WINERcost'18

&

Aeolus4future

FINAL CONFERENCE 2018

"Wind Energy Harvesting...
(...focusing on exploitation of the Mediterranean Area)"

Catanzaro, Italy
21-23 March 2018

Chairs: Charalampos Baniotopoulos, Claudio Borri & Enzo Marino

EDITORS

- **BANIOTOPOULOS C.** (Action & Conference Chair)
- **BORRI C.** (Action Vice Chair & Conference Chair)
- **MARINO E.** (Conference Vice-Chair)
- **BLOCKEN B.** (WG1 Chair)
- **HEMIDA H.** (WG1 Vice-Chair)
- **VELJKOVIC M.** (WG2 Chair)
- **MORBIATO T.** (WG2 Vice-Chair)
- **BORG R.** (WG3 Chair)
- **HAMZA N.** (WG3 Vice-Chair)

March 21-23 2018, Catanzaro Lido, Italy

SCIENTIFIC COMMITTEE

CHAIR: LUGNI C. (Italy) // **ALTERMAN R.** (Israel) // **ARAN J.** (Spain) // **BAKER C.** (UK) // **BAKON T.** (Poland) // **BARD D.** (Sweden) // **BARTOLI G.** (Italy) // **BLOK R.** (Netherlands) // **SERRI L.** (Italy) // **BORELLO D.** (Italy) // **CHAUDHARI A.** (Finland) // **CUNDEVA S.** (FYR Macedonia) // **EFSTATHIADES C.** (Cyprus) // **EFTHYMIOU E.** (Greece) // **TRICOLI P.** (UK) // **BIAGINI P.** (Italy) // **TUNESKY A.** (MK) // **GENC M.S.** (Turkey) // **GLUMAC A.** (Serbia) // **HADJIMITSIS D.** (Cyprus) // **HÖFFER R.** (Germany) // **HOZJAN T.** (Slovenia) // **HUBER S.** (Switzerland) // **HUBOVA O.** (Slovakia) // **JOFFRE S**. (Finland) // **KONECNA L.** (Slovakia) // **LAGERQVIST O.** (Sweden) // **LETTMAYER G.** (Austria) // **MARCIUKAITIS M.** (Lithuania) // **MARKOVIC Z.** (Serbia) // **MOLNAR I.** (Hungary) // **MONTAZERI H.** (Belgium) // **MURPHY P.** (Ireland) // **NETUSIL M.** (Czech Republic) // **NORTON C.** (Ireland) // **PIRES NEVES L.** (Portugal) // **POLAK A.** (Croatia) // **RAM B.** (Denmark) // **REBELO C.** (Portugal) // **REVELL A.** (UK) // **REVHEIM P.P.** (Norway) // **RICCI A.** (Netherlands) // **SCHAUMANN P.** (Germany) // **SEMPREVIVA A.M.** (Denmark) // **SEVERINI L.** (Italy) // **SHIFF G.** (Israel) // **SOKOLOV A.** (Lithuania) // **SPIESS H.** (Switzerland) // **SPITERI STAINES C.** (Malta) // **SRSEN A.** (Croatia) // **STAROSTA K.** (Poland) // **STATHOPOULOS T.** (Canada) // **STAVROULAKIS G.** (Greece) // **STERLING M.** (UK) // **SZLIVKA F.** (Hungary) // **TAMURA Y.** (Japan) // **THOMASSEN P.** (Norway) // **TODOROVIC J.** (Bosnia and Herzegovina) // **TOMLIN A.** (UK) // **UZOL O.** (Turkey) // **VAN BEECK J.** (Belgium) // **VAN HOOFF T.** (Belgium) // **VANDEVELDE L.** (Belgium).

STEERING COMMITTEE

- **BANIOTOPOULOS C.** (UK)
- **BLOCKEN B.** (Netherlands)
- **BORG R.** (Malta)
- **BORRI C.** (Italy)
- **HEMIDA H.** (UK)
- **HÖFFER R.** (Germany)
- **HAMZA N.** (UK)
- **MARINO E.** (Italy)
- **MORBIATO T.** (Italy)
- **VELJKOVIC M.** (Netherlands)

ORGANISING COMMITTEE

BARBANTI G. (Italy) // **VITA G.** (UK) // **VIGLIANTI D.** (Italy) // **MACRÌ P.** (Italy)

SUPPORT OF

http://www.cost.eu/COST_Actions/tud/TU1304

http://www.aeolus4future.eu/

https://www.ingegneria.unifi.it/

https://www.birmingham.ac.uk/schools/engineering/

PATRONAGE OF

http://www.comunecatanzaro.it/

http://ciro.asmenet.it/

http://www.archicz.it/

http://www.criaciv.com/

http://studioseverini.eu

SPONSOR

http://www.gruppomazzei.it/

TABLE OF CONTENTS

WINERcost '18

&

Aeolus future

FINAL CONFERENCE 2018

"Wind Energy Harvesting...
(...focusing on exploitation of the Mediterranean Area)"

Catanzaro, Italy
21-23 March 2018


Morandi Bridge


The Quarryman


Catanzaro


Catanzaro Lido


Isola di Capo Rizzuto


Cirò

FOREWORD

C. Borri, C.C. Baniotopoulos & E. Marino

Conference Chairs, WINERCOST'18 Conference

As widely known, wind represents the second largest, i.e. second most important, source of energy power in Europe. Moving forward, its importance will even increase, as it is made evident by the actions of some most influential political/economical leaders worldwide.

Looking to last years' development, one can surely affirm that Europe focuses on wind energy generation: in 2016 wind energy alone contributed to over 50% of the new installed electric power, with 12,5 GW of new wind turbines (less than 11 GW on-shore, more than 1,5 GW off-shore). According to the report of Wind Europe, in 2016 wind energy has attracted 27 Billion Euro investments of which about 18 Billion offshore. With a total installed of 154 GW, wind energy becomes the second largest source of electrical power generation in Europe, after natural gas and before coal. Now with the increase in land price, the environmental issues related to onshore wind farms, the great offshore-wind resources is evidently clear that offshore technology has the greatest potential. This is also evidenced by the largest share of investments in offshore wind technology in 2016 (over 18 Billion Euro), with a jump of growth of 39% with respect to the previous year.

It is expected this growth to continue in the coming years as, according to accredited estimates, offshore wind energy has the potential to cover the entire European electrical demand. The trend is evident: thanks to the farms in the final commissioning phase, one shall reach soon 16 GW worldwide, while the forecast for 2020 exceeds yet the 24 GW, therefore doubling the capacity (worldwide) within only 4 years. The true key of this trend is the rotor capacity, which has yet reached 8 MW each (s. the WTs installed off the Thames estuary): thanks to such large rotors (diameter: 160m; tower height: about 140m), that cannot certainly be installed onshore, the efficiency of offshore wind farms increases enormously.

The most recently published report of WindEurope (Sept. 2017), describes three possible scenarios (low, central and high) for wind energy capacity installations in 2030 based on Wind Europe's analysis of the potential conditions determining wind energy deployment post-2020. The report considers the central scenario as the most likely, i.e. *"323 GW of cumulative wind energy capacity would be installed in the EU by 2030, 253 GW onshore and 70 GW offshore. That would be more than double the capacity installed at the end of 2016 (160 GW). With this capacity, wind energy would produce 888 TWh of electricity, equivalent to 30% of the EU's power demand. The wind energy industry would invest €239 bn by 2030 and provide*

employment to 569,000 people". Therefore, offshore wind energy becomes more and more competitive on the market against onshore.

All above facts, evidences and figures gave the motivation for dedicating the second and last (Final) Conference of the COST TU1304 action on "Wind energy technology reconsideration to enhance the concept of smart cities" (WINERCOST'18) to offshore wind energy in Southern European seas, i.e. focusing on exploitation of the Mediterranean area. Due to the relevance of this issue for the trends of the European research training programmes, the supervisory board of the project H2020-MSCA-ITN-AEOLUS4FUTURE (2015-2018) has decided to join the promotion of the WINERCOST'18 Conference as its Final discussion forum and dissemination event.

Therefore the programme has been arranged by providing two full days of scientific presentations (6 keynote lectures, 4 plenary technical sessions, 4 parallel sessions) with a 1-day break (2nd day) entirely dedicated to a technical excursion to recently built, large wind farms in Cirò, Crotone/Scandale and Isola Capo Rizzuto. The excursion will especially focus on the technical challenges of building wind farms in mountainous or coastal regions. The unexploited potential of wind energy production will be treated and discussed within the first Keynote lecture, while socio-economic aspects (society acceptance) as well as other rather technical challenges will be faced within Keynote lectures 3, 4 and 5. Amongst the highlights, Keynote lecture 2 will be dedicated to the 10-years long process for authorizing and designing the first offshore wind farm in the Mediterranean (bay of Taranto, South Italy), now eventually under construction. Eventually, Keynote lecture 6 will deal with a promising future technology of energy harvesting, which is not recurring to classical wind turbines.

The AEOLUS4FUTURE community, and especially the research trainees, will have the chance of presenting the results of their (14) PhD Theses, which will be delivered and defended in 2019/'20: the conference will give them a unique chance of receiving comments and useful suggestions for their final work.

Acknowledgements

The Conference Chairs of WINERCOST'18 wish to gratefully acknowledge the contribution of the staff of the Local Organising Support in Catanzaro, Mrs Daniela Viglianti, Arch. G. Macrì, Arch. A. Renda e Mr. D. Schiavello, as well as the scientific support to the coordination team given by G. Barbanti, Florence, and G. Vita, Birmingham.

Last but not least, the logistic supports of the City of Catanzaro, City of Cirò, NOVENERGIA Italia, (Rome, Dr. M. Calzecchi, Eng. A. Del Vecchio) and the sponsorship of Gruppo Mazzei (Mr. G. Mazzei) are gratefully recognised.

KEYNOTE LECTURES

KL1 *Offshore Wind Energy harvesting in Mediterranean area: turning challenges into opportunities*

KL2 *Getting achieved the first offshore wind farm in the Mediterranean sea*

KL3 *Foundation design issues of inshore high power turbines in complex geological sites of Calabria*

KL4 *Towards energy prosuming cities*

KL5 *Measurement-based optimization of structures for renewable energy production*

KL6 *Harvesting energy from fluttering structures*

OFFSHORE WIND ENERGY HARVESTING IN MEDITERRANEAN AREA: TURNING CHALLENGES INTO OPPORTUNITIES

L. Serri[1]*

[1]RSE S.p.A., via Rubattino, 54, Milano, Italy
*Corresponding author: Laura Serri, laura.serri@rse-web.it

ABSTRACT

Offshore wind energy is at present a well-developed sector especially in the Northern European countries. The Mediterranean basin has very different characteristics from the North Europe, where many offshore wind farms are installed. Many different countries face the basin, with very different and generally not coordinated energy policies and regulations. The wind resource is generally lower and the water is generally deeper than in the North Sea. The basin is also crowded with traditional and emerging offshore activities. However, a strong experience and many infrastructures for the offshore installations are present and, in a medium long term, the offshore wind energy sector – mainly based on floating technology- could revitalise the economy of the region starting from the role of ports and shipyards, with a significant number of local job created. Some dedicated tools and projects results to support the development of offshore wind sector in the Mediterranean area are reported. Moreover, in order to decrease the possible conflicts, combinations with other beneficial offshore activities are considered.

1. INTRODUCTION

The 2015 United Nations Climate Change Conference, COP 21, confirmed the importance of the reduction of climate change. A global agreement was signed by a large number of countries to pursue efforts to limit the temperature increase limiting the greenhouse gas emissions [1]. The process undertaken to reach this goal passes through the so called "decarbonisation" of all the economy sectors. At global level, an important contribution to the greenhouse emissions is still ascribable to the electricity sector, even if many efforts have been globally done in this sector since the last decade of the 19th century.

In particular, the European Commission strongly fostered this process with the so called 20-20-20 directive- and subsequent ones [2][3], which, among the others, forced the production of the electricity from renewable sources. At a European level, the main renewable electricity production comes from the already existing big hydropower plants (in Italy as well as in the many Northern countries), and from photovoltaic and wind power plants installed in the last 20 years. In particular, concerning the wind energy, a very important growing rate can be observed in Figure 1, mainly due to the European technological leadership in this sector and to the favourable wind regimes, especially in the North Europe. The Northern European countries are also pioneers (Denmark) and leaders (UK and Germany) in the field of offshore energy.

According to WindEurope[1]'s Central Scenario [5],"323 GW of cumulative wind energy capacity would be installed in the Europe by 2030, 253 GW onshore and 70 GW offshore. That would be more than double the capacity installed at the end of 2016 (160 GW). With this capacity, wind energy would produce 888 TWh of electricity, equivalent to 30% of the Europe's power demand. In this scenario, the wind energy industry would invest €239 bn by 2030 and provide employment to 569,000 people".
Concerning offshore wind, in this scenario, only 0,5 GW of offshore wind capacity is expected to be installed in the Mediterranean basin, still remaining a secondary market in 2030.

[1] European Wind Energy Association

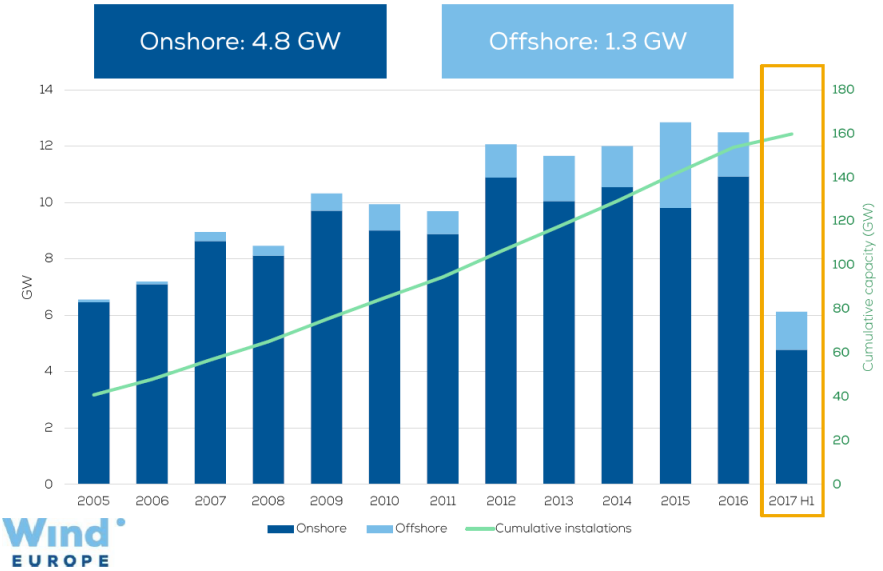

Figure 1. Annual wind capacity installation [4].

In the present paper, the author aims to discuss the possibility of the future development of the offshore wind sector in the Mediterranean area. First, a quick overall view to the offshore wind energy sector in terms of resources, technology, costs, infrastructure, installed capacity and barriers is reported (Chapter 2). Then a focus is done on the Mediterranean basin peculiarities, which can be considered responsible for the delay of the wind energy deployment (Chapter 3). Examples of information and tools, such as WebGIS -Geographical Information System freely accessible from the web, especially developed for the support to RD&D of offshore wind energy sector in Italy and in the overall Mediterranean basin are also reported in the same Chapter. In Chapter 4 some visions for the future deployment of offshore wind energy in the Mediterranean area, based on results of research projects and studies, are suggested with the aim to overcome barriers due to environmental, social and political peculiarities of this offshore area.

2. THE OVERALL CONTEST

2.1. Why offshore wind energy?

Due to the very high growth of onland wind energy installations in the last decades, in many countries there is a significant reduction of onland virgin areas suitable for further new wind energy development: sites with high and good wind resource have been already deployed as well as sites with easy access or mild climate. Moreover in some regions, the lack of social acceptance is growing [6]. In the Northern countries there a significant offshore wind resource – generally higher and less turbulent than the onland one– in combination with shallow waters and sandy sea bottom, conditions that make the installation of offshore wind farms technologically, environmental and economically sustainable.

The offshore wind turbines have become specialised for the offshore environment, with very big and increasing size (i.e. MHI Vestas V164 9.5MW and Siemens-Gamesa Renewable Energy SWT-8.0-154) and some European wind turbine manufacturers (Siemens, Vestas) are the global leaders in the this market. However, the offshore wind projects are more expensive than the onland ones. The wind turbine cost represents 50% of the capital costs of an offshore wind energy project, the remaining costs constituting a market for the manufacturers of the foundations as well as for the offshore installers and operation and maintenance operators. Among the others, the ship industry and the ports can be revitalised by the offshore wind installations, as can be seen in the UK offshore wind energy programs [7][8]. For these reasons many countries started to put in place measures to support this kind of installations, even if a reduction of the overall costs in this sector is required and expected in the next ten-twenty years.

2.1. State of the art of the technology

As already mentioned, the technology of the offshore wind energy is still developing, however some distinctions have to be made. The main difference between the onshore and the offshore technology is the kind of foundations, In the latter case, foundations are structures able to keep the wind turbine anchored to the see bottom and to sustain the huge loads due to the very big wind turbine rotor diameters. There are many different kind of foundations already known and used in the offshore Oil&Gas sector [9]. However, in the case of offshore wind sector, the limited revenues coming from the electricity selling, reduce the affordable costs and consequently the available solutions. In the shallow waters (sea depth lower than 30 m, the most of the actual installed offshore wind foundations) monopile foundations are used. In the transitional waters (sea depth between 30 and 50-60 m) jacket foundations are used and in deep waters (sea depth greater than 60 m) floating structures are expected to be used. The first two types are fixed foundations and these technologies can be considered mature or close to maturity. The floating offshore wind technology is still in the prototypal/demonstration stage [10] [11] [12] [13]with no consensus on the best configuration - see the different trend for Technology Readiness Level [14] for four different floating platform configurations, Figure 2.

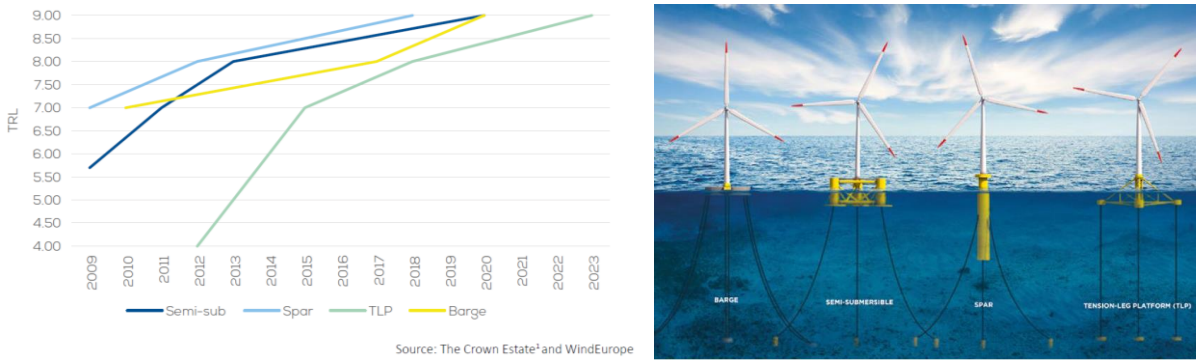

Figure 2. Trend for Tecnology Readiness Level evolution (left) for four different floating platform configurations (rigth) [15].

A mention has to be done to the first small size demonstration of floating wind turbine performed by BlueH in 2008 in the Mediterranean Sea close to the Apulian Region [16].

A strong potential is seen in the medium-long term scenario for the floating offshore wind, primarily in the Mediterranean Sea, where generally the waters become quickly deep moving from the coast, but also in many European (i.e. Portugal, Norway, Canaries) and worldwide offshore areas (i.e. in USA and Japan).

2.2. Wind resource

The offshore wind energy assessment is very important to understand the suitable sites for profiting offshore wind installation. Many efforts have been done to produce more and more precise offshore wind maps and Atlas [17]. However, the lack of distributed and long term offshore wind measurements at hub height leaves a quite high level of uncertainty on these maps. In order to partially overcome this, the New European Wind Atlas -European funded project is ongoing[18]. The New European Wind Atlas will involve the development of new dynamical downscaling methodologies as well as improvements and extensions of the models involved with high temporal and spatial resolution. The new Atlas will provide a unified high resolution and freely available data-set of wind energy resources in Europe. The statistics in the atlas will cover Europe with a resolution 20-30 meters in at least 10 wind turbine relevant heights. The area coverage is the European countries and 100 km offshore plus the Baltic and the North Sea.

The information on the offshore wind resource itself is not enough to determine the viability of an offshore wind project that depends on the overall costs of the produced electricity. On one side, WindEurope analysed and reported the offshore wind load factors2 in the five largest offshore wind markets in 2016 (Belgium, Denmark, Germany, Netherlands, UK). The annual load factors of offshore wind in these countries range from 33.1%-42.9%. The highest monthly load factor was in the UK in December 2016, with a value of 68.2% [19].

On the other side, WindEurope recently published a report –in collaboration with BVG Associates and Geospatial Enterprises, that highlights the economically attractive offshore wind resource that is potentially available to Europe in three sea basins (the Baltic, North Sea and Atlantic from France to the north of the UK) in 2030. The study is based on the determination of the Levelised Cost of Energy (LCoE) in the considered basin, identifying the location of the lowest cost resource [20].

2.3. Installed offshore wind capacity and grid

According to GWEC[3], at the end of 2016 14,384 MW of offshore wind power capacity was installed worldwide. Nearly 88% of this capacity is located off the coast of ten European countries, the remaining is located largely in China, followed by Japan, South Korea and US.

In the first half of 2017, 1244 MW were installed in four European countries: Germany (48%), UK (38%), Belgium (12%) and Finland (2%).

The strong deployment of the North Sea offshore wind energy has been enabled also by many projects and initiatives aimed to develop a reinforced offshore grid. For example in order to achieve the renewable targets up to 2020, the North Seas Countries' Offshore Grid initiative (NSCOGI) was formed as the responsible body to evaluate and facilitate coordinated development of a possible offshore grid that maximises the efficient and economic use of those renewable sources and infrastructure investments [21].

2.4. Opportunities and barriers

As already mentioned, at European level there is a strong expected offshore wind power capacity growth within 2030 (99 GW in the High Scenario [5]) and beyond.

This development and diffusion has been and will be shaped by the barriers of cost, project risk and complexity, capital requirements, and multi-disciplinarity [22].

Moreover, in many countries/regions there are still barriers concerning the permitting processes, the uncertainty of the incentive mechanism and sector policies, conflicts with others sea uses (ref) and lack of acceptance.

Concerning costs, however, the current and future offshore wind energy market can be seen as a big opportunity. According to WindEurope "New investments in offshore wind in Europe continued to grow strongly during 2016. Eleven projects reached the Final Investment Decision (FID) in 2016, with a combined investment value of 18.2bn. […]. In total, 4.9 GW of new capacity was financed across five countries" [19] for an average capital costs of slightly less than 3,7 M€/MW.

Starting from now, many costs reduction scenarios have been developed. i.e. IEA[4] and IRENA[5] calculated a range of LCoE respectively between 90-180 and 100-190 US$/MWh respectively by 2025 [22].

In fig 3 a median LCoE long term cost reduction scenario for the wind energy is reported. It's interesting to see that for the IEA expert group, the main reduction will be for the floating offshore wind

[2] Load factor is the unitless ratio of an actual electrical energy output over a year to the maximum possible electrical energy output over the same amount of time

[3] Global Wind Energy Counci

[4] International Energy Agency

[5] International Renewable Energy Agency

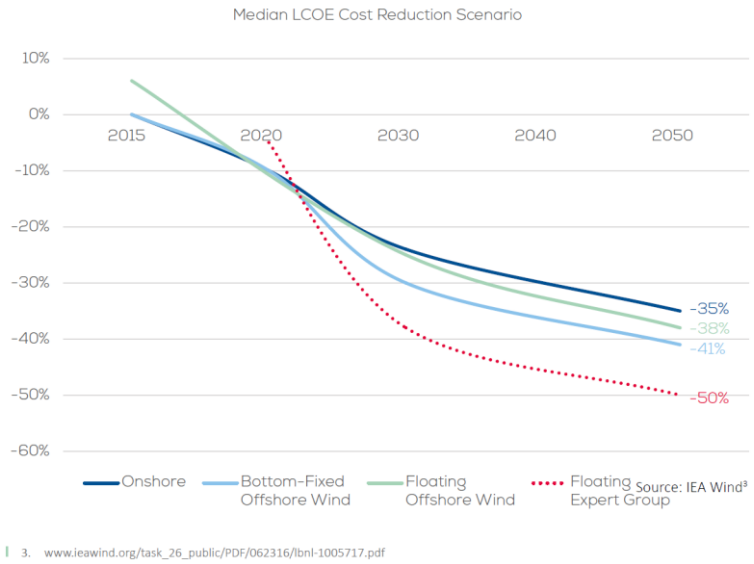

Figure 3. Long term cost reduction scenario for different wind energy technology [15].

Most of the current studies on cost reduction are based on the evaluation of LCoE. This parameter has to be compared with the price of the electricity selling nowadays considered fixed for the whole plant lifetime as in the most of the current energy sales agreements. However, in a long term scenarios, the electricity sales prices could be variable during the plant lifetime depending also on the ancillary services that each wind farm will be able to offer to the grid contributing to its regulation.

3. OFFSHORE WIND IN THE MEDITERRANEAN AREA

3.1. Peculiarities

The Mediterranean area has many peculiarities concerning the offshore wind energy deployment respect to the North Sea area, very well described in the recent review by Soukissian et al. [23].

First of all, more than twenty countries from three continents face the Mediterranean Basin. A minor part of them belongs to the European Community with an already significant production of electricity from renewable sources. The remaining ones have very different energy demand, supply and strategy and very different economies. On one side, a high political instability characterises the Middle East and North Africa countries. On the other side, a great increase in electricity demand is expected in these countries [24][25].

The grid interconnections among the countries are at different stage of development, however ……

In spite of these great dissimilarities, renewable generation – in particular PV and wind generation- could be suitable for the power supply of isolated communities such as the great number of small islands present in the basin or the distant North African rural communities.

The offshore wind resource in the Mediterranean area has been studied for many years [24][26][27][28][29], however the almost total absence of direct long term measurements still leaves a high degree of uncertainty. In general, the average wind speed and consequently the load factor) are lower than in the North Sea at the same levels. The most windy areas are the Lion Gulf and the Eastern part of the Aegean Sea.

In most of the Mediterranean basin, the sea depth becomes quickly considerable even at few kilometres from the coast. Most of the offshore wind potential is expected to be deployed with offshore wind floating systems [30]. The shallow waters of the Adriatic Sea correspond in general to a fair wind resource.

Lower wind resource and deep waters make the offshore wind deployment in this area currently less economically attractive than in the North Sea.

From the environmental point of view the impacts on the species are very different than in other Seas and Oceans due to the specific sensitive species and habitat that characterises the Mediterranean basin, i.e. the protected Posidonia beds [31]. There is a growing need to assess the biological costs and benefits of the offshore wind farm installation in the region. An approach for the evaluation of the potential effects on birds, marine mammals, fish and benthic communities can be found in [25].

The Mediterranean basin is also crowded with a number of already existing offshore activities: transport, fishery, aquaculture and fish farming, Oil&Gas extraction, military use, tourism. The installation of offshore wind farms requires a quite large amount of room and could be in conflict with the other sea uses.

The strong tourist vocation of most of the coastal areas facing the basin and the sea value perception from the Southern Europe population tend to decrease the acceptance of offshore wind farms [32] and offshore structures in general.

However, many countries facing the Mediterranean basin have strong offshore industries, modern and big ports and shipyards. In other words they already have the experience and expertise to successfully afford the offshore wind farm installation, operation and maintenance creating a not negligible number of local jobs in the sector.

3.2. Research Projects and Support Tools

As described in the previous Paragraph, the offshore wind deployment in the Mediterranean Sea will likely occur if the numerous unique aspects will be taken into proper account and if dedicated policies will be put in place. For this reason, some tools have been developed in different national and European projects to support the decision makers.

In the following, the author presents three different approaches, one at national level (Italy) and two at European level.

RSE, the author's organisation, developed in 2007 the offshore maps of the Wind Atlas of Italy [33],

ATLAEOLICO is a WebGIS application with the standard function of navigation [34]. The offshore maps cover a buffer of 40 km off the coastline at four different levels (25, 50, 75 and100 m a.s.l.). The spatial resolution is 1 square km. The annual mean wind speed map at 75 m a.s.l. is shown in Figure 4. A calculation tools allows the user to simulate the installation of an offshore wind farm choosing a site on the map and to make a technical-economic evaluation of the wind farm performances.

Starting from the maps of ATLAEOLICO a more complex WebGIS tool for the coastal and marine special planning, named TRITONE, has been built [35]. Thanks to this tool the user can also see maps concerning the wave and marine current resources and overlap other environmental and socio-economic information such as distance from shore lines (5, 10, 20, 40 km), bathymetry, seabed composition, Tsunami catalogue, MPA information, Posidonia beds presence, use of the coastal areas, use of the sea, touristic indicators, ports characteristics and routes. On the basis of this information, the offshore wind energy feasible potential of Italy within 40 km off the coast has been evaluated to be around 10.5 GW (2.5 GW for fixed foundation technology and 8 GW for floating platforms) [36].

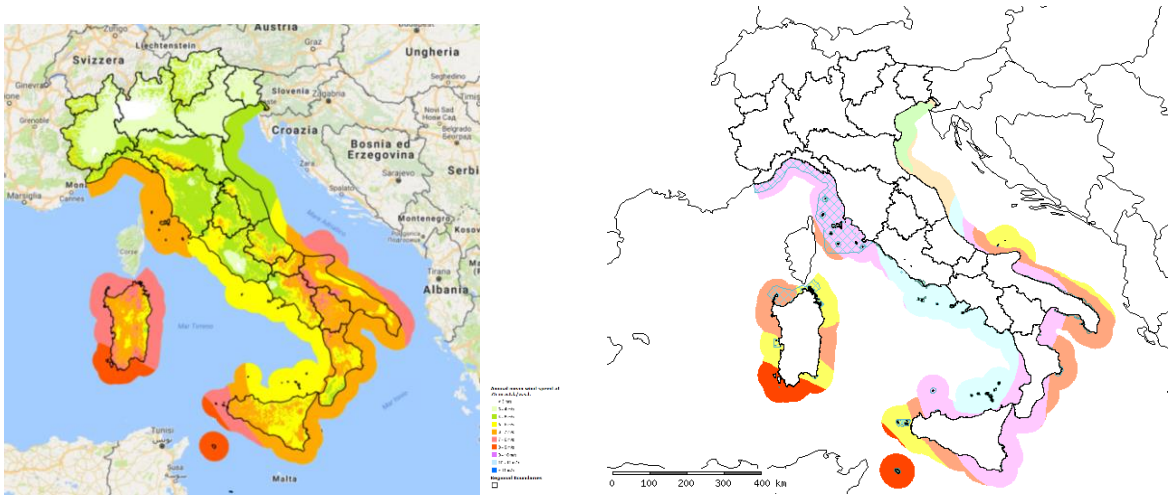

Figure 4. ATLAEOLICO annual mean wind speed map at 75 m a.s.l. (right) and TRITONE specific annual energy production maps at 75 m a.s.l. with information concerning MPA and marine mammals sanctuary area (rigth).

The European funded ORECCA project [37], ended in 2011, was aimed to stimulate collaboration in research activities leading towards innovative, cost efficient and environmentally benign offshore renewable energy conversion platforms for wind, wave and other ocean energy resources, for their combined use as well as for their complementary use such as in aquaculture e.g. biomass and fishes and monitoring of the sea environment e.g. marine mammals, fish and bird life. It was one of the first approach considering the achievement of a cost reduction in the development of offshore renewables sharing the platform and other infrastructure – i.e. the connection to the grid, the installation ship – among different renewable energy converters and/or sharing the area with other offshore activities. ORECCA was also one of the first European project including also the Mediterranean and Black Sea area. One of the outputs of ORECCA was a WebGIS tool, still accessible [38], in which single and combined offshore information about renewable resources (wind, wave and tidal) can be found. An example of ORECCA WebGIS output is shown in Figure 5, that is the annual mean wind speed map at 10 m a.s.l. and combined wind and wave resource maps in the Mediterranean area.

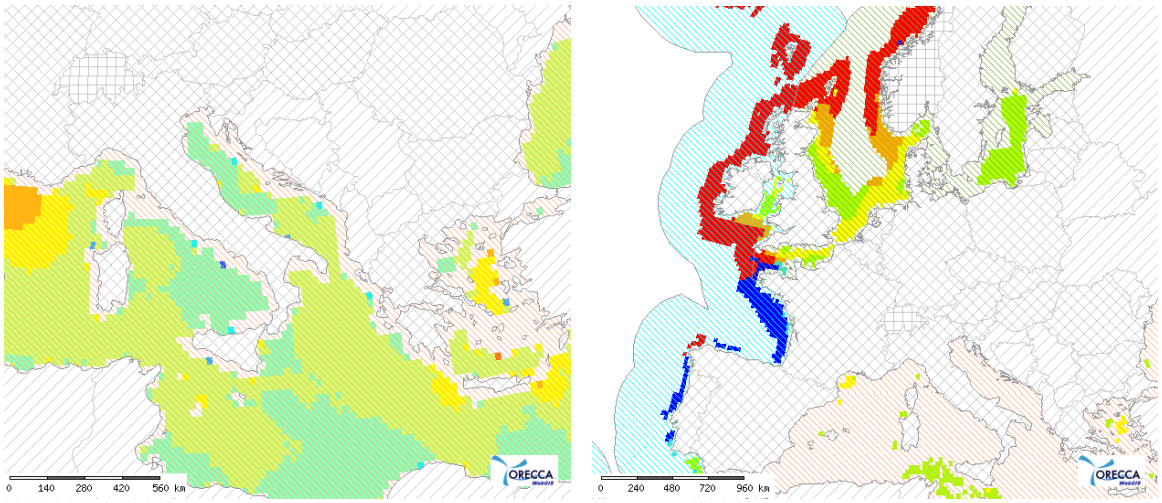

Figure 5. ORECCA WebGIS: annual mean wind speed map at 10 m a.s.l and combined wind and wave resource maps (rigth).

The European funded COCONET project [40], ended in 2016, was dedicated to the Mediterranean area. In particular, COCONET identified groups of putatively interconnected MPAs in the Mediterranean and the Black Seas, shifting from local (single MPA) to regional (Networks of MPAs) and basin (network

of networks) scales. The coastal focus is widened to off shore and deep sea habitats, including them in MPAs Networks. COCONET also individuated areas where offshore wind farms might be installed, avoiding too sensitive habitats but acting as stepping stones through MPAs.

One of the outputs of the project was a Smart Wind Chart, shown in Figure 6, in which the offshore Mediterranean and Black Sea area were classified and scored for the future offshore wind farm installation taking into account the sensitive habitat.

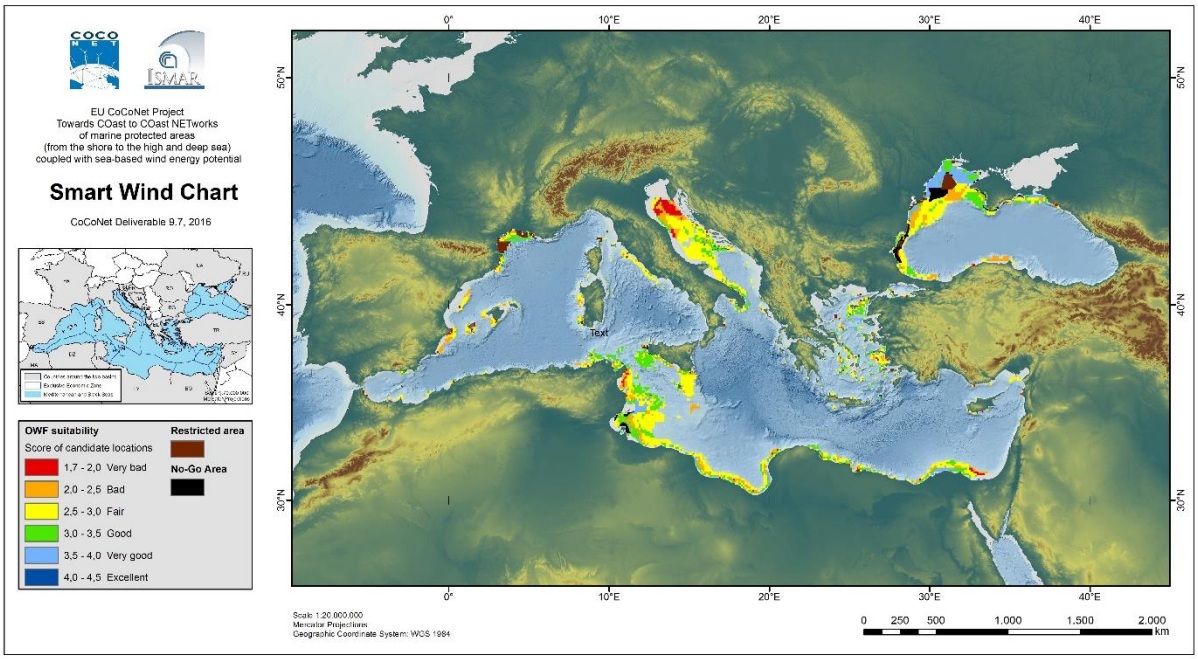

Figure 6. COCONET Smart Wind Chart [41].

3.3. Offshore Mediterranean Wind Farms projects

Another important issue that can speed up the deployment of offshore wind in the Mediterranean area is the presence of offshore wind demonstrator at sea. After the 2008 short campaign [16], no more demonstrator (both for fixed and floating technology) has been installed yet.

Many wind farm projects have started the authorization process, at least in Italy, but they were all rejected even if an incentive tariff for offshore wind electricity production was and is still present in the Italian incentive mechanism. Only one offshore wind farm project on fixed foundations (monopiles) has been authorised. The wind farm, with a total rated power of 30 MW (ten Senvion 3 MW wind turbine with 100 m hub height), will be located in front of Taranto harbour in the Apulian region. The installation of the first turbines is planned for the summer 2018 [41].

The French Environment and Energy Management Agency (ADEME) has approved three floating wind pilot projects in the Mediterranean, one in Gruissan area, another in Faraman area and the last one off Leucate [42][43]. The project winners will install floating systems with different configurations of the floater, all mounting a three blade horizontal axis multi-megawatt wind turbine [44].

To the author's knowledge the four above mentioned offshore wind farm projects are the only authorised projects in the Mediterranean basin.

4. TURNING CHALLENGES INTO OPPORTUNITIES

The offshore wind energy in the Mediterranean area is expected to be deployed in a medium-long term scenario. In this area, the cost reduction is one of the main challenge for creating a significant and affordable market.

From a technological point of view, concerning the wind turbines, dedicated models could be designed and manufactured in order to better exploit the low speed winds characterising the Mediterranean wind. As happened for the photovoltaic sector, some wind turbine manufacturers from Eastern countries will be probably able to supply reliable offshore wind turbines with an expected cost reduction of 30 % respect to the Western competitors -even if the transport is still a challenge. In example, in 2016, China manufactured and installed more than 11000 wind turbines, around 150 offshore [45] [46]. When the Chinese onland wind energy market starts to saturate, the offshore market will grow both for domestic use and for exportation.

Concerning the platforms, most of the offshore wind farms will be floating. According to Figure 3, a significant cost reduction will be achieved when this technology becomes mature. The advantages of the floating technology are: less complicate and cheaper installation, no big dedicated ships are needed –the floating systems can be assembled in a port and towed to the installation site by tug boats. Less environmental impacts both in the installation phase -no noise due to the use of big hammer to fix the monopiles and in the operating phase. In fact these systems are installed in waters depth greater than 50 m [23]. Most of the biodiversity in the Mediterranean is in water with depth lower than 30 m. Floating system can be installed far from the coast reducing the visual impact. “Multipurpose” platforms hosting different offshore renewable conversion devices (wind-waves, wind-marine currents) can be considered too [47]. The Mediterranean ports and shipyards could be revitalised by these offshore activities.

Offshore wind energy could represent a significant contribute in the new energy mix (renewables, diesel generation and storage systems) for the the small islands power supply [48][49][50]. In many of these islands, characterised by strong touristic vocation, the onland wind farm installation has very strong impacts if compared with the offshore installation. A (micro) smart grid will be able to properly address the demand, lowering the costs and the carbon footprint with respect to the traditional diesel generation. The excess of renewable generation due to the fluctuating wind and solar resources can be stored, but also employed in other activities, i.e. desalinisation [51], electric vehicles battery recharge [52], hydrogen production [53]. In the same way, wind energy can also contribute to the power supply of the offshore Oil&Gas extraction platforms [54][55]. Considering that the average Mediterranean Oil&Gas platforms energy demand is generally very low, most of electricity produced by the offshore wind farms will be sent to the grid. However the renewable power supply of the Oil&Gas platforms is greener than the present diesel/gas generation, the co-location of different offshore installations in the same marine area reduces the global visual impact and a joint management of the two activities can optimise the operation and maintenance costs. All these issues are expected to increase the public acceptance of the offshore infrastructures.

The co-location or “multi-use” can be also applied to other offshore activities [56]. The co-location of offshore wind farms and aquaculture and fish farms seems one of the most promising in the Mediterranean area due to the activities requirements and to the expected reduction of the conflicts with the very numerous local fishery communities [57][23]. This could also mitigate the fishing crisis due to the overfishing in the basin. “Over 90% of the fish stocks assessed are over-exploited, and despite recent efforts the situation is not improving. Managing fish stocks is complicated by the fact that many of them are shared with non-European countries.” [58]. New offshore cultivation of algae for food, biomass and biofuel (algae farms) seem to be suitable for the combination with offshore wind farm too [59][60]. The offshore wind farms can be combined with environmental monitoring and can act as a driver for the repopulation/protection of some species, for example with specially designed artificial reef in their foundations [40][56].

A positive impact on the tourism can also be seen when a consistent environmental policy and wind farm associated recreational activities are properly addressed and managed [61].

In January 2015 RSE designed, implemented and launched an e-survey to 90 selected industrial organizations to understand the main challenges and barriers for the offshore wind farm development in Italy [62]. The main obstacles perceived by the responders are: the absence of clear and fast authorization processes, the possible conflicts among different levels of authority, the absence of clear and complete legislation and the lack of relevant incentives and of political support to the specific industrial sector. The technology is perceived as mature by most of the responders. The wind resource, the presence of infrastructure, including the power grid and the interaction with other marine and maritime activities are perceived as adequate. In spite of the absence of offshore wind farms in Italy, a prudent optimism has been registered by a not negligible number of responders interested in the field.

A Roadmap for marine renewable energy (including offshore wind) sustainable development in the Mediterranean Sea is presented in [23]. This Roadmap contains technical, environmental and socio-economics recommendations.

5. CONCLUSIONS

In a medium long term scenario a significant offshore wind energy exploitation can be expected in the Mediterranean area mainly using floating offshore wind turbines.

The main drivers are: to establish stable long term sector policies able to provide clear and proper regulations and support mechanisms, to prove the floating offshore wind technology, to reach an adequate cost reduction, to increase the acceptance by rising the environmental awareness of the local communities. Due to the intensive use of the Mediterranean Sea the combination of offshore wind farm installation with other economic activities could be advantageous.

A deeper understanding of the peculiarities of this area for the offshore renewable energy deployment is still needed. Under the Blue Growth strategy [63], the European Commission is supporting a number of ongoing research projects (i.e. ODYSSEA [64], MUSES [65], PELAGOS [66]).

The harmonisation of the energy strategies and regulations, the share of knowledge, experience and infrastructures among the countries facing the Mediterranean basin is another important challenge to unlock the significant offshore wind potential. Some lessons learnt from the Northern countries could be taken into account as a starting point.

Last but not least, it is desirable that the scientific community and all the stakeholders would be able to find a common language to profitably communicate with the decision makers in order to harvest the offshore wind energy and bring environmental and socio-economic benefits to all the Mediterranean people.

ACKNOWLEDGEMENTS

This work has been financed by the Research Fund for the Italian Electrical System under the Contract Agreement between RSE SpA and the Italian Ministry of Economic Development – General Directorate for Nuclear Energy, Renewable Energy and Energy Efficiency, in compliance with the Decree of March 8, 2006.

REFERENCES

(Web Sites accessed 31st December 2017)

[1] www.cop21paris.org
[2] https://ec.europa.eu/clima/policies/strategies/2020_en
[3] https://ec.europa.eu/energy/en/topics/energy-strategy-and-energy-union/2030-energy-strategy
[4] WindEurope, Wind Energy Outlook, September 2017.
[5] WindEurope, Wind Energy in Europe: Scenarios for 2030, September 2017.

[6] Kontogianni A., Tourkolias Ch., Skourtos M., Damigos D., "Planning globally, protesting locally: Patterns in community perceptions towards the installation of wind farms", Renewable Energy 66 (2014) 170e177.
[7] The Department for Energy and Climate Change, UK Ports for the Offshore Wind Industry: Time to Act, URN 09/511X 5, February 2009.
[8] WindEurope, A statement from the offshore wind ports, June 2017.
[9] https://www.nrel.gov/docs/fy05osti/38135.pdf
[10] www.statoil.com/en/what-we-do/hywind-where-the-wind-takes-us.html?gclid=EAIaIQobChMIuICX19m52AIVCbcbCh39KgdSEAAYASAAEgJXqPD_BwE
[11] http://www.principlepowerinc.com/en/windfloat
[12] http://www.fukushima-forward.jp/english/
[13] https://www.evwind.es/2017/10/13/floating-offshore-wind-turbine-inaugurated-in-france/61390
[14] https://ec.europa.eu/research/participants/data/ref/h2020/wp/2014_2015/annexes/h2020-wp1415-annex-g-trl_en.pdf
[15] WindEurope, Floating Offshore Wind Vision Statement, June 2017.
[16] https://www.technologyreview.com/s/409834/wind-power-that-floats/
[17] https://openei.org/wiki/European_Wind_Atlas:_Offshore
[18] http://www.vindenergi.dtu.dk/english/research/research-projects/newa
[19] WindEurope, The European offshore wind industry, key trend and statistics 2016, January 2017.
[20] WindEurope, Unleashing Europe's offshore wind potential - A new resource assessment, June 2017.
[21] http://www.benelux.int/nl/kernthemas/holder/energie/nscogi-2012-report/
[22] Dedecca, J.G., Hakvoort R. A., Ortt, J.R., "Market strategies for offshore wind in Europe: A development and diffusion perspective" *Renewable and Sustainable Energy Reviews*, *Volume 66*, December 2016, Pages 286-296
[23] Soukissian T.H., Denaxa D., Karathanasi F., Prospathopoulos A., Sarantakos K., Iona A., Georgantas K., Mavrakos S., "Marine Renewable Energy in the Mediterranean Sea: Status and Perspectives", Energies 2017, 10, 1512
[24] Gaudiosi G., Borri C., "Offshore wind energy in the mediterranean countries", Revue des Energies Renouvelables SMEE'10 Bou Ismail Tipaza (2010) 173 – 188173
[25] Bray L., Reizopoulou S., Voukouvalas E., Soukissian T., Alomar C., Vázquez-Luis M., Deudero S., Attrill M.J., Hall-Spencer J. M., "Expected Effects of OffshoreWind Farms on Mediterranean Marine Life", J. Mar. Sci. Eng. 2016, 4, 18; doi:10.3390/jmse4010018
[26] Lavagnini, A., Sempreviva A. M., Barthelmie R. J., "Estimating Wind Energy Potential Offshore in Mediterranean Areas", Wind Energy, Volume 6, Issue 1 January/March 2003 Pages 23–34
[27] http://www.orecca.eu/c/document_library/get_file?uuid=757326c6-102f-4dd3-8790-916755694103&groupId=10129
[28] http://www.powered-ipa.it/it/il-progetto-powered/
[29] http://cordis.europa.eu/result/rcn/181920_en.html
[30] Zountouridou E.I., Kiokes G.C., Chakalis S., Georgilakis P.S., Hatziargyriou N.D., "Offshore floating wind parks in the deep waters of Mediterranean Sea" Renewable and Sustainable Energy Reviews 51 (2015) 433–448
[31] http://ec.europa.eu/environment/nature/natura2000/management/habitats/pdf/1120_Posidonia_beds.pdf
[32] Westerberg V., Jacobsen J.B., Lifran R., "Offshore wind farms in Southern Europe – Determining tourist preference and social acceptance", Energy Research & Social Science, Volume 10, November 2015, Pages 165-179
[33] Botta G., Casale C., Lembo E., Maran S., Serri L., Stella G., Viani S., "THE ITALIAN WIND ATLAS – STATUS AND PROGRESS", European Wind Energy Conference & Exhibition, Milan, Italy, 7-10 May 2007
[34] http://atlanteeolico.rse-web.it/
[35] http://map.rse-web.it/tritone/map.phtml
[36] Airoldi D., Lembo E., Serri L.,"Italian Offshore Wind Potential Evaluation through GIS Tools and Data" EWEA OFFSHORE 2011, The Netherlands Amsterdam, 29 Nov 1 Dec 2011
[37] http://www.orecca.eu/web/guest;jsessionid=88AE9E39453EE43DB577F413BCDEBC46

[38] http://map.rse-web.it/orecca/map.phtml
[39] http://msp-platform.eu/projects/coconet-towards-coast-coast-networks-marine-protected-areas-shore-high-and-deep-sea
[40] http://coconetgis.ismar.cnr.it/documets/COCONET_SWC.jpg/view
[41] https://www.offshorewind.biz/2017/06/14/senvion-turbines-for-first-offshore-wind-farm-in-the-mediterranean/
[42] https://www.offshorewind.biz/2016/11/04/france-approves-two-floaters-in-the-mediterranean/
[43] https://www.offshorewind.biz/2017/11/23/france-to-put-offshore-and-floating-wind-on-fast-track-in-2018/
[44] IEA WIND TCP 79th ExCO Meeting- France presentation (private communication)
[45] *IEA Wind TCP 2016 Annual Report*, China Country Chapter, September 2017 ISBN 978-0-9905075-6-7
[46] GWEC, "Global Wind Report 2016 – Annual market update"
[47] C. Casale, L. Serri, N. Stolk, I. Yildiz, F. Neumann, M. Cantù, "Synergies, Innovative Designs and Concepts for Multipurpose Use of Conversion Platforms", October 2011, *www.orecca.eu*.
[48] Garofalo E., Gargiulo A., Lembo E., Marazzi R., Rondena E., Moneta D., et al., "Sviluppo delle Fonti Energetiche Rinnovabili nelle Isole minori non interconnesse", RSE 15000371, 2014. Rapporto Ricerca di Sistema
[49] Buhagiar, D. and Sant, T., "Combining Offshore Wind and Thermocline Energy Production: Going Beyond Electrical Generation,European Wind Energy Conference in Barcelona, March 2014."
[50] Boero F., FogliniF., Fraschetti S., Goriup P., Macpherson E., Planes S., Soukissian T., The CoCoNet Consortium, "CoCoNet: TOWARDS COAST TO COAST NETWORKS OF MARINE PROTECTED AREAS (FROM THE SHORE TO THE HIGH AND DEEP SEA), COUPLED WITH SEA-BASED WIND ENERGY POTENTIAL", SCIentific RESearch and Information Technology Ricerca Scientifica e Tecnologie dell'Informazione Vol 6, Supplement (2016), I-II e-ISSN 2239-4303, DOI 10.2423/i22394303v6Sp1
[51] Xiaobin He; Chufu Li; Weidong Gu, "Research on an innovative large-scale offshore wind power seawater desalination system", 5-7 Nov. 2010, DOI: *10.1109/WNWEC.2010.5673305*
[52] Ghofrani M.; Arabali A.; Etezadi-Amoli M., "Electric drive vehicle to grid synergies with large scale wind resources", Power and Energy Society General Meeting, 22-26 July 2012, DOI: 10.1109/PESGM.2012.6345662
[53] http://www.h2ocean-project.eu/
[54] Bertani D., Lembo E., Serri L., Guastella S., Panei L., Terlizzese F., "RENEWABLE POWER SUPPLY OF OFFSHORE OIL&GAS PLANTS IN ITALY: RESOURCE ASSESSMENT AND POWER SUPPLY OPTIMISATION", OSES2016, Malta July 2016
[55] Nikhila Gopal, "Use of Hywind in Oil and Gas Platforms to Reduce CO2 and NOx Gas Emissions" NTNU, July, 2016, https://brage.bibsys.no/xmlui/bitstream/handle/11250/2418691/15940_FULLTEXT.pdf?sequence=1
[56] Lacroix D.and Pioch S., "The multi-use in wind farm projects: more conflicts or a win-win opportunity?" Aquat. Living Resour. 24, 129–135 (2011), DOI: 10.1051/alr/2011135
[57] He W., Yttervik R., Olsen G. P.,Ostvik I., Jimenez C., Impelluso T., Schouten J., Bellotti G., "A case study of multi-use platform: Aquaculture in offshore wind farms", EWEA Offshore 2015 – Copenhagen – 10-12 March 2015
[58] https://ec.europa.eu/fisheries/putting-end-overfishing-mediterranean_en
[59] Papandroulakis N., Thomsen C., Mintenbeck, K., Mayorga P., Hernández-Brito J.J:,"The EU-Project "TROPOS \\", https://epic.awi.de/44350/1/Papandroulakis_etal_2017.pdf
[60] https://www.ecofys.com/en/press/ecofys-launches-trial-module-for-seaweed-cultivation-in-offshore-wind-farm/
[61] Westerberg V., BredahlJacobsen J.,Lifran R., "The case for offshore wind farms, artificial reefs and sustainable tourism in the French Mediterranean",Tourism Management, Volume 34,February 2013, Pages 172-183
[62] Serri L., Lembo E., Vannini C., "-survey on offshore wind energy sector in Italy: results of the first launch", Offshore Wind and other marine renewable Energies in Mediterranean and European Seas- OWEMES 8th Ed.© 2015

[63] COMMUNICATION FROM THE COMMISSION TO THE EUROPEAN PARLIAMENT, THE COUNCIL, THE EUROPEAN ECONOMIC AND SOCIAL COMMITTEE AND THE COMMITTEE OF THE REGIONS Blue Growth opportunities for marine and maritime sustainable growth, COM/2012/0494 final
[64] http://odysseaplatform.eu/
[65] https://muses-project.eu/
[66] https://pelagos.interreg-med.eu/

GETTING ACHIEVED THE FIRST OFFSHORE WIND FARM IN THE MEDITERRANEAN SEA

S. Bray[1], A. Severini[1] and L. Severini[2]*

[1]Nicetechnology s.r.l., Taranto, Italy
[2] iLStudio-Engineering & Consulting Studio, Taranto, Italy
*Corresponding author: L. Severini, manager@studioseverini.eu - windfarm@studioseverini.eu

ABSTRACT

The wind today is used to create clean, inexhaustible, efficient energy without producing polluting emissions into the atmosphere. Today, offshore wind energy represents a highly potential sector for Italy. All the wind resources available in our seas are enormous and will certainly be able to meet a significant part of our electricity needs in a cost-effective way.
This document describes the first Italian offshore wind farm that will be realized in the Mediterranean Sea (Taranto Offshore Wind Farm Project). Attention will be focused on both the bureaucratic and planning process implemented, during a long time period, for the practical realization of this project. The objective is to become pioneers in the national offshore wind sector, opening the way for the Italian growth of this type of technology.

1. INTRODUCTION

Wind energy is the energy of the future, available today. The production of wind energy takes place through the use of advanced and extremely reliable technology, which enables you to efficiently exploit a renewable, always available, natural and clean resource. Wind energy brings benefits to local, national and international economies by supporting the development of local labor, job creation both on the producer / investor side and indirectly through suppliers.

As stated by Anev [1], our Country has produced 16 TWh of energy in 2016, covering 16 million households and environmental benefits.

The benefits of wind energy:

- it does not consume raw materials;
- it does not involve drilling, extraction, refining or construction of oil pipelines;
- it does not emit CO_2 or other greenhouse gases;
- it does not involve variability in energy prices;
- it is technological innovation;
- has significant energy potential;
- it does not produce radioactive waste;
- it does not consume fuels;
- has minimal impact on poultry fauna;
- reduces energy dependency and the importation of raw materials;
- brings benefits to the trade balance;
- the wind is available, natural and clean technological energy.

These estimates, however, refer only to the onshore wind compartment. Currently Italy does not have offshore wind farms. One of the major benefits of offshore wind energy is that it is the largest available wind resource, which results in higher levels of production than onshore plants. However, there have been some design proposals: between 2006 and 2013, 15 design ideas have been presented. No one of them has been approved and just one has received the authorization from local, regional and national institutions after a long and difficult bureaucracy.

This project involves the construction of the first Italian offshore wind farm that will be realized in the port of Taranto (Puglia). It is planned to install ten turbines of 3 MW each with a 100 m hub height. They will be located in front of the port of Taranto where the depths of the seabed is between 4 and 18 meters. Turbines will be divided into two groups: 4 nearest to the quay and 6 further off. The delivery and installation of the machines is currently scheduled for the summer of 2018 while their commissioning should take place in the autumn of the same year.

2. ITALIAN OFFSHORE WIND ENERGY

The benefits of achieving international targets in the offshore wind energy from Italy would result in enormous savings, including in economic terms, resulting from the failure to use fossil fuels and the failure to pay penalties. To achieve this goal, it is necessary, within a legal framework, to provide the necessary tools at national and regional level.

Anev [1] said that offshore wind energy is a highly potential sector for Italy today, unfortunately not yet exploited. Over the years, in order to identify potential sites, we have taken into account, besides some environmental, territorial, landscape constraints, also additional measures of both design and environmental protection.

Depending on the constraints above, it is noted that most of the sites capable of implementation are concentrated along the coasts between Abruzzo and Puglia for a value estimated around 550-650 MW.

Other 300 MW could be distributed between some coastal areas of Sardinia and Sicily, if the proximity constraints to the shores was essentially reduced, since in Sicily and Sardinia the depths of seabed is around 30 meters just a few hundred meters far from the coast. Of the 950 MW considered to be achievable, 375 MW could already be installed by 2020 due to the number of projects already developed but not yet unlocked (which unfortunately is hard to come by).

An overview of the future trends of the offshore wind sector in Italy is presented in Figure 1and Figure 2.

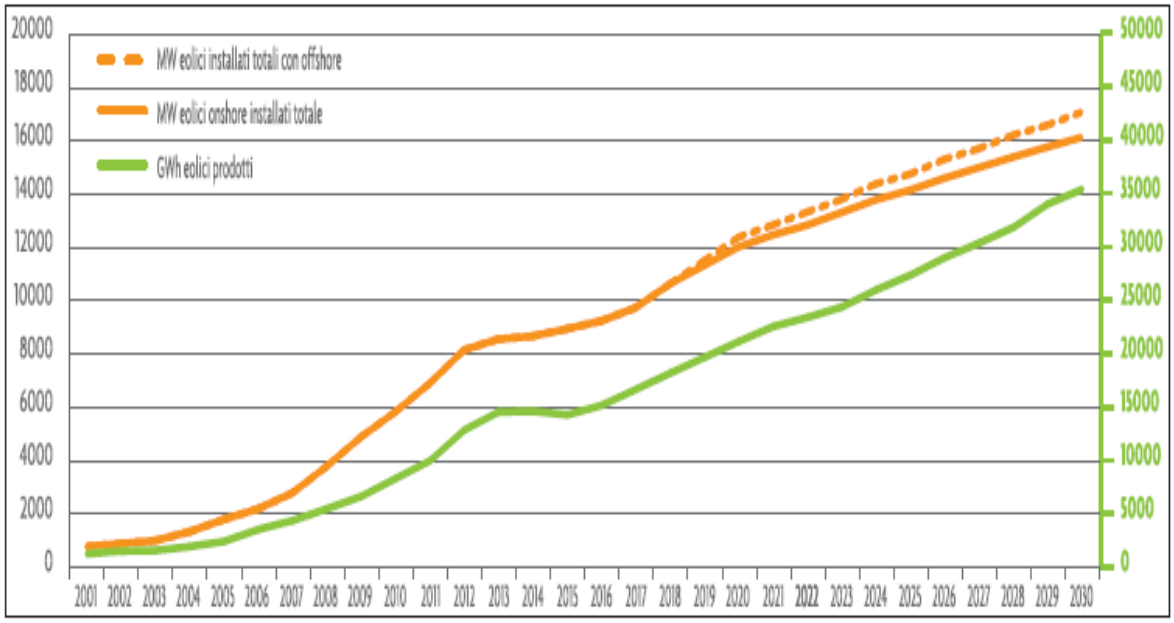

Figure 1. Offshore Wind Energy in Italy – ANEV

REGIONE	OBIETTIVO (MW)	PRODUZIONE (TWh)	TERRITORIO OCCUPATO	PRODUZIONE (kWh) PER ABITANTE	NUMERO DI OCCUPATI
PUGLIA	2.750	5,78	0,00164%	1.416,48	11.614
CAMPANIA	2.000	4,2	0,00179%	717,83	8.638
SICILIA	2.000	4,2	0,00092%	827,75	6.800
SARDEGNA	2.000	4,2	0,00091%	2.533,17	6.765
CALABRIA	1.750	3,68	0,00174%	1.864,54	4.586
BASILICATA	1.250	2,63	0,00104%	4.573,17	4.355
LAZIO	750	1,58	0,00136%	267,49	5.548
MOLISE	750	1,58	0,00104%	5.048,08	3.166
ABRUZZO	700	1,47	0,00058%	1.107,76	3.741
MARCHE	500	1,05	0,00095%	680,05	2.675
TOSCANA	500	1,05	0,00180%	280,45	2.289
UMBRIA	450	0,95	0,00033%	1.060,61	2.114
LIGURIA	250	0,53	0,00069%	334,18	1.061
EMILIA	250	0,53	0,00011%	118,03	771
OFFSHORE	950	2,38	-	-	1.200
ALTRE	300	0,63	0,00002%	28,98	1.877

Figure 2. The Regional Wind Potential: Electrical And Occupational Benefits– ANEV

Today, despite all the proposed projects, just one is going to start: the realization of the first offshore wind farm in the Mediterranean Sea.

The site chosen is Taranto, where the project involves the installation of ten maxi turbines.

The nominal rated power is 30 MW, each turbine can count on a power of 3 MW.

The offshore wind farm will count on 4 turbines along the line of the same landing, to which will be added another 6 turbines placed near the breakwater.

3. TARANTO OFFSHORE WIND FARM PROJECT: PLANNING PROCESS

The first Italian off shore wind farm will arise in the external harbor of Taranto. It represents the first example of offshore wind farm fully endorsed by the Italian Institutions and its realization allows the national and local industrial system to acquire an important primacy of knowledge and skills about the construction of such installations.

The bureaucratic procedure for obtaining the State of Property Concession involved a considerable period of time during which purely administrative issues are intertwined with purely economic-design issues.

A brief description of the entire procedure is shown below:

The State Property Concession of the project area has been formally requested to the Port Authority on 2008. After this date, a period of eight years has taken place during which further authorizations have been requested for the final grant of the Concession.

The required Authorization are as follows:

- The Environmental Compliance Decree, with VIA / VAS procedure, was issued by the Minister of Environment in agreement with Minister of Cultural Heritage and Activities on 24.07.2012;
- The Single Authorization for the construction and operation of the plant was issued by the Ministry of Infrastructure and Transport by Order No. 1 of 27.06.2013.

After obtaining the previous Authorizations, the State of Property Concession has been granted on 03/11/2016.

The favorable opinion expressed by MIBAC (Ministry of Cultural Heritage and Activities and Tourism) is also peculiar:

"... it is possible to share the methodological setting of the project ... structures should not compromise the recognition elements of sites but they have to introduce new perceptual values through non-random projects capable of introducing new forms of spatial relationship with precise alignments and compositional devices. ... the localization of wind turbines ... capable of creating an evocative layout ... is not definable as the pathological alteration of existing visuals ...

At this project goes the merit of having correctly identified the maximum number of site-compatible wind turbines ... unlike how often it can be found in other offshore wind power projects ... out of any relationship with the existing ....

In this particular case, the interference generated by the new wind farm is not dissonant with respect to the present condition of the landscaping interest of the area, whose values are still preserved. "

During these eight years, we have carried out, with quite a few problems, the design of the offshore wind farm by proceeding as follows:

- collection of site specific data: meteo - marine, geological, geophysical, geotechnical data;
- use of the collected data for an initial selection of the most suitable turbines to be used, market research on the relevant turbine manufacturing companies;
- use of the collected data and technical characteristics of the turbines for the foundation design: size, material research and market research on the producers;
- power transmission grid design;
- estimation of the carrying capacity and stiffness parameters of the foundation soil;
- structural and geotechnical analyzes and surveys of the turbine-foundation-soil complex according to Italian Standard (NTC'08) and according to International Standard IEC 61400-1 / 2005;
- possible updating and correction of the final dimensions of foundations;
- logistics and temporary planning of all stages of the project.

The wind farm will consist of 10 turbines of 3 MW each spatially divided into two subgroups of turbines: n.6 (A1) and n.4 (A2) as shown in Figure 3.

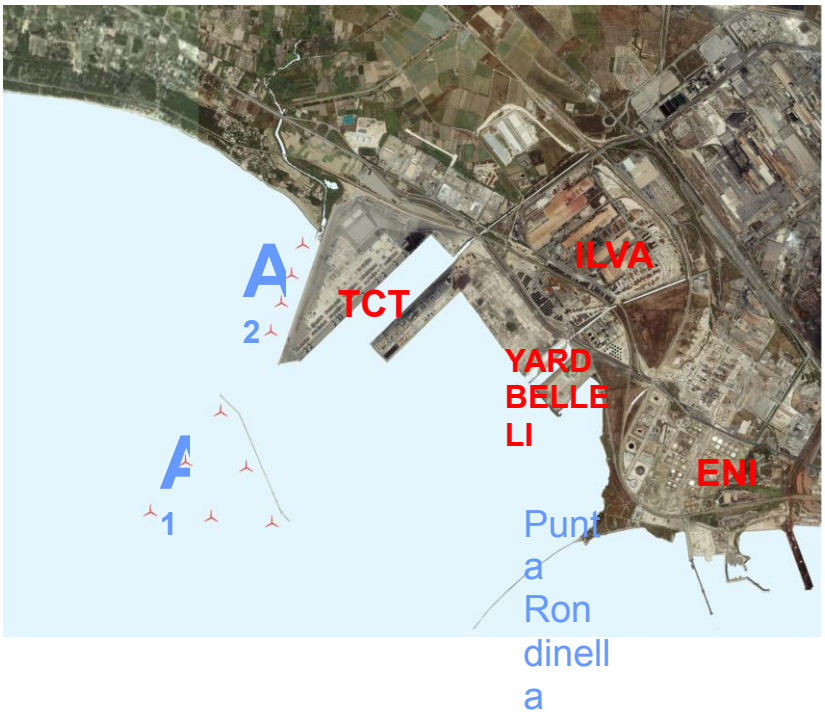

Figure 3. Taranto Offshore Wind Farm – iLStudio (Studio Severini Taranto)

For completeness, in Table 1 the geometric characteristics of the monopiles and the penetration length in the seabed are synthesized.

Table 1. Monopiles geometric features - free length - infixed length

Name	L total length [m]	L above sea level [m]	Seabed height [m]	Muddy layer [m]	L Free length [m]	L penetration length [m]
G01 (PP02)	53	4	-17.1	2.55	23.65	29.35
G06 (PP03)	53	4	-17.9	2.7	24.6	28.4
G02 (PP07)	47.5	4	-13.9	0.4	18.3	29.2
G03 (PP08)	47.5	4	-13.8	2.1	19.9	27.6
G04 (PP01)	47.5	4	-14.3	1.7	20.0	27.5
G05 (PP06)	47.5	4	-15.5	1.5	21	26.5
G07 (PP04)	39.5	4	-6.7	2.3	13.0	26.5
G08 (PP11)	39.5	4	-4.7	4.4	13.1	26.4
G09 (PP12)	39.5	4	-4.5	5.0	13.5	26.0
G10 (PP05)	39.5	4	-3.75	4.2	11.95	27.55

The turbines will be located in front of Taranto harbour where the water depth is between 4 and18 meters and the soil consists predominantly of gray-blue clays (strongly over consolidated). Preliminary investigations for the executive design have been carried out to obtain, with adequate detail, the geotechnical, geophysical and geomorphological characterization of the site.

The geognostic campaign was conducted according to the shared program with Port Authority and Works Management with the aim of integrating and expanding previous campaigns to obtain a detailed knowledge of the site, for the complete project definition of the works in the configuration initially offered.

The knowledge on the geological and geotechnical characteristics of the site has been deepened, following a very detailed campaign.

Electricity production will be sufficient to fuel all port activities and to ensure a broad Green Portuality Program.

Senvion, a German wind turbine manufacturers, has been appointed by Beleolico s.r.l., a Belenergia S.A. affiliate, as the supplier for the 30MW Taranto offshore wind farm. Senvion will provide ten 3.0M122 wind turbines, each with a hub height of 100 meters.

The foundations of the wind turbines will be steel monopiles with a diameter of 4.5 meters. The connection between the tower and the monopile will not carried out with the use of the transition piece (like existing technology) but it will be used a special carpentry piece. The base of the wind turbines will have a diameter of 4.5 meters.

The design and verification of foundations as well as the management of the entire project over all these years has been carried on by iLStudio with the support of Nicetechnology s.r.l..

Furthermore, the agreement signed by Beleolico and Senvion foresees a 25-year full maintenance service contract for the Taranto off shore wind farm.

4. CONCLUSIONS

Wind energy has become a precious and reliable source for electrical supply. It creates benefits in terms of employment, investment, research and economic activity in the electrical and energy sectors. Shortly before the end of 2016, Italy has concluded a renewable energy auction that will see the introduction of approximately 870 MW of energy produced by various renewable sources. The auction results, announced by the Energy Services Manager (GSE), also include a 30 MW offshore wind farm to be developed at the port of Taranto, southern Italy.

The project will be the first offshore wind farm in Italy. It was the only eligible bid to compete with subsidies under the Italian Decree on Renewable Energy Resources in 2015 which had accounted only for 30 MW of offshore wind energy. Belenergia, through the subsidiary Beleolico s.r.l., got the auction in June 2016 with a 2% auction drop (it was also the only participant in the auction). Taranto wind farm provides for 10 turbines of 3 MW each and the installation of the machines will start during 2018.

It should be noted that Studio Severini with the support of Nicetechnology s.r.l. (Via Solito 85, 74121 Taranto - Italy) has managed and fully carried out all the activities necessary for the complete realization of the project: bureaucratic procedure, foundations design, power transmission grid design, structural and geotechnical checks, development of innovative design solutions for secondary carpentry, material research and contact with suppliers.

Future aims will be to investigate in detail the most promising areas for wave power exploitation and promote the developing of prototypes in selected sites in Italy. The objective is to become pioneers in the national offshore wind sector, opening the way for the Italian growth of this type of technology.

REFERENCES

[1] Anev, “Anev-Associazione Nazionale Energia del Vento”, pp.1-24, 2017.

FOUNDATION DESIGN ISSUES OF INSHORE HIGH POWER TURBINES IN COMPLEX GEOLOGICAL SITES OF CALABRIA

P. Biagini[1], G. Bosco[2]* and A. M. Bruna[3]

[1]Professional Civil Engineer, Hamburg, Germany
[2]Department DICEAA, University of L'Aquila, L'Aquila, Italy
[3]Professional Geologist, Rome, Italy
Corresponding author: G. Bosco, giovanni.bosco@univaq.it

ABSTRACT

Designing the foundations of large inshore turbines, with a production capacity of 2MW and above, is generally a relatively straightforward process. In some cases, however, specific geotechnical and structural issues arise, thus requiring the contributions of geological, geotechnical and structural expertise in searching efficient and cost effective solutions. It is the case of variable rock and soil conditions, as in geologically complex settings subjected to tectonics and faulting, and of wind farms along steep or narrow ridges; these are often prone to shallow and deep seated slides, triggered by the local soil and weather conditions and also as a result of severe ground reshaping, often necessary for construction purposes. To contribute to the recognition of such issues, to suggest solutions and procedures for foundation design, to assess the influence of the foundation on the soil-structure interaction and the response of the turbine, this paper report the experience gained from three project cases in Calabria.

1. INTRODUCTION

The majority of the large wind farms completed in Italy are located in hilly and mountainous areas, such as the Pennines at the toe of the Alps; all of them are inland or close to the coast line; no offshore wind farms have been constructed so far. Turbines have production capacities in the range 2MW to 3MW, with generators atop a 90-100 m high tower, and are generally founded on large circular rafts. Depending on the strength and stiffness of the subsoil, these rafts may be placed on piles.

Typical raft diameters are comprised in the range 15 m (2MW on limestone rock) to 19 m (3MW on fractured rocks) and 20 m (2MW stiff soils); these dimensions reduce to 15-17 m for piled rafts. In this case an efficient solution calls for 12-16 piles, diameters 1.2 m or 1.0 m respectively, placed along a circle with a diameter of 12-15 m, in order to maximize resistance to bending. To this aim, also the distance between the pile centres and the edge of the raft is often kept to a minimum, in the range 0.7-1.2 m. Compared to wind actions the dead loads are negligible, especially in the case of steel towers; in fact the total weight of the structure is almost balanced by the weight of the excavated soil, because the raft must be fully embedded to avoid the risk of localized erosions, especially on sloping ground.

The length of the piles depends on local soil conditions, which may be quite variable within the same wind farm. For turbines located on very stiff soils (cemented sands and gravels, hard clays and shales) and soft intact rocks, either in alternating thick layers of thinly interbedded, pile lengths are typically comprised between 6-12 m; when the subsoil consists of loose to medium dense sands, medium to stiff clays, interbedded soils and fractured rocks, pile lengths increase to 15-25 m. For turbines located in flat and depressed areas, or in the vicinity of river estuaries, where the subsoil consists of very thick alluvial deposits of predominantly fine soils, such as normally consolidated clays and silts, it may be necessary to increase pile lengths to 40-50 m, in order to embed their tips into a strong bearing layer, such as marls, shale, clayey shales, hard flysh, gravels.

Because the subsoil conditions are quite variable within short distances in most wind farms, as a result of the complex geological history of the country, it is not uncommon to encounter superimposed layers of rock like materials and fine soils; furthermore, layering is often inclined and folded. For this reason piles are always bored (rotary bucket) and cast in place, sometimes using a bentonite slurry to reduce

disturbance caused by excavation. In this manner the upper cage can be easily reinforced for additional resistance to the horizontal actions that may arise from local instability of the superficial layers.

For the same reason soil investigation is typically based on borehole logs and laboratory tests on intact samples or material retrieved while drilling; in fact in situ testing, such as cone and flat dilatometer, is generally impossible due to the impenetrable layers near ground surface and at various depths.

In this paper, the experience gained from the design and the supervision of construction of the foundations of 67 inshore turbines (2MW) forming three wind farms is reported and described. These three project sites are located on the hilly areas South and West of Crotone and West of Cirò, some 50 to 100 km North of Catanzaro (Figure 1). The first project site (wind farm Isola Capo Rizzuto, **ICR**), near the Crotone-Sant'Anna airport, includes 48 turbines (6 clusters or sections of 8 towers each) with generators resting on two sections tower; the lower 2/3 are made of reinforced precast concrete elements that were post-tensioned on site; the top 1/3 is a metallic element; all turbines were founded on piles. The second project site (Santa Domenica, **SD**), near the village of Scanadale, includes 6 turbines, divided in 2 clusters, all of them with a metal tower and a raft foundation. The third project site (Crociminuti, Malucutrazzo, Irto Scuro, **CMI**), west of Cirò Marina, includes 13 turbines, all with metal tower; eleven have a piled raft and two a large diameter shallow foundation.

2. GEOLOGY OF THE PROJECT SITES

The three wind farms, Isola Capo Rizzuto (**ICR**), Santa Domenica (**SD**), Crociminuti, Malucutrazzo, Irto Scuro (**CMI**) are located in the province of Crotone (KR) and overlook the Ionian coastline of Northern Calabria (Figure 1). The geological, morphological, and tectonic features within each one of these farms and from one to another are quite different and variable; they have strongly affected the selection of turbine sites and the design of their foundations.

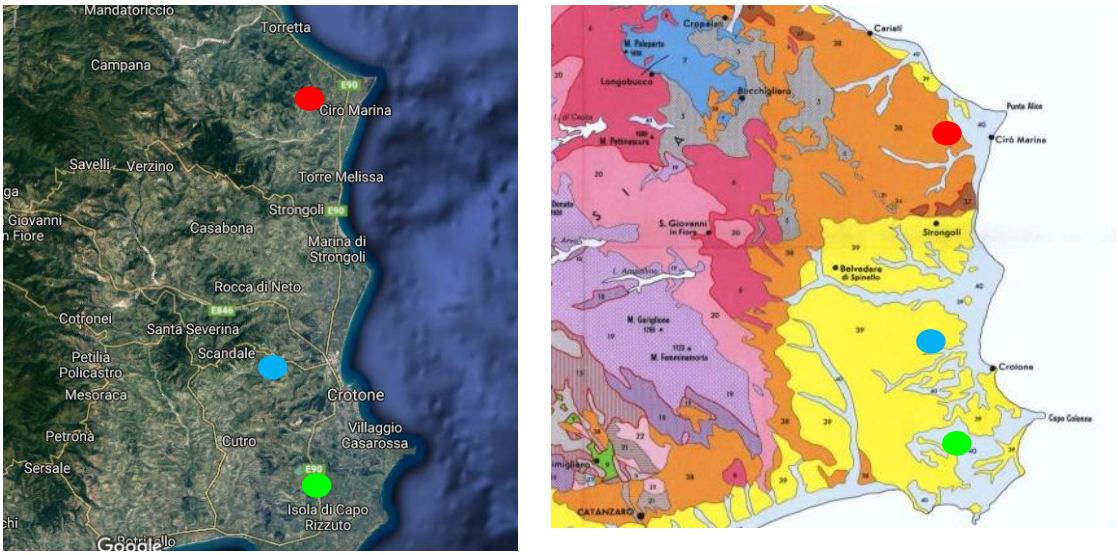

ICR – Calcarenite, sands and clastic deposits, terrassed (Pliocene-Pleistocene-Neogene)

SD – Calcarenite, sands, clays, conglomerates (Pliocene-Pleistocene)

CMI – Clays, marls, sandstones, conglomerates (Miocene-Pliocene)

Figure 1. Location of the wind farms and general geology of the surrounding regions.

The geology of the three project sites, origins from the sedimentary and tectonic processes that have transformed the Calabria coastline and the Ionian Sea into their present state are still occurring. From a lithological point of view, the three farms share some similarities; the subsoil is made of sedimentary deposits that include sandy soils and sandstones and also clayey soils and marls.

The most recent deposits that occupy the central and Southern parts of the Crotone province belong to marine terraces of successive periods (order); they are easily recognized from inland to the coastline. The slope of the ground surface is steeper along the hills that rise inland; instead, the terrain become flatter in the vicinity of the coastline. The shape of the ground and the landscape are determined by the

outcropping of clay deposits, often subjected to the intense erosive processes caused by precipitations; water washout the finer particles, that are transported to the sea, and leaves behind deep gullies.

The Northern areas of the Crotone province maintain some of the lithological features described above but the deposits encountered herein are geologically older. Here, a more advanced tectonic framework has produced folding and faulting. The ground surface is characterized by several cliffs that cut through the stronger and better cemented sandstone; at the toe of these cliffs the debris and the lower clayey deposits are often subjected to extensive sliding. When outcropping and exposed to rain, the marly deposits are prone to intense and rapid weathering, with a resulting reduction of stiffness and a severe loss of shear strength.

Under the above conditions, the design of three wind farms posed various issues from a geological, geotechnical and structural perspective. These are due to the specific ground morphology within each farm, that pushed may turbine sites in the vicinity of slope crests and cliff edges, to the geological and geotechnical characteristics of the outcropping soils, which at places are highly weathered and prone to sliding, to the variability of the shear strength and stiffness of the soils and rocklike materials encountered in the foundations of the turbine, to the extensive erosion processes that continue with time and are still reshaping the terrain.

2.1. Isola Capo Rizzuto (ICR)

The wind farm is located atop clastic deposits of marine terraces. These consists mainly of calcarenite covering sands and conglomerate, all deposited above the basal clay formation locally known as "Argille di Cutro", after the village of Cutro some 20 km West of Crotone. This stratigraphic unit of clayey silts and silty clays has been dated to the Pliocene-Pleistocene period.

As shown in Figure 2 the soil deposition within the farm can be traced along bedding joints that are essentially planar and parallel.

The 48 turbines are distributed atop three morphological terraces (12+12+12), with the lowest one forming a wide plateau.

The site is crossed by a natural stream, flowing between the hillsides; in the steepest area of the sloping territory, this creek has originated a shallow slide.

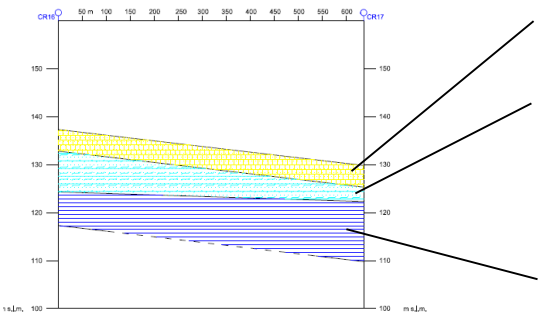

Weathered calcarenite and sands; the calcarenite is (unloaded),

Clayey and sandy silts, grey to yellow, thinly bedded and with locally cemented nodules; stiff to hard;

Terraced marine deposits; Scandale Formation

Silty clays and clayey silts; grey to bluish; Unit of the Crotone Basin – Clays from Cutro

Figure 2. Typical geological cross section along the Isola Capo Rizzuto wind farm.

2.2. Santa Domenica (SD)

The farm consists of two clusters, each one including three turbines; the clusters dot the ridges of two parallel series of hills, North-West to South-East, separated by a local road and a narrow creek.

Along the hillsides the predominant lithological unit can be well recognized; it is the clay member of the "Argille di Cutro". Instead, along the top of the hills, where the turbines have been installed, an essentially granular and coarse formation outcrops; this consists of sands and cemented sands (sandstones) of marine origin. Figure 3 presents the stratigraphic cross sections along the two clusters; these were reconstructed on the basis of the data from the geological survey and the six borehole logs prepared on site during the ground investigation campaign.

The upper sands and sandstones are much more permeable than the lower clay formation, which acts as

an aquiclude. As a result, ground water has been generally detected at the contact between the two formations, with water rising to maximum elevations at some local spots.
Because the permeability of the two layers differs significantly, water emerges along the hillsides, originating superficial erosion and shallow slides. With time deep gullies are excavated and fast flowing waters transport downhill large volumes of the finer soils. These sediments are eventually collected by canals and creeks flowing at the foot of the hills and conveyed to the sea.

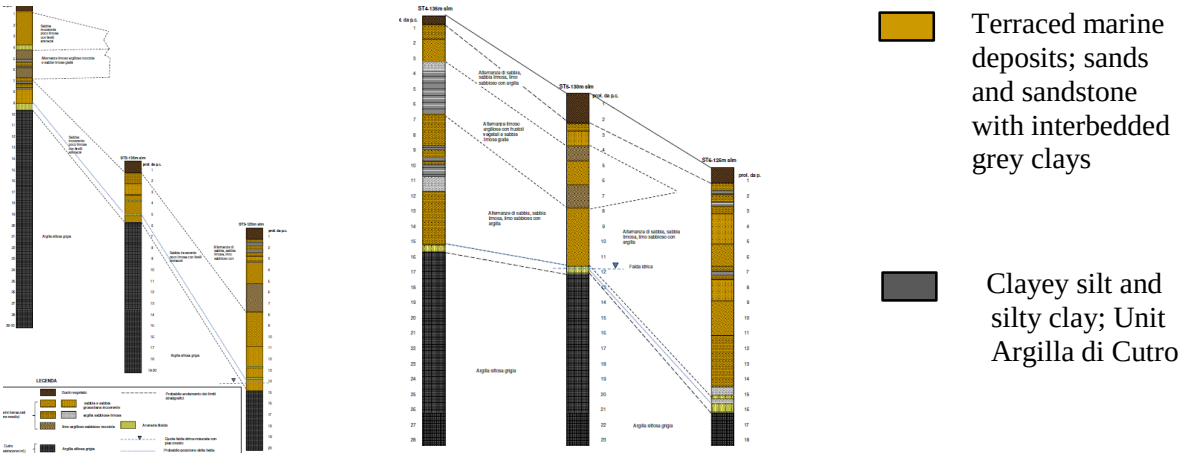

Figure 3. Stratigraphic cross sections through the Santa Domenica wind farm.

2.3. Crociminuti, Malucutrazzo, Irto Scuro (CMI)

The subsoil conditions within this farm are quite variable. The turbines are placed over sedimentary soil and rock deposits, including clays, sands and sandstones, conglomerates, know as “Formazione del Ponda”; these deposits were originated by the erosion of the Sila mountains.

The morphology of the area within the farm results from the geological conditions and the tectonic history of this part of the region; it is characterized by an irregular and undulated terrains from which a series of hills emerge, often cut by steep cliff faces and unstable slopes.

Figure 4 presents a typical stratigraphic cross section along the farm; it was reconstructed from the data collected during the geological studies and surveys and using five borehole logs, prepared during the ground investigation campaign that comprised more than twenty boreholes.

As a result of the combined effects of synclines and anticlines crossed by faults, the subsoil has been broken into separated blocks that have been displaced; thus the different stratigraphic units are dislodged and the hydrogeological continuity has been interrupted.

In most cases the sloping ground follows steeply inclined bedding planes. Where these planes are eroded, deep scarps are formed, giving the land surface a highly irregular shape. When deposited along steep slopes, the clayey and sandy soils may be subjected to sliding; movements may involve large volumes of soils, extending to the base of the toe of the hills.

3. GEOTECHNICAL DESIGN ISSUES

The six clusters of the **ICR** wind farm can be grouped into three couples (1+2, 3+4, 5+6), each couple having relatively uniform subsoil characteristics. Couple 1+2 are located over the plateaus atop the hills descending toward the coast; couple 5+6 are located at the toe of these hills, still elevated above the sea line; couple 3+4 are located on the hillsides. Regardless their position, all towers have the same foundation; an annular raft with outer diameter of 16.4 m, 3.2 m high, embedded entirely in the ground and placed on 14 piles, 1.2 m in diameter. All piles were excavated with a rotary bucket and concreted with a tremie pipe. Occasionally a temporary metal lining was used through the top calcarenite layer. All piles carry the same compressive and tensile loads, $E_{c,d}$ = 3872 kN and $E_{t,d}$ = 509 kN (per pile).

Soil investigation comprised 5 CPT and 1 borehole per tower and laboratory tests on soil samples.

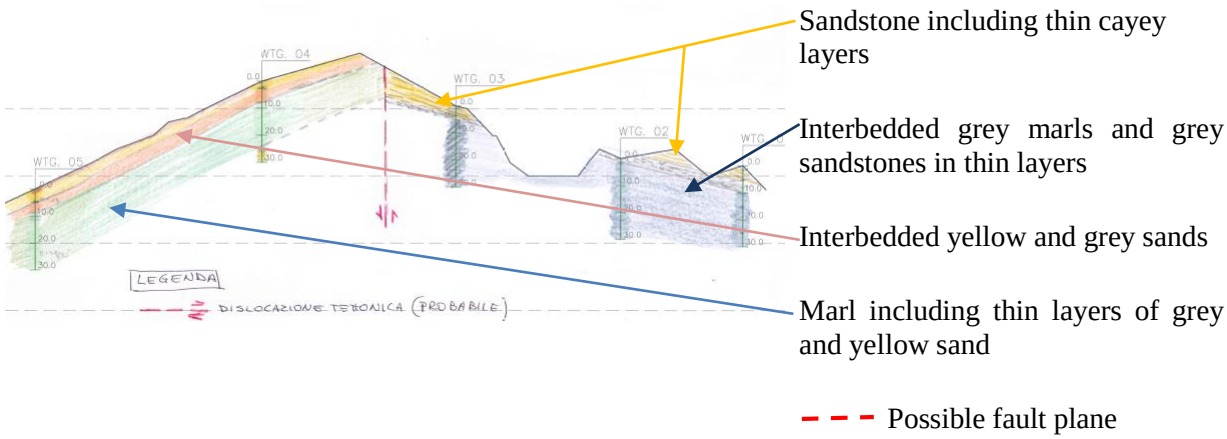

Figure 4. Stratigraphic cross section through the Crociminuti, Malucutruzzo, Irto Scuro wind farm.

The turbines of cluster 1 are located over an essentially flat area, except for local gullies, at elevations 145-165 m m.s.l.; those of cluster 2 are distributed on a more irregular area at elevations 120-160 m m.s.l. with ground sloping at 3°-10°. From a geological-geotechnical point of view the main issue is the presence of an upper thick layer (3-6 m) of calcarenite covering a transition level of sandy clayey silts passing to clayey silts and silty clays that extend to great depths. The calcarenite exhibits a highly variable degree of cementation, from a strongly cemented coarse sand, not penetrated by CPT, to a medium dense sand, locally containing fragments of cemented sand. The lower fine soils (40%-55% clay, 40%-55% silt, 10%-20% sand) are very stiff in the upper 15 m and become hard at greater depths. Using q_c data from the 33 CPT that penetrated the calcarenite, of a total 48 planned for 16 towers, two ranges of values of undrained shear strength c_u are estimated; for depths less than 15 m c_u = 130-180 kPa (q_c = 2-3 MPa); for depths between 15-25 m c_u = 180-230 kPa (q_c = 3-4 MPa). Water was encountered inside 2 boreholes only, at 2 sites of section 2, at a depth of 3.5 m, in the calcarenite layer. At places some minor seepage of rainy water was observed at the interface between the more permeable calcarenite and the underlying fine soils, in comparison essentially impervious. Due to the relatively uniform soil conditions the piles of the 16 towers (sections 1+2) have the same length, 18 m.

Cluster 3 is located at midheight of the hillsides, either on relatively flat areas or on slightly sloping sites, at elevations 90-130 m m.s.l.; cluster 4 is distributed over a more irregular terrain at elevations 60-110 m m.s.l.; in general ground surface slopes at 6°-7°. With the exception of only two towers, also in the clusters 1+2 the subsoil consists of an upper thick layer (3-7 m) of calcarenite often covering a sandy clayey silt level passing to clayey silts that become silty clays and extend to great depths. The thickness of the transition level varies from 3-5 m to 8-10 m; thus the clayey deposit is reached at depths varying between 11-16 m. The lower fine soils (35%-60% clay, 35%-65% silt, 5%-15% sand) are very stiff in the upper 15 m and become hard at greater depths. Using q_c data from the 11 CPT tests, out of 48, different ranges of values are determined for the undrained shear strength; c_u = 120-200 kPa (q_c = 2-3 MPa) for depths less than 15 m and c_u = 220-240 kPa (q_c = 3-4 MPa) for depths less than 20 m and c_u = 250-300 kPa (q_c = 4-5 MPa) for depths 15-25 m. Water was encountered inside 4 boreholes only, sites of 4 turbines of section 3, at depths between 3.5-7.5 m in the calcarenite layer. Pile lengths (16 turbines) vary: 17 m (3), 18 m (2), 19 m (3), 20 m (4), 21 m (1), 22 m (2), 23 m (1).

Clusters 5+6 are located near the base of the hills, at elevations 40-50 m m.s.l., atop a relatively flat plateau, resembling a terrace elevated above the coast line; here the inclination of the ground surface remains below 2°. Similarly to the other cluster, the subsoil consists again of an upper thick layer (4-6 m) of calcarenite that covers a sandy clayey silt level (transition) of variable thickness, 1-6 m, passing to clayey silts that become silty clays and extend to great depths. As before, these lower fine soils show increasing strength with depth. Using q_c data from the 11 CPT tests, out of 48, the following ranges of values are determined: c_u = 90-160 kPa (q_c = 1.5-2.5 MPa) for depths less than 5 m, c_u = 190-250 kPa (q_c = 3.0-4.0 MPa) for depths 5-10 m, c_u = 250-280 kPa (q_c = 4.0-4.5 MPa) for depths 10-15 m, c_u = 250-300 kPa (q_c = 4.5-5.0 MPa) for depths 15-20 m. Water was encountered inside 6 boreholes only, one within section 5, the remaining 5 in section 6; depths range 2.5-4.2 m (3.5 m in section 5), water circulates in the calcarenite layers or through interbedded sand and calcarenite levels. Pile lengths of the

16 turbines (sections 5+6) are less variable: 12 m (9), 14 m (5), 15 m (1), 16 m (1).

The six turbines of the **SD** farm are located along the relatively wide ridges atop the hills rising to 120-150 m m.s.l. on the West of Crotone. Both clusters are aligned in the North-West to South-East direction and are divided by a local road and a narrow creek; three turbines are located at elevations of 130-150 m m.s.l. and three at elevations of 125-135 m m.s.l., North-East (cluster 1) and South-West of the road and the creek respectively. Regardless their position, all towers have the same foundation, a circular raft with diameter of 20 m and maximum height of 3 m, embedded entirely in the ground.

Soil investigation comprised 7 boreholes (6 towers and station) with 2 stand pipe piezometers, 17 SPT, retrieval of samples for laboratory tests, measures of shear wave velocities by means of 4 MASW.

From a geotechnical point of view the main issue is a layered subsoil; an upper thick deposit of mainly granular soils, variously interbedded; a relatively uniform formation of hard silty clays and clayey silts extending to great depths. The upper deposit consists of interbedded silty sands, clayey silts and sands, silty and sandy clays, in layers of variable thickness, 1-3 m reducing to 100-200 mm at places. The total thickness varies in the ranges 4.5 m, 9.0 m, 13.5 m (cluster 1) and 10.0 m, 15.0 m, 15.0 m (cluster 2). At the base a thin layer (0.3-0.5 m) of weakly cemented sandstone is generally visible, locally hidden inside a coarse silty sand layer. The top of the hard clay has variable elevations, 112-130-140 m m.s.l. (cluster 1) and 109-118-120 m m.s.l. (cluster 2).

From in situ and laboratory test results the upper sandy soils appear quite dense, capable to mobilize a friction angle in the range $\varphi' = 32°\text{-}39°$ (lab) to $\varphi' = 40°\text{-}50°$ (SPT). The fine soils, though somewhat variable, appear relatively stiff, with water content 0.08-0.26 and void ratio 0.55-0.62. In the lower deposit the silt content is slightly larger (54%-57%) than the clay fraction (40%-42%), except for one sample (clay 58%, silt 41%); the sand content is always negligible (1%-4%). Water content, degree of saturation and void ratio were comprised in the ranges w_n = 18%-23%, S = 99%-100%, e_0 = 0.48-0.59. From PI values, PI = 10%-15%, a friction angle in the range $\varphi' = 28°\text{-}30°$ was estimated; UU tests yielded values of undrained shear strength in the range c_u = 200-310 kPa, thus typical of hard clays. In accordance, oedometer tests yielded values of the compression index quite low, Cc = 0.1. Inside the 2 piezometers water raised 0.2-1.0 m above the base of the upper deposit; while water circulation is likely to occur in the mostly granular soils, the lower silts and clays are probable free of any kind of seepage; furthermore it cannot be excluded that they are subjected to negative pore pressures.

The thirteen turbines of the **CMI** farm are distributed along the narrow ridges defining the top of the hills on the West of Cirò. From an elevation of 350 m m.s.l. this tiny village overlooks the touristic Cirò Marina, along the coast. The geological history of the area, combined with the tectonic activity of the region, have originated a quite irregular terrain, often disrupted by shallow and deep seated slides, involving large volumes of soil and cutting through local roads. Minor faults have also been detected along the excavations of three foundations. As a result of this natural reshaping of the ground, and due to the specific subsoil stratigraphy, some hillsides are exposed along steep faces on one side, while descend more gently on the opposite direction.

To compromise, construction requirements, excavations, subsoil conditions, and production goals, the turbines are located at different elevations; 6 in the range 300-340 m m.s.l.; 5 in the range 350-380 m m.s.l.; 2 in the range 400-430 m m.s.l. Furthermore, during construction it became necessary to switch to the pile foundation for 1 out of 3 turbines and increase the length of the piles at 1 site. The choice between shallow and piled foundation depended on slope of the ground and subsoil conditions.

Soil investigation comprised 1 borehole per tower, retrieval of soil samples for laboratory tests, 2 down-hole tests for shear wave velocities profiling, 2 stand pipe piezometers.

Regardless their location, all piled foundations have a circular raft with diameter of 16.5 m, maximum height of 3.2 m, 12 piles with diameter of 1.2 m; pile axis are 7.5 m distant from the raft axis. All piles were excavated with a rotary bucket and concreted with a tremie pipe; apart from one site, were trickling occurred while boring, water was not encountered during piling. The two shallow rafts have a diameter of 18.5 m and maximum height of 3.2 m.

Though the design compressive load, $E_{c,d}$ = 4000 kN per pile, is constant throughout the farm, piles have different lengths, 16 m (9 sites), 19 m (1 site), 22 m (1 site) as a result of variable soil conditions. At three sites (shallow foundations) the subsoil consists of soft rocks, sandstones, marls, clayey marls. At four other sites, sands and lightly cemented sandstones with interbedded hard rocks, clayey marls, marly

clays, and marls including sandstones, were encountered (16 m long piles). At three sites, sands and silty clays over sandstones, marls, and clayey marls becoming strongly cemented marls, clayey marls, and strong sandstones were encountered (16 m) occasionally with some water (19 m). At two sites, layers of interbedded sands, hard clays, marly clays, and clayey marls, marly clays, sandstones (soft rocks) and marls and sandstones (moderately strong rocks) were encountered (16 m). At one site moderately stiff clays and marly clays becoming hard in depth were encountered (22 m long piles).

Uniaxial compressive tests yielded values of compressive resistance in the range σ_c = 1-5 MPa for clayey marls and marls with sandstone, σ_c = 0.5-2.0 MPa for lightly cemented sandstones, σ_c = 5-20 MPa and σ_c = 20-60 MPa for moderately to strongly cemented sandstones.

3.1. Design strategies

The variability of the subsoil conditions within the same farm, as enlightened before for three project sites, makes it difficult to plan a geotechnical investigation and select effective testing procedures for determining strength and stiffness parameters for foundation design. As such, a conservative strategy should be adopted, preferring a piled foundation and concentrating the geotechnical investigation on two objectives; the reconstruction of a reliable subsoil stratigraphy at each turbine site; the retrieval of intact and good quality samples for laboratory testing.

In this respect it is easily recognized that superficial layers of soft rocks, though fractured, stiff and hard soils, cemented sands and gravels, make it generally impossible to carry out in situ testing by CPT and-or DMT. Thus drilling of boreholes may prove the only viable and adequate solution; in these cases at least two boreholes per turbine site should be planned, for soil reconnaissance, samples collection, installation of instruments, execution of seismic tests.

Because shear strength of soils depends only on effective stresses, a knowledge of the pore water pressures, their distribution and evolution with depth and time, is fundamental. As such it shall not be overlooked that in dry areas fine soils are often subjected to negative pore pressure, regardless their degree o saturation. Therefore, pore pressures shall be determined using instruments functioning also in the negative range (electric, vibrating wire,.) either retrievable for maintenance or permanently installed in the ground, taking advantage of the boreholes drilled for soil reconnaissance.

Because soil structure interaction analyses require a reliable knowledge of the stiffness characteristics of the foundation soils, 1 borehole at each turbine site should be specifically equipped for a down-hole test; such test shall be performed using seismic modules carrying 2 receivers, to avoid interpretation errors in calculating the shear wave velocity of different soils and rocks at various depths.

3.2. Pile design for compressive and tensile loads

Under variable soil conditions, bored and cast in situ piles might prove the most flexible and efficient solution. Large diameter piles, 1.0-1.2 m, should be preferred, for their capacity to resist horizontal and tensile forces, thus allowing to limit the diameter of the raft; a relatively small raft will in turn reduce the volume of the excavations thus limit the danger of slides in sloping areas.

For purposes of design, the analytical calculation method, based on the results of reliable laboratory tests will very likely yield a reasonably conservative evaluation of the necessary length. Accordingly the compressive resistance is obtained adding two contributions, base resistance and shaft resistance. The former is typically determined as the product of a unit base resistance q_b times the cross section of the pile. The latter is obtained by integrating unit skin friction $q_s(z)$ along depth (z) to the full length of the pile time shaft perimeter. Values of q_b and q_s vary depending on soil type and mode of analysis, drained or undrained. Both of them shall be limited, to avoid excessive settlements and also because skin friction does not increase indefinitely with depth. It is known that full base resistance is mobilized after much greater displacements, and in the order of 10% the diameter of the pile, than those required to develop skin friction, typically 10-15 mm regardless the diameter. On the other hand, measures of strain in piles during load tests show that in soils q_s does not reach values greater than 120-150 kPa.

The general criteria outlined above have been positively applied in designing the piles of the 59 towers within the ICR and CMI wind farms. Calculations have been performed assuming that the different soils and rocks encountered would behave like a two-phase material, obeying the Mohr-Coulomb failure criterion with a linear envelope. Thus, the procedures detailed below were adopted for all piles.

In granular soils unit base resistance was chosen in the range q_b = 2500-4000 kPa, depending on the in situ density. In very hard clays, hard marls and marly clays, lightly cemented sandstones (soft rocks) the range q_b = 3-5 MPa was considered, with q_b related to the degree of cementation, hence the uniaxial compressive strength; in strongly cemented rocks extending well below the tip of the piles values of q_b in the range q_b = 5-10 MPa were adopted. Instead in fine soils, such as moderately stiff to hard clays, q_b was calculated with the well know equation $q_b = (9) (c_u)_{av} + (\sigma_v)$, in which (σ_v) is the total vertical stress at the tip of the pile and $(c_u)_{av}$ is the average undrained shear strength (c_u) of the soils above and below the tip contributing to q_b (c_u determined from lab or in situ tests, CPT, DMT).

Calculation of the unit skin friction follows similar approaches. In granular soils, where pore pressures are easily evaluated, q_s has been determined using the relationship $q_s(z) = (k) (\sigma_{vz}') (\tan \varphi')$, in which (σ_{vz}') is the effective vertical stress at depth (z), (φ') is the effective friction angle of the soil at the same depth and (k) is an empirical coefficient relating (σ_{vz}') to the stress perpendicular to the shaft (σ_{hz}'). A fixed value (k) = 0.7 was always assumed. In soft normally consolidated clays, where the pore pressures can be estimated or calculated to a reasonable level of accuracy, q_s was determined with the equation $q_s(z) = (\beta) (\sigma_{vz}')$ in which (σ_{vz}') has the same meaning as before and $(\beta) = (k_0) (\tan \varphi')$ with $(k_0) = (1 - \sin \varphi')$ as per NC fine soils. It is worth noting that (β) is relatively unaffected by variations of (φ') within the range that typically applies to clayey silts and silty clays, with some sand. In lightly to strongly cemented rocks and especially in very stiff to very hard clays, where it is very difficult to obtain reliable measurements of pore pressures, most often negative, q_s has been calculated using the equation $q_s(z) = (\Psi) [(\sigma_c) / 200]^{1/2}$ with q_s and σ_c expressed in kPa, σ_c being the uniaxial compression strength (σ_c = 2 c_u), while (Ψ) is a material factor that varies for soils and rocks and depends on their strength (Kulhawy et al [1]). For very stiff to hard clays it has been assumed (Ψ) = 50-70; for lightly cemented to moderately cemented rocks it has been assumed (Ψ) = 70-100.

4. SOIL-STRUCTURE INTERACTION

Soil Structure Interaction (SSI) is the procedure commonly used whenever the structural response is influenced by the soil deformation. In the wind turbine foundation analysis the contribution of the soil deformation to the structural dynamics is of crucial interest. In fact the tower bottom loads that every single manufacturer provide to the foundation engineer is strictly dependent on the system frequency. If this last deviates of more than 5% respect to the nominal value, the entire load set needs to be calculated again.

In the standard practice, many analytical formulas have been implemented to calculate the foundation stiffness by considering the foundation as a rigid block. However this calculation implies a ratio between the diameter of the foundation and the height to be less than 10.

For this reason a full SSI, taking into account of the soil and structure deformation is highly recommended in order to achieve the two following important targets:

- Ensure that the stiffness requirements are achieved
- Foundation design optimization

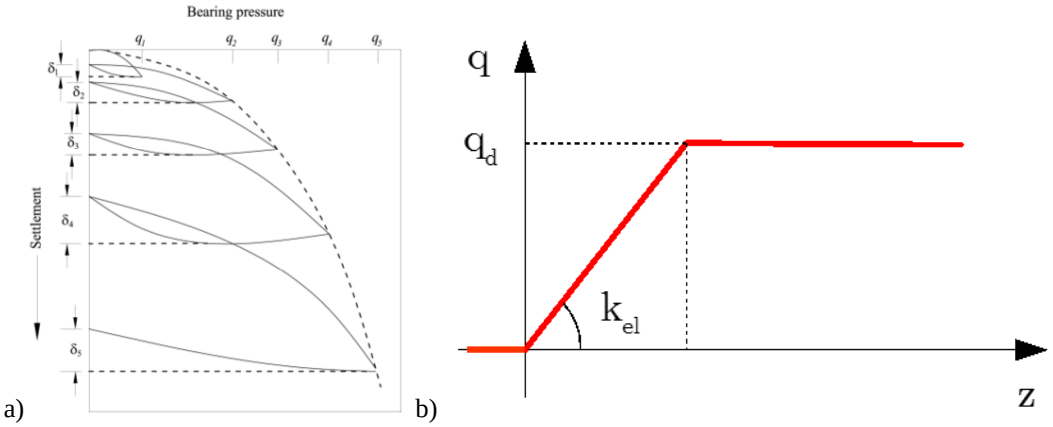

a) b)

Figure 5. Example of soil behavior: (a) actual (b) simplified.

The representation of the soil behavior through a bed of elastic-plastic spring not reacting in tension is a general common way of approaching SSI problems (Figure 5).

In the case of the wind turbine foundation analysis it allows to take into account the plasticization of a portion of soil underneath the foundation under extreme load conditions. In this way the engineer can also verify the preliminary results obtained through the half-moon method for highly eccentric loads.

Another important feature of this method is that several different analysis, for the same load level, can be performed assuming different values of elastic stiffness so as to take into account the progressive decay of the mechanical properties of the soil (time and strain dependent properties). This is even more important when employing static analyses in the design of wind turbine foundations.

The same approach can be used for piled foundations, where again the pile-soil interaction can be analyzed by elastic-plastic s of convenient stiffness.

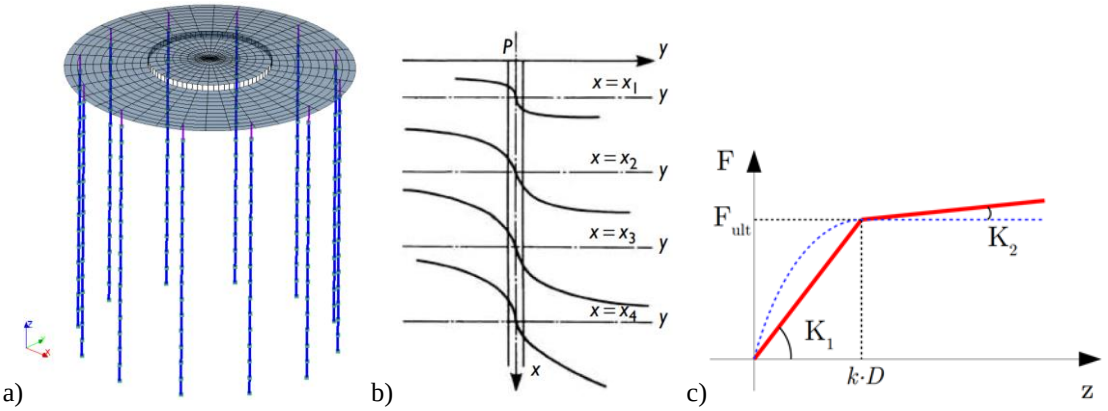

Figure 6. Piled foundation: (a) FE model (b) pile-soil interaction curves and (c) FE soil response curve.

Figure 6 shows the general approach for modeling soil structure interaction in case of piled foundations. Simple elastic-plastic curves or elastic-plastic with hardening can be adopted, depending on the type of soil.

In the case of foundations placed on essentially fine-grained soils, the curves presented in Figure 7 may be adopted as suggested in DNV [7].

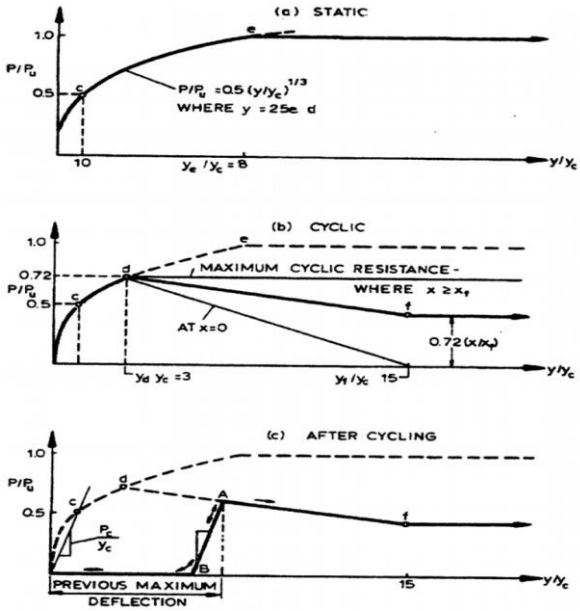

Figure 7. Soil response curves for soft clays [6].

In general the shape of the response curve is not varying very much going from soft clays to weathered rocks, being always present an initial nonlinear softening path, followed by the plastic zone.

It is important, in using the idealized elastic-plastic behavior, with or without hardening, to properly fine-tune the two stiffness values k_1 and k_2 in Figure 6 in order to account properly for the following aspects:

- Short term low-deformation stiffness
- Long-term low-deformation stiffness
- Time dependent effects
- Mechanical properties degradation due to cyclic loads

For this scope several analysis may be conducted under the same load level.

5. CODES AND STANDARD PRACTICE

Design of wind turbines foundation for the Italian market requires some special adaptation to the local building regulations that are prescriptive and supersede the international standards usually employed for this kind of design process.
The Italian regulation for building construction, namely *Norme Tecniche per le Costruzioni* (NTC 2008), has been introduced as per National Decree of the Ministry of Public Works in January 2008.

The NTC 2008 allows to use harmonized standards UNI EN, therefore international standards incorporated into the Italian Institute for Standardization (UNI).

An important paragraph of the Italian code NTC 2008 states "*Possono essere utilizzati anche altri codici internazionali, purché sia dimostrato che garantiscano livelli di sicurezza non inferiori a quelli delle presenti Norme tecniche.*" Literally one can use international regulation other than harmonized UNI EN standards, provided that the level of safety is not less than the one included in NTC 2008.

Now, considering the IEC 61400-1, which is the reference standard for the design of the wind turbines, the following levels of safety, in terms of Partial Safety Factors (PSF) are defined.

Unfavourable loads			Favourable[9] loads
Type of design situation (see Table 2)			All design situations
Normal (N)	Abnormal (A)	Transport and erection (T)	
1,35*	1,1	1,5	0,9

* For design load case DLC 1.1, given that loads are determined using statistical load extrapolation at prescribed wind speeds between V_{in} and V_{out}, the partial load factor for normal design situations shall be γ_f =1,25.

If for normal design situations the characteristic value of the load response $F_{gravity}$ due to gravity can be calculated for the design situation in question, and gravity is an unfavourable load, the partial load factor for combined loading from gravity and other sources may have the value

$$\gamma_f = 1{,}1 + \varphi\varsigma^2$$

$$\varphi = \begin{cases} 0{,}15 & \text{for DLC1.1} \\ 0{,}25 & \text{otherwise} \end{cases}$$

$$\varsigma = \begin{cases} 1 - \left|\frac{F_{gravity}}{F_k}\right|; & |F_{gravity}| \le |F_k| \\ 1; & |F_{gravity}| > |F_k| \end{cases}$$

Figure 8. Partial safety factors from IEC 61400-1.

The PSF in Figure 8 apply to the loads simulated according to the classical theories for the wind turbines and therefore also to the tower bottom loads that are the basis for the foundation design.

In the NTC 2008, when it comes to the foundation design, the same approach as in the Eurocode 7 is used, therefore the following PSF apply to the external loads.

CARICHI	EFFETTO	Coefficiente Parziale γ_F (o γ_E)	EQU	**(A1)** STR	**(A2)** GEO
Permanenti	Favorevole	γ_{G1}	0,9	1,0	1,0
	Sfavorevole		1,1	1,3	1,0
Permanenti non strutturali (1)	Favorevole	γ_{G2}	0,0	0,0	0,0
	Sfavorevole		1,5	1,5	1,3
Variabili	Favorevole	γ_{Qi}	0,0	0,0	0,0
	Sfavorevole		1,5	1,5	1,3

Figure 9. PSF for foundation design according to NTC 2008.

A1 and A2 in Figure 9 are the classical two different approaches for the design. They take into account the different combinations of loads, material (soil) and resistance factors.

Clearly, if one compares the two sets of PSFs, a substantial difference arises for the turbines model whose governing situations are dictated by the abnormal loads cases (factored with coefficient 1.1 in the IEC standard).

In this case, if one has to strictly follow the NTC 2008, he has to use the unfactored design loads (characteristic loads) and re-apply the PSF from NTC 2008. This will lead to an increase of the design load on top of the foundation between about 18% and 36%.

Of course, this difference leads to a considerable increase of the foundation cost, when compared to the same situation in the other European Countries, where the international standards for wind turbines are fully integrated into the design framework.

The interpretation of the Italian Regulation is not yet resolved, as many local Authorities deputed to receive and approve the structural design (Genio Civile) strictly follow the Italian regulation. This ultimately leads to a remarkable inconsistency between the international framework that regulates the certification of the wind turbines and the Italian situation.

It is advisable that in the future the international regulations commonly governing the certification of the wind turbines, like IEC 61400-1 and DNV-GL Guidelines 2010 will be formally accepted and introduced into the Italian standardization system.

This will in the end recognize the wind turbines as a specific type of construction for which, nowadays, a high level of industrialization has led to an extreme accuracy in the evaluation of the effect of the wind load on the supporting structure, with considerable reduction on the loads and structural response calculation uncertainties. These last ultimately justify, together with the reduced lifetime of this kind of structures, the reduced PSF for a certain group of load conditions.

6. POST CONSTRUCTION CONTROLS

Post construction controls executed so far have included pile load tests, topographic measurements of settlements and tilting, visual survey of sloping areas and terrains prone to surface erosion.
For purpose of checking the bearing capacity, piles have been subjected to vertical loads equal to 1.5 the design load for Serviceability Limit State analyses (as indicated in [2]) and also to greater loads, close to the calculated compressive resistance of the pile.
All tests indicate that the piles performed satisfactorily, probably because the inherent conservatism of the calculation procedures described before.
Besides, neither significant settlements nor rotations have been measured so far in the shallow rafts.

7. CONCLUSIONS

The paper has outlined the major design issues when installing 2MW turbines in geologically complex sites. It has been shown that the morphological and stratigraphic conditions must be considered to plan the soil investigation program and to select the type of foundation, shallow or on piles. Large diameter piles are highly recommended where the superficial stiff soils are removed to embed the raft, and in case of soils and sloping grounds prone to surface erosion and sliding. Procedures to design the piles are relatively straightforward; they can be applied in difficult soil conditions to obtain a reliable and reasonably conservative estimate of the compressive resistance of the piles. Special attention shall be devoted to determining soil properties for use in SSI analyses; to this aim the results of down-hole tests

may prove a very helpful mean, especially if accompanied by laboratory dynamic test. Finally it is noted that a better harmonization of the different codes and standards in use by member state within a common international framework, could certainly produce more reliable and cost effective design strategies of such important structures.

ACKNOWLEDGEMENTS

The authors gratefully acknowledge Novenergia Italia s.r.l. for permission to use available data from the soil investigations and design documentation related to the wind farms of Santa Domenica (KR) and Crociminuti, Malucutrazzo, Irto Scuro (KR) in preparing this paper.

REFERENCES

[1] F. H. Kulhawy, K.-K. Phoon, "Drilled Shaft Side Resistance in Clay Soil to Rock", in *Design and Performance of Deep Foundations: Piles and Piers in Soil and Soft Rock, ASCE, Geotechnical Special Publication N.38, P.P. Nelson & T.D. Smith editors*, 1993.
[2] Consiglio Superiore dei Lavori Pubblici, Norme Tecniche per le Costruzioni, di cui al D.M. del 14.01.2008.
[3] EN 1997-1, Geotechnical design - Part 1: General rules, 2005.
[4] CEB-FIP, Model Code 1990, 1991.
[5] CEN EN 1992-1-1, Eurocode 2: Design of concrete structures - Part 1-1: General rules and rules for buildings, 2004.
[6] API RP 2A-WSD-2005, Recommended Practice for Planning, Designing and Constructing Fixed Offshore Platforms - Working Stress Design, 2005.
[7] DNV, Foundations, 1992.

Paper KL4

TOWARDS ENERGY PROSUMING CITIES

Dan van der Horst[1,2]*, Peter Stokes[1], Bohumil Frantal[2], Stanislav Martinat[3,4]

[1]*University of Edinburgh, School of Geosciences,*
Drummond Street, Edinburgh EH8 9XP, United Kingdom.

[2]*Institute of Geonics of the Czech Academy of Sciences, Department of Environmental Geography,*
Drobneho 28, 602 00 Brno, Czech Republic

[3]*Institute of Geonics of the Czech Academy of Sciences, Department of Environmental Geography,*
Studentska 1768, 708 00 Ostrava, Czech Republic,

[4]Cardiff University, School of Geography and Planning, 45 Park Place, Cardiff CF10 3BB, Wales, UK

**Corresponding author: Dan van der Horst, dan.vanderhorst@ed.ac.uk*

ABSTRACT

Energy 'prosumers' are people who generate (renewable) energy for self-consumption. With the 'right' house and good climatic conditions, prosumers may on aggregate become annual net exporters of (green) electricity to the grid. The possibility of zero carbon cities (within the build-up area) may seem less promising; the level of energy consumption per square km will far exceed the capacity for generating renewable energy in the urban space. However yield, efficiency and payback time are not the only criteria by which we can assess the 'potential' of urban renewables; there are wider political, moral and socio-technical reasons why renewables like wind turbines should be *seen* in the city and in other places of energy consumption. Government targets and Kyoto commitments illustrate that a transition to a low carbon economy or society is a normative endeavor that requires joined-up thinking on issues of production and consumption, adaptation and mitigation, social justice for future generations and amongst the current generation; Illustrated with examples of wind energy in the UK, we will explore to what extent the concept of carbon neutral energy prosumption could be scaled up. Whilst the scenarios explore theoretical maximum for wind energy, and are therefore not very 'realistic', we would argue that given the scale of emissions reductions required, radical design (in its broader sense) is needed to disrupt current unsustainable practices and yield significant green win-win situations closer to home, i.e. to the places where we currently (end) use our fossil energy.

1. INTRODUCTION

The term 'prosumer' (being both a producer and consumer), is thought to have been coined by Alvin Tofler. In his 1980 book 'the Third Wave' he describes the industrial revolution (the 'second wave'; the agricultural revolution was the 'first wave') as a process that is characterised by urbanisation around factories and mines; the new industrial cities became primary places of production. He argues that this separation of consumption and production is anomalous and will become again more intimately linked in the coming 'third wave'. Over the course of the last decade, the term prosumer has gained traction in wider academic circles. In direct response to Toffler's work, other scholars of the 'consumer society' (e.g. the sociologist George Ritzer, who reached popular fame with his 1993 book 'the McDonaldization

of Society) have explored the extent to which the 'prosumer' is indeed emerging in the 21st century through growing phenomena like the 'web 2.0' that is characterised by user-generated contents, self-service business models where the consumer provides free labour, participative design of user goods and the co-production of social, medical or environmental knowledge with end-users.

The disconnect between energy generation (often invisible and far away) and energy consumption (just press the button for now; cumulative bills will be sent to you much later) is recognised as a key reason why the problem of unsustainable energy systems has long been so poorly understood by large sections of society[1]. In energy research, attention for energy prosumers has grown hugely in the last decade, tracking the strong uptake of PV in the domestic sector; not only did PV become much cheaper, but also in many western countries the interest rates were so low since the 2007 financial crash that even with low government feed-in tariffs there was quite a competitive return on investment for homeowners buying PV panels. Many of the early experiences with energy smart meters and energy demand shifts in the home, were indeed related to meters that measured the production of electricity from domestic solar panels. For example Keirstead[2] reports 6% demand reduction as a result of people adjusting their electricity consumption to make the most of their domestic PV electricity production. This is a stronger effect than the one reliably reported from the roll-out of smart meters of energy consumption. Demand reduction is a key component in the transition to a low carbon society but in comparison to a switch to renewables, demand reduction is a rather difficult political sale; whilst governments have pursued the generation of renewable energy and the uptake of energy efficient technologies, they have been far more reluctant to try to persuade their citizens to consume less. The fuel protests in the UK in 2000[3] are a good case in point; the government caved in and reduced (environmental) taxation on fossil fuels for transport.

Some academics have criticised the popularity of domestic micro-renewables, pointing out that they do not always provide value for money (relative to other investment options in low carbon technologies). However the value of domestic renewables is not limited to direct emission reductions; as Bergman & Eyre[4] point out, much of the value is indirect; allowing people to engage with the energy system not merely as consumers but as energy citizens; taking low carbon electricity production into their own hand and engaging more critically with their own electricity consumption. In short, we can argue that the rapid growth of domestic energy prosumers has been an important case of early and voluntary adoption of (somewhat) more low carbon lifestyles, notably by a rather mainstream section of the population in terms of income (typically homeowners) and political orientation (attracting people from across the political spectrum).

So how can this success story of energy prosumers be scaled up? Scaling up has the dual potential of getting more people involved and of generating more renewable electricity. Barriers to wider adoption include income, home ownership and types of homes since you need your own roof. Another aspect is technological; what other prosumer technologies can enable a wider uptake and/or more demand reduction? Energy efficiency has a role to play at particular points of intervention, e.g. improve wall insulation during a home refurbishment or get a super efficient freezer or washing machine when the old inefficient one is breaking down. Smart meters can provide people with the baseline information and improved energy literacy to be able to recognise the overall cost effectiveness of making such investments.

This paper is seeking to draw attention to a different form of scaling up; namely energy prosumption beyond the domestic scale. Prosumption at the national or the 'whole energy systems scale' is fairly easy to conceptualise, but in this paper we are interested in energy presumption at a community, city or regional level. What scope is there for some geographical areas to generate much or all of their local energy needs through renewables? And are energy citizens living in such an area indeed willing (individually or collectively) to shift their energy demand to accommodate 'natural' variations in renewable energy generation? Would it not be possible to motivate people to consumer less energy if their region at that stage is faced with a shortage of renewable energy generation? The idea of living within our environmental means is not a new one and even in the electronic world of a 24/7 economy

and an indoor climate managed by a thermostat, we still have some social practices which are sensitive to the weather. For outdoor recreation the examples are plentiful but we can think of some household chores, e.g. doing the laundry on a day when you can hang the laundry outside to dry. `

Within the limited space of this chapter we explore the technical potential for (renewable) electricity prosumption at different sub-national levels. We do this by running a number of scenarios that focus on places characterised by a spatial concentration of energy consumption (motorways, cities) and/or by regulatory and societal barriers to wind energy projects (national parks, cities).

2. METHODOLOGY

We explore wind energy scenarios for different sub-national areas which could be the focus of energy prosumption. Our model that calculates these scenarios extrapolates the average wind speed, provided by the NOABL dataset[5] to the height required to the turbine being modelled. This extrapolated average speed at hub height is then entered into the model, where the Weibull distribution is applied to the figure. The Weibull distribution is an equation to calculate the distribution of wind speeds from an annual average wind speed figure. The power curve for the turbine being employed is entered into the model, with each m/s increment associated with the output that the turbine would produce. An air density factor, based on the elevation above sea level is then applied to the power curve and following this the power is multiplied by the wind probability in each m/s increment. All of these net outputs are multiplied to produce an average output power, which is then multiplied 8760 (the number of hours in a year) to produce a kilowatt-hours per year total. In the final part of the model the following factors[6] are applied: Machine availability factor 0.95, Grid availability factor 0.95, Transmission loss 5%, Array loss 0.90. Further to this a correction factor is applied to the REpower MM82 and Vestas V52 turbines of 31.405% and 32.025% respectively, following the validation process, which is described in more detail below. With this model any point location can provide an estimation of Annual Energy Output (AEO) for a particular turbine. This AEO is then multiplied by the number of turbines that can be suitably located in a 1km²; this provides that output for a 1km² grid cell. This model is run individually for each gird cell data point included in scenario being tested. With a total for each grid cell, the total can be summed together, which produces the total potential for any given area of land.

In this study three different types of turbine were used; the Vestas V90, the REpower MM82 and the Vestas V52 (Table 1).

Table 1: Wind turbines used in the scenarios

Turbine type	Capacity	Hub height used (m)	Blade diameter (m)	Swept area (m²)	Turbines pe 1km² cell
Vestas V90	3MW	80	90	6362	2.469
REpower MM82	2MW	69	82	5281	2.974
Vestas V52	850KW	60	52	2124	7.396

Validation was performed by creating a potential annual energy assessment for a location that already has a wind farm. The AEO made from the model was then compared to that actually produced by the wind farm. Table 2 below shows the validation for the three turbines used in this study. As can be seen, the turbine most accurately modelled is the largest of the three, the Vestas V90, with the other two models overestimating the potential energy from the sites. This

turbine is therefore used in the majority of subsequent comparisons and as a judge of wind energy potential. Furthermore this type of large turbine is a likely candidate for future development, as turbines have been growing in power and size over time. Based on this validation where the REpower MM82 and Vestas V52 are displayed in the results, a correction factor is applied based on the average percentage difference from the actual power generated; 31.405% for the REpower MM82 and 32.025% for the Vestas V52.

Table 2: Validation results

	Vestas V90: 3MW Aikengall Community wind farm	REpower MM82: 2MW Fairburn Estate wind farm	Vestas V52: 850KW turbine. Dun Law Extension wind farm
Average from turbines AEO	8,620 MWh	6,100 MWh	2,868 MWh
Multiplied by no. of turbines	137,920 MWh	122,007 MWh	100,409 MWh
Wind farm actual output 2012	143,485 MWh	70,018 MWh	64,544 MWh
Actual 2012 vs model output*	4.03%	-42.61%	-35.72%
Wind farm actual output 2013	150,845 MWh	97,364 MWh	71,967 MWh
Actual 2013 vs model output*	9.37%	-20.20%	-28.33%

*Calculated as: actual output exceeding model output by x%

The selected scenarios are designed to reflect possible future energy policies and to offer examples of the potential of wind energy. They are designed to be used as a yardstick before further negative analysis of the potential sites for wind farms is taken place. Table 3 below highlights each of the different scenarios with a short explanation. The model findings from the scenarios are presented and discussed in the Results section below.

Table 3: Wind energy scenarios for roads, cities and national parks.

Scenario	Rationale
Total for Scotland	National on-shore wind energy potential (theoretical maximum)
Total for England and Wales	Same as above, for England and Wales
Total Scottish national parks	Lost wind energy potential due to blanket restrictions on wind farms within national park territory.
Total English and Welsh national parks	As above
1km buffer along UK motorways	What if we concentrate wind farms along transport corridors (noisy eye-sores, used for fossil fuel consumption and air pollution).
Single turbine line along all motorways	As above, but a buffer of minimal thickness
1km of all urban areas in Scotland	Strong planning restrictions and public resistance to wind farms near towns; How much potential energy is lost by not developing these areas?
Edinburgh buffer	How wide would a buffer zone of wind farms have to be around the city for Edinburgh, for it to be carbon neutral in electricity use.
Bristol buffer	Same as above, for Bristol (allows comparison to Edinburgh).

3. RESULTS

Following validation different scenarios were tested against each model. We calculated how much wind electricity each area scenario could potentially produce with the Vestas V90, the REpower MM82 or the Vestas V52 wind turbines; the results are listed in table 4. Table 5 compares the findings from table 4 with different alternative/equivalent measures. For bench-marking purposes we use the amount of electricity generated by UK on-shore and off-shore wind farms, which is 12,121 GWh and 7,463 GWh respectively (2013 figures).

Table 4: Potential energy for each scenario using each of the turbines modelled

	Vestas V90		REpower MM82		Vestas V52	
	Total - TWh/y	Average - MWh/y	Total - TWh/y	Average - MWh/y	Total - TWh/y	Average - MWh/y
1km buffer along motorways	75.94	5,704.28	50.01	3,118.18	45.45	1,139.67
1km of urban areas in Scotland	330.17	6,932.06	197.37	3,557.66	188.53	1,366.59
Total English and Welsh Nat. parks	247.22	6,295.61	153.26	3,239.83	146.33	1,243.99
Total Scottish nati-onal parks	111.53	6,331.58	68.80	3,242.24	66.05	1,251.66
All of Scotland	1,394.66	7,441.66	856.24	3,792.62	823.40	1,466.72
All of England and Wales	2,022.92	5,905.71	1,267.91	3,072.74	1,200.8	1,170.28

Table 5: Annual generation potential for each scenario (using Vestas V90) with some benchmark comparisons

	Number of households (3,800KWh)	Drax power stations (26.2TWh)	Elec. consump-tion in London (39.9TWh)	UK electricity (364TWh)
1km buffer along motorways	19,985,376	2.9	1.9	0.21
1km of urban areas in Scotland	86,886,195	12.6	8.3	0.91
Total English and Welsh national parks	65,058,737	9.4	6.2	0.68
Total Scottish national parks	29,349,892	4.3	2.8	0.31
All of Scotland	367,015,547	53.2	34.9	3.83
All of England and Wales	532,346,197	77.2	50.6	5.56

(based on data from Department of Energy & Climate Change, 2013a; Department of Energy & Climate Change, 2013b; Department of Energy & Climate Change, 2013c; Department of Energy & Climate Change, 2014b; Drax Group plc, 2013)

1km around urban areas in Scotland

Following news articles where buffer zones are purposed around urban areas; (Cohen, 2013; Mason, 2013), this scenario examines the wind energy potential within just 1km of urban areas in Scotland. An ideal place for power generation as that ideally generation should be located close to where it is consumed. 330.17TWh could be produced in this 1km buffer which is 24% of the whole of Scotland scenario. England and Wales were not tested as an urban area buffer would result in most of the land area being covered.

National parks scenarios

In the UK, national parks have been off-limit for wind farm developments (only small and micro-wind turbines have been allowed). As such this scenario examines the potential lost by excluding these large parts of the national territory. The total potential for national parks in Great Britain is 358.75TWh per year, or 98.6% of the 364TWh total electricity generated by all sources in the UK in 2012 (Department of Energy & Climate Change). This potential which cannot be developed is a hidden cost to national parks to retain an "unspoilt" view. This is also equivalent to 28.4% more than the 257TWh produced by all European wind farms. This scenario assesses England and Wales national parks separately from Scottish.

England, Wales and Scotland (the whole island of Great Britain) scenarios:

In this scenario the total generating potential for Scotland, England and Wales is shown. With the development of these results most other scenarios can be quickly devised by clipping the resulting data points by the areas in the other scenarios. The total generating potential of 3,417.57TWh per year is the result from all of the land area of Scotland, England and Wales, excluding urban areas and areas over water. This is 106% of the total electricity generated from the 27 EU countries in 2009. This highlights the great potential of the wind, but also that the UK has some of the best wind in Europe.

Motorway scenarios

As noisy and visually unappealing places dedicated to transport that is dominated by fossil fuel guzzling internal combustion engines, motorways are uninhabited corridors of energy consumption where wind turbines are less likely to be heard or be perceived to be 'ruining' the view. The first motorway scenario examines the wind potential of a 1Km buffer around motorways. This area is used in this scenario to generate energy and could provide a huge amount, around; 75.94TWh per year, this is 8% more than all of the Nuclear energy generated in the UK in 2012.

The second motorway scenario locates wind turbines at a set distance apart alongside the carriageway. There is a total of 3,4987km of motorway in the UK and the Vestas V90 has a blade diameter of 90m. Each turbine is to be placed seven blade diameters apart, 630m. The result of this is 5554 points for turbines to be placed, 955 of these are discarded as they are found in urban areas, 36 above water were also removed and 14 have an average wind speed of zero according to the NOABL database (an error of some kind). This leaves 4549 turbines to be placed along the roadway. This is an enormous potential for electricity generation, exceeding the combined out put of onshore and off-shore wind (19,584GWh/year) by a third.

Another consideration for this potential source of electricity is the energy consumed by the vehicles on the motorways themselves. Motorways account for around one per cent of the road network in length, but carried 20.6 per cent of traffic in 2012 (Department for Transport). As a result reducing the carbon released by these vehicles would greatly help reduced the emissions of road traffic. Department of Energy & Climate Change (2013e) and Palmer & Cooper (2013) show that road traffic in the UK uses the equivalent of 39,468,000 tonnes of oil equivalent,

which is equivalent of 459TWh. Assuming that road traffic uses the same amount of energy on motorways as on other roads, and with 20.6% of this energy use is on motorways, this scenario implies an electricity production of 94.554TWh. If all this energy would be used to run electric vehicles, a total of 27.65% of the vehicle traffic on UK motorways could be powered by electricity generated along the road itself.

City buffer scenarios

Tables 11 and 12 show the results for a scenario which examines the size of wind farm required to alone power a whole city. If this wind farm was constructed in the form of a buffer around the city, how thick would the buffer have to be? The energy consumption statistics for UK cities was retrieved from (Department of Energy & Climate Change, 2013b; Department of Energy & Climate Change, 2013c). Two cities were examined in this scenario, Edinburgh and Bristol to provide comparison between different areas of the country. Both have similar populations; Edinburgh has a population of 476,626 compared to Bristol's 428,234, however Tables 13 and 14 indicate that Edinburgh consumes more energy than Bristol, in terms of both electricity and gas.

The results show that a wind farm buffer of 2km would be required in Edinburgh to cover the city's electricity consumption, compared to a wind farm buffer of 3km in Bristol, despite Bristol requiring 588.66GWh per year less than Edinburgh. This highlights the large disparity of wind speeds in the two different areas of the country, with average turbine output in Bristol only 74.69% of that of the average Edinburgh turbine at the 4km buffer. A wind farm buffer around Edinburgh of 2km could save 1,553,200 tonnes of CO2 and cost 26% less than an equivalent size scheme offshore, saving £92,719,529. For total power consumption which includes electricity and gas a buffer size of 7km is required in Edinburgh, a wind farm size of 468km². In Bristol the buffer of 6km would be required, with a wind farm size of 386km². This reflects the higher energy consumption in Edinburgh compared to Bristol. This may be due to the different industries in the two cities, Edinburgh's slightly higher population and due to Edinburgh's colder northern location. The buffers for each city are shown in Figures 1 and 2.

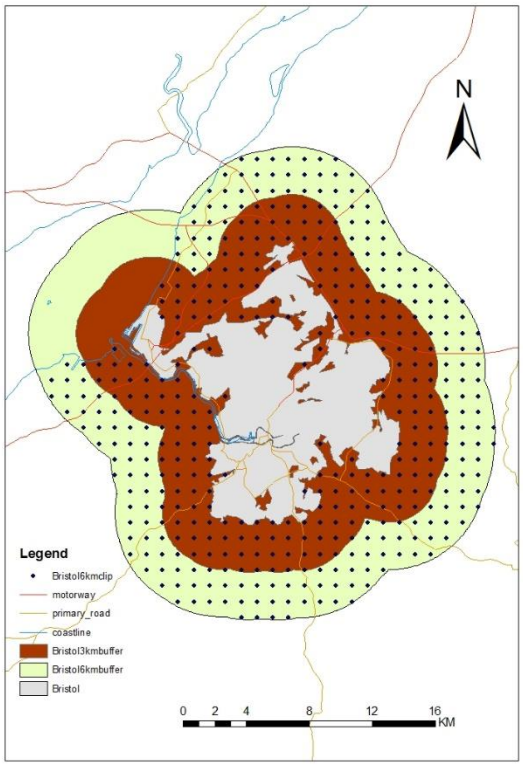

Figure 1: Bristol wind farm buffers

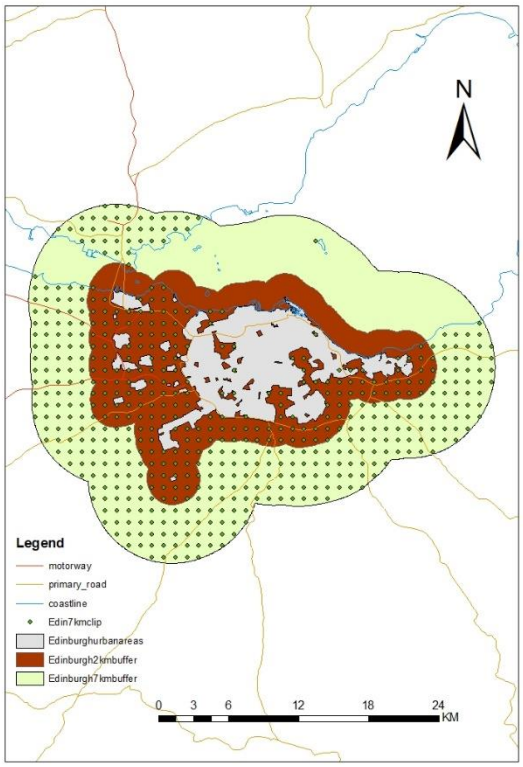

Figure 2: Edinburgh wind farm buffers

Table 6: Results for Edinburgh city buffer wind farm scenario

Buffer size (km)	Turbine average output (MWh)	Total wind farm output (GWh)	Percentage of Electricity	Percentage of Electricity and Gas	1km² of wind farm
10	7,385.78	13,203.22	530	181	724
7	7,229.66	8,229.32	330	113	468
6	7,239.52	7,007.14	281	96	397
5	7,258.28	5,985.84	240	82	338
4	7,312.79	5,001.59	201	69	277
3	7,235.39	3,983.93	160	55	223
2	7,076.36	2,952.85	118	41	169
1	6,870.16	1,713.30	69	24	100

Table 7: Results for Bristol city buffer wind farm scenario

Buffer size (km)	Turbine average output (MWh)	Total wind farm output (GWh)	Percentage of Electricity	Percentage of Electricity and Gas	1km² of wind farm
6	5,567.53	5,278.84	277	112	386
5	5,508.50	4,243.59	223	90	312
4	5,462.05	3,236.77	170	69	240
3	5,443.99	2,419.55	127	51	180
2	5,297.26	1,530.32	80	33	119

Table 8: Total energy consumed in Edinburgh an Bristol (Department of Energy & Climate Change, 2013b; Department of Energy & Climate Change, 2013c)

	Gas (GWh/y)	Electricity (GWh/y)	Total (GWh/y)
Edinburgh	4,796.45	2,493.15	7,289.59
Bristol	2,797.24	1,904.49	4,701.72

Emissions savings

One of the most important reasons in the uptake of renewable energy is the reduction of greenhouse gas emissions, especially CO2. Table 16 shows the amount of CO2 saved by each scenario using onshore wind power as opposed to the current UK power generation mix. Bassi, et al., (The case for and against onshore wind energy in the UK) indicates that wind energy generates between 8 - 20 gCO2/KWh (a figure of 14 gCO2/KWh is used to develop the table below), these carbon costs mostly occur during the manufacturing, transport, installation, operation and decommissioning of turbines. By comparison, the average emissions from power generation in the UK were around 540gCO2/KWh in 2008.

Table 9: Total Tonnes of CO2 saved instead of using current generation mix for each scenario

	Tonnes of CO2 saved/y
1km buffer along motorways	39,946,770
1km of urban areas in Scotland	173,668,126
Total English and Welsh national parks	130,039,404
Total Scottish national parks	58,664,564
All of Scotland	733,590,675
All of England and Wales	1,064,053,578

4. CONCLUSIONS

A demand reduction is a key challenge for developed countries seeking a transition to a low carbon society. The disconnect between electricity supply (far away, hidden) and demand is a key limiting factor to both public acceptance of renewables[7] (why so many, why so big, why here) and to voluntary demand reduction; i.e. we need to enable and encourage people to live more within the regional energy balance, however we chose to define 'region'. At the household level we see early evidence that prosumers are indeed changing their consumption in response to their own PV electricity production. Something similar needs to be stimulated at the regional level. Hence this chapter explores the idea of prosumption at intermediate levels; beyond individual households (where energy production potential is very limited) and below the national scale, where we already consider consumption and production simultaneously since that is the level at which we tend to study whole energy systems. Our scenarios illustrate that on-shore wind energy remains a hugely underutilised resources and that cities and build up areas and their immediate hinterlands have the potential to generate all of their annual electricity needs from locally sited wind turbines. We have created GIS maps to demonstrate and visualise much resource hinterland (in this case; areas covered in wind farms) cities like Bristol and Edinburgh would require to be carbon neutral in terms of annual electricity consumption. The point is not that these super concentrations of wind turbines around cities is necessarily the most appropriate form of renewable energy development, but rather that it is important for us to learn to relate our energy consumption to renewable energy production and recognise the big spatial footprint of renewables (which are spatially not well concentrated) so we can be motivated to significantly shift or reduce our demand whilst living more in harmony with what nature can provide us. The intermittent nature of renewables like wind or solar add an important dimension to this: The more renewables we have, the less frequently we will need to reduce our demand. In other words, the development of local to regional energy prosumption models implies that the more visible and nearby renewable energy technologies become, the more we can consume clean energy cheaply, provided that we are willing to shift our periods of high consumption towards our local sunny spells and windy days.

REFERENCES

[1] Van der Horst D. (2017). Energy landscapes of less than 2 degrees global warming. In: Calvert K. and Solomon B. (eds.) *Handbook on the Geographies of Energy*. Edward Elgar.

[2] Keirstead, J., 2007. Behavioural responses to photovoltaic systems in the UK domestic sector. *Energy Policy*, *35*(8), pp.4128-4141.

[3] Doherty, B., Paterson, M., Plows, A. and Wall, D., 2003. Explaining the fuel protests. *The British Journal of Politics & International Relations*, *5*(1), pp.1-23

[4] Bergman, N. and Eyre, N., 2011. What role for microgeneration in a shift to a low carbon domestic energy sector in the UK? *Energy Efficiency*, *4*(3), pp.335-353.

[5] This model was originally developed by the second author as a dissertation project (Stokes, 2014). Due to space limitations we cannot provide all parameters and references but a full technical report is available on request.

[6] Hossain, J., Sinha, V. & Kishore, V., 2011. A GIS based assessment of potential for windfarms in India. *Renewable Energy*, Volume 36, pp. 3257-3267;

[7] van der Horst, D., 2007. NIMBY or not? Exploring the relevance of location and the politics of voiced opinions in renewable energy siting controversies. *Energy Policy*, Volume 35, pp. 2705-2714

Paper KL5

MEASUREMENT-BASED OPTIMIZATION OF STRUCTURES FOR RENEWABLE ENERGY PRODUCTION

R. Höffer[1*], S. Tewolde[1, 2], H.-J. Niemann[1]

[1]Ruhr-Universität Bochum, Faculty of Civil and Environmental Engineering, Germany
[2]Airwerk GmbH, Germany
Corresponding author: R. Höffer, ruediger.hoeffer@rub.de

ABSTRACT

Model measurements and measurements in full scale at executed structures energy - so called Structural Health Monitoring (SHM) and Condition Monitoring (CM) - is a science and technology developed to monitor and assess the condition of aerospace, civil and mechanical infrastructures and their operation (here, plants for the conversion of renewable are considered) using sensor systems integrated into the structure. SHM is capable to detect, locate and quantify various types of damage in a structure like cracks, corrosion, delamination and loose joint. But also service-related items, such as temperatures, responses of machineries, output values and maintenance effects can be measured (CM). Nowadays the interest toward this technology in the field of renewable energy is increasing due the required economy, efficiency and performance of renewable energy plants. The paper informs about ongoing projects about a) SHM strategies at large off-shore plants, and b) a combined SHM and CM campaign at a physical, outside model of a solar chimney in Egypt. The potentials of model measurements to enable possible optimizations of structures and processes are described.

1. STUCTURAL HEALTH MONITORING OF LARGE OFFSHORE WIND ENERGY CONVERTERS

1.1. Introduction

Off-shore WEC are growing in size of the wind turbine, causing a structural fault or a downtime more important to avoid. Furthermore, off-shore WEC are installed in difficult places to reach, making the maintenance check more difficult to realize and therefore even more important.

Identification of the modal parameters of a full-scale operating wind turbine is particularly difficult, and a lot of researcher have been trying to developed suitable methods to tackle this problem (Carne & James 2010). Classical experimental modal analysis methods cannot be applied because the input force due to the wind cannot be measured. For this reason, Operational Modal Analysis (OMA) methods have to be used to identify the modal parameters from the response of the WEC in operation subjected to unknown random perturbations (Hermans & Van der Auweraer, Brinker et al. 2001, Camberghe 2004, Hoeffer et al. 2015, Bogoevska et al. 2016). The main goals of the monitoring system described in this section are the characterization of the wind turbine tower vibrations and the assessment of the structure's most relevant modal parameters, in order to evaluate its structural and detect eventual abnormal behaviors that may reduce its lifetime and or may imply maintenance activities.Finally, it is possible to estimate the residual life of the structure through fatigue analysis calculation, evaluating in more detail the safety years in operation of the WEC, see (Lachmann 2014).

Offshore wind energy source is becoming increasingly favorable because of its remoteness from people and a better wind source. But with increasing demand for wind energy, the supporting structures of wind turbines are also continuously getting bigger for higher power generation. Therefore, the Structural Health Monitoring (SHM) becomes necessary in order to evaluate the condition of the support structures for operational safety and functionality of the wind turbines.

The SHM is especially more critical for Offshore Wind Energy Converter (OWEC) structures, because of the extreme loading and environmental conditions they are exposed to; for this reason the BSH

(Bundesamt für Seeschifffart und Hydrography) requires that 10% of the OWECs from an offshore wind farm to be equipped with Condition Monitoring System (CMS) to continuously monitor the changes in structural vibration response.

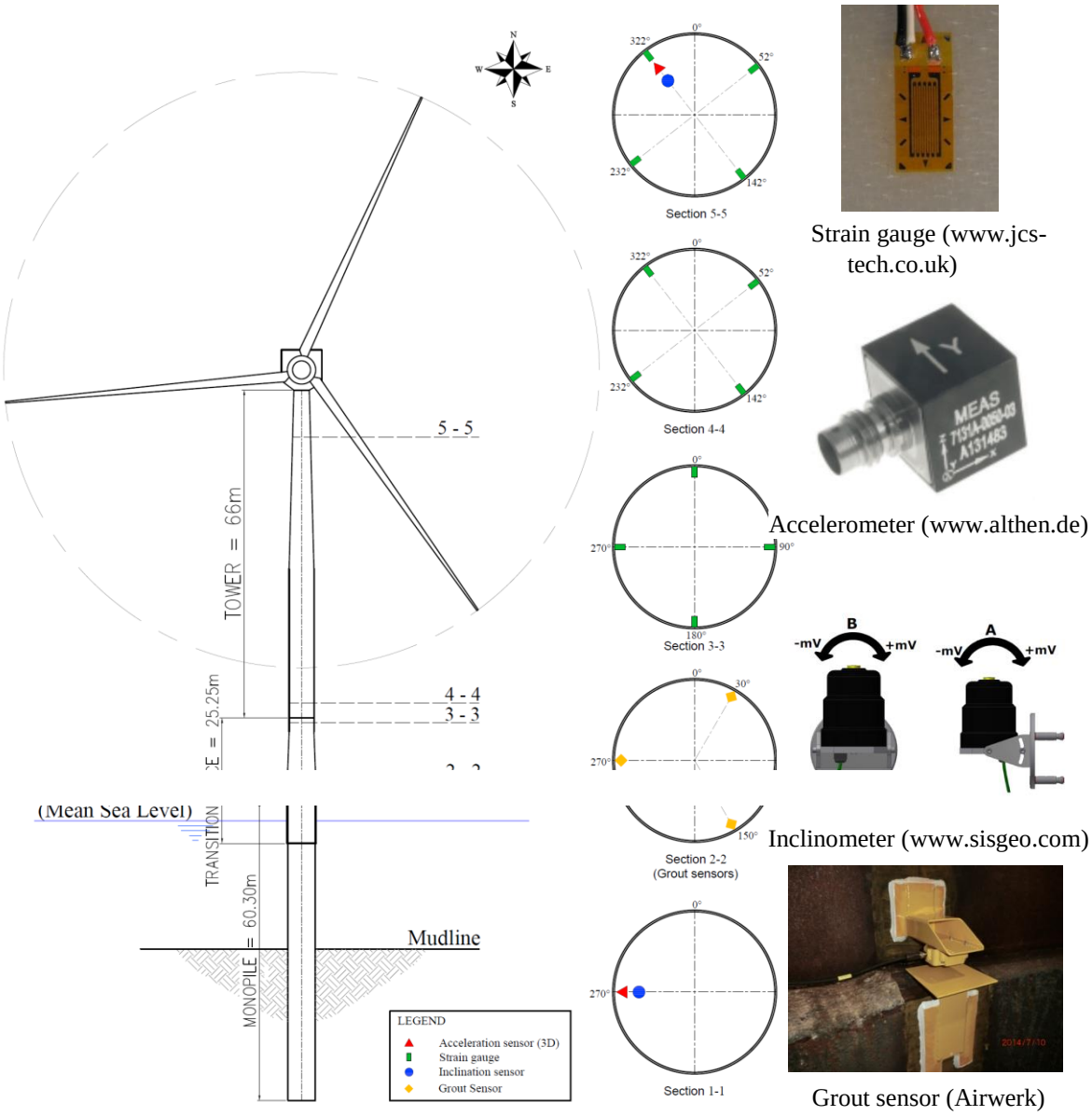

Figure 1.1: Typical sensor positioning for offshore wind energy convertors (Airwerk)

This is not only a benefit from safety point of view, but also from economical as well. The cost for maintenance is about 25 to 30% of the energy generation costs (Wind Stats 2006)and these costs are mainly spent on corrective maintenance (Wiggelinkhuisen et al. 2007). These very expensive costs (and sometimes very dangerous sea conditions) for inspection and maintenance works can be minimized or made when only needed (condition based) with the help of the results obtained from SHM by integrating them to the asset management for operation and maintenance decision making.

1.2. Sensors and delivered information

The main purpose of the strategic sensor positioning is to catch the changes in structural response and be able to tell from the changes in structural response, when deterioration or damage occurs. List of the

most common sensors and the information that can be obtained from them are listed in **Table 1.1** below. Figure 1.1 illustrates the in-situ application of different sensors.

Table 1.1: List of common sensors and available information

Sensor type	Information obtained (used for)
Accelerometer	**Natural frequencies, Mode shapes and Damping** Generally – Damage is inversely proportional to Natural frequency and directly proportional to damping.
Strain gauge	**Fatigue analysis** for remaining life time estimation
Inclinometer	**In Monopile** : Detect failure in foundation **In Transition piece and (or) Tower**: detect failure in grout connection (also as redundant to grout sensors)
Grout sensor	Failure in grout connection
Temperature	Environmental effect compensation

The data obtained from the inclinometers and grout sensors are directly compared to threshold alarm levels. Whenever these alarm levels are exceeded an automatic notification is sent to the responsible person in the form of an email or SMS. These alarm levels are set from designer's recommendation and early stage continuous monitoring (minimum one year) of the healthy structure. And the data obtained from accelerometers and strain gauges are further processed in order to be able to detect changes in structural vibration response, which leads to damage detection.

The response of a structure greatly varies for a particular weather condition and operation. Therefore, it is very important to consider the environmental and operational conditions of the wind turbine for correct and realistic data interpretation and decision.

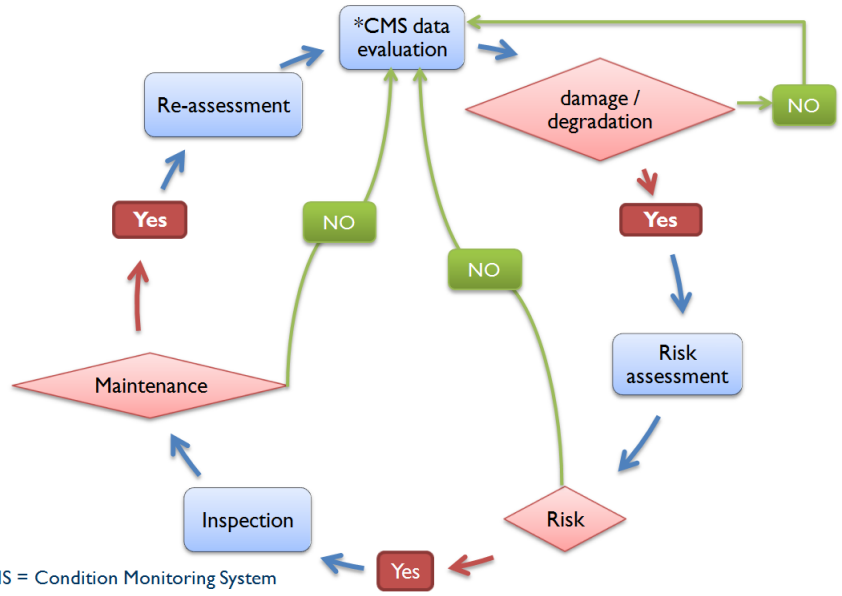

Figure 1.2: Incorporation of SHM in the decision making for inspection and maintenance planning (Airwerk)

1.3. Application

All data obtained from the condition monitoring system is interpreted in such a way that it assures the safe operation of the structure and aids the decision makers for inspection and maintenance planning of the wind turbines.

That is, instead of waiting for the damage until failure occurs and apply corrective maintenance, which is more expensive and most of the time needs stopping the operation of the wind turbines (with more down time), It is more preferable to implement preventive maintenance through SHM which can detect the damage during its initial stages or prevents the damage from deterioration trend monitoring. The scheme shown in figure 1.2 is cost effective and with minimum down time.

2. STRUCTURAL AND CONDITION MONITORING OF A SOLAR CHIMNEY

2.1. Introduction to solar chimneys for the conversion of updrafts

Some 25 years ago Professor Schlaich developed the idea of a power plant which uses the power of the upwind flow in a special chimney. Solar insulation drives the flow. He tested the conceptsuccessfully in a comparatively small scale facility in Spain. The obvious advantages of Schlaich's technology have stimulated various project ideas particularly in Australia but as well in Africa. The chimney dimensions range from 1000 m in height and 130 m in diameter up to 1500 m in height and a diameter of 280 m depending on the required power output of 100 to 400 MW (Harte et al. 2013). The chimney is basically a cylindrical tube designed as a concrete shell structure. The tower height is beyond present experience. Also, models for the wind load which, based provide safe and economic structures, are not tested. A prediction about the performance of the plant is also lacking every validation. Whatever input data is used, experimental campaigns in model scale are appropriate to the challenge of designing these outstanding structures and to optimize it with respect to its efficiency. In section 2, measurements at a 20 m high, fully functional model are described.

2.2. Application Case: Solar chimney plant at Aswan, Egypt

The solar chimney project in Aswan, Egypt, is initiated as one part of the Egyptian-German Research Fund (GERF) project. It is being built near the faculty of Energy Engineering, Aswan University. With an average high temperature of about 40°C for more than half of the year and average annual sunshine of about 4000 hours, which is close to the theoretically maximum annual sunshine hours, Aswan is one of the hottest and sunniest cities in the world. This climatic condition makes the city an ideal place for implementing solar energy harvesting projects from solar updraft tower.

2.3. Structure description

The solar chimney structure has a total height of 20.10m, which consists of an 18.60m high cylindrical steel tower structure welded to the top of a 1.50m high steel frame structure. The supporting structure is anchored to a reinforced concrete foundation (Fig. 2.1).

2.4. Sensor positions

An array of sensors was initially proposed, which was later revised due to financial constraints to fully implement it. Considering that this is a research project, the initially proposed concept was made, so as to allow for system redundancy due to the very high temperatures the sensors will be exposed to and to

enhance the reliability of the data by cross checking the response of more than one sensors when a significant structural change occurs.

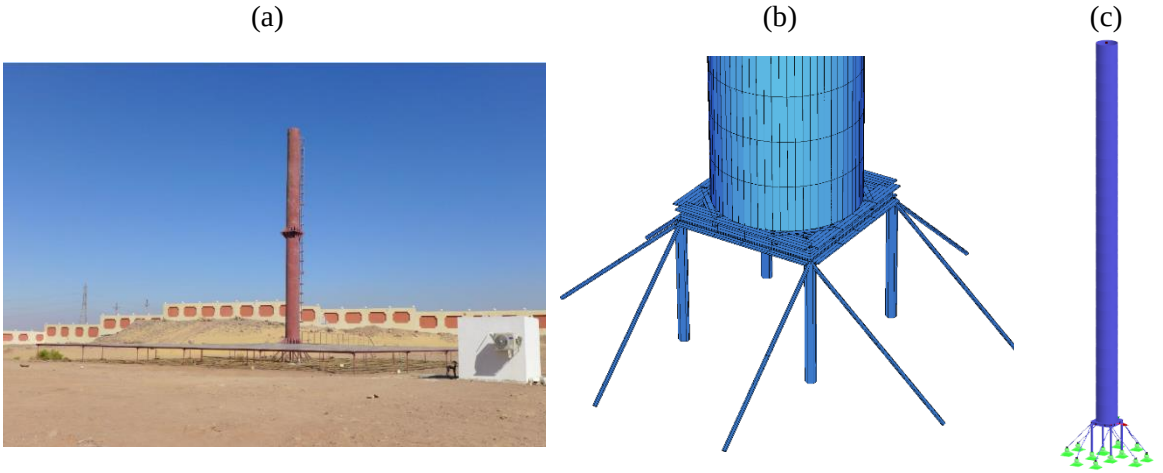

Figure 2.1: (a) Photo of the construction; (b) and (c) FE Models (Bergische Universität Wuppertal)

As shown in the latest revised sensor positions Fig. 2.2, the sensors used can be generally classified as structural and environmental sensors. Three 3D accelerometers are used; one at the top, one at the middle of the tower, and the third one on the top of the concrete foundation to measure ground motion from seismic activity. One 2D inclinometer is used at the top of the tower to measure inclinations. At the bottom of the tower structure, just above the stiffeners, three rosette type strain gauges are to be installed at an angle of 120° to each other, so that it is possible to compute the principal stresses, orientation of principal stresses, shear stress, and also to record the strain time history for fatigue analysis.

2.5. Implementation and expected results

After all the sensors are installed in position, all their channels are to be connected with the I/O modules inside the steel cabinet mounted on the outside surface of the tower (Fig. 2.2). All sensors are to be provided with adequate supports to protect them against physical and environmental damages. Cable routing is also to be done in consideration of the protection of the cables from damages that may result from exposure to extreme heat and physical forces.

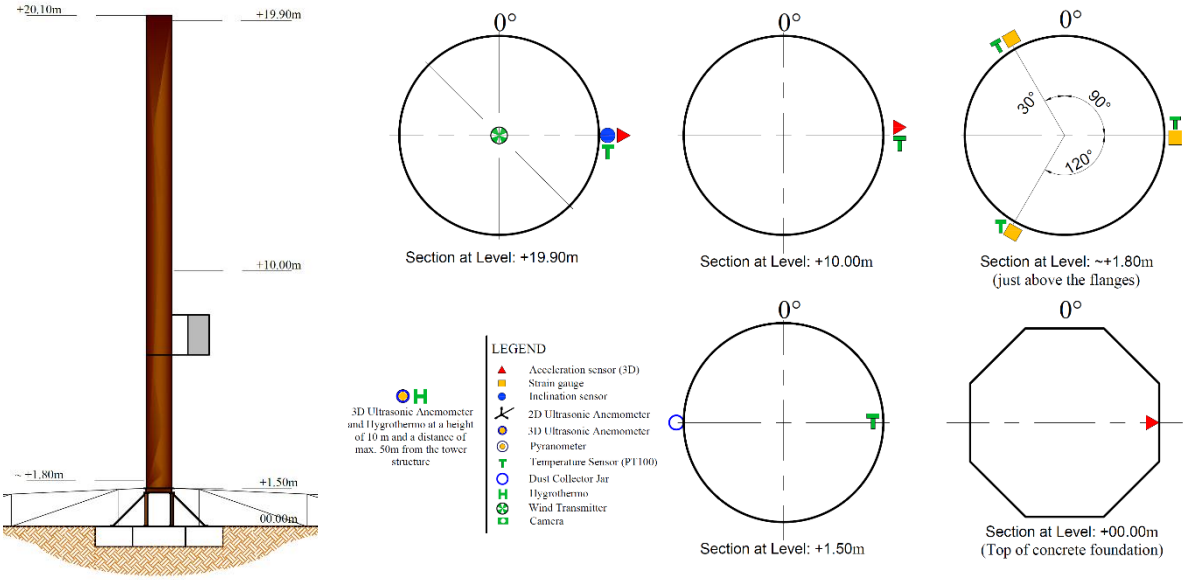

Figure 2.2: Sensor positions and layout

All the I/O modules are in turn connected to the controller (data logger) housed in the cabinet. Then finally, all the data is to be transferred to the computer inside the faculty of Energy Engineering, Aswan University (Fig. 2.3).

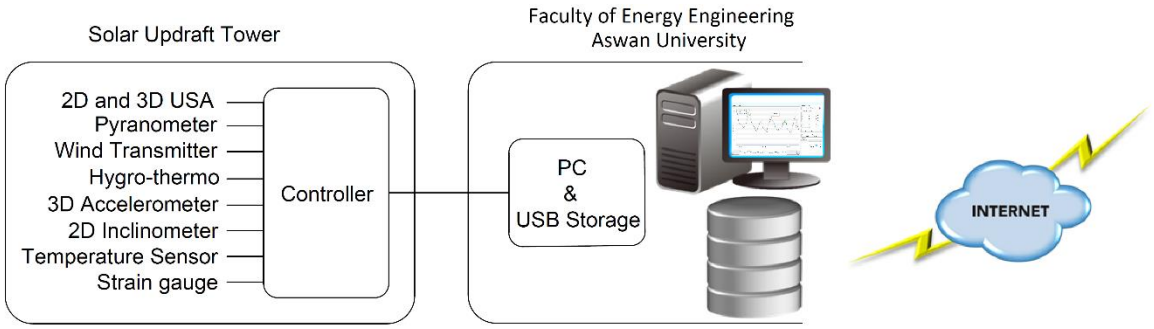

Figure 2.3: General overview of network diagram

This computer serves as a server where the monitoring data is stored. A web interface is also developed, which enables real time data visualization, along with the possibility to select particular channels to visualize - also with a possibility to download a selected data range. LAN ports are required on the server location (the university) for remotely accessing, manipulating and maintaining the data acquisition system.

The results expected from this monitoring system are the real time data visualization, including correlation of the responses from sensors among themselves and with environmental conditions. Also once the threshold limits are defined, an automatic alarm notification can be implemented which sends automatic notification by email or SMS. The data obtained from the accelerometers will be used to extract the modal parameters by using operational modal analysis technique, which makes use of only the output data. The strain time history data recorded by the strain gauges will be used to compute the principal stresses, bending moments and for performing fatigue analysis using the rain flow counting method (Höffer et al. 2015).

This Solar Chimney Project in Aswan, although it is a small scale research project, it can serve as an ideal experimental field for future commercial implementation of the already designed very huge solar updraft towers, some of them reaching up to a height of about 1000m and higher (Harte et al. 2013).

3. CONCLUSIONS

In order to build a reasonable but at the same time effective monitoring system that will capture all necessary phenomena, the optimization of types, number and strategic positioning of sensors, the required sampling frequency and quantity of recorded signals, as well as proper data storage tools and equipment need to be considered. In this paper, planning strategies, as well as preliminary data based estimates of the structural dynamics for two application studies of different real slender structures are discussed. The presented ongoing case studies are targeted at vibration based structural health monitoring strategies capable of delivering valuable information on structural changes by exploiting features extracted only from the measured vibration structural response. The focus of further research is at development of automated damage detection frameworks that will be able to alarm as soon as any

structural damages occur. In turn this allows taking timely action, minimizing the maintenance cost and down time of monitored systems.

Monitoring can be a qualified basis for continuous strength checking of the structure of wind converters. In recent years, structural elements of wind energy converters have been monitored in order to control and steer the blade and gear configuration during power production, to alert about dynamic overloading, and to detect dangerous conditions such as icing. New and modern monitoring concepts aim more at the identification of present or developing damages to provide an advanced estimation of the residual lifetime of the structure of the wind turbine. To this, the applied sensor systems for periodical and/or continuous monitoring are predominantly acceleration sensors, cycle transmitters, strain-gauges, and inductive displacement transducer, where the accuracy of such systems depends strongly on the local peculiarities. Previous sensor systems have mainly been used for sensing purposes within a specified recording concept. By contrast, relatively new applications employ optical displacement detectors or radar interferometers. Both devices are mostly based at an outside reference positions adjacent to the wind energy converter (WEC). The benefits of the structural health monitoring can be summarized as:

- Improve safety and functionality of structures
- Minimize number of Inspection visits and down time

Timely and cost effective maintenance

Service life time extension

New research aims at the detecting of detrimental alterations of system responses including the rotor, the transmitting power train, the gear mechanism, the generator as well as its interaction with the electricity network, and the load bearing structure of a WEC. To this end, the determination of clear indications for present damages or developing deteriorations using a remote observation data base is mandatory. A further target is the use of the sensing data for life cycle management strategies. In the future, special actuators will increasingly be employed as well to be able to instantaneously counteract excessive operational demands. Also, investments for surveying and maintenance of wind energy plants will follow the modern concepts mentioned above. It exists basic concept for the service and repair that can be applied to the structure of wind turbines. The demand is that repair and/or strengthening can be planned and conducted with minimized investments and losses of service time ensuring a reliable serviceability.

ACKNOWLEDGEMENTS

The support through the German-Egyptian Research Fund (GERF) granted by the German Federal Ministry of Education and Research and supervised by DLR (project no. IB023/AS-SO-CH), through the Innovative Training Network “Aeolus4Future” granted as a Marie Skłodowska-Curie action within HORIZON 2020, grant agreement no. 643167, are gratefully acknowledged. In addition, author SB is grateful for the doctoral research scholarships and travel supports provided by the Research School of Ruhr University of Bochum, by the SEEFORM Doctoral School (German Academic Exchange Service DAAD) and by the Civil Engineering Faculty of Skopje, Macedonia.

REFERENCES

Airwerk GmbH, Essen (www.airwerk.com)

Bogoevska S., Spiridonakos M., Chatzi E., Dumova-Jovanoska E., Höffer R., A novel bi-component structural health monitoring strategy for deriving global models of operational wind turbines. *Proceedings of the 8th European Workshop on Structural Health Monitoring,* Bilbao, Spain, 2016.

Brincker R, Zhang L and Andersen P.: Modal identification of output only systems using frequency domain decomposition, Smar Mat. St., 441–445, 2001.

Carne TG and James GH.: The inception of OMA in the development of modal testing technology for wind turbines, Mech Syst Signal Pr, 1213–1226, 2010.

Cauberghe B.: Applied frequency-domain system identification in the field of experimental and operational modal analysis, PhD Thesis, Vrije Universiteit Brussel, Brussels, 2004.

Harte R, Höffer R, Krätzig W B, Mark P and Niemann H. J., Solar updraft power plants, *Engineering structures for sustainable energy generation*. Engineering Structures 56 1698–1706, 2013.

Hermans L. and Van Der Auweraer H.: Modal testing and analysis of structures under operational conditions: industrial applications, Mech Syst Signal Pr., 193–216.

Höffer R.., Tewolde S., Bogoevska S., Baitsch M., Zimmermann S., Barbanti G., Monitoring based identification for structural life cycle management of wind energy converters, *Europe and the Mediterranean towards a sustainable built environment*, SBE16 Malta, 2016.

Hoeffer R., Tewolde S., Haardt H. and Bogoevska S.: Monitoring techniques for the detection of fatigue damages at Wind Energy Converters, WINERCOST Workshop‘Trends and Challenges for Wind Energy Harvesting’, Coimbra, March, 2015.

Lachmann, S.: Kontinuierliches Monitoring zur Schädigungsverfolgung an Tragstrukturen von Windenergieanlagen. Dissertation, Fakultät für Bau- und Umweltingenieurwissenschaften der Ruhr-Universität Bochum, 2014

Wiggelinkhuizen et al. - CONMOW: Condition Monitoring for Offshore Wind Farms, EWEA, EWEC 2007, Milan

Paper KL6

HARVESTING ENERGY FROM FLUTTERING STRUCTURES

Gianni Bartoli[1]* and Luca Pigolotti[1]

[1]CRIACIV @ Department of Civil and Environmental Engineering, University of Florence, Italy
Corresponding author: Gianni Bartoli, gianni.bartoli@unifi.it

ABSTRACT

Energy harvesting from flow-induced vibrations is an appealing recent research field. Several different systems are being investigated; after a critical review of the state of the art, two-degree-of-freedom flutter-based solutions seem to be the most promising. The present work includes some recent results obtained from both experimental and numerical analyses performed at CRIACIV (Interuniversity Research Centre on Building Aerodynamics and Wind Engineering), aimed at investigating the feasibility of a flutter-based harvesters. The critical condition and the response during the post-critical regime have been investigated, as well as the possible role played by turbulence. Collected results suggest the high potentiality of flutter-based generators, and a significant enhancement of performance can be envisaged.

NOMENCLATURE

η, α	=	heaving and pitching degrees of freedom
B, D, L	=	width, depth and length of the model (L)
ρ, ν	=	density ($M \cdot L^{-3}$) and kinematic viscosity ($L^2 \cdot T^{-1}$) of the air flow
I_η, I_α	=	heaving inertial mass (kg) and pitching inertial mass ($M \cdot L^2$)
S	=	static mass unbalance ($M \cdot L$)
$n_{\eta 0}$, $n_{\alpha 0}$	=	still-air heaving and pitching uncoupled frequencies of oscillations (T^{-1})
n	=	frequency during flutter oscillation (T^{-1})
$\xi_{\eta 0}$, $\xi_{\alpha 0}$	=	heaving and pitching ratio-to-critical damping (%)
x_e	=	position of the centre of elasticity, normalized to the section width B
x_m	=	position of the centre of mass, normalized to the section width B
μ	=	ratio between the masses of model and a virtual moved air
r_α	=	radius of polar inertia, normalized to the section width B
γ_n	=	frequency ratio in still air of the uncoupled modes of pitching to heaving
X	=	squared ratio of pitching still-air frequency to flutter frequency
$U_{R\alpha}$	=	reduced flow velocity
$\hat{\eta}$, $\hat{\alpha}$, $\hat{\phi}$, $\hat{n}$	=	heaving and pitching amplitude of oscillations, phase difference and frequency of the motion

1. INTRODUCTION

'Energy harvesting' is the process by which energy is derived from external alternative sources (e.g., solar power, thermal energy, wind energy, salinity gradients, kinetic energy), captured, and stored for providing power. Suitable systems can be developed in order to extract energy from small-scale sources, which are present as ambient background and are free, providing power for low-energy networks. Recent

developments in the field of flow-induced kinetic energy involve systems that exploit vibrations produced by aeroelastic phenomena and water-induced motions.

This is without any doubt a very attractive technique, first of all for a wide variety of applications for self-powered micro-systems: examples are wireless sensors, monitoring devices, structure-embedded instrumentation, remote stations, etc. Furthermore, the devices exploiting dynamic instability, such as classical flutter, are considered to be very promising for their simplicity of operation principle and powerful motion. However, the large-amplitude-oscillation regime entails several scientific aspects that should be solved yet. Indeed, reliable predictive models for the post-critical behaviour are still developing, being feasible to perform stability analyses mainly. Therefore, the study of flutter-based systems usually involves computational simulations or experimental investigations, although requiring specific design of both setups.

In the present work, after an overview of the energy harvesting systems with a focus on the main flutter-based solutions, the most important results obtained at CRIACIV (Interuniversity Research Centre on Building Aerodynamics and Wind Engineering) are discussed.

2. HARVESTING ENERGY FROM DYNAMIC FLUID-STRUCTURE INTERACTION PHENOMENA

In the common practice of wind and aeronautical engineering, dynamic fluid-structure interaction is considered as a dangerous phenomenon, and the design of structures prone to flow-induced vibrations usually focuses on limiting any excursion in the post-critical range. Several aeroelastic phenomena can arise when slender structures are excited to produce cross-flow, self-induced aerodynamic loads with important nonlinear effects. In some cases, the following Limit Cycles of Oscillations (LCO) can exhibit limited amplitudes in a range of flow velocities, as in case of vortex-induced vibrations, or unrestricted LCO with the flow velocity after a critical threshold, as in case of galloping and flutter.

From a different perspective, recent studies on alternative energy production showed the possibility of exploiting fluid-elastic instabilities to capture the flow energy and generate electricity. As an alternative to conventional wind turbines, it is possible to exploit the flow-induced large oscillations at the steady-state to recover energy from the flow through suitable energy conversion apparatus that are able to convert the vibrations into usable power.

Usually, electricity is the final output, and different conversion methods can be applied based on (*e.g.* [1]): (i) electrostatic induction; (ii) electromagnetic induction; (iii) piezoelectric effect. When any transducer is activated, it produces a backward coupling to the mechanical system. This is particular important in the case of piezoelectric transducers, for which the analysis should consider the whole electro-mechanical interaction, while the energy conversion process can be preliminary modelled through additional mechanical damping in the case of electromagnetic induction (*e.g.* [2,3]).

The first studies investigated torsional flutter of non-aerodynamic cross sections [4] while recently wings have been analysed too [5]. The main achievement is dated 1981 and it was reached by McKinney and DeLaurier [7], where an oscillating wing in vertical motion with harmonically prescribed pitching angle (without elastic support) showed competitive efficiency with respect to traditional dam-turbine systems. The technology was then gradually optimized by numerical investigations [7,8]. Higher efficiency was obtained by Isogai *et al.* in 2003, when elastic supports were introduced in the heaving degree of freedom with prescribed pitching oscillatory motion [9,10]. Flapping of rectangular prisms in air was investigated in 2006 [11], and some alternative concepts were studied too [12-14]. Other systems were explored in 2010-2011 considering the flutter oscillations of multibodies [15,16]. The research also focused on flapping foils in water. Experiments demonstrated the hydrodynamic conversion efficiency of foils undergoing harmonic pitching and heaving motions [17], also with continuously controlled parameters [18]. Deeper numerical investigations [19] were performed, and the possibility of multiple arrangements [20] was recently investigated.

In 2008 an alternative promising idea was developed: harvesting through a cantilevered flexible plate in air axial flow [21] was firstly considered. The issue of the fluid-solid-electromagnetic coupling optimization was also faced [22-24].

The first system based on vortex-induced vibrations is dated 2001 [25,26] and dealt with a membrane ‘eel’ in water, placed behind a bluff body. In 2008, Bernitsas *et al.* received the patent for the VIVACE

prototype [27] based on lock-in of cylinders in water. Recently, theoretical investigations have been conducted on the parametric space [28], on the continuous-option of tensioned cables [29] and on the optimal resonant conditions [30].

About galloping, only in-air systems were considered so far: in particular, the wake galloping of two circular cylinders in a tandem configuration [31,32] was studied, while Barrero-Gil *et al.* approached the transverse galloping of a bluff cylinder [33], both showing little efficiency.

For the sake of completeness, it is worth mentioning that very particular solutions were recently explored (*e.g.* [34-37]).

In the following, some of the proposed solutions for flutter-based generators are analysed in more details. Often, comparison will be done according to the values of the so-called 'extraction factor', which represents the ratio between the power related to the aeroelastic loads and the flow power.

If compared to the one adopted for rotary wind turbines, the available flow power can be identified as that of the flow passing through the area swept by the oscillating body; thus, applying the equations of mass, momentum and mechanical energy conservation in this control volume, the Betz analysis of oscillating systems defines the theoretical maximum extraction factor (equal to $16/27 \approx 59\%$). In some theoretical cases, e.g. two devices in a tandem configuration, the limit value may be overcome, due to the effects of diffusion of unsteady momentum and kinetic energy across the time-averaged boundaries.

3. AN OVERVIEW OF FLUTTER-BASED GENERATORS

3.1 Fluttering Membranes

During 2007-2009, the idea of 'flutter windmill' was developed by Tang *et al.* [21,38]: a cantilever flexible plate in axial flow in which the energy conversion considered electrostatic transducers placed along the plate (Fig. 1). Numerical and experimental investigations were conducted, and the predicted extraction factor was about 10%.

Dunnmon et al. [39] and Doaré and Michelin [22] introduced piezoelectric patches, directly installed along the plate. In this case, the system can be designed to achieve a global resonant condition, occurring when the characteristic time of the electric circuit is close to that one of the mechanical system. The optimization of the piezoelectric distribution along the plate allowed to achieve a maximum extraction factor around 20% ([23,24]).

3.2 Flapping Foils

In 1981, the 'wingmill' was the first generator based on the flapping mechanism in an air-flow [6,40]. The system (Fig. 2-left) was a wing model oscillating in vertical motion driven by a prescribed pitching angle, without any elastic support. It was theoretically and experimentally studied, and an extraction factor around 17% at low wind-speed was found. Further numerical and experimental studies showed that efficiency could be increased when both pitching and heaving motions were mechanically driven. In the case of a NACA-0012 hydrofoils, the extraction factor achieved about 35% when imposing a motion phase of 90° and an heaving amplitude of 1.23 times the section chord [18].

An alternative solution for 2-DoF flapping systems was conceived in 2003 by Isogai *et al.* [9], who introduced for the first time an elastic suspension in the translational DoF (Fig. 2-right), developing semi-active (or semi-passive) systems. The rotational DoF continued to be externally driven, in particular prescribing frequency and maximum amplitude, while the translational amplitude was naturally adjusted according to the lifting load. After parametric numerical analyses and optimizations, a maximum extraction factor around 32% was predicted [10].

Zhu *et al.* ([19,41]) worked on a model with a pitching actuator and a damper support (without stiffness) in the heaving DoF, the latter simulated the energy extraction process. The energy extraction at low values of the reduced flow velocity depended on the imposed pitching amplitude. An optimal value of the damping coefficient was found, achieving a maximum extraction factor around 20% when the elastic axis is close to the hydrodynamic center of pressure.

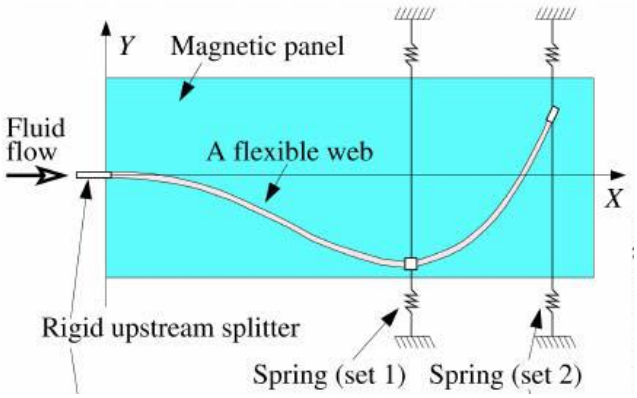

Figure 3. The conceptual design of a flutter-mill (from [21]).

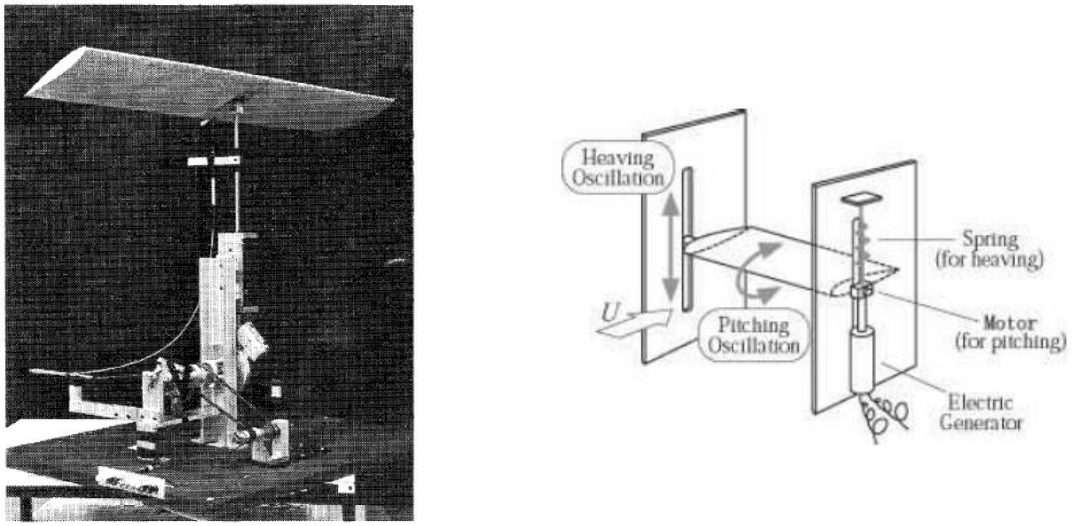

Figure 4. Left: the "wingmill" apparatus (from [6]); right: the concept of flapping wing generator (from [9])

Over the years, more complex solutions were also proposed. A tandem configuration of flapping wings, placed at a certain distance in the streamwise direction and oscillating in quadrature thanks to a specific mechanical device composed by supporting arms and gears, was experimentally studied in water flows [42]. A favourable interactions between downstream foil and wake vortices lead to theoretical extraction efficiencies up to 63%, if estimated for the ensemble of foils.

Very recently, a NACA-0015 model with a flexible tail attached at its trailing edge (Fig. 3) was studied as a possible solution to enhance the performance [43]. As compared to the case of rigid tail, a highly flexible tail can improve the performance, since the lifting load is increased due to the tail participation in the vortex-shedding mechanism.

Flapping bodies with cross section different from the airfoiled shape were investigated only by Matsumoto *et al.* in 2006 [11], who applied the concept of Isogai and co-workers to rectangular cross sections with 5 and 20 width-to-depth ratios. The results demonstrated that the energy extraction in the heaving motion is more rentable.

3.3 2-DOF fluttering devices

Solutions specifically based on the classical-flutter phenomenon were investigated only starting from the period 2009-2011. Bryant and Garcia [16,44] preliminary explored the exploitation of aeroelastic vibrations of a NACA-0012 wing model attached to a cantilever beam with embedded piezo-patches (Fig. 4), and predicted high extraction factors in the range of 32-42%.

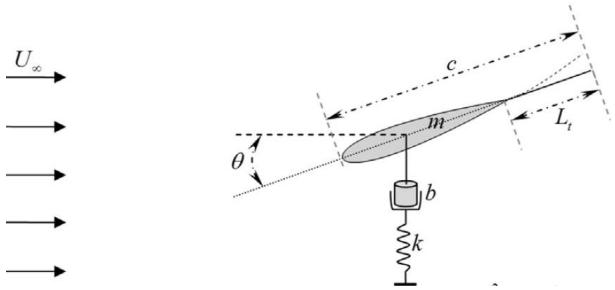

Figure 5. Flexible tail attached at the trailing edge of a foil (from [43]).

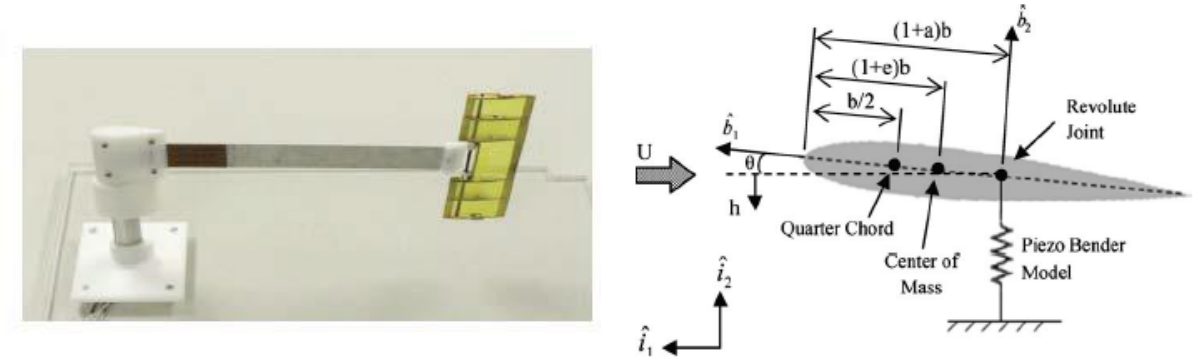

Figure 6. Model tested and schematic of the aeroelastic harvester (from [44]).

Successively, Ertuk *et al.* [12] experimentally investigated the theoretical critical condition for a 2-DoF sectional model of an airfoil with piezoelectric transducers embedded in the supporting elastic structures, activating the energy extraction in the heaving DoF. They investigated the possible role played by nonlinearities inserted in the model, such as a free-play gap (discontinuous stiffness, with a null value in a finite range about the rest position, producing a bilinear behaviour) in the pitching DoF. They also considered a cubic hardening rotational stiffness, in order to anticipate the instability onset and to limit the growth of the oscillation amplitude with the flow speed [45].

Progressively, the same research team discussed the capability of energy production through two different conversion methods, namely piezo-elements, as in the previous cases, and/or electromagnetic transducers in the heaving DoF [46,47]. Linear analyses were conducted by varying several governing parameters, outlining sensitivity maps about the critical condition.

Between 2012 and 2014 further researches were conducted by Abdelkefi *et al.* ([48,49,50]). They explored several similar problems about piezo-aeroelastic wing models, again controlling the role played by nonlinearities and investigating the possibility of anticipating the critical threshold through a suitable choice of the nonlinear pitching/heaving stiffness.

A particular case of flutter-based system was developed by Peng and Zhu [51]. Numerical investigations were conducted on a rigid hydro-foil supported by a spring in the pitching DoF and just a damper in the heaving DoF. An extraction factor of 20% was estimated in optimal conditions.

On the whole, it can be said that 2-DOF fluttering devices are promising because, differently from active or semi-active flapping mechanism as those explained in § 3.2, they experience spontaneous oscillations and their operation can be controlled by suitably designing the governing parameters, as it will be better described in the next paragraphs.

4. CRIACIV EXPERIENCE ON 2-DOF FLUTTER-BASED GENERATORS

CRIACIV wide experience on aeroelasticity motivated and provided the expertise for facing the classical-flutter phenomenon from the energy harvesting point of view [52]. This section summarizes the main results obtained during the last years of research activities on this topic [53-56].

4.1 Parametric linear analyses

The typical 2-DoF flutter system is sketched in Fig. 5, which represents the motion of a sectional model. It considers an elongated rectangular cross section performing transverse (or heaving, η) and rotational (or pitching, α) oscillations about the elastic axis (CE), the latter located at a distance $x_e \cdot B$ from the mid-chord (B is the section chord). Stiffness and damping properties and polar inertia (I_α) are referred to the elastic centre, while heaving inertia (I_η) is referred to to the centre of mass (CM), which is located at a distance $x_m \cdot B = S/I_\eta$ from the former (S is the static mass unbalance).

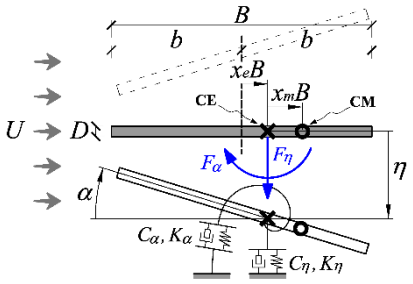

Figure 7. Schematic of the two-degree-of-freedom flutter problem (from [53]).

Moreover, in addition to the ratio-to-critical damping coefficients of heaving $\xi_{\eta 0}$ and pitching $\xi_{\alpha 0}$, the other dimensionless parameters that play a role in the flutter problem are: the mass-ratio $\mu = 2I_\eta/\rho B^2 L$ (being L the model span and ρ the flow density); the still-air uncoupled frequency ratio $\gamma_n = n_{\alpha 0}/n_{\eta 0}$ (being $n_{\alpha 0}$ the pitching and $n_{\eta 0}$ the heaving frequency in still air); the polar inertia radius $r_\alpha B = \sqrt{I_\alpha/I_\eta}$; the normalized form of the flutter motion frequency $\sqrt{X} = n_{\alpha 0}/n$ and the normalized flow speed $U_{R\alpha} = U/n_{\alpha 0}B$.

The analytical linearized model of Theodorsen was used to describe the aeroelastic loads at the instability condition as described in [53,54], solving the flutter problem in the frequency domain.

This analytical approach was used to parametrically explore the stability of the system, testing several sets of governing parameters in order to identify optimal conditions for energy harvesting. Indeed, one of the main goal is to design configurations with as low as possible critical flow speed so to anticipate the cut-in, thus enhancing the operative range and the device performance [54]. Moreover, the power conversion process extracts energy form the fluid-structure system by inducing an equivalent damping into the mechanical system. Thus, the understanding of the system response to increments of the heaving damping is of crucial importance [54].

Key parameters for lowering the critical flow speed are the position of elastic and mass centres, as clear from Fig. 6. In particular, a small mass unbalance downstream of the mid-chord ($x_m \approx 0.06$) produces a local minimum of critical reduced velocity, and it is also fundamental to foster the instability in the presence of a high heaving damping. On the contrary, the optimal position of the elastic axis depends on the heaving damping level, that is on the operative condition of the device, moving toward the upstream quarter-chord as $\xi_{\eta 0}$ increases.

4.2 Experimental setup for large-amplitude oscillations

Experimental tests were conducted in the open-circuit, boundary layer wind tunnel of CRIACIV, in Prato, Italy. The details of the setup have been described in [55].

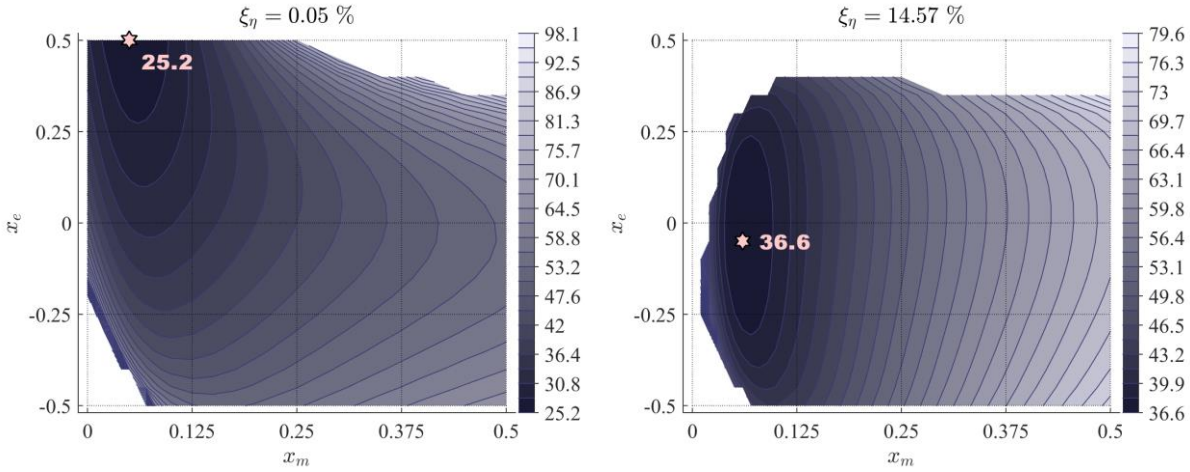

Figure 8. Critical-reduced-velocity maps as a function on mass centre (x_m) and elastic axis positions (x_e), for different levels of heaving damping ($\xi_{\eta 0}$). The other parameters are: $\xi_{a0} \approx 1\%$, $\mu \approx 1400$, $r_a \approx 0.4$, $\gamma_n \approx 1.24$). Figures from [53].

The steel model had a rectangular cross section with sharp edges and it was 100 mm wide (B) and 4 mm deep (D), the smaller dimension being the one facing the wind. The free span of the model (L) was 1004 mm. The model was installed in a peculiar aeroelastic setup (Fig. 7), which was specifically designed to allow large amplitudes of oscillation with linear mechanical parameters.

The heaving elastic suspension was composed by two pairs of leaf springs (shear-type frames) combined with fours coil springs. Each frame was equipped with a clock spring to provide the elastic suspension in the pitching component. Moreover, the model axis was connected to the elastic supporting frames by means of radial ball bearings, in order to decouple the two degrees of freedom. The connection of the flat plate to the end tube allowed to control the position of the elastic centre, while two rocker arms fixed to the model axis were devised to vary the mass centre by adding calibrated masses. The suspension system was sheltered from the flow by means of two screens having a nose following the geometry of a NACA0020 profile.

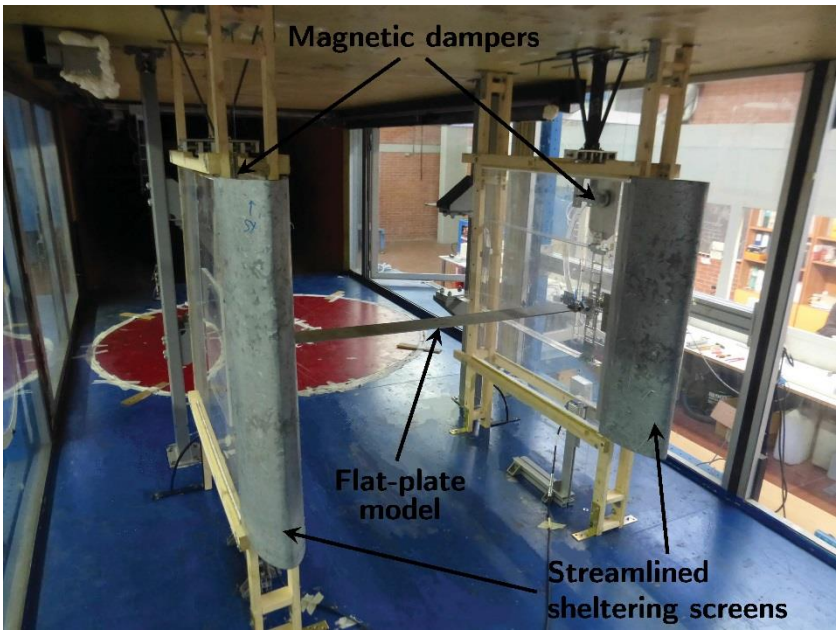

Figure 9. View of the aeroelastic setup inside the wind tunnel.

The motion was recorded through laser displacement transducers and accelerometers, and the sampling frequency was 2000 Hz. The stiffness linearity of the aeroelastic setup, both in the pitching and heaving degrees of freedom, was verified through static tests [55]. For each configuration, free decay tests were performed in still air for different initial conditions, to evaluate the natural frequencies of oscillation ($n_{\eta 0}, n_{\alpha 0}$) and the ratio-to-critical damping coefficients ($\xi_{\eta 0}, \xi_{\alpha 0}$).

Damping devices, based on the eddy-current dissipation generated on an aluminium plate moving between a pair of circular permanent magnets at close distance, were installed to introduce linear viscous damping in the heaving component. Therefore, increments of $\xi_{\eta 0}$ (up to about 18%) simulated the operation of a conversion apparatus.

The tests were conducted both in smooth flow (turbulence intensity lower than 1%, [55]) and in homogeneous turbulence conditions [56]. The mean flow speed was measured through a Prandtl tube installed upstream of the model and corrected through known flow maps to infer the velocity at the model centreline. The Reynolds number (defined as $Re = UB/\nu$, with $\nu = 15$ mm^2/s) during the tests was in the range 33,000 to 107,000.

4.3 Large-amplitude response and the (possibly) destabilizing effect of damping

The large-amplitude regime of oscillation is described in terms of heaving and pitching amplitudes of the equivalent harmonic motion, namely $\hat{\eta}$ and $\hat{\alpha}$, the oscillation frequency $\hat{n}$ and the pitching-to-heaving phase angle $\hat{\phi}$. The results presented hereinafter refer to configurations contained in [53,55], with different frequency ratio (γ_n) and a small mass unbalance downstream of the mid-chord ($x_m = 0.06$); the elastic axis is always located at the upstream quarter-chord ($x_e = -0.25$). Furthermore, for all cases the other governing parameters are: $\xi_{a0} \approx 1\%$, $\mu \approx 1400$, $r_a \approx 0.4$.

As a general comment, Fig. 8 shows that the large-amplitude response ensuing from the classical-flutter instability is characterised by a marked sub-critical bifurcation (the critical condition is identified through the vertical dashed lines, while full and empty markers describes respectively points with increasing and decreasing flow speed). It is apparent from Fig. 8 that the system with $\gamma_n < 1$ shows markedly larger amplitudes for the low damping level, if compared to the similar case with $\gamma_n > 1$. Indeed, the frequency ratio strongly influences the characteristics of the motion, also in terms of pitching-to-heaving phase difference, which indicates an opposite-phase motion for $\gamma_n < 1$ and an in-phase motion for $\gamma_n > 1$. Clearly, in both cases the system could oscillate in the subcritical regime down to flow speeds about 0.6 times lower than the critical one, when either reached from stable oscillations at higher amplitude or triggered from rest with initial conditions large enough to cross the unstable solution branch.

It is commonly expected that increments of damping lead to system stabilisation, postponing the critical condition and reducing the flow-induced effects. This is confirmed by the results for configurations with $\gamma_n > 1$ in Fig. 8. By contrast, a destabilizing effect of heaving damping can arise for other sets of the governing parameters, and in particular for configurations with frequency ratio significantly larger than unity [53]. This behaviour is shown in Fig. 8 for the configurations with $\gamma_n \approx 1.2$: the system became more unstable when increasing the heaving damping up to about 15%, anticipating the instability threshold (vertical dashed lines). Moreover, while the heaving amplitudes of oscillation were practically unaltered, the pitching components were markedly enhanced.

4.4 The role of turbulence

The turbulence effects were preliminary discussed in [56]. The configuration investigated was the one with $\gamma_n > 1$, which showed the largest oscillation amplitudes in the smooth flow case [55]. In the wind tunnel, the homogeneous turbulent flow was produced by a large-size grid placed at a distance of 3.6 m upstream of the model. This arrangement produced a longitudinal turbulence intensity of $I_u = 15\%$ and an integral length scale of about $1.8B$.

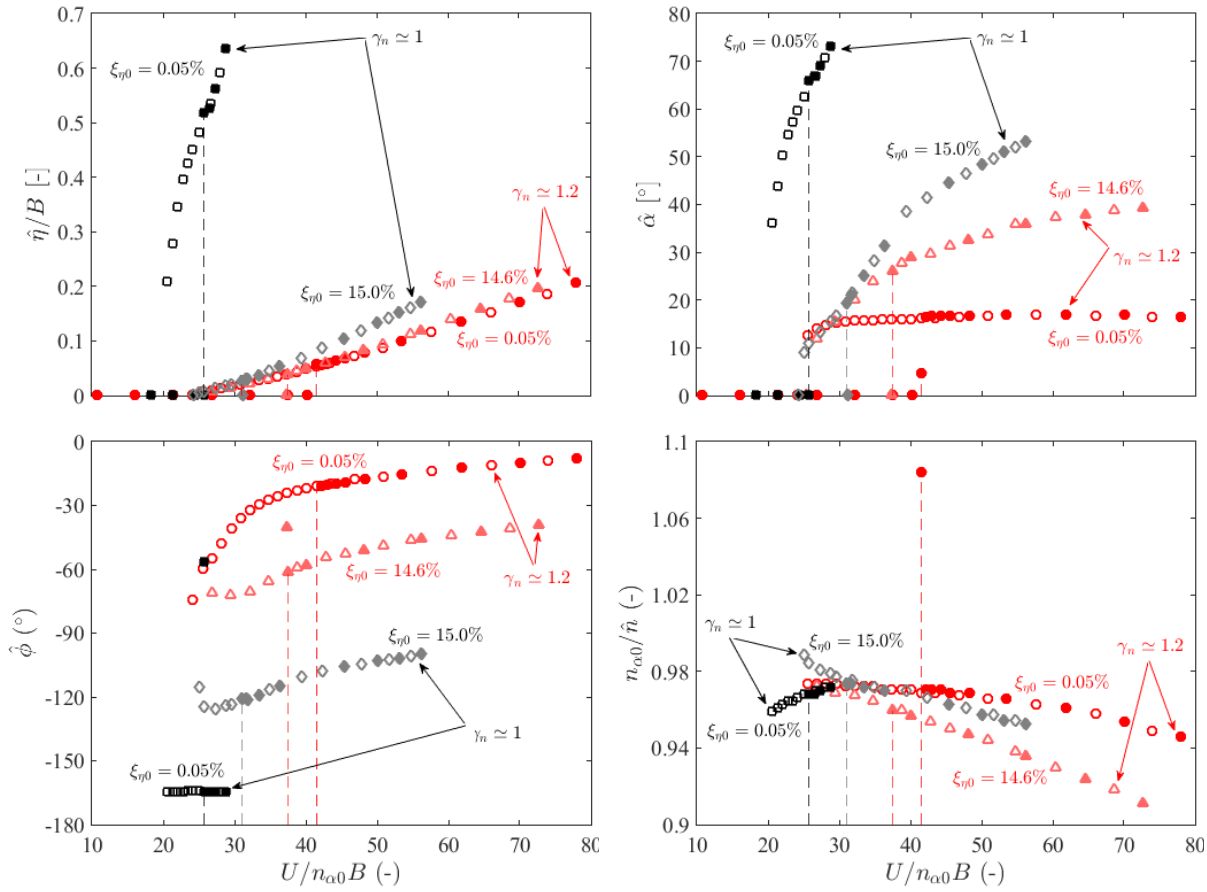

Figure 10. Amplitude-velocity diagrams of heaving, pitching, phase difference and frequency during large-amplitude oscillations, for different levels of heaving damping ($\xi_{\eta 0}$) and frequency ratio (γ_n).

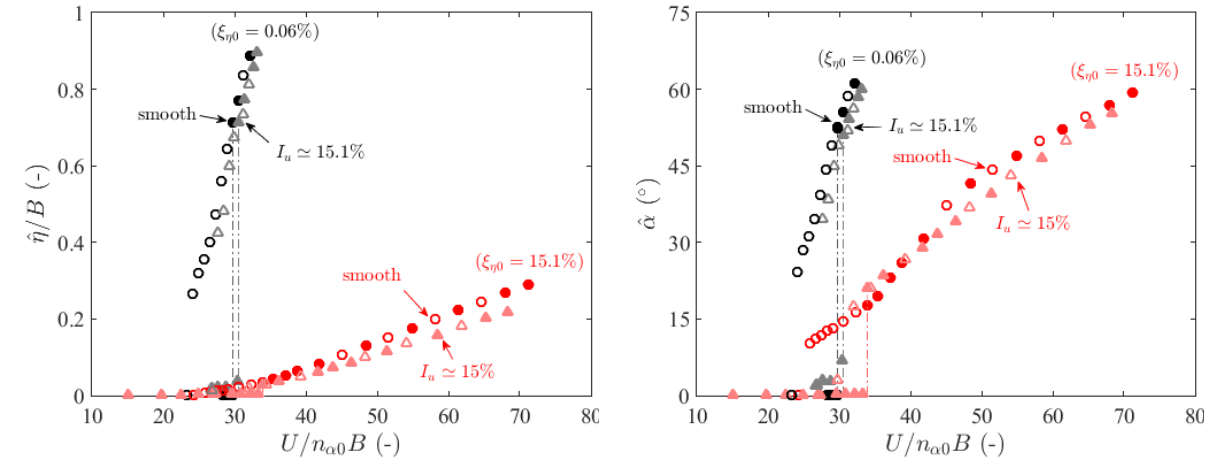

Figure 11. Amplitude-velocity curves for configurations with a still-air frequency ratio lower than unity ($\gamma_n = 0.93$) and different heaving damping ($\xi_{\eta 0}$), when subjected to different turbulence conditions.

The amplitude-velocity curves shown in Fig. 9 point out that the free-stream turbulence seems to affect very little the system response. Indeed, the self-sustained motion still occurs with amplitudes that are very similar to those of the smooth-flow case, and the instability threshold is only slightly postponed. Moreover, the effects of turbulence show a low dependence on the heaving damping level, as it is apparent comparing the behaviour of low- and high-damped configurations in Fig. 9.

5. CONCLUSIONS

Energy harvesting from flow-induced vibrations has recently received a boost, involving research activities aimed to both develop the technological features of the device and improve the scientific understanding of the excitation mechanism.

The state of the art is widespread, since several solutions have been developed depending on the diversity of flow-induced phenomena. Among all, great attention is now being devoted to devices with two degrees of freedom that exploit the flutter excitations, in both water and air flows. For the former, the main technology adopts flapping foils with externally driven motion, while for the latter the sponstaneous flutter oscillations are mainly considered.

The main results obtained at CRIACIV about classical-flutter systems in air flows have been shown.

Results confirm the high potential of flutter-induced motion as energy-harvesting source, controlling the operative range through a specific design of the governing parameters. Moreover, the destabilizing effect of damping is a very peculiar response of the system, since performance enhancements can be simply obtained by increasing the level of extracted energy.

Finally, the investigated flutter-based device is also operative in flows with high turbulence. Thus, this can envisage promising installations in urban environments with the possibility to integrate the system in the future energy network, fostering smart buildings and cities.

ACKNOWLEDGEMENTS

The work has been partially supported by Cassa di Risparmio Firenze Fundation, within the project “New - new energy from wind” (2014-2016).

REFERENCES

[1] S. Roundy, “On the effectiveness of vibration-based energy harvesting”, *J. Intell. Mat. Syst. Str.*, vol. 16, no. 10, pp. 809-823, 2005.

[2] R.L. Harne, “Theoretical investigations of energy harvesting efficiency from structural vibrations using piezoelectric and electromagnetic oscillators”, *J. Acoust. Soc. Am.*, vol. 132, pp. 162–172, 2012.

[3] M.A. Karami and D.J. Inman, “Equivalent damping and frequency change for linear and nonlinear hybrid vibrational energy harvesting systems”, *J. Sound Vib.*, vol. 330, pp. 5583–5597, 2011.

[4] G. Ahmadi, “An oscillatory wind energy convertor”, *Wind Eng.*, vol. 3, no. 3, pp. 207–215, 1979.

[5] L. Caracoglia, “Feasibility assessment of a leading-edge-flutter wind power generator”, *J. Wind Eng. Ind. Aerodyn.*, vol. 98, no. 10–11, pp. 679–686, Oct. 2010.

[6] W. Mckinney and J. De Laurier, “The Wingmill: An Oscillating-Wing Windmill”, *J. Energy*, vol. 5, no. 2, pp. 106–115, 1981.

[7] K. Jones and M. Platzer, “Numerical computation of flapping-wing propulsion and power extraction”, in *AIAA 35th Aerospace Sciences Meeting & Exhibit*, 1997, pp. 1–16.

[8] K. Jones, K. Lindsey, and M. Platzer, “An investigation of the fluid-structure interaction in an oscillating-wing micro-hydropower generator”, in *S.K. Chakrabarti, C.A. Brebbia, D. Almorza, R.A. Gonzalez-Palma (Eds.)*, Southampton, UK: WIT press, 2003, pp. 73–82.

[9] K. Isogai, M. Yamasaki, M. Matsubara, and T. Asaoka, “Design study of elastically supported flapping wing power generator”, in *International Forum on Aeroelasticity and Structural Dynamics, Amsterdam*, 2003.

[10] E. Shimizu, “Multi-objective design study of a flapping wing generator”, in *The 24th International Congress of the Aeronautical Sciences*, 2004, pp. 1–8.

[11] M. Matsumoto, K. Mizuno, K. Okubo, and Y. Ito, “Fundamental study on the efficiency of power generation system by use of the flutter instability”, in *Proceedings of Pressure Vessels and Piping Division Conference, ASME*, 2006, pp. 277–287.

[12] A. Erturk, W. G.R. Vieira, C. De Marqui, and D.J. Inman, “On the energy harvesting potential of piezoaeroelastic systems”, *Appl. Phys. Lett.*, vol. 96, no. 18, pp. 184103, 2010.

[13] F. Fei, J.D. Mai, and W.J. Li, "A wind-flutter energy converter for powering wireless sensors", *Sensors Actuators A*, vol. 173, no. 1, pp. 163–171, Jan. 2012.
[14] S. Frayne, "Humdinger Wind Energy", 2010. Available: http://www.humdingerwind.com/.
[15] S.-D. Kwon, "A T-shaped piezoelectric cantilever for fluid energy harvesting", *Appl. Phys. Lett.*, vol. 97, no. 16, pp. 164102, 2010.
[16] M. Bryant and E. Garcia, "Modeling and Testing of a Novel Aeroelastic Flutter Energy Harvester", *J. Vib. Acoust.*, vol. 133, no. 1, pp. 011010, 2011.
[17] K. Jones, S. Davids, and M. Platzer, "Oscillating-wing power generation", in *Proceedings of the 3rd ASME/JSME Joint Fluids Engineering Conference*, 1999, pp. 1-6.
[18] B. Simpson, F. Hover, and M. Triantafyllou, "Experiments in direct energy extraction through flapping foils", in *Proceeding of the 18th International offshore and polar engineering conference*, 2008, pp. 370–376.
[19] Q. Zhu, M. Haase, and C.H. Wu, "Modeling the capacity of a novel flow-energy harvester", *Appl. Math. Model.*, vol. 33, no. 5, pp. 2207–2217, 2009.
[20] K. Isogai and H. Abiru, "Study of Multi-Wing Configurations of Elastically Supported Flapping Wing Power Generator", *Japan Soc. Aeronaut. Sp. Sci.*, vol. 55, no. 2, pp. 133–142, 2012.
[21] L. Tang, "The Dynamics of Two-Dimensional Cantilevered Flexible Plates in Axial Flow and a New Energy-Harvesting Concept", *PhD thesis, McGill University of Montréal*, 2007.
[22] O. Doaré and S. Michelin, "Piezoelectric coupling in energy-harvesting fluttering flexible plates: linear stability analysis and conversion efficiency", *J. Fluids Struct.*, vol. 27, pp. 1357-1375, 2011.
[23] K. Singh, S. Michelin, and E. De Langre, "The effect of non-uniform damping on flutter in axial flow and energy-harvesting strategies", *Proc. R. Soc. A Math. Phys. Eng. Sci.*, vol. 468, no. 2147, pp. 3620–3635, 2012.
[24] S. Michelin and O. Doaré, "Energy harvesting efficiency of piezoelectric flags in axial flows", *J. Fluid Mech.*, vol. 714, pp. 489–504, 2013.
[25] J. Allen and A. Smits, "Energy harvesting eel", *J. Fluids Struct.*, vol. 15, pp. 1–12, 2001.
[26] G.W. Taylor, J.R. Burns, S.A. Kammann, W.B. Powers, and T.R. Welsh, "The Energy Harvesting Eel: a small subsurface ocean/river power generator", *IEEE J. Ocean. Eng.*, vol. 26, no. 4, pp. 539–547, 2001.
[27] M.M. Bernitsas, K. Raghavan, Y. Ben-Simon, and E.M.H. Garcia, "VIVACE (Vortex Induced Vibration Aquatic Clean Energy): A New Concept in Generation of Clean and Renewable Energy From Fluid Flow", *J. Offshore Mech. Arct. Eng.*, vol. 130, no. 4, pp. 041101, 2008.
[28] A. Barrero-Gil, S. Pindado, and S. Avila, "Extracting energy from Vortex-Induced Vibrations: A parametric study", *Appl. Math. Model.*, vol. 36, no. 7, pp. 3153–3160, 2012.
[29] C. Grouthier, S. Michelin, and E. De Langre, "Energy harvesting using vortex-induced vibrations of tensioned cables", *Phys. Fluids*, pp. 1–11, 2012.
[30] A. Mehmood, A. Abdelkefi, M.R. Hajj, A.H. Nayfeh, I. Akhtar, and A. O. Nuhait, "Piezoelectric energy harvesting from vortex-induced vibrations of circular cylinder", *J. Sound Vib.*, vol. 332, no. 19, pp. 4656–4667, 2013.
[31] H. Jung, S. Lee, and D. Jang, "Feasibility study on a new energy harvesting electromagnetic device using aerodynamic instability", *IEEE Trans. Magnetics*, vol. 45, no. 10, pp. 4376–4379, 2009.
[32] H.-J. Jung and S.-W. Lee, "The experimental validation of a new energy harvesting system based on the wake galloping phenomenon", *Smart Mater. Struct.*, vol. 20, no. 5, pp. 055022, 2011.
[33] A. Barrero-Gil, G. Alonso, and A. Sanz-Andres, "Energy harvesting from transverse galloping", *J. Sound Vib.*, vol. 329, no. 14, pp. 2873–2883, 2010.
[34] D. St. Clair, A. Bibo, V.R. Sennakesavababu, M.F. Daqaq, and G. Li, "A scalable concept for micropower generation using flow-induced self-excited oscillations", *Appl. Phys. Lett.*, vol. 96, no. 14, pp. 144103, 2010.
[35] S. Li, J. Yuan, and H. Lipson, "Ambient wind energy harvesting using cross-flow fluttering", *J. Appl. Phys.*, vol. 109, no. 2, pp. 026104, 2011.
[36] D.-A. Wang, C.-Y. Chiu, and H.-T. Pham, "Electromagnetic energy harvesting from vibrations induced by Kármán vortex street", *Mechatronics*, vol. 22, no. 6, pp. 746–756, 2012.
[37] X. He and J. Gao, "Wind energy harvesting based on flow-induced-vibration and impact", *Microelectron. Eng.*, vol. 111, pp. 82-86, 2013.

[38] L. Tang, M.P. Païdoussis, and J. Jiang, "Cantilevered flexible plates in axial flow: energy transfer and the concept of flutter-mill", *J. Sound Vib.*, vol. 326, pp. 263–276, 2009.

[39] J.A. Dunnmon, S.C. Stanton, B.P. Mann, and E.H. Dowell, "Power extraction from aeroelastic limit cycle oscillations", *J. Fluid. Struct.*, vol. 27, pp. 1182–1198, 2011.

[40] K.H. Ly and V.A.L. Chasteaut, "Experiments on an oscillating aerofoil and applications to wind-energy converters", *AIAA Journal*, vol. 5, pp. 116–121, 1981.

[41] Q. Zhu and Z. Peng, "Mode coupling and flow energy harvesting by a flapping foil", *Phys. Fluids*, vol. 21, pp. 033601, 2009.

[42] K.D. Jones, K. Lindsey, and M.F. Platzer, "An investigation of the fluid-structure interaction in an oscillating-wing micro-hydropower generator", *in WIT Transactions on The Built Environment, vol. 71, 2003, ch. Fluid Structure Interaction II*, pp. 73–82.

[43] J. Wu, J. Wu, F.-B. Tian, N. Zhao, and Y.-D. Li, "How a flexible tail improves the power extraction efficiency of a semi-activated flapping foil system: A numerical study", *J. Fluid. Struct.*, vol. 54, pp. 886–899, 2015.

[44] M. Bryant and E. Garcia, "Development of an aeroelastic vibration power harvester", *in Proceedings of Active and Passive Smart Structures and Integrated Systems*, vol. 7288, 2009, pp. 728812–728812–10.

[45] V.C. Sousa, M. de M. Anicézio, C. De Marqui Jr., and A. Erturk, "Enhanced aeroelastic energy harvesting by exploiting combined nonlinearities: theory and experiment", *Smart Materials and Structures*, vol. 20, pp. 094007, 2011.

[46] C. De Marqui and A. Erturk, "Electroaeroelastic analysis of airfoilbased wind energy harvesting using piezoelectric transduction and electromagnetic induction", *J. Intell. Mat. Syst. Str.*, vol. 24, pp. 846–854, 2012.

[47] J. Dias, C. De Marqui Jr., and A. Erturk, "Hybrid piezoelectric-inductive flow energy harvesting and dimensionless electroaeroelastic analysis for scaling", *Appl. Phys. Lett.*, vol. 102, pp. 044101, 2013.

[48] A. Abdelkefi, M. Ghommem, A.O. Nuhait, and M.R. Hajj, "Nonlinear analysis and enhancement of wing-based piezoaeroelastic energy harvesters", *J. Sound Vib.*, vol. 333, pp. 166–177, 2014.

[49] A. Abdelkefi and M.R. Hajj, "Performance enhancement of wing-based piezoaeroelastic energy harvesting through freeplay nonlinearity", *Theor. Appl. Lett.*, vol. 3, pp. 041001, 2013.

[50] A. Abdelkefi, A.H. Nayfeh, and M.R. Hajj, "Design of piezoaeroelastic energy harvesters", *Nonlinear Dynam.*, vol. 68, pp. 519–530, 2012.

[51] Z. Peng and Q. Zhu, "Energy harvesting through flow-induced oscillations of a foil", *Phys. Fluids*, vol. 21, pp. 123602, 2009.

[52] L. Pigolotti, "On the Flutter Response of Two-Degree-of-Freedom Flat Plates for Energy Harvesting applications", *Ph.D. Thesis, Dept. of Civil and Env. Engrg., Univ. of Florence (IT), and Dept. of Arch., Civil Engrg. and Env. Sciences, Techn. Univ. Braunschweig (DE)*, 2017.

[53] L. Pigolotti, C. Mannini, G. Bartoli, "Destabilizing effect of damping on the post-critical oscillations of flat plates", *Meccanica*, vol. 52, pp. 3149–3164, 2017.

[54] L. Pigolotti, C. Mannini, G. Bartoli, K. Thiele, "Critical and post-critical behaviour of two-degree-of-freedom flutter-based generators", *J. Sound Vib.*, vol. 404, pp. 116–140, 2017.

[55] L. Pigolotti, C. Mannini, G. Bartoli, "Experimental study on the flutter-induced motion of two-degree-of-freedom plates", *J. Fluid. Struct.*, vol. 75, pp. 77–98, 2017.

[56] L. Pigolotti, C. Mannini, G. Bartoli, "Turbulence effects on the post-critical response of flutter-based generators", in: Proceedings of the 7th European-African Conference on Wind Engineering, Liège, Belgium, 4–7 July 2017.

WINERCOST REPORTS

Work Group 2 Report

FROM ON-SHORE & OFF-SHORE TO BUILT ENVIRONMENT WIND ENERGY PROJECTS

Tommaso Morbiato[1]*, Milan Veljkovic[2]

[1]Working Group Lead - R&D Head, CEO, Windcity srl, Progetto Manifattura, Rovereto (TN), Italy
[2]Working Group Co-Chair - Chair Steel and Composites Structures, Technical University Delft, Netherlands
Corresponding author: Tommaso Morbiato, tmorbiato@windcity.it

ABSTRACT

The expertises, activities, advances, and most relevant findings conveyed by Working Group 2 of the COST Action TU 1304 WInd eNErgy Reconsideration to enhance the COncept of Smart ciTies (WINERCOST) are presented in this paper, as an assessment of the 4 years workplan from ON- ,OFF-SHORE Wind Energy Technology (WET) and the respective accumulated expertise, to the Built environment Wind energy (BWT) pilot, demonstration and good practice scale projects.

NOMENCLATURE

WET	=	Wind Energy Technology
BWT	=	Built Environment Wind Energy Technology
UBL	=	Urban Boundary Layer
SRO	=	Specific Rated Outut (kW/m^2)
$W'_{r,el}$		Annual specific work (kWh/m^2/y)
ρ		density of the air (kg/m^3)
CF		Capacity Factor
HAWT/VAWT		Horizontal/Vertical axis wind turbine
NZEB		Nearly-Zero Energy Building

1. INTRODUCTION: WORKING GROUP 2 TERMS OF REFERENCE

According to the Memorandum of Understanding of the COST Action TU 1304 WInd eNErgy Reconsideration to enhance the COncept of Smart ciTies (WINERCOST), the 4 years action workplan is scheduled to be performed by Working Groups (WG) working in parallel and independently; this paper summarizes the activities and findings of WG n°2 (WG2).

During the first 2 years WG2 was called WG2A and focused on the

- WG2A: ON- ,OFF-SHORE Wind Energy Technology (WET) and Built Environment Wind Energy projects (BWT), and the respective accumulated expertise

At the beginning of the third year of the action, the WGs were reconsidered and focus on the synthesis of the accumulated scientific knowledge and expertise applied to BWT projects. WG2 changed focus to coming topics in built environment:

- WG2B: Built environment Wind energy (BWT) pilot, demonstration and good practice scale projects

Considering also the integration of the other two WGs, and in particular WG3 working on societal acceptance, Wind Energy Technology pilot projects and Building-Integrated-Wind Energy Technology

good practice applications were scrutinized to enhance Smart Future Cities concept, whereas a preliminary holistic design approach including the societal acceptance strategies to enhance the Smart Future Cities concept has been investigated.

2. A PORTRAIT OF WORKING GROUP 2

Working Group 2 connects 33 members whose countries of origin are Bosnia and Herzegovina, Cyprus, FYR of Macedonia, Germany, Greece, Italy, Lithuania, Malta, Norway, Poland, Portugal, Serbia, Spain, Sweden, Swiss, Turkey, and UK. The 5 most represented countries are Italy, Greece, Germany, Serbia and Spain, and the internal gender balance of the group is about 1:4. These informations are highlighted as infographics cake charts in Figure 1.

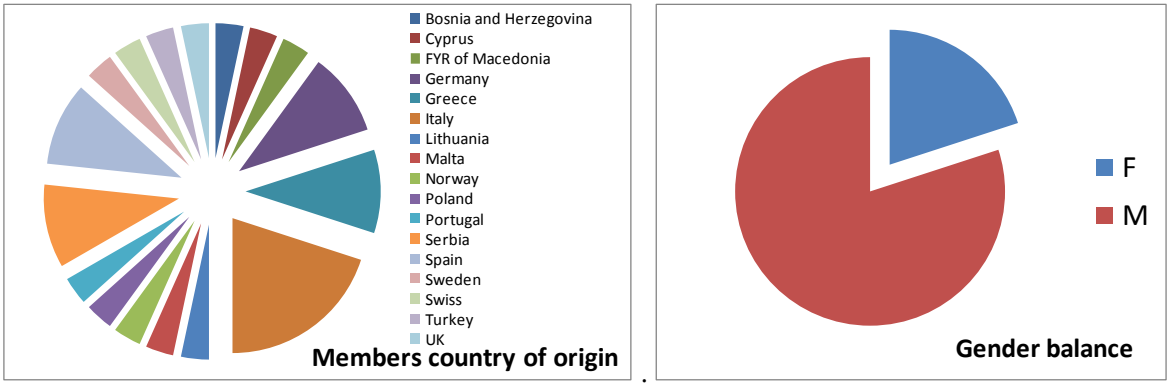

Figure 1. **Members country of origin and Gender Balance for Working Group 2.**

The expertises conveyed by the WG2' members include an extraordinarily wide range of scientific and technological areas that ensured a holistic approach to the wind energy technology reconsideration to enhance the concept of smart cities. The expertise areas of WG2' members include Atmospheric boundary layer and turbulence, Wind power forecasting, Electrical power engineering, Fluid mechanics, Off-shore wind energy technology, Photogrammetry, Remote sensing, Steel structures and applications to Wind Tech, Structural dynamics, System identification & non-linear dynamics, and Wind engineering. The most represented areas of expertise are Steel structures applications to WindTech, Electrical power engineering, Fluid Mechanics, Structural dynamics, and Wind Engineering. These informations are highlighted as infographics cake chart in Figure 2.

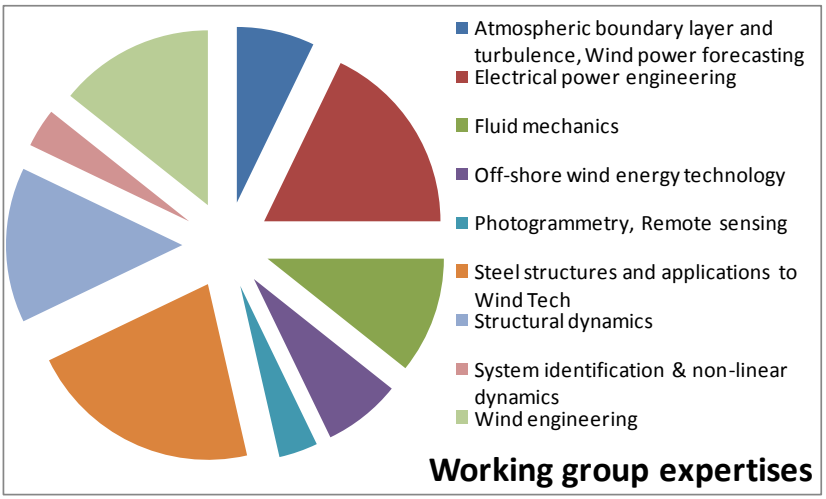

Figure 2. **The areas of expertise of members from Working Group 2.**

3. KNOWLEDGE TRANSITION FROM TRADITIONAL TO BUILT ENVIRONMENT WIND ENERGY PROJECTS

The knowledge transition from traditional to built environment wind energy projects is not an easy matter, as multidisciplinary aspects are involved, well covered by Working Group 2 expertises, and new design criteria apply involving several trade-offs. Furthermore the application of the wind energy technology to the boundary layer generated in the urban environment (UBL) involves special and unprecedented features, such as high turbulence intensity above all.

To this end the activity of WG2 started by scrutinizing the most relevant areas of expertise being Steel structures applications to Wind Tech, Electrical power engineering, Fluid Mechanics, Structural dynamics, and Wind Engineering. The milestone at midterm of the action has been to clearly identify the three main needs whose aggregation composes the knowledge transition core, being in particular: Power and Energy Production examination, Analysis of Technology Readiness Level for built environment, and Integration at Building scale for Wind Energy Projects.

The value proposition principles characterizing scientific & technological research of the group members for the final part of the action are therefore set, and comprise: Structural design for small wind turbine integration in the building, Turbine design for variable winds in Urban Boundary Layer, Electrical connection solutions for smart-grids, Urban context integration and Energy Performance of Building Directive 31/2010. The latter is a goal involving a shared value approach in collaboration with the activity of Working Group 3 dealing with Societal Acceptance.

Table 2. **Knowledge transition from Working Group 2 Expertises to Need Analysis to Value Proposition.**

Working Group 2 Expertises	Need Analysis	Value Proposition
Steel structures applications to Wind Tech	Power and Energy Production examination	Structural design for small wind turbine integration in the building
Electrical power engineering	Analysis of Technology Readiness Level for built environment	Turbine design for variable winds in Urban Boundary Layer
Fluid Mechanics	Integration at Building scale for Wind Energy Projects	Electrical connection solutions for smart-grids
Structural dynamics		Urban context integration and Energy Performance of Building Directive 31/2010
Wind Engineering		

The knowledge transition program followed by WG2 throughout the COST Action is summarized above in Table 1.

3.1. Power and Energy Production examination

In conventional WET the turbines are easily classified by the rated power to swept area ratio. This parameter characterizing WET offer is often referred to as specific rated output (SRO), that is:

$$SRO = \frac{P_{el,\max}(C_p)}{A_D} \tag{1}$$

where power is evaluated according to the theoretical performance of WET through the maximum power coefficient C_p. As highlighted in Figure 3, when considering the most promising power rating range for BWT applications, i.e. the 0,1 to 10 kW, one has to remark the greatest SRO data dispersion among all categories.

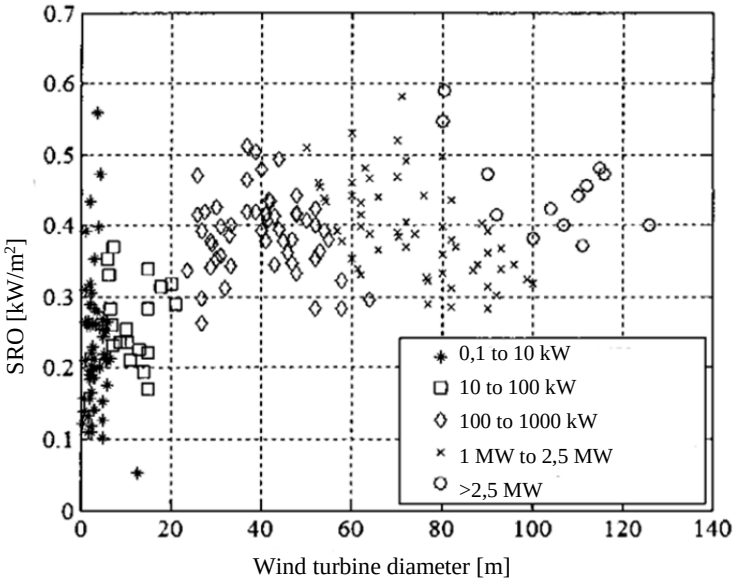

Figure 3. **SRO for different ranges of power rating as a function of the wind turbine diameter (swept area) (adapted from [1]).**

The consistent companion of the SRO parameter is the annual energy production to swept area ratio, which is often referred to as annual specific work (kWh/m^2/y) that is the calculation of the wind energy harvested by the turbine, according to the following (where domain of integration is extended to one year):

$$W'_{r,el} = \frac{1}{A_D} 0.5\rho \int_0^T C_p(t) V_0^3(t) dt \tag{2}$$

The coherence between actual energy records and the calculation according to (2) is very much relying upon the time dependencies of the power coefficient C_p, and of the wind speed distribution assumption V_0. The former tends to coincide with the maximum C_p taken in (1) only if the turbine always works at the optimal tip-speed ratio, while the latter can be reduced to a linear composition of wind speed classes when the most common Weibull distribution applies.

Especially when considering BWT applications, one has to acknowledge that high turbulence intensity of UBL is very much diminishing the amount of time in which the turbine works at the optimal tip-speed ratio, and conversely using a linear composition of Weibull distribution classes to calculate energy, tends to ignore the increased importance of the non-stationary behaviour.

Agencies monitoring renewable energy economics such as the International Renewable Energy Agency (IRENA) record the annual energy production of wind farms, and formulate the fundamental efficiency parameter called capacity factor (CF) as in the first expression of the following equation:

$$CF = \frac{\int_0^T P_{el}(t) dt}{P_{el,\max} \cdot T} \cong \frac{W'_{r,el}}{SRO \cdot T} \tag{3}$$

The expression at second member indicates how the calculation of SRO and annual specific work by (1) and (2) can approximate CF, based on the effective coherence between the technology assumptions and reality.

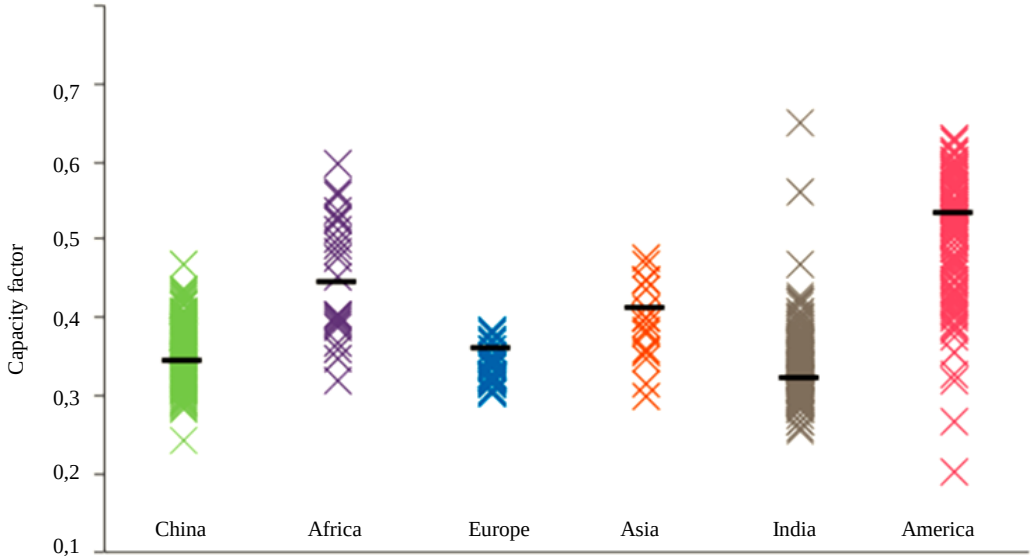

Figure 3. **Capacity factors and weighted averages for commissioned wind farms (Source IRENA, 2015 [2]).**

The reports annually published e.g. by IRENA indicate a great dispersion of CF data by world regions and for the same region (see Figure 3 adapted from [2]). The gap between the actual CF and 1 is conventionally accepted as a measure of the availability and unpredictability mix of the natural resource, although more recently the domain of causes is increasingly extended to: Energy Market drives & Distributors Network Operations (DNOs) feasibility, Technical facilities (O&M), Technology level, Resource quality [2], [3].

The lower values of CF generally obtained (sun and water applications do not differ significantly) are the main obstacle for the time being that impede to consider renewables as an effective alternative system to the primary carbon/nuclear energy supply.

Furthermore, due to the turbulence intensity of UBL introduced above, BWT applications nowadays figure among the lowest CF values highlighted in Figure 3, as remarkably reported by Barlow [4].

Generally speaking therefore, based on the recent acceptance for including Technology level and Resource quality among the CF drivers, research & development in the field of WET and BWT can develop advances & innovation to increase CF, ultimately reducing the gap between renewable and carbon/nuclear systems.

3.2. Technology Readiness Level for built environment

As seen in previous section, UBL affects the behaviour of a conventional wind turbine because in the built environment thanks to high turbulence intensity the non-stationary parts are prevailing. Weibull type distributions or distributions in general become a questionable assumption as a mean of accounting for different classes of wind speed in the total energy production, because of the increased frequency of transient runs. The turbine should be continuously driven in variable speed operations mode, as highlighted in Figure 4. Variable speed operations are not the standard for WET: they are usually regarded as a short transient mode in between long periods of stationary uniform operations at constant wind speed.

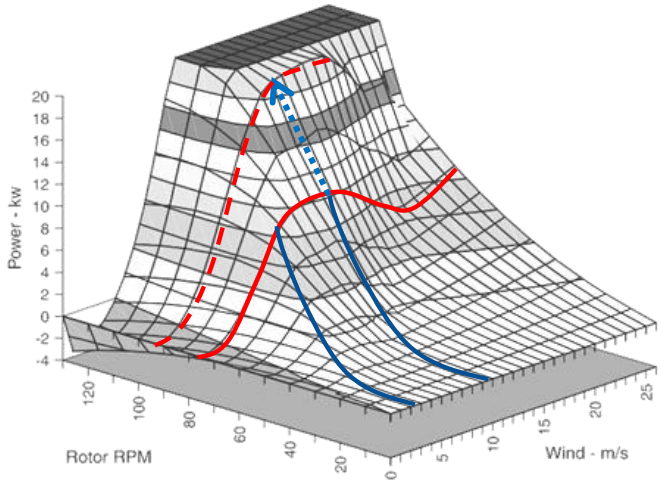

Figure 4. **Variable speed operations mode in a wind turbine: an electronic controller drives the machine through the maxima of a power surface as a function of rotating and wind speed.**

A turbine' architecture whose standard are non-stationary and variable speed operations introduces not only new power electronics challenges, but mainly in terms of the inertia of the machine. In fact the dynamics equation of the system is perturbed at every wind gust by a similar relation:

$$I_{rot}\dot{\omega}_{rot} = M_{rot,B} - M_{gen,A} \tag{4}$$

where generator and rotor due to the turbulent gust undergo different torque A and B, and the new equilibrium point requires moment of inertia and acceleration term. Inertia is increasingly seen as the most critical parameter in particular in BWT, as it turns out to be the driving factor during start-up. According to Battisti [1] and to the surveys carried out in UK by Barlow [4], the inertia of conventional WET applied to BWT appears to be over critical, as start-up is hardly achieved, and CF of BWT remains generally low.

Compared to horizontal axis wind turbines (HAWT), vertical axis (VAWT) are omni-directional for aerodynamics and therefore recommended for use in built environment wind applications (BWT). Hara et al. [5] studied the moment of inertia dependence of VAWT in pulsating winds, showing that the energy efficiency is almost independent of the wind cycle and the moment of inertia under the condition of constant load torque. However, in the case of a long wind cycle and a small moment of inertia, the energy efficiency is expected to vary and is dependent on the torque curves.

3.3. Building integrated wind energy projects

Based on the above findings, it appears therefore not unnecessary to promote TRL advance towards a specific BWT design, introducing also structural design guidelines for Building integrated wind energy projects. VAWT are omni-directional for aerodynamics and therefore recommended to use in BWT. Coupling of vibrations from VAWT to building and viceversa, in a wider range of frequencies due to VAWT mechanics, is a major issue to account for in building integrated wind energy projects. It is often mandatory to integrate in the design of the small wind turbine also specific devices to damp oscillations in case of minor vibration problems, or to fully isolate from vibrations in case of major coupling cases. Of course, increase of installation costs must be carefully addressed and trade-off solutions should be researched.

In case of HAWT the resonant spectrum is possibly less wide, although HAWTs are less indicated for BWT as they are not omni-directional and yawing might result cumbersome in UBL.

4. VALUE PROPOSITION FOR BWT

4.1. Structural design for small wind turbine integration in the building

The integration of distributed generation from wind energy at the building scale is a mandatory achievement in order to define the characteristics of the Nearly-Zero Energy Building (NZEB) introduced by EU Commission. While in case of VAWTs the design of extra-dampening and isolators could be the most relevant, in case of HAWT some authors as Gluhovič et al. [6] propose innovative numerical simulations where the dynamic loads from the rooftop turbine are added to the building load case scenario, and the ISO 10137 acceleration limits for building occupants are evaluated.

4.2. Turbine design for variable winds in Urban Boundary Layer

The winds encountered in UBL by BWT are variable, and therefore the self-starting issue of VAWT becomes even more crucial, as the machine can hardly accelerate in the short time windows allowed by the wind gusts. The self-starting issue of lift driven VAWTs is well known and is due to the local minimum in the standard power curve at low tip-speed ratios. A small mitigation can be offered by using cambered blade profiles, while a sound variable geometry rationale is illustrated in Figure 5: the family of power curves is obtained by letting vary the pitch angle of the blade from 0° (bold red curve, fixed geometry) to 30° (dotted red curve), with the result of progressively eliminating the local minimum that prevents self-start. Conversely though, the self-starting variable-pitch turbine has the drawback of canceling the higher tip-speed ratio region of the power curve, thus reducing the power coefficient to a 25% of the fixed geometry lift driven VAWT, i.e. similar to that of a drag driven VAWT.

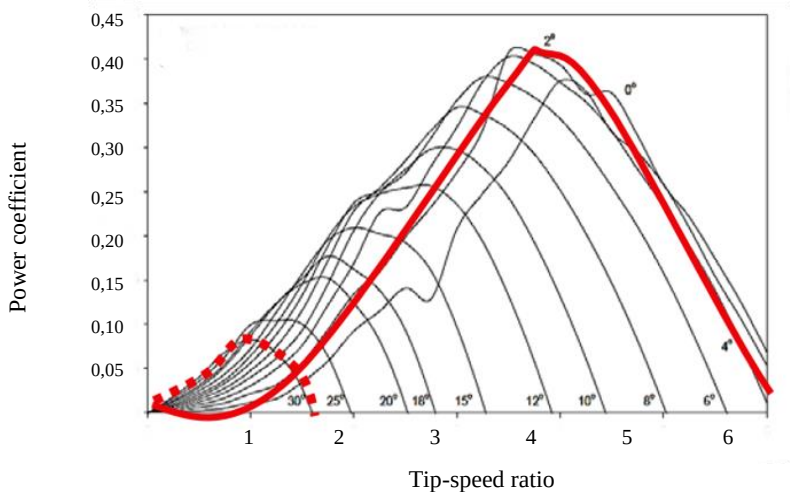

Figure 5. **The family of power curves obtained in a variable pitch lift-driven VAWT from 0° pitch (fixed geometry VAWT) to 30° pitch.**

New aerodynamic concepts are therefore needed in VAWT dynamics for BWT applications to allow self-starting while securing efficiency of variable geometry turbines at higher tip-speed ratios, by means of active or more sustainable passive principles, e.g. variable geometry might be integrated to both blade pitch and inertia (as in [7]).

4.3. Urban context integration and Energy Performance of Building Directive 31/2010

Research and innovation policies and actions should focus from now on in penetration of wind energy at the distributed generation scale, i.e. system integration at the building scale, thus completing the matching with the NZEB concept for WET. Safety and comfort for occupants should be addressed, e.g. through the guidelines from structural analysis introduced above, smart metering for grid/storage solutions coupling should be facilitated to easily integrate the building in the smart-grid, and micro-siting techniques should be defined as design criteria, spanning from the integration of simplified anemometry campaigns used as inlet, to CFD simulations designed to find aerodynamic ramps for optimal turbine positioning (Figure 6).

Figure 6. CFD techniques used in micro-siting for optimal positioning of wind turbines in BWT [8].

4.4. Electrical connection solutions for smart-grids

To increase the percentage of wind energy distributed generation in the power grid it is essential to know the maximum permissible feed-in power that will not deteriorate the quality and reliability of the supply for other customers. Cundeva et al. [9] yet found out that, at least when the hosting capacity of the network is set by the harmonic emission, in a relevant case study the wind turbines can be connected to medium-voltage network without any additional measures.

5. CONCLUSIONS

Spanning from the expertise in WG2, to the selection of an appropriate need analysis focusing in BWT challenges, it has been possible to highlight throughout the findings of the Action several pilot & good practice projects to enhance wind energy at the building scale in the Smart Future Cities concept.

REFERENCES

[1] L. Battisti, "Impianti motori eolici" *LBE*, Trento, 2014.

[2] IRENA, "Renewable Power Generation Costs in 2014" *International Renewable Energy Agency.*, 2015.

[3] IEC 61400-26, "Availability for Wind Turbines and Wind Farms – Technical Specifications", International Electrotechnical Committee, 2012

[4] J. F. Barlow, D. R. Drew, "Wind Flow in the Urban Environment," in *"Trends and Challenges for Wind Energy Harvesting", WINERCOST Workshop, 30-31.03.2015*, 2015, pp. 15–24.

[5] Y. Hara, K. Hara, and T. Hayashi, "Moment of Inertia Dependence of Vertical Axis Wind Turbines in Pulsating Winds", International Journal of Rotating Machinery, ID 910940, 2012

[6] N. Gluhovič, M. Spremič, M. Pavlovič, Z. Markovič, "Numerical Study of Vibrations in a Steel Building Induced by Roof Mounted Small Scale HAWT", in "*Proceedings of the International Conference on Wind Energy Harvesting", WINERCOST17*, 2017

[7] T. Morbiato, Wind turbine, Patent WO 2015071863 A1, CN106415004A, EP3069019A1, US20160290316, 2015

[8] T. Morbiato, T. Pascon, Windcity srl consultancies internal archive

[9] S. Cundeva, M. Bollen, D. Schwanz, "Hosting Capacity of the Network for Wind Generators set by Voltage Magnitude and Distortion Levels", in "*Proceedings of the International Conference on Wind Energy Harvesting", WINERCOST17*, 2017

TECHNICAL SESSION 1.1

Wind Characteristics and Loads

THE INTERNATIONAL CONFERENCE ON
WIND ENERGY HARVESTING 2018
21-23 March 2018
Catanzaro, Italy

Paper TS1.1.1

VIBRATION MONITORING OF AN HAWT IN WIND TUNNEL

Mirjana Ratkovac[1], Rüdiger Höffer[1], Thomas Andrianne[2*]

[1]Wind Engineering and Flow Mechanics, Ruhr-Universität Bochum, Germany
[2]Department of Aerospace and Mechanical Engineering, University of Liège, Belgium
Corresponding author: Thomas Andrianne, t.andrianne@uliege.be

ABSTRACT

This work presents a monitoring strategy of the blade vibration of a small scale Horizontal Axis Wind Turbine (HAWT). The instrumentation consists in three wireless accelerometers located at the tip of each blade and a load balance on the tower. A time and frequency domain analysis of the acceleration signals is performed in the case of a misalignment of the rotor with respect to the wind. The resulting unsteady aerodynamic loading leads to aeroelastic vibrations of the blades, which are measured and analysed. The demonstration apparatus is installed in a wind tunnel where flows with three types of isotropic turbulence are simulated: low turbulence (<1%), medium turbulence (10%) and high turbulence (15%). It is shown that the instrumentation of the blades by wireless accelerometers is able to capture the small flapwise vibrations due to the dissymmetry of the flow and corresponding aerodynamic loading.

NOMENCLATURE

a_x, a_y	=	Acceleration in the flapwise (x) and edgewise (y) directions (g)
F_x, F_y	=	x and y components of the base shear force (N)
g	=	Standard gravity (9.81 m/s^2)
I_u	=	Longitudinal turbulence intensity (%)
L_{ux}	=	Integral length scale (m)
β	=	Rotor misalignment (°)
Ω	=	Rotational frequency (RPM)

1. INTRODUCTION

Structural health monitoring (SHM) systems have large application in the wind turbine industry in order to help ensuring the safety and functionality of the structure during its lifetime. In comparison to the expensive corrective and time scheduled maintenance strategies, SHM systems allow preventive, condition based maintenance, by utilizing the data collected from sensors for damage and faults detection. While the drivetrain monitoring systems are widely applied, the SHM of the rotor-blade system and support structure is still in the development phase, relying on the planned inspections [1]. A detailed overview of different monitoring strategies can be found in [1,2], for the whole wind turbine structure and in [3] focusing on the wind turbine blades.

According to the Caithness Windfarm Information Forum report [4] that summarises the wind turbine accident data to 30 September 2017, the most common type of failure is blade related failure, followed by structural failure and fire. The cost of the wind turbine blades is around 15-20% of total wind turbine cost and damage on the blade can lead not only to blade failure, but also to rotor imbalance and additional structural damage [2] on the entire turbine. Blade damage is due to various factors, such as fatigue at the blade root section, or the overload caused by pitch-yaw control errors [1]. A number of methods for

blade monitoring was tested in the past. Loh et al. [5] tested blade damage detection strategy using accelerometers in the laboratory on the shake table, with motor-induced blade rotations and in the field using small-scale wind turbine with ambient wind load. Song et al. proposed a health monitoring strategy for wind turbine blades using a piezoceramic-based wireless sensor network [6]. Ou et al. compared mode-based and statistics-based blade damage detection strategies using an experimental blade equipped with a set of accelerometers for sensoring an artificially induced damage [7]. In a study published in 2014, an aeroelastically scaled model of a wind turbine is tested in the boundary layer test section of the wind tunnel of the Politecnico di Milano, featuring active individual blade pitch and torque control [8]. The authors of this study address also the limitations of the current technology for measuring the misalignment of rotor and wind direction and an adequate yaw actuation for rotor realignment. Rotor misalignment generates additional loading on the wind turbine structure and can contribute to a progress of fatigue damages.

In this study, the vibration-based monitoring strategy of wind turbine blades is presented. The instrumentation consists of three wireless accelerometers located at the tip of each blade. The strategy is based on the analysis of the acceleration signals in the case of a misalignment of the rotor with respect to the wind. Blade vibration spectra are not only influenced by structural characteristics of the blade but also by the wind excitation spectra, which is dependent on the wind conditions. The resulting unsteady aerodynamic loading leads to aeroelastic vibrations of the blades, which are measured and analysed. The demonstration apparatus is installed in a wind tunnel where three types of incoming flows are simulated: low isotropic turbulence (<1%), medium isotropic turbulence (10%) and high isotropic turbulence (15%).

2. EXPERIMENTAL SET-UP

The blade vibration of a small-scale horizontal axis wind turbine was tested in Wind Tunnel Lab at the University of Liège using three wireless accelerometers (A1-A3) located at the blade tips. Figure 1 shows the experimental set-up with the medium turbulence grid. The tests were run using three different wind flows, low turbulence (no grid), medium turbulence (grid 1) and high turbulence flow (grid 2). The yaw angle is fixed using a steel bar in order to achieve a misalignment between the rotor and the wind flow.

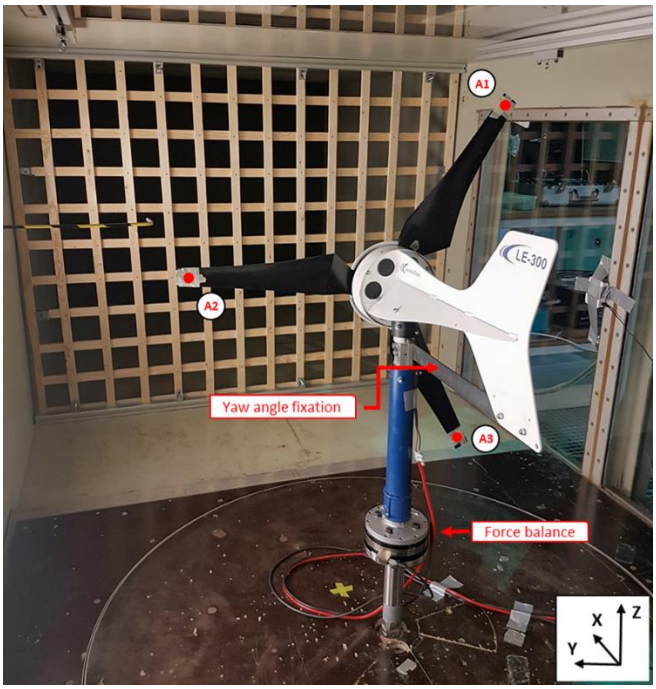

Figure 1. Wind tunnel experimental set-up and instrumentation

2.1. HAWT LE-300

The tests are carried out on a small scale Horizontal Axis Wind Turbine (HAWT), model LE-300, designed and manufactured by the UK Company Leading Edge. Table 1 shows the main technical characteristics and nominal operating conditions. During the experiment, the nominal operational point was reached by adjusting the wind velocity and the value of a variable load resistance. Despite the small size of the accelerometers (see section 2.2.1), their presence has an effect on the aerodynamic performance of the blades. In addition, the HAWT is located in the aeronautical test section of the wind tunnel (2m width by 1.5m high) leading to a blockage effect of 26%. This important value strongly influences the flow around the blades. It is assumed that due to the blockage effect, the operational point reached during the tests was 633RPM (instead of rated 800 RPM) and 24V, for a wind speed of 8m/s. Note that this discrepancy between the nominal value proposed by the constructor and the ones corresponding to the wind tunnel tests does not limit the conclusions drawn in this work. Indeed, the objective is to investigate the possibility to monitor the aeroelastic behaviour of a generic HAWT, not to characterise the aerodynamic/electrical power performances of a given turbine.

Table 1. HAWT LT-300 technical information

Rotor Type	1m diameter, 3-Blade upwind
Blade Material	Glass Reinforced, UV resistant Nylon
Rated Output	85 W @ 8m/s @800 RPM
Peak Output	300 W
Cut-in speed	3 m/s
Generator Type	3-Phase Brushless NIB rotor PMA
Output Voltage	24V

2.2. Instrumentation

2.2.1. Accelerometers

Blade vibrations are measured using three 3-axis wireless sensors (A1-A3) developed by IOTree, a start-up company emanating from the Microsys laboratory of University of Liège. The sensors have the capability to measure accelerations in the range ±16g. Acquisition frequency was set to 200 Hz, since the expected first two natural frequencies are in the range below 100 Hz [9] and can be captured according to the Nyquist-Shannon theorem. Sensors are positioned at the tip of each blade, as shown in the Figure 1 and 2, with x-axis sensor component measuring the flapwise vibrations, which are of the main interest for this study. The acceleration in the y-direction is an edgewise acceleration, while the z-component is the radial acceleration, which was saturated (above 16g) and not of interest in this study. The effect of the sensors on the height of the natural frequency and stiffness of the blade was investigated in [9].

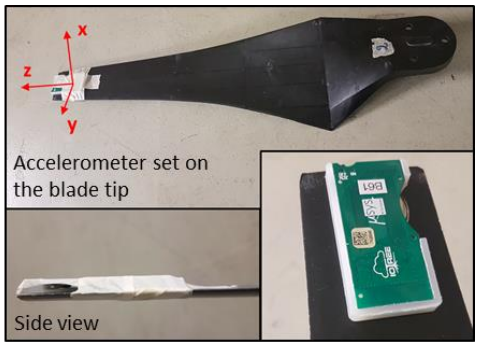

Figure 2. Example of one accelerometer located at the blade tip

2.2.2. Force balance

A force balance is mounted on the support structure of the wind turbine, at the height of 27.5 cm measured from the turn table. A 6-components load sensor by ATI Instrumentation (model omega 160) is used. The acquisition frequency of the force sensor is also 200 Hz, 3-component shear forces and bending moments can be measured. In the analysis, shear force (x-component, facing the wind, and y-component, perpendicular to the wind) are analyzed. Due to differences of the acquisition systems, it was not possible to synchronize acceleration and force measurements. The duration of both measurements is set to 10s for each value of the misalignment of the rotor with respect to the incoming flow.

2.3. Modal-analysis

Information on the modal parameters for the investigated wind turbine can be found in [9]. However, due to the changes in the experimental set-up regarding the force balance at the support structure and minor changes in the characteristics (weight and size) due to the wireless accelerometers, modal properties of the single blades and complete wind turbine structure were investigated by means of free decays tests. The clamped blades were given an initial displacement and then released. During the test, the accelerometer was mounted at the tip of each blade and acceleration was measured. The complete wind turbine structure was analyzed using the impact on the support structure. Vibrations are monitored by the force balance and by the wireless accelerometer at the top of the wind turbine support structure.

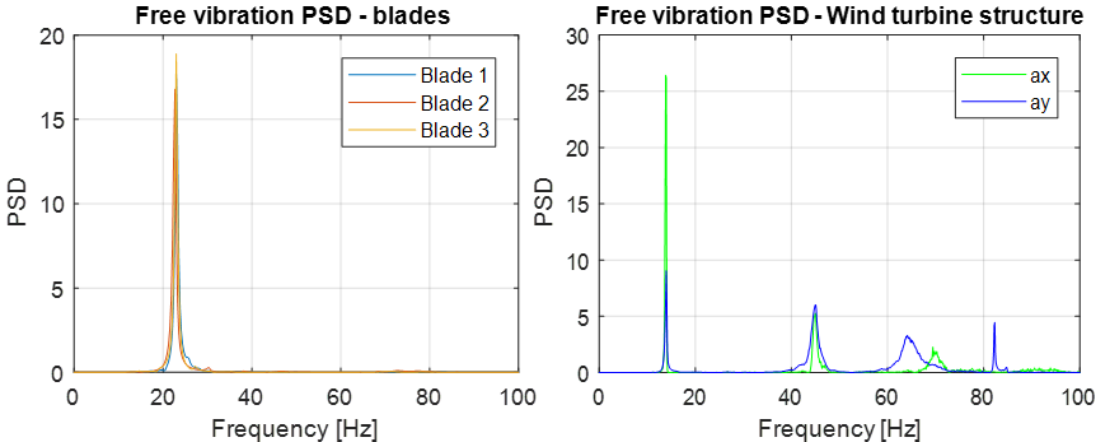

Figure 3. Power spectral density of the free vibration acceleration signals

It is observed from the spectra of figure 3 that the three blades have their 1st mode at around 23Hz. It corresponds to the first bending mode of the blades. Global modes can be observed in the spectra of ax and ay measured through free vibration tests of the complete wind turbine (see right plot of figure 3). The first natural frequency at 13.84 Hz belongs to the supporting structure of the wind turbine. In the previous study this frequency was not encountered. However, the wind turbine structure is changed and force balance is added in the lower half of the turbine tower, which explains the reduced stiffness and lower eigenfrequency of the support. The remaining modes describe the movement of the rotor and relative movement of the blades, as explained in [9]. For this study, the frequencies of the single blades are of the main interest. The list of modal parameters is shown in the Table 2.

Table 2. Selected modal properties of the wind turbine blades and wind turbine structure

Mode 1	**Single blades 1st mode**		**Wind turbine structure**	
	Eigenfreq. [Hz]	Damping [%]	Mode	Eigenfreq. [Hz]
Blade 1	23.1	1.7	1	13.8
Blade 2	22.6	1.7	2	44.9
Blade 3	22.9	1.8	3	60.1
			4	69.4
			5	82.2

3. METHODOLOGY

The blade vibrations are analysed in the framework of a time-frequency analysis of the response signals obtained by the wireless accelerometers on the blades and the force balance at the wind turbine support structure. The FFTs of the both types of signals were analysed and compared in order to assess the use of accelerometers for the blade health monitoring.

Two types of tests were conducted, at high RPM and at low RPM, in order to compare the level of vibrations for these two scenarios. First, the wind turbine was tested near the nominal operating conditions in a uniform flow with a velocity of 8m/s and an output voltage of 24V, with high RPM (633 RPM for 0° misalignment). Then, a second type of test was conducted under low operating conditions with the same velocity of the flow (8m/s), but with controlled low RPM and voltage output (108 RPM and 3.5V for 0° misalignment).

In both cases, three types of turbulent flows were simulated using passive grid generators. The characterisation of these grids can be found in Vita et al. [10]. Table 3 summarizes the flow features:

Table 3. Simulated flow characteristics

	Iu [%]	**Lux [m]**
Low turbulent flow	1%	0.012
Medium turbulent flow	10%	0.066
High turbulent flow	15%	0.079

4. RESULTS AND DISCUSSION

Figure 4 shows the variation of the rotational speed and loads (in terms of mean value and standard deviation), as a function of the misalignment. It is observed that the rotational speed is slightly reduced when the rotor leaves the perfect alignment (0°) and reaches -15° and 15°, where the reduction is limited to 10% of the value at 0° (633RPM). For larger misalignment values, ($|\beta| \geq 20°$), the rotational speed drops suddenly by 85% (to 108RPM) whereas the load resistance remains unchanged (R=16.2 Ω). This fact is attributed to the large change in the effective flow velocity and angle of attack of the flow on the blades: the root of each blade shows large angles leading to stall of the flow and the tip region shows lower angles, responsible for lower aerodynamic loading [11]. The resulting aerodynamic loading is decreasing leading to a smaller mechanical torque, rotation speed and electrical power output.

The stall phenomenon is characterized by its strong unsteadiness, which results in time varying excitation forces. In consequence it is expected to measure large fluctuations of the aerodynamic loads measured on the tower of the turbine. Nevertheless, the opposite observation is done in the lower plot of figure 4: the standard deviations of the forces are reduced by a factor of 4. This is obviously in accordance with the reduction of the rotation speed and hence due to the corresponding reduction of the inertial forces from the blades. In addition, the yaw moment (Mz) is not strongly impacted by the misalignment of the rotor: its mean value is slightly affected but the standard deviation value is reduced by the deceleration of the rotor as the yaw angle reaches +/- 20°.

On the basis of these observations it is concluded that the measurement of the loads is not able to give a full picture of the vibration behavior of the blades. For this reason, the rest of the study focuses on the signals measured by the accelerometers at the tip of the blades.

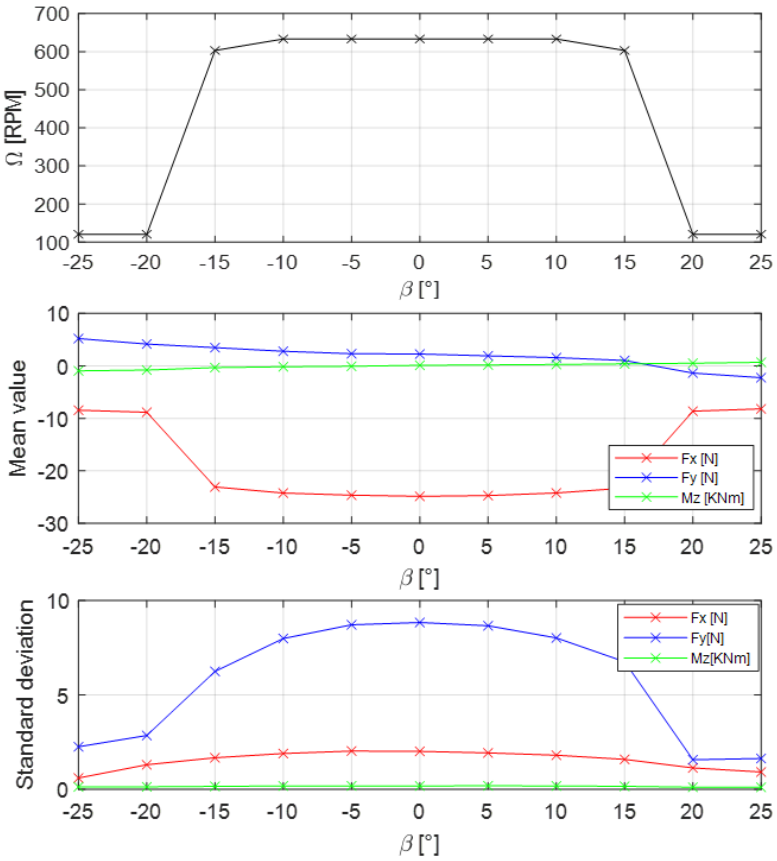

Figure 4. Rotation speed and loads on the turbine in low turbulence and high RPM configuration

Figure 5 shows the time signals of an accelerometer in the x and y directions. It is observed that the acceleration ay vary between -1g and +1g, as expected in this direction. On the other hand, the x component has a non-zero mean (around 0.3g). This value can be explained by the non-alignment of the x-direction of the accelerometer with the rotation axis of the turbine leading to the unintended measurement of a part of the centripetal acceleration. The right plot of figure 5 (spectrogram) shows the frequency content of the flapwise acceleration (ax) as a function of the misalignment angle. It is observed from this plot that the rotation frequency is constant (around 1.8Hz, i.e. 108RPM) over the entire range of misalignment. In this range, it appears that the aerodynamics of the rotor is not modified by the change of yaw angle and the effects of flow separation cannot be detected for a specific value of β. Another important observation concerns the strong peaks between 20Hz and 30Hz, around the first modal frequency of the blades (23Hz, see table 2). As a consequence, the first bending mode of the three blades is excited by the flow when the turbine operates at this low RPM configuration.

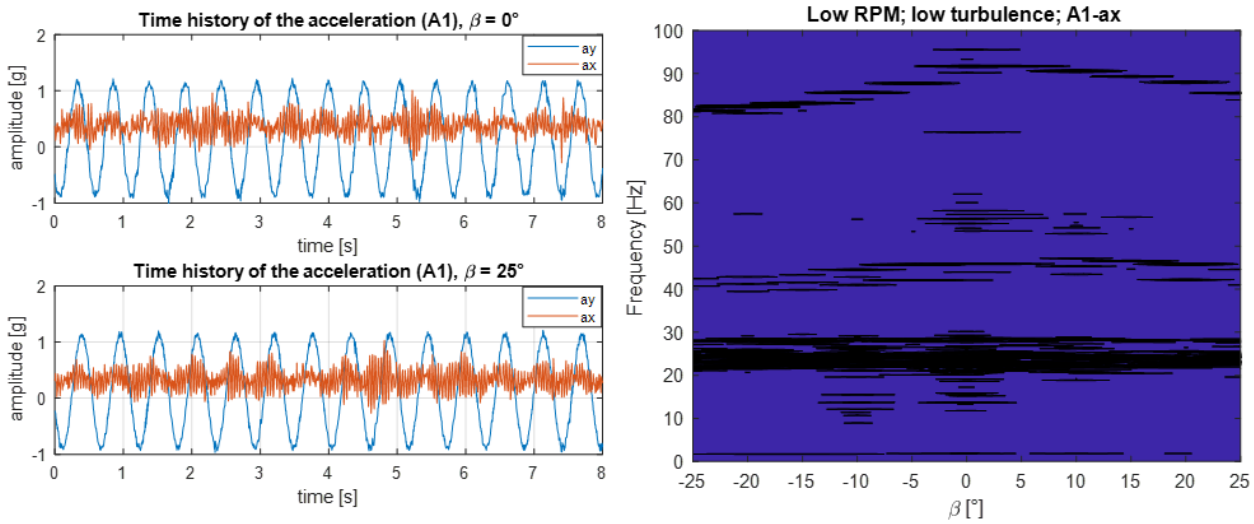

Figure 5. Time history and spectrogram of the acceleration for low RPM operating conditions, 108 RPM.

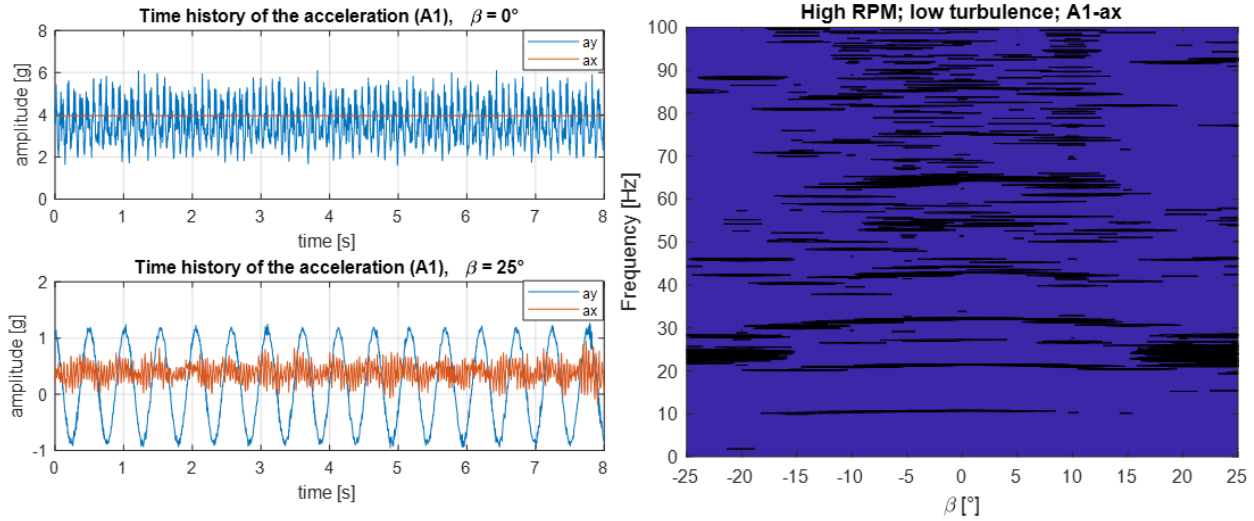

Figure 6. Time history and spectrogram of the acceleration for the high RPM operating conditions, 633 RPM

The behaviour is rather different in the case where the high RPM configuration is considered. In this case, the upper left plot of figure 6 (corresponding to β=0°) shows that the y-component of acceleration of the blade varies between 2g and 5g. In the same figure, the x-component has a mean value of around 4.5g. These values can be explained as stated previously, due to a non-alignment of the accelerometer with respect to the rotation axis. The bottom plot of figure 6 corresponds to the deteriorated situation, where β =25°, and the time signal are similar to the ones of figure 7.

The frequency content of the flapwise (x-direction) acceleration is presented by the spectrogram in the right plot of figure 6. In the range -15°/15° no pronounced vibration along the first mode is observed. Instead, the rotation frequency (at 10.5Hz) appears together with its harmonics (21Hz and 31.5Hz). Then other peaks are observed for higher frequencies. The absence of vibration of the blades along the x-direction is attributed to the stiffening effect due to the high rotation frequency of the rotor. In addition, the effective angle is close to the optimal value (~8°), where attached flow conditions are met, leading to large aerodynamic forces characterised by small fluctuations.

Finally, the effect of turbulence on the frequency content of the x and y components of the acceleration at the tip of the blades is analysed in figure 7. The left spectrograms show the first bending mode of the blade in the spectra of the flapwise acceleration outside the range -15°/15° only. Out of this range, a

large peak is observed between 20Hz and 30Hz. The width of the peak increases as the turbulence of the wind increases. Two phenomena are taking place: (i) the buffeting response due to the flow separation (effect of blade-induced turbulence) and (ii) the turbulent response of the blade due to the incoming flow. The right spectrograms of figure 7 present the frequency content of the edgewise acceleration (ay). In the limited range -15°/15° a sharp peak around 10.5Hz is measured, corresponding to the rotation frequency of the rotor. Out of this range the lowering of the rotation frequency is captured (1.8Hz).

5. CONCLUSIONS

This paper presents a new set of experimental results dedicate to investigate the monitoring possibilities for blades of an HAWT. Experiments are carried out on a small scale HAWT in a wind tunnel. The sensors are wireless accelerometers and a load balance. A misalignment of the rotor of the HAWT is imposed in order to create a dissymmetric aerodynamic loading on the blades over a period of oscillation. The tests are performed in three different types of flow (from low turbulence to high turbulence). In addition, two sets of rotation frequencies of the rotor are tested at the same wind velocity by changing the value of the load resistance.

On the basis of this large amount of experimental data, the following conclusions are drawn:

- When increasing the yaw angle, the aerodynamics of the rotor is decreased. At nominal conditions (no misalignment) the entire blade operates in attached flow conditions with a small amount of fluctuations of the aerodynamic loading. For large yaw angles (beyond +/- 20°) the rotor decelerates as a result to the reduction of the relative angle of attack of the flow on the blades. It leads to a limited power output of the turbine, combined with the excitation of the first bending mode of the blade (around 23Hz). This mode is not excited at nominal conditions because of (i) a stabilizing effect due to the gyroscopic effect and (ii) the flow excitation is less important.
- The blade vibrations as described above for large values of the yaw angle cannot be detected from the measurement of the loads and moment at the tower of the HAWT. The mean and standard deviation of these loads are more influenced by the inertial effect due to the rotation of the blades. Hence, the aeroelastic behaviour of the loads cannot be derived from a measurement based on the tower.
- The turbulence of the incoming flow has an important effect on the frequency content of the accelerations at the tip of the blades: the number of peaks and their width is increasing when increasing the level of turbulence. The vibrations of the blades are a combination of buffeting response (body-induced turbulence due to flow separation around the blade) and turbulent response (turbulent flow from the passive grid as a simplified model of the atmospheric wind).

More work is planned in the analysis of the signals. In particular, the comparison of the time signal of accelerometers as a function of their azimuthal position in the disk will be performed. The objective is to investigate the blade response over a revolution as a function of the misalignment. New tests will be performed using the gyroscopic capabilities of the sensor in order to have an accurate information about the azimuthal position. During these new wind tunnel tests, more misalignment angles will be tested in order to refine the understanding of the aerodynamic excitation in the range where the flow does not approache the blades in an optimal manner.

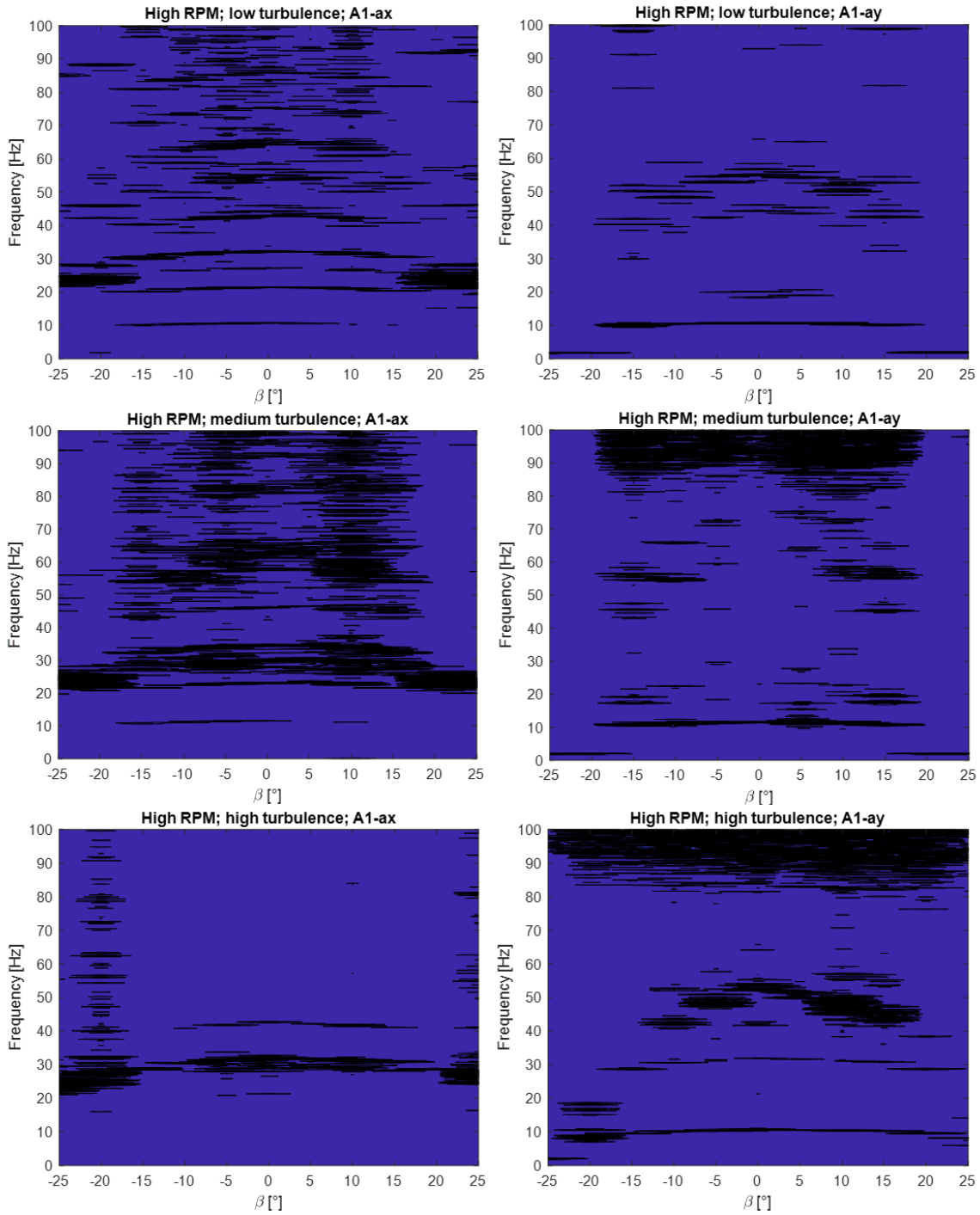

Figure 7. Spectrograms showing the frequency content of acceleration signals for different misalignment degree

ACKNOWLEDGEMENTS

The authors acknowledge with thanks the support of the European Commission's Framework Program "Horizon 2020" through the Marie Skłodowska-Curie Innovative Training Networks (ITN) "AEOLUS4FUTURE - Efficient harvesting of the wind energy" (H2020-MSCA-ITN-2014: Grant agreement no. 643167) and support of the start-up company IOTree.

REFERENCES

[1] D. Coronado and K. Fischer, "Condition Monitoring of Wind Turbines: State of the Art, User Experience and Recommendations," Report, Fraunhofer Institute for Wind Energy and Energy System Technology IWES Northwest, 2015.

[2] C. Ciang, J. Lee and J. Bang, "Structural health monitoring for a wind turbine system: A review of damage detection methods," *Measurement Science and Technology*, vol. 19, no. 12, p. 20, 2008.

[3] B. Yang and D. Sun, "Testing, inspection and monitoring technologies for wind turbine blades: a survey", *Renewable and Sustainable Energy Reviews*, vol. 22, p. 515-526, 2013.

[4] "Summary of Wind Turbine Accident data to 30 September 2017," *Caithness Windfarm Information Forum*, 2017. Available Online: http://www.caithnesswindfarms.co.uk/.

[5] C.H. Loh, K.J. Loh, J.S. Yang, W.Y. Hsiung and Y.T. Huang, "Vibration-based system identification of wind turbine system", *Struct. Control Health Monit*., vol. 24, 2017, Online: (wileyonlinelibrary.com). DOI: 10.1002/stc.1876

[6] G. Song, H. Li, B. Gajic, W. Zhou, P. Chen and H. Gu,"Wind turbine blade health monitoring with piezoceramic-based wireless sensor network", *International Journal of Smart and Nano Materials*, vol. 4, no. 3, p. 150-166, 2013. DOI:10.1080/19475411.2013.836577

[7] Y. Ou, E.N. Chatzi, V.K. Dertimanis and M.D. Spiridonakos, "Vibration-based experimental damage detection of a small-scale wind turbine blade", *Structural Health Monitoring*, vol. 16, no. 1, p. 79–96, 2017.

[8] C.L. Bottasso, F. Campagnolo and V. Petrović, "Wind tunnel testing of scaled wind turbine models: Beyond aerodynamics", *Journal of Wind Engineering and Industrial Aerodynamics*, vol. 127, p.11–28, 2014.

[9] M. Dawans, "Development of an experimental platform dedicated to wind turbine default detection", Master thesis, University of Liège 2016.

[10] G. Vita, H. Hemida, T. Andrianne and C. Baniotopoulos, "Generating atmospheric turbulence using passive grids in an expansion test section of a wind tunnel", Submitted to the *Journal of Wind Engineering and Industrial Aerodynamics, WINERCOST'17 Special Issue "Wind energy Harvesting"*

[11] M.S. Jeong, S.W. Kim, I. Lee, S.J. Yoo, K.C. Park, "Impact of yaw error on aeroelastic characteristics of a horizontal axis wind turbine blade", Renewable Energy 60 (2013) 256-268.

CFD BASED ENERGY OUTPUT ESTIMATION OF ROOF MOUNTED WIND TURBINES IN URBAN ENVIRONMENTS

Marius Paraschivoiu[1*], Aierken Dilimulati[1] and Ted Stathopoulos[2]

[1]Department of Mechanical, Industrial and Aerospace Engineering, Concordia University, Canada
[2]Department of Building, Civil and Environmental Engineering, Concordia University, Canada
Corresponding author: marius.paraschivoiu@concordia.ca

ABSTRACT

This paper presents a methodology to evaluate the wind power potential of roof mounted wind turbines. The methodology utilizes both computational fluid dynamics and meteorological data in an effort to estimate the energy production of a specific turbine placement. Energy yield calculations of a Darrieus turbine placed at 4 corners of a building are presented for both a low and high density urban environments.

NOMENCLATURE

Cp	=	Power Coefficient
U_{ref}	=	Reference wind velocity for the simulations [m/s]
U_{cp}	=	Wind velocity calculated at control points [m/s]
U_{wind}	=	Wind velocity data from meteorological statistics [m/s]
U_{actual}	=	Estimated wind velocity at turbine rotor [m/s]

1. INTRODUCTION

The deployment of wind turbines in an urban environment necessitates adequate prediction tools to select the best location to maximize wind energy production. Computational approaches are emerging as very powerful tools for this purpose and provide the ability to simulate an entire urban area [1]. The wind energy potential at a specific location can be assessed by physically measuring the wind characteristics at that location for a long period of time. A novel approach based on Computational Fluid Dynamics (CFD) can be used to have a preliminary idea of the wind potential in a specific area and also to better identify, if needed, the best location to take the measurements [2]. In addition, as more urban deployment of wind turbine is being considered, a CFD tool becomes essential to identify the locations on existing buildings that have higher wind speeds. This paper presents a cost-effective tool that estimates wind power for urban communities. The challenge is to combine an accurate CFD tool with meteorological data. In [3] the authors conclude that "the simulated results by using realizable k-epsilon model indicate that the calculated velocities agree well with the measured data". In this paper we present the computational fluid dynamics approach and the combination with actual wind data to estimate the energy output for two actual buildings in the vicinity of Montreal, Canada. We study both a low building density area and the downtown area which is a high building density area.

2. CFD BASED METHODOLOGY

The deployment of small turbines in an urban area requires accurate tools to estimate the wind energy available at specific mounting sites. Wind resource assessment can be carried out using a three-dimensional computer model of the geometry followed by the simulation of the flow using Computational Fluid Dynamics (CFD) in a similar approach to evaluating pedestrian comfort [4]. The wind from eight different directions is simulated on a virtual model of the site in order to calculate the wind speed at different control points (receivers) placed near or on buildings representing the mounting placement of turbines. The simulation results are then combined with wind statistics from a local meteorological station to assess the wind potential at the control points.

2.1. Geometry Construction

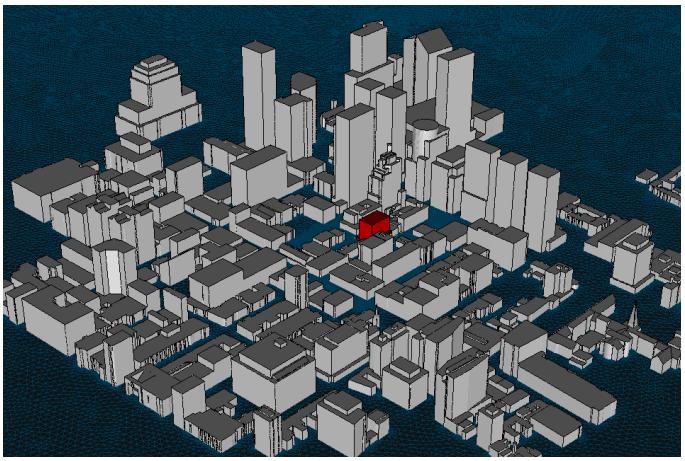

Figure 1: 3D CAD Model of the high building density site.

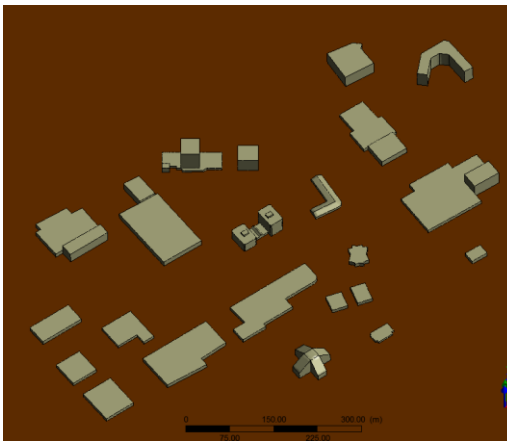

Figure 2: 3D CAD Model of the low building density site.

The geometry of a site is constructed from a 3D CAD model either available from the city or reconstructed from an aerial view. The geometry is verified and corrected in order to have the exact heights of the buildings and the topology of the ground. Figures 1 shows the model of the high building density (HBD) site which is part of downtown Montreal, Canada. Figure 2 shows the model of a low building density (LBD) site which is a commercial in a suburban region of Montreal called Point-Claire. The two regions are affected by the same winds but the building density and the heights will significantly change the local winds.

2.2. Mesh Construction

The mesh construction consists of discretizing the computational volume into volumetric elements that are used in the computations. A typical computational domain is an octagonal prism with a height of 10H (H is the height of the highest building in the area considered) as shown in Figure 3. A distance of 10H in each one of the eight directions from the urban area considered defines the size of the octagon. The mesh is concentrated using basic 3D tetrahedrons cells and triangular prisms near the ground surface. The high building density test case, shown in Figure 4, is more demanding computationally as the highest building is very tall. In this case the building zone covers a radius of 500 m and the boundaries are 1000 m from the edge of the building zone. The height of the computational domain is 1000 m from the ground. The surface mesh for the HBD zone is shown in Figure 5 which leads to a total number of 6 million elements.

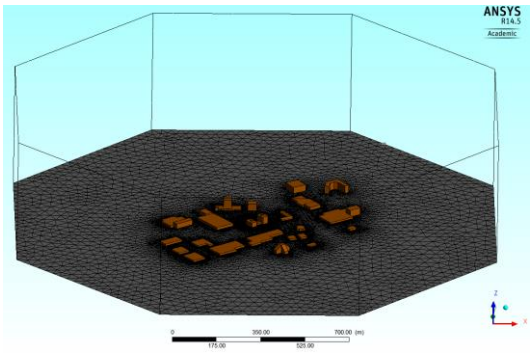

Figure 3: Surface mesh and computational domain for LBD.

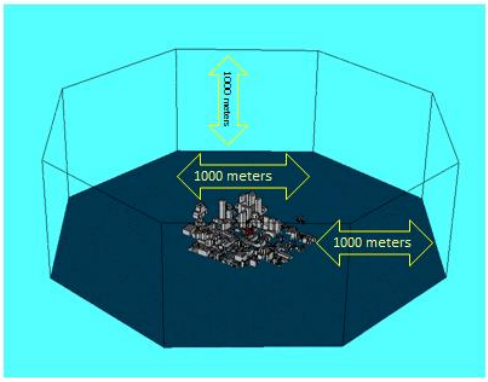

Figure 4: Surface mesh and computational domain for HBD.

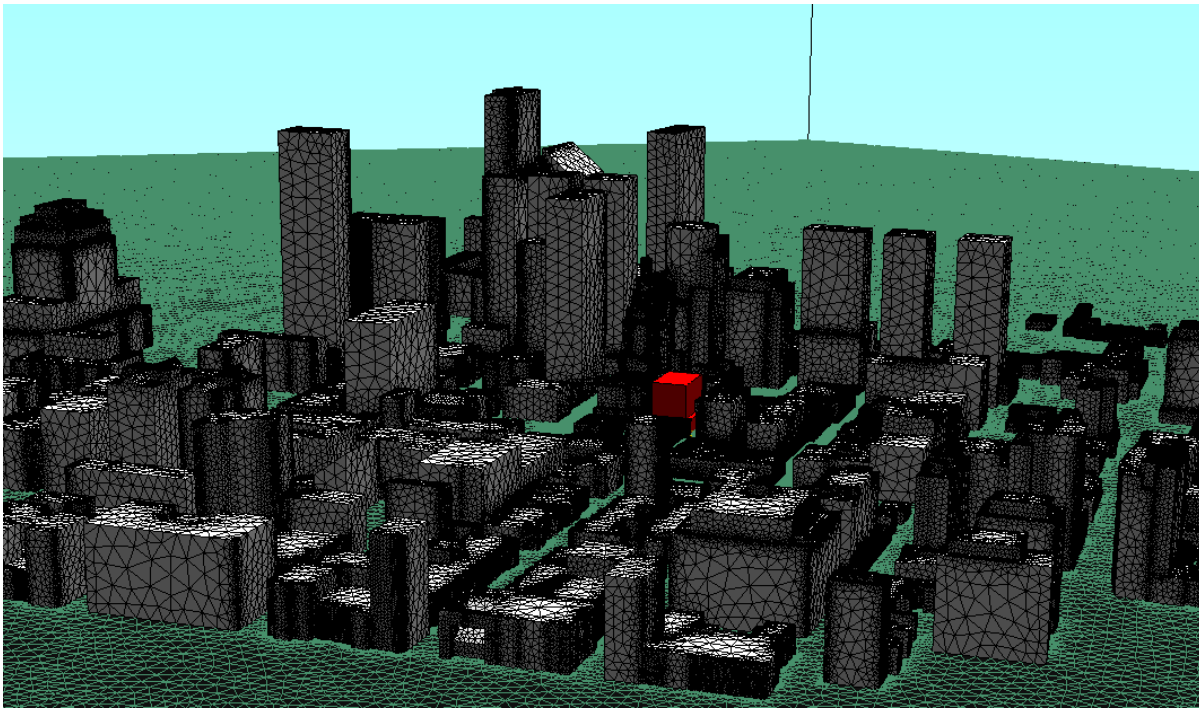

Figure 5: Surface mesh over the buildings.

2.3. Wind flow simulations

All three wind velocity components at each node of the mesh are obtained by solving a large system of equations resulting from discretizing the Reynolds-Average-Navier-Stokes (RANS) equations. A calculation for each one of the 8 wind directions is performed. A typical reference wind of 5 m/s at 10 m height is used as an inlet boundary condition along with other turbulence parameters for ABL flow simulations. The inflow atmospheric boundary layer is a key component of the simulation. Current approaches used in conjunction with the K-epsilon Realizable turbulence model are to impose a mean wind speed, turbulent kinetic energy and turbulent dissipation rate [5]. The wind speed at each one of the receivers and for each wind direction is used for the statistical analysis necessary to calculate the wind potential. The frequency distribution of hourly mean wind speed and direction from a

meteorological site, combined with the simulation value of the wind speed for each direction, is used to assess the wind speed distribution at the control points which represent possible wind turbine locations.

3. ENERGY OUTPUT CALCULATION

The average wind speed at each receiver from each wind direction is reported in Table 1 for the LBD site and in Table 2 for the HBD site. This average velocity (U_{cp}) is scaled with the reference velocity (U_{ref}) of 5 m/s so that any wind velocity can be related to the statistical hourly mean wind speed and direction. Introducing the a wind velocity at the rotor as U_{actual} and the resulting incoming wind as U_{wind} , the following relation is used to relate all the wind velocities:

$$U_{actual} = \frac{U_{wind} U_{cp}}{U_{ref}} \tag{1}$$

Using the frequency of the U_{wind} applied to U_{actual} will provide the energy output produces by the turbine for the specific time period considered. The wind rose indicating the frequency and the wind speed for the Montreal region is reported in Figure 6. This data is used both the LBD and HBD sites.

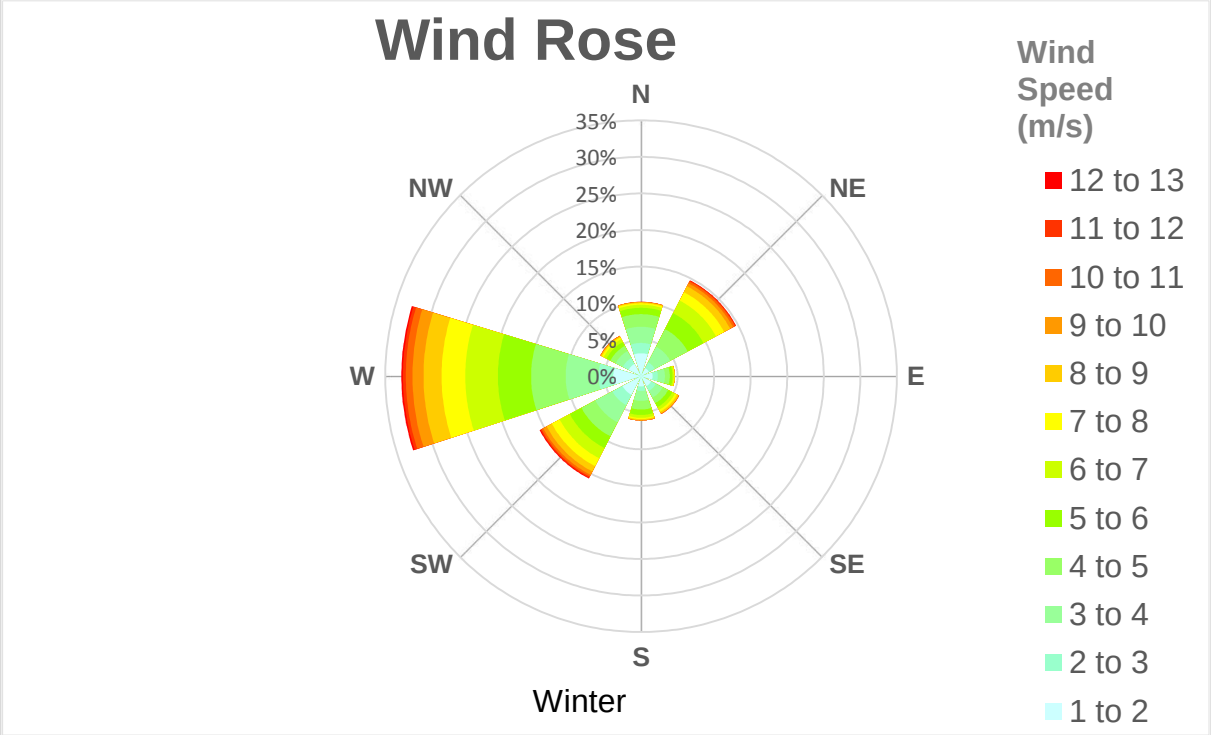

Figure 6: Winter Wind Rose for the Montreal, Canada region.

3.1. Location of control points

Control points can be placed anywhere in the computational domain. In this work, four control points are placed at the corner of a building as seen from the top in Figure 7 and from the side in Figure 8 for the LBD case. Figures 9 and 10 show the same for the HBD case.

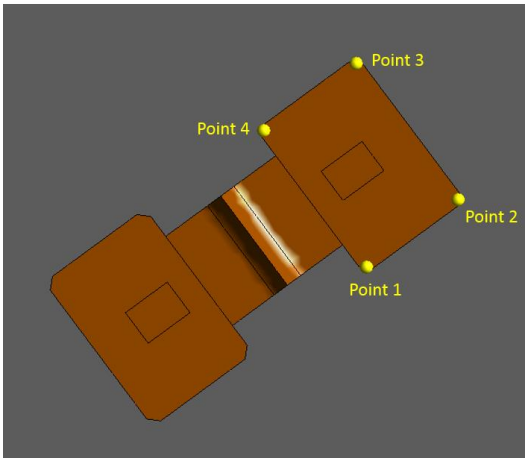

Figure 7: Top view of the control points for LBD.

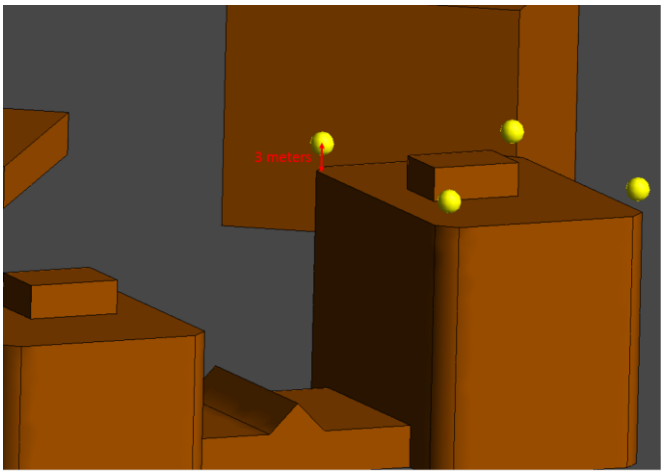

Figure 8: Isometric view of the control points identifying the locations where the turbine can be located for LBD.

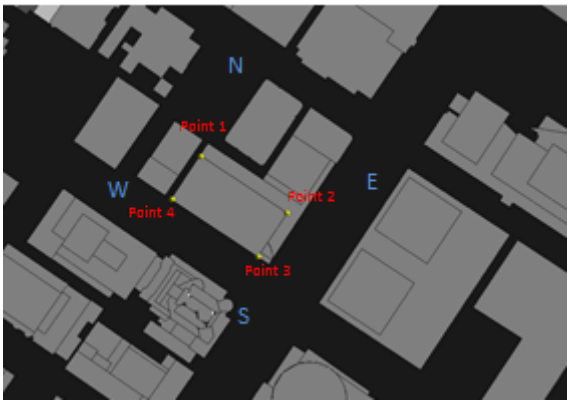

Figure 9: Top view of the control points for HBD.

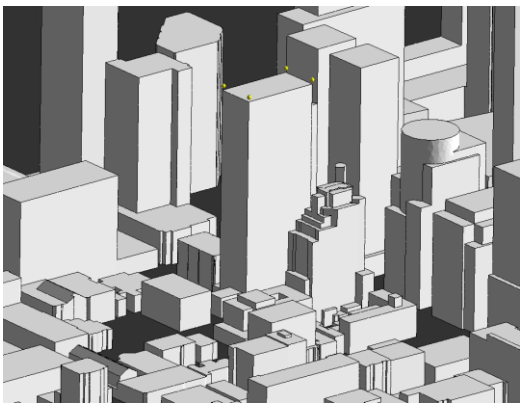

Figure 10: Isometric view of the control points identifying the locations where the turbine can be located for HBD.

3.2. Case 1: Calculation of energy yield during winter for a LBD site

Table 2 provides energy production in winter of a small Darrieus turbine placed at each of the four corners. The power coefficient used for this turbine when mounted on a building is 0.40 based on CFD work published in [6]. This turbine has an area of 2.595 m^2 facing the wind which is a small turbine. In this work, only the winter months are used to calculate the energy output. It can be seen that control point 4 offers the higher energy production while control point 2 is the lowest. The main wind direction in winter is from the west so the control point 4 is the most exposed, nevertheless the placement at control points 1 and 3 also offer energy outputs that are only 10 to 15% lower.

Table 1. Average velocity (U_{cp}) at each control point for LBD.

Average Velocity (m/s)								
	N	**NE**	**E**	**SE**	**S**	**SW**	**W**	**NW**
Point 1	5.9910	5.1900	7.6620	7.9070	8.0750	7.8370	6.4680	5.2340
Point 2	7.6220	6.3810	7.6640	8.0250	7.6480	7.5010	3.6710	5.6600
Point 3	7.4860	6.4970	6.9510	7.4490	6.3010	6.9160	6.4580	6.1080
Point 4	7.2520	6.3790	5.5360	5.3110	8.0260	7.7570	6.8960	4.8970

Table 2. Estimated energy output for winter months for LBD.

Energy (kWh)				
Control Point	1	2	3	4
Energy	667	472	651	746

3.3. Case 1: Calculation of energy yield during winter for a HBD site

The same turbine is place at the four corners of the building shown in Figure 9 and 10. The estimation of the energy production reveals that all four locations produce significantly less than in the LBD site. This is surprising because the building is significantly taller. The building in the LBD case is about 1/3 of the height of the building in the HBD case nevertheless energy production at point 3 is only about 40% of the energy production at point 4 at the LBD site. These results confirm the need to perform this type of study as the local wind patterns significantly affect the energy production. To further illustrate this behavior, the wind velocity iso-contours at the HBD site at the height of the turbines are presented in Figure 11. It is clear that the wake of the adjacent building is affecting the turbines.

Table 3. Average velocity (U_{cp}) at each control point for HBD.

Average Velocity (m/s)								
	N	**NE**	**E**	**SE**	**S**	**SW**	**W**	**NW**
Point 1	4.5790	3.4350	1.6050	2.2810	3.1030	3.6550	3.8810	4.1610
Point 2	3.7280	3.5580	1.3080	1.6490	3.5410	2.6660	3.1950	3.5670
Point 3	3.1600	4.7400	2.2520	5.3030	6.1660	5.6750	5.0900	4.1870
Point 4	4.5350	2.4930	1.6960	4.0160	3.9520	4.3910	4.2910	4.2800

Table 4. Estimated energy output for winter months for HBD.

Energy (kWh)				
Control Point	1	2	3	4
Energy	115	73	297	149

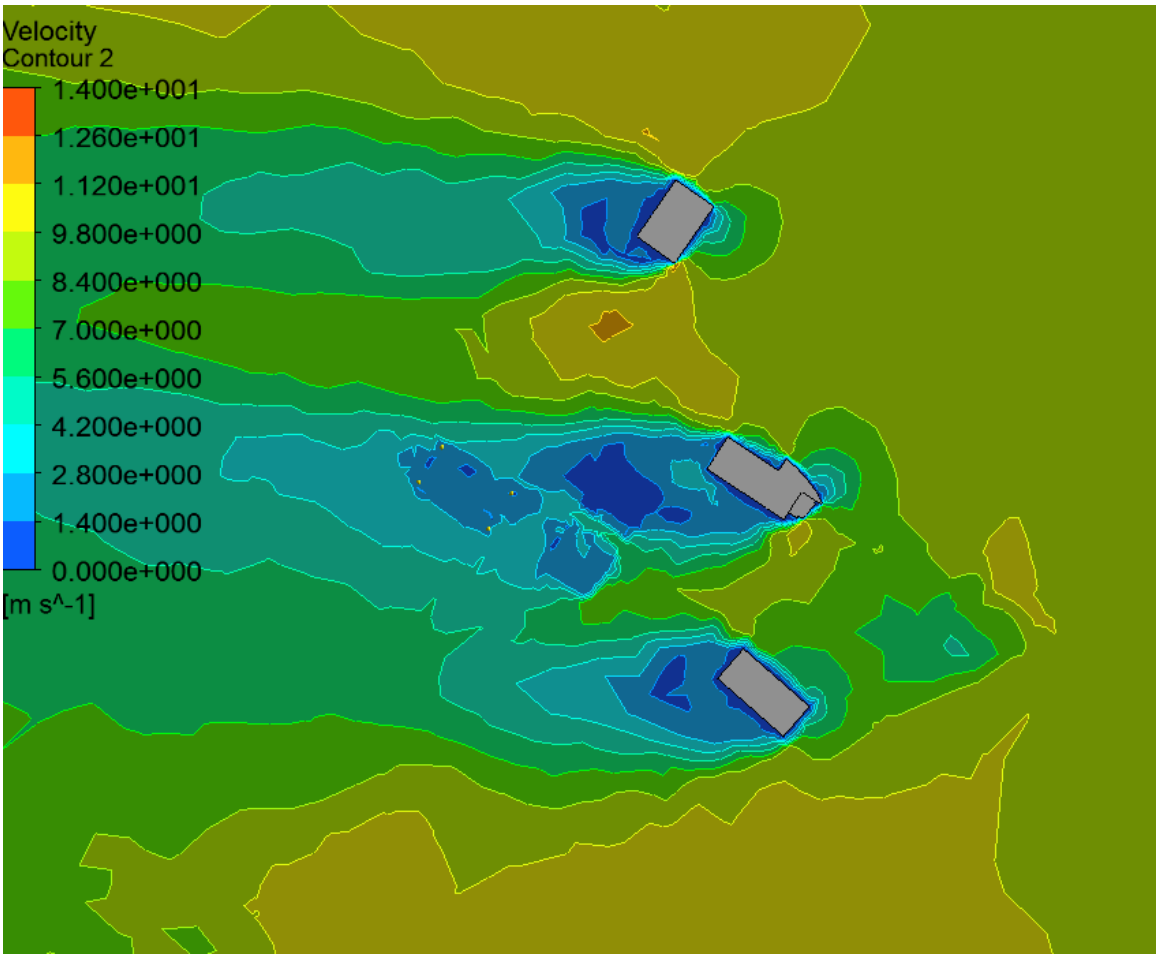

Figure 11: Velocity iso-contours at 149 m from the East wind.

4. CONCLUSIONS

This paper presents the methodology to evaluate the energy potential of roof mounted turbines in urban environments. A case study of a Darrieus wind turbine placed at one of the 4 corners of a building in two urban settings in Montreal is presented and discussed. This study illustrates that there is a significant effect of the site. A High Building Density HBD site leads a low energy production even if the buildings are much higher. For a Low Building Density LBD, the wind is less affected by surrounding buildings. In the case studies here, the best turbine placement at the LBD site offers a 60% higher energy output that the worst case on the same building. A turbine placed at the best location is estimated to produce close to 3000 kWh per year (749 for the winter months) which, in this case, is a good energy output for the small turbine considered. Finally, the methodology presented here-in is very powerful and can be used to analyse multiple sites and turbines simultaneously.

REFERENCES

[1] Aierken Dilimulati Ted Stathopoulos and Marius Paraschivoiu , Wind Turbine Designs for Urban Applications: A Case Study of the Shrouded Diffuser Casing for Turbines, accepted Journal of Wind Engineering & Industrial Aerodynamics

[2] Amir Bashirzadeh Tabrizi, Jonathan Whale, Thomas Lyons, Tania Urmee, Performance and safety of rooftop wind turbines: Use of CFD to gain insight into inflow conditions, Renewable Energy, Volume 67, 2014, Pages 242-251

[3]An-Shik Yang, Ying-Ming Su, Chih-Yung Wen, Yu-Hsuan Juan, Wei-Siang Wang, Chiang-Ho Cheng, Estimation of wind power generation in dense urban area, Applied Energy, Volume 171, 2016, Pages 213-230

[4] B. Blocken, W.D. Janssen, T. van Hooff, CFD simulation for pedestrian wind comfort and wind safety in urban areas: General decision framework and case study for the Eindhoven University campus, Environmental Modelling & Software, Volume 30, 2012, Pages 15-34

[5] Bert Blocken, Ted Stathopoulos, Jan Carmeliet, CFD simulation of the atmospheric boundary layer: wall function problems, Atmospheric Environment, Volume 41, Issue 2, 2007, Pages 238-252, ISSN 1352-2310

[6] Samson Victor and Marius Paraschivoiu, Performance of Darrieus Turbine on the roof of a building, submitted Transactions of the Canadian Society for Mechanical Engineering.

NUMERICAL AND EXPERIMENTAL INVESTIGATION OF ENERGY POTENTIAL OF HIGH-RISE BUILDING USING IRWES SYSTEM

O. Hubova[1], M. Macak[2]

[1]Department of Structural Mechanics, Slovak University of Technology, Slovakia
[2]Department of Mathematics, Slovak University of Technology, Slovakia
*Corresponding author: O. Hubova, olga.hubova@stuba.sk

ABSTRACT

This article deals with numerical and experimental investigation of air flow at the top of high-rise building situated in Bratislava city center. Determination of the wind flow in roof area and optimal design of input area give us information on possibility of use the integrated roof energy system IRWES. It will be designed for application on existing building. Possible variants of small Vertical Axis Wind Turbine - VAWT are based on mean wind speed around 8m/s, see [1]. Optimal roof design should give us optimal distribution of mean wind velocity. CFD simulation using ANSYS and k -ε model of turbulence and experimental measurements in BLWT wind tunnel in Bratislava were used and compared.

NOMENCLATURE

IRWES	=	Integrated Roof Wind Energy System
VAWT	=	Vertical Axis Wind Turbine
I_v	=	Intensity of turbulence (%)
α	=	Local angle of wind attack (rad)
z_0	=	Roughness length (m)
v_m	=	Mean wind velocity (m/s)
v_{ref}	=	Reference wind speed (m/s)
ρ	=	Density of air (kg/m^3)

1. INTRODUCTION

In the broader central zone of Bratislava the intensive construction of high-rise buildings began lately. Because the buildings are oriented along the Danube River, the northwest wind flow is dominant, as it is seen from the wind-rosette in Fig. 1. The orientation of some high-rise objects that are shown in models in the BLWT tunnel (see Fig. 3) is suitable for using the wind power. Average wind speeds measured over the last 10 years by the Slovak Hydro Meteorological Institute give good information about the city's wind conditions (see Fig.1).

2. METHODOLOGY

The high-rise buildings in Bratislava, as seen in Fig. 3, have a total height of 90 to 124 m. In the upper part, it is possible to use the IRWES system, if the building is suitably oriented towards the predominant wind flow. In the first phase, the selected building was investigated using CFD simulation in the ANSYS program, where we will deal with the mean wind velocity distribution inside the upper part of the building, where small wind turbine VAWT is envisaged, see Fig. 4.

The average mean wind speed during the year at a height of 10 m above the ground is about 5 m/s - see Fig.1. The gradient of the wind velocity up to 200 m is expressed in relation 1 and shown in Fig. 2.

$$v_m(z) = c_r(z) \cdot c_o(z) \cdot v_b = 0{,}19 (z / z_{0,II})^{0,07} \ln(z / z_0) \cdot v_{ref} \quad (1)$$

(a) 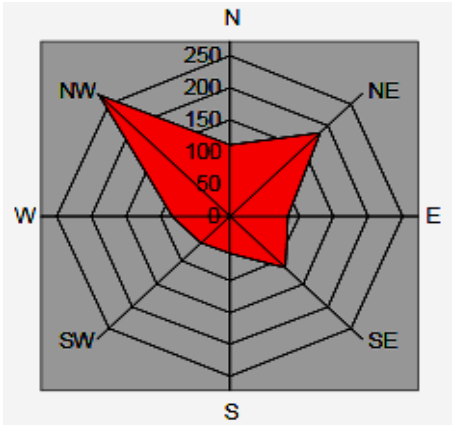

(b) 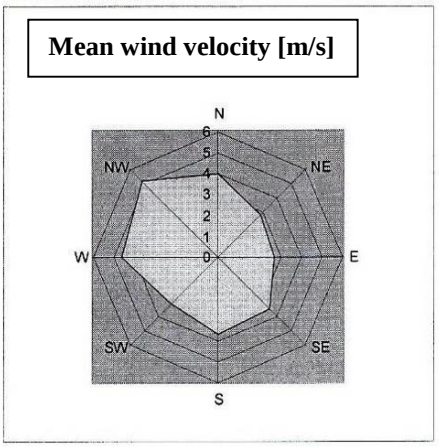

Figure 1. Wind-rosette (a) and mean wind velocity in Bratislava city center (b)

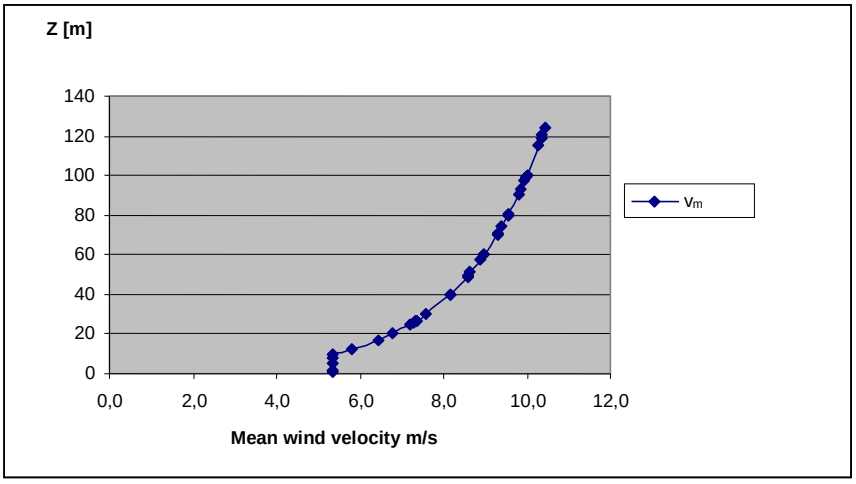

Figure 2. Gradient mean wind velocity profile in Bratislava city

(a) 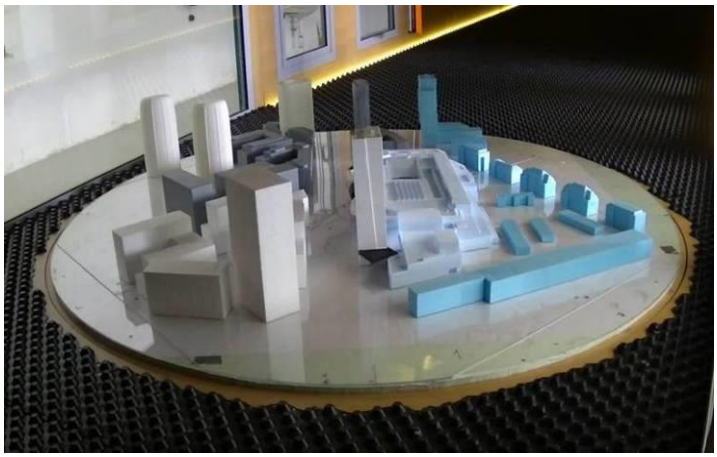 (b) 

Figure 3. Models of buildings in scale 1:300 in turbulent wind in BLWT (a), selected high-rise building (b).

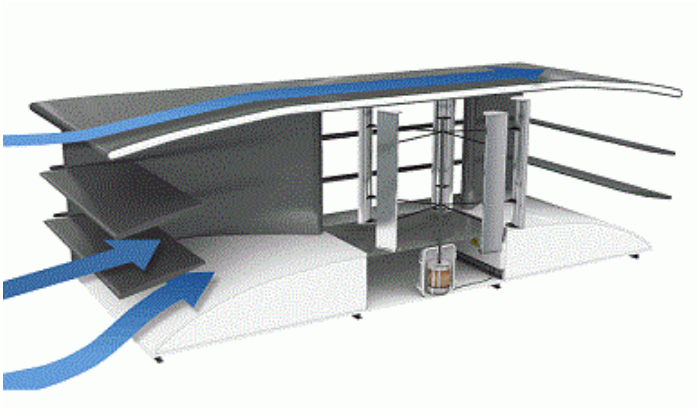

Figure 4. IRWES system

At the top of the selected object, we tried to create space for 3 small wind turbines where the optimal shape would ensure the acceleration of the wind flow.

Geometry of the model was derived from the existing building with specific façade structure in Bratislava, see Fig 3 (b). Building is 105m high with elliptic cross-section with dimension 48 × 27m.

3. CFD SIMULATION

3.1. Description of the top of building

Possible free space in top of the building is on two technical floors in roof of the building. According to façade structures there are possibilities to integrate three wind turbines. Cross-section of the middle section is 5 × 12m and 5 × 10m for side section. We want find the optimal inlet/outlet shape for using IRWES system (see Fig.5.).

(a) 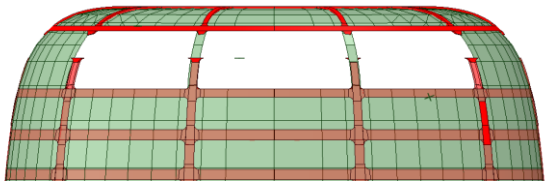 (b) 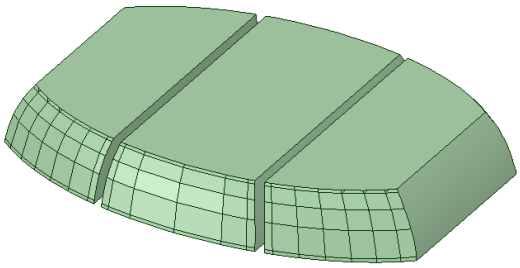

Figure. 5. Illustration of specific facade structure with empty space (a) , Shape of the three sections (b).

3.2. Computation domain and generated mesh

Model of building was created according to an existing building. The computational domain has size 1×0.6×0.4 km^3 (l×w×h), corresponding with block ratio 2%, which is below the recommended maximum value of block ratio 3% [8,9]. The distance from the object to the inlet was 400m.

We created mesh using Meshing implemented in ANSYS [10]. The size function was set on proximity and curvature with medium relevance centre. The element size on surface of the building was 1 m with the size function set on curvature. The element size on surfaces of the designed wind turbine inlet/outlet was 0.25 m with the size function set on curvature. 2 071 521 elements with 387 717 nodes which were transformed in Fluent [10] to polyhedral mesh with 455 303cells, 2 895 448 faces and 2 376 340 nodes were generated.

3.3. Numerical model, boundary conditions and solver setting

For the solution of the 3D steady RANS equations with standard *k-ε* model [11] we used CFD code ANSYS Fluent [10]. For near-wall treatment, the standard wall functions by Launder and Spalding [11] were used. The inlet boundary conditions of the domain are defined by the vertical profiles

$$v(z) = \frac{v^*}{\kappa} \ln \frac{z + z_0}{z_0}, \tag{2}$$

where *v(z)* is mean wind velocity at height *z*, v* is shear velocity, z_0 is aerodynamic roughness height (z_0=0.7), κ is von Karman constant (κ = 0.42), v_{ref} = 10.98467 m/s at a reference height z_{ref} = 100 m. Additional inputs for *k-ε* model are equation for turbulent kinetic energy k, and turbulence dissipation rate ε as follows:

$$k = \frac{u^{*2}}{\sqrt{C_\mu}}, \quad \varepsilon(z) = \frac{u^{*3}}{\kappa(z + z_0)}, \tag{3}$$

where

C_μ =0.09 is a model constant. The outlet boundary is defined as pressure outflow and the side and upper boundary as zero gradients (symmetry). The bottom of the computational domain is modeled as a slip wall. All computations were run as pressure-based, steady, without production limiter. As the solution method SIMPLE pressure-velocity coupling scheme with second order spatial discretization was used, for transient formulation was used second order implicit method. Solution was initialized by hybrid initialization with default setting.

3.4. Design of inlet/outlet shape

Wind pattern for three empty sections on top of the building for wind direction 90° gave us following results:

- for middle section the best location for the wind turbine is centre top of these section,
- for side sections, the best location is top, for left section left top and for right section the best location is top right.

According to these observations we designed symmetric shape of the inlet/outlet wind turbine space 3 × 3m. For modeling of the surfaces, we used spline. Side surfaces were created with tangent 45° on outer end and 0°randent in centre. The bottom surface was modeled using spline with 0° tangent on both ends. The upper surface was flat, see Fig. 6.

Wind pattern for designed wind turbine inlet/outlet space for wind direction 90°can be seen see in Fig. 7.

(a) 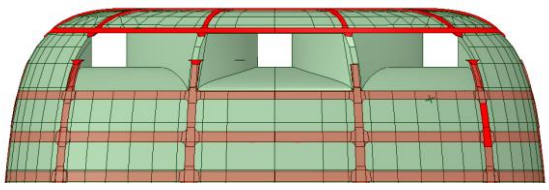 (b) 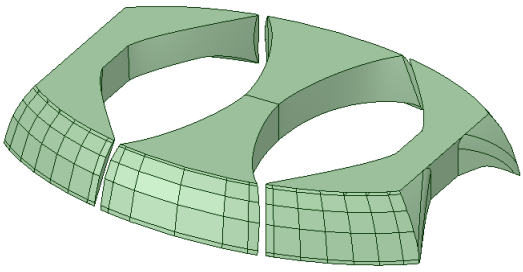

Figure 6. Illustration of designed wind turbine inlet/outlet space (a), Shape of the designed sections (b)

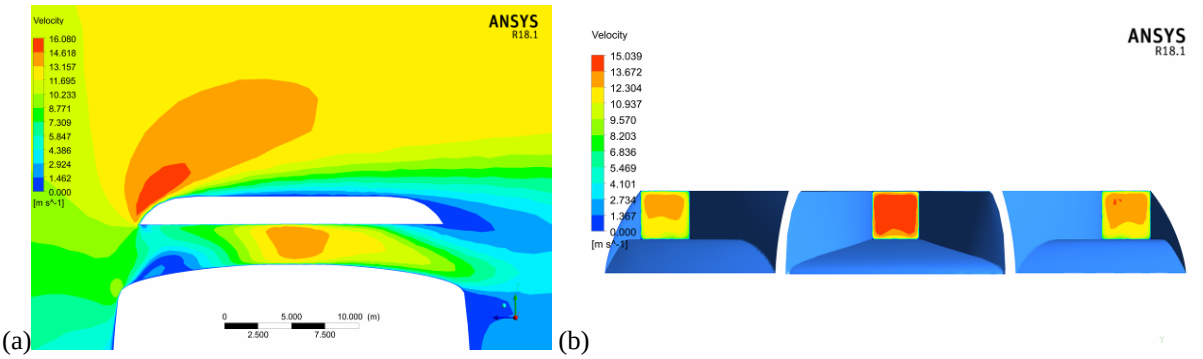

(a) (b)

Figure 7. Cross-section wind pattern (a), Wind pattern in the middle of three sections (b)

4. WIND TUNNEL EXPERIMENTAL MEASUREMENTS

Experimental measurements were performed in Boundary Layer Wind Tunnel of Slovak University of Technology in Bratislava. Wind tunnel was designed with open circuit scheme (see Hubova et al. [3], [6]") with overall length 26, 3 m and two operation sectors of cross-section 2.6 x 1.6 m and with adjustable ceiling. Front operation sector provides steady wind flow up to the velocity 32 m/s (115 km/h). Rear operating sector (ROS) is suitable for detection of effects caused by turbulent wind flow with velocity from 0.3 to 18 m/s. The turbulent wind flow is created in rear operating space. In our case, the roughness of floor was created by plastic film FASTRADE 20 and 150 mm barrier. From the evaluation of the vertical mean velocity profiles, it seems that this modification of floor of tunnel is in the match with terrain category III - IV (closely to IV) with roughness length $z_0 = 0.7$(m), according to ACSE [4], EN 1991-1-4 [5] and Wieringa [7].

By using 3D print technology, model of the structure in scale 1:300 with rough façade was created. To measure the mean wind speed in the open top of building, we use the Irwin omni directional probes, see Fig.8, which were evaluated using a digital pressure scanner DSA 3217 from Scanivalve and we obtain average wind speeds and standard deviations. The model was placed on a rotating table (Fig. 9), which was used for simulation of various wind directions with step of rotation 15°. Pressure taps were placed on the façade in height 92.7m (30.9 cm on model) and 97.8 m (32.6 cm on model) to measure external wind pressure.

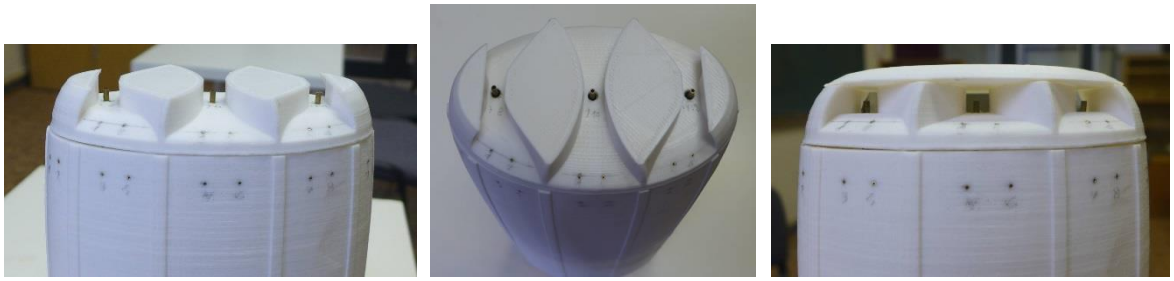

Figure 8. View of model and the position of vertical wind turbine at the position of Irwin probes and top of building for experimental measurements of external wind pressure coefficients

Reference wind speeds were selected so as to fulfill flow similarity of prototype and model. Velocities were chosen with regard to ACSE [4]. In all positions measurements were made for 3 reference velocities (6.95, 8.68 and 10.98 m/s). Similarity of the wind flow around real structure and model of structure during tests was ensured using Reynolds number higher than recommended value 10^4. Reference wind velocities were measured in height H= 33.6 cm (100.8 m on real structure) at the position of wind turbine (without the model) by ALMEMO probe. Average temperature during tests was 15.4°C, barometric pressure was 100 920 Pa and air density was 1.215 kg/m^3. Reynolds numbers for 3 reference velocities reached values ($7.4 \cdot 10^4$, $9.2 \cdot 10^4$, $1.17 \cdot 10^5$).

(a)  b) 

Figure 9. 3D model of the structure in BLWT for wind direction 90° (a), Northwest view of future development (b)

5. RESULTS

We have compared the results of the numerical simulations and experimental measurements and obtained information on the average wind speeds at the VAWT site. Experimental measurements also took into account the influence of free ends of high objects that reduce pressures and wind speed wind at the top of buildings.

Due to the significant increase in small vortices at the entrance, that have been experimentally and numerically detected, it is necessary to insert a rectifying grid that will optimize the flow in inlet region.

The wind velocity values obtained experimentally for reference wind velocity 10.98 m / s are shown in Figure 10.

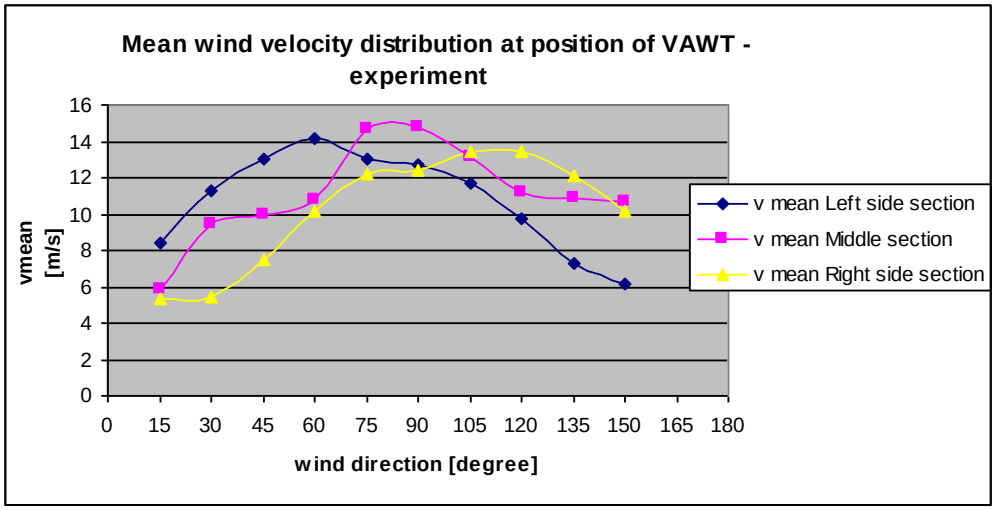

Figure 10. Mean wind speed distribution for different wind direction

Comparison of the mean wind velocity and external wind pressure coefficient obtained by CFD simulation and experimental measurement for 3 reference wind speeds showed a good match. Considering the annual average wind speed at about 100m above sea level v Bratislava, see Fig. 2, we compared the wind acceleration at the turbine site at a reference wind speed of 10.98 m/s. Comparison of experiment and CFD simulation is shown in the graph in Fig. 11.

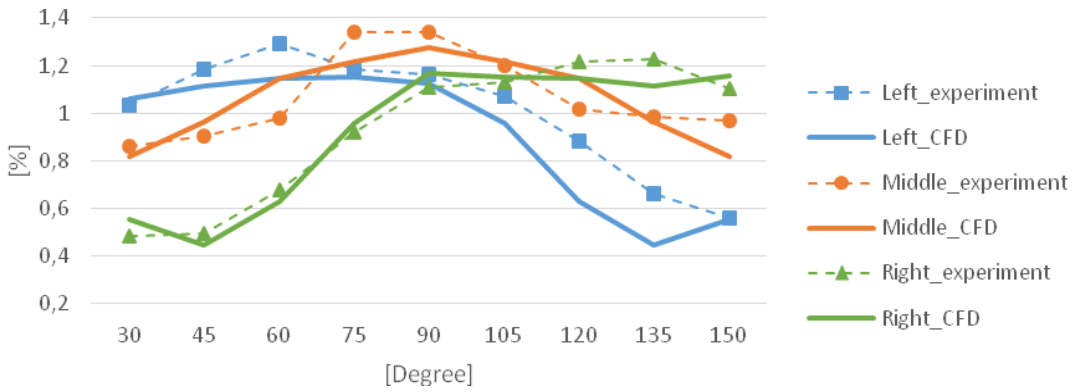

Figure 11. Comparison of wind acceleration in space of wind turbines for different wind directions

Comparison of the experimentally measured coefficients of external wind pressure on the building facade with computer simulation is shown in the graphs in Fig.12.

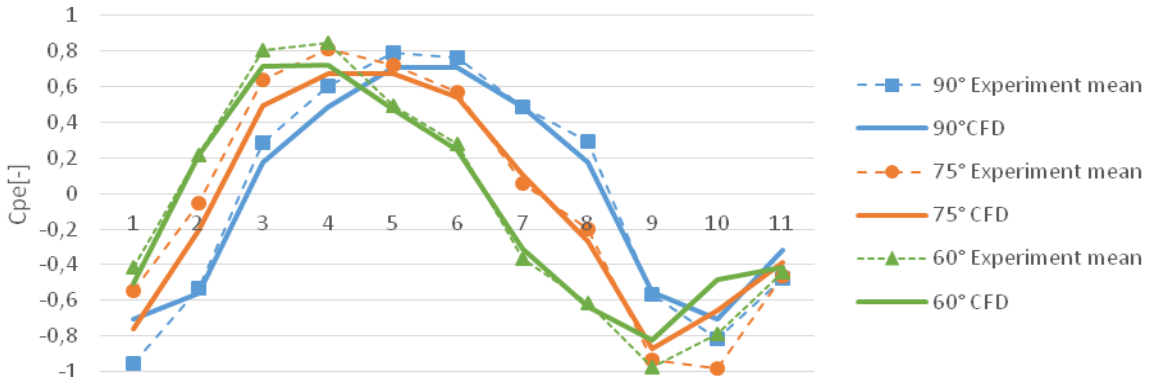

Figure 12. Comparison of external wind pressure coefficient on facade of building at height 92.7m for different wind directions

6. CONCLUSIONS

The wind speed distribution results obtained by CFD end experimental measurements in BLWT allow us to select a suitable VAWT type, see Battisti et al. [1] in this area and height above ground in Bratislava city center. In accordance with power curves Fig.7 in [1] it appears that three-bladed configuration H-rotor DU06W200 and 2-bladed H rotor NACA0018 will have maximal annual energy output. The wind energy potential is based on average local wind velocities as well as the IRWES wind energy characteristics. Annual energy output for wind velocity higher than 8m/s for the considered turbines and three buildings should give 70 MWh/year.

ACKNOWLEDGEMENTS

The presented results were achieved under sponsorship of the Grand Agency VEGA of the Slovak Republic (grant. reg. 01/0265/16) and Grand Agency APVV-15-0522 and with the support of the TU1304 COST action “WINERCOST”.

REFERENCES

[1] L. Battisti, A. Brighenti, E. Benini, M.R. Castelli, "Analysis of Different Blade Architectures on small VAWT Performance", In: Journal of Physics: Conference Series 753 (2016) IOP Publishing 1088/1742-6596/753/6/062009.

[2] A. B. Suma, R. M. Ferraro, B. Dano, and S. P. G. Moonen, "Integrated Roof Wind Energy System" In 2nd European Energy Conference, Maastricht, The Nederlandes. (2012).

[3] O. Hubova, P. Lobotka, "The multipurpose wind tunnel STU", In Civil and Environmental Engineering Scientific - Technical Journal. ISSN 1336-5835, EV 3293/09, Volume 10th, Issue 1/2014, pp. 2 - 9.

[4] ACSE Manuals and Reports on Engineering Practice, no.67. Wind Tunnel studies of buildings and structures Aerospace Division of the American Society of Civil Engineers, ISBN 0-7844-0319-8, 1999.

[5] EN 1991-1-4 Eurocode 1: Actions on structures-Part 1-4: General actions-Wind actions, 2005

[6] O. Hubova, P. Lobotka, "The Natural Wind Simulations in the BLWT STU Wind Tunnel". Vienna: TGM - Federal Institute of Technology, 2014, In: ATF 3rd Conference on Building Physics and Applied Technology in Architecture and Building Structures. E-Book of reviewed papers Vienna, Austria, 6.-7.5.2014, pp.78-84 ISBN 978-3-200-03644-4

[7] J. Wieringa, "Representative Roughness Parameters for Homogeneous Terrain", In: Boundary Layer Meteorology, 63, 323-363, 1993.

[8] J. Franke, et al., "Best practice guideline for the CFD simulation of flows in the urban environment" COST Office Brussels (2007).

[9] Y. Tominaga, "AIJ guidelines for practical applications of CFD to pedestrian wind environment around buildings", J Wind Eng and Aerod. 2008. 96, (10-11) 1749-1761.

[10] ANSYS Inc., ANSYS Fluent User's Guide, Release 18.1 (2017).

[11] D.C. Wilcox, "Multiscale model for turbulent flows". In: AIAA 24th Aerospace Sciences Meeting. American Institute of Aeronautics and Astronautics, 1986. ISBN: 978-1-84821-001-1.

IMPACT OF THE ENVIRONMENTAL CONDITIONS ON OPERATION OF WIND TURBINES

Tomasz Bakoń[1]*, Anna Kozikowska[1] and Paweł Obstawski[1]

[1]Faculty of Production Engineering, Warsaw University of Life Sciences – SGGW, Poland
Corresponding author: Tomasz Bakoń, tomasz_bakon@sggw.pl

ABSTRACT

This article presents selected issues of erosion and contamination of wind turbines blades and their impact on aerodynamics which directly affects the obtained performance of wind power plant. The main focus is on meteorological and biological factors such as wind and particles of sand and dust carried with it as well as rain and insects.

1. INTRODUCTION

Market of wind turbines needs new technologies and solutions that will increase the design performance, resistance to external factors and will reduce number of breakdowns and lower the operation costs. The conditions, in which wind turbine operates, are also very important as well as the possibility of mitigating their negative actions on construction. Well – designed wind turbine blades are characterised by a good stiffness, the lowest possible weight, durability, resistance to soiling, icing and lightning. There are new solutions for protecting blades surface from erosion including the prototype of robot to detect early the damages [3].

The effect of meteorological factors is significant when designing and then using different type of buildings such as wind turbines. The stronger the wind is, the more energy wind power plant produces. However, the same wind that carries particles of different sizes and contamination, but also the temperature, humidity, UV radiation, ice or rain impact the construction of wind turbines, especially blades, and change their aerodynamics and obtained performance.

2. IMPACT OF WIND

During the conversion of wind energy into mechanical energy wind turbine blades are exposed to static and dynamic loads. This is why they must be sufficiently strong. Their designs are mainly based on the technologies that are used in aviation. The most common are profiles divided with regard to pressure distribution. These are conventional, laminar flow and special airfoils which differ from each other in geometrical parameters. One of the most widespread are NACA airfoils.

The type of material used in the production of blades directly affects the shape of the airfoil. The wind turbine blades are made from glass fiber reinforced by polyester, epoxide resin, carbon fiber or kevlar. These materials are characterised by high fatigue strength and low weight, but on the other hand they have high production costs. Another material (rarely used) is wood reinforced by epoxide resin or different plastics. There are also blades made from steel and aluminium, but they are heavy and fatigue sensitive and used only in rotors with very small diameter.

The tip of the wind turbine blade with a length of ca. 40 m cut the air with the rated speed of ca. 230 km/h. The further away from the central point, the larger is the angle of the wind flowing around the blade. In order to keep the optimal angle of attack along the entire length, it is necessary to torque the rotor blades. This solution helps the rotor to operate more efficiently.

Aerodynamic losses reduce the performance of wind turbines. Due to the air viscosity and imperfect smoothness of blades surface, there appear losses caused by air friction. Defects of the profile result in detaching the air stream and creating vortices. The scale of these losses, that are one of the biggest,

depends mainly on aerodynamic drag coefficient which can be improved by more precise smoothening blades surface. The inductive losses occur mainly on the external tips of the blades as the result of the air pressure compensation on both of their sides. There are also screw motion losses of the air that flows away behind the moving blades due to deviation of the air stream in the tangential direction, losses of the flowing air that are caused by increased pressure in front of the blades and partial escaping of the air from the moving blades, losses of the air that flows away as the effect of vortex disturbances of the air stream [14].

Destructive impact of wind. Rotating blades of the wind turbine produce electricity thanks to blowing wind. But at the same time this wind can cause damages of the moving components. The reason of it are too strong and gusty winds, that sometimes may take the form of the tornado. Winds blowing with high velocities can break wind turbine blades and, as a consequence, they become totally destroyed. Figure 1 shows the wind turbine with three blades which were damaged by the tornado. The photo was taken in Kansas (USA) in 2012. Radars at a height of ca. 90 m recorded the value of 267 km/h of wind velocity on that day which was high enough to cause the failure of many wind turbines that were located on that farm. When there are a large number of variables, it is hard to predict what values of wind velocity may begin the damaging process of the blades. The components separated from the wind turbine blades can be dangerous for people and objects that are close to it [3, 10].

Figure 1. Wind turbine blades destroyed by tornado [10].

3. IMPACT OF DUST AND SAND

Sand and dust are the particles which move together with air masses. These fractions differ in sizes (dust is smaller than the sand), but both of them negatively affect the surface of wind turbine blades. The higher the wind velocity is, the stronger the grains hit the blades coating and after some time of operation the damages may significantly lower the efficiency of the energy conversion from wind stream to mechanical energy. Hence, wind power plants located close to the sandy areas such as deserts or beaches are exposed to increased erosion. It is similar to offshore wind turbines that are affected by sea salt.

Erosion of wind turbine blades. The most exposed site to erosion is the leading edge of the wind turbine blade. Figure 2 shows the changes on the leading edge of the blades that are caused by particles carried with the wind within over 10 years of operation. The damages of the top coating are visible and they change the aerodynamic characteristics of the airfoil. Thus, the repair is needed which results in higher maintenance costs and reduces operational readiness . If the erosion will not be stopped at the right time, the sand may erode into fiberglass blade skin and destroy integrity of its structure. Additionally, copper mesh that is usually embedded on the surface of the composite skin and protects from the lightning strike, may be removed locally in the place of erosion. As the lightning strikes tend to be concentrated at the outboard section of the blade, the erosion damage may degrade lightning protection where it is most necessary.

Another problem connected with the erosion of blades surface and sandy areas is so called “corona effect” which means that the ionising air cause electric discharge. In order to prevent damage to the fiberglass structure from the rain or sand erosion, metallic abrasion strips are bonded to the blade leading edge and they form hard surface that absorbs kinetic energy of the rain drop or sand particle. Metallic materials are especially good at rain erosion protection, but it is not the same with the impacting sand particles which gradually erode away the metallic pieces. This phenomenon usually occurs near the outboard blade tip where the velocity is high and sand particles impact with the greater kinetic energy. They often oxidise and cause the corona discharge in sandy environments (figure 3) [18, 23].

Figure 2. Impact of sand and dust particles on wind turbine blade [5].

Figure 3. The corona effect at the time of landing of the helicopter [13].

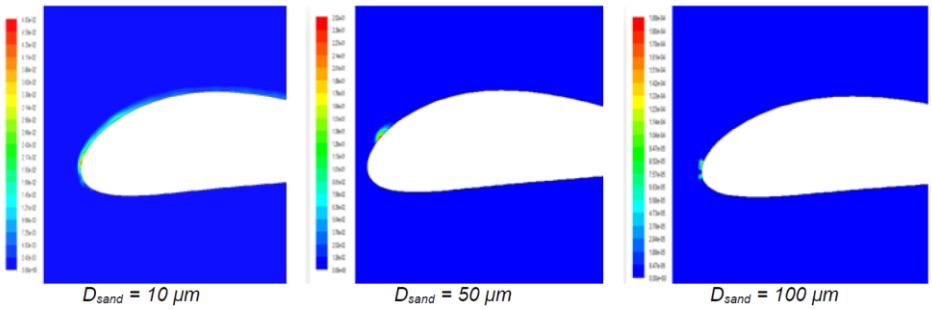

Figure 4. The results of mass deposition for different particle diameters, the angle of attack $\alpha = 0°$, wind velocity V = 6 m/s and sand – to – air loading ratio Q = 0,001 [8].

Accumulation of dust on the blades surface. Figure 4 shows models predictions of the mass distribution over the blades surface. The simulations were performed using CFD model [8]. Moreover, the contours of deposited mass are noticeable to show the areas on the airfoil that are mostly vulnerable to contamination by dust particles. The bigger the particles sizes are, the less distribution of mass occurs and the area of surface contamination is smaller. The increase of particles diameter results in less sticking efficiency and less mass deposition, although the chance of impacting blades surface is increased as well as number of impacted particles. The reason is that bigger particles are inertia – dominated which means they are not so influenced by the flowing air. On the other hand, small particles follow the flow path.

Increasing the attack angle (figure 5, 20° angle) causes increase of deposited mass especially on the pressure side which significantly distorts the flow around the blade. As a consequence, the lift coefficient decreases as well as the produced energy. Thus, pitch – regulated system is better to control the power of wind turbine in a dusty environment than stall – regulated system. This is due to a character of pitch – regulated system that allows to control the power by rotating the blade around its axis toward lower angles of attack.

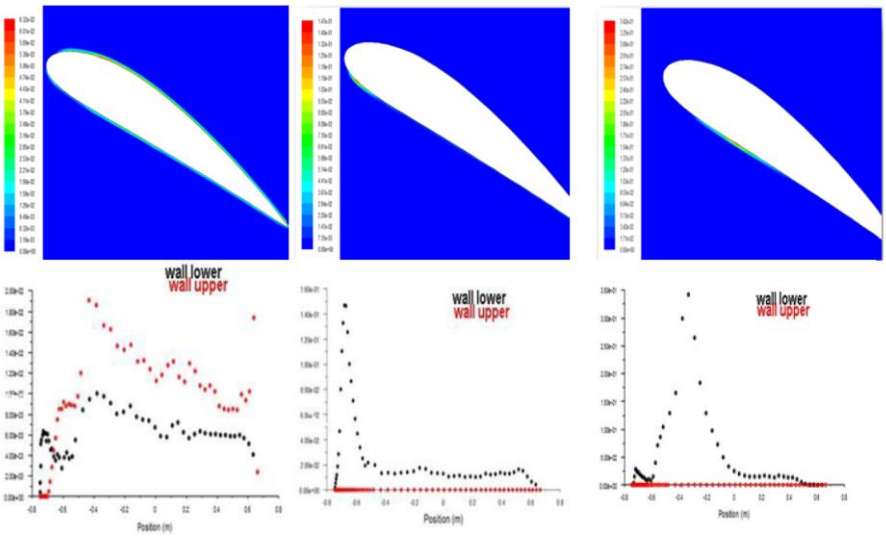

Figure 5. The results of mass deposition for different particle diameters the angle of attack α = 20°, wind velocity V = 6 m/s and sand – to – air loading ratio Q = 0,001 [8].

This means less deposited mass and less drops in power for the same conditions. Since, pitch – regulated turbines shall be installed in dusty areas. In case of using stall – regulated system it is important to clean blades surface in every 1 – 3 months in order to reduce the drop in performance (to 10 – 20 %) [8].

The studies performed in Greece [15] focused on the problems of planning wind farm on a high plateau that occur when for example neighbouring lignite basin field. The analysis were conducted using WRA – Wind Resource Analysis modelling methodology with data of wind speed and wind direction measured for more than a year on three meteorological masts.

Table 1. Impact of dust accumulation on blades surface for three wind farms located near the lignite basin field [15].

The three proposed wind farms	Without dust accumulation	With dust accumulation losses (1 month accum. [1%])	With dust accumulation losses (9 months accum. [18%])
East			
Net CF	19,0 %	18,7 %	15,4 %
Net [MWh/MW]	1660,0	1644,2	1357,2
North			
Net CF	19,0 %	18,8 %	15,5 %
Net [MWh/MW]	1660,0	1644,4	1359,0
West			
Net CF	23,0 %	22,9 %	18,9 %
Net [MWh/MW]	2027,0	2006,4	1654,7

The air that is contaminated by different sizes rock materials significantly affects the performances of wind turbines. Neighbouring the mine results in accumulation of dispersed dust on the rotor blades which noticeably changes the power curve of wind turbines. The maximum dispersion distance for 10 µm particles and the wind speed value of 3,9 m/s in the emitting source was estimated 6,3 km away from the source. According to this, the distance is important factor when planning the localization for wind farms close to mine area. If dust is accumulated on blades of pitch – regulated turbines for 1 month, the mean power loss is less than 5 %. However, when the accumulation continues for 6 or 9 months the power loss can reach up to 12% and 18%, respectively.

Table 1 shows the results of conducted simulations regarding to effects of dust accumulation on the blades surface of wind turbines. Net capacity factor (Net CF) and net operating hours (Net index) were calculated for three localization of wind farms. The values of Net CF and Net index decrease with the duration of dust accumulation. There are noticeable differences in power losses (up to 17 %) between 1 and 9 months of accumulation [15, 21].

The tests performed in China [17] mainly concentrated on changes of aerodynamics properties of wind turbine blades that depend on roughness surface conditions due to accumulated contaminations. The values of lift and drag coefficient were taken into account and they were compared with the values obtained for clean airfoil surface. The NACA 63-430 airfoil was chosen for the experiment, because of its common use in wind turbines structure. Figure 6 shows the changes of lift coefficient depending on angle of attack. Two curves, that are shown in the graph (figure 6), were developed based on the experimental data and numerical simulation.

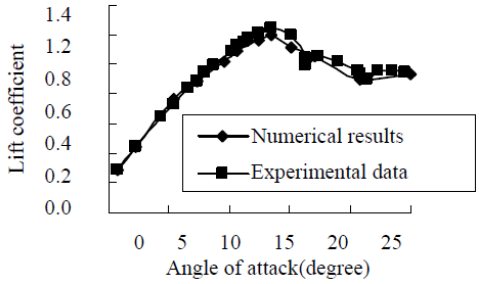

Figure 6. Comparison of lift coefficient curves for NACA 63-430 airfoil [17].

4. IMPACT OF RAIN

Rain as well as sand and dust can cause the erosion of wind turbine blade surface (Figure 7). Its negative impact depends on droplet size, intensity and duration of rainfalls and also tip velocity that may cause the increase of impact force. The degradation of the blades surface may proceed faster in regions with strong winds and heavy rainfalls.

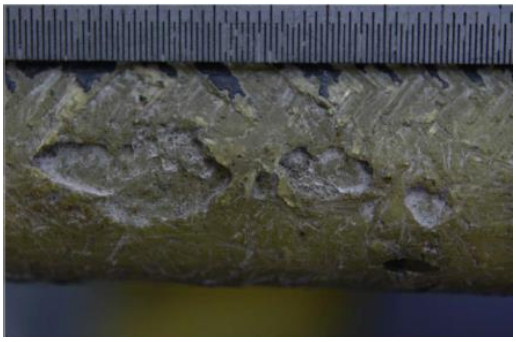

Figure 7. Erosion of the leading edge of the wind turbine blade removed from the service [19].

The Scottish studies [16] were carried out to map the erosion effects of the rainfall rate against tip velocity. The uncoated composite made from epoxy resin and reinforced by fiberglass was used in the experiments. The droplets impacting the sample surface were characterised by constant diameter of 2,5 mm, rainfall intensity of 20 – 40 mm/hour and tip velocity of 40 – 60 m/s. The 40 minutes tests proved that the increase of tip velocity has greater impact on mass loss than the increase of rainfall intensity (figure 8). It means that the velocity of wind turbine blades plays more important role in erosion process than the relevant conditions in which the turbine is situated.

The size and shape of rain droplets are also significant in process of blades surface erosion. Large drops can cause larger erosion damages of blades coating, even at lower velocities. This is because large drops are characterised by higher hammer pressure on the surface and there is the possibility of varying the pressure distribution over the impacted area. Some researchers claim that not the mass of a distorted water drop is so much important at the moment of an impact but the radius of curvature at the point of

contact. Distorted drops with radii of curvature greater than their initial diameters shall proportionately cause more damages [1, 19].

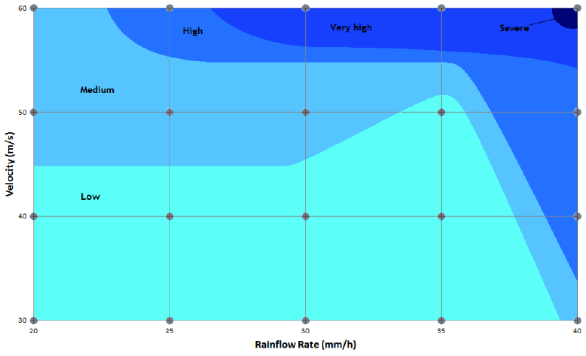

Figure 8. Mass loss of the composite material depending on the impact velocity and intensity of rainfall [16].

The angle of impact also affects the process of surface erosion. The normal component of a droplet impact velocity is mainly responsible for the damage while the tangential component in most cases has little effect. However, for ceramics and hard polymers at high impact velocity the tangential component of a droplet may equally significantly damage the surface as the normal component.

The erosion rate depends on the temperature of the environment and the liquid drops. Experiments have shown that the erosion rate increases with the rise in water temperature which might be the result of the reduction of the liquid viscosity. The increase of the viscosity causes the increase of the velocity of the outward flowing liquid and it affects the surface by experiencing more shear damage.

The liquid that is trapped in the bottom of pits formed on eroded surfaces can reduce the negative impact of rain. Water shall act like a cushion at the moment of impact and mitigate the process of erosion. If the droplet hits wet surface, the liquid film deforms and, as a consequence, the pressure on surface is less than if it was dry. Another explanation is that the impact pressure decreases due to dispersion of wave as it passes through the liquid layer [19].

5. IMPACT OF BILOGICAL FACTORS

Besides weather conditions, biological factors such as flying insects, algae and lichens have also influence on operation of wind turbines (figure 9).

There were performed some studies that analysed flying insect population at height of 100 m above the ground in southern Great Britain. Researchers discovered that the most common species of insects were aphids and drosophila melanogaster known as the fruit fly. At present it is hard to find information about complex studies on insect population at different heights. However, in case of wind turbines the most important thing involving flying insects is that their debris accumulate on the blades surface and cause deterioration in the aerodynamic characteristics [11].

Double stall or multiple stall effect can be caused by defective yaw control system, badly designed blades or accumulation of various contamination such as debris of flying insects on the leading edge of wind turbine blades. First observations of this phenomenon were made on the wind farm located in California (USA).

It was noted that the output power had more than one level for the same wind velocity and its value was sometimes half lower than the designed one. There were performed some studies on the aforementioned wind farm referred to this phenomenon but the source of the double stall effect was not found as “the Insect Hypothesis” was not considered [6].

The Insect Hypothesis. The behaviour of flying insects mostly depend on weather conditions (figure 10). It is assumed that the contamination of blades surface increases only when insects are close to the wind turbine that is in operation. The insects mainly fly when there is no rain, little wind (the velocity lower than 7 m/s), and the ambient temperature is higher than 10 °C. Under this conditions, the flying insects will increasingly contaminate the blades surface near the stagnation point where the velocity of the air stream is low and the flow becomes insensitive to contamination. This means that the output power is not affected. Above certain wind velocity, when the insects do not fly, the level of

contamination maintains constant. When the velocity is high, the attack angle of the blade is large and the suction peak (the area of minimum pressure and maximum air velocity) shifts to the contaminated site. In this case the flow disturbance depends on the level of contamination that accumulates on the blades surface and results in the decrease of the stall angle. It is important to note that the smaller the stall angle, the lower the output power. The design power level of the wind turbine shall be reached again if the blades are clean or when it rains during the operation of the turbine [7].

Figure 9. Wind turbine blade covered by algae and lichens [2] (left) and by debris of beetles [9] (right).

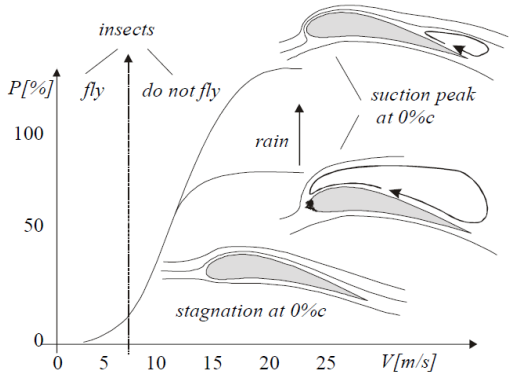

Figure 10. Double stall phenomenon as the result of insects behaviour in different weather conditions [7].

6. CONCLUSIONS

Proper operation of wind turbines depends on proper functioning of rotor blades. First of all, they have to be characterised by good aerodynamic parameters. Unfortunately, it is hard to achieve optimal conditions because of the meteorological and biological factors. Both sand and rain, but also the wind and contamination accumulating on the blades surface such as dust and insects debris cause the erosion of the blades coating. This deteriorates the aerodynamics of blades and the obtained performances of wind turbine are lower (table 2).

Desert areas, coasts, open – pit mines and another sources of dust can increase the accumulation of contamination [4]. However, the impact of some factors is not related to the specific location, which for instance refers to flying insects that collide with blades and cause negative phenomenon called double stall. Therefore, it is very important to clean regularly the surface of rotating components, and especially the leading edge of blade that is mostly susceptible to erosion and accumulation of contamination.

Table 2. Impact of contamination on change in annual energy production of wind turbine [22].

Blade state	***Annual Mean Wind Velocity***		
	6 m/s	***7 m/s***	***8 m/s***
Clean	0 %	0 %	0 %
Moderate contamination	0 %	0 %	0 %
Severe contamination	-1 %	-2 %	-2 %
Extreme contamination	-13 %	-11 %	-10 %

REFERENCES

[1] W.F. Adler, Particulate impact damage predictions, *Wear. 186–187, Part 1 (1995)*, pp. 35-44

[2] Altitec Wind Power Service, Do Blades Matter – How to maintain them, conference materials, 2013, p. 14

[3] T. Bakoń, Wind Turbines Damages and Non-invasive Methods of Early Detection, *elektro.info* 11/2011, pp. 46-49

[4] T. Bakoń, Impact of selected exploitation factors on photovoltaic cells efficiency, *elektro.info* 5/2015, pp. 82-84

[5] Braendler Engineering, Blade Inspection, Damage and Maintenance, conference materials, Hamburg 2013, p. 32

[6] G. P. Corten, H. F. Veldkamp, Insects can halve wind-turbine power, *Nature*, 2001, vol. 412, p. 1

[7] G. P. Corten, H. F. Veldkamp, Insects Cause Double Stall, conference materials, *13th IEA expert meeting on the Aerodynamics of Wind Turbines*, Stockholm 1999, pp. 1-3

[8] A. Diab, H. Salem, A Preliminary Study on the Performance Degradation of a Wind Turbine Blade in Dusty Environments, Ain Shams University, Egypt, pp. 2-4

[9] Double stall, http://www.bladecleaning.com/problematica_EN.htm

[10] T. Farney, Tornadoes and Wind Turbines!, http://toryfarney.blogspot.com/2013/02/tornadoes-and-wind-turbines.html

[11] G. Fiore, M. S. Selig, A Simulation of Operational Damage for Wind Turbine Blades, conference materials, *32nd AIAA Applied Aerodynamics Conference*, Atlanta 2014, pp. 6-7

[12] S. Gumuła, Energetyka wiatrowa, *Wydawnictwo AGH*, Kraków 2006

[13] Israel Defense Forces, Chopper's Blades Give Off a Ring of Lighthttps, https://www.pinterest.com/pin/31103053646481443/

[14] W. Jagodziński, Silniki wiatrowe, *Państwowe Wydawnictwa Techniczne*, Warszawa 1959

[15] C.J. Koroneos, E.A. Nanakib, G. Xydis, Comparative wind farm planning on a high plateau: Dust dispersion as a sitting constraint, *„Land Use Policy" 2014*, vol. 39, Elsevier, pp. 22-33

[16] D. Nash, C. Siddons, M. Stack, An experimental approach to analyzing rain droplet impingement on wind turbine blade materials, *University of Strathclyde*, 2015, pp. 4-5

[17] J. Ou, N. Ren, Dust Effect on the Performance of Wind Turbine Airfoils, *Journal of Electromagnetic Analysis & Applications* 2009, no. 1, pp. 102-107

[18] M. Ples, Wyładowanie koronowe,

http://weirdscience.eu/ Wy%C5%82adowanie%20koronowe.html

[19] Z. Shizhong, Accelerated rain erosion of wind turbine blade coatings, *Technical University of Denmark*, 2014

[20] W. Sobieraj, Aerodynamika, *Wydawnictwo WAT*, Warszawa 2014

[21] I. H. Seo et al., Numerical prediction of fugitive dust dispersion on reclaimed land in Korea, *„Transactions of the ASABE"* 2010, vol. 53, no. 3, pp. 891–901

[22] C. J. Spruce, Power performance of active stall wind turbines with blade contamination, conference materials, *Vestas*, 2006, pp. 2-7

[23] W. Thomas et al., Enhanced erosion protection for rotor blades, conference materials, *Hontek Corporation*, Teksas 2009, pp. 1-2

Paper TS1.1.5

THE INTERNATIONAL CONFERENCE ON
WIND ENERGY HARVESTING 2018
21-23 March 2018
Catanzaro, Italy

FLOW SIMULATION AROUND MULTI WIND TURBINES USING IN CITIES

Ferenc Szlivka[1], Ildikór Molnár [2], Gábor Sándor *

[1]Department of Civil and Mechanical and Safety Engineering, University of Budapest, Hungary
[2] Department of Civil and Mechanical and Safety Engineering, University of Budapest, Hungary
*Corresponding author: Gábor Sándor, *rodnas.robag@gmail.com*

ABSTRACT

The operation of more wind turbines derived from the principle of wind energy is simulated in our article with the help of CFD code. Our aim is to develop a type of wind generator which produces energy more efficiently. In our case study the two or more impellers are pushed to each other and they are connected as gears. So they use smaller space in an urban environment. In this type of wind generator are two or more rotors very close to each other. There are two or more rotors in one column or more rotors in horizontal or vertical mounted on bigger building faces. To calculate the theoretical performance of the dual or more impeller wind turbine we have done CFD (Computational Fluid Dynamics) analysis on the flow field around the impellers.

NOMENCLATURE

P	=	Performance (W)
C_p	=	Performance factor
λ	=	Speed ratio factor

1. INTRODUCTION

Renewable energy sources are increasingly part of our life in the field of energy supply. Nowadays, the technologies which can ensure sustainable energy supply are available. Using wind energy is a potentional opportunity to produce more MW electricity with wind turbines. In our experience, there is more and more demand for public energy initiatives. If a community or local council launches an energy investment, it can be considered as a public initiative. Where the legal environment allows it, the community can actively take part in the investment and the members can ensure their own energy supplies. Thus, they become energy providers and consumers. As a result, they increase their independence and improve the local economy. Current wind turbines are located further from the residential areas mostly due to their large size which has negative impact on the landscape. Therefore, all the advantages that cities can offer are ignored and the wind channel between buildings is not used. When wind turbines are installed in urban areas, their size is mostly 2-3 meters, which enables us to gain 1,5-2 kW energy in the case of 10 m/s wind velocity. In the EU member countries, so in Hungary as well, the concept of public energy is more widely known, which means common commitment to energy awareness. The main aim of this community is to use sustainable energy in the households of the community with the help of their own energy supplies. The most common option is the usage of solar energy but using micro wind turbines is another possible option. [4; 7]

[1] Professor, [2] Associate, [*] Student, Institute of Mechatronics and Vehicle Engineering, Öbuda University, 1081 Népszínház utca 8., Budapest, Hungary/[1] szlivka.ferenc@bgk.uni-obuda.hu, [2] molnar.ildiko@bgk.uni-obuda.hu, [*] rodnas.robag@gmail.com

2. METHODOLOGY

The process of pressure balance is influenced by the terrain and the rotation of the Earth. The performance of the wind is proportional to the third power of velocity.

$$P = \frac{1}{2}\rho v_1^3 A\ [W] \tag{1}$$

The performance originating from the wind can be calculated in more ways. We choose the Betz equation as this method does not focus on the flow field around the blades just with the gained performance. The ideal model can be seen on Figure 1., where v is the velocity between blades and v_1 is the inlet velocity and v_2 is the outlet velocity. The surface of the turbine is S, the surface of the inlet wind is S_1 and the surface of the outlet wind is S_2.

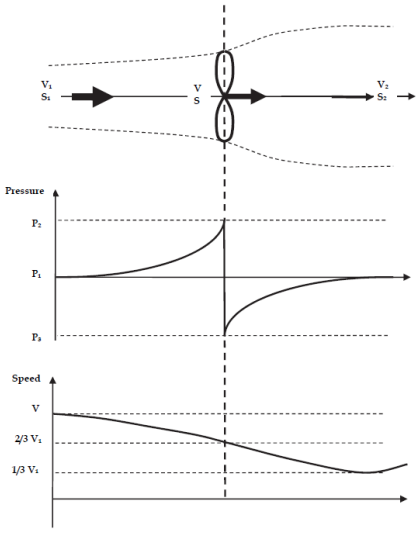

Figure 1. Betz model

The so called performance factor C_p is the quotient of the gained performance and the wind performance available.

$$C_p = \frac{P_{extr}}{P} \tag{2}$$

$$P_{extr} = \frac{1}{4}\rho S(v_1^2 - v_2^2)(v_1 + v_2) \tag{3}$$

The performance factor is a proportion without a measurement unit. This indicates the efficiency of turbines, which means how much power is gained from the wind flow. Equation 4 shows the power factor taking the speed ratio into consideration.

$$C_p = \frac{1}{2}(1 - b^2)(1 + b) \tag{4}$$

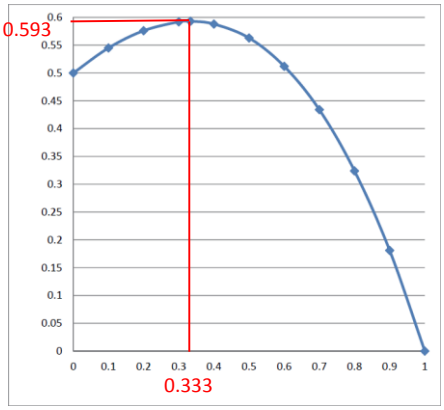

Figure 2. The performance factor in function of velocity ratio [2]

Based on the results of Figure 2, the highest efficiency can be reached at 1/3b. We get the maximum power factor by inserting this (1/3b) into equation 4. So this is the maximum theoretical performance that we can achieve. 40% of the wind energy available is lost but this can be more in practice. As a result, the maximum performance value of the wind turbine:

$$P_{max} = \frac{16}{27}\frac{\rho}{2}V_1^3\frac{\pi D^2}{4} \quad [W] \tag{5}$$

An important feature of the blades is the speed ratio λ which is the quotient of the circumference velocity and the wind velocity.

$$\lambda = \frac{v_k}{v_1} \tag{6}$$

The speed ratio factor is influenced by the number of blades, n. In order to reach the maximum performance, the fewer the blades of a wind turbine are, the faster it needs to rotate.

In Hungary the most common wind turbine is the horizontal one with three blades impeller. Figure 3 indicates the connection between the performance factor and the speed ratio in the case of three blade impellers and ideal impellers. [2; 6; 9]

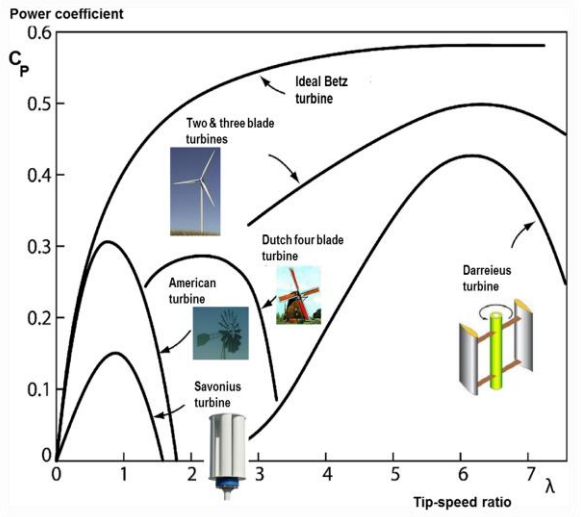

Figure 3. Connection between the performance factor and the speed ratio [2]

You can clearly see from the theoretical equation that the gained performance is proportional with the third power of velocity and it increases in a linear way with a surface of the impeller. If we want to make use of the wind power in the city, we need to cover as many areas as possible with wind turbines. What

is even more important is to locate the turbines on surfaces where the wind is faster due to the attributes of the buildings. To make the best use of the surface, we already have some positive results from earlier researches. [8; 10]

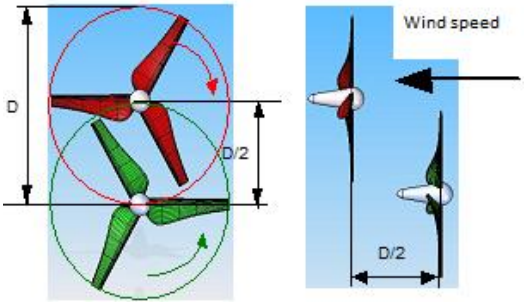

Figure 4. Impeller layout

The two impellers rotate opposite each other and in opposite direction. Not just two but more turbines can be installed on buildings as Figure 5. shows.

Figure 5. Turbines on buildings

The layout which can be seen on Figure 4. can be combined with the layout of Figure 5. In this case the turbines would be found in two rows and the distance between the rows would be D/2 and the distance between impellers would also be D/2. The turbines of the first row would rotate clockwise while the turbines of the back row would rotate in the opposite direction with synchronized rpm. The rotation of the impellers would be with a 60 angle difference like in the case of gears. We are currently working on such model. (Fig. 8.) For the time being, due to computer capacity and time capacity, we can only have limited results. If we increase the surface we can reach better performance. Another way to increase the performance is to find or create areas where the wind velocity is higher. Unfortunately cities are places where the natural wind flow and inflation above the ground are distorted. The thick layer (200- 2000 meters) of the atmosphere is called atmospheric inflation, which is directly affected by the features of the underlying terrain. The atmospheric inflation is where human activity takes place. The flow in the inflation is characterised by a disorganised, turbulent motion. The structure of the flow depends on the complex system of mechanic and thermic turbulent vortexes which are interrelated. Turbulence can be described as the difference between the speed value and the average value and as the extent of the fluctuation of the velocity. The flow in the atmospheric inflation is considerably influenced by the relief, the vegetation and the buildings. A complicated turbulent flow forms around buildings, which is illustrated in Figure N in the case of a detached square building and in the case of terraced houses. If the detached square building is hit by perpendicular wind velocity, the flow field around the building can be divided into five parts. [1;3]

- the first part: a vortex in the shape of a horse shoe forms along the front wall and the side walls of the building
- above the vortex in the shape of the horse shoe, stagnation point forms on the front wall of the building and the flow speeds up towards the edges of the front wall
- a stalling part forms at the top and the sides of the building
- behind the building stalling bubbles are formed
- the flow is undisturbed above and next to the building

The flow is considerable influenced by the stalling of the inflation, which can occur if the pressure rises along the solid wall in the direction of the flow. If the buildings are located relatively far from each other, the flow around the buildings is considered as separate flow. With the reduction in the distance between buildings, stalling bubbles affect each other and the flow rises. [3]

3. RESULTS

We can clearly see from the results of the simulations, that a stalling bubble forms above the building. But above this stalling bubble, there is a flow field where the wind velocity is higher (red zone). If we install the wind turbine in this zone, the wind is expected to reach the impellers with greater inlet velocity than in other fields even if it is an undisturbed one. If the front wall of the building is made chamfered to different extent, the size of stalling bubbles is reduced and the size of the zone with higher velocity increases.

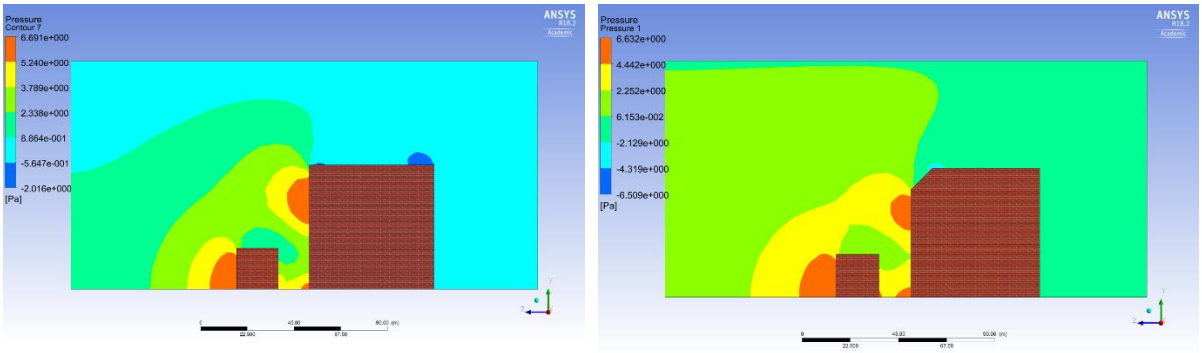

Figure 6. Pressure field around buildings

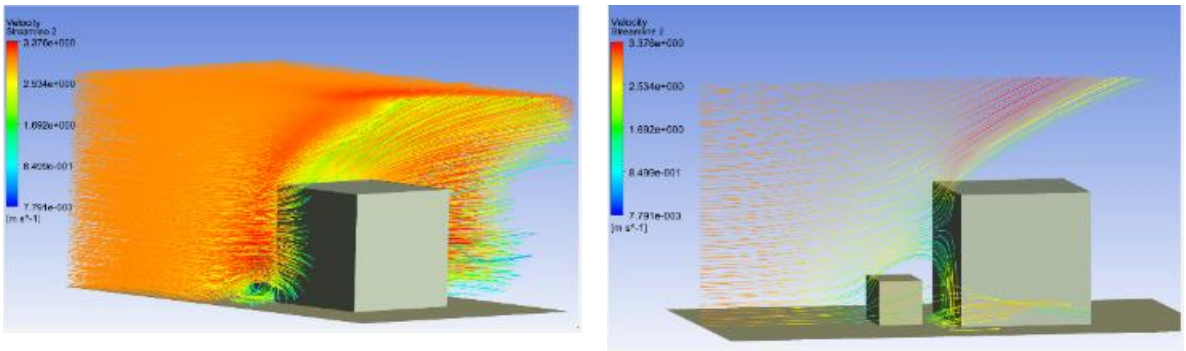

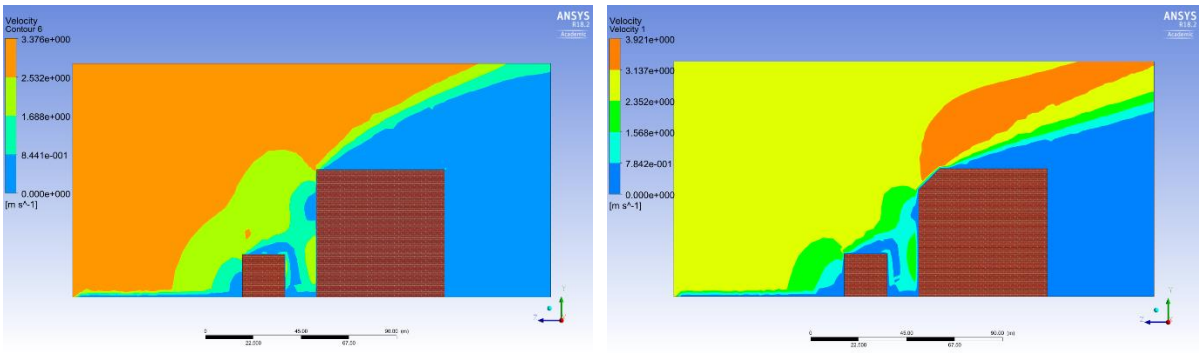

Figure 7. Velocity field around buildings

In the first case, wind direction is assumed to be perpendicular with constant speed of 3 m/s as an average wind speed in dense cities. In the second case wind profile power law relationship will be given as an initial condition (7), where:

$$\frac{v}{v_r} = \left(\frac{h}{h_r} \right)^{\lambda} \qquad (7)$$

v is the wind speed *[m/s]* at the height of h *[m]*, $\boldsymbol{v_r}$ is the known wind speed at a reference height h_r and λ is a coefficient that depends on the surface structure and the equilibrium position of the atmosphere.

Figure 8 shows the windmill around the buildings. Due to the asymmetric inflow, several large vortex structures appear in the field. The results show the part of the higher building where the installation of wind turbines is recommended. A The maximum wind velocity is located near the edge of the underlying building (v = 13 m / s)

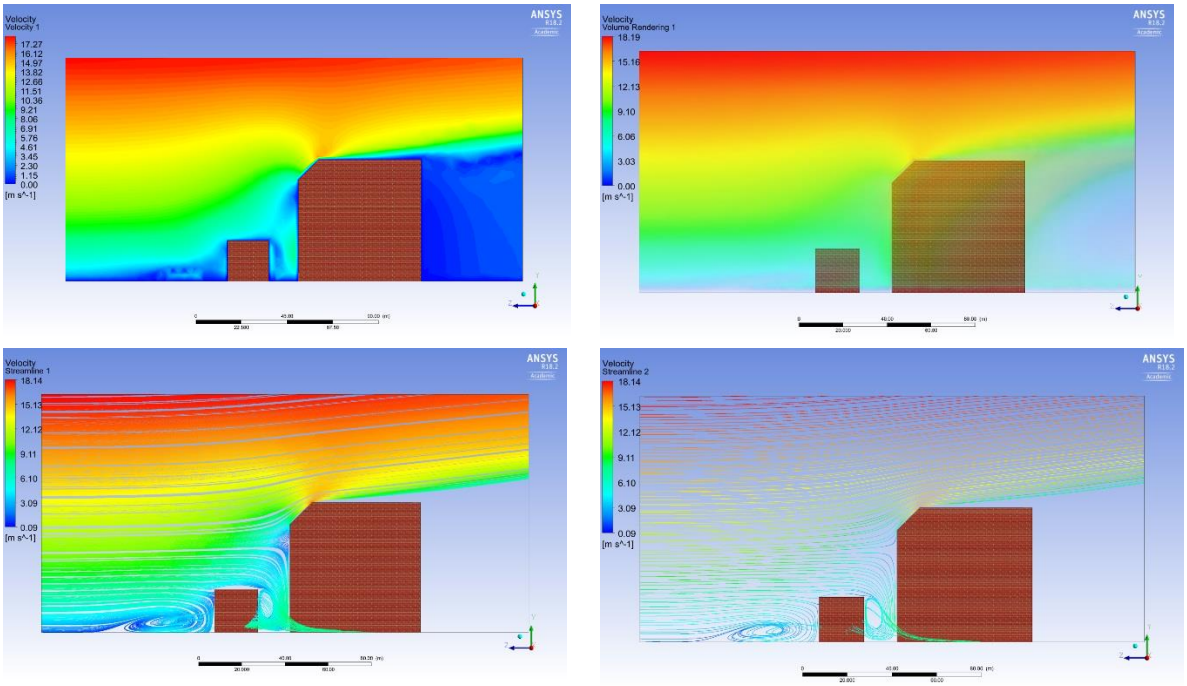

Figure 8. Wind speed exponential function

The practical significance of these observations can be multifaceted and useful for a city-building program aimed at revitalizing a space.

4. CONCLUSIONS

Besides solar energy, wind energy also a major factor in the "green energy" aspect that should be taken advantage of. In urban circumstances the flow of the wind is more predictable therefore it is worth to be utilized paying attention to various components such as impact on humans. Under the given conditions the goal is to obtain more benefit from this fluid energy. From the point of view of installing wind turbines, it is important to pay attention to places with larger wind areas in urban environments. Computing Fluid Dynamics (CFD) calculations help to map this. In the urban environment, the occurrence of a vertical axis wind turbine is becoming more common, despite its low efficiency.

During the preliminary Computing Fluid Dynamics (CFD) simulations it have been concluded that the multi-rotor configuration is more effective than the single-rotor construction. Further measurements and simulations are based on the multiple impeller is situated in a given infrastructure. (Fig. 8.) [5]

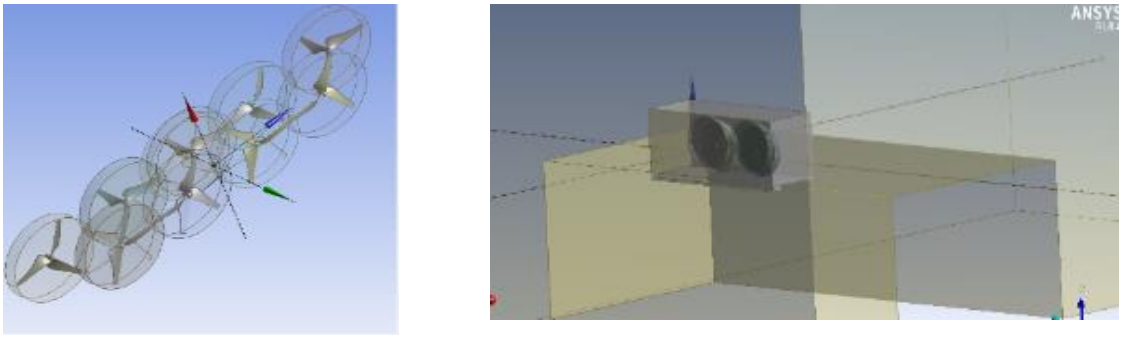

Figure 8. Wind turbines in two rows (CFD)

REFERENCES

[1] Dr. Molnar Ildiko, Dr. Szlivka Ferenc, „Víz - és szélenergia hasznosítás," MÜTF - TÁMOP-4.1.2.A/2-10/1 Projekt, MÜTF, 2012, p. 87.

[2] Scribd, Magdi Ragheb and Adam Ragheb, "Wind Turbines Theory - The Betz Equation and Optimal Rotor Tip Speed Ratio," in Fundamental and Advanced Topics in Wind Power, intech, 2011, pp. 19-38.

[3] Bottyán, Z., Gyöngyösi, A. Z., Wantuch, F., Tuba, Z., Kurunczi, R., Kardos, P., Horváth, G. (2015). Measuring and modeling of hazardous weather phenomena to aviation using the Hungarian Unmanned Meteorological Aircraft System (HUMAS).Idojaras, 119(3), 307-335.

[4] European Wind Energy Assiciation (2002): Wind Energy. The Facts Brussels. European Communities

[5] Tony Burto (2006): Wind Energy Handbook, Wind Energy Consultant, Carno, UK, 618 p.

[6] N. SCHREMPF, L. TÓTH, I. PATAY: Wind energy potential estimation in Hungary, hae Journals.org, TÁMOP 4.2.1.B-11/2/KMR-2011-0003

[7] Wilkes J. Moccia J. Dragan M.: (2012) Wind in power, European statistics (EWEA) http://www.ewea.org/fileadmin/ ewea_documents/documents/publications/statistics/Stats_2011.pdf

[8] T.S. No, J.-E. Kim, J.H. Moon and S.J. Kim: Modeling, control, and simulation of dual rotor wind turbine generator system, Renewable Energy Volume 34 ,10, 2009

[9] Vad, János: „Incorporation of Forward Blade Sweep in the Non-free Vortex Method of Axial Flow Turbomachinery Rotor" Periodica Polytechnica ser. Mech. Eng. Vol. 45, No. 2, 2001, pp.: 217– 237.

[10] Szlivka,F., Bencze, F., Kemény, Gy., 1989, "Ventilator rotor of axial flow fan", No: 209 012: NSZO:F04D-029/38 Vad, J., 2001, "Incorporation of Forward Blade Sweep in the Non-free Vortex Method of Axial Flow Turbomachinery Rotor", Periodica Polytechnica ser. Mech. Eng.. Vol. 45, No. 2, pp. 217–23

TECHNICAL SESSION 1.2

Dynamics, Structures and Materials

THE INTERNATIONAL CONFERENCE ON
WIND ENERGY HARVESTING 2018
21-23 March 2018
Catanzaro, Italy

Paper TS1.2.1

ASSESSING THE IMPACT OF EARTHQUAKE AND WIND LOAD IN THE PERFORMANCE-BASED DESIGN OF WIND TURBINE TOWERS

Pedro Martinez-Vazquez[1], Michaela Gkantou[1] and Charalampos Baniotopoulos[1]*

[1]School of Engineering, Civil Engineering Department, The University of Birmingham, Edgbaston, B15 2TT, Birmingham, United Kingdom
Corresponding author: Pedro Martinez-Vazquez, P.Vazquez@bham.ac.uk

ABSTRACT

Strength reduction factors (SRFs) are typically used for the performance-based design of structures located in seismic areas. This enables to calibrate their inelastic response to pre-determined ductility levels based on building classification schemes. The standard procedures to estimate SRF's however ignore the presence of wind, which may lead to non-conservative designs. Previous research has shown that the combined action of wind and earthquakes can considerably magnify strength demands of buildings designed to perform under specific ductility levels. The proposed research is therefore concerned with the estimation of design forces acting on a hybrid steel wind turbine tower located in shore with and without wind actions. It is seen that meaningful combinations of wind and earthquake load can increase the strength demand of hybrid wind turbine structures in up to 50% for the tubular section and up to 81 % across the lattice segment. This raised the ductility demand of those structures from 1 to up to 3 and 6.5 respectively, thus suggesting that the structure is susceptible to undergo inelastic performance when subject to multi-hazard conditions.

1. INTRODUCTION

In the past decades, regions across the world have been identified where the energy production of Class I and Class II wind energy increases exponentially. This is largely due to the availability of natural resources, technological developments and qualified labour. The fast growing of energy generation however requires careful consideration of the type of infrastructure that can fulfil the demands in terms of strength, resilience and innovation. In earthquake-prone regions, tectonic and environmental conditions make infrastructure often susceptible to earthquakes and wind effects both during construction and once in operation. Notwithstanding that, current engineering practice disregards their simultaneous occurrence even though past earthquake records show that further ground accelerations can occur within days or even hours from main events. Examples of this include the earthquake that hit the Sichuan Province in China in 2008 (Ms =7.9) which was followed by 12 weeks with 42 aftershocks ranging in magnitude between $5 < Ms < 6.4$, killing over 87,000 and leaving over £56bn in losses [1]. The earthquake that hit Nepal in 2015 (Ms =7.8) killing more than 8,000 [2] was followed by 30 aftershocks of $Ms < 5$ occurring within three weeks and killing 200 more. More recently, the earthquakes that hit Ecuador in 2016 (Ms = 7.8) killing over 600, were followed by over 55 aftershocks in the first 24 hours [3].

Past research has contributed to better understand the mechanisms through which extreme load events affect infrastructure. Martinez-Vazquez [4] showed that the combination of earthquakes and wind would decrease the value of strength reduction factors that are calculated by ignoring the impact of wind during earthquake events whilst the joint probability of occurrence of such natural events could not be ignored because it would lead to non-conservative designs. Kiyomiya et al. [5] suggested that wind turbines have adequate earthquake resistance provided these are designed against typhoons, which could be the case of offshore wind turbines but is not shared practice for onshore infrastructure design. Furthermore, Diaz and Suarez [6] demonstrated that operational earthquake combined with design wind load tend to over-stress the tower section hence increasing the strength demand established under isolated wind conditions. The present paper thus aims at enhancing our understanding of multi-hazard load conditions

and their effect on wind energy infrastructure through the analysis of strength and ductility demands imposed by combinations of earthquake and wind load acting on a hybrid tall wind turbine. The study also scrutinises the joint probabilities of occurrence of meaningful multi-hazard events.

2. EARTHQUAKE RECORD DATABASE

Earthquake records of magnitude $5.3 \leq Ms \leq 7.36$ recorded on alluvium and with distances from geological faults of up to ~57 km were downloaded from the PEER ground motion database. These records are assumed to be representative of alluvium and firm soils once it has been shown in [7] that without much variation they would produce similar strength demands to structures located on either soil type. These records have a duration which oscillates between 30 and 80 s and were measured at a time interval of 0.1s. The list of historic earthquake records is provided in Table 1.

Table 1. Earthquake record database

#	Earthquake(s)	Magnitude	Epicentral Distance Km	vs_{30} ms^{-1}	PGA g
1-2	Helena Montana-01, 10/31/1935, Carroll College, 180 / 270	6	2.86 / 2.92	593.35/551.82	0.16
3-4	Northwest Calif-01, 9/12/1938, Ferndale City Hall, 45 / 224	5.5 / 5.8	53.88 / 53.77	219.31	0.15 / 0.11
5-6	Izmir Turkey, 12/16/1977, Izmir, L / T	5.3	3.21	535.24	0.42 / 0.13
7-8	Dursunbey Turkey, 7/18/1979, Dursunbey, L / T	5.34	9.15	585.04	0.18 / 0.24
9-10	Imperial Valley-02, 5/19/1940, El Centro Array #9, 180 / 270	6.95	6.09	213.44	0.25 / 0.15
11-12	Northern Calif-01, 10/3/1941, Ferndale City Hall, 225 / 315	6.4	44.68	219.31	0.10 / 0.12
13-14	Northern Calif-03, 12/21/1954, Ferndale City Hall, 44 / 314	6.5	27.02	219.31	0.16
15	Borrego Mtn, 4/9/1968, El Centro Array #9, 180	6.63	45.66	213.44	0.13
16-17	San Fernando, 2/9/1971, Castaic - Old Ridge Route, 21 / 291	6.61	22.63	450.28	0.32 / 0.28
18-19	San Fernando, 2/9/1971, LA - Hollywood Stor FF, 90 / 180	6.61	22.77	316.46	0.22 / 0.16
20	San Fernando, 2/9/1971, Lake Hughes #1, 21	6.61	27.4	425.34	0.15
21-22	San Fernando, 2/9/1971, Lake Hughes #12, 21 / 291	6.61	19.3	602.1	0.38 / 0.28
23-24	Imperial Valley-06, 10/15/1979, Bonds Corner, 140 / 230	6.53	2.66	223.03	0.52 / 0.77
25-26	Imperial Valley-06, 10/15/1979, El Centro Array #4, 140	6.53	7.05	208.91	0.48 / 0.27
27-28	Imperial Valley-06, 10/15/1979, El Centro Array #5, 140 / 230	6.53	3.95	205.63	0.33 / 0.38
29-30	Imperial Valley-06, 10/15/1979, El Centro Array #7, 140 / 230	6.53	0.56	210.51	0.34 / 0.47
31-32	Kern County, 7/21/1952, Taft Lincoln School, 21 / 111	7.36	38.89	385.43	0.14 / 0.15
33-34	Taiwan SMART1(45), 11/14/1986, SMART1 C00, EW / NS	7.3	56.01	309.41	0.12 / 0.15
35-36	Taiwan SMART1(45), 11/14/1986, SMART1 O02, EW / NS	7.3	57.13	285.09	0.16 / 0.24
37-38	Cape Mendocino, 4/25/1992, Petrolia, 0 / 90	7.01	8.18	422.17	0.58 / 0.66
39-40	Landers, 6/28/1992, Lucerne, 260 / 345	7.28	2.19	1369	0.65 / 0.61

3. WIND TURBINE TOWER MODEL

With the aim to investigate the structural performance under the joint occurrence of earthquake and wind, a hybrid wind turbine tower has been considered. Details of the considered structure are given at [8]. The wind tower and information of the cross-sections are shown in Figure 1. The examined wind tower consists of 60 m tube at the upper part and 60 m lattice structure at the lower part which support an NREL 5 MW Class AII turbine [9]. The hybrid system was selected as it has been identified as an alternative to optimise safety and durability whilst keeping the solution economically and environmentally sustainable.

To evaluate the structural response due to wind, Ashes software [10] has been used. Ashes uses the blade element momentum (BEM) algorithm for aerodynamics and combines it with the finite element (FE) solver for the evaluation of the induced structural behaviour, thus accounting for the interaction between elastic, viscous and inertial forces of the structure and the external aerodynamic forces. A Normal Turbulence Model (NTM) which embody the requirements for loads resulting from the atmospheric turbulence during normal operating conditions has been developed and incorporated into

the model. The wind flow was assumed to be parallel to the hub axis and 600 seconds simulations were subsequently performed. Noting that the first 30s of each simulation, during which the simulated flow was not fully developed yet, were disregarded, hence eliminating dynamic transient effects.

The hybrid wind tower model was imported into SAP2000 [11] where the earthquake database obtained from PEER could be loaded. Upon evaluation of the natural frequencies of the wind tower model, time history linear modal analysis, considering a damping factor equal to 5%, was performed. For the scope of the present study, it was considered sufficient for the earthquake analysis to model the wind turbine with structural mass, whilst assuming earthquake and wind events to be randomly off-phase.

For both the wind and earthquake analyses, the time histories of the elemental forces and the nodal displacements were extracted in critical positions of both the lattice and the tubular part. The mean, maximum and minimum values of the output data were also evaluated.

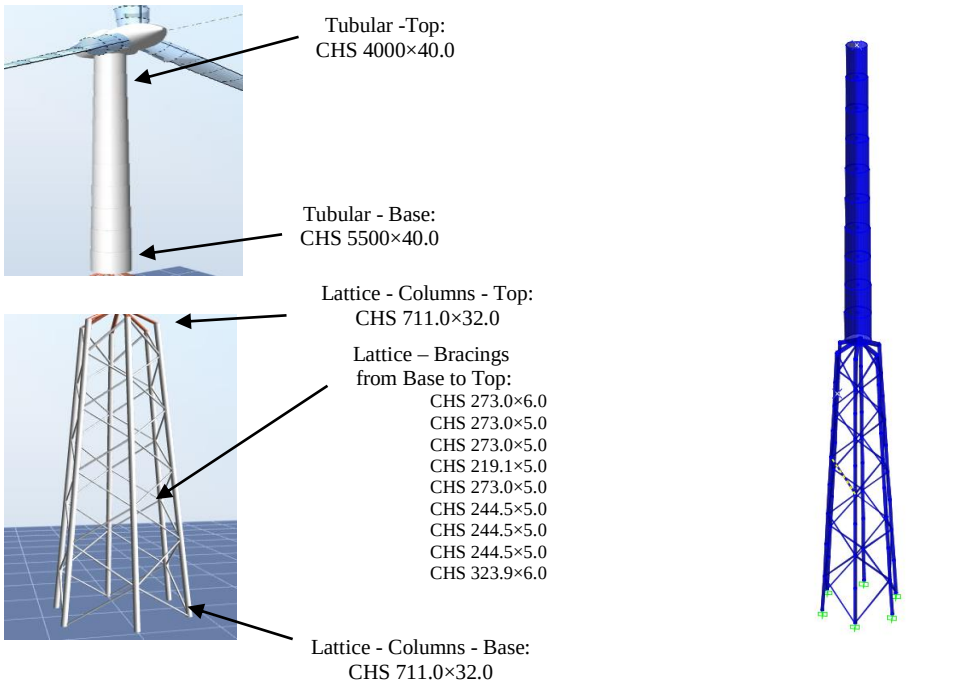

a) Model in Ashes [10] b) Model in SAP2000 [11]

Figure 1. Hybrid wind turbine tower model

4. PROBABILITIES ASSOCIATED TO WIND AND EARTHQUAKE EVENTS

Eurocode 1 [12] associates wind design loads to a 50-year return period whose probability of annual exceedance is P_{50} = 0.02. The norm also provides Eq. (1) to scale the 10-min design wind velocity for other probability levels.

$$C_{prob} = \left[\frac{1-K\cdot ln(-ln(1-p))}{1-K\cdot ln(-ln(0.98))}\right]^{n} \quad (1)$$

In Eq. (1) K is a shape parameter that depends on the coefficient of variation of the extreme-value distribution, n is a constant number, C_{prob} is the probability factor and p represents probability. Eurocode 1 recommends K = 0.2 and n = 0.5.

$$log_{10}N = a - bM \quad (2)$$

On the other hand, the Gutenberg-Richter law quoted in Eq. (2) establishes a relationship between frequency of earthquake events recorded within a year and their magnitude. In this equation, N

represents the number of events having magnitude $\geq M$ and a, b are site-dependent constants. It follows that Eq. (1) and (2) can be used to infer the magnitude of earthquake events associated to probability values (P_{EQ}) which, paired with those related to wind (P_W), match the standard probability of wind-resisting design i.e. $P_{EQ} \cdot P_W = 0.02$. This is shown in Table 2 for a set of randomly selected locations across the world, assuming that the 50-year return period design velocity equals 20 m/s. Wind velocities associated to higher values of P_W are also shown in Table 2.

Table 2. Probabilities associated to earthquake and wind events

	Probability of Exceedance, Seismic Magnitude per Country, or Wind Velocity								*a*	*b*
P_W	0.02	0.05	0.1	0.25	0.5	0.75	0.9	1	-	-
C_{prob}	1	0.95	0.90	0.84	0.78	0.75	0.68	0.52	-	-
$\bar{U}$ (ms^{-1})	20	18.92	18.05	16.75	15.53	14.49	13.68	10.33	-	-
P_{EQ}	1	0.4	0.2	0.08	0.04	0.027	0.022	0.02	-	-
India[1]	3.19	3.67	4.04	4.52	4.88	5.09	5.19	5.24	4.35	0.83
UK[2]	2.06	2.44	2.74	3.12	3.42	3.59	3.66	3.71	3.82	1.03
Turkey[3]	1.96	2.48	2.87	3.39	3.78	4.01	4.11	4.17	3.21	0.77
Greece[4]	4.86	5.13	5.33	5.59	5.79	5.91	5.96	6.00	8.99	1.5
Switzerland[5]	3.54	3.96	4.27	4.68	5.00	5.18	5.26	5.31	5.1	0.96
Global Data[1]	6.36	6.73	7.02	7.39	7.68	7.84	7.92	7.96	8.44	1.06

[1] [13]; [2] [14]; [3] [15]; [4] [16]; [5] [17]

According to the data shown in Table 2, $\bar{U} = 10.33$ m/s would always be exceeded in a year whilst $\bar{U} =$ 18.92 m/s ,18.05 m/s, and 16.75 m/s, considerably exceed the probability of the design wind speed. The joint occurrence of earthquake and wind events as listed in Table 2, match the single probability associated to the design wind load, and define a sub-set of multi-hazard scenarios that tend to magnify the strength and ductility demand of constructions.

5. JOINT EFFECTS OF WIND AND EARTHQUAKE LOADING

On the basis of the probabilities presented in Table 2, it was deemed critical to further investigate the joint occurrence of earthquake and wind events. Earthquake (EQ) events refer to those listed in Table 1 whereas local wind is assumed to have certain average velocity (U). The following four combinations were thus scrutinised: i) U=20 m/s and EQ #11 i.e. 6.4 Ms; ii) U=18.92 m/s and EQ #15 i.e. 6.63 Ms; iii) U=18.05 m/s and EQ #37 i.e. 7.01 Ms; iv) U=16.75 m/s and EQ #32 i.e. 7.36 Ms.

Typical wind and the earthquake time histories of response are shown in Figure 2.

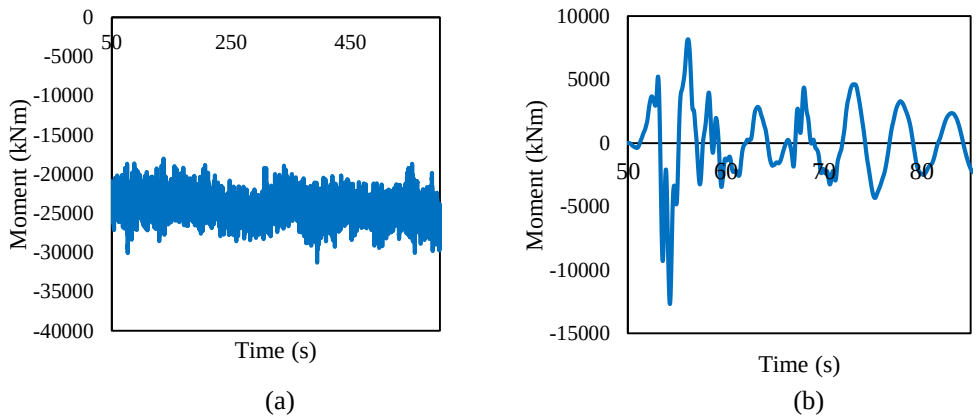

Figure 2. (a) In-plane bending moment time histories – Bottom of tubular part: Wind speed 18.05 m/s (b) In-plane bending moment time histories – Bottom of tubular part: EQ37, Ms 7.01

6. STRENGTH AND DUCTILITY DEMANDS ASSOCIATED TO MULTI-LOAD SCENARIOS

To evaluate the strength demands for multi-hazard scenarios, the ratio of the joint occurrence of earthquake and wind over the individual occurrence of wind was evaluated. In particular, cases related to in-plane bending moments at the bottom of the tubular part: M_{EQ+W}/M_w, and of the axial forces of the columns at the bottom of the lattice part: F_{EQ+W}/F_w. The results of these analyses are shown in Table 3. As anticipated, some of these values are higher than unity - which correspond to increased strength demands derived from wind and earthquake events.

Table 3. Strength demands for the considered hybrid wind turbine tower

		(Earthquake+Wind) / Wind			
		U20+EQ11	U18.92+EQ15	U18.05+EQ37	U16.75+EQ32
		Axial Force			
LATTICE BOTTOM - COLUMNS	max	1.064	1.193	1.799	1.185
	min	1.077	1.181	1.810	1.215
	mean	1.000	1.003	1.001	1.001
		Bending Moment			
TUBULAR - BOTTOM	max	1.020	1.370	1.405	1.270
	min	1.031	1.496	1.453	1.439
	mean	1.000	1.136	1.001	1.002

Furthermore, ductility demands can be estimated based on their relationship with strength reduction factors (SRFs) and structural period, as in [4]. Such relationship is reflected in Eq. (3).

$$R_\mu = \frac{F_y(\mu = 1)}{F_y(\mu = \mu)} \tag{3}$$

Where $\mu = \frac{u_{max-inelastic}}{u_y}$ represent structural ductility, R_μ is the SRF and F_y is the force required to keep the structural performance within a target ductility level (μ). Noting that the value of R_μ changes with the structural period (T). Furthermore, in [4] the mass distribution across a building is characterised with the parameter $\Gamma = \frac{M^*}{\sqrt{H^2+W^2+L^2}}$ where M^* represent generalised mass and H, W, and L are the height, width, and chord of a prismatic structure. For a wind turbine, the denominator of the equation that defines Γ can be replaced by a measure of the volume enclosing the structure - which in the present investigation resulted in a value of Γ equal to 6.61 Ton/m.

The relevant strength reduction factors (SRFs) presented in [4] are reproduced here in Figures 3 and 4, for cases where $\overline{U} = 15$ m/s and 20 m/s and when Γ takes values of 1.91, 60.43, and 17.78.

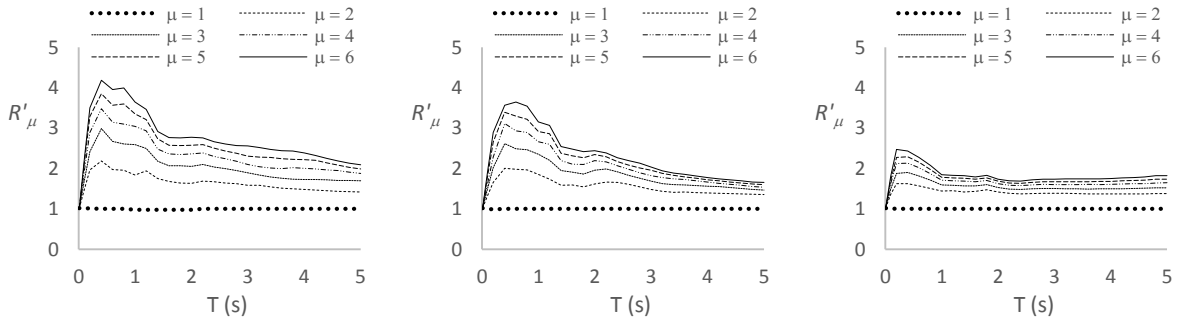

(a) $\Gamma = 60.43, \overline{U} = 15\ ms^{-1}$ (b) $\Gamma = 17.78, \overline{U} = 15\ ms^{-1}$ (c) $\Gamma = 1.91, \overline{U} = 15\ ms^{-1}$

Figure 3. Strength reduction factors estimated for $\overline{U} = 15$ m/s
Adapted from [4]

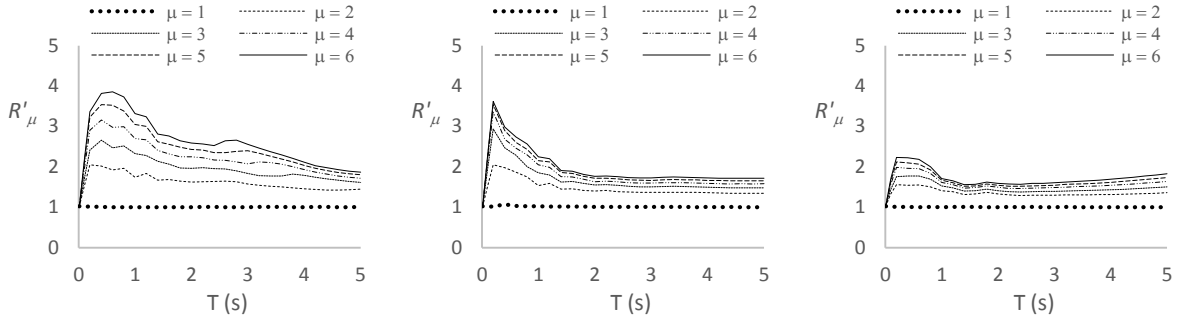

(a) $\Gamma = 60.43, \overline{U} = 20\ ms^{-1}$ (b) $\Gamma = 17.78, \overline{U} = 20\ ms^{-1}$ (c) $\Gamma = 1.91, \overline{U} = 20\ ms^{-1}$

Figure 4. Strength reduction factors estimated for $\overline{U} = 20$ m/s
Adapted from [4]

In Figures 3 and 4, SRFs associated to earthquake and wind events are represented by R'_μ. That is to dinguish between values derived from multi-load conditions with respect to those determined for earthquake actions only which are typically presented as $R_\mu$in the literature.

The magnification of strength demand listed in Table 3 can now be expressed in terms of ductility demand, as suggested by Eq. (3). Noting that a value $\mu = 1$ means that the structural performance remains within the linear-elastic range. By interpolation of the curves shown in Figures 3 and 4 and taking into account the critical values for each wind velocity level, the ductility demands associated to the wind turbine towers discussed here can be established, as shown in Table 4.

Table 4. Ductility demands (μ) for the considered hybrid wind turbine tower

		U20+EQ11	U18.92+EQ15	U18.05+EQ37	U16.75+EQ32
LATTICE BOTTOM - COLUMNS	Peak	1.217	1.544	6.498	1.503
TUBULAR - BOTTOM	Peak	1.083	3.059	2.699	2.542

The period of the hybrid wind turbine equals 4.75 s. This falls in a region where, according to Figures 3 and 4, the value of the R'_μ changes rapidly across ductility levels. That is characteristic of SRFs estimated for structures subject to high winds [4]. It can be observed in Table 4, that strength demands quoted in Table 3 lead to ductility demand levels that correspond to inelastic performance. The tubular segment would require a ductility of up to ~3 whilst the lattice components would require a ductility of ~6.5. Bearing in mind that these results relate to particular earthquake events and are therefore not conclusive regarding the potential change of the performance level, they do suggest that there is a potential damage to infrastructure associated to the correlation of natural events.

7. CONCLUSIONS

The present paper focused on the strength and ductility demands when the earthquake and the wind occur simultaneously for a hybrid wind turbine. It was shown that earthquake and wind effects tend to modify the performance level of wind energy infrastructure. Even though there are no records of such extreme events causing failure to wind turbine towers, the frequency of occurrence of earthquakes of medium to high intensity is not rare, according to [18] that reports a total of 418 ground motions of 7.01 < Ms < 9.9 in the last 50 years whilst 62 and 11 of those events were seen in the period 2011-2016 and during 2016, respectively. The recent earthquake events recorded in Mexico which killed dozens was

followed by a second national emergency as Hurricane Katia made landfall across the Gulf coast [19]. It thus seems necessary to consider multi-hazard scenarios during the design process seemingly through a more detailed analysis of risk. It is also worth to note that the fast growth of technology for clean energy generation is leading towards the increase the height of wind turbine towers which demands further measures to mitigate the impact of extreme natural events.

REFERENCES

[1]. Daniell JE, Vervaeck A, Khazai B, Wenzel F, 2012. Worldwide CATDAT Damaging Earthquakes Database in conjunction with Earthquake-report.com - Presenting Past and Present Socio-Economic Earthquake Data.
[2]. Amos J, 2015. Unsettled earth continues to rattle Nepal. BBC News -12 May
[3]. Shankar S, 2016. Ecuador earthquake: death toll soars, aftershocks reported. International Business Times – 18 April.
[4]. Martinez-Vazquez P, 2017. Strength reduction factors for the combined action of wind and earthquakes. Structures and Buildings. DOI: dx.doi.org/10.1680/jstbu.16.00086.
[5]. Kiyomiya O, Rikiyi T, Van Gelder HAJM, 2002. Dynamic response analysis of onshore wind energy power units during earthquakes and wind. Twelfth International Offshore and Polar Engineering Conference. Kitakyushu, Japan, May 26-31.
[6]. Díaz O, Suárez LE, 2014. Seismic analysis of wind turbines. Earthquake Spectra, 30(2): 743-765.
[7]. Miranda E, 1993. Site-dependent strength reduction factors. Journal of Structural Engineering ASCE 119(5): 1319–1338.
[8]. Gkantou M, Martinez-Vazquez P, Baniotopoulos C, 2017. On the structural response of a tall hybrid onshore wind turbine tower. In the proceedings of X International Conference on Structural Dynamics, EURODYN 2017
[9]. Jonkman J, Butterfield S, Musial W, Scott G, 2009. Definition of a 5-MW reference wind turbine for offshore system development. National Renewable Energy Laboratory, Golden, CO, Technical Report No. NREL/TP-500-38060.
[10]. Ashes 2.2.3, Simis, 2017. Available from http://www.simis.io/. [Accessed 7 January 2017]
[11]. Computers and Structures, Inc (CSI), 1999. SAP2000: Integrated structural design and analysis software. Berkeley, CA: Computer and Structures, Inc.
[12]. European Standard, 2010. Eurocode 1: Actions on structures – Part 1-4: General actions – Wind actions. European Committee for Standardization, Brussels.
[13]. Sharma RD, Gupta S and Kumar S, 1999. Application of extreme-value distribution for estimating earthquake magnitude-frequency relationships. Journal of Earthquake Technology 388(36): 15–26.
[14]. NERC, 2017. Seismicity and earthquake Hazard in the UK. British Geological Survey. Environmental Science Centre Keyworth, Nottingham, United Kingdom.
[15]. Bayrak Y, Öztürk S, Koravos GC, Leventakis GA, Tspanos TM, 2008. Seismicity assessment for the different regions in and around Turkey based on instrumental data: Gumbel first asymptotic distribution and Gutenberg-Richter cumulative frequency law. Natural Hazards and Earth Sciences 8(1): 109-122
[16]. Papazachos, BC, Kiratzi AA, Karacostas BG, 1997. Toward a homogeneous moment-magnitude determination for earthquakes in Greece and the surrounding area. Bulletin of the Seismological Society of America, 87(2): 474-483.
[17]. Wiemer S, 2000. Earthquake Statistics and Earthquake Prediction Research. Institute of Geophysics, Zürich, Switzerland. http://www.physics.buffalo.edu/phy410-505/midterm/img/wiemer-earthquake-prediction.pdf - [Accessed on 29.04.17].
[18]. NOAA, 2017. Earthquake data and information. National Centers for Environmental Information – National Oceanic and Athmospheric Administration. Available at https://www.ngdc.noaa.gov/hazard/earthqk.shtml [30.04.17].
[19]. ABC News, 2017. Death toll 61 in Mexico quake as hurricane hits Gulf coast. http://abcnews.go.com/International/wireStory/magnitude-earthquake-hits-southern-mexico-felt-capital-49695666 [Accessed on 17.09.17]

THE INFLUENCE OF A ROOF MOUNTED SMALL-SCALE HAWT ON HEADED STUDS FATIGUE RESISTANCE

Isidora Jakovljevic[1]*, Nina Gluhovic[1], Milan Spremic[1], Zlatko Markovic[1]

[1]University of Belgrade Faculty of Civil Engineering, Department for Materials and Structures, Serbia
Corresponding author: Isidora Jakovljevic, isidora.jakovljevic@yahoo.com

ABSTRACT

Installation of small-scale wind turbines in urban regions can gain higher energy efficiency, considering that energy production takes place at the place of its consumption. The aim of this work is to investigate effects of installation of a small-scale horizontal axis wind turbine (HAWT) on a roof structure of an existing building. This paper is focused on fatigue resistance of headed studs that are preinstalled in the building roof composite steel-concrete deck to ensure shear connection and that are indirectly dynamically loaded during wind turbine operation. Turbulent wind profiles with mean wind speeds from 3 m/s up to 15 m/s are generated and applied on the model of HAWT with 5 m rotor diameter using Ashes software package. Time-dependent forces and bending moments induced by wind turbine operation are applied on the composite roof deck model. Based on the time-history of transverse force in the composite steel-concrete beam and wind speed records during a year, fatigue cumulative damage of headed studs is calculated according to Eurocode. It is obtained that installation of HAWT do not significantly affect residual life of headed studs with reference to fatigue.

1. INTRODUCTION

Sustainable development principles lead to increased usage of renewable energy resources, as it is a wind energy. Considering the idea of high energy efficiency by producing and consuming electrical power at the same place, it is intended to install small-scale wind turbines in urban regions. However, due to the lack of free open areas in urban environment, the preferable solution is installation of small-scale wind turbines on building roofs.

A possible shortcoming of wind turbine mounting on the building's roof is related to increased vibrations that may affect human comfort and serviceability of equipment in a building [1]. However, another potential problem is related to the fatigue resistance of specific structural details of a building structure. Frequent stress fluctuations in construction elements caused by dynamic nature of wind loading and rotation of wind turbine blades, affect cumulative fatigue damage of certain details. Especially sensitive to fatigue damage are welded connections, as it is the connection between headed stud shear connectors and steel beams or profiled steel sheeting in steel-concrete composite buildings.

In this paper it is investigated how fatigue resistance of headed studs preinstalled in the roof steel-concrete composite beam is affected by installation of the small-scale horizontal axis wind turbine (HAWT) on the building roof. It is assumed that building is previously designed without an intention of installing wind turbine, which is mounted subsequently. The considered wind turbine is a small-scale HAWT with 5 m rotor diameter and 5 m tower height, that operates at wind speeds up to 15 m/s. HAWT model is developed using Ashes software package [2]. Calculation of fatigue damage accumulation factor is done according to EN 1993-1-9:2005 [3] and EN 1994-1-1:2004 [4].

2. METHODOLOGY

Model of small-scale HAWT with 5 m rotor diameter and 5 m tower height is developed using a multi-body analysis software package Ashes [2], that integrates finite element analysis (FEM) and blade element momentum theory (BEM). Model of small-scale HAWT is developed by scaling a standard NREL_5MW onshore wind turbine through dimensions scaling with factor 0.04 (Figure 1) [1]. However, as *wind turbine with local scaling of dimensions does not always give appropriate*

masses for different wind turbine parts, it was necessary to manually define masses for wind turbine elements. *Mass of the support tower and RNA structure (rotor-nacelle assembly) in comparison to the mass of the whole wind turbine of* 553 kg *is approximately 50 % each.* The developed HAWT is a direct drive turbine without pitch control system *with rated power of 2.4 kW. It is assumed that wind turbine does not operate at wind speeds above 15 m/s.*

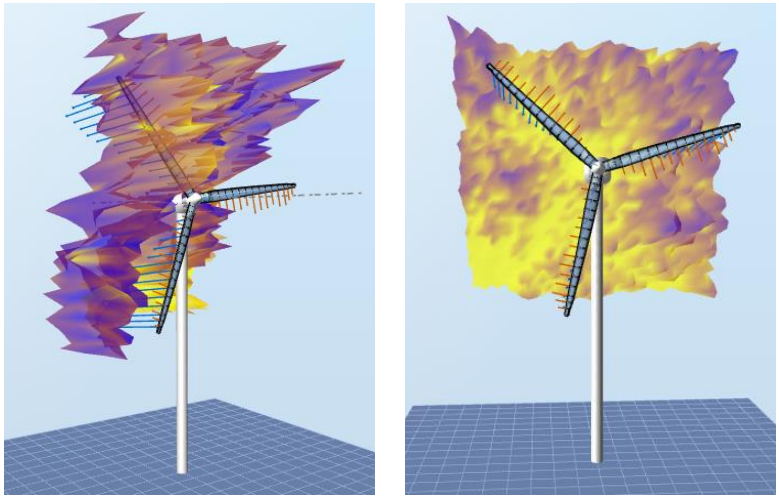

Figure 1. Model of the small-scale wind turbine and the tower in Ashes software.

Turbulent wind profile is generated in TurboSim module integrated in Ashes software [2]. In order to model spatial distribution, wind field is defined in certain number of grid points. The time history loading is generated for set values of mean wind speeds during time period of 60 seconds and applied on wind turbine model.

The obtained wind turbine support reactions due to applied wind loading of mean wind speeds from 3 to 15 m/s are presented on Figure 2. It is important to highlight that results presented in Figure 2 are filtrated from results of Ashes software in order to give proper graphical presentation, and that real data contain more fluctuations. However, wind turbine support reactions with real fluctuations are used for fatigue analysis of headed studs, in order to give realistic prediction of fatigue cumulative damage.

The time-history response of the composite roof beam due to dynamic loading generated by HAWT operation is analysed in Sofistik FE software [5]. The overall dimensions of the building roof are 24x24 m, as it is shown in Figure 3. Design of all elements is performed according to requirements given in EN 1994-1-1:2004 [4]. Steel-concrete deck is composed of 330 mm high steel I beams connected by shear connectors to the 160 mm thick concrete deck. Headed studs that connect steel beams and concrete deck are ductile shear connectors, which number provides partial shear connection, according to EN 1994-1-1:2004 [4]. The adopted headed stud's diameter is 16 mm and the distance between headed studs is 300 mm.

In order to investigate shear studs fatigue damage, HAWT position is assumed to be in the most unfavourable place, in the middle of the composite beam span, at the central position of the analysed roof structure, as presented in Figure 3.

Reaction loads induced by wind turbine operation (Figure 2) are applied on Sofistik model as time-histories of forces and bending moments. For investigation of headed studs fatigue damage, time period of 60 seconds of HAWT operation is taken into account. Headed studs' shear stress is calculated according to linear elastic theory, using the results of dynamic analysis performed in Sofistik. Shear stress results for applied wind loading of mean wind speeds of 3, 6, 9, 12 and 15 m/s during 60 seconds of HAWT operation are presented in Figure 4. For stress range counting, a rain flow method is performed.

The analyse of headed studs fatigue lifetime is based on a year record of wind speed for the site near the town of Vršac in Serbia [6]. Wind speed histogram obtained from the record is presented in Figure 5. As wind turbine operation is analysed for five different wind speeds, it is adopted that number of stress

range cycles for certain wind speed corresponds to the frequency of that wind speed and lower wind speeds.

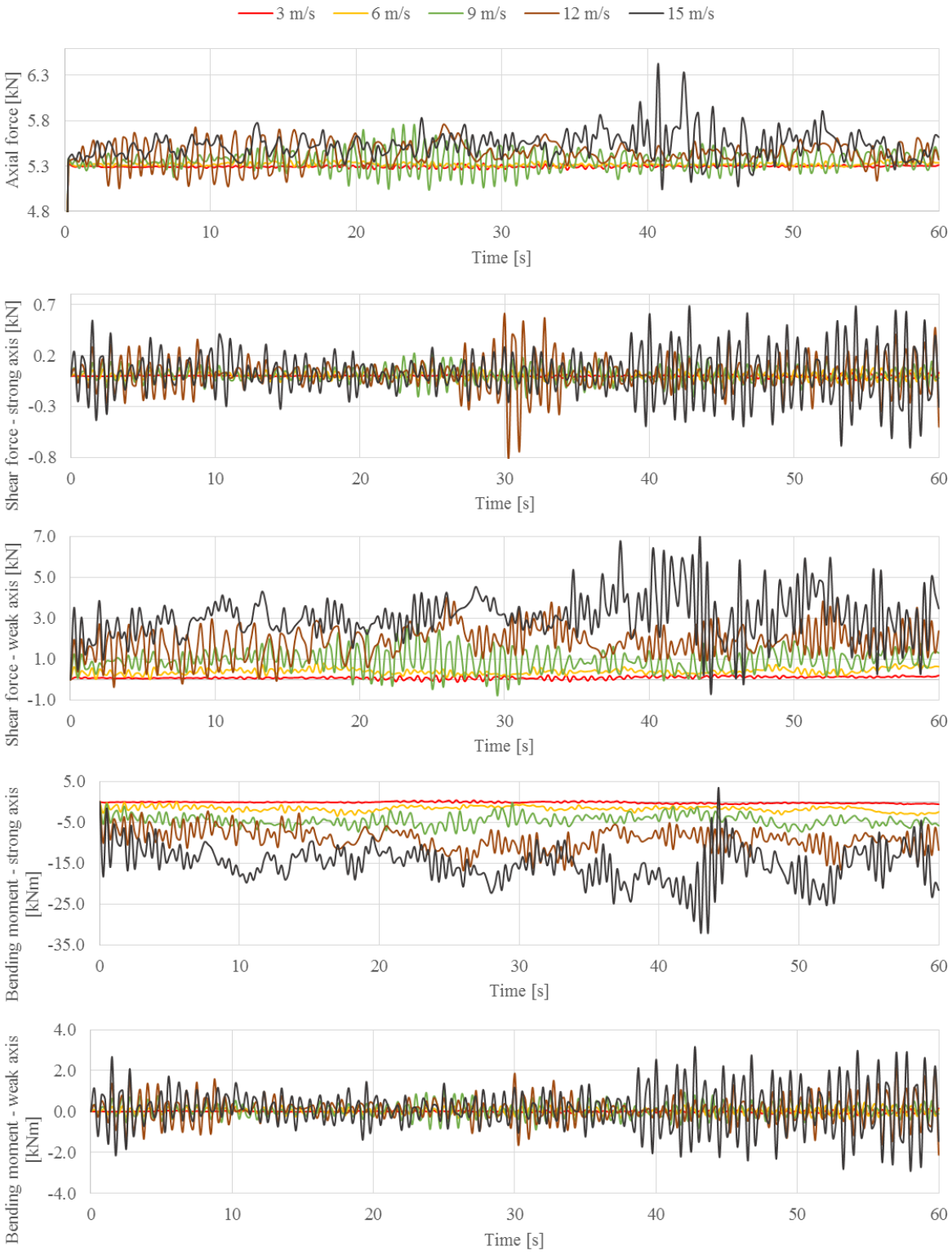

Figure 2. Time-history of wind turbine support reactions for different mean wind speeds.

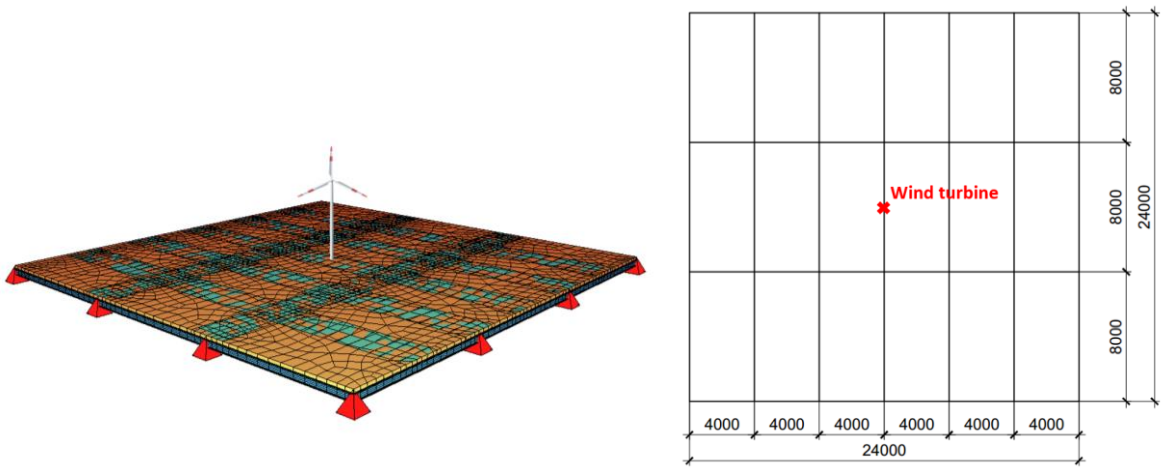

Figure 3. Layout of roof beams.

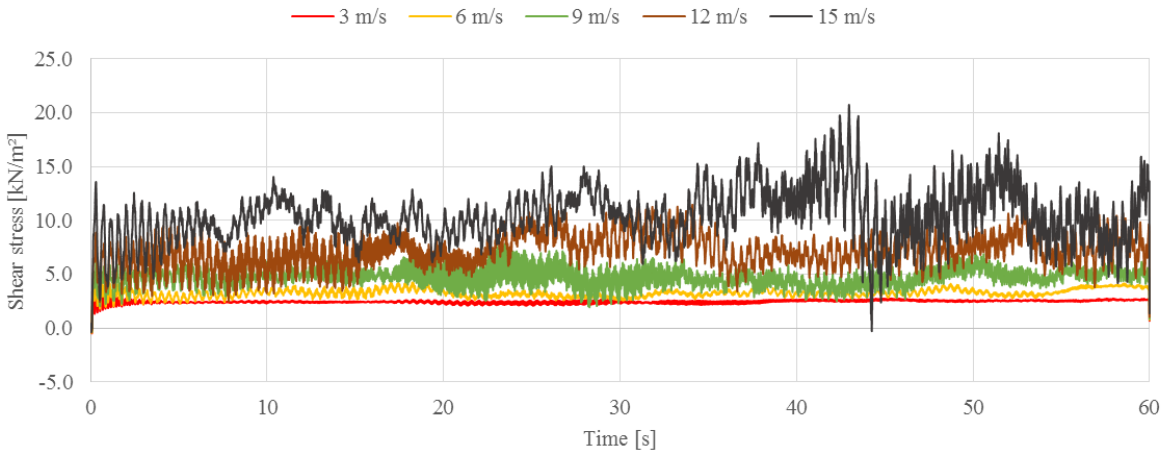

Figure 4. Time-history of shear stress in headed studs for different mean wind speeds.

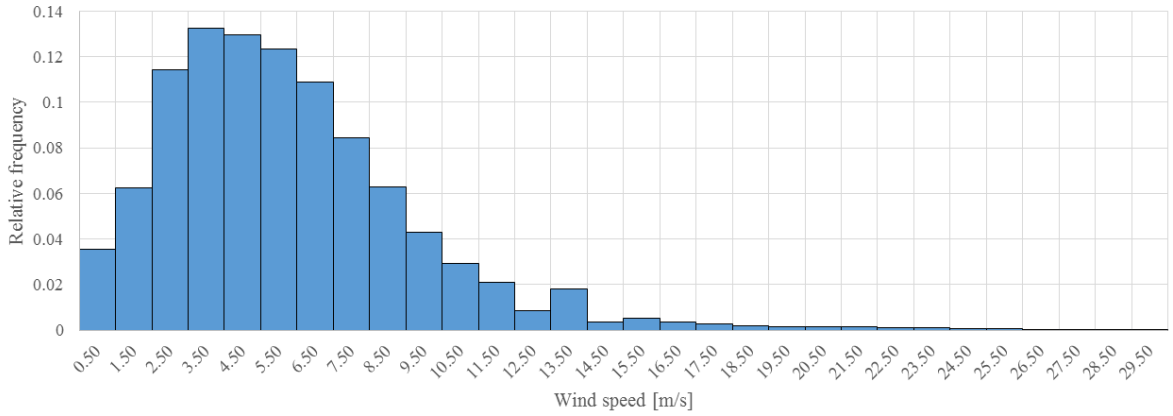

Figure 5. Wind speed histogram.

3. RESULTS

Taking into concern floor response during 60 seconds of wind profile application on the wind turbine and results of rain flow counting procedure, stress range histograms for each wind speed are obtained and presented in Figure 6.

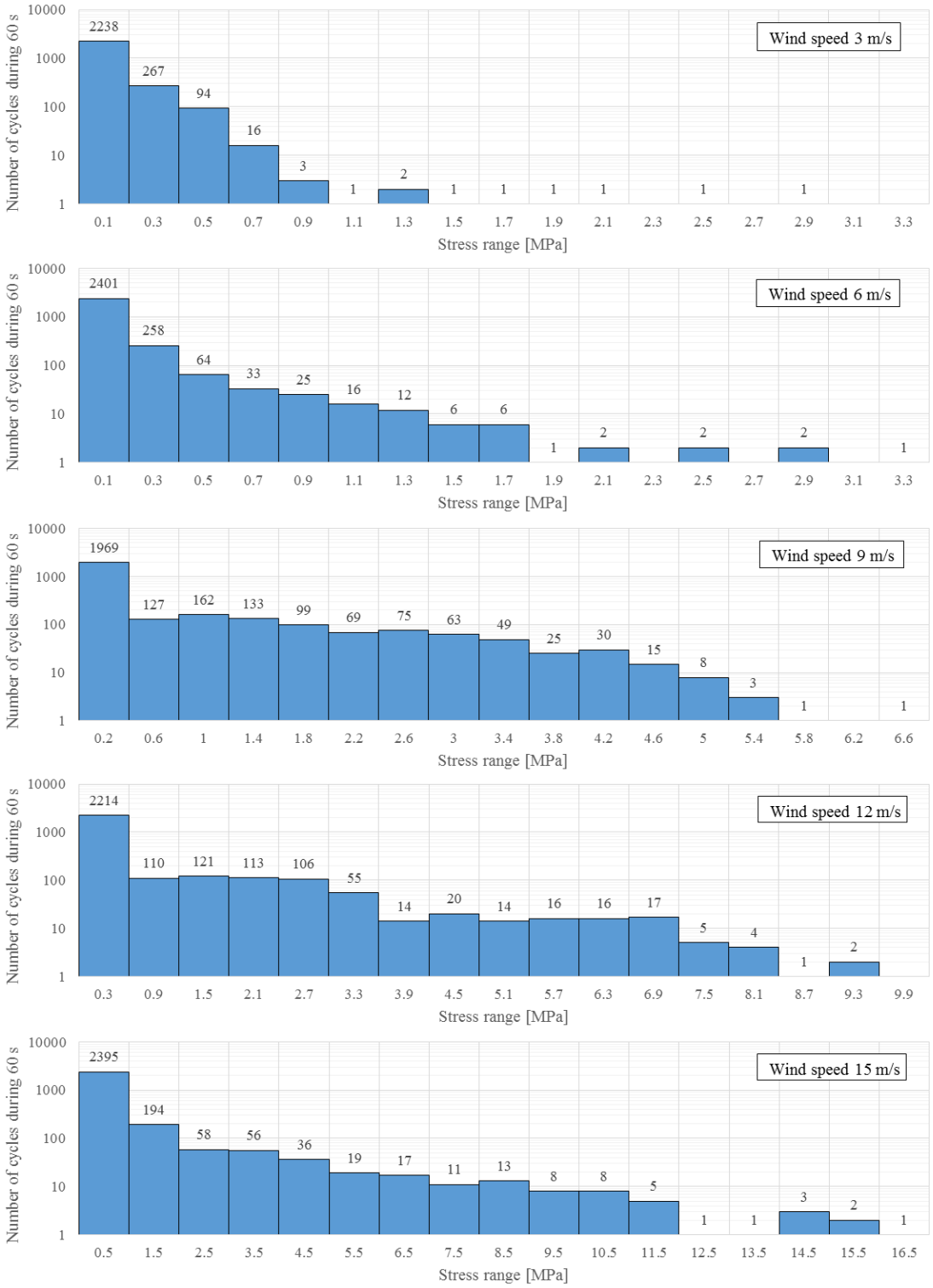

Figure 6. Stress range histograms for different mean wind speeds.

According to EN 1993-1-9 [3] and EN 1994-1-1 [4], accounting wind speed records and stress range histograms, damage accumulation factor for shear studs is calculated. The detail category of headed suds defined in EN 1994-1-1 is 90 MPa, while S-N curve has the slope 1:8 [4]. Adopted partial safety factors for fatigue strength and fatigue load are both 1. It is assumed that HAWT design life is 20 years. The

obtained damage factor equals $2.18 \cdot 10^{-6}$, that is much smaller than limiting value of 1. Therefore, the influence of the mounted wind turbine on fatigue life of headed studs preinstalled in the composite steel-concrete slab is very small.
The parameter study is performed by varying distance between shear studs. Results presenting damage accumulation factor are given in Table 1.

Table 1. Damage accumulation factor depending on distance between headed studs.

distance between headed studs [mm]	damage accumulation factor
300	$0.02 \cdot 10^{-4}$
400	$0.23 \cdot 10^{-4}$
500	$1.27 \cdot 10^{-4}$
600	$5.71 \cdot 10^{-4}$

Again, it could be noticed that fatigue damage due to wind turbine operation on the building roof is not remarkable. In the case of shorter distances between studs, shear stress in each stud is lower and therefore it is followed by smaller damage factor. Conversely, in the case of larger interspaces between headed studs, higher damage factors are obtained. However, all presented outcomes show that fatigue damage is negligible.
Additionally, the other possible failure on the connection of shear stud and beam flange, through the base material is tested. According to the time-history of direct stresses in the upper beam flange, detail category of 80 MPa and bilinear S-N curve with slopes 1:3 and 1:5 [3], damage accumulation factor is calculated. Adopted partial safety factors for fatigue strength and fatigue load are 1.15 and 1, respectively. The calculated damage factor equals 0, as all considered direct stress ranges are bellow cut-off limit and according to Eurocode [3] do not contribute to the fatigue damage.
The results lead to conclusion that fatigue failure generated by HAWT operation on the building roof could be neglected. Shear stress ranges to which shear studs are exposed as well as direct stress ranges in the base material, are very low and therefore do not significantly contribute to the cumulative damage.

4. CONCLUSION

Installation of a wind turbine on a roof of an existing building in urban environments requires consideration of dynamic loading on a structure, that had not been analysed during structure design. Wind turbine subsequent implementation could significantly affect the resistance of structural elements or serviceability of the structure. The influence of frequent stress fluctuations in construction elements on reduction of element's fatigue resistance due to installation of small-scale HAWT on the building roof is presented in this paper. The construction detail which is analysed is welded connection between headed studs and steel beam in a composite steel-concrete roof deck.
According to the results of the performed analysis, following conclusions could be stated:

- fatigue life of headed studs in a roof deck is satisfied for a HAWT design life of 20 years,
- damage accumulation factor is remarkably smaller than limiting value of 1, even in the case of longer distances between shear studs along composite steel-concrete beam,
- installation of small-scale HAWT on the roof deck of the existing building which is analysed in this paper does not affect life of headed studs and fatigue failure could be neglected. Also, in the case of different building structure geometry significant differences in fatigue damage results are not expected.

REFERENCES

[1] N. Gluhović, M. Spremić, M. Pavlović, and Z. Marković, "Numerical study of vibrations in a steel building induced by roof mounted small scale HAWT" in "*WINERCOST '17 International Conference on Wind Energy Harvesting*", *Coimbra, 20-21.04.2017,* 2017, pp. 196-199.

[2] http://www.simis.io/ 08.02.2016

[3] EN 1993-1-9: Eurocode 3 – Design of steel structures. Part 1-9: Fatigue. Brussels, Belgium: European Committee for Standardization (CEN), 2005.

[4] EN 1994-1-1: Eurocode 4 – Design of composite steel and concrete structures. Part 1-1: General rules and rules for buildings. Brussels, Belgium: European Committee for Standardization (CEN), 2004.

[5] https://www.sofistik.com/ 15.04.2017

[6] Ž. Đurišić, and J. Mikulović, "Assessment of the wind energy resource in the South Banat region, Serbia," *Renewable and Sustainable Energy Reviews*, vol. 16, no. 5, pp. 3014-3023, June 2012.

THE INTERNATIONAL CONFERENCE ON
WIND ENERGY HARVESTING 2018
21-23 March 2018
Catanzaro Lido, Italy

Paper TS1.2.3.

PROBABILISTIC ASSESSMENT OF THE PEAK RESPONSE OF HORIZONTAL AXIS WIND TURBINES TO WIND AND SEISMIC ACTIONS

A.M. Avossa[1]*, C. Demartino[2], M. Vardaroğlu[1], F. Ricciardelli[1]

[1]Department of Engineering, University of Campania "Luigi Vanvitelli", Italy
[2]College of Civil Engineering, Nanjing Tech University, China
*Corresponding author: A.M. Avossa, albertomaria.avossa@unicampania.it

ABSTRACT

This study presents some results on the peak response assessment of a 5-MW, land-based Horizontal Axis Wind Turbines (HAWTs) support structure, under the combined effects of wind and seismic loads. Using a decoupled approach, simulations of the wind and seismic loads effects are performed separately applying a specific model to define the aerodynamic damping and then joined. Then, the probabilistic assessment of the multi-hazard peak response parameters was developed from Monte Carlo simulations of the tower structure subjected to different wind and seismic loads scenarios.

1. INTRODUCTION

The rapid growth and expansion of the wind energy industry worldwide has brought the construction of wind turbines also to areas characterized by high seismic hazard. Although, these unmanned structures can be considered of moderate importance regarding the safety and reliability classification, the prevention of their structural failure associated with the combined effects of wind and earthquakes is of crucial importance, especially from an economic point of view, to avoid losses of the invested capital and ensure returns. The increase of the electric production is related to the increase of the rotor diameter and hub height since the power produced by the wind is proportional to the third power of wind speed as well as the square of the rotor radius. However, the increase of the mass of the Rotor-Nacelle Assembly (RNA) induces larger tower base moment demand, due to the combined effect of wind and seismic loads. Consequently, the multi-megawatt HAWTs have become very slender structures heavily loaded on top and characterized by a long period, whereby the seismic load effects may govern their structural design.

In response to these new trends and design challenges, several researchers have investigated different aspects of the implications that seismic loads have considering wind turbine design and assessment. The first numerical investigations carried out by Bazeos et al. [1], and Lavassas et al. [2] were focused on the tower support structure. Moreover, Bazeos et al. [1] also presented a comparative analysis of the dynamic response, using models of different complexity: full shell-element, beam column, and s-DoF. In a more recent paper, Witcher [3] used models that explicitly simulated the rotor along with the turbine tower, to evaluate the seismic response of a 2 MW upwind turbine in different scenarios. A more comprehensive review of the current literature concerning the seismic response of wind generators, was provided by Prowell and Veers [4], together with the proposal of a simplified approach to be used for the seismic design assessment of tower heights ranging from 24 m to 90 m, and generally associated with 50 kW and 5 MW power output, respectively. The results also showed that for wind generators, equipped with a blade pitch control system, the leading design loads would be the seismic actions, as the turbine increased in size. Prowell et al. [5] developed shake table tests on a full scale 65 kW Nordtank wind turbine, imparting earthquake motions in the two principal horizontal directions (parallel and perpendicular to the axis of rotation of the rotor). They concluded that the importance of taking into account the seismic demand within the design process increases as the wind generator increases in

capacity. Moreover, it was detected that higher mode effects could be relevant for large wind turbines. Prowell et al. [6,7] pointed out that some earthquake ground motions can produce in the NREL 5 MW HAWT a demand in terms of bending-moment at the tower base section, higher than the one derived from extreme wind loads in operational, emergency shutdown and parked simulations.

International Standards and Guidelines such as IEC 61400-1 [8] and ASCE-AWEA RP2011 [9] recommend practice on the design of wind turbine support structures that accounts for the combination of seismic loads with operational loads. In these documents, the use of uncoupled analyses is also considered. To address this issue, the combination of separate wind and earthquake responses in the time domain is desirable. However, the use of the uncoupled approach involves the definition of an appropriate level of aerodynamic damping, representing the aeroelastic effects, but only a few data are available in the literature for this purpose. Recently, Valamanesh et al. [10] suggested a closed-form approach for the definition of the fore-aft and side-to-side aerodynamic damping ratios to be used for HAWTs. This formulation was considered as a suitable way to account for the effect of the aerodynamic damping in the seismic analysis of HAWTs through a multibody dynamic analysis.

Within this topic, the authors have recently presented some results on the vulnerability assessment of HAWTs under the combined effect of wind and seismic actions, based on a decoupled approach of an aeroelastic model of HAWTs [11]. In this paper, starting from the same approach, more refined results on the peak response assessment of a 5-MW land-based HAWT subjected to multi-hazard wind and seismic actions, are presented and discussed.

2. METHODOLOGY

The National Wind Technology Center (NWTC) has developed a report containing the features of the 5 MW NREL reference turbine [12]. The model is produced to represent a standard definition for studies of engineering considerations for large on-shore and off-shore wind turbines. This wind generator is used herein to evaluate the impact of the combined wind and seismic loading conditions on wind turbine tower. The wind turbine is an upwind, three-bladed, variable speed and variable pitch machine. The wind generator has a rotor diameter of 126 m with cut-in, rated, cut-out wind speeds V_w of 3 m/s, 11.4 m/s, and 25 m/s, respectively (Fig. 1a). The algorithm that controls the pitch and rotor speed is developed to optimise the power output for any wind speed. Cut-in speed divides the zone where the generator torque is zero and no power is extracted from the wind by the zone where the wind is used to accelerate the rotor for start-up. The rated wind speed is associated with the state when the pitch control is activated, and the blades start to be rotated, so that torque and generated power remain constant for higher wind speeds. Cut-out wind speed is the state when the rotor shuts down in high wind conditions, to avoid structural damage. For steady state conditions, the trends of rotor speed and blade pitch versus wind speeds ranged between the cut-in and the cut-out states are reported in Fig. 1b.

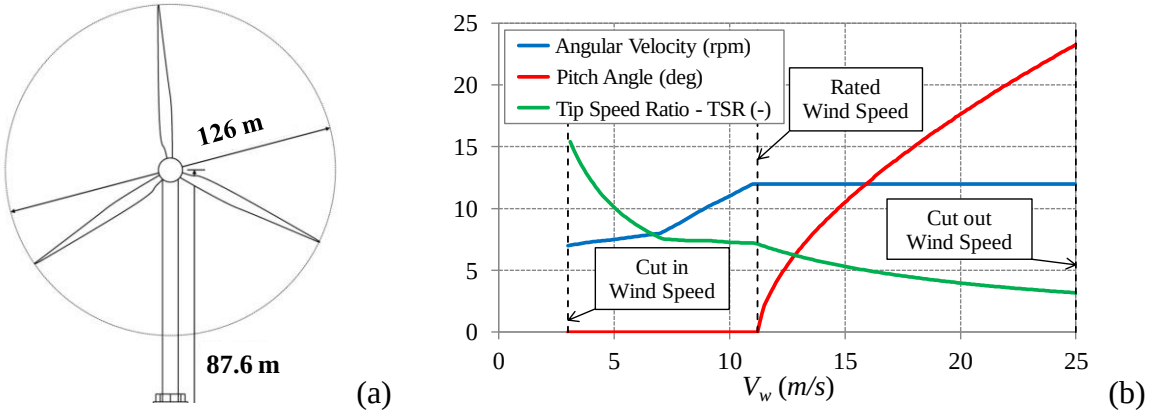

Figure 1. 5MW land-based HAWT: (a) geometry of tower and rotor; (b) values of rotor speed Ω, blade pitch, and tip speed ratio (TSR) versus wind speed.

In particular, the trends of the angular velocity of the rotor, Ω, and of the Tip Speed Ratio TSR (ratio between the blade tip velocity and the wind speed), are shown. The results presented in this paper,

related to the operational conditions, are based on combinations of wind speed, rotor speed, and blade pitch, whereas the results given for the parked condition are based on a fixed rotor with feathered blades.

2.1. Aeroelastic model and uncoupled approach

An essential aeroelastic model, representing the dynamic response of the HAWT structure, can be expressed by the general equations as follows:

$$\boldsymbol{M_{HAWT}}\ \ddot{\boldsymbol{x}} + \boldsymbol{C_{HAWT}}\ \dot{\boldsymbol{x}} + \boldsymbol{K_{HAWT}}\ \boldsymbol{x} = \boldsymbol{F_{aerodyn}}\left(\boldsymbol{U}, \ddot{\boldsymbol{x}}, \dot{\boldsymbol{x}}, \boldsymbol{x}\right) - \boldsymbol{M_{HAWT}}\ \boldsymbol{I}\ \ddot{x}_g\left(t\right) \tag{1}$$

where $\boldsymbol{M_{HAWT}}$, $\boldsymbol{C_{HAWT}}$ and $\boldsymbol{K_{HAWT}}$ are the structural mass, damping and stiffness matrices of the overall dynamic system, respectively; $\ddot{\boldsymbol{x}}$, $\dot{\boldsymbol{x}}$ and $\boldsymbol{x}$ are the time-dependent acceleration, velocity, and displacement vectors, respectively; $\boldsymbol{F_{aerodyn}}$ ($\boldsymbol{U}$, $\ddot{\boldsymbol{x}}$, $\dot{\boldsymbol{x}}$, $\boldsymbol{x}$) is the load vector due to the aerodynamic forces on the rotor blades, $\boldsymbol{M_{HAWT}}\,\boldsymbol{I}\,\ddot{x}_g(t)$ is the seismic force vector, wherein $\boldsymbol{I} = [1,1,1,\ldots..,1]^T$ is the influence coefficient vector and $\ddot{x}_g(t)$ the input ground acceleration, and $\boldsymbol{U}$ is the turbulent wind field.

In this study, the aerodynamic and the seismic loads, applied to the structural model of the HAWT, were calculated by decoupling the aerodynamic response of the rotor from the dynamic response of the tower structure. Based on this assumption, the aerodynamic forces are defined using a quasi-steady approach as [13]:

$$\boldsymbol{F_{aerodyn}}\left(\boldsymbol{U}, \ddot{\boldsymbol{x}}, \dot{\boldsymbol{x}}, \boldsymbol{x}\right) = \boldsymbol{F_{aerodyn}}\left(\boldsymbol{U}\right) - \boldsymbol{C_a}\left(\boldsymbol{U}\right)\cdot\dot{\boldsymbol{x}} \tag{2}$$

in which the aerodynamic forces are decoupled in a load vector of the aerodynamic forces acting on the rotor blades and in an aerodynamic damping matrix, $\boldsymbol{C_a}$, in this case only related to the mean wind speed in the fore-aft direction, V_w.

First, the response of the rotor with flexible blades, neglecting the elastic behaviour of the tower, is evaluated. Then, the dynamic loads deriving from the first step are imposed to the FEM model of the tower where the aerodynamic damping is embedded. The approximate structural response of the HAWT is evaluated by applying the wind thrust of the rotor and the seismic excitation to a dynamic model of the tower structure, neglecting any feedback. The HAWT tower structure is modelled using a FEM software (i.e., OpenSees). Two separate linear time-history analyses were developed: (i) the first applying the wind loads as a time-dependent rotor thrust to the tower top; (ii) the second one applying the seismic excitation as a tower base acceleration boundary condition. Within this decoupled approach, the effects of the aeroelastic interaction are taken into account including in the model an appropriate level of aerodynamic damping [14].

2.2.1 Aerodynamic model

The aerodynamic response evaluation of the wind turbine was performed using the FAST code, developed by Jonkman and Buhl [15] at the National Renewable Energy Laboratory (NREL). FAST is specifically developed to simulate the turbine dynamic response and is capable of predicting both extreme and fatigue loads of two- and three-bladed horizontal axis wind turbine. The code uses a modal combination formulation with limited degrees of freedom to simulate the wind turbine behaviour in the time domain. The structural response is calculated by solving the equations of motion using multi-body dynamics formulation with elements whose flexibility is defined by summing specified mode shapes for different components. For given values of the mean wind speed and turbulence intensity, a wind velocity field is generated by Turbsim [16] and is used as input for the aerodynamic analyses carried out in FAST; the latter produces as output the time-history of the rotor thrust at the top of the tower, due to the wind in the operational and parked scenarios. The results of the FAST simulation are then applied to the tower FEM model as an external loading in addition to the seismic actions.

2.2.2 Structural model

The dynamic structural model of the HAWT was developed in OpenSees [17] using Euler-Bernoulli cantilever beams (Elastic Beam-Column Element) discretized by 11 nodes into 10-beam elements, connected to a rigid foundation.

Thus, the effects of the pile and soil flexibility were not taken into account in this paper. The section properties of the tower elements are calculated from the stiffness properties given for the reference wind turbine. The steel material used for the tower has a Young modulus of 210 GPa, Poisson ratio of 0.3 and density of 8500 kg/m^3. This density value is higher than the steels typical value of 7850 kg/m^3 to implicitly account for paint, bolts, welds, and flanges that are not considered in the tower thickness data [12]. The RNA mass is lumped at the top node, while the tower mass is concentrated at each corresponding node of the cantilever beam, representing the flexible model of the tower. The final structural model was tuned by adjusting the tower stiffness properties to match the first and second bending modes in all directions according to the structural model of the prototype 5 MW HAWT proposed by NREL [12]. A sketch of the tower structural model and the external loads, rotor thrust, and seismic input is shown in Fig. 2a. Within the decoupled approach above mentioned, the equation of motion for the tower structure can be expressed as:

$$\boldsymbol{M_T}\ \ddot{\boldsymbol{x}} + \boldsymbol{C_T}\ \dot{\boldsymbol{x}} + \boldsymbol{K_T}\ \boldsymbol{x} = \boldsymbol{F_{Rotor}}(t) - \boldsymbol{M_T}\ \boldsymbol{I}\ \ddot{x}_g(t) \tag{3}$$

where $\boldsymbol{M_T}$, $\boldsymbol{C_T}$, and $\boldsymbol{K_T}$, are the tower mass (tower and RNA masses), damping and stiffness matrices, respectively; $\ddot{\boldsymbol{x}}$, $\dot{\boldsymbol{x}}$ and $\boldsymbol{x}$ are the time-dependent vectors of the kinematic parameters of the tower; $\boldsymbol{F_{Rotor}}(t)$ is the rotor thrust load vector, whose only non-nil component is that applied at the top node, $\boldsymbol{M_T} \cdot \boldsymbol{I}\ \ddot{x}_g(t)$ is the seismic force vector. The total damping model is assumed as the sum of the structural damping and the aerodynamic damping, calculated for each parked/operational condition through the closed form approach suggested by Valamanesh and Myers [10]. For the structural damping, the mass and stiffness proportional coefficients of the Rayleigh model are calculated, while the aerodynamic damping is embedded in the model through a viscous damper placed at the top of the tower.

2.2.3 Aerodynamic damping

The aerodynamic damping is an effect due to the velocity of a vibrating structure inducing a change in the aerodynamic forces, which generally reduce the dynamic response of the structure. This effect is related to the velocity term in the equation of motion producing feedback effects and is additive with structural damping [14]. In a decoupled approach, the aerodynamic damping is the key point to take into account the aeroelastic effects. In this paper, the estimation of the aerodynamic damping was developed using the closed form approach suggested by Valamanesh and Myers [10]. This solution, starting from the BEM theory, is based on some simplifying assumptions: (i) the flexibility of the rotor blades is neglected and (ii) a steady, uniform wind oriented perpendicular to the rotor plane is considered for its derivation. This approach allows to accurately consider aerodynamic damping within the software that has more refined structural analysis features. As above mentioned, the decoupling approach can be applied since wind actions and seismic excitation can be seen as independent phenomena.

For the specific case of the NREL 5-MW HAWT, the aerodynamic damping ratio was calculated in the fore-aft and side-to-side directions, using the approach proposed by Valamanesh. A value of the air density of 1.25 kg/m^3 was considered in the calculations. The results are represented in Fig. 2b as a function of the wind speed in the range of 0 – 25 m/s for both parked and operational conditions. The predictions of the aerodynamic damping, in the fore-aft direction, outcome in a maximum value of 0.1% for the parked condition, and in higher values ranged between 2.24% and 5.34% for operational conditions. The predictions for the side-to-side direction outcome in lower values of aerodynamic damping, ranging between 0.3% and 1.5% (mean value of 1%) for the operational condition. These values are quite consistent with those suggested by ASCE/AWEA RP2011 [9], which, however, provide the same value for all the direction of vibration.

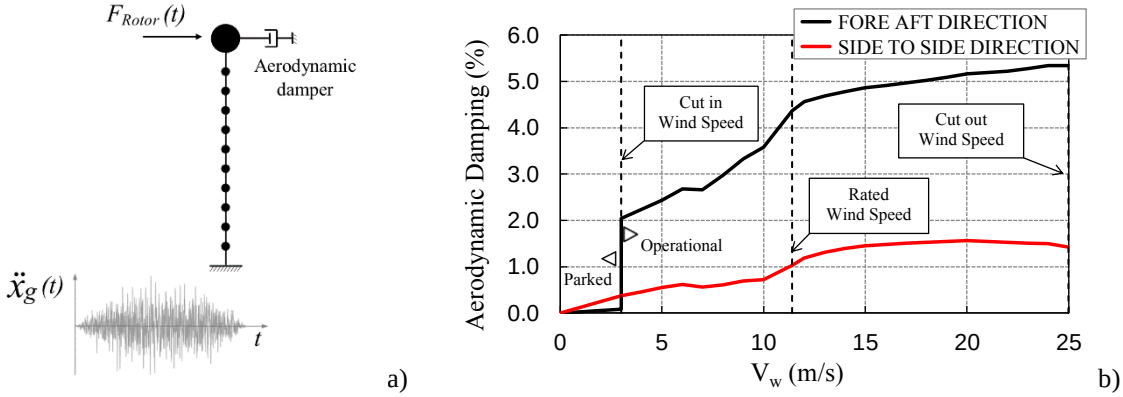

Figure 2. a) Structural model with aerodynamic damping; b) aerodynamic damping in the fore-aft and side-to-side directions for 5-MW land-based HAWT.

3. RESULTS

3.1. Wind and seismic actions

To properly simulate the wind loads on the blades, the simulation of random wind field velocity time histories is required. For given values of the mean wind speed and turbulence intensity, a wind field can be generated by TurbSim and will be used as an input for the aerodynamic analyses developed with FAST [15]. TurbSim is a stochastic, full-field, turbulent-wind simulator that uses a statistical model to numerically simulate time-histories of three-component wind-speed vectors [16]. TurbSim is able to support the spectrum proposed by Kaimal et al. [18] to simulate the wind fluctuations.

The seismic action can be represented by a set of recorded, simulated or artificial inputs. Some specific rules can be found in EC8 [19]: the corresponding acceleration response spectra have to match, on average, the peak ground acceleration and the shape of the elastic response spectrum for 5% damping defined for the site. Moreover, EC8 provides further indications for the generation of artificial inputs, concerning the duration and the spectral shape.

3.2. Aerodynamic and seismic response of the wind turbine

The outcome of the combined effects of turbulent aerodynamic and seismic loads on the structural response of a HAWT was evaluated on the above mentioned decoupled dynamic model of the 5 MW, land-based turbine developed by NREL.

To define the wind action and consider various wind load combinations with seismic excitation, 12 different wind speeds were selected, ranging from 3 m/s to 25 m/s, evaluated at the hub height (equal to 87.60 m), to be tested on the model. For the parked and operational cut-in scenario, the same value of wind speed equal to 3 m/s was set. The rated wind speed of the turbine (11.4 m/s), associated to the state where the pitch control algorithm is activated, was also included in the range, as the final value of 25 m/s that corresponds to the operational cut-out scenario.

The roughness value for z_0 equal to 0.05 m for all the wind scenarios and directions is assumed, that characterize areas with low vegetation and isolated obstacles.

For each value of the mean wind speed, 50 turbulent wind fields (grid 21 x 21 with a step of 6.50 m) were generated using Turbsim [16]. A Normal Turbulence Model (NTM) and medium turbulence characteristic of class B, as defined by the IEC-61400 standard [8], were assumed. The mean wind speed profile for all the wind speed conditions here accounted for is shown in Fig. (3a).

Each wind field was applied to the Aerodyn module of the FAST program, so as to calculate the aerodynamic response of the rotor in time domain, for each mean wind speed level (parked and operational condition), obtaining 50 rotor thrust time-histories. In Fig. 3b the mean values (black points), the maximum values (red points) of the rotor thrust, and their average across the wind speed (black and

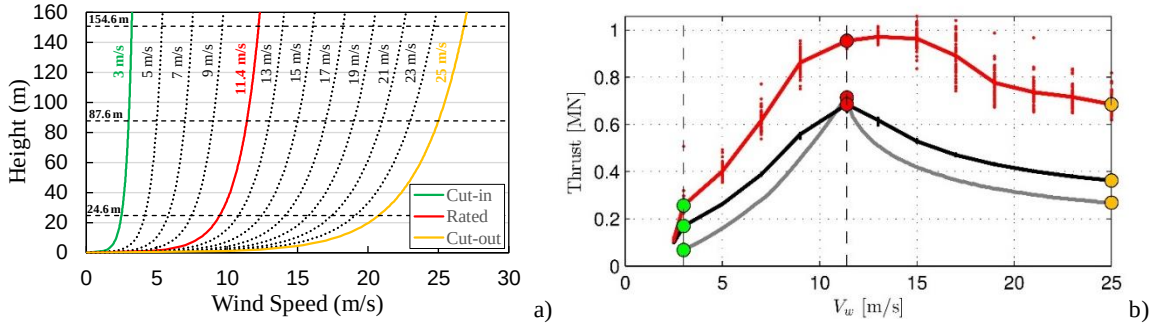

Figure 3. a) Mean wind speed vertical profile; b) Mean (black point and line) and maximum (red points and line) values of the rotor thrust compared with the results of the Blade Element Momentum theory (grey line).

red continuous lines) are shown. It can be observed that the rotor thrust is strongly related to the wind speed and pitch control mechanism in the blades that change the load pattern significantly (Fig. 1b). The rotor thrust increases up to wind speeds reaching the value of 11.4 m/s (rated condition), and decrease for increasing values of wind speed up to 25 m/s (cut-out). This trend is in good agreement with the corresponding one calculated through the BEM theory (grey continuous line). The observed differences are mainly due to the model assumed for the definition of the wind loads: turbulent wind field, in the first case, and steady-state wind condition in the second case. It is important to mention that turbulence effects, taken into account in the generation of the random wind fields, play a crucial role in the calculation of the maximum rotor thrust values that result relatively higher than those derived with the BEM theory, with an increase of 33.7% observed for the operational rated condition.

Each thrust time history was then applied to the top node of the tower structural model, so as to evaluate the corresponding structural response parameters in the fore-aft direction resulting from the linear dynamic time-history analysis.

The structural model was then analysed under the fifty artificial accelerograms. These input signals were generated using the SeismoSignal software, with a total duration of 25s, and a strong motion length of 15s. Their mean spectrum is never lower than 90% of the corresponding EC8 elastic spectrum Type 1 for class of soil C, with 5% damping ratio. These accelerograms were scaled to a peak ground acceleration ranging from 0 to 1g.

Each ground motion was then applied as a boundary condition at the base of the tower in either the fore-aft or side-to-side direction, and linear dynamic time-history analyses were carried out to evaluate the corresponding seismic response parameters.

For all the time-history analyses, the aerodynamic damping magnitude was set for each parked and operational condition at values here calculated for the fore-aft and side-to-side directions, using the closed-form solution proposed by Valamanesh [10] (Fig. 2). On the other hand, the structural damping was assumed to be equal to 1% of critical for all directions [8].

3.3. Probabilistic assessment of the peak response

The structural response of the 5 MW HAWT tower subjected to the combined actions of wind and earthquake was evaluated using Monte Carlo simulations. For each working condition, the maximum value of the structural parameters was assessed for each combination of wind load (acting in fore-aft direction) and the seismic excitation applied in the fore-aft or side-to-side directions. The time-history response to wind load was calculated for a duration of 600s, and the ground motion was applied in the simulation after 400 s, allowing the transient behaviour of the turbine at the beginning of the simulation to diminish and not to affect the seismic response.

The outcome of the wind and seismic effects on the parked and operational wind turbine was analysed in terms of tower base bending moment and base shear, total drift ratio and rotation at the tower top. In fact, each wind response time history of the structural parameter was then combined with each seismic response time-history of the same parameter, so to obtain in the fore-aft and side-to-side directions a total of 2500 response time histories for each scenario (1 parked and 12 operational wind speed levels).

The variations of the GEV Probability Density Function parameters (shape κ, scale σ, and location μ), of the maximum base bending moment depending on the wind speed for increasing values of peak ground acceleration a_g, are shown in Fig. 4.

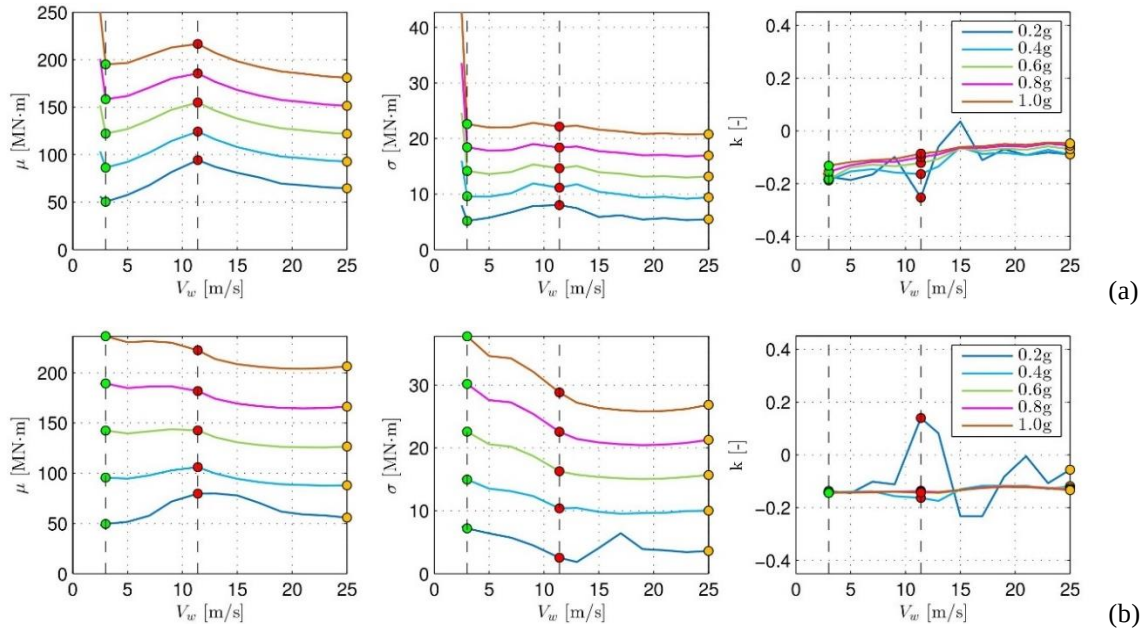

Figure 4. GEV parameters (shape parameter κ, scale parameter σ, location parameter μ) of CDF fitting the multi-risk HAWT peak base bending moment, for different wind scenarios combined with earthquake acting along the, (a) fore-aft direction, (b) side-to-side direction.

By observing Fig. 4, it can be seen the general increase of the location and scale parameters with a_g for all wind speeds. Usually, the maximum demand in terms of all the structural response parameters is associated with the operational rated scenario. However, it is noted that for the high value of peak ground acceleration (a_g > 0.6g) only the parked condition gives larger results if compared to the others, due to the absence of aerodynamic damping. Therefore, the parked scenario reveals to be critical for high values of peak ground acceleration.

Similar trends are observed for the combination of wind and seismic loads acting in the fore-aft direction and side-to-side direction, respectively. In these other cases, all the scenarios associated with wind speed values less than 11.4 m/s are more demanding if compared to the operational rated one for high values of peak ground acceleration. However, in these last cases, it is noted that the parked scenario becomes critical starting from a lower value of the peak ground acceleration (a_g > 0.5g).

Finally, it is observed that the trends of the shape parameters tend to stabilize at a constant negative value for peak ground accelerations larger than 0.4g. In these cases, the probability distribution can be represented using a reverse Weibull or Type III Extreme Value Distribution.

4. CONCLUSIONS

In this study, the probabilistic assessment of the peak response of a land-based horizontal axis wind turbine HAWT subjected to the combined effects of wind and seismic actions is calculated through Monte Carlo simulations. The analyses were carried out using two open-source software (i.e. FAST and OpenSees) to minimize costs. For the first time, the GEV parameters of the maximum base bending moment depending on the wind speed for increasing values of peak ground acceleration, are calculated.

The role played by the seismic loads if combined with the operational wind loads is presented and discussed. The results in terms of variation of the GEV parameters of the base moment expressed as a function of wind speed for increasing values of peak ground acceleration show that the maximum demand is associated with the operational rated scenario. However, it is noted that for a high value of peak ground acceleration, the parked condition only gives greater results if compared to the others,

becoming dominant for high values of peak ground acceleration, higher than 0.6g for seismic action in the fore-aft direction and 0.5g in the side-to-side one.

REFERENCES

[1] N. Bazeos, G.D. Hatzigeorgiou, I.D. Hondros, H. Karamaneas, D.L. Karabalis, and D.E. Beskos, "Static, seismic and stability analyses of a prototype wind turbine steel tower", *Eng. Struct.,* vol. 24, pp. 1015-1025, 2002.

[2] I. Lavassas, G. Nikolaidis, P. Zervas, E. Efthimiou, I. Doudoumis, and C. Baniotopoulos, "Analysis and design of the prototype of a steel 1-MW wind turbine tower", *Eng. Struct.,* vol. 25, pp. 1097-1106, 2003.

[3] D. Witcher, "Seismic analysis of wind turbines in time domain", *Wind Energ.,* vol. 8, pp. 81-91, 2005.

[4] I. Prowell, and P. Veers, *Assessment of Wind Turbine Seismic Risk: Existing Literature and Simple Study of Tower Moment Demand.,* Sandia National Laboratories: Albuquerque, NM, USA, 2009.

[5] I. Prowell, M. Veletzos, A. Elgamal, and J. Restrepo, "Experimental and numerical seismic response of a 65 kW wind turbine", *J. Earthquake Eng.,* vol. 13, pp. 1172-1190, 2009.

[6] I. Prowell, *An Experimental and Numerical Study of Wind Turbine Seismic Behavior.,* University of California: San Diego, CA, USA, 2011.

[7] I. Prowell, A. Elgamal, C. Uang, J.E. Luco, H. Romanowitz, and E. Duggan, "Shake table testing and numerical simulation of a utility-scale wind turbine including operational effects", *Wind Energ.,* vol. 17, pp. 997-1016, 2014.

[8] International Electrotechnical Commission, *Wind Turbines - Part 1: Design Requirements,* IEC 61400e1 Ed, 3: Geneva, Switzerland, 2005.

[9] ASCE/AWEA RP2011, *Recommended Practice for Compliance of Large Land-Based Wind Turbine Support Structures,* American Society of Civil Engineering: Reston, VA, USA, 2011.

[10] V. Valamanesh, and A.T. Myers, "Aerodynamic Damping and Seismic Response of Horizontal Axis Wind Turbine Towers", *J. Struct. Eng.,* vol. 140, no. 11, 2014.

[11] A.M. Avossa, C. Demartino, P. Contestabile, F. Ricciardelli, and D. Vicinanza, "Some results on the vulnerability assessment of HAWT subjected to wind and seismic actions", *Sustainability,* vol. 9, p. 1525, 2017.

[12] J. Jonkman, S. Butterfield, W. Musial, and G. Scott, "Definition of a 5-MW reference wind turbine for offshore system development", *Technical Report NREL/TP-500-38060,* 2009. Available from: https://www.nrel.gov/docs/fy09osti/38060.pdf

[13] C. Demartino, and F. Ricciardelli, "Aerodynamic stability of ice-accreted bridge cables", *J. Fluids Structures,* vol. 52, pp. 81-100, 2015.

[14] D.J. Salzmann, and J. Van der Tempel, "Aerodynamic Damping in the Design of Support Structures for OffshoreWind Turbines", In: *Proceedings of the Copenhagen Offshore Conference,* Copenhagen, Denmark, 2015.

[15] J.M. Jonkman, and M.L. Buhl Jr, *Fast User's Guide.,* NREL: Golden, CO, 2005.

[16] B.J. Jonkman, "TurbSim user's guide. Technical report NREL/TP-500-46198", *National Renewable Energy Laboratory,* Golden: CO, 2009.

[17] F. McKenna, G.L. Fenves, M.H. Scott, and B. Jeremic, "Open system for earthquake engineering simulation (OpenSees) [program]. Version 2.4.6", *Pacific Earthquake Engineering Research Center,* University of California at Berkeley: United States, 2013.

[18] J.C. Kaimal, J.C. Wyngaard, Y. Izumi, and O.R. Cote, "Spectral characteristics of surface layer turbulence", *Q. J. R. Meteorol. Soc.,* vol. 98, pp. 563-589, 1972.

[19] EN 1998–1, Eurocode 8, *Design of Structures for Earthquake Resistance, Part 1: General Rules, Seismic Actions and Rules for Buildings,* European Committee for Standardization: Brussels, 2004.

THE INTERNATIONAL CONFERENCE ON
WIND ENERGY HARVESTING 2018
21-23 March 2018
Catanzaro Lido, Italy

Paper TS1.2.4.

AN AUTONOMOUS REAL-TIME DECISION TREE FRAMEWORK FOR MONITORING & DIAGNOSTICS ON WIND TURBINES

Imad Abdallah, Vasilis K. Dertimanis, and Eleni N. Chatzi[1]*

[1]Department of Civil, Environmental and Geomatic Engineering, ETH Zurich, Switzerland
Corresponding author: Eleni N. Chatzi, chatzi@ibk.baug.ethz.ch

ABSTRACT

This paper describes a conceptual framework for real-time monitoring and diagnostics, root cause analysis of faults and quantitative risk assessment in the context of operation and maintenance of wind turbine components. An autonomous software-hardware solution is proposed that implements a real-time decision tree learning algorithm for smart monitoring and diagnosis of the state of structural and mechanical components on wind turbines. A decision tree is a machine learning algorithm that classifies the outcome of events resulting in a "flow-chart" like structure, laying a path from an initiating event to an end state of a system, with each event associated with a probability of occurrence. A paradigm of the proposed conceptual framework focuses on the tower substructure of the wind turbine indicating the potential of the approach with respect to the design of specialized software for monitoring and diagnostics of both new and existing installations.

1. INTRODUCTION

The key concept lies in running the wind turbine (WT) telemetry data through a decision tree learning algorithm in real time for detecting faults, errors, damage patterns, anomalies and abnormal operation (i.e., "end states"). The framework is illustrated in Figure 1, with an early investigation appearing in a recent work [1]. A decision tree essentially comprises a machine learning tool for classification of event outcomes. For a given initiating event, multiple end states are possible, linking each event to an associated probability of occurrence. Once built and trained, and given a new set of real-time measurements, the decision tree may be used to predict "end states" and classify (discover) previously unknown "end states". In addition to being a natural fit for learning from big data on WT fleets, the use of decision trees is motivated by the ease of their implementation and interpretation as compared to alternative quantitative data-driven tools. The proposed framework implements:

- Hardware-software package, able to acquire and fuse in real-time both condition monitoring (CM) (e.g. electric power output, rotor speed) and specialized structural health monitoring (SHM) data (e.g. tower accelerations, strains on blade) from WT components (e.g. blades, gearbox, tower, etc.).
- Computational core: autonomous object-oriented decision tree learning algorithm, Bayesian network (BN) based computation of probabilities and root-cause discovery algorithm.
- Distributed cloud-based data storage and analytics of long term historical data, which interfaces with the real-time decision tree software unit. Hence, the toolkit does not need to save data and do heavy computations locally on remote WT.
- Online user interface to visualize the output from the decision tree (decision support tool).

2. METHODOLOGY

There currently exists a significant dislocation between data derived from CM systems (e.g. power output, rotor speed), and data obtained from specialized SHM (e.g. tower acceleration, strain on blades). The framework exploits the continuous and combined inflow of both types of information to maximize the utility of both measuring systems to owners and operators of WTs, further allowing the development

of a decision-support kit for predictive maintenance. The efficient fusion of CM and SHM data sources constitutes a "Big Data" problem, as large amounts of data are continuously sampled at high and diverse rates from thousands of WTs within a wind farm. This can be achieved through the integration of a distributed cloud based data storage and analytics system (i.e. Hadoop, Spark), and as consequence results in a reduction in the cost of handling and manipulating of said data.

Several decision tree algorithms formerly proposed by the machine learning community (i.e. ID3, C4.5, C5.0, J48, and CART) can be explored in the classification and discovery of "end states", which will assist technicians in the field in their inspection and maintenance of WT components. An innovation is being introduced in the form of object-oriented decision tree learning [3]. To this end, a WT is viewed as a multilayered system of objects (e.g. structure, controller, actuator, etc.) that are defined on the basis of abstract superclasses, attributed with specific properties and methods. The limitation appears when the component displays a behavior with feedback (i.e., after a repair or update in the system) or for evolving systems (e.g. when new sensors are integrated or aging of the system), which implies a need to establish several decision trees based on the possible ordering of the events or based on new initiating events. One way around this is to map the decision trees learners into Bayesian Networks (BN) for further assessment of the conditional probabilities [5, 6]. The integration of the decision tree learning algorithm and BN delivers updated probability of occurrence associated with each event and end state, which would form a solid indicator of the risk of future failure of any given component.

Owners, operators and manufacturers of WTs spend significant time, budget and effort on discovering root causes of faults, damages and failure of components on WTs. An important outcome of the real-time decision tree software is the automatic capability to trace a path from the end state (e.g. blade damage) to the initiating event (e.g. wrong parameters in control system), thus providing the decision maker with timely and salient insights into the root causes [4], including probability of each root cause.

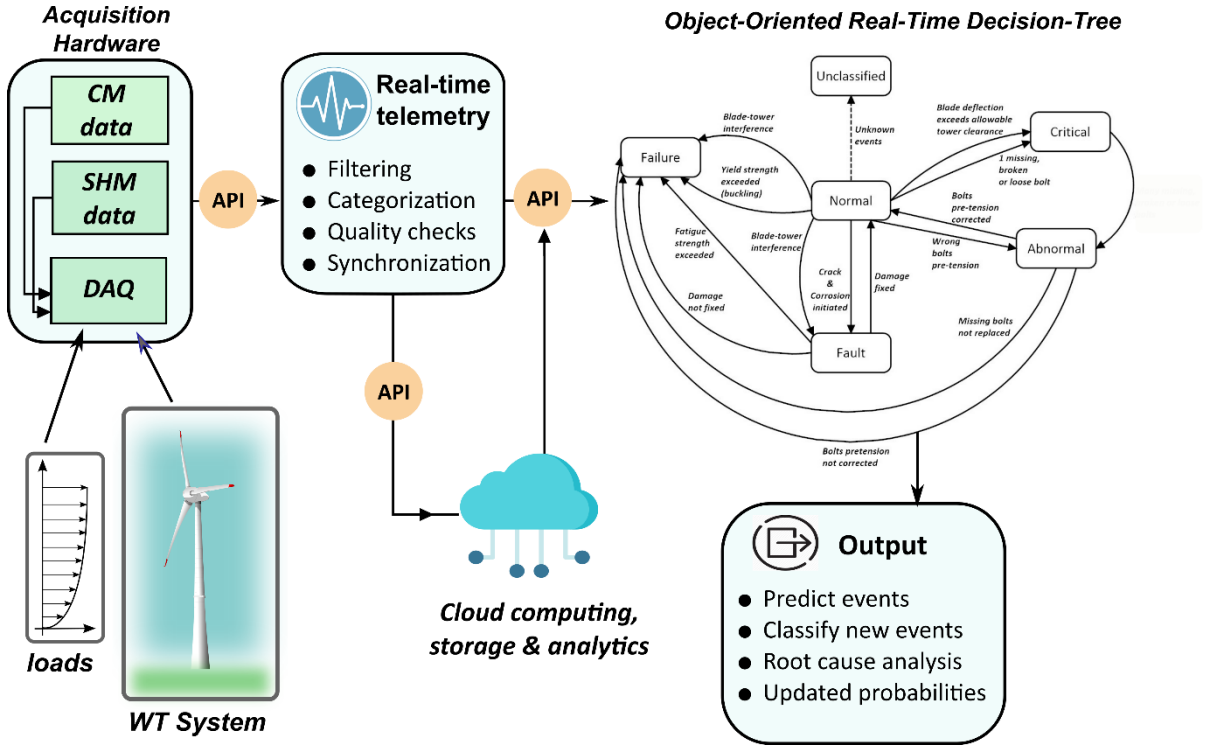

Figure 1: Graphical summary of the proposed framework.

3. RESULTS

As an indicative example of our framework, we focus on the representation of tower component of the WT. A tower object is an instance of the tower class, which is a child of the "structure" *superclass* and inherits its *properties* and *methods*. The tower's structural response is assumed to be affected by the interaction forces that are developed with its neighboring sub-structures, namely the foundation and the rotor-nacelle assembly, which are also instances of the corresponding foundation and nacelle classes, again children of the structure superclass. Figure 2 displays an indicative decision tree for the tower. The properties of the state class are clearly indicated, along with events that have been specifically defined for this object. We note the presence of an *unclassified* state and *unknown* events in Figure 2. The decision tree would, based on the real–time telemetry from the tower, learn those unknown events and the corresponding unclassified states. In a fully probabilistic framework, all the events among the different states must be attributed with corresponding conditional probabilities, which are initially assigned during the design stage and updated accordingly with respect to the actual structural behavior based on the real-time telemetry. The latter could be achieved by combining both sensors, which provide a direct indication of the structural response at the measurement points, and estimators, which can be utilized in order to estimate the structural response in unmeasured spots along the tower [7]. The term estimator could refer to, but is not restricted to, Kalman filters, surrogate models, and reduced time marching simulators which could be run in near real-time.

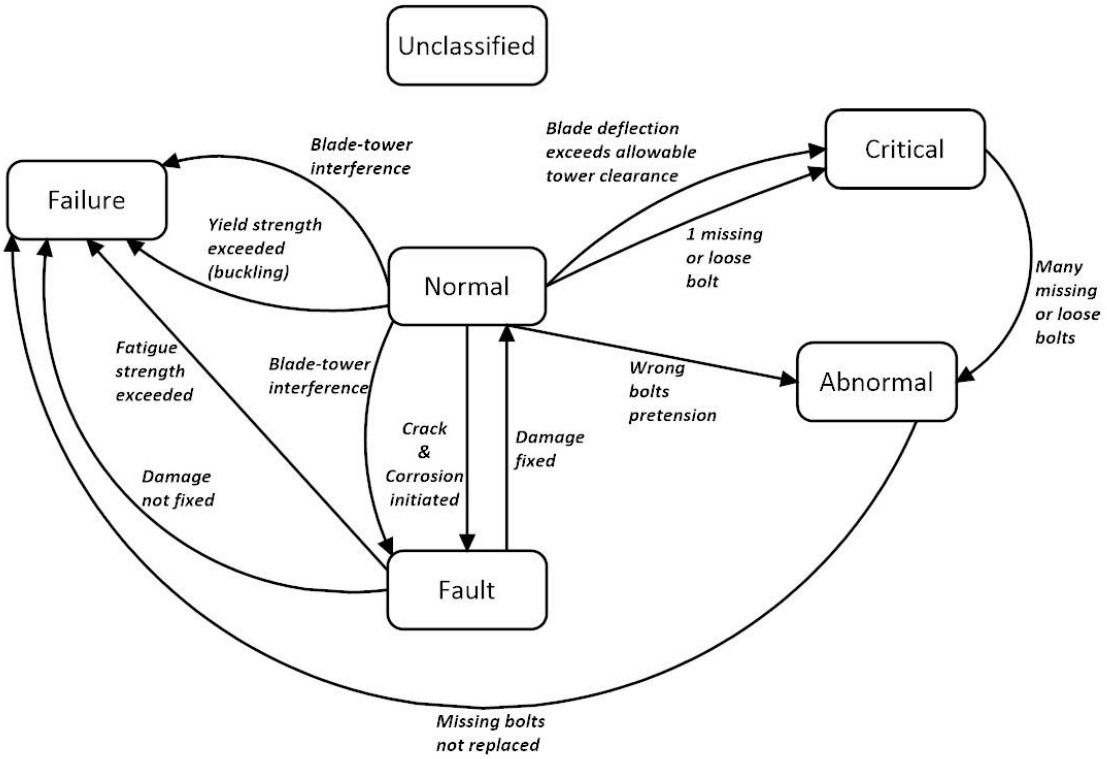

Figure 2: Example of an object-oriented decision tree of a wind turbine tower.

4. CONCLUSIONS

As generally the largest component of operation and maintenance costs is inspection, maintenance & repair, we stipulate that the proposed autonomous decision tree framework would form a "protection suit" from cradle-to-grave and promises significant potential in establishing wind energy as a robust, reliable and highly efficient renewable infrastructure. The hardware-software solution is to be implemented on both new as well as existing WTs. As such, our solution bears the direct benefit of extending the operating life of existing WTs, currently limited to a mere 20-25 years average lifespan. A preventive approach to maintenance planning further helps reduce operation and maintenance costs in the long-term, which disproportionally increase near an advanced WT life-stage. The framework may

eventually be adopted by various industries and infrastructure that provide critical services to society such as bridges, power lines, hydropower dams, internet networks, tunnels and transportation infrastructure can readily benefit from such a framework.

ACKNOWLEDGEMENTS

The authors would like to acknowledge the support of the European Research Council via the ERC Starting Grant WINDMIL (ERC-2015-StG #679843) on the topic of Smart Monitoring, Inspection and Life-Cycle Assessment of Wind Turbines.

REFERENCES

[1] I. Abdallah, V. Dertimanis and E. Chatzi, "Data-driven identification, classification and update of decision tress for monitoring and diagnostics of wind turbines", 2nd ECCOMAS Thematic Conference on Uncertainty Quantification in Computational Sciences and Engineering, UNCECOMP 2017, Rhodes Island, Greece, 15–17 June 2017.

[2] G. D. Wyss and F. A. Duran, "OBEST: The object based event scenario tree methodology", Technical Report SAND2001-0828, Sandia National Laboratories, Albuquerque,

[3] A. X. Zheng, J. Lloyd and E. Brewer, "Failure Diagnosis Using Decision Trees", Proceeding ICAC 2004 Proceedings of the first international conference on automatic computing, p. 36-43, 2004.

[4] G. Bearfield and W. Marsh, "Generalising event trees using bayesian networks with a case study of train derailment". In International Conference on Computer Safety, Reliability, and Security, SAFECOMP 2005, pages 52–66, Fredrikstad, Norway, 2005.

[5] D. Jassens, G. Wets, T. Brijs, K. Vanhoof, T. Arentz and H. Timmermans, "Integrating Bayesian Networks and decision trees in a sequential rule-based transportation model", Euro. J. Oper. Res. 175 (1), 16-34, 2006.

[6] A. Vitina, S. Lüers, A. Wallasch, V. Berkhout, A. Duffy, B. Cleary, L. Husabø, D. Weir, R. Lacal-Arántegui, M. Hand, E. Lantz, K. Belyeu, R. Wiser, M. Bolinger and B. Hoen, "IEA Wind Task 26: Wind Technology, Cost, and Performance Trends in Denmark, Germany, Ireland, Norway, the European Union, and the United States: 2007–2012", International Energy Agency, 2015.

[7] Tatsis, K. Dertimanis, V., Abdallah, I., Chatzi, E., "A substructure approach for fatigue assessment on wind turbine support structures using output-only measurements", In X International Conference on Structural Dynamics, EURODYN 2017, Procedia Engineering 2017, 199: 1044-1049

Paper TS1.2.5.

THE INTERNATIONAL CONFERENCE ON
WIND ENERGY HARVESTING 2018
21-23 March 2018
Catanzaro Lido, Italy

LESSONS LEARNED FROM PRACTICAL STRUCTURAL HEALTH MONITORING OF OFFSHORE WIND TURBINE SUPPORT STRUCTURES IN THE NORTH SEA

S. Tewolde[1, 2*], R. Höffer[1], H. Haardt[2], J. Krieger[2]

[1]Ruhr-Universität Bochum, Faculty of Civil and Environmental Engineering, Germany
[2]Airwerk GmbH, Germany
**Corresponding author: S. Tewolde,* simon.tewolde@rub.de

ABSTRACT

With the increasing demand for transition towards renewable energy sources, the clean energy produced from offshore wind is rapidly progressing not only in the amount of energy produced but also in minimizing the energy costs. As a result, offshore wind turbines are getting bigger and being built in deeper waters for higher energy production. Advancement in technology is also significantly contributing for innovative designs and construction methods. Furthermore, to increase the reliability and minimize the operation and maintenance (O&M) costs, risk based inspection and maintenance planning is being implemented through Structural Health Monitoring (SHM). As of January 2017, 72% of the installed offshore wind capacity in Europe is located in the North Sea. In this paper, for a bottom-fixed offshore wind turbine in the North Sea, the concept of SHM, data analysis strategy, results and applications presented. The experiences, challenges and lessons learned are also discussed for implementing SHM on floating offshore wind turbines.

ABBREVIATIONS

BSH	=	BSH - Bundesamt für Seeschifffahrt und Hydrographie (German Federal Maritime and Hydrographic Agency)
CMS	=	Condition Monitoring System
DNV GL	=	Det Norske Veritas and Germanischer Lloyd
EF	=	Eigen frequency
EMODnet	=	European Marine Observation and Data Network
FLOW	=	Far and Large Offshore Wind
FOWT	=	Floating Offshore Wind Turbines
MP	=	Monopile
O&M	=	Operation and Maintenance
OSS	=	Offshore Substation
OWT(s)	=	Offshore Wind Turbine(s)
RBIM	=	Risk Based Inspection and Maintenance
SHM	=	Structural Health Monitoring
TP	=	Transition Piece
VBSHM	=	Vibration Based Structural Health Monitoring

1. INTRODUCTION

In the transition from fossil fuels based energy resources in to renewables, wind energy is playing an important role. As a result by 2020, wind energy is expected to cover about 16.5% of the electricity demand in European Union (EU) [1]. This figure was only 1% in 2000. Especially offshore wind energy

has a tremendous potential to significantly contribute for achieving this goal and further. But for a complete transition from fossil fuels to renewable energy sources, producing only a clean energy is not enough. The renewable energy sources also need to be more reliable and their costs more affordable compared to the non-renewable energy sources.

As for every young industry, the energy cost for offshore wind energy was initially high. But the increasing need to minimize cost pushed for technological advances. As a result, offshore wind turbines are being built bigger and taller in deeper waters and harsh sea conditions for higher power production. In addition, technological improvements without changing the dimensions of the wind turbines have also played a significant role in maximizing power production, such as use of higher grade magnets, redesigning of gear boxes and development of more effective cooling systems. These improvements have enabled commercial deployment of 8MW wind turbines and prototype tests for up to 9.5MW wind turbines [2, 3, and 4]. The major wind turbine manufacturers have already developed concepts to realize a 10MW+ wind turbines by 2020. These bigger wind turbines are also best suited for floating platforms. 80% of the offshore wind energy potential in European seas are located at sea water depths of more than 60m, where fixed bottom type offshore wind turbines are not economically and technically feasible [5]. This makes floating offshore wind turbines as the future of offshore wind energy industry in Europe. The map below (Figure 1) generated from (European Marine Observation and Data Network) EMODnet website [6] shows the distribution of sea water depths in Europeans seas.

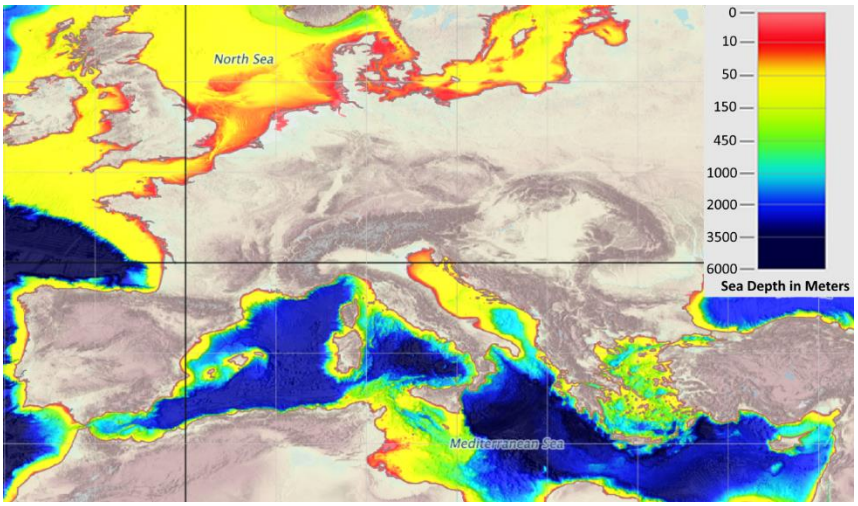

Figure 1. European Seas water depth distribution, map generated from EMODnet [6]

The advances in technology and many other improvements in design, material and construction methods have significantly contributed to decreasing the cost of offshore wind energy. According to a conclusion of a study carried out by FLOW (Far and Large Offshore Wind), about 40% reduction in the cost of offshore wind energy can be achieved between 2013 and 2023 [7]. FLOW was a research program in the Netherlands consisting of thirteen companies and research institutions working together on innovations for reducing the cost of offshore wind energy.

A similar study by DNVGL also estimated that a cost reduction of about 40% can be achieved. Many stakeholders claim that this reduction is needed to secure the future of wind energy industry [8]. The DNVGL report further broke down the cost reduction contribution percentages from different activities, such as; finding a better way of doing things through innovative research and development activities that could contribute in 12% cost reduction. It was also proposed that reducing risks and increasing reliability could result in 7% cost reduction, which is the core aim of this paper.

2. STRUCTURAL HEALTH MONITORING (SHM)

Wind turbines, especially OWTs, are ever getting bigger and being placed in more challenging environments for achieving higher power production. For a relatively new industry, as the upper boundary is pushed further and further, it may result in more risks and increasing operational and

maintenance (O&M) costs. That was the reason BSH - Bundesamt für Seeschifffahrt und Hydrographie (German Federal Maritime and Hydrographic Agency) recommended that, all offshore wind farm operators in the German bight should install a Condition Monitoring System (CMS) on 10% of the offshore wind turbines in an offshore wind farm [9]. For offshore wind turbines, it is estimated that around 25 to 30% of the energy cost is spent on maintenance, mainly corrective maintenance [10, 11 and 12]. Therefore, assessing and managing risk in line with the recommendations of ISO 31000 [13] could help to identify structural performance parameters to obtain the most possible benefit from designing and implementing an SHM system. SHM reduces uncertainty by providing information on the performance of the structure being monitored. Reducing uncertainty results in reduced risk. In this way the results of SHM could contribute to risk reduction and increase in reliability. This in turn results in cost reduction through informed decisions on O&M scheduling. The idea is to plan an inspection or maintenance activity only when it is required, not too early or not too late. This is commonly known as Risk Based Inspection and Maintenance (RBIM).

2.1. Global monitoring concept

In the past many different methods have been used for detecting damages in large civil engineering structures; such as visual inspection, use of dye penetrants and acoustics. But almost all the methods are local, in which every part of a structure needs to be investigated before the structure being inspected could be declared safe. This, in most cases was very tedious and involves uncertainty from human factors. For offshore structures, such methods are simply impractical. Therefore, Vibration Based Structural Health Monitoring (VBSHM) is used for damage detection in OWT structures. The concept involves installation of an array of sensors on a structure, in order to monitor parameters of the structure which are damage sensitive (figure 2).

2.2. Structural Health Monitoring system

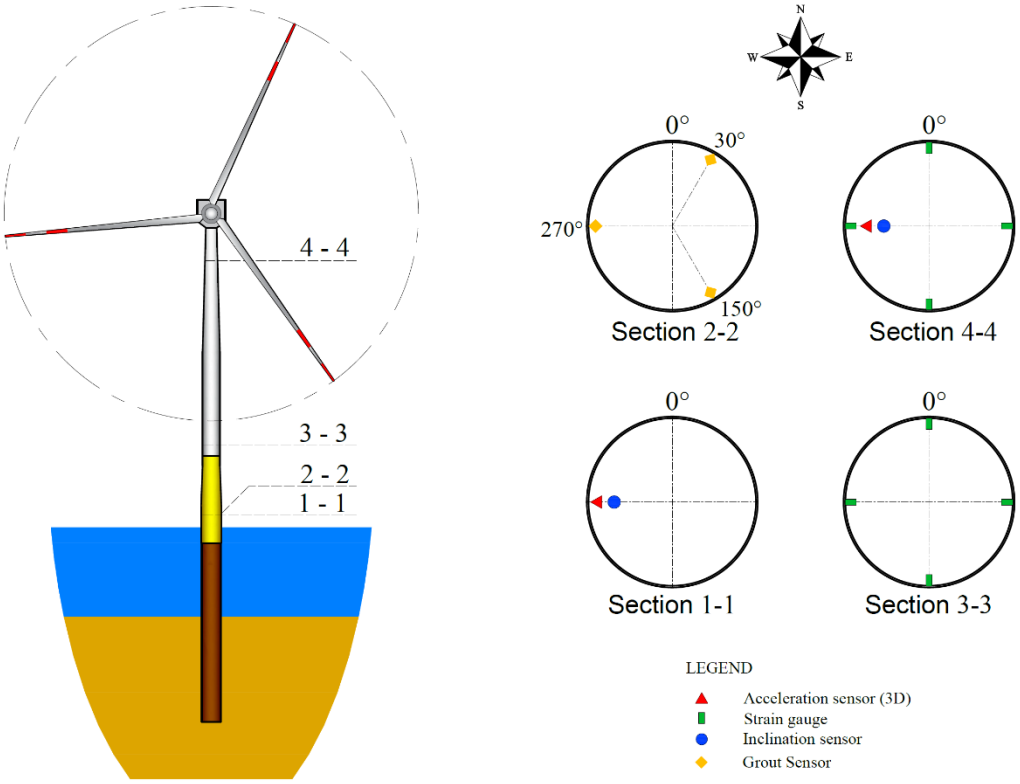

Figure 2. Typical installed sensor types and locations at an offshore wind turbine

The installed monitoring system on the offshore wind turbine structures commonly consist of vibration, environmental and operational sensors. The vibration sensors mainly consists of acceleration sensors,

inclinometers, strain gauges and displacement transducers. While the environmental sensors include wind, wave and sea state data and the operational sensors include power, blade RPM, yaw angle and pitch angle.

The OWT under consideration in this paper (figure 2) consists of; 2x 3D acceleration sensors at two levels, 2x 2D inclination sensors at two levels, 4x strain gauge sensors at two levels and 3x displacement transducers (grout sensors), the scheme may be referred to in figure 2 and the photos of the installed sensors by airwerk GmbH may also be referred to in figure 3.

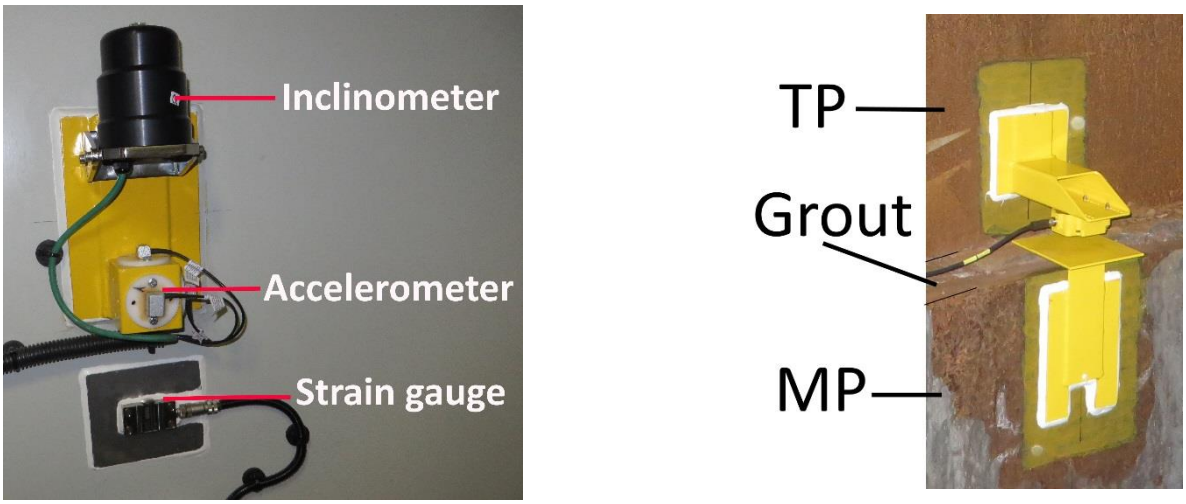

Figure 3. (left) Installed sensors at section 4-4 (270°N) of figure 2, (right) one of the grout sensors installed at section 2-2 of figure 2

Data collected from all the monitored OWTs is transferred to the offshore server in the Offshore Sub Station (OSS) platform. Then, the data is transferred to onshore through internet for further analysis.

2.3. Data analysis strategy

Considering the huge amount of data collected from the continuous SHM, the data analysis strategy is semi-automatic and classified in to three iterative stages of increasing complexity level (Figure 4).

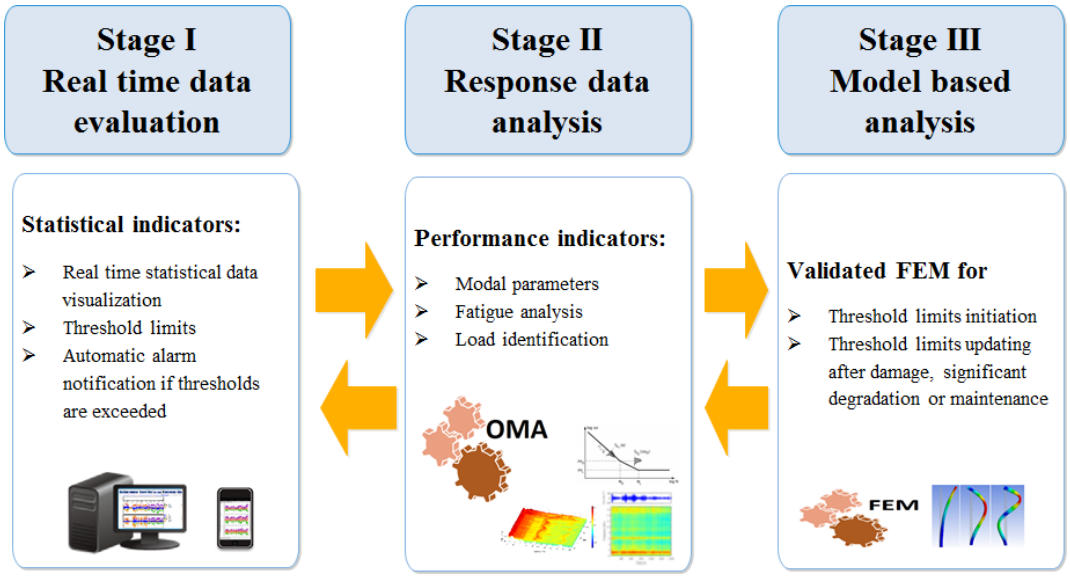

Figure 4. Iterative data evaluation strategy

The data evaluation strategy is called iterative, as the three stages continuously (iteratively) support each other for updating the threshold limits of the different parameters being monitored. This is important, as the initial threshold level recommendations (usually from designers) are more conservative. For example; experiences from many offshore wind farms show that, the measured first Eigen frequencies of the as built structures are higher than the design Eigen frequencies, which means that the as built offshore wind turbine structures are stiffer than their design. This is most of the time caused by underestimation of the foundation soil stiffness during design phase.

In this iterative data evaluation strategy, the first stage consists of real time statistical data analysis and comparison to predetermined threshold levels, above which alarm notifications are activated, whenever exceeded. The second stage makes use of acceleration sensor raw data for computing dynamic parameters of the structure by modal analysis. Also the strain gauge data are used for load identification and fatigue analysis through rain flow counting. Stage III makes use of validated Finite Element Model (FEM) for initial determination of the threshold values for stages I and II. This stage also helps for updating the threshold limits after damage, significant degradation or maintenance.

2.4. Data Analysis Results

The data analysis results show the ongoing status of the structure's integrity. In stage I, the 10 minute statistical data values are compared in real time against predefined threshold values. For example, figure 5 shows one day data plot of the three displacement transducers (grout sensors), which indirectly measure the damage of the grout connection through the movement (slippage) of the transition piece (TP) relative to the monopile (MP). The TP and MP are joined together by a high strength and shear key reinforced grout annulus injected between them (figure 2, right and figure 5, bottom right). The purpose of using the grout connection is for correcting the pile inclination error while driving, so as to achieve the required verticality for the bolted connections. The one day data plot in Figure 5 shows that, the two threshold limits recommended by designer (**± 3mm** and **± 6mm**) were not reached on that day. The maximum and minimum records due to operation for that day were with in **± 0.6mm.**

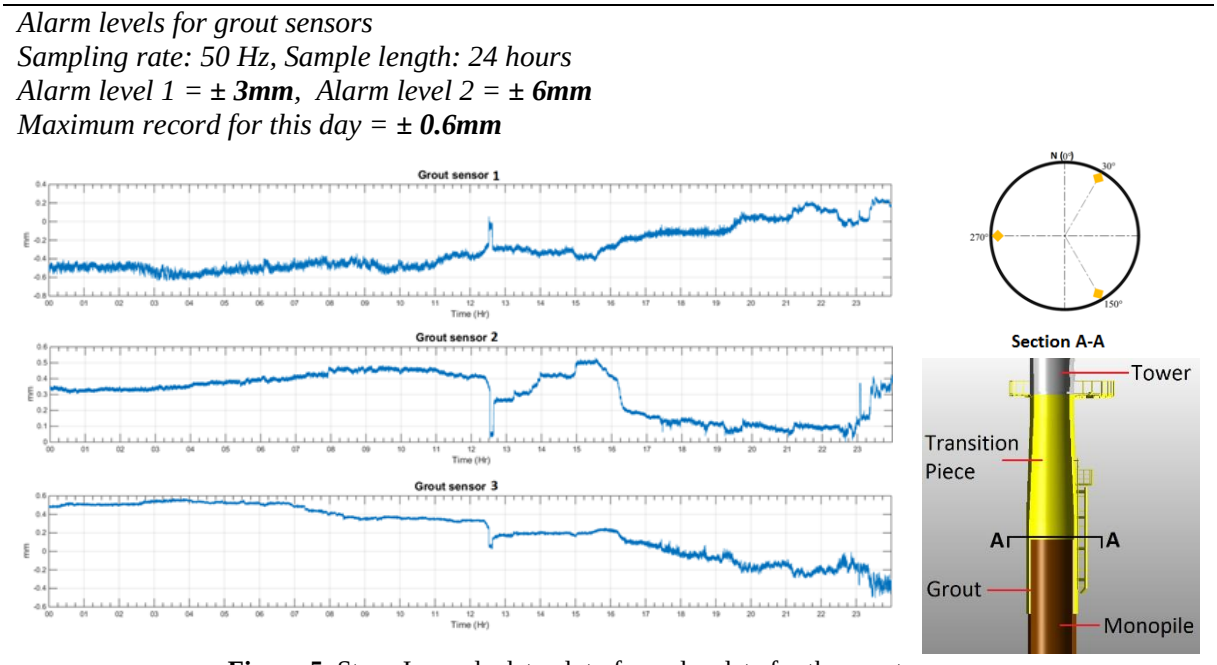

Figure 5. Stage I sample data plot of one day data for the grout sensors

Figure 6 shows stage II data analysis results. The plot on the left shows, the identified as built Eigen frequencies (EFs) computed from acceleration time history data recorded during the early stage operation of the offshore wind turbine. These calculated EFs are to be used as healthy state reference EFs against which future computed EFs are to be compared for detecting damage or changes in boundary conditions. Energy based methods are also used to analyze the acceleration data for damage detection.

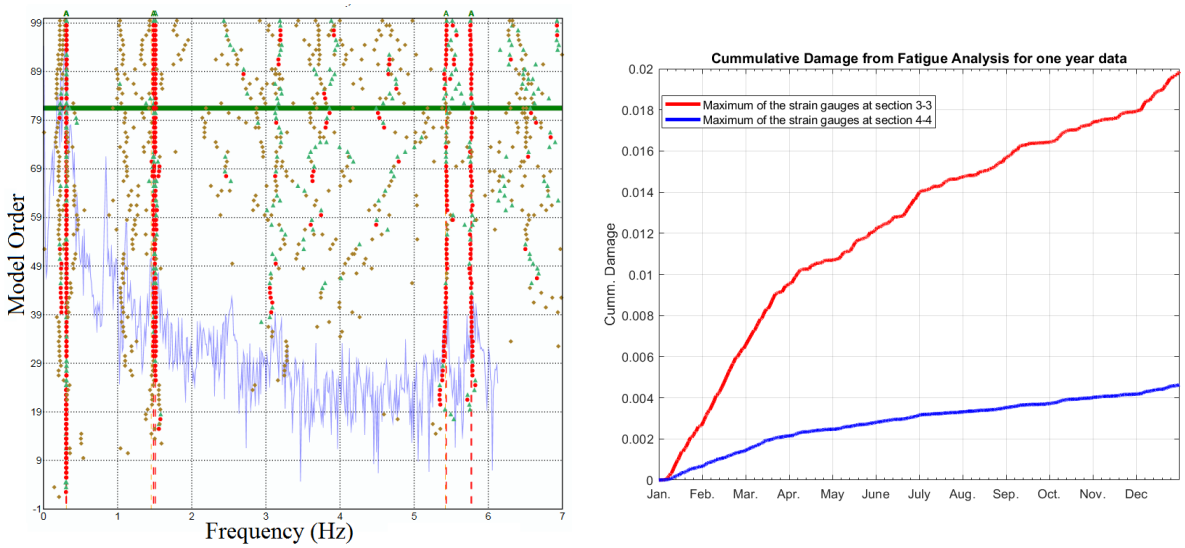

Figure 6. Stage II data analysis results Eigen frequencies (left), Cumulative damage from fatigue analysis of one year strain gauge data at two levels

Figure 6, right shows accumulated damage for one year strain gauge data at two measurement levels. The results are used for estimating the remaining life time of the structure and for justification of possible service life time extension beyond the design life. Figure 7 shows results from stage III, in which a damage (change in boundary condition) scenario of progressive scouring is simulated on an FE model validated using the as built EFs computed in stage II (figure 6, left). The result can be used for initiating thresholds for this scenario and it also shows that, the second EF is the most sensitive to scouring [15].

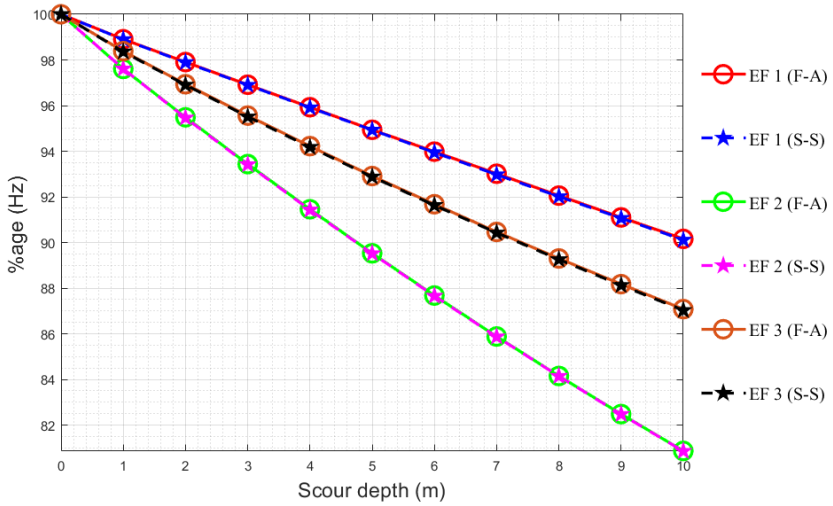

Figure 7. Stage III result: Sensitivity of Eigen frequencies to simulated progressive general scouring

2.5. Application

The SHM data analysis results are used to continuously and remotely observe the structural integrity. This can then be used to justify the reduction in number of annual periodic inspections to be made. For example in Germany, according to BSH regulations annual periodic inspection should be made on 25% of the OWTs in an offshore wind farm [9]. The annual periodic inspection includes checking of the grout connection integrity through manual measurement of the TP slippage. The SHM data from the grout sensors, when compared against the manual measurements at the same locations proved to be much more reliable and consistent. The final goal is to integrate the SHM data analysis results to the O&M to aid the operators for decision making through Risk Based Inspection and Maintenance planning.

3. CHALLENGES

The main challenge for the SHM in offshore wind industry has been full and effective integration of the SHM data results to O&M, in such a way that the wind farm operators could have the end result in a very simplified and directly usable way. For example, as simple as a traffic light indicators, so that it may directly be used for risk based inspection and maintenance plan decision making.

Another challenge is that, most wind farm operators do not show much interest in the results that could be obtained from analyzing the monitoring data. The first reason is that; the SHM was not initially part of the project planning. Its value would have been more understood and appreciated, if it was implemented according to the recommendations of ISO 31000 to mitigate or reduce the risks after first identifying, analyzing and evaluating them. The second reason is that, most of the OWTs are currently in their early operation stage (and within the typical 5 year warranty period from manufacturers). For example; in Germany, the first generation offshore wind turbines have been in operation for the past seven years. As a result, in many cases, huge amount of data is just being accumulated without analysis. Although BSH no more insists on monitoring 10% of the OWTs in an offshore wind farm, still most operators follow the 10% recommendation.

4. LESSONS LEARNED

The wind farm operators' interest is expected to grow as their turbines age. But they also need to be convinced that SHM is not only about following regulations or for formality purpose. When the SHM data analysis results are properly integrated to the project management, significant inspection and maintenance cost savings could be achieved. But in order to achieve this, the early stage SHM data analysis results are very important to determine the as built properties of the structure and establish the healthy state reference parameters.

For example, data analysis results from early stage monitoring showed that the as built EFs are usually higher than the design EFs. The same also for fatigue analysis results. These are very important findings, which indicate a possibility of service life time extension of the turbines beyond their design life time. The integration of the SHM results in O&M decision making is not yet fully realized. Researches are being made on this topic to present the monitoring results in a very simplified way to be directly used by the operators for inspection and maintenance decision making.

5. MONITORING CONCEPT FOR FLOATING OFFSHORE WIND TURBINES

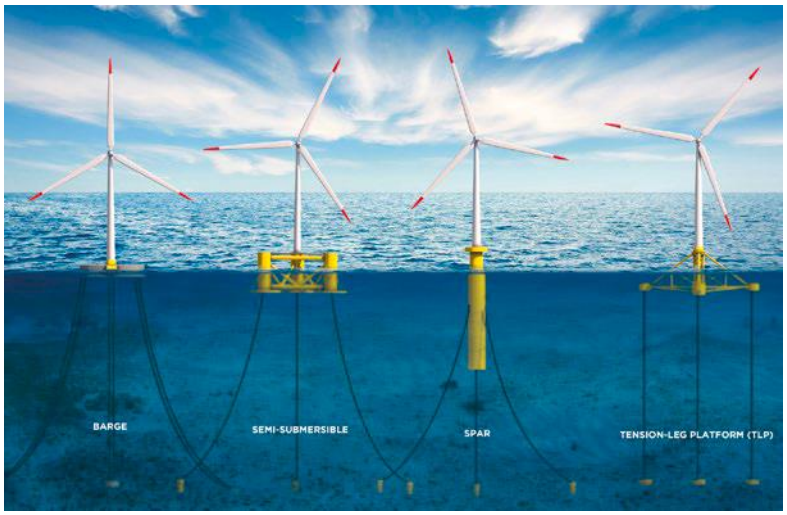

Figure 8. Common sub-structure design types for floating offshore wind turbines [5]

Floating Offshore Wind Turbine (FOWT) structures are basically different from fixed bottom OWT structures. The FOWTs could have several types of substructures. The most common sub-structures types are barge, semi-submersible, spar buoy and tension-leg platform (figure 8) [5]. The first three are

loosely anchored to the sea bed making the installation process easier, while the fourth one is not easy to install but results in a more stable structure.

The advantages of FOWTs compared to the fixed bottom OWTs are; foundation costs are very low, can be implemented without geotechnical or water depth constraints, no grouted connection, very less work on offshore site as the whole structure could be built onshore and towed to the offshore site, possibility of towing the whole structure back to the shore for major repairs and very easy decommissioning. But of course the structures are highly dynamic and all components need to be designed accordingly. Also performing minor maintenances might sometimes be difficult and the structures are prone to corrosion as greater part of the structure is located close to the splash zone (water surface).

In this section, a general instrumentation scheme is proposed for the support structure (tower and substructure) of a large FOWT. These recommendations are made based on the experiences gained from SHM of fixed bottom OWTs. It is highly recommended to follow the procedures of ISO 31000 for adopting it to a particular substructure type.

The proposed vibration sensors should consist of accelerometers, inclinometers and strain gauges. The strain gauges should be installed at the foot of the turbine tower from inside. This region, similar to the instrumentation scheme and fatigue analysis result of the fixed bottom case (figure 2 and figure 6 right respectively), is more prone to higher fatigue damages resulting from changes in geometry and thickness compared to the substructure (tower support) below. It is also recommended to install 3D accelerometers at the top, middle and bottom of the tower. The 3D accelerometer at the tower bottom is also used as redundancy for the strain gauges at the same level. Generally, compared to accelerometers and inclinometers, strain gauges do not last very long in an offshore condition. A 2D inclinometer is recommended to be installed together with the 3D accelerometer at the tower top. 2D inclinometers (or preferably 3D accelerometers) are proposed to be installed one at the top (from inside) for each of the platform columns (if above water level).

For realistic interpretation of the SHM data evaluation results from vibration sensors, it is very important to also have the operational, environmental and sea state data.

REFERENCES

[1] Wind Europe “Wind energy in Europe: Outlook to 2020” September 2017.
[2] Siemens Wind Power GmbH & Co.KG. Product flier: SWT-8.0-154
[3] www.4coffshore.com. 4C Offshore Ltd. Accessed on 17.10.2017
[4] MHI Vestas Offshore Wind A/S
[5] Wind Europe. Floating Offshore Wind Vision Statement. June 2017
[6] European Marine Observation and Data Network (EMODnet) Bathymetry. Generated on 17.10.2017
[7] Rolf de Vos. FLOW competitive through cooperation. 2016
[8] DNV GL. Offshore wind: a manifesto for cost reduction
[9] Federal Maritime and Hydrographic Agency (BSH). “Design of Offshore Wind Turbines”. 2007
[10] Operation and Maintenance costs compared and revealed, Wind Stats Vol.19, No.3, 2006
[11] Wiggelinkhuizen et al. - CONMOW: Condition Monitoring for Offshore Wind Farms, EWEA, EWEC 2007, Milan
[12] Miedema, R. (2012). Offshore Wind Energy Operations & Maintenance Analysis. Hoge school van Amsterdam.
[13] ISO 31000: Risk Management – Principles and Guidelines
[14] Wang L. and Chan T. H.T. (2009). Review of vibration-based damage detection and condition assessment of bridge structures using structural health monitoring. Queensland University
[15] S. Tewolde, R. Höffer, H. Haardt. Validated model based development of damage index for Structural Health Monitoring of offshore wind turbine support structures. X International Conference on Structural Dynamics, EURODYN 2017, Rome, September 10-13, 2017

TECHNICAL SESSION 2.1

Markets, Strategies, Policies and Socio-economics

THE INTERNATIONAL CONFERENCE ON
WIND ENERGY HARVESTING 2018
21-23 March 2018
Catanzaro Lido, Italy

Paper TS2.1.1

URBAN WIND ENERGY: SOCIAL, ENVIRONMENTAL AND PLANNING CONIDERATIONS

Ruben Paul Borg [1*], Neveen Hamza [2], Conor Norton [3], Christos Efstathiades [4], Mantas Marciukaitis [5]

[1] Faculty for the Built Environment, University of Malta, Chairman WINERCOST WG3
[2] University of Newcastle, United Kingdom, Vice Chairman WINERCOST WG3
[3] Dublin Institute of Technology, Ireland
[4] Municipality of Limassol, Limassol, Cyprus
[5] Lithuanian Energy Institute, Lithuania

Corresponding author: Ruben Paul Borg, ruben.p.borg@um.edu.mt

ABSTRACT

Wind power has an important role as a renewable energy source for energy security of supply and in supporting sustainable development. The integration of renewable sources of energy generation nearer to consumers within the built environment forms one of the main strategies for smart cities. Wind energy Technologies and related structures and infrastructure are expected to form an integral part of the Smart Cities of the future. Past experience has shown that wind technology very often receives significant opposition from the communities. The paper presents key issues concerning social, environmental and planning considerations of wind technology in the urban environment. The outcome of the WINERCOST survey and the Urban Wind Energy focus group are discussed in the context of current research in this field. The assessment leads to the development of key principles for a strategy to enhance the Smart Cities Concept by effectively introducing Urban Wind Energy.

NOMENCLATURE

SMWT	=	Small and Medium Wind energy Technologies
BWT	=	Built Environment Wind Technology
UWT	=	Urban Wind Technology

1. INTRODUCTION

Wind power continues to have a major role as part of the emerging global shift to diversify sources of the energy supply and its mix, to spur sustainable development and security of energy supply. According to Global Wind Energy Council (GWEC), the deployment of wind power has more than tripled since 2007, surpassing 318 gigawatts (GW) of cumulative installed capacity, with the highest shares of cumulative installed capacity in China (91 GW), the United States (61 GW), and Germany (34 GW)[1]. The International Energy Agency (IEA) technology roadmap for wind power targets a 15–18% share of global electricity production by 2050. The roadmap targets 2300–2800 GW of installed wind power capacity which will prevent up to 4.8 gigatonnes (Gt) of future carbon dioxide (CO2) emissions per year [2]. Despite the increase in research and development of stand-alone wind turbines and wind energy generation from wind farms, the increase in commercially available wind turbines for wind generation within urban environments still remains a niche market.

In this framework, COST Action TU1304 WINERCOST (WINd Energy technology Reconsideration to enhance the COncept of Smart ciTies) addressed the objective of wind energy integration into urban and suburban built environment and identified methods towards the acceleration of related applications to overcome technological, societal and other barriers [3]. For the purposes of this research activity, the COST Action aimed at gathering the existing knowledge on onshore and offshore wind energy

technology and addressed the built environment wind energy technology. The aim was to provide the necessary tools and to contribute towards the strategy for Future Smart Cities. The integration of renewable sources of energy generation nearer to its consumers within the Built environment forms one of the main strategies for smart cities. Wind energy Technologies (BWT) and related structures and infrastructure are expected to form an integral part of the Smart Cities of the future. As past and current experience with wind energy shows, large WT moving structures very often receive significant opposition from the communities. This is most often relevant for new technologies and changes in society, and may relate to aesthetics, nuisance, processes or communication issues.
The aim of this paper is to present key issues concerning social, environmental and planning considerations of wind technology in the urban environment. The paper presents the outcome of the WINERCOST survey which was conducted during 2014-2015. The survey responses covered a wide geographic distribution across European Countries in particular and were intended to address the challenges of Urban Wind Technology. Furthermore, Focus Group discussions concerning Urban Wind Energy were analysed also in the context of current research in this field. The assessment led to the development of key principles for a strategy to enhance the Smart Cities Concept by effectively introducing Wind Technology Projects in the built environment.

2. URBAN WIND ENERGY

The climate and energy package of the European Union, consists of binding legislation which aims to ensure that the European Union meets its ambitious climate and energy targets for 2020 [1].These targets, known as the "20-20-20" targets, set three key objectives for 2020:

- A 20% reduction in EU greenhouse gas emissions from 1990 levels;
- Raising the share of EU energy consumption produced from renewable resources to 20%;
- A 20% improvement in the EU's energy efficiency.

The major contributors to locally produced renewable energy are principally photovoltaic systems, solar panels and combined heat power systems, whereas there is also a significant potential contribution from small and medium (15kW-100kW) wind turbines. In recent years, a significant growth in the sector of small and medium turbines has been noted with further expansion of this sector being expected in the coming years.

Khorsand et al [5] note that the transition towards low-carbon energy sources including wind energy, requires higher levels of public interaction. While the ultimate contribution of wind energy relies as much on technological advancements and policies as on societal considerations. The authors assessed the influence of region, community involvement, and several IEA-recommended practices on social acceptance of wind energy projects among residents from cities in four OECD and three non-OECD countries with a wide geographical coverage. The results indicate inter-urban variations among the generally high levels of acceptance reported, especially among residents of cities in developing countries with lower domestic CO_2 emissions. In addition the authors reported that the level of community involvement in a hypothetical wind energy project had a positive effect on acceptance, and respondents from cities in countries with the highest installed wind capacity reported the greatest sensitivity towards involvement. Acceptance to the IEA-recommended practices was predicted across all cities. However the authors reported that fair distribution of earnings and costs was the only significant individual predictor. These economic considerations, combined with increased community involvement, are reported to be very important to facilitate future development of wind energy [5].

Countries worldwide have set national targets for renewable energy production and many governments are committed to increasing production. However Teschner et al [6] report that obtaining permission to site installations is becoming increasingly difficult. Large tracts of land taken up for renewable energy production are becoming intensely contested and therefore countries seeking to meet their renewables targets are directing attention also towards tapping the potential in the urban environment through

smaller-scale facilities including small-scale wind turbines (SSWT). This however presents new challenges. Teschner et al [6] present a review on the land-regulation aspects of siting SSWT in countries that already have experience with such installations including the USA, UK and New Zealand. The authors further report on a comparative analysis of the land-related regulations and practices in Spain (Catalonia) and Israel. They analysed legal and policy documents and carried out field work through in-depth interviews with key-stakeholders in both jurisdictions. Different approaches of planning systems to new technologies were analysed. It was reported that despite their shared objective factors, the two jurisdictions have adopted an almost opposite approach to regulating SSWTs. They report that the incorporation of an unknown technology within the city requires a change of mind-set both among the officials and among the city residents. The authors suggest that a more effective regulatory framework can therefore include a combination of strategic thinking, an experimental approach and the capacity to learn from cross-national comparative experiences [6].

3. METHODOLOGY

3.1. Wind Energy Technology Reconsideration and Smart Cities.

The feasibility of installations of Small and Medium Wind energy Technologies (SMWT) in urban areas is significantly influenced by the acceptance of the local communities. A catalogue on social acceptance at the European level does not exist yet, although there have been some preliminary initiatives in international energy fora. This results from a different understanding and acceptance of SMWT. Nevertheless a thorough investigation of the social acceptance criteria is required and needs to be based on the existing knowledge about wind power in general, SMWT and the first examples of wind power in the built environment. This required research in different countries based on case studies. It is therefore crucial to discuss European energy policy and strategy for advancement of the BWT with consumers, municipalities, industry (turbine manufacturers) and grid operators. The investigation of optimized centralised or de-centralised grid-integration needs to be considered [8]. During Phase 1 of the WINERCOST Action, existing knowledge on on-shore, off-shore WT and other application of wind energy structures in particular BWT including Building-Integrated-Wind-Energy Technology applications, was assessed. During Phase 2 of the WINERCOST Action, the activities focused on the development of a strategy to enhance the Smart Cities Concept by effectively introducing WT projects in the built environment. The activities also addressed barriers for technological implementation, possible non-technical negative effects such as noise, production/installation costs, logistics, reliability, integrity, system robustness, aesthetic and European energy policy as well as societal acceptance issues. In this sense, the WINERCOST network of BWT-stakeholders looked into research needs and research and development actions for the future of BWT in urban environments [3].

3.2. Challenges in Wind Energy Technology in the Built Environment

The integration of renewable sources of energy generation nearer to its consumers within the Built environment forms one of the main strategies for smart cities. Built environment Wind energy Technologies (BWT) and related structures and infrastructure are expected to form an integral part of the Smart Cities of the future. Wind Technologies are expected to be integrated into urban spaces and closer to spaces were people. As past and current experience with wind energy shows, large WT moving structures very often receive significant opposition from the communities. This is most often relevant for new technologies and changes in society, and may relate to aesthetics, nuisance, processes or communication issues. Therefore, acceptance issues have to be considered when addressing new technologies including in particular BWT, both in the general planning as well as for integration in specific projects. The factors that need to be considered carefully include aspects related to policy, legislation, planning and environmental issues. Communication and processes also need to be respected while industry needs to address the challenges to design and produce socially acceptable products. WINERCOST Working Group 3 gathered information on the current state of public acceptance for wind turbines considering their increasing presence as near urban wind farms and integrated in building

structures in various European countries. Secondary information resources were reviewed such as published legislations and research comparing findings to surveys and interviews with stakeholders, interested parties and groups in society. Based on the findings of this assessment, some approaches were developed for future implementation. In the last phase, the main criteria for a strategy for stakeholder dialogue was proposed bringing together the authorities, industry and research entities to test the approaches and to prepare the ground for the BWT to become reality through implementation in Smart Cities. The aim was to provide an improved understanding of the challenges in the implementation of WT in the Built Environment with a focus on social, environmental and strategic planning aspects of Urban Wind Energy Technology. This was achieved through two phases of activity: Phase A focused on non-technical issues of WET including societal acceptance, European energy policy and municipalities-researchers-industries dialogue. Phase B focused in more detail on societal acceptance, European BWT policy and other non-technical BWT issues. The activity had to objective to contribute to the advancement of the Wind Energy harvesting in the urban habitat by enhancing the Future Smart City concept. The methodology was based on a survey with stakeholders and focus group discussions during the course of the project. Urban Wind Technology was also considered as a more effective reference to the consideration of wind energy technology in the Built Environment.

3.3. Survey Methodology

The survey developed within the project was intended for different stakeholders. The survey was disseminated online with various stakeholders in various regions and countries of Europe. It was based on 8 questions, intended to get a response concerning the challenges of Urban Wind technology (Table 1). It included also general questions concerning background information on the country or region of origin and activity, the area of activity and years of activity of the participant.

Table 2. WINERCOST Survey: Social, Environmental & Planning Considerations.

Ref.	Survey Question
1	In your opinion, what are the main benefits of Urban Wind Technology?
2	How has Urban Wind Technology been delivered and managed so far in your region?
3	What are the main planning and environmental considerations relating to Urban Wind Technology in your region?
4	What are the main concerns and issues regarding social acceptance of Urban Wind Technology in your region?
5	Are you aware of any policies, guidelines or legislation relating to Urban Wind Technology in your region? If yes, please provide references.
6	Are you aware of any financial incentives to support Urban Wind Technology in your region? If yes, please provide references.
7	Are there any notable successes or failures in Urban Wind Technology in your region? If yes, please provide references.
8	Do you think that the implementation and adoption of Urban Wind Technology needs to be improved in your region? If yes, please provide details.

4. RESULTS & DISCUSSION

The survey results were gathered from more than 150 participants with a wide geographical distribution and with a varied experience. The survey was a preliminary exercise intended as a first step to identify core issues and establish key areas for more detailed assessment with reference to social, environmental and planning considerations. The outcome paved the way for focus group discussions carried out in

different groups in different regions across Europe with reference to the WINERCOST participants and different stakeholders. The key areas are presented in Table 2.

Table 2. WINERCOST Key Areas.

Ref.	Key Areas
A	General Considerations for the Implementation of Wind Energy Technology in the Built Environment.
B	Social Acceptance and UWT
C	Environmental and Life Cycle Engineering Considerations and UWT.
D	Strategic Planning Considerations and UWT
E	Architecture and UWT
F	The Role of the Local Authority
G	Wind Resource and UWT
H	Developments in Engineering and UWT

4.1. General Considerations for the Implementation of UWT

The survey responses indicted a general trend in favour of large scale off shore wind farms rather than Urban wind energy. This can be attributed to bias in favour of larger development, clearer legislative frameworks and already established community consultation procedures and media coverage than for wind turbines in urban settings. Responses pointed towards the perception of in-sufficient market uptake of urban wind turbines, notable failures reported in the media, perceptions concerning noise, failure of mechanical parts and poor energy yield when compared to manufactures' expected yield. Reference was made to the perception that other renewables such as PV technology would have a shorter return on investment when compared to Urban wind turbines. Furthermore there was reference to a lack of a true understanding of site specific and contextual environmental analysis; although most countries have a wind energy resource map that is published online (www.rensmart.com), there was a general feedback that these maps were not accurate and presented annual average readings rather than urban context specific readings. Reference was made to the need to make the same considerations for wind farms when being placed in rural environments near rural settlements and how these affect the landscape and natural environment. In addition NIMBY related issues were noted to be of relevance and a barrier to the uptake of this technology.

4.2. Social Acceptance

The societal acceptance of urban wind generation is significantly affected by past experience, media influence and perceived environmental concerns. In addition concerns relating to noise and vibrations, flicker and other negative impacts were evident and a barrier to implementation of urban wind technology. Furthermore the perceptions concerning the impact of large on-shore and off-shore wind structures on the landscape were noted to have a significant influence on societal acceptance. Technological developments are recent and urban wind energy is not yet part of the urban environment with the consequence that the public is not used to urban wind energy.

4.3. Environmental and Life Cycle Engineering Considerations

Significant concerns reported refer to noise, vibration and flicker and the effect on wellbeing of inhabitants in urban areas. The perceptions regarding the relative impact and effectiveness of different renewable energy sources in the urban environment are noted. The relative environmental impact of the PV technologies and urban wind energy can be better assessed through a life cycle assessment and life cycle cost analysis including an assessment of the initial costs and actual output.

4.4. Strategic Planning Considerations

Urban environments present significant challenges in land use planning and redevelopment and regeneration. There are significant opportunities for integration of new technologies including urban wind energy particularly in the regeneration and site redevelopment. This is the case for example of industrial sites. The effective implementation also requires the contribution of different specialists through an inter-disciplinary approach and by bringing different stakeholders together.

4.5. Architectural considerations

Building augmented wind turbines are, for performance reasons, only integrated in towers and one-off iconic structures. These are still being seen by the public and design teams alike as a token gesture to sustainability and environmental values. It is indicated that the regeneration of industrial sites and renewal of degraded urban areas is more likely to result in societal acceptance and to benefit from integration of Urban wind technology. In this case urban wind technology can be effectively presented as part of the design solution in regeneration and not as an add-on. The levels of acceptance of wind turbines as a symbol of sustainable architecture have been questioned and have shown that the use of rotating blades for symbolism over buildings, such as the case of the Hertz 50 building in Berlin and Temple Bar in Dublin were more damaging to trust in the technology than under-performing UWT or those that were kept stationary due to technical reasons.

4.6. The Role of the Local Authority

The local authority have a critical role in the implementation of urban wind energy. Policy framework and criteria for assessment of the impacts of urban wind energy can be promoted by the local authorities in order to ensure effective consideration of these technologies through a comprehensive approach. Public perceptions and their engagement with the market dictates growth patterns and can underpin incentivisation schemes and government policy.

4.7. Wind Resource

There is a general concern as to the knowledge on the wind resource and the performance of wind energy technology in urban areas. Further research is necessary in order to ensure a better understanding on the performance of wind energy technology within the built environment.

4.8. Developments in Engineering

The developments in engineering provide effective solutions to past challenges in the integration of wind energy technology in the built environment. The perceptions of failure may reflect past experience of people. In this regard, demonstration projects can be effective in promoting successful integration of wind technology in the built environment.

5. CONCLUSIONS

Social, environmental and planning considerations offer significant challenges for wind energy technology. The challenges are even more significant for UWT in the Built Environment. Acceptance of Wind Technology, is a wide field with a large number of factors to be taken into account including economic, planning, ecological and health issues.

Abohela et al [9] and Grieser et al [10] argue that the main impediments regarding faster market diffusion are diverse, and predominantly encompass a lack of understanding of appropriate siting, technological standards and also a non-transparent regulatory framework with respect to planning and building laws as well as support schemes and a negative public perception of the feasibility and performance of the wind turbines. Grieser et al [10] research indicates that Small wind turbines in

urban areas today are only profitable under very favourable condition in suburban and rural siting and are coupled to a storage system. The evaluation of the profitability of SWT under urban conditions crucially depends on a reliable prediction of yields. Compared to the planning procedure of large-scale wind energy projects, the investment in SWT commonly takes place without a detailed ex-ante feasibility assessment accounting for the specific urban conditions. Abohela et al [9] highlight the impact of the built environment configuration and even the roof shape on the effect of accelerating wind and the performance of the wind turbine. Hamza [11] compares between intended design outcome and public perception of wind integrated generation in the built environment. lack of trust in the public trust for the uptake of wind turbines in urban areas is underpinned by the discrepancies between intentions and actual performance on site increase negative perceptions and the desire to uptake this technology. Khorsand et al [5] point out that social acceptance is sustained by a sense of fair distribution of earnings and benefits from the wind energy generation installations, there was no difference between urban or rural dwellers in various cities examined. The research indicates that government and institutional commitment to provide clear legislations are needed to support incentivization schemes but more crucially there is a need for clearer mechanisms of the benefits and community distribution to improve public perception.

Municipal and community-based energy and climate policies are key for the implementation of UWT in the built environment. The strategy should be based on existing programmes and on past experience, but Wind Technology should also link with the concept of "smart cities". The cities and urban environments offer challenges for redevelopment but also opportunities for integration of new technologies in the urban areas and the built environment, particularly for site redevelopment as in the upgrading of industrial sites. UWT and wind energy harvesting in the urban habitat promises to contribute towards the concept of the Future Smart City. The effective implementation of the integration of UWT in smart cities requires the contribution of different experts from specialised fields and necessitates an inter-disciplinary approach. This can be achieved through a collaborative approach by bringing different stakeholders together and through the assessment of case studies and the adaptation of existing experience.

Societal acceptance of urban wind generation is affected by past experience, media influence and perceived environmental concerns. Building augmented wind turbines are for performance reasons only integrated in towers and one off iconic structures, therefore still being seen by the public and design teams alike as a token gesture to sustainability and environmental values. Although research suggests that public perceptions and acceptance of micro wind generation maybe supported by value believes and excitement in participation in new forms of technology, there is no evidence found that this is the case on the ground. Public perceptions and their engagement with the market dictates growth patterns and can underpin incentivisation schemes and government policy. Similarly this also affects building regulations. The eventual development of Architectural styles and the integration of renewables are directly affected by all of the above factors. New technological developments that can demonstrate an improved expected performance from the Urban wind technology adapted for urban built environment applications is considered relevant. Regeneration of industrial sites and renewal of degraded urban areas are more likely to result in societal acceptance and benefit from integration of Urban wind technology, where Urban wind technology is presented as part of the design solution in regeneration.

REFERENCES

[1] GWEC (Global Wind Energy Council) Global Wind Report, Annual Market Update|2013 (2014) Available at: http://www.gwec.net/wp-content/uploads/2014/04/GWEC-Global-Wind-Report_9-April-2014.pdf
[2] IEA (International Energy Agency) Technology Roadmap, Wind Energy: 2013 Edition (2013) Available at: http://www.iea.org/publications/freepublications/publication/wind_2013_Roadmap.pdf
[3] WINERCOST, TU1304, Memorandum of Understanding, COST Association, Brussels, 22nd November 2013..

[4] European Commission, Climate Action, http://ec.europa.eu/clima/policies/package/index_en.htm, Accessed 12th March 2015.
[5] Khorsand I., Komos C., MacDonald E., Crawford C (2015) Wind energy in the city: An interurban comparison of social acceptance of wind energy projects, Volume 8, pp. 66–77 Energy Research & Social Science
[6] Na'ama Teschnera, Rachelle Alterman, (2017) Preparing the ground: Regulatory challenges in siting small-scale wind turbines in urban areas, Renewable and Sustainable Energy Reviews, Elsevier
[7] Baniotopoulos C., (2016), "Wind Energy Technology Reconsideration to Enhance the Sustainability Features of Smart Future Cities," in "Europe and the Mediterranean: Towards a Sustainable Built Environment", SBE16-Malta, 16-18.03.2016, 2016, pp. 465–466.
[8] Borg, R.P.; Huber S.; (2015), Social, Environmental and Planning Coniderations of Wind Energy Technology in the Built Environment. Work Group 3: Introduction, WINERCOST Action TU1304, International Conference, Coimbra Portugal.
[9] Abohela I, Hamza N. and Dudek S, (2013) Effect of roof shape, wind direction, building height and urban configuration on the energy yield and positioning of roof mounted wind turbines, Renewable Energy 2013, 50, 1106-1118.
[10] Griesera, B, Sunak Y., Madlenerb, R. (2015) Economics of small wind turbines in urban settings: An empirical investigation for Germany. Energy policy, Volume 78, June 2015, Pg. 334–35
[11] Hamza N (2016). The sustainable high rise building: renewables and public perceptions. In: The Sustainable High Rise Buildings in urban zones. Springer.
[12] Huber, Stefanie; (2015), An overview of non-technical issues of Wind Energy and Smart Cities, WINERCOST Action TU1304, International Conference, Coimbra Portugal.
[13] Bertasiene, Agne; Borg, Ruben Paul; Azzopardi, Brian; (2015), A review of Life Cycle Impact Analysis of Wind Turbines, WINERCOST Action TU1304, International Conference, Coimbra Portugal.
[14] Norton C., (2015), Planning and environmental considerations for the development of wind energy in the urban environment, WINERCOST Action TU1304, International Conference, Coimbra Portugal.
[15] Efstathiades C., (2015), The role of local authorities in the engagement of small wind turbines in urban areas, WINERCOST Action TU1304, International Conference, Coimbra Portugal..
[16] Hamza N., 2015, Urban wind energy: exposing sustainability symbolism or a hidden existence, WINERCOST Action TU1304, International Conference, Coimbra Portugal.
[17] Marčiukaitis M., Katinas V., Gecevičius G., (2015). Analysis of economic, environment, social factors and efficiency of wind turbines in Lithuania, WINERCOST Action TU1304, International Conference, Coimbra Portugal.

TECHNICAL SESSION 3.1

Smart Cities and Environmental Aspects

THE INTERNATIONAL CONFERENCE ON
WIND ENERGY HARVESTING 2018
21-23 March 2018
Catanzaro Lido, Italy

Paper TS3.1.1

IMPACT OF THE BREEZE ON OFFSHORE WIND DEVELOPMENT: PRELIMINARY STUDY IN A SOUTHERN ITALY COASTAL SITE

E. Avolio[1]*, C. R. Calidonna[1], T. Lo Feudo[1], D. Gullì[1] and A. M. Sempreviva[2]

[1]ISAC-CNR, Lamezia Terme, Italy
[2]DTU, Roskilde, Denmark
*Corresponding authors: E. Avolio,C.R. Calidonna e.avolio@isac.cnr.it, cr.calidonna@isac.cnr.it

ABSTRACT

We present an experimental and modelling study to evaluate the interaction between the synoptic and coastal breeze regimes on the daily development of the vertical wind profiles in a Southern Italy coastal site. The study aims to be useful for the optimization of the layout and location of wind farms, onshore and offshore, and for the refining of an existing modelling system for the short-term and long-term forecast of power production.
In this preliminary study, we considered an intensive experimental campaign in summer 2009, where several meteorological data, from surface measurements to vertical profiles, were taken into account; for this campaign, high-resolution atmospheric simulations were performed with the Weather Research and Forecasting (WRF) mesoscale meteorological model. Here, we present results of the evaluation of WRF output in simulating the offshore sea breeze extent and to characterize the potential impact of the breeze on the offshore power production.

1. INTRODUCTION

The increasing growth of wind turbines, and the placing of wind farms in coastal areas on either side of the coastline, demand a careful study of the characteristics of the coastal flow in both horizontal and vertical directions. In such areas, the flow dynamics is very complex due to the combination of atmospheric processes at different spatial scales. In wind energy, the extension of the sea breeze cell is of special interest, for placing a wind farm in either sides of the coastline in order to optimize the wind farm layout and to forecast the power production pattern. Numerical Weather Prediction (NWP) models, and specifically mesoscale models, are ideal to investigate spatial variation of the sea breeze circulation, even if their spatial resolution often does not allow to accurately locating the coastline and describe other physiographic features.

The breeze system in a coastal area is triggered by the sea-land differences in temperatures and heat capacities. For the sea breeze, during sunny days, the sun heats the soil, the air is warmed and lifts; the difference of thermal pressure between land and sea establishes, and it causes air at the surface to flow landward and air returning back seaward above.

To better understand the phenomenon, the sea breeze system can be described as a mesoscale circulation cell, resulting of differential heating between the sea and the land. A schematic description can be found in Miller [4], also depicted in figure 1, while the processes of heating gradient vertical expansion and upper and lower pressure gradient formations describe the upward theory of sea breeze development.

This study is focused on the Calabria region, about 50 km wide and elongated 300 km in the north-south direction in the Central Mediterranean (Figure 2). The experimental area (Lamezia Terme site) is flat and at the end of a west-east valley (the *Marcellinara gap*) that crosses the peninsula acting as a connecting channel between the Tyrrhenian and Ionian seas and surrounded by mountains.

This area is a natural laboratory to study land-sea interaction in complex terrain. The coastal flow is characterized by the interaction between synoptic winds and sea-breeze circulation. The synoptic wind comes usually from the west [1]. Furthermore, sea breeze and land breeze act in phase with upslope and downslope winds to determine stronger and more persistent breeze system.

Studies were conducted in the area using different approaches both by mesoscale models and short experimental campaign [1,2] to characterize the local circulations and their interaction with large scale flow over the area. From these studies, conducted at Lamezia Terme site [1,2], followed that: (i) sea breeze cells develops during the summer with wind profiles reflecting the daily cycle of stability over land; (ii) sea breeze always develop in sunny days all year around with different strength; (iii) with moderate westerly synoptic flow, the sea breeze acts modulating the background wind, while the weak nocturnal return flow is blocked because it is in the opposite direction of the main wind. In these cases, wind profiles are more toward neutrality.

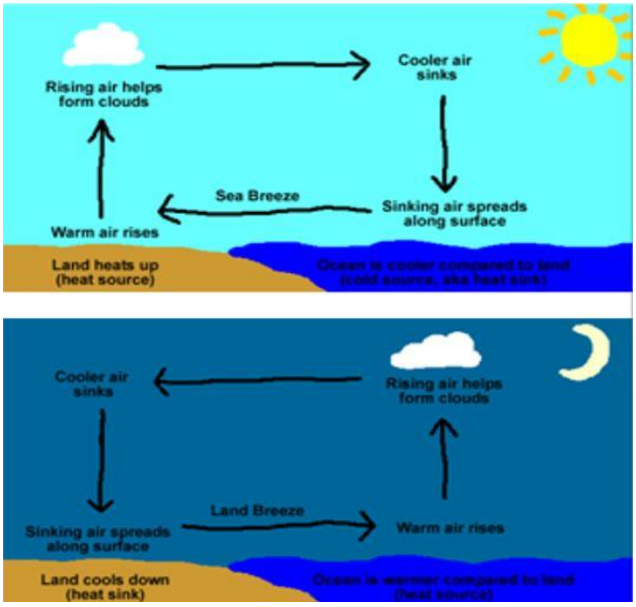

Figure 1. Schematic breeze descriptionMiller [4].

Analyzing the wind characteristics during the campaign, and considering other past studies in the same experimental area, the coastal flow was then classified in breeze (i), semi breeze (ii) and synoptic (iii).

In this context, mesoscale models can help in understanding the amplitude of this modulation and refine the characteristics of the flow regimes with respect to the large-scale situation.

Here, we present an experimental and modelling study of the interaction between the synoptic and coastal breeze regimes on the daily development of the vertical wind profiles in a Southern Italy coastal site.

We consider data from an intensive experimental campaign in summer 2009 (from 15 July to 6 August), where several meteorological observations are available; in this preliminary work, we select two specific case studies extracted from the campaign. High-resolution atmospheric simulations with the Weather Research and Forecasting (WRF) mesoscale meteorological model were performed, using different parameterization schemes.

2. EXPERIMENTAL AND MODELING SET-UP

The experimental site is located in Calabria Region, at about 500 m from the coastline at the west end of the only sea-to-sea valley around 30 km wide (the narrowest part of the region along west-east direction). The location and the instrumentation operative in the area are showed in figure 2.

For the 2009 experimental campaign, we used data from a surface station and a meteorological mast for surface variables, and vertical wind profiles measurements from wind Lidar (Windcube WLS7-0012, LEOSPHERE) and Sodar (DSDPA.90-24, METEK). Such wind profilers are based on different principles optics and sounding respectively, and they respond to aerosol and thermal activity giving complementary information in vertical backscatter signal depending on weather conditions.

For the modeling approach we used the WRF-ARW model (Skamarock et al., 2008) [3] version 3.4.1 to simulate the local scale flow during the measurement campaign. Three nested domains were adopted; 27, 9, 3 km grid spacing respectively, using the NCEP GFS analyses (0.5-degree horizontal resolution) as boundary conditions. Several PBL parameterizations schemes were tested in order to perform useful sensitivity tests.

Figure 2. Experimental site with Zephir wind-lidar and its location in Mediterranean Area.

The main purpose of the modeling effort was to characterize the simulated wind and the model performance at Lamezia Terme coastal site during different weather conditions, using observations of wind and other atmospheric parameters.

3. DISCUSSION

Considering the classification of the different wind regimes mentioned above, and taking into account the measurements collected during the campaign, the following case studies were preliminarily analysed: a synoptic flow case (18 July) and a sea breeze case (15 July).

Figure 3a shows a cross section from the WRF simulation on 15th July 2009 at 12 UTC. This case is a pure breeze and, as we can see, wind plotting shows the behaviour of the flow as shown in figure 1 and descripted above. In this situation the breeze mechanism is evident both on the Tyrrhenian and Ionian Sea, with different spatial extension.

Figure 3b shows a cross section from the WRF simulation on 18th July 2009 at 12 UTC. In this case the flow is synoptic; it's easy to note that the currents are more intense respect to the breeze case and constantly directed from the west at all levels, also preventing the returning current from the land at upper levels.

A further analysis is performed, regarding the study of the offshore wind spatial evolution, throughout the extraction of the time series for wind speed and direction, both at 10 and 100 m, in six point of a specific transect from the land to offshore the Tyrrhenian Sea (Figure 4a).

We report the results for only the 15 July breeze case. In Figure 4b we reported the daily evolution of the wind direction for the six points aforementioned, both at 10 and 100 m.

For the 10 m height, observed time series (black dots in the top panel) from the meteorological mast are also reported. There is a general agreement between the simulated wind (mainly those extracted at t1 and t2 point, nearest the experimental site) and the observation.

At 10 m the model is able to well reproduce the main directions of the wind and to simulate the breeze orientation after the 8 UTC. During daytime there is a general agreement between the simulated wind

in the different points and the observations. During nigh time, between 0 and 9 UTC, the directions are quite different depending on the position of the offshore point. As we move away from the coast out to sea, simulated directions become westward; the analysis of the change of directions with the distance from the coast provides useful information about the cell breeze extent. This is a potentially very practical tool to facilitate the optimization of the layout and the location of wind farms onshore and offshore.

At 100 m we can only evaluate simulated directions in the chosen sites on the map; in this case, the directions are in general agreement. Are an exception the locations nearest the coastline from the 0 to 5 UTC and the farthest from the 16 to 19 UTC. Comparing 10m and 100 m it seems that the modelled sea breeze develops first in the lower levels and extends to higher levels later in the early afternoon.

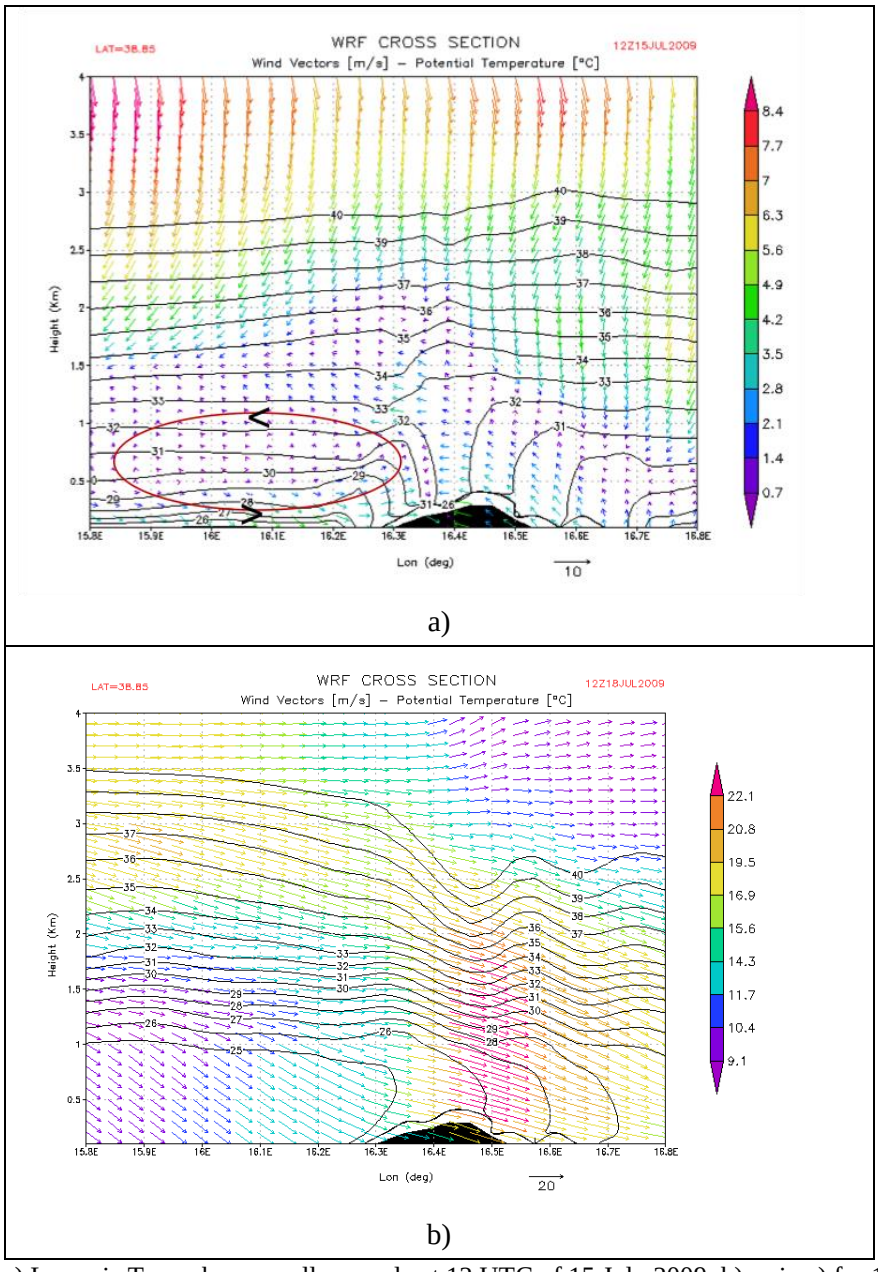

Figure 3. a) Lamezia Terme breeze cell example at 12 UTC of 15 July 2009; b) as in a) for 18 July 2009.

As we can see from the figure 3a, the vertical cell breeze extent is greater than 100m; so it's not surprising that wind behaviours at 10 and 100m are similar and in general agreement with the schematic breeze system descripted above (figure 1).

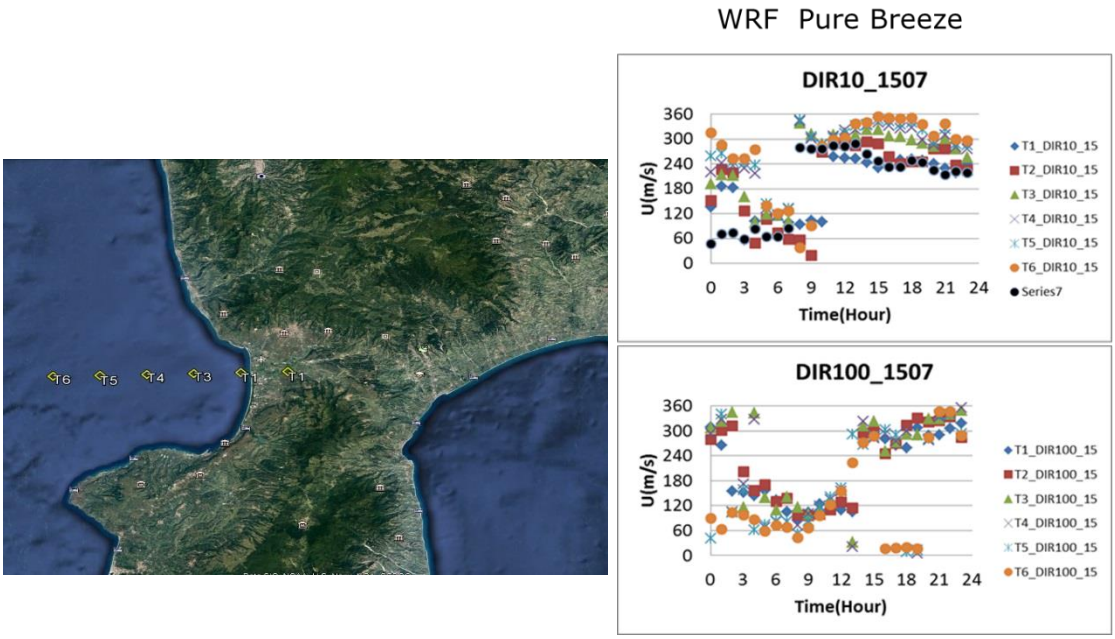

Figure 4. a) left. Offshore transect for the wind spatial evolution; b) right. Daily time series for wind direction on 15 July at 10m (top) and 100m(bottom). Figure 4b shows that the modelled sea breeze develops first in the lower levels and extends to higher levels later in the early afternoon. Looking at the spatial variation, it seems that the most offshore points T3-T6 feel also the influence of the further offshore flow pattern.

4. CONCLUSIVE REMARKS AND FUTURE WORK

In view of future wind farm installations in the Mediterranean coastal offshore area, attention must be paid to the sea-land breezes system extension that might play an important role in the patterns of power production. Only a well calibrated model chain system can help to understand these spatial patterns. Therefore, we undertook a preliminary investigation of the performance of a model system in simulating the evolution of a sea breeze flow considering two case studies representative of synoptic and sea-breeze flow episodes selected from an intensive measurement campaign.

Future work will focus on studying how the offshore extent of different sea breeze types is sensitive to the boundary layer parameterization scheme adopted by the mesoscale model, in order to perform useful sensitivity tests and to individuate an optimal configuration for the WRF model.

Our principal scope is to extend this study to a much longer period of time; in Lamezia Terme experimental site, since July 2013, are routinely measuring a met mast at 10m and a wind Lidar (10 - 300m) profiles and an operational modelling system (based on WRF) for the high resolution weather forecast at this costal site. This set-up gives us a comprehensive data-set to be analysed in order to deeply study the breeze phenomenon.

From these first analysis follow that the sea breeze tends to introduce coastal wind patterns that can influence the power production.

A well placed offshore wind farm can take advantage of coastal breeze systems; however, it is crucial to understand the impact of different local and mesoscale regimes and their interaction influence the power production patterns associated to different local and mesoscale patterns.

ACKNOWLEDGEMENTS

This work was partially supported by the project I-AMICA Infrastructure PON03_00363and it is within the collaboration between DTU and CNR-ISAC in the frame of European Energy Research Alliance, Joint Programme “Wind Energy”, EERA-JPWIND Sub Programme “Wind Conditions”. The 2009 intensive campaign was partially supported by FP6-MOBILITY - Human resources and Mobility in the specific programme for research, technological development and demonstration "Structuring the European Research Area" under the Sixth Framework Programme 2002-2006. MODOBS (Atmospheric modelling for wind energy, climate and environment applications: exploring added value from new observation technique) network Project ID 19369.

REFERENCES

[1] Federico, S., Pasqualoni, L., Sempreviva, A. M., De Leo, L., Avolio, E., Calidonna, C. R., & Bellecci, C. (2010). The seasonal characteristics of the breeze circulation at a coastal Mediterranean site in South Italy. Advances in Science and Research, 4, 47-56. DOI: 10.5194/asr-4-47-2010.

[2] Avolio, E., Federico, S., Miglietta, M.M., T. Lo Feudo, Calidonna, C.R., Sempreviva, A.M.: Sensitivity analysis of WRF model PBL schemes in simulating boundary-layer variables in southern Italy: An experimental campaign, Atmospheric Research, Volume 192, p.58-71 (2017).

[3] Skamarock, W.C., Klemp, J.B., Dudhia, J., Gil, D.A., Barker, D.M., Duda, M.G., Huang, X.- Y., Wang, W., Powers, J.G., 2008. Description of the Advanced Research WRF Version 3. National Center for Atmospheric Research. Boulder, Colorado, USA.

[4] Miller, S. T. K., B. D. Keim, R. W. Talbot, and H. Mao (2003), Sea breeze: Structure, forecasting, and impacts, Rev. Geophys., 41, 1011, doi:10.1029/2003RG000124, 3.

EVALUATION OF THE WIND RESOURCES IN WARSAW BASED ON THE ONSITE MEASUREMENTS AND NUMERICAL MODEL

Katarzyna Starosta , Andrzej Wyszogrodzki

Institute of Meteorology and Water Management National Research InstituteWarsaw, Poland
katarzyna.starosta@imgw.pl;andrzej.wyszogrodzki@imgw.pl
phone:+48 22 56 94 132; phone +48 22 56 94 131

ABSTRACT

The aim of this study is to provide an analysis of the wind power conditions in the urban space. The study uses 2016 year observational data from five meteorological stations located in a diverse area of Warsaw. Observational data were used to evaluate numerical forecasts from the COSMO numerical weather prediction model run at a resolution of 2.8 km. Wind speeds and directions were calculated as well as frequency classes for different time intervals: months, years and selected hours. Research will be continued with the new parameterization of urban space introduced in the model.

Key words : meteorology, climatology, wind power, smart city, wind speed and direction, numerical weather forecasts, weather forecast verification, post-processing.

1. INTRODUCTION

The population of large urban areas is growing rapidly. By 2050 it is predicted that two-third of global population will be the city inhabitants. As the cities constantly grow the high-end technology is being utilized to manage urban development, which leads to the concept of Smart Cities - friendly and intelligent infrastructure for their citizens [1]. One of the key factors of this concept is the promotion of green energy from renewable sources. In recent years, there is observed significant development of new wind turbine and photovoltaic installations (up to 20% of total power production by 2020 according to European Union Directive), especially in the urban environment. Municipal office in Warsaw provides support for the development of new power micro-installations in urban neighbourhoods until 2020 [2]. Illuminated road signs and information boards, park lighting, as well as small locally quiet turbines with a vertical axis of rotation on the roofs and walls of the building combined with photovoltaic installations already appear in the city space of Warsaw. Currently, the first housing estate in Warsaw is being built (Jasminowy Mokotów, Fig 1), with the power provided exclusively by the wind energy. There, at the stage of construction by Skanska company it is used only green energy from the wind, which reduces negative impact on the environment already at the stage of investment implementation.

Figure 1. Wind energy from innogy.pl has provided power to the construction site of a new housing developer Skanska - Jaśminowy Mokotów in Warsaw.

Another important problem for cities is the smog and air pollution. A high quality wind conditions form weather forecasting model may be necessary to calculate either the optimal wind conditions for the energy harvesting or ventilation index for the different city areas. Thus, in this work we provide assessment of the use of COSMO numerical weather prediction (NWP) model for wind speed and wind direction forecasting in the urban space. The visual representation of results is prepared with the help of WRPLOT software [3].

2. METHODOLOGY

- **Numerical Weather Prediction COSMO model at IMWM-NRI**

The COSMO model used in this study run at IMGW-NRI operationally four times per day using two nested domains at horizontal resolutions of 7 km and 2.8 km (Fig 2).

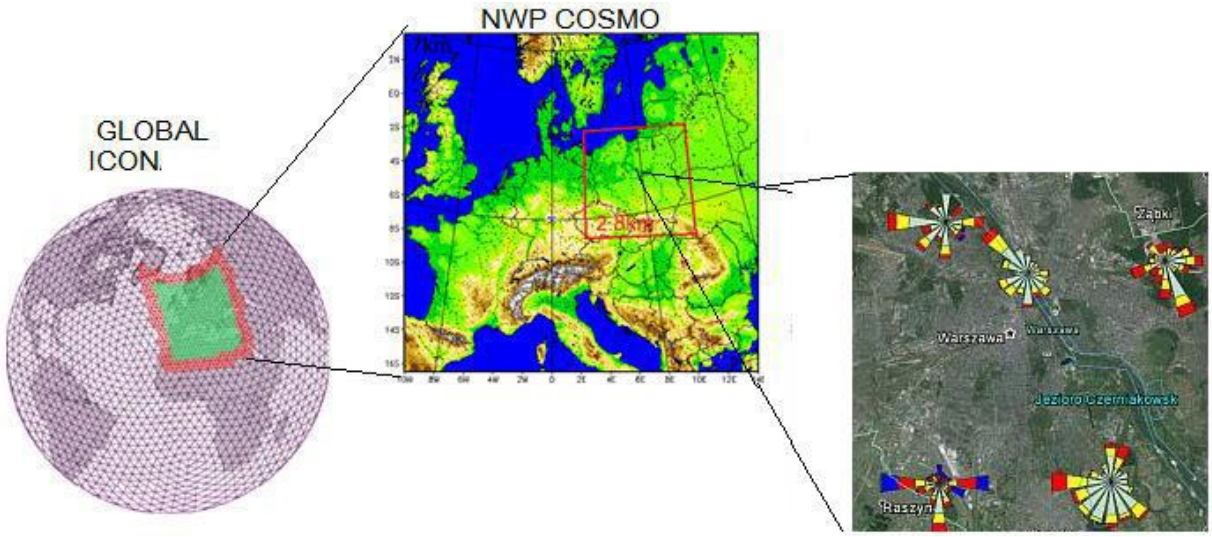

Figure 2. COSMO model configuration at IMGW-PIB (center). Locations of the observational stations within city of Warsaw - data from March 2015 (right).

COSMO model runs in a deterministic mode using initial (IC) and boundary (BC) conditions from ICON global model. Implemented in the COSMO observational data assimilation (DA) system is based on the nudging technique to improve forecast quality. DA allows for ingesting weather data measurements - as these carried out at SYNOP stations acquired from the WMO/GTS network. The model is starting at 00, 06, 12, 18 UTC and produces 78 hour and 36 hour forecasts respectively at 7 and 2.8km resolutions. See Table 1 for more details of the operational setup.

Table 1.Operational setups of the COSMO-PL models

Horizontal Grid Spacing [km]	7	2.8
Domain Size [grid points]	415 x 445	380 x 405
Forecast Range [h]	78	12
Initial Time of Model Runs [UTC]	00 06 12 18	1h frequency
Model Version Run	5.01	
Model providing LBC data	ICON	COSMO PL 7
LBC update interval [h]	3h	1h
Data Assimilation Scheme	Nudging	

For further applications a new version of COSMO model is currently being adapted at IMGW-NRI, which has implemented urban canopy parameterization (UCP) based on the TERRA_URB (Wouters) version of the surface layer parameterization. The UCP utilize modified roughness length accounting for the structure and type of buildings, roads, parks and rivers within the city area. These parameters are affecting meteorological conditions as winds which are the single most important source of free kinetic energy and a major factor determining the urban air quality.

- **Observational network within the city of Warsaw**

In the current studies, the results of numerical model COSMO at 2.8 resolution is verified with the data from urban meteorological stations. For this purpose we utilise data from two WMO network stations located in Warsaw at Okęcie and Bielany and three additional automatic stations from KLIMAT project (Fig 3.): ZOO, ECK, Wilanów.

- Synoptic station Warszawa Okęcie (N52º09'46",E20º57'40")
- The climatological station Warszawa Bielany (N 52º16'53",E 20º57'48")
- Zoological Garden ZOO Praga North (N52º15'27",E21º01'31")
- Palace Museum – Wilanów (N52º09"47",E21º15'10")
- Heat and power plant ECK – Kawęczyn (N52º15'48",E21º07'41")

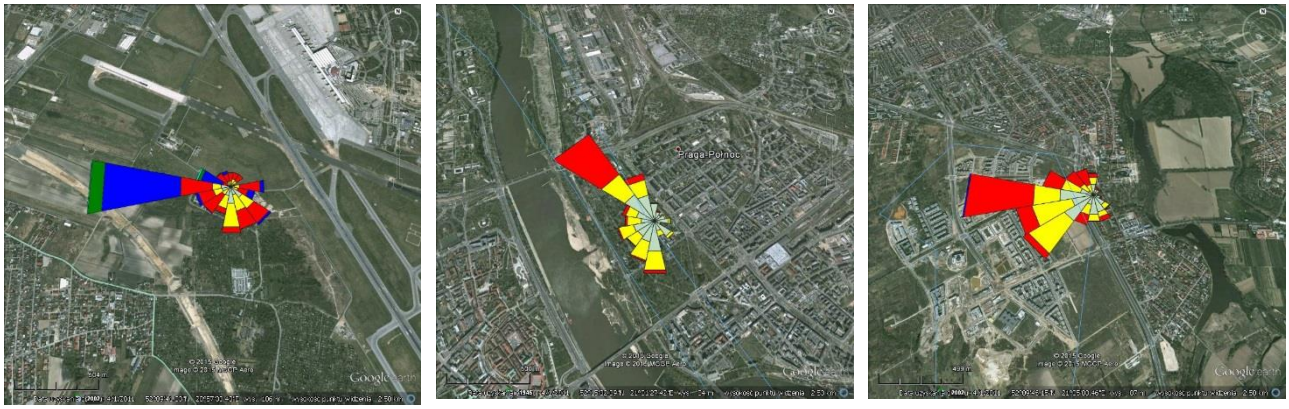

Figure 3. Location of stations and wind roses in January 2015 (left Okęcie, middle ZOO, right Wilanów)

The stations are located in various areas of Warsaw, and were chosen to account for an impact of the city structure on the daily course of wind speed and wind direction. The open-air stations are the synoptic station Okęcie, located on the territory of the international airport in the south-western part of the city, and the ECK station located in the Kawęczyn, heat and power plant, in the north-eastern part of the city. The Bielany station is located within the Institute of Meteorology and Water Management in the northern part of the city, in the open space, between buildings and green areas. The Zoo station is located in the zoological garden not far from the Vistula River. Wilanów station is located in a park near the Wilanów palace and is surrounded by trees.

3. POTENTAIL FOR THE WIND HARVESTING IN WARSAW

Poland has a transitional climate between the maritime climate (Atlantic) from the west and continental from the east of the country [4]. Accordingly, the weather conditions in the individual years are highly variable. Warsaw which has 1.8 million inhabitants is located in the central part of Poland on the Mazovian Lowland on the Vistula river. This is a favorable wind energy zone, with the wind energy potential of 750-100 kWh / m2 / year. One of the crucial factors is the efficiency of the new generation of wind power installations as the vertical turbines, whose design allows to achieve high efficiency without the need for construction of tall masts. The vertical turbines can operate even in low wind speeds of 0.6-0.8 m/s, exceeding the power output from the traditional turbines. The

power of a single turbine varies from 2 to 50 kW, which can produce up to 3.6 times more electricity than a photovoltaic and nearly 50% more than traditional windmills.

In order to support the micro-wind installations and housing estate with renewable energy planned in Warsaw suburban zones, the detailed analyzes of observational and COSMO wind data (24-hour forecasts) were performed for the whole year 2016, accounting for the annual, seasonal, monthly and hourly wind variability [5].

- **Model-observation data verification in different periods of time**

By analysing the annual course of wind speed at the stations location (Figutre 4), we see parallel courses for all stations with high speeds in the autumn and winter season and the lowest speeds in the summer season of 2016. The highest speeds, taking into account all stations, were observed in December and the lowest in September and these two months were selected for a more detailed analysis. However, the speed differences between the observations at the stations are considerable. The highest speeds were observed at the Okęcie station, which results from the low urban development around the airport, as well as the fact that winds in the western direction have an advantage over the whole year. We also observe the lowest values of wind speed at Wilanów and Zoo stations.

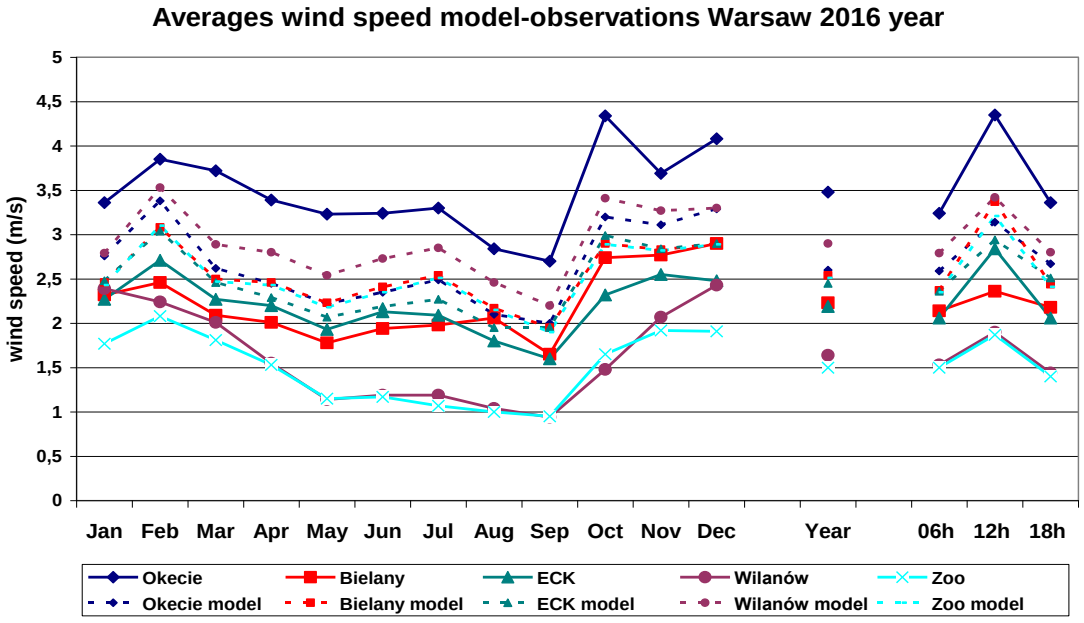

Figure 4. Monthly wind speed form observations and model, Warsaw 2016

Comparing the observational data with the COSMO model forecasts, we can see that for the tested set of locations differences between model predictions are in general smaller than between observations. Only for the Okęcie station, the forecasted wind speeds are lower than those observed, for other stations they are higher than observations. The best forecast results are for the ECK station where the differences between the forecast and the observation are smallest and the worst for the Wilanów station, where the observed values are much lower than forecasted. Moreover, we observe much higher wind speeds during the day (12 o'clock) than during the night (06 and 18 o'clock).

The Figure 5 show the resultant vector, i.e. a sum of all wind vectors for a given station. In the forecasted data, there is no clear difference between the average wind directions for individual stations. However, in the observational data, we can see the influence of the station's location on the change in the mean wind direction. The two stations of Zoo and Bielany located in the Vistula valley

clearly stand out from the others. For the Zoo station it is a deviation of the wind direction to the north-west, while for the station Bielany to the south-east.

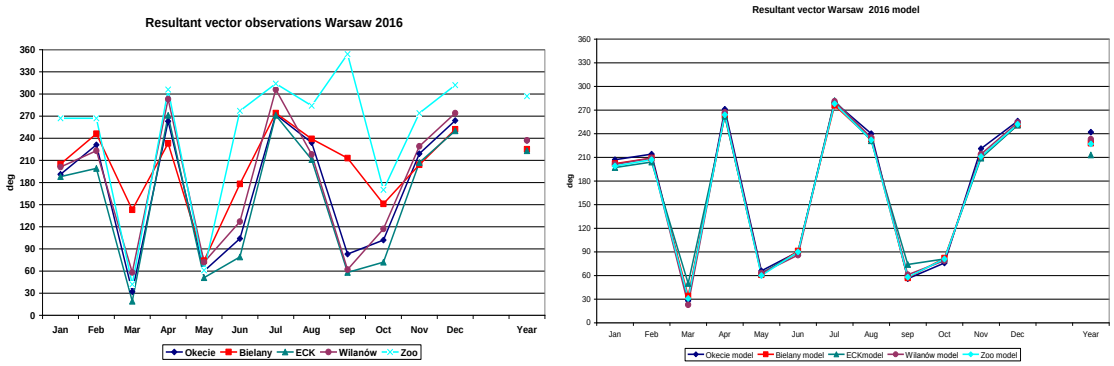

Figure 5. Resultant vector of wind within the city of Warsaw 2016 (left observations, right model)

- **Winds statistics for 2016 year.**

The Figure 6 presents the seasonal variability of the calm winds based on the station observations. The greatest number of calm winds in the observational data occurs from May to October. The most cases with calm winds is observed at the Wilanów station with an annual average of over 4% and a maximum of 10% in September. The impact on this situation has the position of the station in the park and its surrounding by the tall trees.

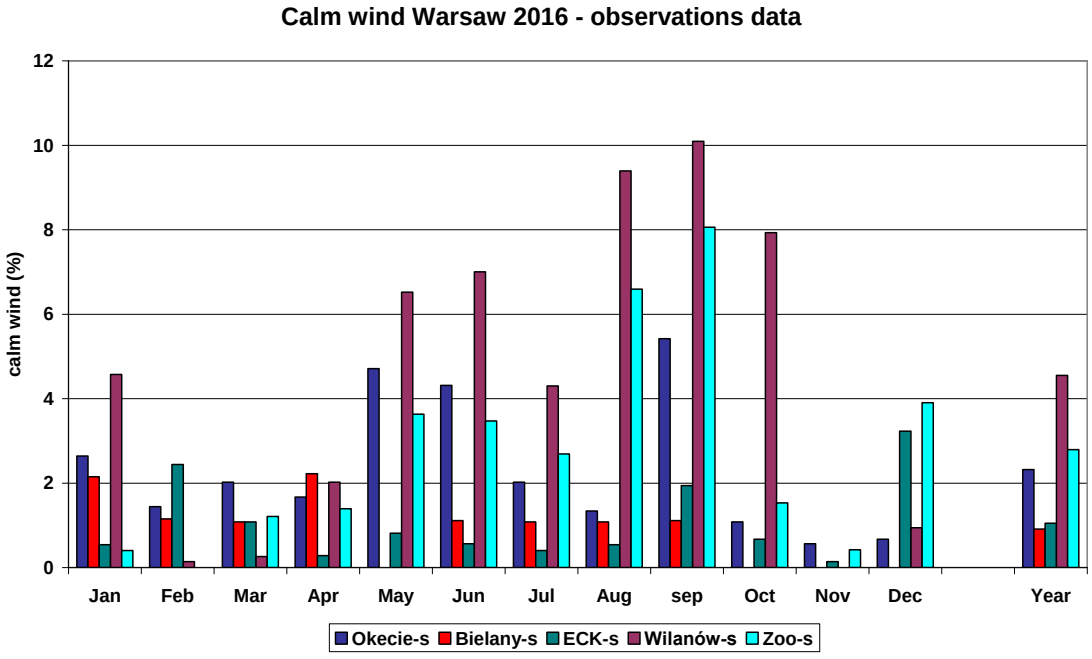

Figure 6. Calm winds in the city of Warsaw 2016 – observation data

A lot of calm winds is also observed at the Zoo station and Okecie - more than 2% per year. We observe the least calm wind cases at the Bielany and ECK stations. In the model generated data the number of calm wind is practically non-existent, it is lower than 0.5%.

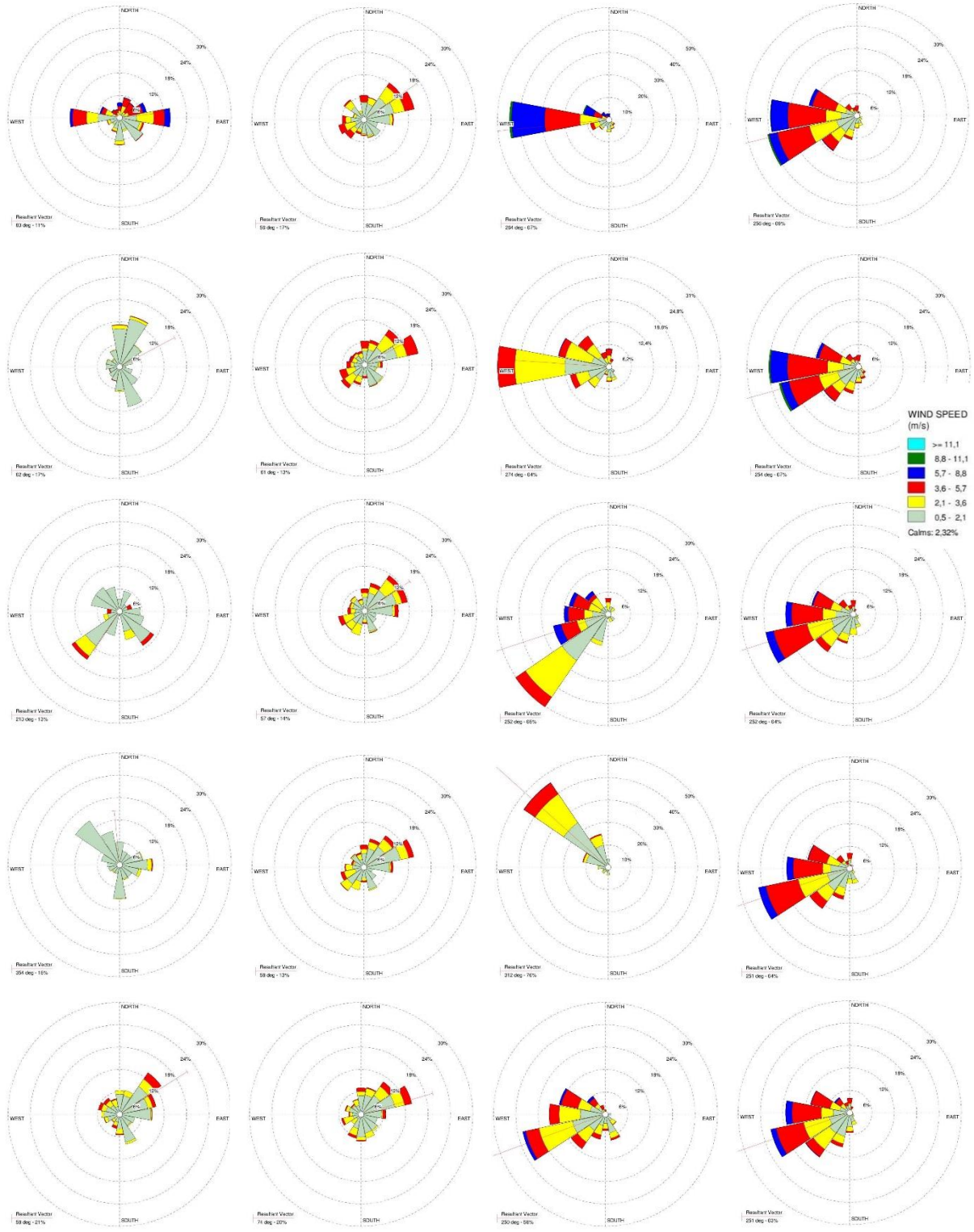

Figure 7. Wind roses from model and observations during 2016. From the top : Okęcie , Wilanów, Bielany, Zoo, ECK From left: September observation, September model, December Observation , December model.

In the Figure 7 we are presenting model-observation wind speeds and directions at station locations for two selected months in 2016 (September and December) in the form of wind roses. We observe different wind speeds and directions observed at all stations with weakest winds during September and

strongest in December. On the other hand, the forecast data from the COSMO model for all stations have a similar course, so they do not always take into account the individual conditions of the station's location. In September, with weak winds, the differences in directions and speeds observed at stations are higher than in December, the month with the strongest winds. There is a clear change of direction to the northwest at the Zoo station which is related to the proximity of the Vistula River. At Bielany station also the wind directions are different from the forecasted ones.

The compatibility of the forecast with the observations in strong winds in December is much better. The directions predicted in the model are more dispersed than observed. The forecasted wind speeds, outside the Okęcie station, are higher than those observed. A clear change in the observed wind direction to the north-west is at the Zoo station. When comparing the stations, the smallest error in the forecast occurs for both months at the ECK station.

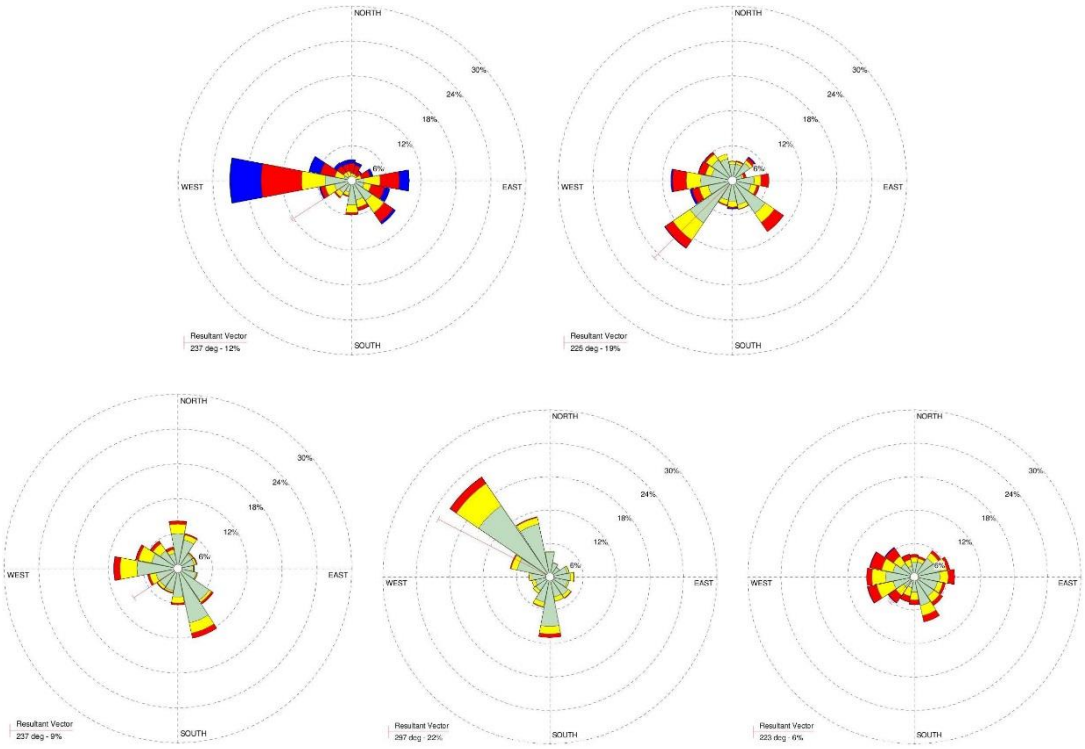

Figure 8. Wind roses observations, year 2016; upper panels from left: Okęcie, Bielany, lower panels from left: Wilanów, , Zoo, ECK

At Figure 8 we are observing very diverse annual directions and wind speeds at stations. Located on the south-west of Warsaw, the Okęcie airport station has prevailing winds from the west. At the Zoo station, the north-westerly direction of the wind is associated with the course of the Vistula River. The ECK station in the north-eastern part of the city is characterized by quite dispersed winds from various directions. At Wilanów and Bielany stations, the wind directions are also related to the local conditions.

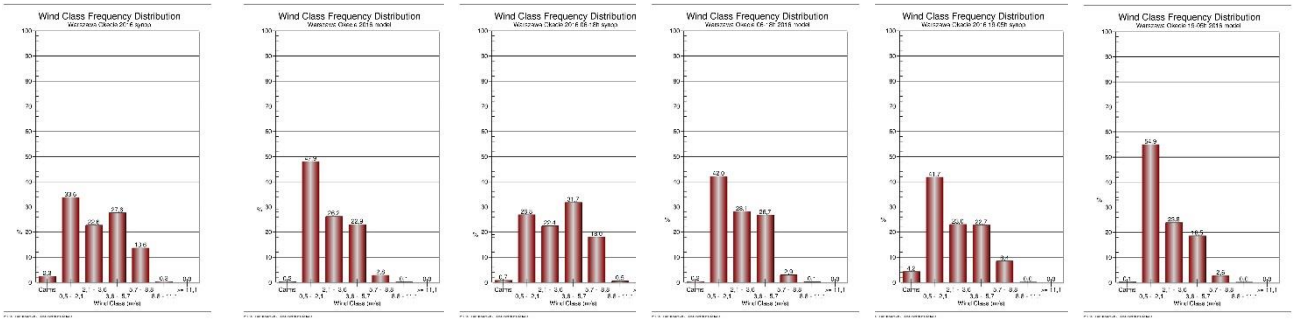

Figure 9. Wind class frequency distribution Okęcie 2016 from left : observation, model, 06-18h observation, 06-18h model, 19-05h observation, 19-05h model

By analyzing the frequency classes for the wind speed at Okęcie (Figure 9), we see a favorable wind distribution for the possibilities of wind energy. Stronger winds with an average value above 3.6 m/s are 42% per year, and winds from 2.1 to 3.6 m/s exceed 22%. When analyzing the distribution during the day, we observe a decrease in weak wind speeds to 27% (0.5-2.1 m / s). However, we see an increase (up to 50%) in classes with higher wind speeds (over 3.6 m/s). At night the wind speed is lower, winds from 0.5-2.1 m/s are the highest class and amount to 42%, but still winds over 2.1 m/s account for 50%. The model forecasted data from the Okęcie indicate a greater number of weak winds than is apparent from the data observed at station.

4. CONCLUSIONS

Meteorological data from station observations together with the results of numerical weather forecasts are the basis for assessing amount of wind energy at a given area. Our results show that in Warsaw there are areas with a good potential for wind installations. In the outskirt districts of Warsaw, to limit coal combustion, it is planned to use wind energy in the single-family houses. Currently, small wind turbines with photovoltaic panels are also used in street lamps in parks as well as for lighting road signs. Further extension of this study, and the use of COSMO model version with UCP parameterization [6] will enable us to obtain more accurate forecasts in any grid points within the city. The verification and post-processing of the model data give us the opportunity to improve our research on meteorological conditions for renewable energy in the urban environment.

ACKNOWLEDGEMENTS

The authors would like to thank for making available data from the project IMGW-PIB “KLIMAT”.

REFERENCES

[1] Oke. T.R. Initial guidance to obtain representative meteorological observation at urban sites. WMO/TD-No.1250 2006

[2] Action Plan for renewable energy sources for Warsaw .Warsaw City Office - August 13, 2014 r. (in polish)

[3] Lakes environmental software WRPLOT View http://www.weblakes.com/products/wrplot/

[4] Starosta K., and Wyszogrodzki A.: Assessment of model generated wind energy potential in Poland. COSMO News Letter No. 16, 2016

[5] Starosta K., and Wyszogrodzki A.: Urban wind analysis in Warsaw. COSMO News Letter No. 17, 2017

[6] Wouters, H., M. Demuzere, K. De Ridder, and N. P. van Lipzig, 2015: The impact of impervious water-storage parametrization on urban climate modelling. Urban Climate, 11, 24–50

THE INTERNATIONAL CONFERENCE ON
WIND ENERGY HARVESTING 2018
21-23 March 2018
Catanzaro Lido, Italy

Paper TS3.1.3.

LIFE CYCLE ANALYSIS OF ONSHORE WIND TURBINE TOWERS

Michaela Gkantou[1*] and Charalampos Baniotopoulos[1]

[1]School of Engineering, Civil Engineering Department, The University of Birmingham,
Edgbaston, B15 2TT, Birmingham, United Kingdom
**Corresponding author: Michaela Gkantou, M.Gkantou@bham.ac.uk*

ABSTRACT

In order to quantify the environmental impacts of wind energy and to assess to what extent this source of energy is green, life cycle analysis (LCA) is performed. Studies examining the life cycle performance of onshore wind turbine towers are thoroughly discussed in this paper. Initially, the definition of the LCA and the steps applied for its execution are presented. A typical system boundary is given and the main conclusions from LCA studies on onshore wind turbine towers are summarised, showing that the manufacturing stage causes the largest environmental impact, while recycling acts in a favourable way. A gap in literature on the life cycle analysis of tall onshore wind turbine towers is identified and in the final part the gathered knowledge is utilised to examine the LCA of a 185 m hybrid wind turbine tower.

1. INTRODUCTION

Wind farms have considerably contributed to an increase in the renewable energy production across the globe. With annual installations of +10 GW since 2009 in Europe, 2017 was possibly a record year (14 GW) [1]. By 2020 it is expected that the wind energy becomes Europe's largest renewable source, with a total capacity of 200 GW, surpassing hydro-power. Until that time, member states try to come up with their energy commitments, while wind energy makes significant contributions. It is remarkable that according to Wind Europe's Central Scenario, 323 GW of cumulative wind energy capacity, equivalent to 30% of the EU's power demand, would be installed in the EU by 2030 [1].

As a matter of fact, wind energy uses the kinetic energy of the wind and produces a clean form of energy, free of contamination and carbon emissions, with significantly lower impact on the resources and the environment compared to traditional fossil technologies. It has been reported that in 2016 with 341,320 wind turbines spinning around the world, over 637 million tonnes of CO2 emissions were avoided globally [2]. However, in order to really quantify to what extent this source of energy is clean and to subsequently find ways in making wind power an even cleaner source of energy, life cycle analysis (LCA) should be performed. Studies focusing on the life cycle performance of onshore wind turbines towers [3-12] are discussed in this paper. The gathered knowledge is subsequently used for the execution of LCA of a 185 m hybrid [13] wind turbine tower.

2. LIFE CYCLE ANALYSIS – AN OVERVIEW

Life cycle analysis is a comprehensive methodology for the quantification of potential environmental impacts of a product or a system over its life cycle from raw material extraction to final disposal at the end of their service life. Commonly referred as cradle-to-grave analysis, LCA is a holistic approach carried out by registering all environmental impacts associated with the material acquisition, processing, manufacturing, use and disposal or recycling in the end-of-life stage. This approach

provides a conceptual framework in order to make sustainable choices and is therefore used by companies for product development and for more sustainable supply chain management. To achieve this, the following four stages are implemented:

- *Definition of goal and scope of analysis:* The system boundaries, methodologies, requirements, assumptions and limitations are defined.
- *Inventory Analysis*: The recourses of all inputs and outputs of the system are collected.
- *Impact assessment:* Different parameters like global warming, acidification, effects on human health are used to evaluate the potential environmental impacts associated with those inputs and outputs.
- *Interpretation:* The significance of the potential environmental impact of the system is assessed.

Life cycle analysis is a time-consuming scientific process that requires rigorous knowledge of the influencing factors and the execution of extensive calculations. To make its realisation easier, a series of LCA software, tools and databases have been developed. Additionally, norms have been framed (e.g. [14, 15]), ensuring that life cycle assessments are carried out in accordance with standardized principles. In Europe, guidelines to assess the sustainability of construction works are given in [16], [17] and [18] for framework, building and product level respectively.

3. LITERATURE ON LCA OF ONSHORE WIND TURBINE TOWERS

A series of studies focusing on the LCA of onshore wind turbine towers around the globe are summarised in Table 1, where the type of tower, the hub height, the wind turbine size, the considered location and the applied softwares are included. As can be seen, past studies have focused on tubular steel or concrete towers with a hub height up to 124 m, leaving the environmental impacts of taller towers unexplored. In addition to this, past studies have dealt with common forms of towers, while research on hybrid towers is missing. Note that hybrid towers efficiently combine steel tubular with lattice parts, thus allowing to fulfil the required safety and durability verifications, whilst keeping the solution potentially economically and environmentally sustainable.

In most cases, a lifetime of 20 years has been assumed and the analyses have been conducted in accordance with [14, 15]. A typical system boundary is shown in Figure 1. This first stage which includes the scope definition and the limitations varies significantly from one LCA to another and should be carefully considered. A sensitivity analysis can be performed in order to estimate the effects on the outcome of a study of the chosen methods and data [11].

The results of the life cycle analysis of the wind turbine towers are commonly assessed by calculating various environmental indicators (e.g. Global Warming Potential (GWP), Acidification Potential (AP), Eutrophication Potential (EP)) and the energy payback time (i.e. how long the wind energy system has to operate in order to generate the amount of energy that was required during its entire life; the energy payback time is calculated as the ratio of the of total primary energy requirements of the system throughout its life cycle to the annual electricity generated by a system). The LCA results are usually presented in percentage charts and grouped either per structural component (e.g. foundation, tower, nacelle, rotor) or per life stage (e.g. manufacture, transport, erection, operation/maintenance, dismantling).

For the considered studies, the energy payback indexes were found lower than 1 year [3, 12], and in some cases only 1.3 months [4]. The largest environmental impacts were unambiguously caused due to the manufacturing stage of wind turbines [3, 9], followed by the transport phase [5, 9]. The smallest contribution is related with the operation phase in studies [5] and [8]. The component which affects most importantly the environment is the foundation [7]. The size of the wind turbines appears to be an insignificant factor in optimising their life cycle energy performance and the embodied energy component of wind turbines over their service life [6]. With regard to the towers, the use of concrete could be favorable if the cement and aggregates are delivered from the immediate vicinity [9]. For steel towers, even though a large amount of steel is required for production, its final impact is reduced

because steel can be recycled [8] and the steel towers can be reused (partially or completely) [10]. Apart from the blades, which are made of composite materials and the foundation which is made of concrete, 80% of a wind turbine system can be recycled nowadays [8]. A future research focus point could deal with recycling technologies for composite materials and existing end-of-life treatment technologies, where lack of data has been reported [12].

Table 1. Literature on LCA of onshore wind turbine towers.

Publication	Year	Type of tower	Hub Height (m)	Wind Turbine Size (MW)	Location	Software
[3]	2008	steel tube	55	0.66	Italy	-
[4]	2008	steel tube	45, 46, 60	0.66, 0.60, 1.75	Taiwan	-
[5]	2009	concrete	124	4.50, 0.25	France	SimaPro (http://simapro.com/)
[6]	2009	steel tube	60, 80	0.85, 3.0	Australia	-
[7]	2009	steel tube	70	2.0	-	SimaPro (http://simapro.com/)
[8]	2012	steel tube	105, 65	1.8, 2.0	Spain	Gemis (http://iinas.org/gemis.html)
[9]	2013	concrete, steel tube	80	1.423	Germany Denmark China	-
[10]	2014	concrete, steel, composite	80, 100, 150	2.0, 3.6, 5.0	Brazil	Gabi (http://www.gabi-software.com/international/index/)
[11]	2015	steel tube	80	2.0	-	Gabi 7 dfx (http://www.gabi-software.com/international/software/gabi-dfx/)
[12]	2016	steel tube	92.5	2.3, 3.2	North America	SimaPro (http://simapro.com/)

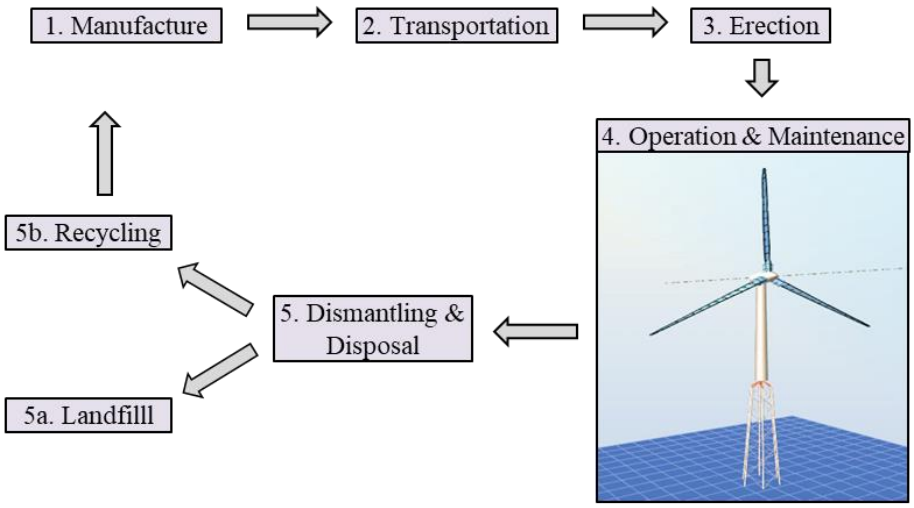

Figure 5. Typical system boundary for life cycle analysis in onshore wind turbine towers (adapted from [8]).

4. LIFE CYCLE ASSESSMENT OF A HYBRID WIND TURBINE TOWER

Having collated useful information on the LCA of onshore wind turbine towers, the life cycle performance of a 185 m tall hybrid wind turbine tower has been examined. A preliminary study is presented hereafter, while more in depth research is currently underway.

Following the boundaries shown in Figure 1, all life stages from production of the materials to the end-of-life have been considered. The connection to the grid that is out of scope of the present study has been left aside. The lifetime of the turbines was set to be 20 years. At the most crucial stage of collecting the required data, the maximum possible level of detail that would not sacrifice the accuracy of the obtained results has been pursued. The Life Cycle Inventory (LCI) focused on gathering information on the primary components of a wind turbine tower.

The hybrid tower examined consists of a 120 m lattice structure (bottom part) and a 65 m tubular tower (upper part). The lattice part is supported at a 6-legged braced structure comprising S355 cold-formed polygonal sections. The tubular part has a diameter ranging from 4500 mm at the base to 3500 mm at the top with 27 mm plate thickness. In line with [13], an NREL 5 MW wind turbine with a total mass of 340 ton has been considered. The rotor consists of the blade hub which is made from cast iron and the nose cone and the three blades which are made from fiberglass and epoxy. The nacelle, the most complex component which is responsible for converting the kinetic energy into electricity, is composed of a group of materials including fiberglass, cast iron, copper, aluminium and steel. The largest share in the mass distribution of the whole structure belongs to the reinforced concrete foundation.

Further to the collection of the material quantities, a series of assumptions and definitions were determined for each life cycle stage. In the *manufacture* stage, the production of the raw materials along with the energy embodied for their manufacture have been considered. For the *transportation* stage, the components were assumed to be prefabricated on the factory with length up to 30 m, wherever possible. In addition to the energy generation during transport, the impact of the emissions due to the extraction and production of fuel has also been considered. Site preparation, mobile crane and strand usage have been included in the *erection* stage. For the *operation & maintenance* stage, energy use equal to 1% of the annual generation has been considered. The latter depends on the quality of the site with respect to the wind resource. In accordance with [7], 2000 operational hours leading to a total annual production of 10 GWh have been assumed. In the *end-of-life stage*, the final decommissioning that might potentially have high impact on the environment has also been taken into account. Recycling has been considered in a closed loop approach, meaning that the recycled products have equivalent material properties to the virgin ones. Steel was assumed to be 85% recyclable, with an average material loss rate of 15%. Finally, the paint used in the rotor, nacelle and tower, the surface treatment in the tower as well as grid losses were excluded from the analysis.

To facilitate LCA execution, GEMIS (Global Emission Model for Integrated Systems) software [19], a freely available database and material flow analysis tool has been used. The software finds applications in different fields including construction, energy, transport and food. It is noteworthy that Gemis has been successfully applied to examine the environmental impacts of wind turbine towers [8]. A pool of 1150 products (i.e. inputs and outputs of processes), 9766 processes (i.e. activities for energy or material conversion) and 131 scenarios (i.e. selection of processes) covering data from more than 50 countries are currently available, whereas additional data can be imported by the user. Upon LCA performance, the air emissions, the greenhouse gases, the water effluents, the solid wastes and the resources use can be obtained in tabulated and graphical forms. For the present study, the following data needed to be imported into the software: i) the materials and their masses in tonnes; ii) the transportation type and the distances in tonne-kilometre; iii) the residues in tonnes. The carbon emissions (in tonnes CO2 equivalent) and the cumulative energy requirements (in MWh) have been subsequently exported.

The total energy was found equal to 2.9 GWh, an improved value compared to that reported for a 2 MW wind turbine tower in [8]. 1.05e06 kg CO2 equivalent were evaluated for the whole life cycle, a better value than that corresponding to a 150 m steel tower reported in [10]. The energy payback time was found to be 3.5 months. The distribution of the carbon emissions among the components is shown in Figure 2(a), where, as expected, the foundation has the biggest contribution. The cumulative energy

requirements for the life cycle stages are presented in Figure 2(b). In line with past studies [3, 9], the biggest share belongs to the manufacturing stage.

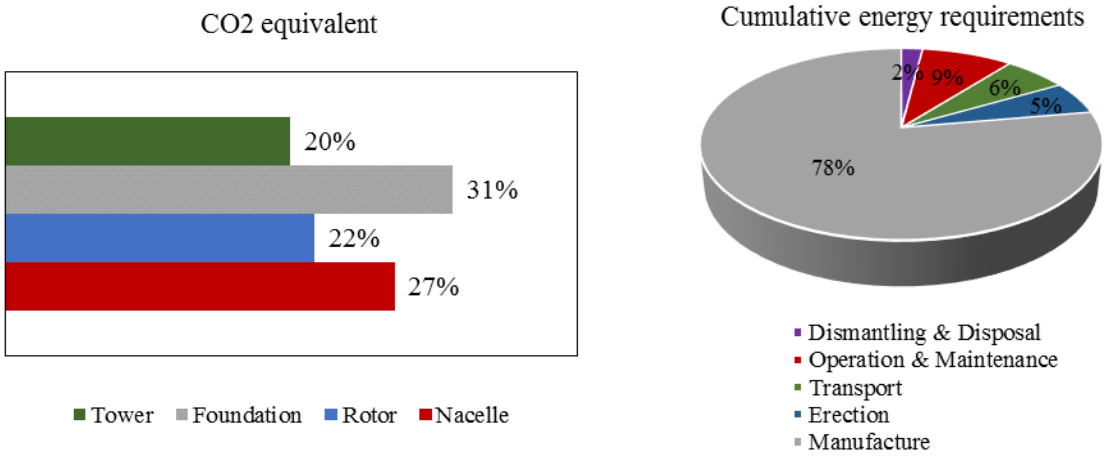

a) per component b) per stage

Figure 2. Preliminary results of life cycle analysis of a 185 m hybrid wind turbine tower.

5. CONCLUSIONS AND FUTURE WORK

With recent demands for taller wind turbine towers with enhanced capacities, comes a respective increase in the energy required for their manufacture and a need to investigate whether the latter can be sufficiently justified by equivalent increases in the energy yield of the system. Upon comprehensive literature review, a gap in knowledge on the life cycle analysis of tall hybrid wind turbine towers has been identified. The life cycle performance of a tall hybrid tower has been assessed, showing that the hybrid structure could be a promising solution with significant environmental benefits. A sensitivity analysis comparing the LCA of different kind of wind turbine towers is currently underway. The study is expected to reveal how the sustainability performance [20] is influenced. These research studies aim to demonstrate which component and stage is the most critical and thus to optimise the eco-friendly performance accordingly.

ACKNOWLEDGEMENTS

The research leading to these results has received funding from the Research Fund for Coal and Steel (RFCS) under grant agreement RFSR-CT-2015-00021. The authors acknowledge the financial support of TU1304 WINERCOST Action to their participation to “The International Conference On Wind Energy Harvesting 2018”.

REFERENCES

[1] Wind in Europe. European statistical data support, 2017. Available online at https://windeurope.org/.

[2] Global Wind Energy Council (GWEC). Wind in numbers, 2017. Available online at http://gwec.net/.

[3] Ardente, F., Beccali, M., Cellura, M. and Brano, V.L., 2008. Energy performances and life cycle assessment of an Italian wind farm. Renewable and Sustainable Energy Reviews, 12(1), pp.200-217.

[4] Lee, Y.M. and Tzeng, Y.E., 2008. Development and life-cycle inventory analysis of wind energy in Taiwan. Journal of Energy Engineering, 134(2), pp.53-57.

[5] Tremeac, B. and Meunier, F., 2009. Life cycle analysis of 4.5 MW and 250W wind turbines. Renewable and Sustainable Energy Reviews, 13(8), pp.2104-2110.

[6] Crawford, R.H., 2009. Life cycle energy and greenhouse emissions analysis of wind turbines and the effect of size on energy yield. Renewable and Sustainable Energy Reviews, 13(9), pp.2653-2660.

[7] Martínez, E., Sanz, F., Pellegrini, S., Jiménez, E. and Blanco, J., 2009. Life cycle assessment of a multi-megawatt wind turbine. Renewable Energy, 34(3), pp.667-673.

[8] Guezuraga, B., Zauner, R. and Pölz, W., 2012. Life cycle assessment of two different 2 MW class wind turbines. Renewable energy, 37(1), pp.37-44.

[9] Oebels, K.B. and Pacca, S., 2013. Life cycle assessment of an onshore wind farm located at the northeastern coast of Brazil. Renewable energy, 53, pp.60-70.

[10] Gervásio, H., Rebelo, C., Moura, A., Veljkovic, M. and da Silva, L.S., 2014. Comparative life cycle assessment of tubular wind towers and foundations–Part 2: Life cycle analysis. Engineering structures, 74, pp.292-299.

[11] Razdan, P. and Garrett, P., 2015. Life Cycle Assessment of Electricity Production from an onshore V110-2.0 MW Wind Plant. Vestas Technical Report. Copenhagen, Denmark.

[12] Bonou, A., Laurent, A. and Olsen, S.I., 2016. Life cycle assessment of onshore and offshore wind energy-from theory to application. Applied Energy, 180, pp.327-337.

[13] Gkantou M, Martinez-Vazquez P, Baniotopoulos C, 2017. On the structural response of a tall hybrid onshore wind turbine tower. In the proceedings of X International Conference on Structural Dynamics, EURODYN 2017.

[14] ISO 14040, 2006. Environmental management – life cycle assessment – principles and framework. In: International organization for standardization. Geneva, Switzerland.

[15] ISO 14044, 2006. Environmental management – life cycle assessment – requirements and guidelines. In: International organization for standardization. Geneva, Switzerland.

[16] BS EN 15643-2, 2011. Sustainability of construction works – Assessment of buildings Part 2: Framework for the assessment of environmental performance.

[17] BS EN 15978, 2011. Sustainability of construction works – Assessment of environmental performance of buildings - Calculation method.

[18] BS EN 15804:2012+A1, 2013. Sustainability of construction works – Environmental product declarations - Core rules for the product category of construction products.

[19] GEMIS. Version 4.9., 2017. Global Emission Model for Integrated Systems. Öko-Institut. Freiburg, Germany. Available online at http://iinas.org/gemis.html

[20] Schaumann, P. and Bechtel, A., 2014. Sustainability Assessment and Relevant Indicators of Steel Support Structures for Offshore Wind Turbines. In Operations Research Proceedings 2012 (pp. 351-356). Springer, Cham.

WINERcost '18

&

Aeolus4future

TECHNICAL SESSION 3.2

Grid Integration, Operations and Control

THE INTERNATIONAL CONFERENCE ON
WIND ENERGY HARVESTING 2018
21-23 March 2018
Catanzaro Lido, Italy

Paper TS3.2.1.

MODEL PREDICTIVE CONTROL FOR FLOATING OFFSHORE WIND TURBINES. WHAT DO WE NEED TO KNOW ABOUT THE FUTURE WIND

C. Gallego-Castillo[1*], V.A. Riziotis[2], A. Cuerva[1], D.I. Manolas[2] and O. Lopez[1]

[1]DAVE (ETSIAE) Universidad Politécnica de Madrid, Spain
[2]Department of Mechanical Engineering, National Technical University of Athens, Greece
**Corresponding author: C. Gallego-Castillo* cristobaljose.gallego@upm.es

ABSTRACT

Model Predictive Control (MPC) is applied for the case of a floating offshore wind turbine (FOWT), with the objective of reducing fluctuations in both generator speed and tower-top fore-aft motion, by using collective pitch as control variable. The analysis focuses on the information about the incoming wind perturbations required by the MPC controller. To this end, five scenarios were defined in order to characterise different operational situations in terms of LiDAR availability and SCADA usage. Results suggested that, for the case of turbulent wind, the contribution of LiDARs (as compared with using SCADA data) could not justify its cost. Furthermore, the availability and use of high-frequency SCADA data was found to be the main driver for improving the MPC controller performance.

NOMENCLATURE

x	=	State vector
w	=	Wind speed at hub height (input)
Θ_d	=	Demanded collective pitch (input)
Ω_g	=	Generator speed (output)
a_{FA}	=	Tower top acceleration in the fore-aft direction (output)
k	=	Prediction horizon (time steps)

1. INTRODUCTION

The continuous upscaling of wind turbines experienced in the last decades resulted in flexible structures with increasingly complex dynamics. This complexity is mainly due to aeroelastic effects, as well as couplings between different elements (blades, tower, drive train, etc.). In addition, offshore configuration adds complexity due to a new loading source (waves) and, for the case of floating offshore wind turbines (FOWTs), new degrees of freedom (DOFs) related to the floater motion.

Under this scenario, the role of the control system has experienced a noticeable shift While traditional control strategies focused mainly on maximising energy capture during operation, modern control designs include also as primary objectives enhancing stability and reducing loads [1]. This calls for new control concepts. Indeed, conventional feedback controllers typically show limited capabilities for reducing loads because they are usually based on rotor measurements, meaning that they can only provide delayed compensation due to the rotor inertia [2]. Model Predictive Control (MPC) represents a clear path for improvement, the main reason being that MPC provides optimal control actions based on the expected evolution of the plant in the near future.

Two key aspects underlie the potential improvements of MPC: (i) the fidelity of the plant model employed by the MPC controller to foresee the plant dynamic response, and (ii) the quality of the available information concerning the incoming system perturbations (in this case, the incoming wind).

Concerning (i), a vast majority of works equip MPC controllers with a wind turbine model too simple to capture aeroelastic features. In this work, we overcome this issue by using an innovative model with 22 DOFs. Concerning (ii), LiDAR technology has been postulated as a natural candidate to cope with this issue. However, the benefits provided by LiDAR must be assessed objectively [3]. In addition, the lack of LiDAR massive deployment nowadays leads to an open question: could SCADA measurements assist MPC reasonably? Or, in other words, to what extent and in which way MPC performance depends on the quality on the incoming wind information? These questions represent the main framework of this work.

2. METHODOLOGY

MPC was implemented for the case of the active tower damping problem of a FOWT. To this end, we considered the linearised dynamics of a FOWT around a certain steady state, given by the following discrete-time state space model:

$$\mathrm{x}_{t+1}=\mathrm{A}\mathrm{x}_t+\mathrm{B}\begin{pmatrix} w_t \\ \theta_{d,t} \end{pmatrix}, \tag{1}$$

$$\begin{pmatrix} \Omega_{g,t} \\ a_{FA,t} \end{pmatrix}=\mathrm{C}\mathrm{x}_t+\mathrm{D}\begin{pmatrix} w_t \\ \theta_{d,t} \end{pmatrix}. \tag{2}$$

Constant matrices $\mathbf{A}, \mathbf{B}, \mathbf{C}$ and $\mathbf{D}$ were obtained from linearising a non-linear FOWT model with 22 DOFs [4]. This model captures the main aeroelastic modes of the system, namely, tower modes (fore-aft and side-side), rotor modes (collective and whirling flap, edge and pitch modes), drive train mode (torsional deformation) and floater modes (surge, sway, heave, roll, pitch and yaw). Periodicity was suppressed through Multi-Blade Coordinate transformation [5]. In the present work, only full load (variable pitch) mode was considered.

MPC computes, at each time step *t*, the optimal value for the control variable, $\theta_{d,t}$, in order to minimise the expected fluctuations of Ω_g and a_{FA} over a time window $[t, t+k]$, where k represents the prediction horizon. The relative importance between the two objective variables is determined through the weights W_{Ω_g} and $W_{a_{FA}}$. In order to perform this computation, the controller needs information about the incoming wind perturbations over the considered time window. The accuracy of this information varies according to LiDAR availability and/or SCADA usage. In order to characterise different operational situations, the following five scenarios were defined:

· *Perfect forecast*: The incoming wind is assumed to be known. This situation is non-realistic, even for LiDAR assisted control. However, the case is interesting as the related outputs represent an upper limit of the MPC controller performance.

· *LiDAR*: The incoming wind is assumed to be constant and equal to its average over the following 4 seconds. This situation mimics a LiDAR assisted configuration, provided that LiDARs act as a low-pass filter of the incoming wind speed [2, 6].

· *SCADA (averaged)*: The incoming wind is assumed to be constant and equal to its average over the past 4 seconds. This situation assumes that the SCADA acts as a low-pass filter of wind speed records.

· *SCADA (direct)*: The incoming wind is assumed to be constant and equal to the current measurement. This situation assumes a high performance of the SCADA, which provides updated information at a high rate (in this case, each 0.05 seconds).

· *Mean*: The wind perturbation is set to zero, that is, the expected wind is assumed to be equal to steady conditions. This case provides the lower limit of the MPC controller performance.

In the literature, usually only one or two of these scenarios are considered for the same analysis, drawing partial conclusions about the impact of the incoming wind knowledge on the controller performance. Figure 1 reflects the defined scenarios for time *t*=85 s.

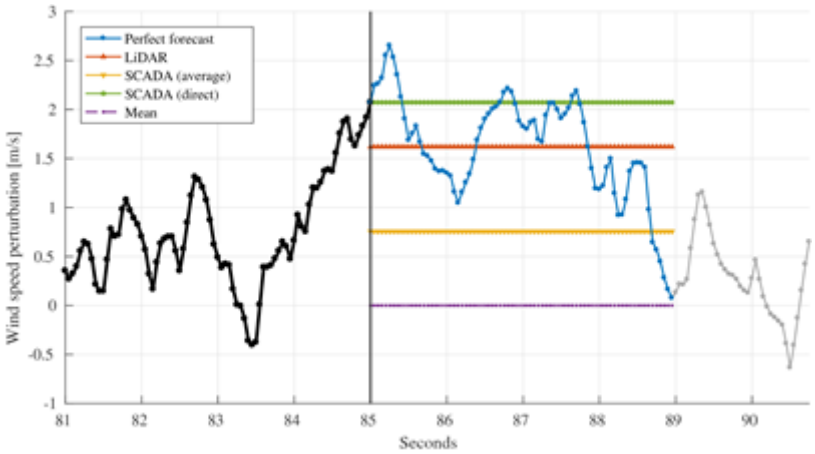

Figure 1. Different scenarios for the wind speed perturbation preview

3. RESULTS

For this analysis, the 5-MW NREL baseline wind turbine [7] mounted on a spar-buoy floater was employed. Full load with turbulent wind (category C) at 15 m/s was considered in a calm water environment (hydrostatic loads enabled, wave loads disabled). Ten minute simulations were performed with a time step of 0.05 seconds. A prediction horizon of k=80 steps (4 seconds) was considered. No constraints were implemented for the MPC in order to explore the impact of the different scenarios on the required pitch rate (which usually should not overcome 10º/s).

Figure 2.a shows the standard deviation of the two output variables, σ_{Ω_g} and $\sigma_{a_{FA}}$, for the five defined scenarios and for different controller configurations ($W_{a_{FA}}$values from 0.01 to 1 andW_{Ω_g}=1). Note that increasing values of $W_{a_{FA}}$are related to decreasing values of $\sigma_{a_{FA}}$. The black dots represent the particular case of $W_{a_{FA}}$=0.1. Figure 2.b reflects the maximum pitch rate observed during the simulation, as a function of $W_{a_{FA}}$.

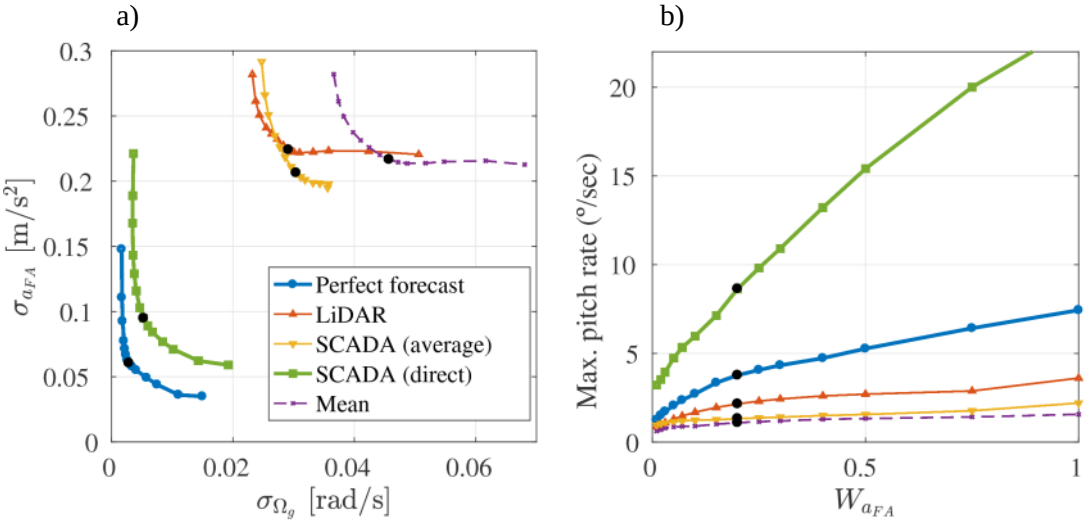

Figure 2. MPC results for the five defined wind preview scenarios (see text for details).

Figure 2.a reflects the boundaries of the feasible trade-offs between the conflictive objectives provided by the MPC for the five different operational configurations. This diagram can be employed to set$W_{a_{FA}}$ according to pre-defined objectives (for example, keeping tower-top fore-aft acceleration below a certain value). However, as the variance of the tower-top acceleration is reduced (as a consequence of increasing $W_{a_{FA}}$), figure 2.b shows an increase of the maximum pitch rate required. This variable usually is limited to 10º/s, meaning that results related to $W_{a_{FA}}$ values providing higher pitch rates should be taken carefully.

The SCADA (direct) scenario, as expected, provides a boundary of trade-offs inferior to that of the Perfect forecast scenario (i.e. higher standard deviations). It can be observed that, while there is room for reducing notably the tower-top acceleration from that of the reference configuration (black dot), it must be noted that the maximum pitch rate is already close to 10º/s for the reference configuration. The increase of this variable with $W_{a_{FA}}$ is very pronounced, and represents the main limitation of this scenario.

Results for LiDAR and SCADA (average) scenarios are one order of magnitude higher than those obtained for the two previous scenarios. However, the increase of maximum pitch rate with $W_{a_{FA}}$ shows lower slope. In addition, it can be remarked that the advantage of LiDAR over SCADA (average) is not clear. This is important as long as one of these strategies implies LiDAR installation, suggesting that, for the turbulent wind case and for the defined targets (minimise tower-top acceleration and generator speed fluctuations), the contribution of LiDARs as compared with using SCADA data could not justify its cost.

As a consequence of the previous comments, the availability and use of high-frequency SCADA data (i.e. SCADA (direct) scenario) can be considered as the main driver for improving the controller performance.

Figure 3 shows the impact of the prediction horizon on the controller performance. The two plots on the left (3.a) show the standard deviation of the two output variables computed for W_{Ω_g}=1 and $W_{a_{FA}}$=0.1, for different prediction horizons from 1.5 seconds to 10. On the right, figure 3.b shows the impact of the prediction horizon on the maximum pitch rate observed. Note that the black dots in figure 3 represent the same controller configurations as in Figure 2.

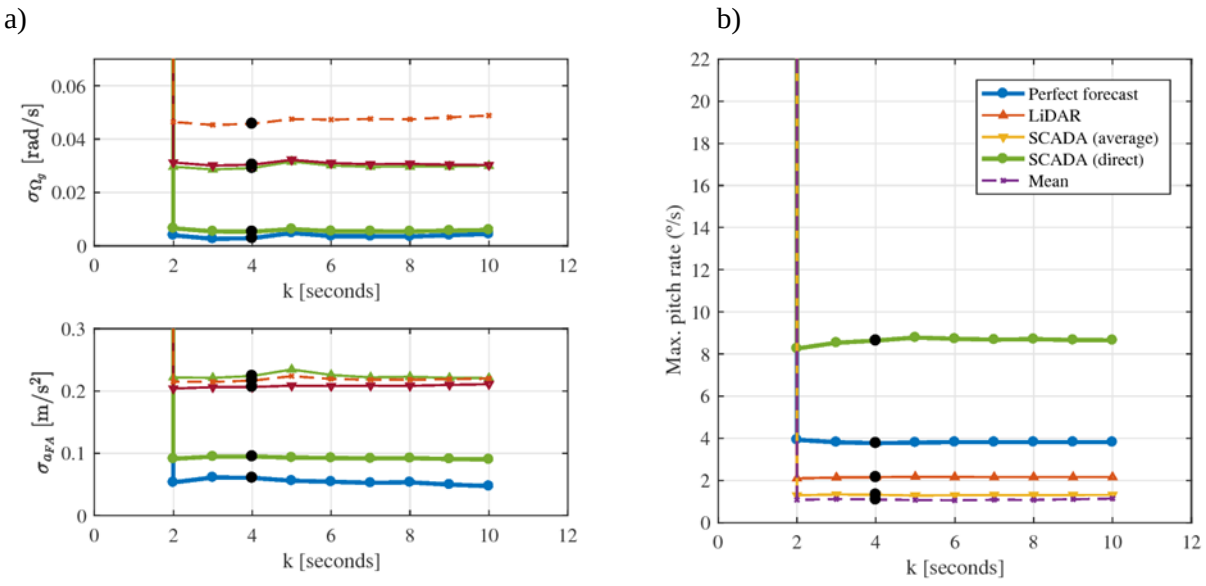

Figure 3. Impact of the prediction horizon on the MPC results.

Figure 3 shows that the prediction horizon has a very limited impact on the controller performance, as long as its value does not go below 2 seconds. The low impact of larger prediction horizons is in good agreement with existing literature (see [3,6]). The unstable behavior observed for horizons below 2 seconds could be attributed to the fact that the MPC fails in capturing and counteracting the fore-aft motion, this being characterised by a period of 2.2 seconds [4]. In this regard, a good practice in MPC implementation is that the horizon of an MPC controller even without stability guarantees shall cover the expected duration of dynamic effects [8]. Note also that increasing unnecessarily the prediction horizon is not recommended, since performance is not improved, but the computational cost associated to the control problem resolution increases notably.

Finally, figure 4 shows the same type of results as in figure 2, but obtained for onshore configuration. Results are qualitatively similar. A remarkable difference is that, for perfect forecast and SCADA direct scenarios, the standard deviation of the tower top acceleration shows a lower limit clearly higher in offshore configuration (around 0.035 and 0.06 m/s^2) as those observed for onshore (around 0.01 and 0.025 m/s^2). This could be due to the floater motion, reflecting a higher difficulty for stabilizing a variable with different contributions to its dynamics (tower fore-aft, floater pitch and floater surge). Actually, this could also explain the fact that the weight related to the tower top acceleration, $W_{a_{FA}}$ had to be below 1 for the offshore case (while for the onshore, values up to 6 were acceptable) in order to prevent instabilities in the results. Consequently, one cannot expect the same degree of controllability of the tower top acceleration for the offshore configuration as that obtained for the onshore case.

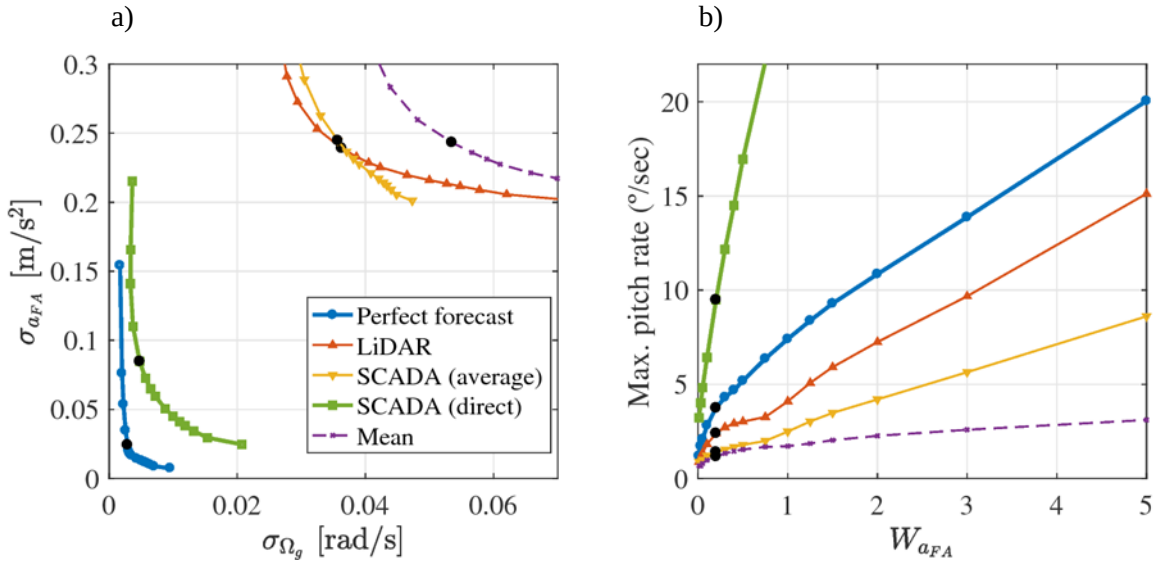

Figure 4. MPC results for the onshore configuration.

4. CONCLUSIONS

The following conclusions can be drawn from the performed analysis:

· For the considered problem (active tower damping problem in full load with turbulent wind), the use of LiDAR did not provide a clear advantage as compared with the use of averaged information gathered by the SCADA.

· A noticeable improvement was observed when SCADA measurements were employed with a high frequency update (and not averaged). This suggests that the availability and use of high-frequency SCADA data could be considered as the main driver for improving the controller performance. However, this came at the expense of a noticeable increase in the pitch rate.

· An analysis on the prediction horizon of the controller, *k*, showed instabilities for values close to the time scales of the tower fore-aft mode (~2 seconds). In general, a 4 second horizon was considered reasonable, and no improvement was observed for larger horizons.

· A comparison with results obtained for the onshore configuration revealed a more limited capability of controlling the tower-top fore-aft acceleration in the offshore case. This was attributed to the existence of several sources contributing to the dynamics of this variable, namely the tower deflection, the floater surge displacement and the floater pitch deflection.

ACKNOWLEDGEMENTS

This research was conducted within the Spanish Plan Estatal de Investigación Científica y Técnica y de Innovación 2013-2016 of the Ministerio de Educación, Cultura y Deporte, whose support is gratefully acknowledged.

REFERENCES

[1] E.A. Bossanyi, "Wind Turbine Control for Load Reduction", *Wind Energy*, vol. 6, no. 3, pp: 229–244, 2003.

[2] D. Schlipf, P. Grau, S. Raach, R. Duraiski, J. Trierweiler, and P.W. Cheng, "Comparison of linear and nonlinear model predictive control of wind turbines using LiDAR", in "*American Control Conference", Portland, OR, USA , 04-06.06.2014*, 2014, pp. 3742–3747.

[3] E.A. Bossanyi, A. Kumar, and O. Hugues-Salas, "Wind turbine control applications of turbine-mounted LiDAR", *Journal of Physics: Conference Series.*, vol. 555, no. 1:012011, 2014.

[4] S. Koukoura, "Aeroelastic analysis of floating turbines using reduced order models", Diploma Thesis (in Greek), NTUA, 2015.

[5] G. Bir and J. Jonkman, "Aeroelastic Instabilities of Large Offshore and Onshore Wind Turbines", *Journal of Physics: Conference Series.*, vol. 75, no. 1:012069, 2007.

[6] C.L. Bottasso, P. Pizzinelli, C.E.D. Riboldi, and L. Tasca, "LiDAR-enabled model predictive control of wind turbines with real-time capabilities", *Renewable Energy*, vol. 71, pp: 442–452, 2014.

[7] J. Jonkman, S. Butterfield, W. Musial, and G. Scott, "Definition of a 5-MW reference wind turbine for offshore system development", technical report NREL/TP-500-38060, Golden, CO, National Renewable Energy Laboratory, 2009.

[8] G. Takcs and B. Rohal-Ilkiv, "Model Predictive Vibration Control: Efficient Constrained MPC Vibration Control for Lightly Damped Mechanical Structures", *Springer Publishing Company*, 2014.

INTEGRATION OF WIND POWER INTO POWER DISTRIBUTION GRID

Jovan Todorovic[1]

[1]Power Transmission Company of Bosnia and Herzegovina, ELEKTROPRENOS BiH, a.d. Banja Luka, jovan.todorovic@elprenos.ba

ABSTRACT

This paper describes integration of wind power generation within power distribution grid. Although, wind turbines connected to distribution grid have minor impact on a power system stability, there are certain technical requirements and constraints set by the Distribution System Operator (DSO). The analysed case study is grid integration of two wind turbines, 1 MW and 0.6 MW installed power, into 20 kV distribution grid. The goal of this analyse is, besides description of technical requirements set by the DSO, estimation of stability sensitivity of these wind turbines. The analyse goes beyond the DSO requirements but some results are more indicative to give insight of wind power generation influence onto power distribution grid.

1. INTRODUCTION

Grid integration of wind turbines is being become complex task, in recent years. Intermittent and unpredictable production from renewable sources imposes new challenges to Transmission System Operators (TSOs) to keep power system in stable operation mode. Significant participation of wind power in a power system jeopardize power production/consumption balance, i.e. power system stability. An electric power produced by wind turbines need to be injected into distribution/transmission grid in the most efficient way to fulfil technical, economic and environmental requirements. An optimal grid integration solution is very case dependent, so each project has to be evaluated individually.

Rapid development of renewable generation technology, followed by proper regulatory subsidy policies and electricity price increase, have motivated households to invest in distributed renewable generation unit, predominantly solar and wind power. This trend influences on transmission and distribution grid, so a supplied region is not passive any more but active [1]. It changes both, power grid design and development approach, consequently.

Harmless influence on a power system stability is the one of the reasons why stability of wind turbines, connected to distribution grid, isn't being scrutinized as for large-scale units connected to power transmission grid. Furthermore, stability improvements in wind turbines, like capacitor banks and power electronics, shouldn't be cost effective comparing to amount of wind power installed into distribution grid. When applying for a power grid connection, a Distribution System Operator requires (DSO) that a wind generator produces power in allowed range of output voltage, total harmonics distortion (THD), flickers, usually.

The technical requirements, when connect wind turbines into power distribution grid, aren't as extensive as for the large-scale wind turbines connected to transmission grid, but responsible DSO imposes some, anyway. This paper describes DSO requirements of one such project proposal. The analyzed case study is grid integration of two wind turbines, WT1 installed power of 1 MW, hub

height 70 m and blades diameter of 54 m and WT2 installed power of 0.6 MW, hub height 55 m and blades diameter of 44 m. The wind turbines have to be connected to 20 kV distribution grid.

2. SOFTWARE TOOL

All simulations and calculations are performed in software package Power System Simulation for Engineers (PSS/E). It is professional software tool designed for simulation of large high voltage transmission networks predominantly, but MV and LV distributions networks can be simulated as well.
Vast of models (power generation/transmission/distribution element models, used in simulation) can be found in the PSS/E Model Library, both for stationary and dynamic calculations, making work with this software very "User friendly". This software uses advanced user graphical interface with possibility of connecting implemented tools necessary for various calculations and simulations. Also, it is possible to create advanced textual and graphical reports based on calculation results [2][4].

3. MODEL CREATED AND ANALYZED

The simulation model is created in PSS/E software tool. The analyzed case is integration of two wind turbines, WT1 1.0 MW and WT2 0.6 MW installed power. The generators are synchronous machines with salient pole. The interface between grid and turbine is AC/DC/AC convertor, enabling stable production wind generator in various operating circumstances (Figure 1). The cut in wind speed is 3-5 m/s, cut out 25 m/s and nominal wind speed is 12-13 m/s.

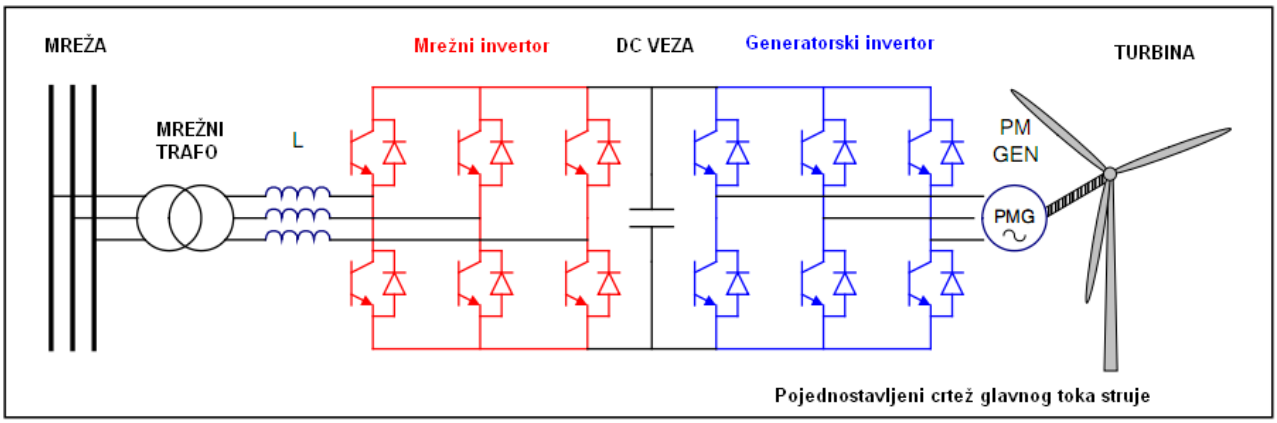

Figure 6. The principal layout of wind generator, AC/DC/AC convertor and 20/0.4 kV wind turbine transformer

Once a model completed, gives you opportunity for creation of reports, either textual or graphical, and for desired part of network (selected elements, selected region, designated distribution area, desired voltage transmission/distribution voltage level etc.). The one such report, the steady state power flow report of the wind turbines connected to distribution network, is presented in Figure 2 [2][4].

The power flow calculations and voltage profiles are obtained by *Newton-Raphson* iterative procedure.

The *Newton-Raphson* iterative method converged and power flow steady state is achieved with all voltages and currents in allowed limits.

4. GRID INTEGRATION CALCULATIONS

The WT1 and WT2 are connected to 110/20 kV power substation by 20 kV overhead transmission lines at distance 2.0 km and 1.4 km, respectively. This solution increases investment costs, but increases reliability, since the wind turbines are independent on each other, i.e. each wind turbine has its connecting 20 kV line. Also, the installed power capacity of both wind turbines could be connected

to lower voltage level, what could decrease investment costs of grid integration. But, DSO had already been created development plans for that distribution grid with 20 kV grid voltage level, so there was no

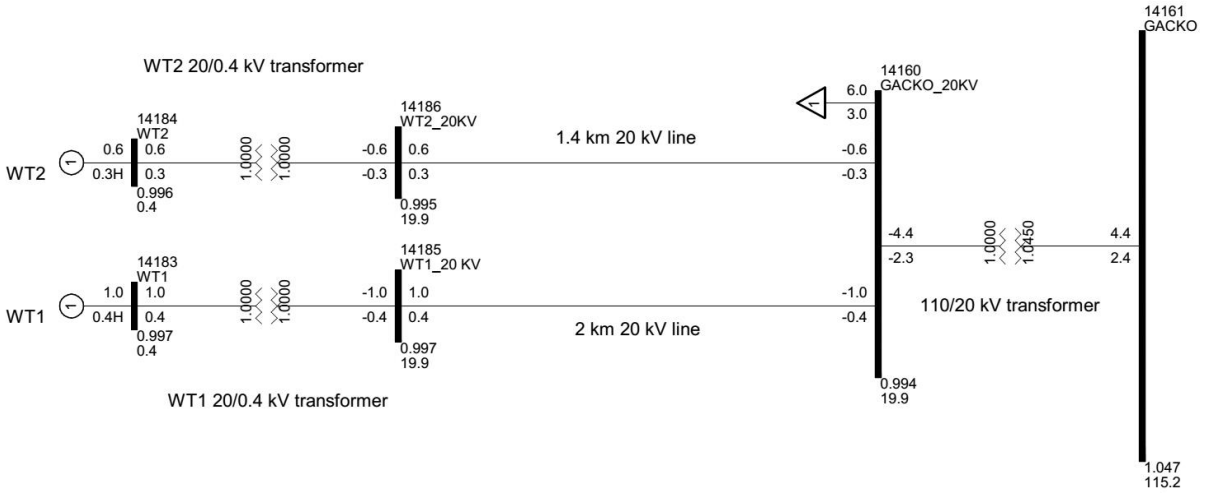

Figure 2. Power flow results in the one phase graphical report

option for the voltage level selection. For this project, the installation site was already chosen by the project proposers, so the connection distance to distribution line stands as input constant value.

The generator voltage is 0.4 kV, connected to 20 kV distribution network by 20/04 kV wind turbine transformer. The produced power is either consumed by local consumption, simulated on 20 kV side, or evacuated to transmission grid by 110/x kV power substation (Figure 2).

The power substation TS 110/20 kV Gacko has 110/20 kV, 20 MVA transformer with the nominal transformer ratio 115/20 kV with ±10% regulation range.

The short circuit currents analyses have to prove that the selected power equipment have to withstand in the extreme conditions of failures, as long as protection equipment clear a fault. The Grid Codes for the TSO and DSO assigned limits for the short circuit currents for all voltage levels. So, the maximal allowed current for 110 kV voltage level is 31,5 kA and for 20 kV voltage level is 16 kA. Table 1 presents the output report from the three-phase short circuit calculations at 110 kV and 20 kV busbars, in the vicinity of WT 1 and WT 2. The report provides and the contributions to the total short circuit current from the adjacent branches/transformers, also.

```
 .               PSS/E SHORT CIRCUIT OUTPUT                    HOME BUS IS  14161.
 .                                                             GACKO       110.00.
 .                                                                                .
 . *** FAULTED BUS IS:  14161 [GACKO       110.00] ***              0 LEVELS AWAY  .
 AT BUS  14161 [GACKO       110.00] AREA   30  (KV L-G) V+: /  0.000/    0.00

 THEV. R, X, X/R: POSITIVE  0.06102  0.19983    3.275

                                                    T H R E E   P H A S E   F A U L T
 X--------- FROM ----------X AREA CKT   I/Z       /I+/     AN(I+)     /Z+/     AN(Z+)   APP
X/R
  14103 [BILECA        110.00]    30 1   AMP/OHM    2262.8    -86.12      16.98      73.19
3.311
  14160 [GACKO_20KV   20.000]    30 1   AMP/OHM     380.4   -102.37       1.19      87.46
22.576
                           TO SHUNT  (AMPS)      0.0     0.00
               TOTAL  FAULT  CURRENT  (AMPS)   2630.1   -88.44
```

```
------------------------------------------------------------------------------

 .               PSS/E SHORT CIRCUIT OUTPUT                     HOME BUS IS  14185.
 .                                                              WT1_20 KV   20.000.
 .                                                                                .
 . *** FAULTED BUS IS:  14185 [WT1_20 KV   20.000] ***             0 LEVELS AWAY  .
 AT BUS  14185 [WT1_20 KV   20.000] AREA   30  (KV L-G) V+: /  0.000/    0.00

 THEV. R, X, X/R: POSITIVE  0.12495  0.46383    3.712

                                                  T H R E E   P H A S E   F A U L T
 X--------- FROM ----------X AREA CKT   I/Z       /I+/     AN(I+)     /Z+/     AN(Z+)   APP
X/R
  14160 [GACKO_20KV   20.000]    30 1   AMP/OHM    4484.1    -86.16       1.01      52.60
1.308
  14183 [WT1            0.4000]    30 1   AMP/OHM    1567.1   -104.98       0.00       0.00
0.000
               TOTAL  FAULT  CURRENT  (AMPS)   5988.8   -91.00

------------------------------------------------------------------------------

 .               PSS/E SHORT CIRCUIT OUTPUT                     HOME BUS IS  14186.
 .                                                              WT2_20KV    20.000.
 .                                                                                .
 . *** FAULTED BUS IS:  14186 [WT2_20KV    20.000] ***             0 LEVELS AWAY  .
 AT BUS  14186 [WT2_20KV    20.000] AREA   30  (KV L-G) V+: /  0.000/    0.00

 THEV. R, X, X/R: POSITIVE  0.11625  0.43405    3.734

                                                  T H R E E   P H A S E   F A U L T
 X--------- FROM ----------X AREA CKT   I/Z       /I+/     AN(I+)     /Z+/     AN(Z+)   APP
X/R
  14160 [GACKO_20KV   20.000]    30 1   AMP/OHM    4897.3    -86.61       0.79      49.55
1.173
  14184 [WT2            0.4000]    30 1   AMP/OHM    1561.0   -105.45       0.00       0.00
0.000
               TOTAL  FAULT  CURRENT  (AMPS)   6394.7   -91.13
```

Table 1: The output reports from the short circuit calculations at 110 kV and 20 kV busbars

For this case, the short circuit current analysis proves that integration of new power facilities (WT1 and WT2 with block transformers and 20 kV distribution lines) will not increase short circuit power level in the local grid, significantly. The short circuit currents are below maximal allowed level, so no need reinforcements in the power grid equipment.

5. MAXIMAL INSTALLED ALLOWED POWER

The responsible DSO, when estimate connection of generators, requires the test of allowed production power. In Eq. (1), the total installed power S_{inst} has to be less then $S_{sc}/50*k$,

$$S_{inst} \leq \frac{S_{sc}}{50} k \tag{1}$$

where S_{inst} is the total installed power in the connection point,

S_{sc} is the short circuit power in the connection point,

k is coefficient dependent on maximal starting generator current, k=1 for the synchronous machines with salient pole.

The connection point of WT 1 and WT 2 is 20 kV busbar in TS 110/20 kV Gacko. The short circuit power in this point is 294 MVA, the total installed power is 1.6 MW. Checking the Eq. (2):

$$1.6 = S_{inst} \leq \frac{S_{sc}}{50} k = \frac{294}{50} 1 = 5.8 \tag{2}$$

it shows that installed WT 1 and WT 2 have fulfilled the test of allowed production power.

6. POWER QUALITY

A voltage fluctuation in frequency range of 0 - 25 Hz, can be recognized as irritating oscillation of lightbulbs light, is called flickers. Flickers can be caused either in normal wind turbine operation or during power equipment handling. For these wind turbines, the power quality depends on AC/DC/AC convertor, predominately.

The flickers coefficient C_f tells about wind turbine ability to produce flickers. This coefficient depends of wind speed, phase angle of equivalent network impedance, wind turbine installed power and short circuit power. The C_f is provided by the wind turbine producer, or responsible independent institution, based on typical testing of a wind turbine with same or similar characteristics as wind turbine in construction. The wind turbine producer has provided the table of flickers emission for the various average wind speed, phase angle of equivalent network impedance and short circuit power.

After construction completed, the on-site measurements in real operation conditions have to prove guaranteed C_f values. The responsible DSO requires $C_f \leq 20$, what these WT1 and WT2 have fulfilled.

The Voltage Total Harmonic Distortion (THD)(%), defined by Eq. (3), is contribution rate of sinusoidal frequency parts which are product of elementary sinusoidal voltage harmonic frequency. According to the responsible DSO Grid Code:

$$THD(\%) = \frac{100}{U1} \sqrt{\sum_{h=2}^{40} U_h^2} \tag{3}$$

where U_1 is voltage of elementary order and U_h ,defined by Eq. (4), voltage of h-order,

$$U_h = |Z_{net,h}| I_h \tag{4}$$

$$|Z_{net,h}| = \sqrt{{R_{50}}^2 + (2\pi f L_{50})^2} \tag{5}$$

where $|Z_{net,h}|$, defined by Eq. (5), is absolute impedance value, R_{50} and L_{50} are values in the Point of Common Coupling (PCC) what can be obtained from power flow calculations.

The h-order harmonic current value I_h can be obtained by Eq. (6):

$$I_h = \left(\frac{I_h}{I_n}[\%]\right) \frac{I_n}{100} \tag{6}$$

where (I_h/I_n [%]) is harmonic value, provided from the wind turbine producer table and I_n is nominal wind turbine current.

The responsible DSO allows maximal THD of 6.5 % for the MV distribution grid. The calculations performed prove that WT1 and WT2 produces THD lower then maximal allowed.

7. STABILITY CALCULATIONS - SMALL SIGNAL STABILITY

A system ability, affected by small disturbances, to stay in synchronism is called static stability or small-signal system stability. These small disturbances in a power system are very often phenomenon, and can be caused by small variations in power consumption or production. As the consequences, there could occur:

- Continuous rotor angle increase caused by insufficient synchronous momentum component,
- Rotor oscillations with higher amplitudes caused by insufficient damping momentum component.
-

The system response on small disturbances depends on many factors, stationary operation state/point, power system characteristics, synchronous generator exitation current regulation, etc. In most of cases, the problem of small disturbances are dependent on a damping momentum component.

The dynamics in the power systems can be described by the set of differential equations. The small signal stability is based on the assumption that for the small disturbances, the system can be assumed as linear around equilibrium point – around steady state. The most common approach in dynamic study analyses is to use linear analysis in order to calculate eigenvalues matrix. If the real parts of eigenvalues are negative, the analyzed system is considered as static stable [5][3].

The dynamic model of the analyzed power system is created in the PSS/E module for dynamics. The dynamics data for the wind turbines (electrical and mechanical parts) are provided by the wind turbines producer. The eigenvalues of WG 1 and WG 2 are presented in Figure 3 and Figure 4, tested when WG1 is on and WG2 if off (Figure 3) and vice versa in Figure 4. These Figures show that the real parts of eigenvalues are negative, so each generator is static stable for the analyzed cases.

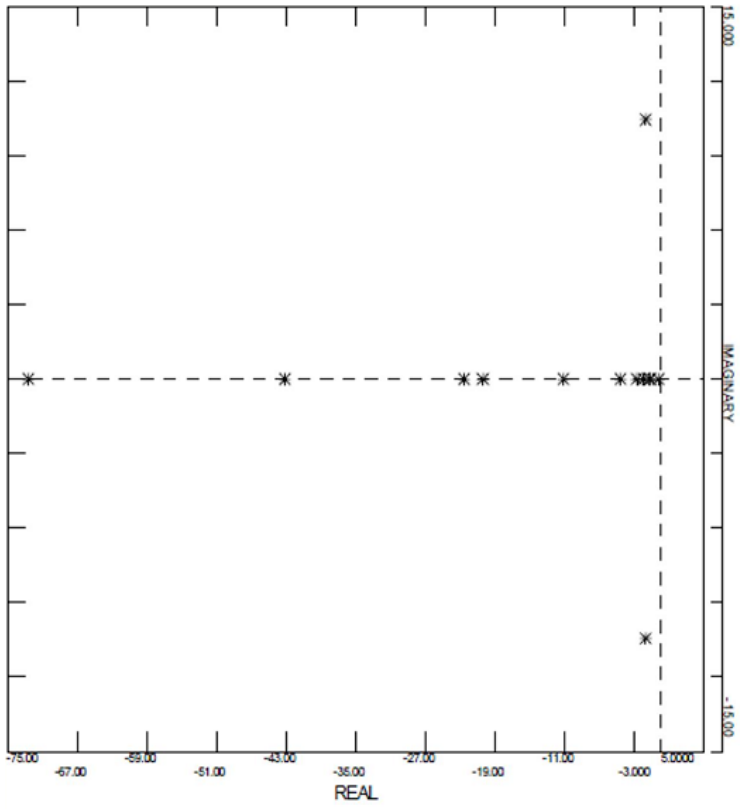

Figure 3. The eigenvalues of G1_WT1

The connection distances for both wind generators, WT 1 and WT 2, are rather short, 2 km and 1.4 km respectively. The short connection distance means low impedance between generation and strong grid what further improves stability.

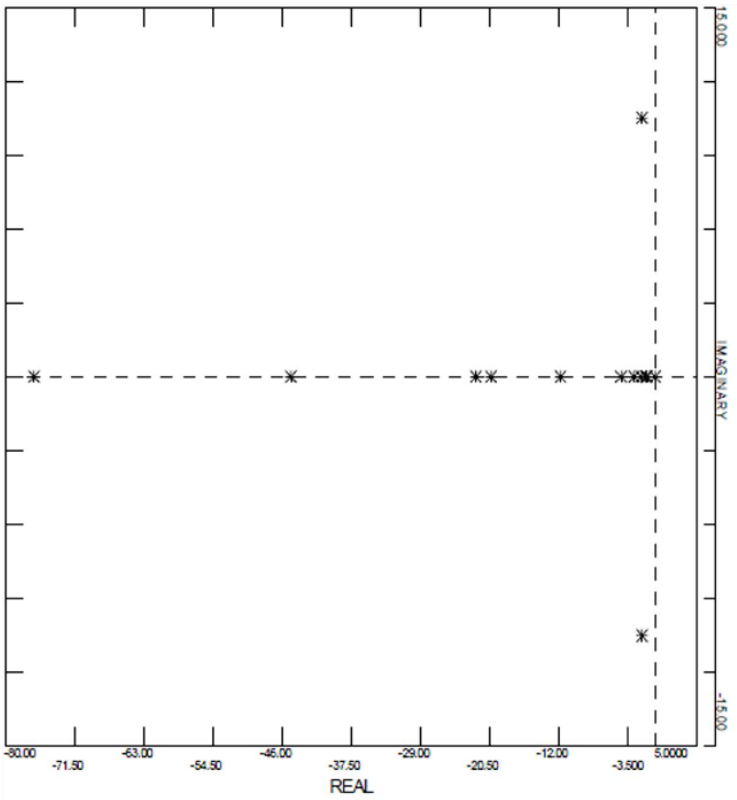

Figure 4. The eigenvalues of G2_WT2

It is known, from the system stability theory, that a generation connected at long radial transmission line could cause system instability under some operating circumstances. So, this could be main task for a new study, i.e. to evaluate influence of connection point on the system stability.

8. CONCLUSIONS

The power grid integration of the wind turbines, WT1 1.0 MW and WT2 0.6 MW, has been simulated in the PSS/E software tool. This software is able to provide all necessary tools and calculations to simulate any possible scenario of wind turbines connection into transmission/distribution power grid.

The connection point and distribution grid voltage level have been selected as input constant data. All calculations and simulations performed, power flow analysis, short circuit analysis, test of maximal allowed power, power quality of generated power have proven that connection of WT1 and WT2 doesn't jeopardize power system stability and reliability in any of possible power system operating conditions. The WT1 and WT2 are in stable operation area for each simulated scenario and the small signal stability is confirmed, also.

The calculations and tests performed hint that WT1 and WT2 are coupled with distribution grid in very stable and reliable way.

REFERENCES

[1] Todorovic J., "Renewable and Distributed Sources within Smart Energy Regions", *3rd International*

Exergy, Life Cycle Assessment, and Sustainability Workshop & Symposium (ELCAS3), July, 2013, Nisyros, Greece.

[2] PSS/E31 Help Documentation/ Program Application Guide/Volume II/ *Basic Power Flow Activity*

Applications.

[3] PSS/E31 Help Documentation/ Program Application Guide/Volume II/ *Linear Analysis*.

[4] Electricity Coordinating Center Ltd., Belgrade, Serbia, personal communication, December, 2016.

[5] Goran Andersson, *Power System Dynamics and Stability*, KTH Stockholm, September 1999.

THE INTERNATIONAL CONFERENCE ON
WIND ENERGY HARVESTING 2018
21-23 March 2018
Catanzaro Lido, Italy

Paper TS3.2.3.

MODULAR AXIAL-FLUX DIRECT DRIVE PERMANENT MAGNET GENERATOR FOR WIND TURBINE APPLICATIONS

Aydın Başkaya[1], Ozan Keysan[2]

[1] TUBITAK MAM Energy Institute, Ankara, Turkey
[2]Department of Electrical and Electronics Engineering, Middle East Technical University, Ankara, Turkey

ABSTRACT

According to fault statistics of wind turbines, most of the cases are related to gear-box failures. Mechanical losses and heat losses are again result from these gear-box drive train systems. In this paper axial-flux permanent magnet direct drive topology is investigated because of its high energy yield and lower maintenance problems due to its modular direct-drive concept. Proposed generator has electrical output power of 5 MW at 12 rpm. Outer stator axial flux concept will be used in the generator. In this paper, cost based design optimization procedure is carried under 9 different wind speed conditions in order to get a more realistic design. Wind speed data is taken from a real field based measurement values of a sample wind power plant (WPP) located in Çanakkale, Turkey. In order to verify the analytical design method, first a sample 50 kW AFPM design is simulated by using FEA and critical parameters, such as air gap flux density, and induced emf values are compared with the analytical results. Comparison results of the designed generator supported the proposed analytical method. It is observed that in the proposed design, PMs contribute most in the total cost while PM mass is the least dominant component in total mass. When increasing importance of "reliability", "modularity" and "fault-tolerance" taken into account, it is expected that the proposed modular AFPM generator system will contribute significantly in the MW level wind energy harvesting technologies both in onshore and offshore.

NOMENCLATURE

SCIG	=	Squirrel Cage Induction Generator
DFIG 3G	=	Doubly-fed induction generator system with 3 stage gearbox
PMSG DD	=	Direct-drive permanent magnet synchronous generator
PMSG 1G	=	Permanent magnet synchronous generator with 1 stage gearbox
EESG DD	=	Direct-drive electrically excited synchronous generator
T	=	Torque(Nm)
AFPM	=	Axial-flux Permanent Magnet Machine
B_{ag}	=	Air gap flux density
FEA	=	Finite Element Analysis
GA	=	Genetic Algorithm
	=	Peak of the fundamental frequency air gap flux density
$E_{ph,peak}$	=	Peak value of the induced emf per phase
w_m	=	Angular speed(rad/s)
THD	=	Total Harmonic Distortion

1. INTRODUCTION

As the world's energy consumption increases it becomes inevitable to employ renewable energy sources for different types of applications. Modern wind energy utilization by means of wind turbines started 40 years ago due to search for alternative energy sources except oil, whose deficiency and high prices were a global crisis issue. Besides, air pollution and other environmental problems made it indispensable to search for clean and renewable energy sources such as wind. To summarize, OPEC crisis in 1970s and environmental problems worked as a catalyst in development progress of wind turbines. Nowadays, there are different types of wind turbines exist in the market both in mechanical and electrical aspects. Global trend is going above 5MW of output power per turbine and especially generator technologies are under development in order to maximize produced energy [1]-[3].

Wind energy has become more popular than ever in the last few decades. Global annual installed wind capacities between 2001 and 2016 are given in Figure 1. As it can be seen from graph, wind energy harvesting has an increasing trend. According to annual market update report of GWEC (Global Wind Energy Council), it's expected to reach 791 GW of global cumulative wind energy capacity by 2020. As the usage of this technology increases more reliable and efficient designs becomes preferable by both manufacturers and customers. According to [5], today 83 countries use wind energy harvesting applications commercially and 24 countries have installed wind power capacity of more than 1GW.

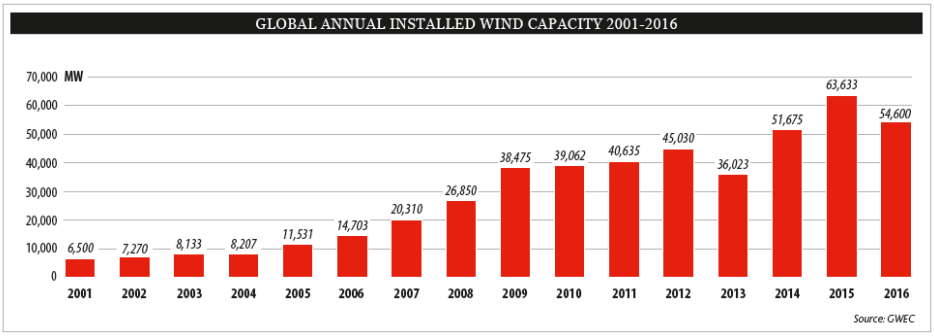

Figure 1. Worldwide yearly installed wind capacity 2001-2016 [4]

Evolution of wind turbine sizes and fraction of power electronics stage capacities can be seen in Figure 2. As the sizes and power levels of wind turbines are increased, importance of efficiency and grid connection subjects also increased. Because wind power plants gradually becomes inevitable parts of electrical grids in most countries and they are expected to conform grid codes and fault ride through capabilities.

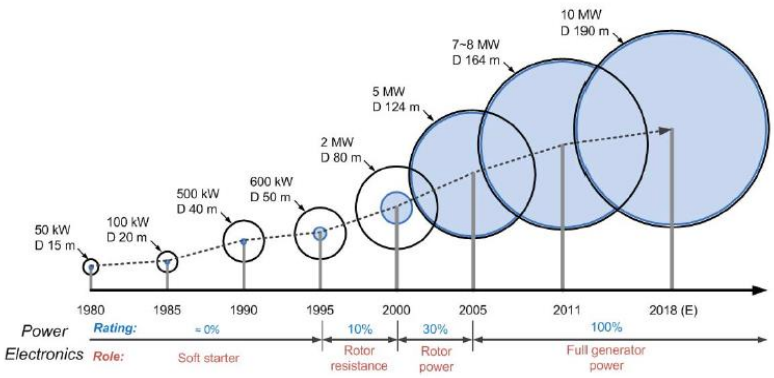

Figure 2. Evolution of wind turbines [6]

There are different types of generator topologies regardless of their magnetic flux paths that are used during their operation. These can be grouped as SCIG, WRIG, DFIG 3G, PMSG DD, PMSG 1G and EESG DD. Gearboxes are used in order to pair the low speed hub with the high speed generator shaft. However, gearboxes result in high mechanical wear, decreased efficiency and lower life-span. Therefore, wind energy systems with geared drivetrain need regular maintenance.

Failure rates and corresponding downtimes for different parts of generator are obtained in [3] and given in Figure 3. Most of the reasons of operation interrupts of wind turbine systems are related with gear-box error. They usually need periodical maintenance which means extra cost and generation interrupts during these periods. Main purpose of using direct-drive system is to reduce failure rates and maintenance costs due to eliminated gear-box part from the generator.

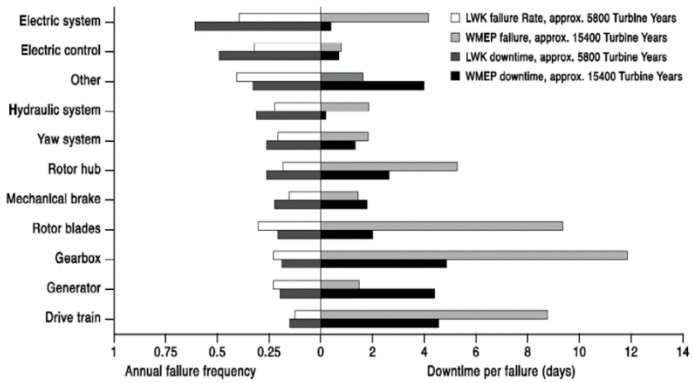

Figure 3. Failure frequency and downtime for different part of wind turbine [3]

In this paper, a Direct Drive Axial Flux Permanent Magnet wind turbine generator is chosen and designed because of its high reliability, high torque density and volume advantages. Designed and proposed generator has output power of 5 MW at 12 rpm. Gearless drive train is chosen especially for increased overall efficiency and reduced maintenance costs. Proposed generator also has a modular structure, thus reliability and high efficiency is desired even in a fault-state. Parameters of the designed machine will be chosen according to genetic algorithm optimization and FEA validation. Output power is defined according to formula,

$$P=T.w_m \quad (1)$$

Torque of an electrical machine increases inversely proportional to the rotational speed, if the rated power is kept constant. When scaling up the turbine sizes, amount of material is increased in order to maintain the air gap against deflection forces between stator and rotor parts. This means direct drive machines are heavier than other types of machines. Torque/volume and mass/torque parameters are important during the design of the generator system. More material also means extra cost which is a disadvantage for this type of generators. Direct drive concept thus is usually designed with a large diameter and small pole pitch to increase the efficiency, to reduce the active material and to keep the end-windings losses small. Active material refers to electromagnetic structure while inactive part means mechanical structure.

2. METHODOLOGY

2.1. Analytical Design

Axial-flux air cored generator system is chosen in this paper because of its electromagnetic and sizing benefits. Outer stator concept is employed. Instead of using conventional slotted or slotless concept, new C-type core limbs are chosen for the rotor structure. There is no slot structure (i.e TORUS type) in the proposed design, and stator windings are attached to the outer stator nacelle part. Modular construction is a brand-new concept in wind turbine systems, which enables getting better

assemble and disassemble (maintain and repair) conditions. Proposed concept also allows each module to work individually and thus provides better fault-tolerance. Single stage of the proposed AFPM generator is given in Figure 4.

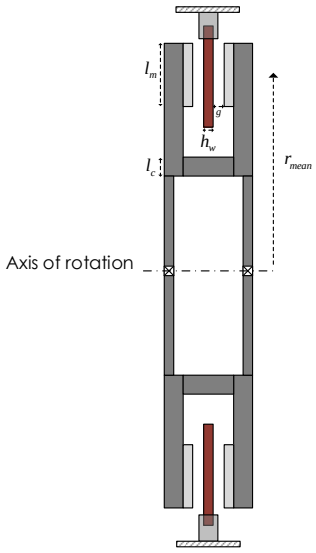

Figure 4. Single stage of the proposed AFPM generator side view

General overview of the proposed generator is given in Figure 5. In this figure, six axially stacked generator blocks are presented. However, this figure includes only 4 poles section of the proposed system, for the sake of simplicity. There is a (4/3) ratio between the coil pitch and the pole pitch in order to achieve maximum flux linkage and induced voltage.

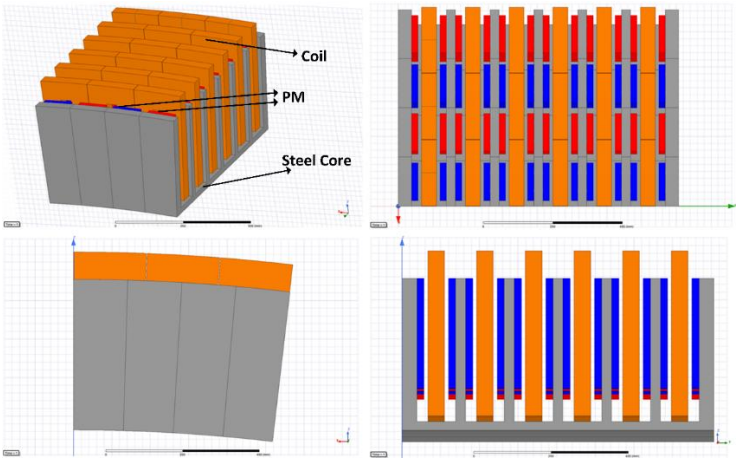

Figure 5. 4-pole section of the proposed axial flux PM generator.

Leakage fluxes in this paper are assumed for the magnet-magnet leakage direction in the air gap and added to magnetic circuit of the design. Top view of the C-cores showing the fluxes and flux paths including the mentioned leakage reluctances S_1 and leakage fluxes ϕ_1, is given in Figure 6. In analytical design calculations, it is assumed that flux density in the airgap has a square waveform nature. Therefore, calculated analytical air gap flux density B_{ag}, is the flat-top value of mentioned square wave. However, in reality this flux density waveforms are sinusoidal rather than square wave due to magnet shapes and leakage fluxes. Thus, peak value of the fundamental frequency component of the square waveform is utilized in calculations of flux linkage and induced emf [7]. In Figure 7, mentioned square waveform of analytical calculation and sinusoidal fundamental component of airgap

flux density are shown. As can be seen from this figure, width of the square wave is related to magnet pitch-to-pole pitch ratio α_i .

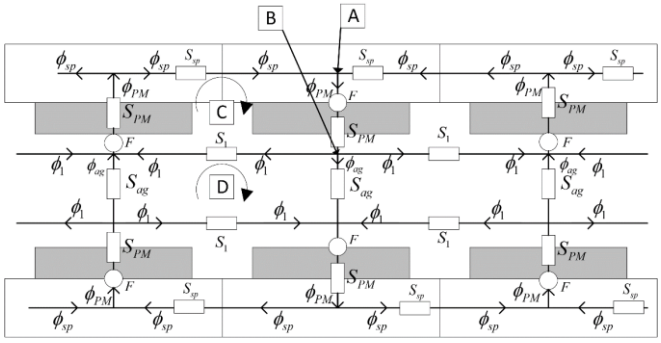

Figure 6. Top view of the C-cores for reluctances and flux paths included leakage effect.

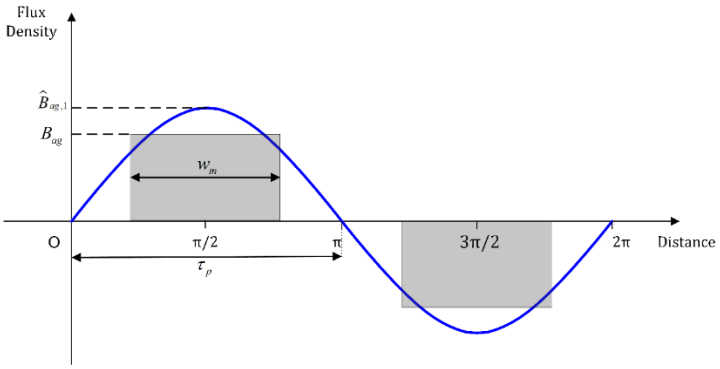

Figure 7. Calculated airgap flux density square waveform (grey) and its sinusoidal fundamental frequency component (blue).

Peak value of the fundamental harmonic value of the air-gap flux density B_{ag} is given as follows [7],

$$B_{ag,1} = \frac{4}{\pi} \mathrm{B}_{ag} \sin(\alpha_i \frac{\pi}{2}) \tag{2}$$

Structural deflection is related to mechanical stability. Since proposed design has air-cored stator, there will be no attraction force between stator and rotor [8]. However, C cores try to close the airgap against each other and result in deflection in the air gap clearance. Main reason of this deflection is strong magnetic attraction forces between magnets in the air gap clearance. Ratio of this deflection with respect to airgap clearance is significant parameter in terms of structural modelling of the generator [9]. This type of deflection is shown in Figure 8. In literature, air gap deflection is generally allowed between 10-20% [9]-[11]. It is desired to keep this ratio below reasonable ratio of 10% in our design. To model the structural deflection at 2D, beam model is employed [12].

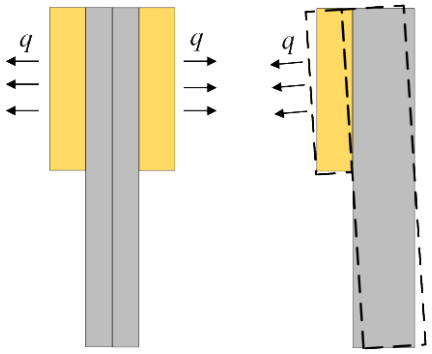

Figure 8. C-core deflection due to magnetic forces

Main heat resources in the proposed generator are copper losses of the windings and eddy losses. However, eddy losses are relatively very low with respect to copper losses because of low speed and low electrical frequency operation [13]. Therefore, current density control is the main focus of this design. When insulation class of windings (F class-155^o [14]) and operational thermal limits of permanent magnets (N50-type magnet-80^{o}C [15]) are taken into account, forced cooling methods are more reasonable rather than natural cooling methods for such a MW-level generator. Cooling of the machine is chosen as forced air cooling in order to improve electrical loading performance. Additionally, forced air cooing improves the magnet thermal performance and prevents them from demagnetization at extreme conditions such as short circuit faults [16]. In this study, thermal network of the machine is neglected. However, this disadvantage is compensated by forcing the optimization algorithm to converge to higher efficiency ratings. Therefore, we can determine a reference current density (A/mm^2) value at 100^o C operating temperature according to chosen cooling technique. Then, calculation of the temperature rise for windings ΔT can be found by using a rational relationship between "I^{2}R" losses and current density given as follows,

$$\Delta T = \frac{(100 - T_{ambient})}{J_{ref}^2} J^2 \tag{3}$$

where reference current density J_{ref} is selected as 7A/mm^2 [17], [18], [19].The schematic diagram of the direct driven PMSG is presented in Figure 9 below.

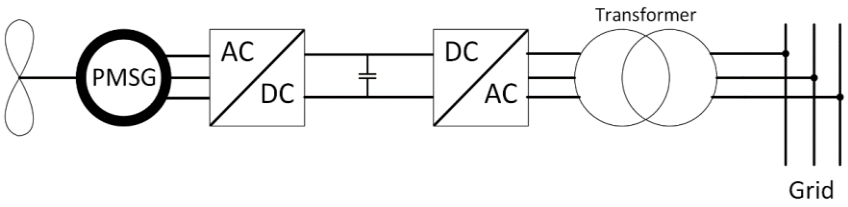

Figure 9. Schematic diagram of the direct-driven PMSG

In order to verify the design equations and techniques used in this study, air gap flux density and induced emf per phase values are chosen for the comparison. For this purpose, a 50 kW/60 rpm sample AFPM generator design is considered and evaluated in the optimization problem. Then, optimization results and FEA results for this sample design are compared. In Table 1 below, comparison of the selected verification parameter values and related error rates are summarized. Error values show that analytical results and finite element analysis results have small differences. Therefore, it may be concluded that analytical equations can be used in the optimization for the proposed AFPM generator design.

Table 1. Comparison of the critical parameters of analytical and FEA results for the sample AFPM design.

Parameter	Analytical	FEA	Error
($B_{ag,1}$)	0.67 T	0.65 T	3%
($E_{ph,peak}$)	1496 V	1600 V	6.5%

2.2. Optimization

15 of design parameters of the proposed AFPM generator are determined in this study by using GA optimization approach based on the analytical equations and cost minimization principles. The required optimization procedure is performed by MATLAB optimization toolbox. For this purpose, three different codes, which include the necessary design equations, are written and tested in the MATLAB environment. These scripts mainly perform; "optimization main handling and saving

performance parameters", "iterative loop for required multi-speed operation calculation" and finally "main design calculation of the generator for a given set of variables". Optimization of the proposed design is based on the cost optimization. In this study, seven different constraints are added in a form of penalty functions to the main objective function. Resulting objective function in which the penalty functions are included is given as follows,

$$F(\mathrm{x}) = 1.2(\mathrm{cost}_{steel} + \mathrm{cost}_{copper} + \mathrm{cost}_{magnet} + \mathrm{cost}_{structure}) - f_{income}(\mathrm{x}) + \sum_{i=1}^{7} p_i(\mathrm{k}_i) \quad (4)$$

where $p_i(\mathrm{k}_i)$ and k_i are the penalty function for i[th] constraint and penalty coefficient for i[th] penalty function. Income function $f_{income}(\mathrm{x})$ is utilized in order to include the effects of energy ratio and time probability of the wind in the total energy production for a proposed generator. This function is calculated as follows,

$$f_{income}(\mathrm{x}) = P_o \, price_{elec} \, f_{avail} \, f_{time} (365*24) \quad (5)$$

where P_o is the net output power from the generator, $price_{elec}$ is the electricity price per kWh sold by the WPP and taken as 7.3 ¢ (USD dollar cent) in this study [20], f_{avail} is the availability factor for proposed wind turbine and taken as 0.9 and finally f_{time} is the time probability of the related wind speed.

Optimization flowchart is given in Figure 10.

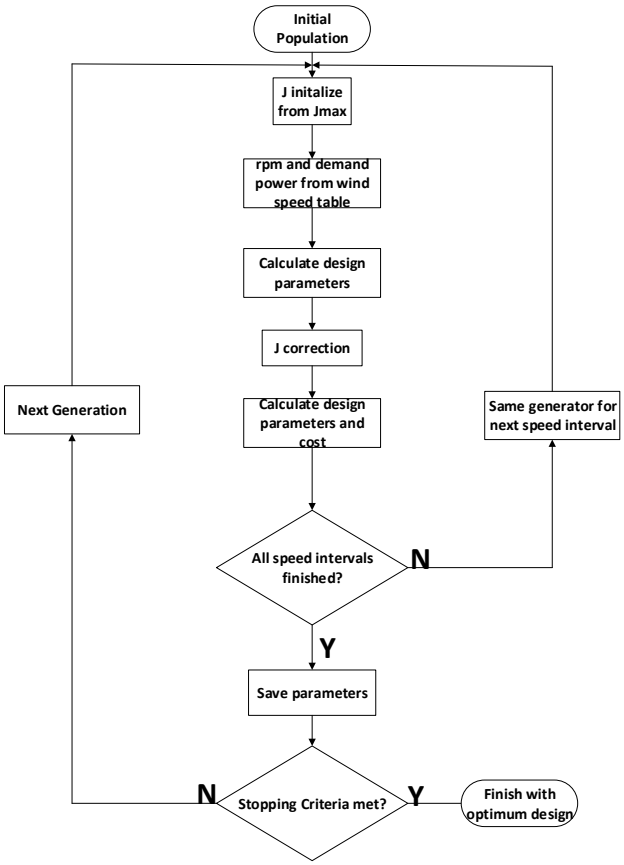

Figure 10. Optimization flowchart

First, an initial population is created by the MATLAB optimization tool based on the predetermined optimization configurations. Then, the reference wind speed data is taken from wind-speed data table. Current density is initially assigned as the half of the upper limit of the current density, namely $J_{max}/2$. Then this current density value, rpm value and demanded power are used together with the created random independent variables in order to calculate the design parameters of the generator. After the first design calculation, current density value is adjusted according to efficiency of the design and reference current density values calculated for steady state and short circuit fault conditions. Then a final design calculation is made for the current rpm interval. This calculations are repeated for all 9 operating conditions for the same design to evaluate performance of the generator at different wind speeds. Cost function is calculated according to objective function defined in Equation (4) by considering the energy ratios of the different wind speed intervals given in the reference wind-speed data table. Then, termination criteria are checked in order to stop the optimization process. This procedures are repeated until termination criteria are satisfied and the optimal design is achieved. Design optimization of the proposed AFPM is carried out in 9 different wind speed conditions with respect to the given time probabilistic densities. For this purpose, wind speed measurement data of a sample WPP, located in Çanakkale/Turkey, are used. Penalty function purposes and their corresponding coefficient values are given in Table 2.

Table 2. Objective function penalty table

Penalty Function	**Constraint**	**Penalty Coefficient**	**Coefficient Value**
p_1	Efficiency	$k_{1-1,1-2}$	$k_{1-1}=5\text{x}10^4$ $k_{1-2}=3\text{x}10^7$
p_2	Deflection	k_2	10^5
p_3	Axial length	k_3	10^5
p_4	Outer diameter	k_4	10^8
p_5	Temperature	k_5	10^5
p_6	Power	$k_{6-1,6-2}$	$k_{6-1}=0.1$ $k_{6-2}=1$
p_7	Voltage	k_7	10^6

In the optimization algorithm, every candidate individual is evaluated for nine wind speed conditions. Fitness function is obtained by summing all cost values for these speed conditions. Therefore, it can be said that fitness function itself not obviously shows exact cost of the proposed generator. Instead, it shows how suitable and low cost solution it becomes throughout the 200 generations. Optimization considers not only initial material cost but also power generation income and selects suitable parameters among the search space. Therefore, more material cost and mass can be preferred for the sake of a better energy generation income.

Algorithm calculated the design parameters of the proposed AFPM generator based on a power generation reference of a commercial 5MW PMSG wind turbine under aforementioned wind conditions. In addition, algorithm also considers the wind speed time probabilistic and related

generation incomes. Performance ratings of the optimized AFPM generator under 9 different wind speeds are given in Table 3 including the field-based wind speed probabilities.

Table 3. Optimized generator performance ratings

Wind Speed	**Time Prob.**	**Rpm**	J **(A/mm^2)**	$V_{ph,rms}$ **(V)**	$I_{ph,rms}$ **(A)**	**Desired Power (kW)**	**Input Power (kW)**	**Output Power (kW)**	**Efficiency (%)**
4 m/s	31,9%	1	1.37	24.4	414.1	195	244	182	74.5
5 m/s	10,7%	1	2.10	19.5	636.4	420	372	223	60.0
6 m/s	11,2%	2.9	1.69	84.3	512.0	786	874	777	88.8
7 m/s	10,1%	4.8	1.62	146.9	489.1	1296	1385	1293	93.4
8 m/s	9,0%	6.7	1.71	208.0	518.7	1943	2049	1942	94.7
9 m/s	8,3%	8.6	1.85	268.7	558.3	2699	2829	2700	95.4
10 m/s	6,3%	10.5	1.95	329.4	588.5	3487	3639	3490	95.8
11 m/s	4,7%	12	2.03	377.1	615.5	4174	4346	4178	96.1
12 m/s	7,5%	12	2.47	371.4	746.9	5000	5230	4992	95.4

The most salient features of the proposed AFPM generator at rated speed are given in Table 4. Optimized parameters are very important because they will be used in the finite element modelling and verification of the proposed AFPM generator.

Finally, mass components and material cost components of the proposed generator are investigated. According to results of these components, structural steel is the most dominant (about 61%) mass component while it is the less dominant (about 17%) in terms of material cost. Permanent magnet (PM) is the most dominant (about 66%) cost component while it is the least dominant (about %9) mass component. Since optimization is based on the cost of the design, algorithm converged to heavier and larger design solution. However, mass of the most expensive component, namely PMs, is minimized.

Table 4. The most salient features of the proposed AFPM generator at 12 rpm

Feature	Value	Feature	Value
Mean radius	4.71 m	Air gap flux density (fundamental-peak)	0.51 T
Stator outer diameter	9.9 m	Air gap flux density (flat-top)	0.46 T
Rated speed	12 rpm	Phase reactance	0.111 Ω
Air gap	10 mm	Phase resistance	0.020 Ω
Number of poles	216	Power factor	1
Number of turns	42	Total mass	119.4 tonne
Axial length	1.0 m	Total copper loss	206.9 kW
Number of axial stack	6	Total eddy loss	30.1 kW
Voltage per phase (rms)	371.88 V	Efficiency	95.4%
Induced emf per-phase (rms)	395.6 V	Total cost (including labor)	$ 1.56 M
Current per phase	746.9 A	Total Electricity Generation (annual)	11.73 GWh
Net output power	4992 kW	Total Generation Income (annual)	$ 857k

3. RESULTS

Design parameters of the optimized generator will be used in the 3D FEA modelling and analysis in order to verify the electromagnetic and electrical performance of the proposed AFPM generator. ANSYS Maxwell® software is employed for the 3D finite element simulations. As mentioned previously, air gap flux density and no-load induced emf values are investigated during the analyses. In addition, full load analysis of the proposed AFPM generator is performed in order to calculate the phase voltages and coefficient of eddy losses on the permanent magnets.

In the magnetostatic simulations, air gap flux density is investigated and results of FEA are compared with analytical results. Combined graphical representation of the air gap flux density results are shown in Figure 11. According to these FEA results, air gap flux density characteristics of the proposed design and comparison with analytical calculation results are summarized in Table 5.

Table 5. Comparison of the analytical and FEA results for the air gap flux density

Property	FEA	Analytical	Error
Air gap flux density - (peak)	0.474 T	0.459 (flat-top) T	3.1%
Air gap flux density fundamental- (peak)	0.502 T	0.516 T	2.7%

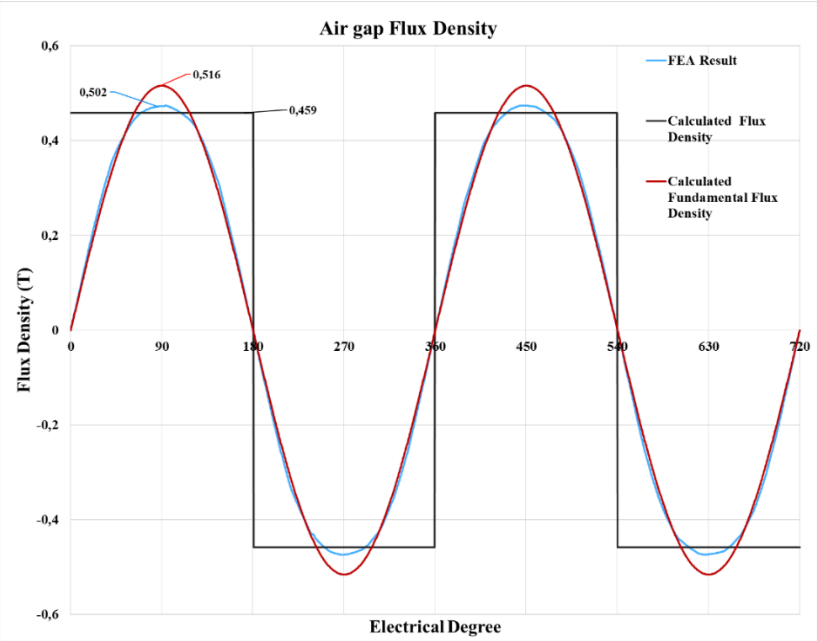

Figure 11. Air gap flux density graph with analytical results for the 5 MW design.

In the transient analyses, no-load induced emf, full-load phase voltage and coefficient of eddy losses on the magnets are investigated. Comparison of the analytical results and FEA for the no-load induced emf is given in Table 6.

Table 6. Comparison of the analytical and FEA results for the induced emf per-phase

Property	FEA Value (V)	Analytical Value (V)	Error
Induced emf per-phase rms (E_a - rms)	394.5	395.6	0.27%

Comparison of the analytically calculated results with FEA results for the phase voltage is given in Table 7 below. As it can be seen from this table, error rate is 1.81%. Since the proposed generator has an air-cored structure, inductance values are very low and the inductance effect on the resulting phase voltage are very low. Moreover, generator operates at low frequencies, hence phase reactance values do not become dominant in the calculation of the phase voltage. Therefore, analytical design method is verified with FEA in terms of phase voltage values. In addition to phase voltage value verification, observed phase voltage waveforms from FEA are subjected to THD analysis in MATLAB/Simulink and it is found as 2% per winding which is suitable in terms of low power electronic losses on the converter side.

Table 7. Comparison of the analytical and FEA results for the phase voltage

Property	FEA Value (V)	Analytical Value (V)	Error
Phase voltage	365.25	371.88	1.81%

Finally in the last part of the transient FEA analyses, coefficient of eddy losses on the magnets during the full-load operation of the proposed AFPM generator is investigated. For this purpose eddy loss of

the one unit of PM in FEA is calculated than loss density for eddy currents is estimated as 18 kW/m^3. A view of this kind of circulating eddy current vectors are depicted in Figure 12.

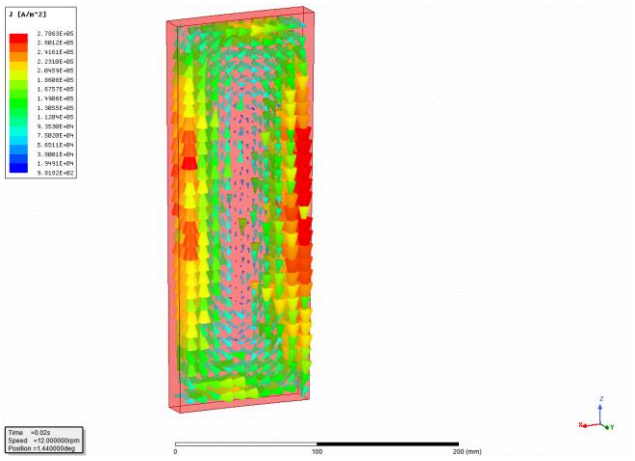

Figure 12. Eddy current density vectors on magnet block

According to results of the different stages of FEA evaluations presented in this paper, it can be concluded that the proposed design of AFPM generator is verified in terms of electromechanical performance. Error rates, phase voltages and harmonic contents of the proposed design were found at an acceptable level.

4. CONCLUSIONS

To sum up, a modular direct drive 5MW 12 rpm AFPM generator is analytically designed, optimized under realistic conditions by GA and verified by FEA in this paper. As it can be shown in air gap flux density plots and error tables given in previous sections, proposed design methodology has high accuracy. This topology is selected due to its higher energy yield, higher efficiency, reliability and axial length advantages. Modular design of the proposed generator allows easier and cheaper transportation, installation and repair conditions thanks to its lighter total mass per axially-stacked machine configuration. Direct drive system allows generator to operate more efficient due to eliminated gearbox. However, large outer diameter, which is optimized as 10 meters in this study, and highly magnet price dependent overall cost are the biggest challenges for the proposed design.

REFERENCES

[1] S. Debnath and M. Saeedifard, “A new hybrid modular multilevel converter for grid connection of large wind turbines,” *IEEE Trans. Sustain. Energy*, vol. 4, no. 4, pp. 1051–1064, 2013.

[2] S. Debnath, J. Qin, B. Bahrani, M. Saeedifard, and P. Barbosa, “Operation, Control, and Applications of the Modular Multilevel Converter: A Review,” *IEEE Trans. Power Electron.*, vol. PP, no. 99, pp. 1–1, 2014.

[3] P. Samuel, R. Gupta, and D. Chandra, “Grid Interface of Wind Power With Large Split-Winding Alternator Using Cascaded Multilevel Inverter,” *IEEE Trans. Energy Convers.*, vol. 26, no. 1, pp. 299–309, Mar. 2011.

[4] Global Wind Energy Council (GWEC), “Global Wind Statistics Report 2016,” 2016.

[5] V. Yaramasu, B. Wu, P. C. Sen, S. Kouro, and M. Narimani, “High-power wind energy conversion systems: State-of-the-art and emerging technologies,” *Proc. IEEE*, vol. 103, no. 5, pp. 740–788, 2015.

[6] F. Blaabjerg, “Future on Power Electronics for Wind Turbine Systems,” *IEEE J. Emerg. Sel. Top. Power Electron.*, vol. 1, no. 3, pp. 139–152, 2013.

[7] A. E. Fitzgerald, J. Charles Kingsley, and S. D. Umans, *Electric machinery*, Sixth. McGraw-Hill Higher Education, 2003.

[8] O. Keysan, A. S. McDonald, and M. Mueller, "A direct drive permanent magnet generator design for a tidal current turbine(SeaGen)," *2011 IEEE Int. Electr. Mach. Drives Conf. IEMDC 2011*, pp. 224–229, 2011.

[9] A. S. McDonald, "Structural analysis of low speed, high torque electrical generators for direct drive renewable energy converters," University of Edinburgh, UK, 2008.

[10] H. Polinder, D. Bang, A. S. Mcdonald, and M. A. Mueller, "10 MW Wind Turbine Direct-Drive Generator Design with Pitch or Active Speed Stall Control," in *2007 IEEE International Electric Machines & Drives Conference (IEMDC)*, 2007, pp. 1390–1395.

[11] M. A. Mueller, A. S. McDonald, and D. E. Macpherson, "Structural analysis of low-speed axial-flux permanent-magnet machines," *IEE Proceedings-Electric Power Appl.*, vol. 152, no. 6, pp. 1417–1426, 2005.

[12] C. Rans, S. Teixeira, and D. Freitas, "Bending Deflection – Macaulay Step Functions." [Online]. Available: https://ocw.tudelft.nl/wp-content/uploads/Deflection-via-step-functions.pdf. [Accessed: 16-Aug-2017].

[13] O. Keysan, A. S. McDonald, and M. Mueller, "Integrated Design and Optimization of a Direct Drive Axial Flux Permanent Magnet Generator for a Tidal Turbine," in *International Conference on Renewable Energies and Power Quality - ICREPQ'10*, 2010.

[14] "NEMA Insulation Classes." [Online]. Available: http://www.engineeringtoolbox.com/nema-insulation-classes-d_734.html. [Accessed: 27-Sep-2017].

[15] "Neodymium Magnets | Arnold Magnetic Technologies." [Online]. Available: http://www.arnoldmagnetics.com/en-us/Products/Neodymium-Magnets. [Accessed: 27-Sep-2017].

[16] V. Ruuskanen, "Design Aspects of Megawatt-Range Direct-Driven Permanent Magnet," Lappeenranta University of Technology,PhD Thesis, 2011.

[17] A. Parviainen, M. Niemela, J. Pyrhonen, and J. Mantere, "Performance comparison between low-speed axial-flux and radial-flux permanent-magnet machines including mechanical constraints," *IEEE Int. Conf. Electr. Mach. Drives, 2005.*, pp. 1695–1702, 2005.

[18] A. Parviainen, "Design of Axial-Flux Permanent-Magnet Low-Speed Machines and Performance Comparison between Radial-Flux and Axial-Flux Machines," Lappeenranta University of Technology, PhD Thesis, 2005.

[19] J. Braid, A. van Zyl, and C. Landy, "Design, analysis and development of a multistage axial-flux permanent magnet synchronous machine," *Africon Conf. Africa, 2002. IEEE AFRICON. 6th*, vol. 2, pp. 675–680, 2002.

[20] "Rüzgar Santralleri (RES) YEKDEM Geliri." [Online]. Available: http://www.enerjiatlasi.com/epias/res-yekdem-geliri. [Accessed: 23-Oct-2017].

THE INTERNATIONAL CONFERENCE ON
WIND ENERGY HARVESTING 2018
21-23 March 2018
Catanzaro Lido, Italy

Paper TS3.2.4.

ENERGY HARVESTING SYSTEM FOR THE POWER SUPPLY OF A SHUNT PIEZOELECTRIC SYSTEM DEVELOPED FOR VIBRATION SUPPRESSION

Georgios K. Tairidis[1], Konstantinos Marakakis[1], Panagiotis Koutsianitis[1], Georgia Foutsitzi[2], Georgios E. Stavroulakis[1]*, Jean-Francois Deü[3] and Roger Ohayon[3]

[1]School of Production Engineering and Management, Technical University of Crete, Greece
[2]School of Management and Economics, Technological Educational Institute of Epirus, Greece
[3]Structural Mechanics and Coupled Systems Laboratory, Conservatoire national des arts et métiers, France
Corresponding author: Georgios E. Stavroulakis, gestavr@dpem.tuc.gr

ABSTRACT

Mechanical energy harvesting attracted a lot of scientific interest during the last two decades. Shunt piezoelectric systems are used for vibration damping. The addition of energy harvesting can be proved very effective. The proposed implementation will be restricted to the collection of the necessary amount of energy in order to make the system self-sustained, thus to achieve zero energy consumption. This technology has a potential of making structures, in particular wind energy ones, more quiet and safer.

1. INTRODUCTION

Smart structures incorporate sensors, actuators, and controllers in order to respond and/or suppress excitations which, in turn, are caused by external and/or unknown reasons. Several smart materials such as piezoelectrics or piezoceramics, shape memory alloys, electrostrictive and magnetostrictive materials, fiber optics etc. can be employed in structures in order to provide them with smart characteristics. An important remark is that due to the nature of the piezoelectric effect, the combination of both functions, i.e. sensing and actuation, is possible. Due to this capability, an increasing interest in passive control of vibrations by shunted piezoelectric transducers with electrical impedances is observed. Shunt piezoelectric systems are also widely used, as the method of shunt damping using piezoelectric materials is a popular method for the vibration suppression of smart flexible structures [1], [2]. In addition, energy harvesting can be added to a structure with shunt circuits in order to provide the small amount of energy which is required for the controller.

Several investigations are proposed in the recent literature. For example, in [3] an analytical modelling of electromechanical piezoelectric bimorph beams under multidirectional excitation is presented, and the combinations of parameters in order to optimize maximum energy harvesting are sought.

In [4] the effect of structural dynamics on voltage generation from dual coupled cantilever based piezoelectric vibration energy harvester systems is investigated. A comparison of two important techniques for the formulation of the electromechanical piezoelectric equations for power harvesting system applications is carried out in [5]. The investigation shows the interconnection between the fundamental physical parameters of charge- and voltage-type equations and the electrical systems. These techniques can be used to many applications. For example, in [6] a smart composite turbomachine blade serves as a test structure for optimum piezoelectric patch positioning. From the investigation it turned out that for a given total patch region, many small patches surpass a single large patch. In addition, a blade with optimized piezo position has a 34.5% higher generalized electromechanical coupling coefficient.

As for the energy harvesting capabilities on shunted piezoelectrics, several papers can be found in literature. For example, in [7] a technique for self-adapting harvesting response capabilities for the tuning of the frequency band and the power amplitude of the harvesting devices is proposed. An efficient and robust broadband power generation for application in self-powered wireless sensor devices is suggested by Lumentut et al. in [8]. Moreover, in [9] the implementation of an autonomous switching resistor–inductor (*R–L*) shunt circuit for the control of structure vibration is presented. The resulting switch shunt circuit, does not require power for its operation and is proved to be effective. Experiments have shown that the automatic R-L switching branch achieves a reduction in vibration reduction of 8 dB, whereas R shunts achieves damping of only 1.5 dB.

The studied techniques have the potential to suppress vibrations and noise of flexible structures, both of importance for urban applications of wind energy turbines.

2. METHODOLOGY

The shunt vibration damping is based on the connection of an electrical impedance to a structurally bonded piezoelectric transducer (see Figure). No external sensors are required. Moreover, if designed properly, piezoelectric shunt damping can guarantee stability of the whole shunted system [10]. The main concept is based on a series inductor-resistor network which can significantly reduce vibration of a single structural mode. The network, along with the innate capacitance of the piezoelectric component, is tuned to the resonance frequency of the mode to be damped.

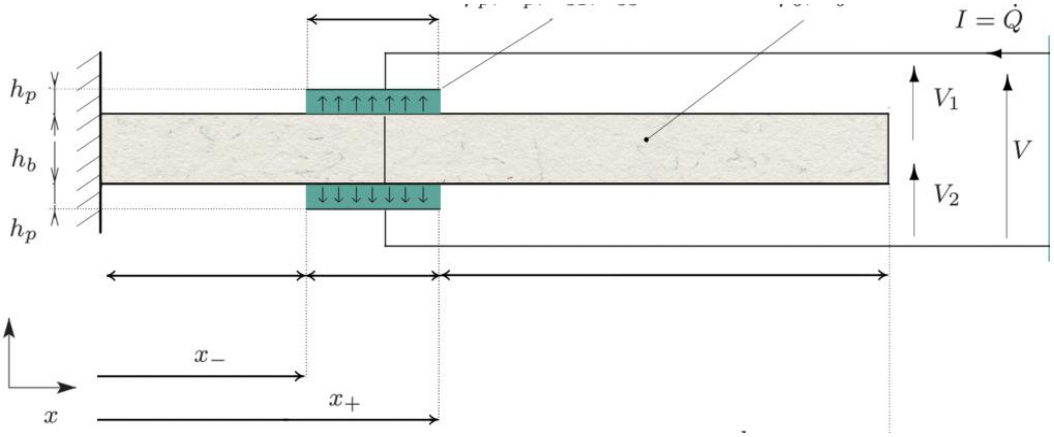

Figure 1: A beam model with a resonant shunt piezoelectric circuit

Furthermore, through harvesting, the system becomes self-sustained. This technology as a whole can provide better and safer structures, by reducing fatigue, noise and vibration and enhancing efficiency. The proposed system can be applied to simple structures, such as beams and plates, however it can be extended to bigger designs, such as wind turbine piles. The energy harvester which is considered here is based on modal analysis techniques, that is on the internal characteristics of the beam structure with the bonded piezoelectric patches and shunt circuits. The estimation of the energy production (*En*) from each piezoelectric element of the structure for every eigenvector is given as:

$$En = \frac{1}{2} E \left(\frac{\Delta u}{L}\right) V \tag{1}$$

where E is the elastic modulus, L is the length of the beam and V is the volume of the structure. The quantity Δu is given as:

$$\Delta u = \left(\varphi_i^j - \varphi_{i+1}^j\right) \frac{h}{2} \tag{2}$$

where φ_i^j and φ_{i+1}^j are the ith and i+1th element respectively of the jth eigenvector and *h* is the height of the beam.

3. RESULTS - CONCLUSIONS

A single piezoelectric patch is placed near the fixed end of the beam as shown in Figure . The length of the beam (*L*) is 0.170 m with cross-sectional area (*A*) of 0.002x0.02 m^2. The elastic modulus (*E*) of structure is 72x10^9 N/m^2 and the mass density (ρ) of the beam is 2800 kg/m^3 [11].

The structure is discretized using the finite element method into 41 elements (42 nodes), with three degrees of freedom per node, yielding to a system with 126 degrees of freedom. The piezoelectric patch is placed at the elements 2 to 6 occupying 5 elements. In the present investigation, the first four eigenmodes of the system are studied. At each case, a different shunt resonant circuit is connected to the piezoelectric patch. The values of the inductance *L* and the resistance *R* are given as [11]:

$$L = \frac{\sqrt{2k_{c,i}^2}}{C\omega_i(1+k_{c,i}^2)} \ , R = \frac{1}{C\omega_i^2(1+k_{c,i}^2)} \tag{3}$$

where $k_{c,i}$ is the coupling factor for the ith mode, C is the capacitance of the piezoelectric patch, and ω_i is the ith eigenfrequency.

For the first eigenvector, the maximum amount of energy is 4.84·10^5 J and appears at the 7th element. Similarly, as for the second mode, the maximum energy is found at the 26th element and it is equal to 1.38·10^7 J. For the third eigenmode the maximum amount of energy, which can be harvested through the piezoelectric materials, is 1.17·10^8 J and appears at the 32nd element. Finally, for the fourth vector, an amount of 3.92·10^8 J can be collected at the 35th element. The results of the harvesting system are given schematically in the Figure 2 and Figure 3 below.

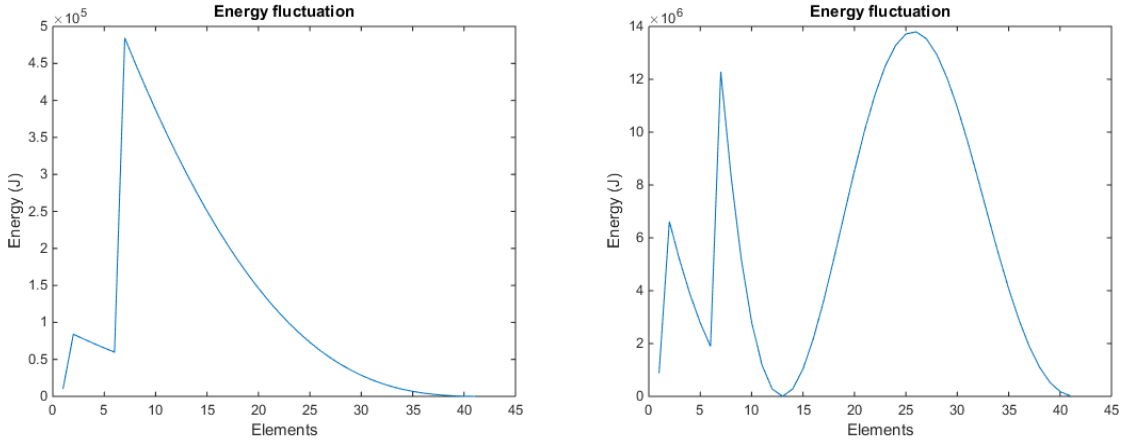

Figure 2: The fluctuation of energy for the 1st and the 2nd eigenvector

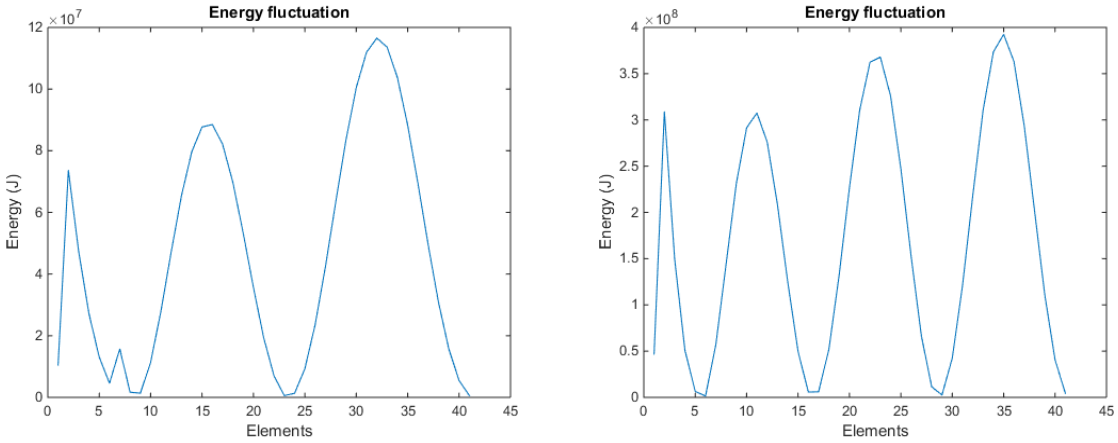

Figure 3: The fluctuation of energy for the 3rd and the 4th eigenvector

ACKNOWLEDGEMENTS

The work of Georgios Tairidis has been supported by a postdoctoral research grant through the "IKY fellowship of excellence for postgraduate studies in Greece – Siemens programme".

Georgios Tairidis also gratefully acknowledges the French Embassy in Greece and the French Government for the funding of his visit to the Structural Mechanics and Coupled Systems Laboratory of the institute Conservatoire national des arts et métiers though a fellowship of the program "Séjours scientifiques de haut niveau" for new researchers, as well as Professor Jean-Francois Deu and Professor Roger Ohayon of Conservatoire national des arts et métiers for their precious assistance and cooperation.

REFERENCES

[1] J.-F. Deu, W. Larbi, R. Ohayon and R. Sampaio, "Piezoelectric Shunt Vibration Damping of Structural-Acoustic Systems: Finite Element Formulation and Reduced-Order Model," *J. Vib. Acoust*, vol. 136, no. 3, p. 031007 (8 pages), 2014.

[2] W. Larbi , J.-F. Deu and R. Ohayon, "Finite element reduced order model for noise and vibration reduction of double sandwich panels using shunted piezoelectric patches," *Applied Acoustics*, vol. 108, pp. 40-49, 2016.

[3] M. F. Lumentut and I. M. Howard, "Analytical modeling of self-powered electromechanical piezoelectric bimorph beams with multidirectional excitation," *International Journal of Smart and Nano Materials*, vol. 2, no. 3, pp. 134-175, 2011.

[4] K. S. Yee, Z. Shakir Radeef, O. Z. Chao, Y.-H. Huang, . C. W. Tong and Z. Ismail, "Zubaidah Ismail. Structural dynamics effect on voltage generation from dual coupled cantilever based piezoelectric vibration energy harvester system," *Measurement*, vol. 107, pp. 41-52, 2017.

[5] M. F. Lumentut and I. M. Howard, "Intrinsic electromechanical dynamic equations for piezoelectric power harvesters," *Acta Mech*, vol. 228, pp. 631-650, 2017.

[6] F. Bachmann, A. E. Bergamini and P. Ermani, "Optimum Piezoelectric Patch Positioning: A Strain Energy-Based Finite Element Approach," *Journal of Intelligent Material Systems and Structures*, vol. 23, p. 1576, 2012.

[7] M. F. Lumentut and I. M. Howard, "Effect of shunted piezoelectric control for tuning piezoelectric power harvesting system responses - analytical techniques," *Smart Mater. Struct.*, vol. 24, 2015.

[8] M. F. Lumentut and I. M. Howard, "Electromechanical analysis of an adaptive piezoelectric

energy harvester controlled by two segmented electrodes with shunt circuit networks," *Acta Mech*, vol. 228, pp. 1321-1341, 2017.

[9] D. Niederberger and M. Morari, "An autonomous shunt circuit for vibration damping," *Smart Mater. Struct*, vol. 15, p. 359, 2006.

[10] R. S. Moheimani and A. J. Fleming, Piezoelectric Transducers for Vibration Control and Damping, London: Springer-Verlag, 2006.

[11] O. Thomas, J.-F. Deü and J. Ducarne, "Vibrations of an elastic structure with shunted piezoelectric patches: efficient finite element formulation and electromechanical coupling coefficients," *Int. J. Numer. Meth. Engng*, vol. 80, pp. 235-268, 2009.

TECHNICAL SESSION 4.1

Work Packages 1 and 5 - Aerodynamic Performance of Wind Turbines

Paper TS4.1.1

THE INTERNATIONAL CONFERENCE ON
WIND ENERGY HARVESTING 2018
21-23 March 2018
Catanzaro, Italy

Influence of Airfoil Maximum Thickness on Aerodynamic Performance of Vertical Axis Wind Turbines

Abdolrahim Rezaeiha[a]*, Hamid Montazeri[a,b], Bert Blocken[a,b]

[a]Building Physics and Services, Department of the Built Environment, Eindhoven University of Technology, P.O. Box 513, 5600 MB Eindhoven, The Netherlands
[b]Building Physics Section, Department of Civil Engineering, KU Leuven, Kasteelpark Arenberg 40 – Bus 2447, 3001 Leuven, Belgium
Corresponding author: a.rezaeiha@tue.nl

ABSTRACT

Airfoil shape can significantly influence the aerodynamic performance of vertical axis wind turbines (VAWTs). However, while the symmetric NACA airfoil series are widely used for VAWTs, the effect of parameters, which define the shape of an airfoil, on the aerodynamic performance of VAWTs has not yet been extensively studied. The current study, therefore, intends to systematically investigate the effect of airfoil maximum thickness t_m on the aerodynamic performance of VAWTs for different tip speed ratios (λ). Unsteady Reynolds-Averaged Navier-Stokes (URANS) calculations are performed on high-resolution gird. The results show that the optimum t_m decreases from 24%c (airfoil chord) to 12%c when λ increases from 2.5 to 5.5. As higher λ corresponds to lower variations of angle of attack (α) of the blades, the better performance of thinner airfoils at such λ is associated to their higher C_l/C_d at such α. Higher stall angle could explain the higher C_P of thicker airfoils at low λ. The current findings could support the optimization of airfoils for VAWTs.

1. INTRODUCTION

Vertical axis wind turbines (VAWTs) have recently received growing interest. The renewed interest, which is mainly for offshore applications [1] and in the built environments [2], stems from advantages including omni-directional capability, low manufacturing, installation and maintenance costs, lower noise, robustness, reliability and scalability. Many studies have focused to further clarify the underlying physics of VAWTs, which is highly driven by complex flow phenomena such as dynamic stall and blade-wake interactions [3].

Characterization and improvement of the aerodynamic performance of VAWTs have also been the center of attention where many operational and geometrical parameters such as tip speed ratio λ [4], solidity [5], number of blades [6], pitch angle [7], turbine shaft size [8] have been studied. Earlier studies have shown the important impact of the airfoil shape as it can significantly influence the aerodynamic performance of VAWTs. However, the employed airfoils for VAWTs are mainly the symmetric NACA airfoil series, which have been originally designed for aeronautical applications, i.e. helicopters. An extensive literature study shows that high-fidelity numerical studies on airfoil shapes for VAWTs have been performed for random lists of airfoils. Singh et al. [9] and Asr et al. [10] experimentally studied three different airfoils on VAWTs while their focus was on starting behavior of the turbine rather than characterizing the effect of the airfoil shape on the aerodynamic performance of the turbine. Mohammad [11] and Elkhoury et al. [12] numerically studied several symmetric and asymmetric airfoils for VAWTs, while the comparison of the computational settings employed in these studies were not in line with the minimum requirements for computational settings suggested by CFD guidelines in the literature [13, 14] which have compromised the accuracy of these calculations.

To the best of our knowledge, therefore, a systematic analysis of the effect of parameters defining the shape of the airfoil on aerodynamic performance of VAWTs for different operating conditions has not

yet been performed. These important parameters include airfoil maximum thickness t_m, position of maximum thickness, leading edge radius, maximum camber and position of maximum camber.

The current study, therefore, intends to investigate the effect of t_m on the aerodynamic performance of VAWTs for different λ values from 2.5 to 5.5. t_m varies from 10 to 24% corresponding to NACA0010-NACA0024 airfoils. The evaluation is based on extensive verification and validation.

The outline of the paper is as follows: the computational settings and parameters are presented in section 2 where the geometrical and operational characteristics of the turbine, computational domain and grid, solver settings and verification and validation studies are discussed. Section 3 presents the CFD results. The conclusions are provided in section 4.

2. COMPUTATIONAL SETTINGS AND PARAMETERS

The geometrical and operational characteristics of the wind turbine are described in Table 1. To simulate the turbine rotation, a computational domain with a rotating core is created where a sliding grid interface with the surrounding fixed domain is employed. The domain width, the distance from the turbine center to the domain inlet and outlet are 20d, 10d and 25d, respectively. Note that the dimensions of the computational domain are chosen based on the CFD guidelines in the literature [13, 14]. The diameter of the rotating core is 1.5d. A high-resolution computational grid consisting of approximately 400,000 quadrilateral cells is generated where the maximum y^+ on the blade walls are below 4 for all cases. The commercial CFD code ANSYS Fluent 16.1 is used to perform the simulations. Incompressible unsteady Reynolds-averaged Navier-Stokes (URANS) simulation are performed in combination with the 4-equation transition SST model. Second-order temporal and spatial discretization and the SIMPLE pressure-velocity coupling scheme are used. The azimuthal increment is 0.1° and the data sampling is initiated after 20 turbine revolutions to reach a statically steady solution. The boundary conditions are uniform velocity inlet, zero gauge pressure outlet, symmetry sides and no-slip walls. The computational settings are according to the guidelines by Rezaeiha et al. [13, 14]. The evaluations are based on extensive verification and validation [7, 8, 13].

Table 1. Geometrical and operational characteristics of the VAWT.

Parameter	Value	Parameter	Value
Number of blades, n	2	Airfoil chord, c [m]	0.06
Diameter, d [m]	1	Shaft diameter [m]	0.04
Height, H [m]	1	Freestream velocity, U_∞ [m/s]	9.3
Solidity, σ [-]	0.12	Freestream total turbulence intensity	5%

3. EFFECT OF AIRFOIL MAXIMUM THICKNESS

Symmetric NACA airfoil series with $10\%c \leq t_m \leq 24\%c$ (see Fig. 1) are employed to investigate the effect of airfoil maximum thickness on the aerodynamic performance of VAWTs within a wide range of λ values from 2.5 to 5.5. The airfoils have their maximum thickness at 30% of the chord from the leading edge.

Turbine power coefficients C_P calculated for the last turbine revolution with the different airfoils, shown in Fig. 1, are depicted in Fig. 2a for different values of λ. The comparison shows that at high λ (≥ 3.5), thinner airfoils outperform the thicker airfoils while this reverses for $\lambda < 3.5$ where thicker airfoils yield in higher C_P. To further clarify the effect of t_m on C_P, Fig. 2b shows the variations of C_P versus t_m for different λ values. It can be seen that for $\lambda = 2.5$, as t_m increases, C_P monotonically increases. The improvement of 294% is achieved when t_m increases from 10% to 24%. For $2.5 < \lambda \leq 5.5$, however, there exists an optimal t_m ($t_{m,opt}$). By increasing λ from 3.0 to 4.5, the $t_{m,opt}$ asymptotically reduces from 18%c to smaller value of 12%c (see Fig. 3).

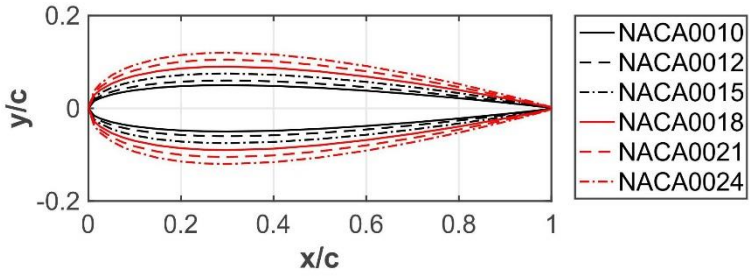

Figure 1. Profiles of the studied airfoils.

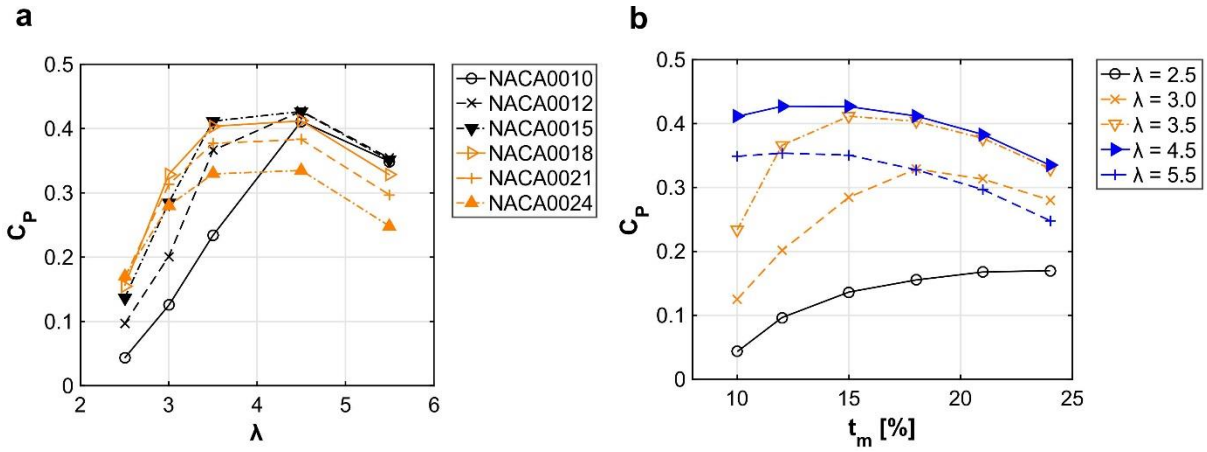

Figure 2. Power coefficient for the last turbine revolution (a) versus tip speed ratio for airfoil with different maximum thickness, 10-24%; (b) versus airfoil maximum thickness for different tip speed ratios, 2.5-5.5.

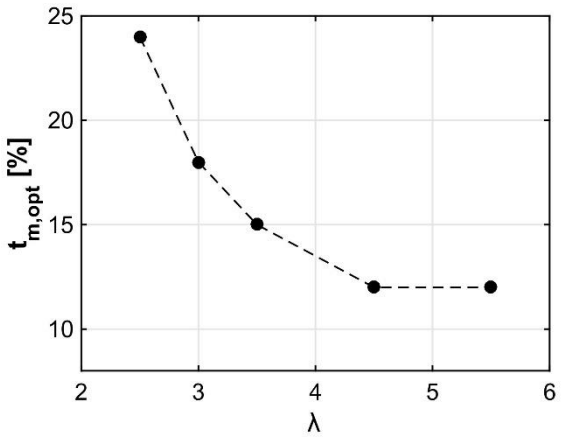

Figure 3. Optimal airfoil maximum thickness versus tip speed ratio.

Turbine instantaneous moment coefficient C_m during the last revolution for turbines with different airfoils at is illustrated in Fig. 4 for different values of λ. It can be seen that the higher C_P corresponding to thicker airfoils at low λ (< 3.5) could be mainly associated to their higher stall angle. This is inferred from later drop of C_m for thicker airfoils within $45° \leq \theta \leq 90°$. In addition, the softer stall behavior of these airfoils also is influential on variation of C_m within the aforementioned θ: the thinner airfoils go through a sudden drop in C_m while this drop is more gradual for thicker airfoils. The better performance of thinner airfoils at λ > 3.5 is mostly attributed to their higher C_l/C_d prior to stall. Note that λ > 3.5 corresponds to smaller variations of angle of attack on blades, which means that the blades mostly operate prior to stall and the flow is mostly attached.

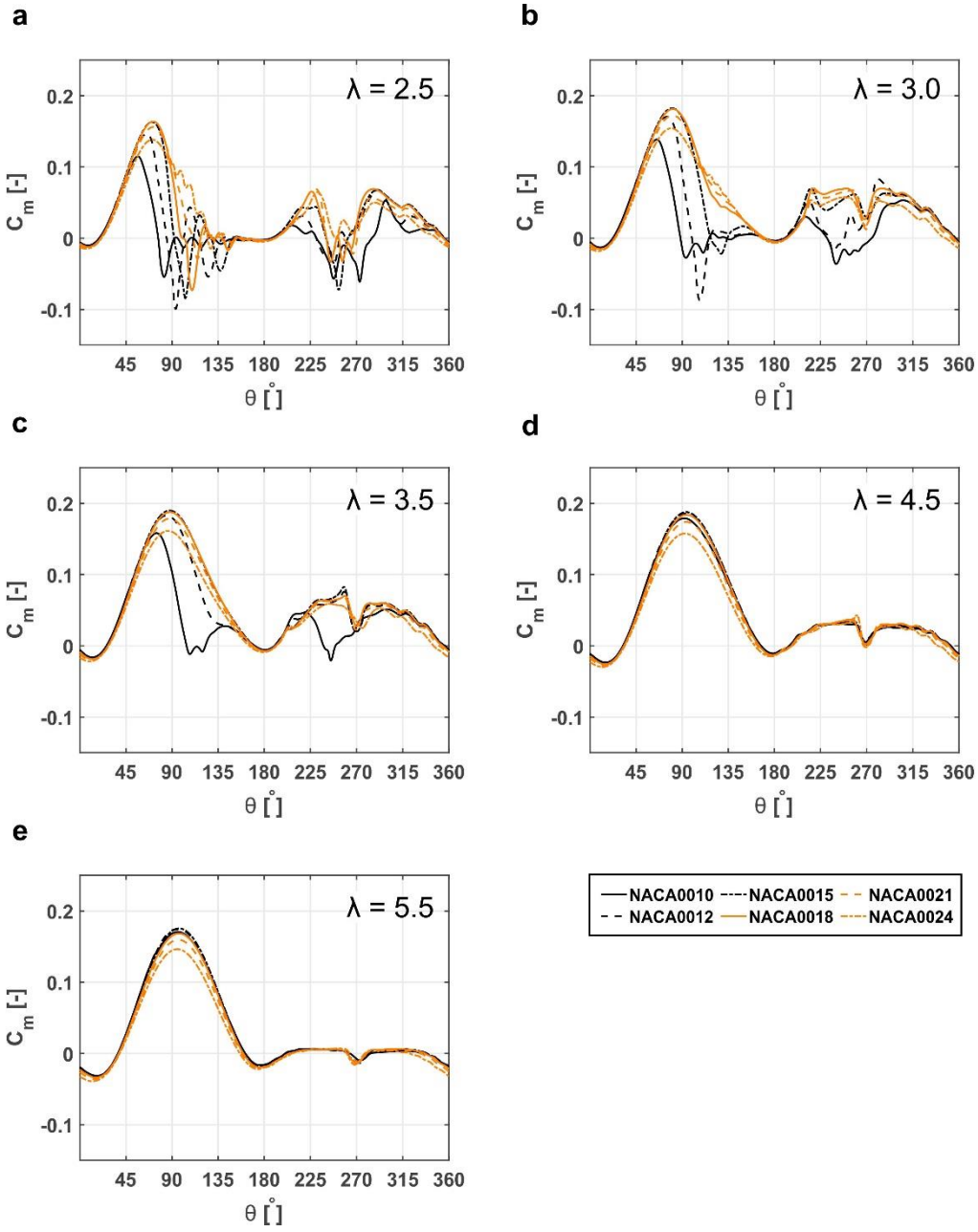

Figure 4. Instantaneous moment coefficient (during the last turbine revolution) at different tip speed ratios for airfoils with different maximum thickness, 10-24%.

4. ACKNOWLEDGEMENT

The authors would like to acknowledge support from the European Commission's Framework Program Horizon 2020, through the Marie Curie Innovative Training Network (ITN) AEOLUS4FUTURE - Efficient harvesting of the wind energy (H2020-MSCA-ITN-2014: Grant agreement no. 643167) and the TU1304 COST ACTION "WINERCOST". The authors gratefully acknowledge the partnership with ANSYS CFD. This work was sponsored by NWO Exacte Wetenschappen (Physical Sciences) for the use of supercomputer facilities, with financial support from the Nederlandse Organisatie voor Wetenschappelijk Onderzoek (Netherlands Organization for Scientific Research, NWO). The 2nd author, Hamid Montazeri, is currently a postdoctoral fellow of the Research Foundation – Flanders (FWO) and is grateful for its financial support (project FWO 12M5316N).

5. CONCLUSIONS

CFD simulations are performed to systematically investigate the effect of airfoil maximum thickness on aerodynamic performance of VAWTs at different tip speed ratios. The results reveal that the optimum t_m asymptotically decreases from 24%c at $\lambda = 2.5$ to 12%c at $\lambda = 5.5$. The better performance of thicker airfoils at small λ could be a result of their higher stall angle and soft stall behavior while higher C_l/C_d of thinner prior to stall explains their improved C_P at higher λ. The Weibull distribution of wind speed at potential installation locations, e.g. urban or sub-urban areas, can be employed to identify the most dominant wind speed regime and the corresponding λ so that the airfoil that yields the highest annual energy power (AEP) can be selected. To fully characterize the influence of airfoil shape on the aerodynamic performance of VAWTs, our future studies will investigate the effect of other important parameters defining the shape of the airfoil such as position of maximum thickness, leading edge radius, maximum camber and position of maximum camber.

6. REFERENCES

[1] Bedon G, Schmidt Paulsen U, Aagaard Madsen H, Belloni F, Raciti Castelli M, and Benini E, "Computational assessment of the DeepWind aerodynamic performance with different blade and airfoil configurations," *Applied Energy,* vol. 185 (2), pp. 1100-1108, 2017.

[2] Li QS, Shu ZR, and Chen FB, "Performance assessment of tall building-integrated wind turbines for power generation," *Applied Energy,* vol. 165, pp. 777-788, 2016.

[3] Simão Ferreira C, van Kuik G, van Bussel G, and Scarano F, "Visualization by PIV of dynamic stall on a vertical axis wind turbine," *Experiments in Fluids,* vol. 46 (1), pp. 97-108, 2008.

[4] Parker CM and Leftwich MC, "The effect of tip speed ratio on a vertical axis wind turbine at high Reynolds numbers," *Experiments in Fluids,* vol. 57 (5), 2016.

[5] Li Q, Maeda T, Kamada Y, Murata J, Shimizu K, Ogasawara T, Nakai A, and Kasuya T, "Effect of solidity on aerodynamic forces around straight-bladed vertical axis wind turbine by wind tunnel experiments (depending on number of blades)," *Renewable Energy,* vol. 96, pp. 928-939, 2016.

[6] Li Qa, Maeda T, Kamada Y, Murata J, Furukawa K, and Yamamoto M, "Effect of number of blades on aerodynamic forces on a straight-bladed Vertical Axis Wind Turbine," *Energy,* vol. 90, pp. 784-795, 2015.

[7] Rezaeiha A, Kalkman I, and Blocken B, "Effect of pitch angle on power performance and aerodynamics of a vertical axis wind turbine," *Applied Energy,* vol. 197, pp. 132-150, 2017.

[8] Rezaeiha A, Kalkman I, Montazeri H, and Blocken B, "Effect of the shaft on the aerodynamic performance of urban vertical axis wind turbines," *Energy Conversion and Management,* vol. 149 (C), pp. 616-630, 2017.

[9] Singh MA, Biswas A, and Misra RD, "Investigation of self-starting and high rotor solidity on the performance of a three S1210 blade H-type Darrieus rotor," *Renewable Energy,* vol. 76, pp. 381-387, 2015.

[10] Asr MT, Nezhad EZ, Mustapha F, and Wiriadidjaja S, "Study on start-up characteristics of H-Darrieus vertical axis wind turbines comprising NACA 4-digit series blade airfoils," *Energy,* vol. 112, pp. 528-537, 2016.

[11] Mohamed MH, "Performance investigation of H-rotor Darrieus turbine with new airfoil shapes," *Energy,* vol. 47 (1), pp. 522-530, 2012.

[12] Elkhoury M, Kiwata T, and Aoun E, "Experimental and numerical investigation of a three-dimensional vertical-axis wind turbine with variable-pitch," *Journal of Wind Engineering and Industrial Aerodynamics,* vol. 139, pp. 111-123, 2015.

[13] Rezaeiha A, Kalkman I, and Blocken B, "CFD simulation of a vertical axis wind turbine operating at a moderate tip speed ratio: guidelines for minimum domain size and azimuthal increment," *Renewable Energy,* vol. 107, pp. 373-385, 2017.

[14] Rezaeiha A, Montazeri H, and Blocken B, "Towards accurate CFD simulations of vertical axis wind turbines at different tip speed ratios and solidities: guidelines for azimuthal increment, domain size and convergence," *Energy Conversion and Management,* vol. 156 (C), pp. 301-316, 2018.

Paper TS4.1.2

THE INTERNATIONAL CONFERENCE ON
WIND ENERGY HARVESTING 2018
21-23 March 2018
Catanzaro, Italy

AIRFOIL TRAILING-EDGE NOISE PREDICTION USING A STOCHASTIC SOUND SOURCE GENERATION TECHNIQUE

A. H. Kadar[1*], S. Le Bras[1] and W. Desmet[2]

[1]Siemens Industry Software N.V., Leuven, Belgium
[2]Department of Mechanical Engineering, K.U. Leuven, Belgium
Corresponding author: A. H. Kadar, a.h.kadar@gmail.com

ABSTRACT

In this study, a Computational Aeroacoustics (CAA) method is presented for the prediction of trailing-edge noise. The numerical strategy is based on the use of a Random Particle-Mesh (RPM) method to compute noise sources, and the resolution of Acoustic Perturbation Equations to propagate sound waves. RPM is a stochastic method that allows to model flow generated noise sources. It reconstructs turbulent velocity fluctuations from target turbulent kinetic energy and length scale distributions. These target quantities are obtained from a preliminary incompressible Reynolds-Averaged Navier-Stokes simulation. The performance of the CAA method is evaluated by simulating the flow around a controlled-diffusion airfoil at a Mach number of 0.047 and a Reynolds number based on the airfoil chord length of 1.6×10^5. The results are found to be in good agreement with Large Eddy Simulation results and experimental measurements from literature. In particular, the trailing edge noise radiated in the far-field region is successfully predicted.

NOMENCLATURE

CAA	=	Computational Aeroacoustics
CFD	=	Computational Fluid Dynamics
DNS	=	Direct Numerical Simulation
LES	=	Large Eddy Simulation
RPM	=	Random Particle-Mesh Method
RANS	=	Reynolds-Averaged Navier-Stokes
APE	=	Acoustic Perturbation Equations

1. INTRODUCTION

Wind turbine noise is now a growing concern [1] due to the close proximity of wind farms to human living areas. The aerodynamic noise, generated by the passage of the air flow over the turbine blade, is a major component of wind turbine noise emissions. Several mechanisms have been identified in the literature [2] to be responsible for flow-induced noise from wind turbines, including turbulent inflow noise, trailing-edge noise and tonal noise due to the interaction of blade wake and turbine tower. Trailing-edge noise is a dominant source of wind turbine aerodynamic noise [3,4]. It results from the scattering of the boundary layer disturbances into acoustic waves at the airfoil trailing-edge, as illustrated in Figure 1.

In order to predict trailing-edge noise, Computational Aeroacoustics (CAA) can be used. Among several CAA approaches available in the literature [5], hybrid methods are a popular way to proceed. In such methods, the computation of the acoustic sources is decoupled from the sound wave propagation. Usually, a Computational Fluid Dynamics (CFD) simulation is first carried out in the flow region in order to determine the noise sources. The radiated noise in the near field region is then estimated by resolving acoustic propagation equations. Several CFD strategies can be found in the literature in order

to compute noise sources. Some of them are presented in Figure 2 as a function of the computational cost. The use of high-fidelity, turbulent scale resolving approaches such as Direct Numerical Simulation (DNS) or Large Eddy Simulation (LES) leads to accurate noise predictions. However, these methods remain computationally expensive for industrial applications involving complex geometries and high-speed flows.

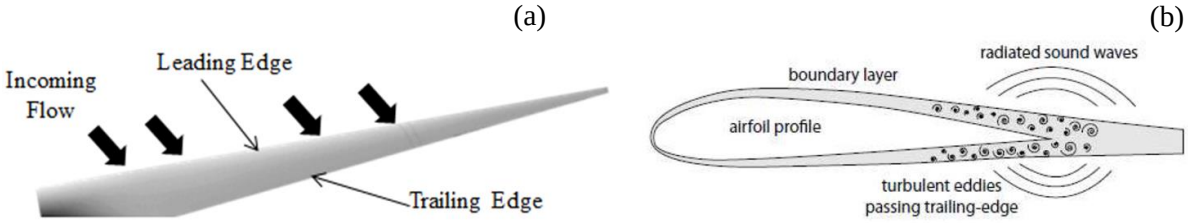

Figure 1. (a) Representation of a wind turbine blade and (b) illustration of the noise generation at the trailing-edge [6].

Alternatively, in order to reduce the computational effort, stochastic methods such as Random Particle-Mesh (RPM) method can be used in combination with Reynolds-Averaged Navier-Stokes (RANS) simulations in order to model the unsteady noise sources. The RPM approach, originally introduced by Ewert et al. [7-9], consists in synthesizing turbulent velocity fluctuations that accurately represent statistical mean flow quantities provided by a preliminary RANS simulation. RANS computes a steady state of the mean flow, and is therefore computationally less expensive than LES/DNS.

Figure 2. Examples of CFD approaches for hybrid CAA applications

In the present work, a hybrid CAA approach based on RPM for noise source computation is considered. The sound wave propagation is then carried out by solving Acoustic Perturbation Equations (APE-4) [10]. The CAA strategy is applied to predict trailing-edge noise radiated from a controlled-diffusion (CD) airfoil [11-14]. This paper is organized as follows: in section 2, the CAA strategy based on RPM is described. Section 3 is dedicated to the application of the CAA strategy to predict trailing-edge noise from the CD airfoil. The acoustic predictions in the far-field region are compared with LES results from literature [12] and available experimental data [13,14].

2. COMPUTATIONAL STRATEGY BASED ON RPM

A schematic overview of the hybrid CAA approach using the stochastic source generation method is shown in Figure 3.

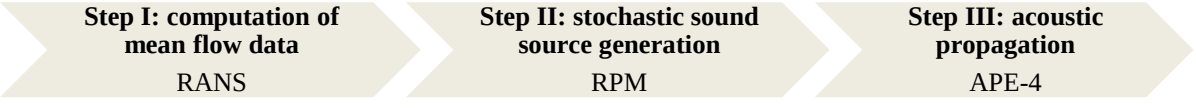

Figure 3. Schematic representation of the CAA approach based on RPM.

The numerical strategy is composed of three steps. In step I, a RANS simulation is performed in order to compute the mean velocity field and the statistical properties of turbulence including the turbulence kinetic energy, the integral length scales and the integral time scales.

Step II is dedicated to the sound source reconstruction. The turbulent velocity fluctuations are stochastically generated using the Random Particle-Mesh (RPM) method introduced by Ewert et al. [7-9]. In the present work, the purely Lagrangian approach of Dieste[15] is used for computing the velocity fluctuations by filtering a stochastic white-noise field. The method requires as input the mean velocity field and the statistical properties of turbulence computed in step I. The velocity fluctuations generated by the RPM method accurately reproduce the target turbulence statistics provided by RANS. The velocity fluctuations are then used to define the vortex sound source term introduced in step III.

In step III, in order to determine the acoustic pressure radiated in the near-field region, the acoustic perturbation equations (APE-4) [10] are solved in time domain using a Discontinuous Galerkin (DG) solver [16,17]. The propagation equations are given by

$$\frac{\partial \acute{p}}{\partial t} + \bar{c}^2 \nabla \cdot \left(\bar{\rho} \acute{\boldsymbol{u}} + \frac{\acute{p}}{\bar{c}^2} \overline{\boldsymbol{u}} \right) = 0,$$

$$\frac{\partial \acute{\boldsymbol{u}}}{\partial t} + \nabla (\overline{\boldsymbol{u}} \cdot \acute{\boldsymbol{u}}) + \nabla \left(\frac{\acute{p}}{\bar{\rho}} \right) = -\acute{\boldsymbol{L}}$$

The quantities with bar $\bar{.}$ denote mean-flow variables and quantities with prime $\acute{.}$ indicate fluctuating quantities. The variables $p, \boldsymbol{u}$ and ρ denote the pressure, velocity vector and density respectively, and $\bar{c}$ denotes the sound speed. The vortex sound source term $\acute{\boldsymbol{L}}$ is given by

$$\acute{\boldsymbol{L}} = (\boldsymbol{\omega} \times \boldsymbol{u})\acute{},$$

where $\boldsymbol{\omega}$ is the vorticity vector. The source term $\acute{\boldsymbol{L}}$ can be approximated by discarding the non-linear terms as follows

$$\acute{\boldsymbol{L}} \cong \overline{\boldsymbol{\omega}} \times \acute{\boldsymbol{u}} + \acute{\boldsymbol{\omega}} \times \overline{\boldsymbol{u}}$$

where, the mean velocity $\overline{\boldsymbol{u}}$ and the mean vorticity $\overline{\boldsymbol{\omega}}$ are obtained from RANS in step I and the fluctuating quantities $\acute{\boldsymbol{u}}$ and $\acute{\boldsymbol{\omega}}$ are computed from RPM in step II. In practice, the source term is interpolated from the RPM mesh to the DG mesh. The mean velocity field is not considered for the acoustic propagation, which is supposed to be a good approximation for flows at low Mach number. Finally, a Kirchhoff integral method [18] is applied in order to extrapolate the acoustic pressure to the far-field region.

3. APPLICATION TO CD AIRFOIL

The CAA strategy based on RPM is applied to predict the trailing-edge noise radiated from a controlled-diffusion (CD) airfoil derived from the Valeo automotive cooling module. This airfoil configuration has been thoroughly investigated both numerically [11,12] and experimentally [13,14]. It is therefore a good case in order to study the performance of the hybrid CAA approach before going towards the simulation of more complex wind turbine blade profiles.

A 2-D representation of the CD airfoil is shown in Figure 4. The airfoil has a chord length C_L of 0.1356 m, and a span length L of 0.3 m. The chord length and airfoil cross-section are constant in the spanwise direction. An angle of attack α=8^0 is considered. The flow around the airfoil is characterized by a Mach number of 0.047 and a Reynolds number based on the chord length of 1.6×10^5.

Figure 4. Representation of the CD airfoil.

The hybrid CAA approach applied to the CD airfoil case is illustrated in Figure 5. As the airfoil cross-section is constant in the spanwise direction, the computation can be reduced to a 2D problem. As presented in section 2, first, an incompressible 2-D RANS computation is performed using the SST k-ω turbulence model. The RANS computational domain is presented in blue in Figure 5a. For details about the RANS simulation, the reader can refer to [17]. Then, the RPM stochastic method is applied in 2D to synthesize turbulent velocity fluctuations. For airfoil trailing-edge noise, it is known that the sound sources are located close to the trailing-edge where the turbulent kinetic energy level is high. Therefore, the RPM domain is restricted to a rectangular box including the trailing-edge and the airfoil wake. This box is delimited in red in Figure 5a. A time snapshot of the equivalent sources of sound $\acute{\boldsymbol{L}}$, computed on the RPM grid is shown in Figure 5b. In the final step, the aeroacoustic noise sources estimated from RPM are provided to the acoustic propagation solver in order to determine the acoustic pressure in the near field region, as shown in Figure 5c. Finally, the extrapolation of the acoustic spectra in the far-field region is performed using the Kirchhoff integral method [18]. Note that for comparisons with the data of the literature, a 2D to 3D correction [8] is applied to the acoustic spectrum obtained from RPM.

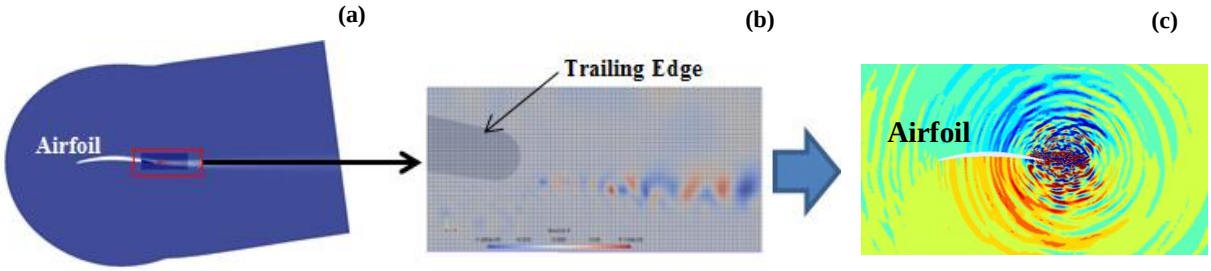

Figure 5. Hybrid CAA approach applied to the CD airfoil case: (a) RANS computational domain (in blue) with the RPM domain (delimited in red). (b) Time snapshot of the Aeroacoustic noise sources computed on the RPM grid, and (c) Time snapshot of the acoustic pressure field radiated in the near-field region.

The far-field sound pressure level computed at an angle of 90^0, and at a distance of 2 meters from the airfoil trailing-edge, is represented in Figure 6. The frequency spectrum obtained from CAA+RPM is compared with data from LES[12] and experiments[13,14]. The CAA-RPM results are in good agreement with the experimental data, within a maximum difference of 5 dB. The CAA-RPM spectrum compares well with the LES spectrum over the frequency range [400Hz-1500Hz].

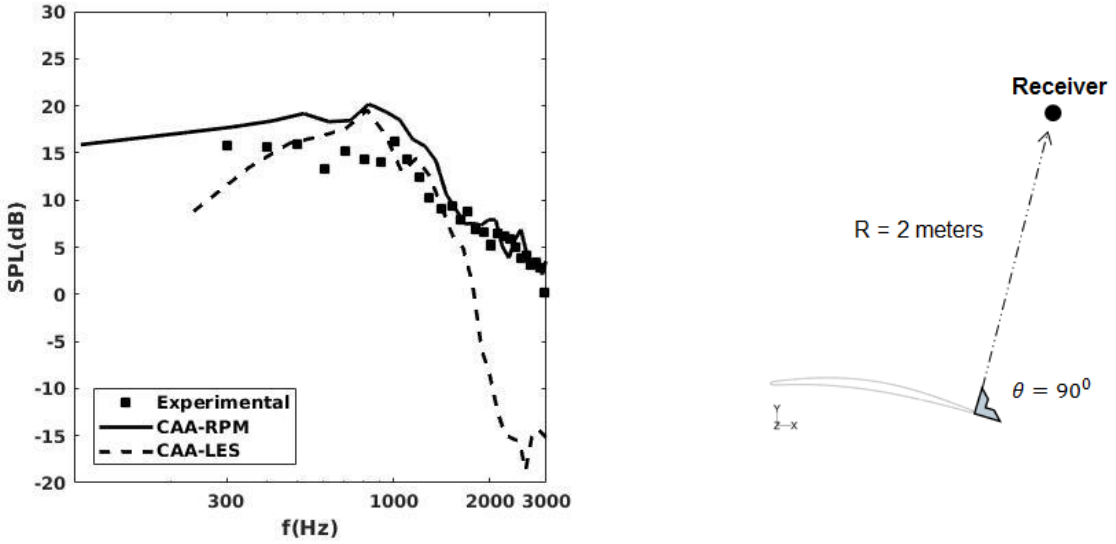

Figure 6. Comparison of the sound pressure levels at a distance of 2 meters and an angle of $\mathbf{90^0}$ from the airfoil trailing edge: CAA-RPM, CAA-LES[12] and ▪ experiment[13,14].

4. CONCLUSIONS

In this paper, a hybrid CAA approach is presented wherein the aeroacoustic sources are stochastically generated using a Random Particle-Mesh (RPM) technique. This approach only requires steady RANS CFD data as inputs, and is therefore less computationally expensive than high-fidelity CFD approaches such as LES/DNS. The hybrid CAA approach based on RPM is applied in 2D to predict the trailing-edge noise radiated from a airfoil with constant cross-section in the spanwise direction. The flow around the airfoil is at a low Mach number of 0.047 and a Reynolds number based on the airfoil chord length of 1.6×10^5. The acoustic results show a good agreement with the data from the literature, which demonstrates that the CAA strategy based on the RPM technique can be used in 2D to compute trailing edge noise. The next step is now to extend this CAA strategy to 3D in order to apply it to complex wind turbine blade profiles, where the flow cannot be computed by a 2D simulation.

ACKNOWLEDGEMENTS

The authors acknowledge with thanks the support of the European Commission's Framework Program "Horizon 2020", through the Marie Skłodowska-Curie Innovative Training Networks (ITN) "AEOLUS4FUTURE - Efficient harvesting of the wind energy" (H2020-MSCA-ITN-2014: Grant agreement no. 643167) to the present research project.

"The computational resources and services used in this work were provided by the VSC (Flemish Supercomputer Center), funded by the Research Foundation - Flanders (FWO) and the Flemish Government – department EWI".

REFERENCES

[1] J. H. Schmidt, and M. Klokker, "Health effects related to wind turbine noise exposure: A systematic review," *PloS one*, *9*(12), e114183, 2014.

[2] T. F. Brooks, and R. H. Schlinker, "Progress in rotor broadband noise research," *Vertica*, vol. 7, no. 4, pp. 287-307, 1983.

[3] R. H. Schlinker, and R. K. Amiet, "Helicopter rotor trailing edge noise," in *AIAA, Aeroacoustics Conference, 7th, Palo Alto, CA, 5-7.10.1981, 1981*, pp. 26.

[4] S. Oerlemans, P. Sijtsma, and B. M. López, "Location and quantification of noise sources on a wind turbine," *Journal of sound and vibration*, vol. *299*, no. 4, pp. 869-883, 2007.

[5] S.K. Lele, and J.W. Nicholas, "A second golden age of aeroacoustics?," *Philosophical Transactions of the Royal Society A: Mathematical, Physical and Engineering Sciences*, vol. 372, no. 2022, pp. 20130321-20130321, Jul. 2014.

[6] M. Collison, L. Desvard, and R. Stimpson "Vortex Shedding Noise Reduction of a Mixed Flow Fan: Experimental and Numerical Investigation," in *"International conference on Fan noise, Technology and Numerical methods", Lyon, 04.2015*, 2015.

[7] R. Ewert, J. Dierke, J. Siebert, A. Neifeld, C. Appel, M. Siefert, and O. Kornow, "CAA broadband noise prediction for aeroacoustic design," *Journal of sound and vibration*, vol. 330, no. 17, pp. 4139–4160, Apr. 2011.

[8] R. Ewert, C. Appel, J. Dierke, and M. Herr, "RANS/CAA Based Prediction of NACA 0012 Broadband Trailing Edge Noise and Experimental Validation," in *"15th AIAA/CEAS Aeroacoustics Conference", Miami-Florida, 11-13.05.2009*, 2009, pp. 3269.

[9] R. Ewert, "Broadband slat noise prediction based on CAA and stochastic sound sources from a fast random particle-mesh (RPM) method," *Journal of Computers and Fluids*, vol. 37, no. 4, pp. 369–387, May. 2008.

[10] R. Ewert, and W. Schroder, "Acoustic perturbation equations based on flow decomposition via source filtering," *Journal of Computational Physics*, vol. 188, Issue 2, pp. 365–398, July. 2003.

[11] M. Wang, S. Moreau, G. Iaccarino, and M. Roger, "LES prediction of wall-pressure fluctuations and noise of a low-speed airfoil," *Internationl Journal of Aeroacoustics*, vol. 8, no. 3, pp. 177–197, May. 2009.

[12] P. Martínez-Lera, J. Christophe, and C. Schram, "Computation of the self-noise of a controlled-diffusion airfoil based on the acoustic analogy," *International Journal of Aeroacoustics*, vol. 16, no. 1-2, pp. 44–64, Feb. 2017.

[13] S. Moreau, D. Neal, and J. Foss, "Hot-wire measurements around a controlled diffusion airfoil in an open-jet anechoic wind tunnel," *Journal of fluids engineering*, vol. 128, no. 4, pp. 699–706, Dec. 2005.

[14] S. Moreau, M. Henner, G. Iaccarino, M. Wang, and M. Roger, "Analysis of flow conditions in freejet experiments for studying airfoil self-noise," *AIAA Journal*, vol. 41, no. 10, pp. 1895–1905, Oct. 2003.

[15] M. Dieste, "Random-vortex-particle methods applied to broadband fan interaction noise," *Doctoral dissertation, University of Southampton* 2011.

[16] B. Vanelderen, W. De Roeck, and W. Desmet, "Flow noise prediction of confined flows using synthetic turbulence and linearized Euler equations in a hybrid methodology," in "*19th AIAA/CEAS, Aeroacoustics Conference", Berlin-Germany, 27-29.05.2013*, 2013, pp. 2267.

[17] A.H. Kadar, P. Martinez-Lera, C. Schram, W. De Roeck, W. Desmet, and M. Tournour, "Trailing-edge noise prediction using synthetic turbulence and acoustic perturbation equations in a hybrid methodology," in "*23rd AIAA/CEAS, Aeroacoustics Conference", Denver- U.S.A, 5-9.06.2017, 2017,* pp. 3846.

[18] J. Scott, A. Pilon, A. Lyrintzis, and T. Rozmajzl, "A numerical investigation of noise from a rectangular jet," in "35th *AIAA, Aerospace Sciences Meeting & Exhibit", 35th, Reno, NV, 6-9.01.1997.*

Paper TS4.1.3

THE INTERNATIONAL CONFERENCE ON
WIND ENERGY HARVESTING 2018
21-23 March 2018
Catanzaro, Italy

TRAILING EDGE NOISE PREDICTION OF AN AIRFOIL BASED ON WALL PRESSURE SPECTRUM MODELS

Yakut Cansev KÜÇÜKOSMAN [1], Julien CHRISTOPHE[1]. Christophe SCHRAM[1]

[1] von Karman Institute for Fluid Dynamics, Sint-Genesius-Rode, Belgium

ABSTRACT

In this study, a far-field noise prediction of a wind turbine airfoil section is carried out by using Amiet's semi-analytical model to predict far-field noise emitted at the trailing edge. Two-dimensional steady Reynolds Averaged Navier-Stokes computations are performed for DU96-W-180 type airfoil at 4^o angle of attack with a Reynolds number of $\mathrm{Re} = 1.13x10^6$. One statistical model: Panton & Linebarger and six different semi-empirical models: Goody, Rozenberg, Catlett, Kamruzzaman, Hu & Herr and Lee are performed to predict the wall-pressure spectrum near the trailing edge. The statistical model is evaluated by using the boundary layer information obtained from the Reynolds Averaged Navier-Stokes computations, on the other hand, the semi-empirical models are based on the normalization laws obtained by the experimental investigation. The semi-empirical models which are developed from the airfoil experimental data better predict the experimentally obtained far-field trailing-edge noise than the models developed from the flat-plate data. Regarding the model input parameters, it is found that it is not always feasible to obtain boundary parameters in the presence of the high adverse pressure gradient flow. However, the boundary layer profiles are more accessible to obtain which are required by the Panton & Linebarger model. Furthermore, the prediction lies in the range of 2 dB even though, the velocity fluctuations are recreated from an anisotropy factor of a flat plate.

NOMENCLATURE

RANS	=	Reynolds-Averaged Navier-Stokes
ZPG	=	Zero Pressure Gradient
APG	=	Adverse Pressure Gradient
Re	=	Reynolds Number
PSD	=	Pressure Spectrum Density
C	=	Chord (m)
ω	=	Angular Frequency
b	=	Span (m)
l_y	=	Spanwise Correlation Length
$\mathcal{L}$	=	Aeroacoustic Transfer Function
ϕ_{pp}	=	Wall Pressure Spectra
U_c	=	Convection Velocity (m/s)
ρ_∞	=	Density (kg/m^3)
U_∞	=	Freestream Velocity (m/s)

1. INTRODUCTION

The increasing demand for wind energy in the urban areas raises the importance of the noise issues due to the acoustic annoyance they cause in their immediate environment [1]–[3]. The effective noise prediction tools with a low CPU and high accuracy are needed for the early design stage of the wind turbines.

The predominant wind turbine noise production mechanism is associated with the turbulence that develops along the blade surface and scatters at the trailing edge as acoustic waves [4], [5]. This noise

mechanism is associated with the wall-pressure fluctuations beneath a turbulent boundary layer which are scattered by a sharp trailing edge. Kraichnan [6] was the first one who expressed the wall-pressure fluctuation for a flat plate based on the solution of the Poisson equations for incompressible flow. The pressure fluctuation can be obtained from the two-point correlation of the wall-normal velocity fluctuations and the mean velocity profile. Panton & Linebarger [7] obtained the inputs of Kraichnan formulation by an empirically determined analytical expression. Lee et al. [8] showed that these inputs can be obtained directly from the RANS simulations by performing the analyses for a backward step. Remmler et al. [9] performed this analysis on both a flat plate and airfoils. The investigation on the wall-pressure spectrum has served to develop semi-empirical approaches by re-scaling the pressure spectrum. Goody [10] presented a model for zero pressure gradient (ZPG) flow where the Reynolds effects have taken into account by the time-scale ratio, R_T. Moreover, the ω^{-5} decay at the higher frequencies is compensated by adding a term in the denominator. Later, Rozenberg et al. [11] have modified the expression by considering the adverse pressure gradient flow (APG) where they have added additional terms such as the Clauser's parameter [12] and the Coles's parameter [13] to characterize the flow type. Catlett et al. [14] also modified the Goody model for APG flows where they have performed an experiment on a flat plate with different trailing edge configurations. Kamruzzaman et al. [15] proposed another model based on Goody's model where they developed their model by using airfoil measurement data. Hu and Herr [16] argued that the parameter that drives the APG flow should be the shape factor and the scaling factor for the pressure should be the dynamic pressure. From this approach, they have presented another wall-pressure spectrum model. Lastly, Lee and Villaescusa [17] extended the Rozenberg model to provide a better universal match.

In this paper, the comparison of the six different semi-empirical wall-pressure models which are Goody, Rozenberg, Catlett, Kamruzzaman, Hu & Herr and Lee as well as one statistical model which is Panton & Linebarger will be investigated on a cambered airfoil where the adverse pressure gradient is expected to be high. Later, the far-field trailing edge noise prediction will be obtained by Amiet's model which requires the input of wall-pressure spectrum and will be compared with an experimental data to validate the best approach.

2. AMIET'S ANALYTICAL MODEL FOR TRAILING EDGE NOISE

Amiet's theory provides an analytical model to compute the far-field trailing edge noise by considering the scattering of a wall pressure gust convected past the trailing edge [18]. The far-field acoustic PSD (S_{pp}) for trailing edge in the midspan plane at a given observer location, x=(R,θ,z=0) can be written as:

$$S_{pp}(\boldsymbol{x},\omega) = \left(\frac{sin\theta}{2\pi R}\right)^2 (kC)^2 b|\mathcal{L}|^2\, l_y(\omega)\, \phi_{pp}(\omega) \tag{1}$$

where C is the chord length, b is the semi-span, ω is the angular frequency, l_y is the spanwise correlation length, $\mathcal{L}$ is the aeroacoustic transfer function [19], and ϕ_{pp} is the wall pressure spectrum. The spanwise correlation length based on the convection velocity, U_c and a model constant b are computed by the Corcos model [20] as:

$$l_y(\omega) = \frac{bU_c}{\omega} \tag{2}$$

3. WALL PRESSURE SPECTRUM MODELS

This section introduces two different approaches to predict the wall-pressure spectrum. The statistical model is based on the integration of a Poisson equation for pressure. The general input for this model is the velocity profile and the wall-normal pressure fluctuations. The semi-empirical models are based on re-scaling of the pressure spectrum by the boundary layer parameters. The general input for these models is the velocity profile which is obtained through a RANS simulation. The assumptions that have been applied for both methodologies will be explained in the following sub-sections.

3.1. Statistical Model

The wall pressure spectrum is computed by a statistical model proposed by Panton & Linebarger [7] and later revisited by Remmler et al. [9]. The formulation is based on Navier-Stokes equation by reforming it as a Poisson equation for pressure. With the assumption of statistically stationary and homogeneous flow in streamwise and spanwise directions, the Poisson equation can be solved by using the Green's function technique as:

$$\phi(k_1) = 8\rho^2 \iiint_0^\infty \frac{k_1(\omega)^2}{|k|(\omega)^2} e^{-|k|(\omega)\left(y+\tilde{y}_2\right)} S_{22}\left(y,\tilde{y},\omega\right) \times \frac{\partial\langle U_1\rangle}{\partial y}\frac{\partial\langle U_1\rangle}{\partial \tilde{y}} \mathrm{d}y\mathrm{d}\tilde{y}\mathrm{d}k_3 \qquad (3)$$

where $|k| = \sqrt{k_1^2 + k_3^2}$, U_1 is the streamwise velocity and y is the wall-normal direction. The energy spectrum of the vertical velocity fluctuations S_{22} is given as:

$$S_{22}(y,\tilde{y},\omega) = \frac{\overline{u_2'(y)}\overline{u_2'(\tilde{y})}}{\pi^2}\Lambda^2 \int \int_0^\infty R_{22}\, cos(\alpha\tilde{k_1}(\omega)\tilde{r_1}) cos(\tilde{k_3}\tilde{r_3})\mathrm{d}\tilde{r_1}\mathrm{d}\tilde{r_3} \qquad (4)$$

where u_2' is the root mean square of the wall-normal velocity fluctuations, Λ is the integral length scale and α an anisotropy scaling for the streamwise structures compared to the spanwise turbulent length scales. The velocity correlation function R_{22} is modeled according to Panton & Linebarger [7]:

$$R_{22} = [1 - \frac{\tilde{r}^2}{2\sqrt{\tilde{r}^2+\tilde{y}^2}}]e^{-\sqrt{\tilde{r}^2+\tilde{y}^2}} \qquad (5)$$

with $\tilde{r}^2 = \tilde{r_1}^2 + \tilde{r_3}^2$. The non-dimensional parameters were used by modifying the integration coordinates and the wave numbers with the integral length scale, $\tilde{r_i} = r_i/\Lambda$, $\tilde{k_i} = k_i\Lambda$ and $\tilde{y} = (y - \hat{y})/\Lambda$. Monte Carlo method was used to perform the integration [9] since it is hard to perform a fivefold integration numerically. The wall-normal velocity fluctuations are obtained through introducing an anisotropy factor which is obtained from a flat plate boundary layer using a Reynolds stress transport model and is defined for each component as $\beta_i = \overline{u'_i}^2/2k$ [9]. Panton & Linebarger [7] was specified the length scale, Λ, 1.5 times the Prandtl mixing length, l_m. From the simulation, the Prandtl mixing length scale can be assumed as $L = \frac{l_m}{C_m}$ where L is calculated as the ratio of the turbulent kinetic energy and the turbulent dissipation rate:

$$L = C_\mu \frac{k^3/2}{\epsilon} \qquad (6)$$

C_m is a turbulence model constant and was chosen as 1.9 for $k-\omega$ SST [9], C_μ is given as 0.09 and the turbulent dissipation, ϵ, is calculated as $\epsilon = k \cdot \omega$.

3.2. Semi-empirical models

The general form of the semi-empirical models can be expressed in this form:

$$\frac{\varphi_{pp}}{\varphi^*} = \frac{a(\omega^*)^b}{[i(\omega^*)^c + d]^e + [fR_T^g\omega^*]^h} \qquad (7)$$

The parameters, *a-h*, determine the shape of the spectrum in Eq. (7), which are parametrized by experimental data. The parameter *a* only responsible by shifting the amplitude of the spectrum. The ω^2 slope observed at low frequencies are regulated by the parameter *b*. The parameters change the overlap region are *b*, *c* and *e*. The slope at high frequencies is adjusted by the parameter b and h. The overlap region to high frequency transition is adapted by the parameters *f* and *g* with a combination of time-scale ratio, R_T which sets the length of the transition domain. The maxima point on the pressure spectrum is weakly dependent to the parameter *d*. Lastly, *i* parameter is introduced even though it is equal to 1.0 for all the models except the Rozenberg model. The non-dimensional parameters are introduced as φ^* for the pressure scale and ω^* for the frequency scale where each scaling factor differs

from each model. In this paper, six different semi-empirical models: Goody, Rozenberg, Catlett, Kamruzzaman, Hu & Herr and Lee are investigated. The corresponding parameters and scaling factors are given in the following section:

Goody Model

The Goody model [10] is developed for zero pressure gradient flow and extends the overlap region by taking into account the Reynolds effect. Moreover, this model is considered as a base model for the Adverse Pressure Gradient (APG) wall-pressure spectrum models.

a =	3.0	d =	0.5	g =	-0.57	R_T =	$(\delta/U_e)/(\nu/u_\tau^2)$
b =	2.0	e =	3.7	h =	7.0	φ^* =	$\tau_w{}^2\delta/U_e$
c =	0.75	f =	1.1	i =	1.0	ω^* =	$\omega\delta/U_e$

where δ is the boundary layer thickness, τ_w is the wall shear stress and U_e is the freestream velocity.

Rozenberg Model

Rozenberg et al. [11] extended the Goody model by introduceing three parameters which consider the APG effect such as Zagarola-Smits's parameter [21], $\Delta_* = \delta/\delta^*$, where δ^* is the displacement thickness, Clauser's equilibrium parameter [22], $\beta_c = (\theta/\tau_w)(dp/dx)$ where θ is the momentum thickness and Coles' wake parameter [13], Π.

a =	$\left[2.82{\Delta_*}^2(6.13\Delta^{-0.75}+d)^{\,e}\right]\left[4.2\left(\frac{\Pi}{\Delta_*}\right)+1\right]$	g =	-0.57
b =	2.0	h =	$\min\left(3{,}19/\sqrt{R_T}\right)+7$
c =	0.75	i =	4.76
d =	$4.76(1.4/\Delta_*)^{0.75}[0.375e-1]$	R_T =	$(\delta/U_e)/(\nu/u_\tau^2)$
e =	$3.7+1.5\beta_c$	φ^* =	$\tau_{\max}{}^2\delta^*/U_e$
f =	8.8	ω^* =	$\omega\delta^*/U_e$

Catlett Model

Catlett et al. has developed another model based on the Goody model from a flat plate experiment with three different trailing-edge configurations. They have observed a better fit with the experimental data when the parameters, *a-h*, are defined as a power-law function in the form of a Reynolds number and a Clauser's parameter.

a =	$e^{7.98(\beta_\Delta Re_\Delta^{0.35})^{0.131}-10.7}+3.0$	g =	$38.1(\beta_\delta H^{-0.5})^{2.11}-0.5424$
b =	2.0	h =	$0.797(\beta_\Delta Re_\Delta^{0.35})^{0.0724}+7.310$
c =	$20.9(\beta_\delta Re_\delta^{0.05})^{2.76}+0.912$	i =	4.76
d =	$0.328(\beta_\Delta Re_\Delta^{0.35})^{0.310}+0.397$	R_T =	$(\delta/U_e)/(\nu/u_\tau^2)$
e =	$-1.93(\beta_\delta Re_\delta^{0.05})^{0.628}+3.872$	φ^* =	$\tau_w{}^2\delta/U_e$
f =	$-2.57(\beta_\delta Re_\delta^{0.05})^{0.224}+2.19$	ω^* =	$\omega\delta/U_e$

where $\beta_{\delta,\Delta} = \frac{\delta,\Delta}{q}\frac{dP}{dx}$ with $q = 0.5\rho U_0^2$ is the dynamic pressure and U_0 is the local freestream velocity. The Rotta-Clauser parameter [23] is defined as, $\Delta = \delta^*\sqrt{(2/C_f)}$ where $C_f = \tau_w/q$ is the skin friction coefficient. The following Reynolds numbers are defined as: $Re_{\delta,\Delta} = \frac{(\delta,\Delta)U_e}{\nu}$ and $H = \delta^*/\theta$ is the shape factor.

Kamruzzaman Model

Kamruzzaman et al. [24] proposed another wall-pressure spectrum model based on the Goody and Rozenberg models. This model is developed by considering various airfoil configurations with a wide range of Reynolds number.

a =	$0.45[1.75(\Pi^2\beta_c^2)^{0.5(\mathrm{H}/1.31)^{0.3}}+15]$	e =	2.47	i =	1.0
b =	2.0	f =	$1.15^{-2/7}$	R_T =	$(\delta^* u_\tau^2)/(U_e\nu)$
c =	1.637	g =	-2/7	φ^* =	$\tau_w{}^2\delta^*/U_e$
d =	0.27	h =	7.0	ω^* =	$\omega\delta^*/U_e$

Hu & Herr Model

Hu & Herr [16] developed this model with a flat plat experimental data where the favourable and adverse pressure gradients were created by a rotatable NACA0012 airfoil.

a =	$(81.004\mathrm{d}+2.154)\cdot 10^{-7}$	e =	$1.13/(1.169\ln(H)+0.642)^{0.6}$	i =	1.0
b =	1.0	f =	7.645	R_T =	$\delta u_\tau/\nu$
c =	$1.5(1.169\ln(H)+0.642)^{1.6}$	g =	-0.411	φ^* =	$q^2\theta/U_\tau$
d =	$10^{-5.8\cdot 10^{-5}Re_\theta H-0.35}$	h =	6.0	ω^* =	$\omega\theta/U_0$

Lee Model

Lee and Villaescusa [17] proposed an extended version of the Rozenberg model to provide an accurate prediction. All the parameters are kept the same as the Rozenberg model except for *h*, *d* and *a*. The parameter h is defined as $h=\min(5.35,0.139+3.1043\beta_c,19/\sqrt{R_T})+7$ if h = 12.35 then, h= $\min\left(3,19/\sqrt{R_T}\right)+7$. For low pressure gradient flows, the Rozenberg model exhibits high amplitudes for low and middle frequency range. Thus the *d* parameter is modified as $d=\max(1.0,1.5\mathrm{d})$ when $\beta_c<0.5$. Lastly, the parameter a is modified to adjust the spectrum amplitude for high pressure gradient flows as $a^*=\max(1,(0.25\beta_c-0.52)a)$.

4. COMPUTATIONAL SETUP

The two dimensional (2D) steady RANS computations are performed by the open source OpenFOAM with DU96-W-180 wind turbine airfoil. The operating conditions are chosen from the BANC benchmark [25] as the following; the freestream velocity, $U_\infty = 60$ m/s, the Reynolds number, $Re = 1.13\times10^6$, the density, $\rho_\infty = 1.164$ kg/m^3, the chord of the airfoil is $C = 0.3$ m and the angle of attack, $\alpha = 4^\circ$. The domain and grid dependency tests are performed as preliminary investigation.

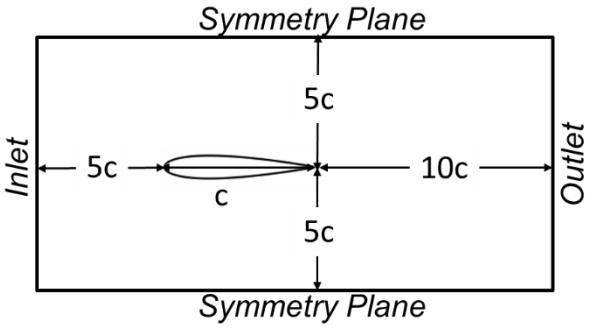

Figure 1. The main domain configuration (Case #1)

The two dimensional (2D) steady RANS computations are performed by the open source OpenFOAM. The inlet flow field assumed to be turbulent for the simulation and $k-\omega$ SST model, proposed by Menter [26] was used since only the global variables are needed for the semi-analytical noise prediction method. At inlet, flow properties are calculated based with a weak turbulence intensity of 0.5%. Zero flux boundary conditions are imposed at outlet. On the airfoil surface, no slip condition for velocity, the adaptive wall functions are used for k, ν_t and ω. Pressure is set to be zero at inlet. At top and bottom boundaries of the domain, symmetric boundary conditions are applied. The simulations were performed by an incompressible OpenFOAM solver called *simpleFOAM* with second order accurate schemes and applying the relaxation for all the variables. θ is the view angle for noise prediction, and equals to 90° when it is orthogonal to the streamwise direction. Far-field noise predictions were computed at an observer distance of r = 1 and a wetted span of b = 1 m. The mesh was created with ANSYS ICEM meshing tool. The mesh topology is based on the C-Grid type, which is here combined with an H-Grid, to optimize the skewness of the cells. It is assured that y^+ value is less than 1 to achieve the grid independence.

5. COMPARISON OF THE WALL-PRESSURE SPECTRUM MODELS

The boundary layer parameters required from the semi-empirical models are given in the Table 1. These values are extracted from the velocity profile at the x/c=0.99 from the leading edge normal to the airfoil surface. The wall-pressure spectrum predicted by different models are given in Figure 2. It should be noted that due to the lack of experimental data for the wall-pressure spectrum, only the models will be compared within themselves. The predictions for the suction side shows a general behavior except for the Goody and Catlett models. When investigating in details, it is observed that the Kamruzzaman, Lee and Panton & Linebarger models deviate maximum $\pm$ 4 dB among them. Contrary to this, the pressure side does not exhibit any general behavior. Furthermore, it should be also pointed out that the Rozenberg and Lee models are unable to predict due to the high favorable adverse pressure gradient.

Table 2. Boundary layer parameters at the x/c=0.99 from the leading edge

	δ/C	δ^*/C	θ/C	U_e/U_∞	Π	β_c
Suction side	0.0409	0.0167	0.0065	0.921	11.54	21.11
Pressure side	0.0189	0.0039	0.0026	0.0897	1.07	-2.55

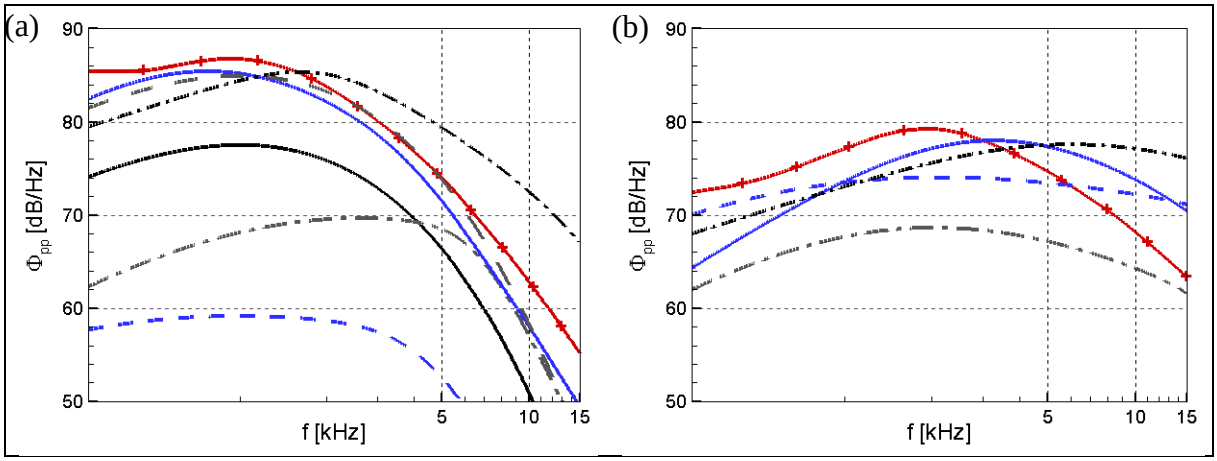

Figure 2. Wall-pressure spectrum prediction by different models at the x/c=0.99 from the leading edge; a) suction side, b) pressure side; Goody (- - -), Rozenberg (——), Catlett (-·-·-), Kamruzzaman (——), Herr & Hu (-··-··), Lee (- - -) and Panton & Linebarger (——).

6. FAR-FIELD NOISE PREDICTION

The far-field noise prediction by different models are compared with an experimental data from LWT [27] in Figure 4. The Goody model which is developed for zero-pressure gradient flow performs poorly in the presence of adverse pressure gradient flow. Even though, the Catlett model is developed for adverse pressure gradient flow, it exhibits a poor performance. The main reason for this could be the fact that the model is developed on a flat plate with different trailing-edge configurations rather than tuning it with an airfoil data. The same explanation could be valid for the Herr & Hu model where the adverse pressure gradient is created by rotating an airfoil and the measurement was taken on a flat plate. Although, the Rozenberg model is validated for airfoil data, a poor prediction is observed for high pressure gradient flow. This discrepancy is considered in the development of the Lee model where an increment of maximum 7 dB is observed below 10 kHz by modifying the parameter *a*. However, it should be noted that the three models which are Goody, Rozenberg and Lee perform the same for the frequencies greater than 10 kHz. The reason for that since these frequencies are emitted by the pressure side which is unpredictable for the Rozenberg and the Lee models, that side is predicted by the Goody's model. Lastly, the Kamruzzaman model performs a good prediction when the simplicity of its parameters is considered. The Panton & Linebarger's statistical model shows a good comparison with an experimental data. The discrepancies observed in the middle and high frequency ranges could be due to the anisotropy factor that is applied to obtain the wall-normal fluctuations. It has been observed that the anisotropy factor obtained from a flat plate is unrepresentative to re-create the fluctuations on an airfoil surface where the APG is really high.

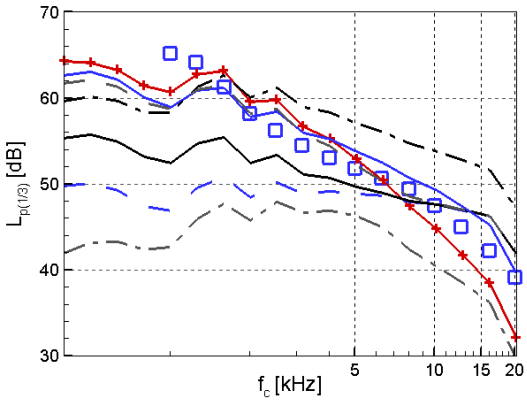

Figure 3. Far-field noise prediction by Amiet's theory with different wall-pressure models and comparison with an experimental data; Goody (- - -), Rozenberg (——), Catlett (-·-·-), Kamruzzaman (——), Herr & Hu (-··-··), Lee (- s) and Panton & Linebarger (——) and experimental data from LWT (○).

7. CONCLUSIONS

The trailing-edge noise prediction is performed by using Amiet's semi-analytical model combined with RANS simulations. The wall-pressure spectrum which is a milestone of the Amiet model is determined by two different approaches. The first one is to obtain the wall-pressure spectrum from the semi-empirical models which are tuned to the experimental data. In the second approach, the wall-pressure spectrum is obtained through the integration of the Poisson equation. The semi-empirical models only require the velocity profile which is normal to the airfoil surface near the trailing edge to determine the boundary layer parameters. In addition to the velocity profile, the kinetic energy and the specific dissipation profile are needed for the statistical model. Six different semi-empirical models namely; Goody, Rozenberg, Catlett, Kamruzzaman, Herr & Hu and Lee with a statistical model, Panton & Linebarger model are investigated. The comparison with an experimental data was only performed for the far-field noise prediction.

The wall-pressure spectrum prediction reveals that the Kamruzzaman, Lee and Panton & Linebarger model perform a similar behavior for the suction side. However, the pressure side does not exhibit any behavior. Furthermore, the Rozenberg and Lee models are unable to predict the wall-pressure spectrum for the pressure side due to the high favorable pressure gradient.

The comparison with an experimental data from LWT shows that the basic model, Goody, performs very poorly in the presence of adverse pressure gradient. Even though, Catlett and Herr & Hu models are developed for adverse pressure gradient flows, they have performed poorly. The reason could be that the experimental data in use was a flat-plate instead of an airfoil. The models which are developed for an airfoil data perform better except Rozenberg model due to the high adverse pressure gradient. The Lee model which is modified for high adverse pressure gradient flow performs in the range of ± 3 dB. The Kamruzzaman model also exhibits a good performance in the range of ± 3 dB by considering its simple formulation. Lastly, Panton & Linebarger model predicts well the middle range whereas under-predicts around 2 dB for the higher frequencies.

As a last remark, the parameters which are needed for semi-analytical models are not always feasible to obtain, especially in the presence of high adverse pressure gradient flow. On contrary, the input profiles for the Panton & Linebarger model are accessible and this model performs in the range of of ± 2 dB even though, the velocity fluctuations are recreated with an anisotropy factor obtained from a flat-plate.

ACKNOWLEDGEMENTS

The authors gratefully acknowledge the support of the European Commission's Framework Program "Horizon 2020", through the Marie Skłodowska-Curie Innovative Training Networks (ITN) "AEOLUS4FUTURE - Efficient harvesting of the wind energy" (H2020-MSCA-ITN-2014: Grant agreement no. 643167).

REFERENCES

[1] A. Bockstael, L. Dekoninck, B. De Coensel, D. Oldoni, A. Can, and D. Botteldooren, “Wind turbine noise: annoyance and alternative exposure indicators.”

[2] K. P. WAYE and E. ÖHRSTRÖM, “PSYCHO-ACOUSTIC CHARACTERS OF RELEVANCE FOR ANNOYANCE OF WIND TURBINE NOISE,” *J. Sound Vib.*, vol. 250, no. 1, pp. 65–73, 2002.

[3] J. H. Schmidt and M. Klokker, “Health effects related to wind turbine noise exposure: a systematic review.,” *PLoS One*, vol. 9, no. 12, p. e114183, 2014.

[4] M. F. Barone, “Survey of Techniques for Reduction of Wind Turbine Blade Trailing Edge Noise,” 2011.

[5] S. Oerlemans, M. Fisher, T. Maeder, and K. Kögler, “Reduction of Wind Turbine Noise Using Optimized Airfoils and Trailing-Edge Serrations,” *AIAA J.*, vol. 47, no. 6, pp. 1470–1481, Jun. 2009.

[6] R. H. Kraichnan, “Pressure Fluctuations in Turbulent Flow over a Flat Plate,” *J. Acoust. Soc. Am.*, vol. 28, no. 3, pp. 378–390, 1956.

[7] R. L. Panton and J. H. Linebarger, “Wall pressure spectra calculations for equilibrium boundary layers,” *J. Fluid Mech.*, vol. 65, no. 2, p. 261, Aug. 1974.

[8] Y.-T. Lee, W. K. Blake, and T. M. Farabee, “Modeling of Wall Pressure Fluctuations Based on Time Mean Flow Field,” *J. Fluids Eng.*, vol. 127, no. 2, pp. 233–240, Sep. 2004.

[9] S. Moreau and S. Remmler, “Computation of Wall-Pressure Spectra from Steady Flow Data for Noise Prediction,” *AIAA J.*

[10] M. Goody, “Empirical Spectral Model of Surface Pressure Fluctuations,” *AIAA J.*, vol. 42, no. 9, pp. 1788–1794, Sep. 2004.

[11] Y. Rozenberg, G. Robert, and S. Moreau, “Wall Pressure Spectral Model Including the Adverse Pressure Gradient Effects.”

[12] F. H. Clauser, “Turbulent Boundary Layers in Adverse Pressure Gradients,” *J. Aeronaut. Sci.*,

vol. 21, no. 2, pp. 91–108, Feb. 1954.
[13] D. Coles, "The law of the wake in the turbulent boundary layer," *J. Fluid Mech.*, vol. 1, no. 2, pp. 191–226, 1956.
[14] M. R. Catlett, J. M. Anderson, J. B. Forest, and D. O. Stewart, "Empirical Modeling of Pressure Spectra in Adverse Pressure Gradient Turbulent Boundary Layers," *AIAA J.*, vol. 54, no. 2, pp. 569–587, Dec. 2015.
[15] M. Kamruzzaman, D. Bekiropoulos, T. Lutz, W. Würz, and E. Krämer, "A Semi-Empirical Surface Pressure Spectrum Model for Airfoil Trailing-Edge Noise Prediction," *Int. J. Aeroacoustics*, vol. 14, no. 5–6, pp. 833–882, Oct. 2015.
[16] N. Hu and M. Herr, "Characteristics of Wall Pressure Fluctuations for a Flat Plate Turbulent Boundary Layer with Pressure Gradients," in *22nd AIAA/CEAS Aeroacoustics Conference*, 2016, p. 2749.
[17] S. Lee and A. Villaescusa, "Comparison and Assessment of Recent Empirical Models for Turbulent Boundary Layer Wall Pressure Spectrum," in *23rd AIAA/CEAS Aeroacoustics Conference*, 2017, p. 3688.
[18] R. K. Amiet and R. K., "Noise due to turbulent flow past a trailing edge," *J. Sound Vib.*, vol. 47, no. 3, pp. 387–393, Aug. 1976.
[19] M. Roger and S. Moreau, "Back-scattering correction and further extensions of Amiet's trailing-edge noise model. Part 1: theory," *J. Sound Vib.*, vol. 286, no. 3, pp. 477–506, 2005.
[20] G. M. Corcos, "The structure of the turbulent pressure field in boundary-layer flows," *J. Fluid Mech.*, vol. 18, no. 3, p. 353, Mar. 1964.
[21] M. V ZAGAROLA and A. J. SMITS, "Mean-flow scaling of turbulent pipe flow," *J. Fluid Mech.*, vol. 373, pp. 33–79, 1998.
[22] F. H. Clauser, "Turbulent Boundary Layers in Adverse Pressure Gradients," *J. Aeronaut. Sci.*, vol. 21, no. 2, pp. 91–108, Feb. 1954.
[23] J. Rotta, "On the theory of the turbulent boundary layer," 1953.
[24] M. Kamruzzaman, D. Bekiropoulos, T. Lutz, W. Würz, and E. Krämer, "A Semi-Empirical Surface Pressure Spectrum Model for Airfoil Trailing-Edge Noise Prediction," *Int. J. Aeroacoustics*, vol. 14, no. 5–6, pp. 833–882, 2015.
[25] M. Herr *et al.*, "Broadband Trailing-Edge Noise Predictions—Overview of BANC-III Results," in *21st AIAA/CEAS Aeroacoustics Conference*, 2015.
[26] F. R. Menter, "Two-equation eddy-viscosity turbulence models for engineering applications," *AIAA J.*, vol. 32, no. 8, pp. 1598–1605, Aug. 1994.
[27] M. Herr *et al.*, "Broadband Trailing-Edge Noise Predictions—Overview of BANC-III Results," in *21st AIAA/CEAS Aeroacoustics Conference*, 2015, p. 2847.

Paper TS4.1.4

THE INTERNATIONAL CONFERENCE ON
WIND ENERGY HARVESTING 2018
21-23 March 2018
Catanzaro, Italy

TURBULENT INLET BOUNDARY CONDITIONS FOR LARGE EDDY SIMULATION: A URBAN WIND ENERGY TEST-CASE

Giulio Vita[1]*, Hassan Hemida[1], Ashvinkumar Chaudhari[2] and Charalampos Baniotopoulos[1]

[1]Dept. of Civil Engineering, School of Engineering, University of Birmingham, United Kingdom
[2]Centre of Computational Engineering and Integrated Design (CEID), Lappeenranta University of Technology, Finland
Corresponding author: Giulio Vita, g.vita@bham.ac.uk

ABSTRACT

This paper reports on an investigation on numerical techniques to include turbulence at the inlet of Large Eddy Simulations (LES). Computational Fluid Dynamics (CFD) is promising as a technique to support wind tunnel results and provide a thorough understanding of the flow field. LES in particular may represent a breakthrough in the correct modelling of turbulence as found in complex geometrical configuration, such as in the urban environment. In fact, the poor understanding of local features of urban and buildings flows is the main reason of the lack of a convincing positioning strategy for Wind Energy Converters (WEC) in such conditions. Nevertheless, Wind Energy is considered a promising way of harvesting wind energy in built areas, as it slashes infrastructural wind energy costs. Developing a successful numerical technique would therefore improve our understanding of the inflow to be considered for urban wind turbines, help us model the effect of turbulence on the aerodynamic performance and eventually assess a positioning strategy which could in turn improve the current poor performance of this technology.

NOMENCLATURE

CFD	=	Computational Fluid Dynamics
FST	=	Free Stream Turbulence
LES	=	Large Eddy Simulation
SGS	=	Sub-Grid Scale model
WEC	=	Wind Energy Converter
WT	=	Wind Turbine

1. INTRODUCTION

Urban Wind Energy (UWE) is currently taking an ever-increasing role in the broad wind energy panorama [1]. Besides the debatable contribution to the energy demand or the matching between the energy consumption/production site, there are other reasons to further investigate UWE as a worthy niche of wind energy [2]. In fact, Small Wind Market is showing an exponential growth, involving numerous companies, investors and workplaces (Figure 1). Moreover, the unsuccessful UWE applications, as they are visible to the inhabitants of the urban environment affect the whole public perception and social acceptance of wind energy [3].

Unfortunately, many issues are responsible for the small or big failure of applications [4]. In particular, the aerodynamics of wind turbines (WTs) located in built areas is challenging and only few studies have shed light on how a WT responds to turbulent inflow structures [5]. For this reason, the positioning strategies for urban WTs are largely based on non-technical considerations: the classification of UWE applications is itself questionable [6].

In this work, a computational methodology based on Large Eddy Simulation is developed in order to include turbulent inlet boundary conditions to WTs and/or aerofoils simulations. A brief overview of existing techniques will be given, with reference to the two families of techniques: precursor simulation and synthetic turbulence methods.

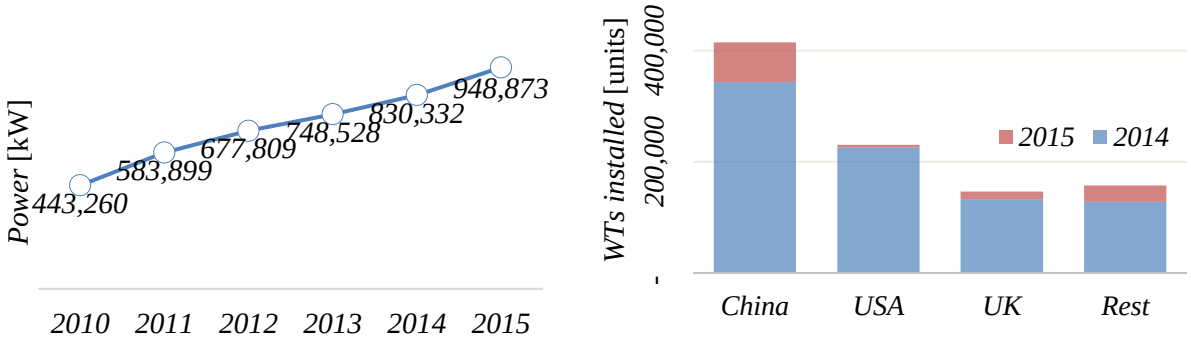

Figure 1. Cumulative Installed Power Capacity for Small WECs: 2016 Statistics ©WWEA [1].

2. METHODOLOGY

2.1. Experimental validation dataset

The experiment by Hemida et al. [7] provides the validation dataset for the numerical model. A series of wind tunnel experiments has been carried out at the Atmospheric Boundary Layer (ABL) Wind Tunnel Lab of the Ruhr-University of Bochum (RUB), within the scope of the COST-Action TU1304 WINERCOST. The RUB wind tunnel has a cross section of *1.6m* × *1.8m* and a length of *9.4m*, in an open tunnel configuration with fan behind the test section (Fig.2a). The ABL is simulated equipping the wind tunnel inlet with a castellated barrier, turbulence generator fins, and roughness cubes (from *3.6cm* to *1.6cm*) working as roughness elements (Fig.2c). The high-rise building model has a 1:300 scale, with a height-to-width ratio of $H/D=3$, where $H=400mm$ and $D=133.3mm$. Fig.2b shows the model mounted on the rotating test table of the wind tunnel.

Results include the velocity pattern above the rooftop, measured using a hot wire anemometer at different locations of the roof, schematised in Fig.2d) and surface pressure on the rooftop. However, this technique does not account for reversed flow, so results have been interpreted accordingly to detect separation. A specific focus has been given to turbulence intensity; it has been measured re. the velocity components in the *y* and *z* directions, *u* and *w*, for $z/D>0.1$. Time histories of each signal have been obtained using a length window of *131s*, and all results are referred to the width of the model $D=133.3mm$ and the reference velocity $u_{ref}=u(z=H)=15.85m/s$ (Fig.2c).

The measurements of the velocity around the models have showed (as expected) that near the surface the flow is reversed, because of a separation bubble. Above $z/D\sim0.3$, turbulence intensity declines to about *0.1* for both *u* and *w*, matching the one present in the upstream flow. This suggests that the building affects turbulence intensity up to a height of about one third of its width. Fig. 4c shows that wind velocity has the maximum increase of about *25%* at about $z/D\sim0.3$, at the centre of the roof (Pos.2). This is just above the shear layer between the separation region and the upstream flow, which is in agreement with previous experiments [8]. At the upstream edge (Pos. 4'), the maximum velocity occurs at a lower height, meaning that the it is maximised downstream to Pos.1. Beneath the maximum velocity area, the flow is highly turbulent. The turbulence intensity has its minimum value at the middle of the building, also for different directions of the wind. It has also been found that different direction yield separation cone vortices, which have a smaller size and height than the normal direction.

The inlet profile of mean velocity and turbulence intensity are shown in Fig.2c. Fig.2d shows the measurement for Pos. 1 and 2. These values provide a very useful validation dataset, as the flow field is normally disregarded in studies about building aerodynamics in favour of the surface pressure field, which is more commonly considered.

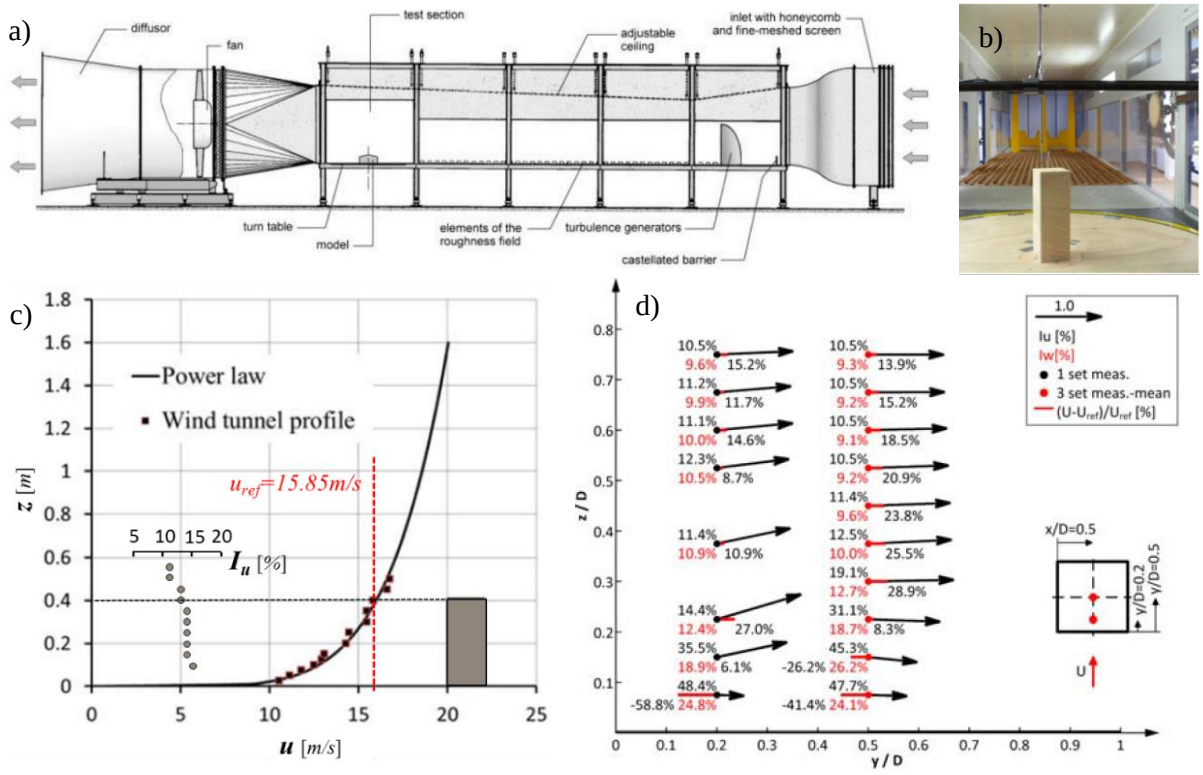

Figure 2. a) Wind Tunnel of the Ruhr-University Bochum; b) photo of the wind tunnel with the model mounted on a turning table; c) Wind-tunnel velocity profile ahead of the model; d) Velocity vectors, I_u and I_w as measured at pos. 1 and 2.

2.2. Numerical simulations

Large Eddy Simulation (LES) is a compromise between Direct Numerical Simulation (DNS) and Reynolds-Averaging of Navier Stokes equations (RANS). The first method computes all turbulent scales up to dissipation, while the latter models most of the turbulent scales using a suitable turbulence model. LES solves most of the turbulent scales, modelling a portion of them based on the definition of a filter, which in the large majority of models is defined based on the size of the mesh cells. The sub-grid scale SGS model is defined on the concept that at small scales turbulence has roughly universal characteristics rather independent on the geometry considered [9].

A turbulent inlet can be generated in two ways. A way is to model the upstream part of the wind tunnel, which is responsible of the development of the ABL in the experiment (method A). This approach accounts as a sort of virtual wind tunnel to be modelled. However, a great amount of caution is needed for computational accuracy, as with such large domains and strict mesh requirements, the convergence of the simulation as well as their cost is at stack. A very promising alternative is to introduce noise in the equations by using appropriate time-varying boundary conditions (method B). Two general methodologies exist to generate fluctuating inlet conditions for LES: 1) precursor simulation and 2) synthetic turbulence methods [10]. These two approaches are complementary rather than alternative [11]. The precursor simulation methods rely on a previous simulation that gives a database of fluctuating conditions to be used as inlet for the LES model of interest, thus reproducing inlet with the expected statistics of turbulence. Synthetic methods on the other hand improve convergence and accuracy without having a physical meaning for the inlet itself [12].

A steady state RANS (Reynolds Averaged Navier-Stokes) simulation has also been developed using the k-ω SST turbulence model, to get a brief idea of the flow pattern and check if the mesh requirements are met. The objective is to have a rough estimation of the turbulent quantities at stake. A preliminary comparison with the LES (Large Eddy Simulation) approach is then proposed, in order to discuss the importance of modelling the fluctuating statistics. In fact, even though the RANS approach has shown

good viability for the estimation of the averaged fields, it is hindered by the modelling of fluctuating statistics [13, 14]

A block structured mesh has been constructed, having $y^+ \sim 1$ and choosing the blocking strategy in order to limit the along-flow size of the elements to respect the CFL condition which imposes $Co<1$. This has brought to the choice of a time step of $\Delta t=5e^{-5}$ for the LES model presented. The Smagorinsky-Lilly model has been chosen as Sub-Grid Scale model (SGS), with the use of the van Driest damping function[1], as implemented in the OpenFOAM® software v.2.3.1.

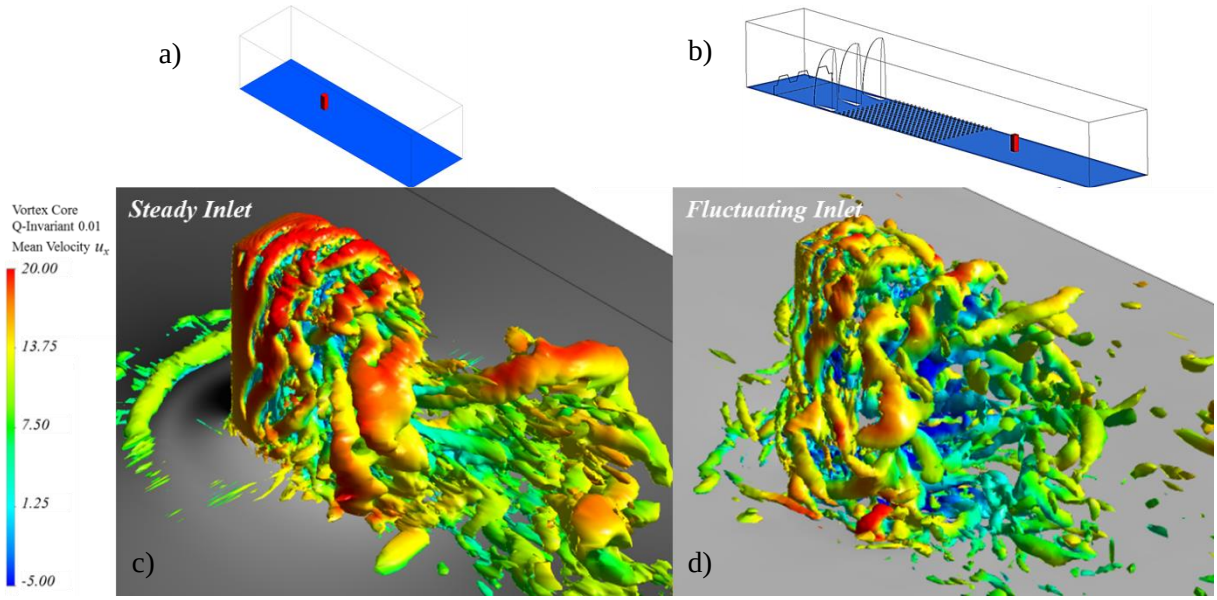

Figure 3. Fluctuating and steady inlet for LES simulation. a) and b) computational domain, c) and d) flow pattern in terms of velocity-invariant Q=0.1.

3. RESULTS AND DISCUSSION

These two methodologies have been used to model the effect of turbulence on WECs that is found at a suitable location for the positioning of WTs within the built environment, such as the high-rise building as described in Section 2.1. The aim is to understand the effect of the turbulent inlet conditions on the development of statistics at the location of interest which is the rood top, where eventually a WEC could be placed. For this preliminary study, two models have been developed to compare the performance of turbulent inlet generation against an LES model which considers the development of the flow and its characteristics. In this paper, the methodology (A) is compared with a steady state case, where a laminar inlet boundary layer profile is imposed at the inlet. The two computational domains are shown in Fig. 3a and b respectively. The flow field is indicated as steady and fluctuating. From a qualitative assessment of results presented in Fig. 3, it can be argued that the flow field looks less organised in the fluctuating case, as many flow structures from upstream roughness elements contribute to the break of vortices, rather than the separated flow due to the bluff body. However, the shedding of the vortices, i.e. the frequency at which vortices are shed from the separation corners of the building, can be considered basically unchanged. This can be quickly assessed by considering the iso-vorticity map, where the vortex cores are roughly placed at the same distance in both cases.

Arguably, for wind energy purposes, the two cases provide a similar flow pattern, which in turn can represent a major simplification of a possible methodology of introducing turbulence effects on WEC performance, when placed close to a bluff body.

[1] A damping function, such as the one formulated by Van Driest $l_{sgs}=C_{sgs}\Delta\left(1-e^{-y^+/A^+}\right)$, where $A^+=26$, lowers the value of the model constant C_{sgs} or C_s in those regions of the flow where viscosity effects become preponderant. In fact, the Smagorinsky model uses a fixed constant to take into account the SGS effects, potentially yielding an unphysical behaviour. The eddy viscosity reads $\nu_{sgs}=\left(C_{sgs}\Delta\right)^2\left|\tilde{S}\right|=\left(C_{sgs}\Delta\right)^2\sqrt{2\widetilde{S_{ij}}\widetilde{S_{ij}}}$ where the Smagorinsky model constant has been set to $C_s=0.17$.

A better estimation of the accuracy of the two simulation is given in Fig. 4, where the steady and fluctuating case are compared with the RANS simulation for the most common turbulence statistics.

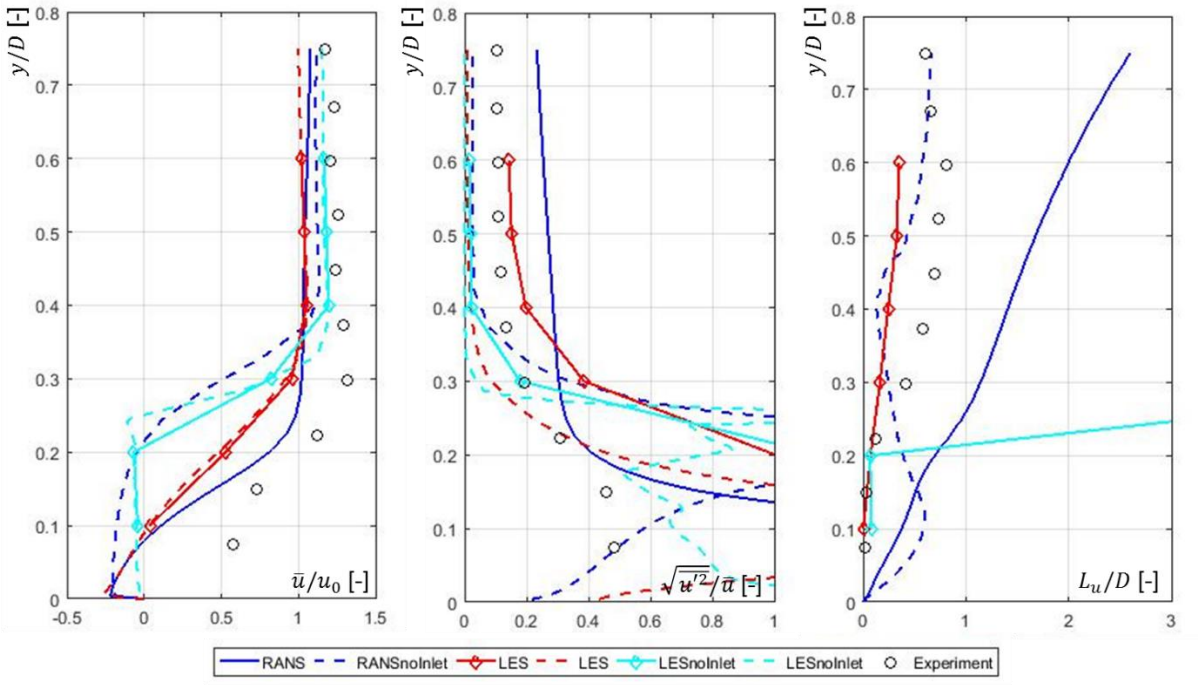

Figure 4. Respectively Average Velocity, Turbulence intensity and integral length scale of the high-rise bulding testcase with comparison of inlet geometry and no inlet for both RANS and LES.

The LES simulation with fluctuating inlet is the closest to the experimental data in modelling turbulence intensity and integral length scale. Not surprisingly, the RANS model performs better in modelling the mean flow. It is rather evident how the steady inlet case does not capture the physics of the flow. However, a closer look to the measured signals clarifies the mismatch between the different techniques. In Fig. 5 the experimental data is plotted together with the steady and fluctuating inlet simulations. Due to the preliminary nature of the simulations it is evident how the fluctuating signal matches peaks of the fluctuating one, while the steady one is rather damped and much shorter. This is also confirmed by the spectra, which are plotted in Fig. 6 for positions 2 and 3 at two different heights. The spectra overlap quite well at lower frequencies, while the diverge at the highest. This is also due to the difference in the length of the signal and in the nature of the chosen sub-grid scale model, which interacts with the solved vortex structures.

LES simulation, although potentially powerful in producing highly accurate data, has still to become viable due to the practicality of the LES approach. That is why the usage of boundary condition fluctuating techniques might be the forthcoming solution to the practical LES usage.

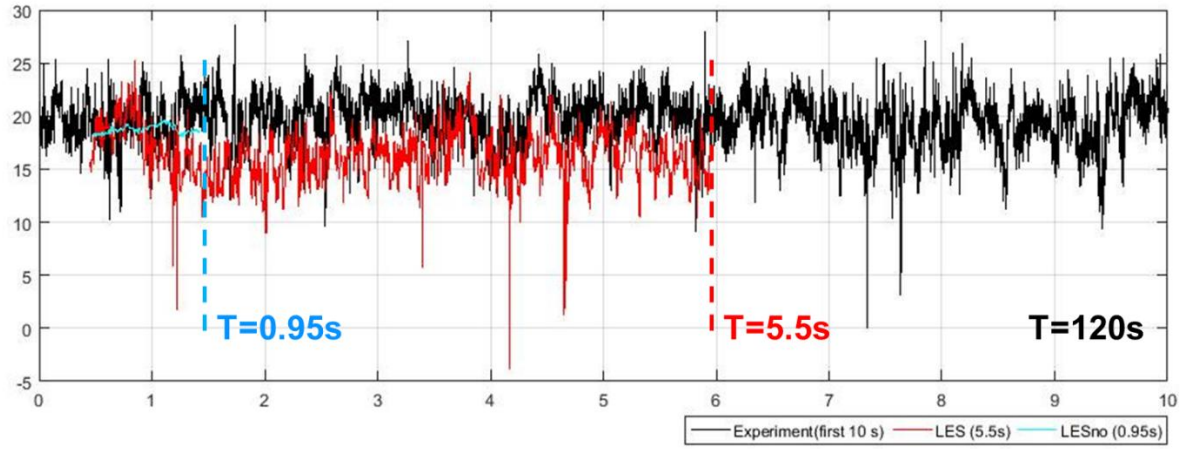

Figure 5 – Time histories of velocity signal for experiment, steady and fluctuating inlet.

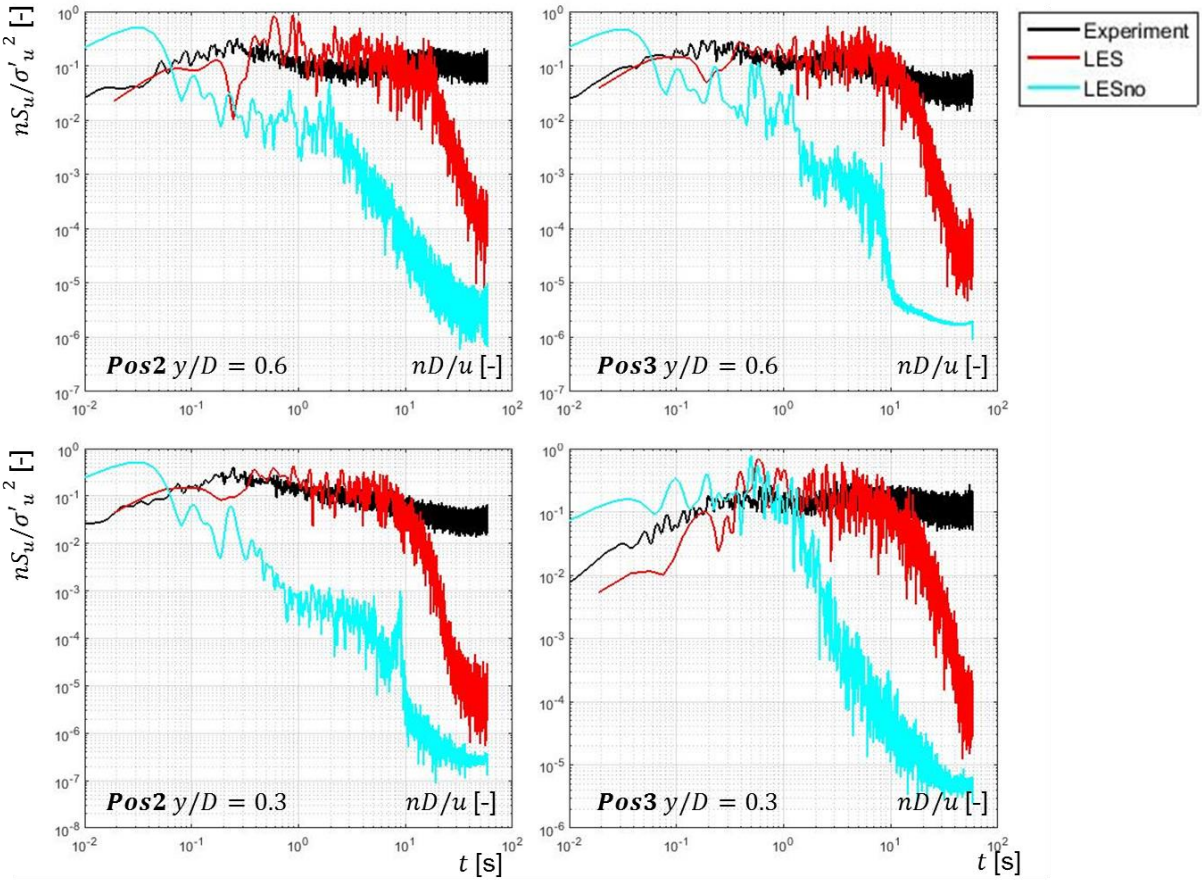

Figure 6 – Energy spectra at different positions and heights.

A methodology based on turbulent inlet generation is expected to greatly improve accuracy and reliability of results and provide a powerful tool for the optimization of wind energy harvesting in the urban environment and further engineering applications which require a thorough understanding of the inflow. However, the physical significance of results has to be ascertained. That is why an STSM has been organised in collaboration with the Centre of Computational Engineering and Integrated Design (CEID) of the Lappeenranta University of Technology (LUT) with the support of Dr. Ashvinkumar Chaudhari. The STSM has the purpose of investigating the possibilities implemented in OpenFOAM to introduce numerical noise with statistics having physical meaning at the inlet of LES. Over the duration of the STSM several OpenFOAM tutorials have been developed. Results will be compared to the

modelled LES high-rise building to understand the limitation of the simplified approach offered by a variety of turbulent inlet conditions. A reference box case, comprising of a grid inlet, is considered. The generation of virtual grid turbulence has been implemented splitting the inlet boundary into a wall and an inlet region respectively. In this way turbulence is produced at the interface between the wall boundary and the inlet. It is found in literature that this technique reproduces grid generated turbulence virtually [15] with a good degree of approximation. However, it is extremely important to choose periodic boundary conditions at the boundaries of the box, which in turn needs to have a specific size and mesh resolution. The same computational domain and mesh is then used to include turbulent inlet synthetic turbulence. The turbulentInlet random fluctuations generator is used in comparison with two techniques developed respectively at the ETH [16] and found in the github repository [17].

In Figure 1, the flow field as computed using the inlet virtual grid and the random turbulentInlet is shown. The numerical noise introduced using random fluctuation with a given amplitude is responsible for the higher maximum velocity of Fig. 7a, while in Fig 7b the maximum velocity corresponds to the inlet velocity, calculated considered the porosity of the virtual grid. In Fig. 8, the Energy spectrum of the longitudinal component of the velocity field is plotted for the two cases. It is evident how the inertial range region of the spectrum does not develop, hence raising doubts on the validity of the boundary condition. At the high end of the spectrum, the behaviour follows the -5/3 law, as for the smallest scales the sub grid scale model is responsible for the resulting flow field. In this preliminary account of results, one can conclude that the generation of virtual turbulence with given statistics requires a great deal of attention, as results strongly vary with the size of the domain, the resolution of the mesh and the duration of the simulation.

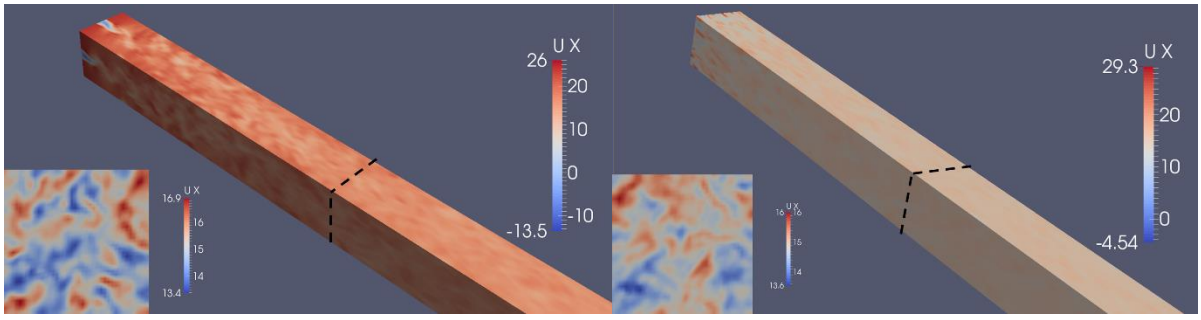

Figure 7 – a) Turbulence box generated with virtual grid and b) random fluctuation generator, with detail of instantaneous velocity field.

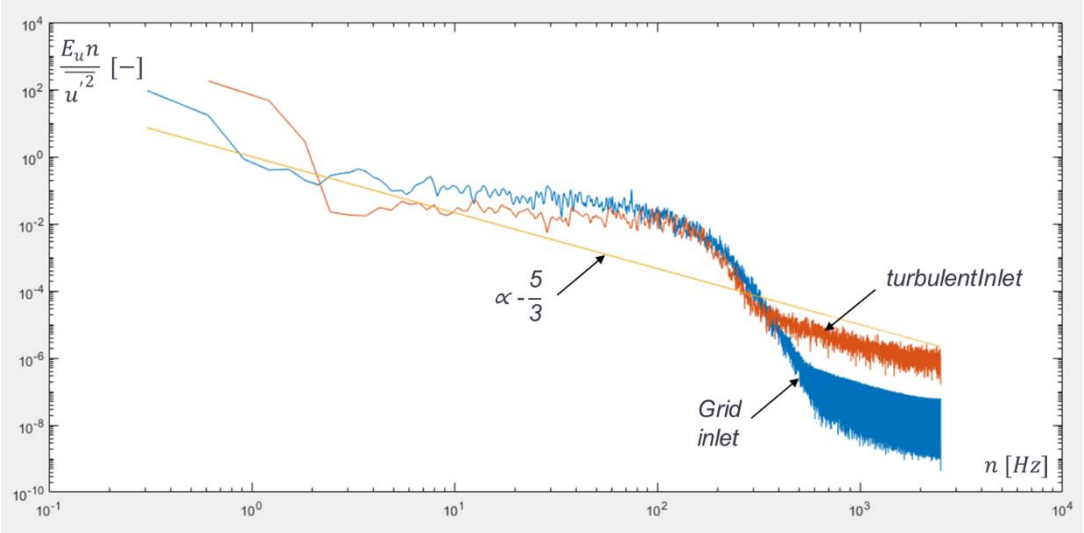

Figure 8 – Energy Spectrum for different turbulent inlet generation techniques with -5/3 law comparison.

Results gained using the turbulent inlet techniques will be compared with actual physical results from the LES simulation of the wind tunnel setup. The aim is to provide a suitable simple and fast technique

to generate a fluctuating turbulence field having certain turbulence characteristics as in the experiment. In is questionable whether the inclusion of random fluctuations at the inlet of the steady simulation would help the convergence and robustness of the LES simulation towards the experimental results.

It will be the topic of further research from the authors to find out.

ACKNOWLEDGEMENTS

The authors acknowledge with thanks the support of the European Commission Framework Program "Horizon 2020", through the Marie Skłodowska-Curie Innovative Training Networks (ITN) "AEOLUS4FUTURE - Efficient harvesting of the wind energy" (H2020-MSCA-ITN-2014: Grant agreement no. 643167), to the present research project. The authors also acknowledge with thanks the WINERCOST TU1304 COST Action for having provided them with a plethora of collaboration activities related to small wind technology.

REFERENCES

[1] Gsänger, S., & Pitteloud, J.-D. (2015). Small Wind World Report 2015. Retrieved from www.wwindea.org
[2] Enevoldsen, P., & Sovacool, B. K. (2016). Examining the social acceptance of wind energy: Practical guidelines for onshore wind project development in France. Renewable and Sustainable Energy Reviews, 53, 178–184. https://doi.org/10.1016/j.rser.2015.08.041
[3] Hamza, Neveen. (2015). URBAN WIND ENERGY EXPOSING SUSTAINABILITY SYMBOLISM WINERCOST Workshop 'Trends and Challenges for Wind Energy Harvesting', Coimbra, 30-31 March 2015.
[4] Balduzzi, F., Bianchini, A., & Ferrari, L. (2012). Microeolic turbines in the built environment: Influence of the installation site on the potential energy yield. Renewable Energy, 45, 163–174. https://doi.org/10.1016/j.renene.2012.02.022
[5] Devinant, P., Laverne, T., & Hureau, J. (2002). Experimental study of wind-turbine airfoil aerodynamics in high turbulence. Journal of Wind Engineering and Industrial Aerodynamics, 90(6), 689–707. https://doi.org/10.1016/S0167-6105(02)00162-9
[6] Walker, S. L. (2011). Building mounted wind turbines and their suitability for the urban scale—A review of methods of estimating urban wind resource. Energy and Buildings, 43(8), 1852–1862. https://doi.org/10.1016/j.enbuild.2011.03.032
[7] Hemida, H., Šarkic, A., Gillmeier, S., Höffer, R., Experimental investigation of wind flow above the roof of high-rise building, WINERCOST Workshop "Trends and Challenges for Wind Energy Harvesting", Coimbra, Portugal, 30-31March 2015, p.25-34.
[8] H. Hemida, "Large-eddy simulation of the above roof flow of a high-rise building for micro-wind turbines," in 11th UK Conference on Wind Engineering, 2014.
[9] Pope, S. B. (2000). Turbulent Flows. Cambridge University Press (Vol. 1). https://doi.org/10.1088/1468-5248/1/1/702
[10] Tabor, G. R., & Baba-Ahmadi, M. H. (2010). Inlet conditions for large eddy simulation: A review. Computers & Fluids, 39(4), 553–567. https://doi.org/10.1016/j.compfluid.2009.10.007
[11] Lund, T. S., Wu, X., & Squires, K. D. (1998). Generation of Turbulent Inflow Data for Spatially-Developing Boundary Layer Simulations. *JOURNAL OF COMPUTATIONAL PHYSICS*, *140*, 233–258.
[12] Chaudhari, A. (2014). Large-eddy simulation of wind flows over complex terrains for wind energy applications. Lappeenranta University of Technology.
[13] B. Blocken, T. Stathopoulos, and J. P. A. J. van Beeck, "Pedestrian-level wind conditions around buildings: Review of wind-tunnel and CFD techniques and their accuracy for wind comfort assessment," Build. Environ., vol. 100, pp. 50–81, 2016.
[14] Ozmen, Y., Baydar, E., & van Beeck, J. P. A. J. (2016). Wind flow over the low-rise building models with gabled roofs having different pitch angles. Building and Environment, 95, 63–74. https://doi.org/10.1016/j.buildenv.2015.09.014
[15] T. Blackmore, W. M. J. Batten, and A. S. Bahaj, "Inlet grid-generated turbulence for large-eddy simulations," Int. J. Comut. Fluid Dyn., vol. 27, no. 6–7, pp. 307–315, Jul. 2013.
[16] M. C. Immer, "Time-resolved measurement and simulation of local scale turbulent urban flow," 2016.
[17] E. Asgari and M. Tadjfar, "Assessment of four inflow conditions on large-eddy simulation of a gently curved backward-facing step," J. Turbul., vol. 18, no. 1, pp. 61–86, Jan. 2017.

Paper TS4.1.5

THE INTERNATIONAL CONFERENCE ON
WIND ENERGY HARVESTING 2018
21-23 March 2018
Catanzaro, Italy

NUMERICAL ANALYSIS OF URBAN WIND ENERGY POTENTIAL USING ACTUATOR DISK MODELS: A CASE STUDY FOR THE BAHRAIN WORLD TRADE CENTER

Zahra Seifollahi Moghadam[1]*, Hamid Montazeri[1,2], and Bert Blocken [1,2]

[1]Department of Built Environment, Eindhoven University of Technology, Eindhoven, Netherlands
[2]Department of Civil Engineering, KU Leuven, Leuven, Belgium
** Corresponding author: Zahra Seifollahi Moghadam, z.seifollahi.moghadam@tue.nl*

ABSTRACT

Wind energy is expected to cover about 14% of the EU's electricity demand by 2020. Several studies have been performed to develop technologies for wind turbines and to provide a better understanding of wind energy harvesting. However, while the vast majority of these studies focused on offshore and onshore wind energy potential, recent studies have shown that there exist incentives to harvest wind energy in the built environment where it is possible to take advantage of flow channeling effects and local flow acceleration around buildings. CFD is a useful tool to investigate the wind energy potential in urban areas. However, there is a lack of evaluation of urban wind energy potential with taking into account the presence of wind turbines. However, the computational modeling of the aerodynamics of wind turbines in complex urban areas is a challenging task because of the complex interaction of wind flow around buildings and turbines. This interaction can be taken into account in CFD simulations using wind turbine models such as the Actuator Disk Models. This paper, therefore, provides CFD simulations of wind flow around a tower in which horizontal axis wind turbines are integrated. The Actuator Disk Model is used to implicitly consider the presence of the wind turbines. The focus is on the World Trade Center (WTC) tower in Bahrain. The results show that for the case in which the wind turbines are modeled, the estimated power output of the turbines is 15% lower in comparison with that of the case where only the building is modeled.

1. INTRODUCTION

Wind energy harvesting has advanced from offshore and onshore to the built environment. Harvesting of wind energy in urban areas introduces a number of advantages. The urban wind turbines can be integrated in existing buildings and city infrastructures or renovation projects. This can also reduce the carbon emissions associated with the electricity delivered to the built environment and energy losses in power lines and electric devices [1]. In spite of these advantages, urban wind turbines are experiencing a number of issues. One of the main limitations is related to the complexity of wind flow in urban areas. For example, in regions with low wind speed and high turbulence intensity, the performance of wind turbines can significantly be reduced [2].
Computational Fluid Dynamics (CFD) has been widely used to investigate the wind energy potential in urban areas. Several studies have been performed to investigate wind conditions around single high-rise buildings for installation of micro wind turbines. Guidance on the most effective height and location for wind turbine installations on the roofs of tall buildings is provided in e.g. Ref. [3]. The feasibility of wind power utilization for generic high-rise buildings is investigated in e.g. Ref. [4]. The impact of several parameters such as the roof shape, the building height and the surrounding buildings has also been studied [5,6].
In CFD studies, a deep understanding of interaction of flow around buildings and turbines is crucial for an accurate estimation of urban wind energy potential [7]. In the vast majority of previous CFD studies, however, wind turbines were not taken into account as the explicit modeling of wind turbines is computationally expensive. Virtual wind turbine models such as the Actuator Disk Model (ADM), therefore, have been developed and used in which the turbine is modeled as a porous medium [8].

So far there is a lack of evaluation of urban wind energy potential with taking into account the presence of wind turbines. This paper, therefore, provides CFD simulations of wind flow around a tower in which horizontal axis wind turbines are integrated. The Actuator Disk Model is used to implicitly consider the presence of the wind turbines. The focus is on the World Trade Center (WTC) tower in Bahrain. The evaluation is based on validation with wind-tunnel measurements of wind speed for a reduced-scale model of the WTC.

2. NUMERICAL SIMULATION

The Bahrain WTC (Fig. 1(a)) is a 240-meter-high tower consisting of two 50-storey sail shaped office towers. The towers are connected by three bridges, each holding a 29-meter-diameter horizontal-axis wind turbine. Wind-tunnel measurements have been performed for a reduced-scale model of the tower (excluding the bridges and the wind turbines). The computational model is made based on the reduced-scale model used in the wind-tunnel measurements. The computational domain and grid are created based on the best practice guidelines by Tominaga et al. [9] and Franke et al. [10]. The generated grid is shown in Figure 1(b). The CFD analysis has been performed using the commercial CFD code ANSYS Fluent. The steady RANS equations are solved in combination with Realizable k-ε turbulence model. The pressure-velocity coupling is done using the SIMPLE scheme. Second-order discretization schemes are used for both the convection terms and the viscous terms of the governing equations. The gradients are computed using the least-squares cell based method. At the inlet of the domain, neutral atmospheric boundary layer inflow profile of mean wind speed U (m/s) is imposed. The turbulent kinetic energy boundary condition is applied based on the measured data.

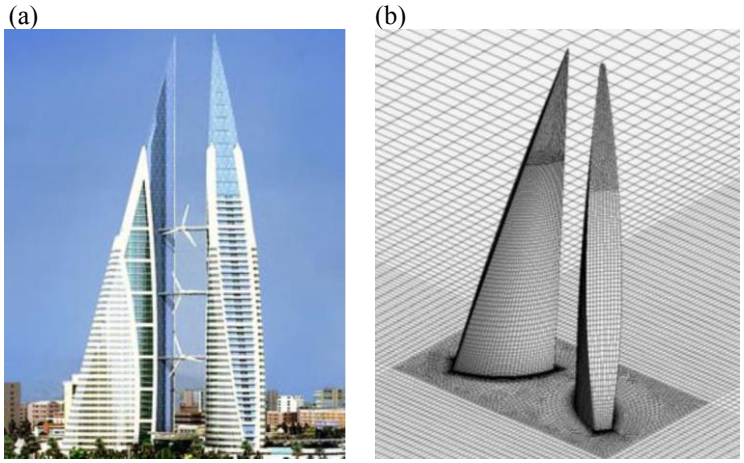

Figure 1. (a) Bahrain World Trade Center[2], and (b) corresponding computational grid (14 million cells).

A grid-sensitivity analysis has been performed to reduce the discretization errors and the computational time. The concept of the Grid Convergence Index (GCI) is used [11] for uniform reporting of grid refinement studies. Figure 2 shows the variation of normalized streamwise velocity at the location of the turbines with number of cells. It can be seen that there is oscillatory behavior in velocity field when computational grid is not sufficiently fine. The computational grid with around 14 million cells is chosen for the rest of the study, which yields a GCI value of 2.7% for streamwise velocity averaged at turbine locations. The validation study is performed for different wind directions of 0□, 15□ and 30□. The results are presented in Figure 3. The agreement is fairly good with average deviations of 6.9%, 6.97% and 5.64% for wind directions of 0□, 15□ and 30□, respectively.

2.1. Actuator Disk Modeling of wind turbines

In this study, the Actuator Disk Model (ADM) is used, in which the turbine disk is modeled as a porous medium that introduces a pressure drop in the flow [8]. The coefficients for this porous medium is calculated using turbine power curve and the combination of conservation of mass, momentum and

[2] Reference: http://inhabitat.com/bahrain-world-trade-center-has-wind-turbines/

energy for one dimensional actuator disk model. Figure 4 illustrates the computational grid including the disk for the ADM.

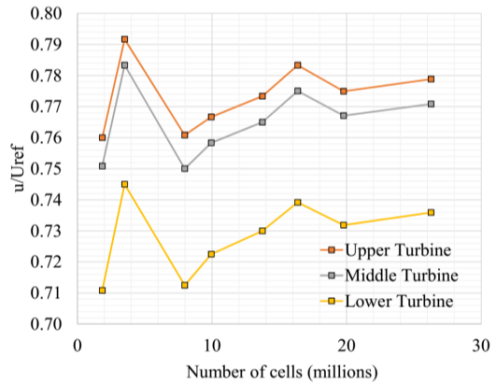

Figure 2. Variation of normalized streamwise velocity at turbine locations with number of cells

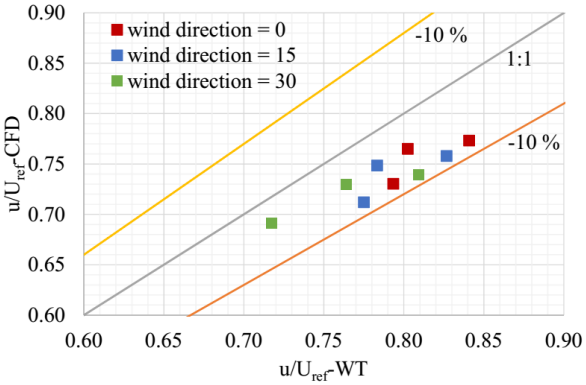

Figure 3. Comparison of numerical and experimental results for normalized streamwise velocity at turbine locations

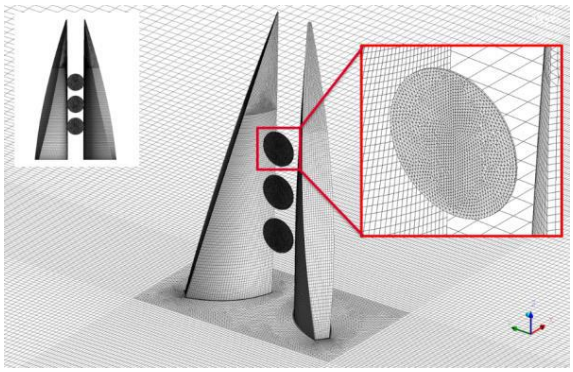

Figure 4. Generated grid for turbine disks and towers for Bahrain WTC

3. RESULTS

Figure 5 shows contours of the normalized streamwise velocity at horizontal planes at the turbine locations. It can be seen that the special arrangement of the towers can concentrate and accelerate the wind flow between the towers, where the turbines are located.

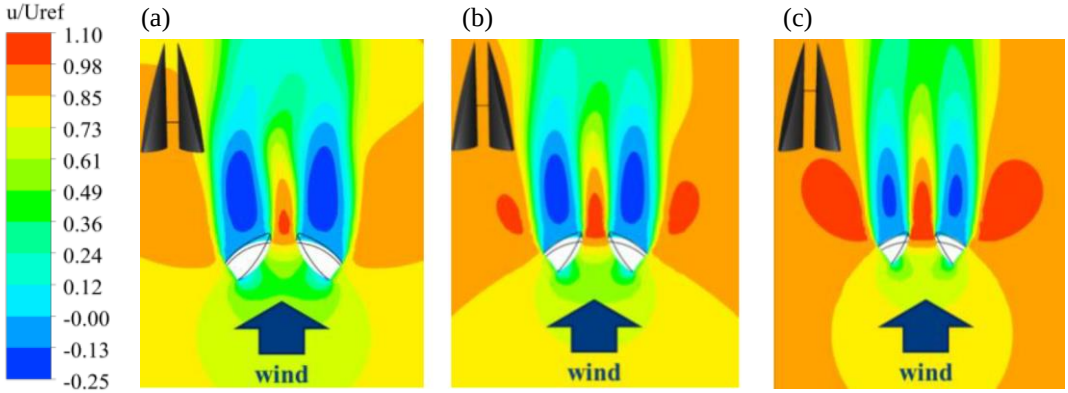

Figure 4. Generated grid for turbine disks and towers for Bahrain WTC

The results for the case with porous medium ADM is presented in Table 1, where Δm is the disk thickness and *a* is the turbine induction factor. In cases 1 and 2 the values for the induction factor are averaged for the whole range of freestream velocities, while the disk thickness is doubled in case 2. In case 3, the induction factor is not averaged to investigate the effect of averaging on the accuracy of simulations. It can be seen that higher velocity inductions occur at the turbine planes compared to the

case in which the towers are not taken into consideration. In this case, the average power output of wind turbines using these three cases is 5.8, 7.3 and 15% less than that of the case without wind turbines.

Table 1. Values for area averaged of u/U_{ref} at 60 cm distance upstream of the disk face

	Towers only	ADM (case 1) $\Delta m = 30$ [cm]	ADM (case 2) $\Delta m = 60$ [cm]	ADM (case 3) $\Delta m = 30$ [cm] with *a* distribution
Turbine upper	7.91E-01	7.63E-01	7.56E-01	7.22E-01
Turbine middle	7.69E-01	7.40E-01	7.33E-01	6.97E-01
Turbine lower	7.21E-01	6.95E-01	6.89E-01	6.55E-01

4. CONCLUSIONS

CFD simulations of wind flow around a tower are performed to investigate the effect of interaction of flow around buildings and turbines on wind energy potential. The Actuator Disk Model is used to implicitly take into account the presence of the wind turbines. The focus is on the World Trade Center (WTC) tower in Bahrain. The results show that for the case in which the wind turbines are modeled, the power output of the turbines can be 15% lower in comparison with that of the case where only the building is modeled.

ACKNOWLEDGEMENTS

The authors would like to acknowledge support from the European Commission's Framework Program Horizon 2020, through the Marie Curie Innovative Training Network (ITN) AEOLUS4FUTURE - Efficient harvesting of the wind energy (H2020-MSCA-ITN-2014: Grant agreement no. 643167) and the TU1304 COST ACTION "WINERCOST". The authors gratefully acknowledge the partnership with ANSYS CFD. The 2nd author, Hamid Montazeri, is currently a postdoctoral fellow of the Research Foundation – Flanders (FWO) and is grateful for its financial support (project FWO 12M5316N).

REFERENCES

[1] F. Toja-Silva, A. Colmenar-Santos, M. Castro-Gil, Urban wind energy exploitation systems: Behaviour under multidirectional flow conditions - Opportunities and challenges, Renew. Sustain. Energy Rev. (2013). doi:10.1016/j.rser.2013.03.052.
[2] L. Ledo, P.B. Kosasih, P. Cooper, Roof mounting site analysis for micro-wind turbines, Renew. Energy. (2011). doi:10.1016/j.renene.2010.10.030.
[3] P. Blackmore, Building-mounted Micro-wind Turbines on High-rise and Commercial Buildings:, 1 edition, IHS BRE Press, Garston, Watford, 2010.
[4] L. Lu, K.Y. Ip, Investigation on the feasibility and enhancement methods of wind power utilization in high-rise buildings of Hong Kong, 2009. doi:10.1016/j.rser.2007.11.013.
[5] I. Abohela, N. Hamza, S. Dudek, Effect of roof shape, wind direction, building height and urban configuration on the energy yield and positioning of roof mounted wind turbines, Renew. Energy. (2013). doi:10.1016/j.renene.2012.08.068.
[6] F. Toja-Silva, O. Lopez-Garcia, C. Peralta, J. Navarro, I. Cruz, An empiricalâ€“heuristic optimization of the building-roof geometry for urban wind energy exploitation on high-rise buildings, Appl. Energy. 164 (2016) 769–794. doi:10.1016/j.apenergy.2015.11.095.
[7] A.-S. Yang, Y.-M. Su, C.-Y. Wen, Y.-H. Juan, W.-S. Wang, C.-H. Cheng, Estimation of wind power generation in dense urban area, (2016). doi:10.1016/j.apenergy.2016.03.007.
[8] T. Javaherchi, S. Antheaume, A. Aliseda, Hierarchical Methodology for the Numerical Simulation of the Flow Field around and in the Wake of Horizontal Axis Wind Turbines : Rotating Reference Frame , Blade Element Method and Actuator Disk Model, Wind Eng. 38 (2014) 181–201. doi:10.1260/0309-524X.38.2.181.
[9] Y. Tominaga, A. Mochida, R. Yoshie, H. Kataoka, T. Nozu, M. Yoshikawa, T. Shirasawa, AIJ guidelines for practical applications of CFD to pedestrian wind environment around buildings, J. Wind Eng. Ind. Aerodyn. 96 (2008) 1749–1761. doi:10.1016/j.jweia.2008.02.058.

[10] J. Franke, A. Hellsten, H. Schlünzen, B. Carissimo, Best practice guideline for the CFD simulation of flows in the urban environment, 2007.
[11] P.J. Roache, Qunatification of uncertainty in computational fluid dynamics, Annu. Rev. Fluid Mech. 29 (1997) 123–160. doi:10.1146/annurev.fluid.29.1.123.

TECHNICAL SESSION 5.1

Work Packages 2 and 3 - Wind Turbine substructure

FATIGUE ANALYSIS ON INNOVATIVE 10 MW OFFSHORE JACKET STRUCTURE USING INTEGRATED DESIGN APPROACH

Ana Glisic[1*], Ngoc-Do Nguyen[2] and Peter Schaumann[3]

[1,3]Institute for Steel Construction, Leibniz Universitaet Hannover, Germany
[2]DNV GL – Energy, Hamburg, Germany
**Corresponding author: Ana Glisic,* glisic@stahl.uni-hannover.de

ABSTRACT

The fatigue limit state (FLS) of fixed offshore wind turbine structures is critical and difficult to handle. As it is the most common design driving criteria for offshore structures, the simulation and calculation of this phenomenon must be as accurate as possible. Research is needed to improve the current design. There are mainly two design approaches available: Integrated design approach (IDA) and Sequential design approach (SDA). The IDA, described in this paper, considers the coupled structural analysis of a whole wind turbine system exposed to wind- and wave-induced loads in an aero-hydro-elastic solver. The results given by solver are loads series, which are afterwards used for obtaining the stress series with stress concentration factors (SCF) included. The stresses are processed in terms of rainflow counting and finally, fatigue damage of a critical K-joint is obtained externally, to avoid the use of damage equivalent loads (DEL) as by default in the solver, but to calculate it by means of the Efthymiou principle. The whole procedure with methods is explained in this paper.

NOMENCLATURE

OWT	=	Offshore Wind Turbine
IDA	=	Integrated Design Approach
SDA	=	Sequential Design Approach
FLS	=	Fatigue Limit State
SCF	=	Stress Concentration Factor

1. INTRODUCTION

Steel jackets are support structures employed for offshore wind turbines (OWTs) in deeper waters, due to the higher stiffness at the footprint and the smaller surface facing the wave loads compared to the monopiles which are dominating the offshore wind turbines market. Furthermore, when talking about the new OWT installations in the EU in year 2016, jackets have a significant increase to 12% of all OWTs installed, compared to the year 2015 (Fig.1).

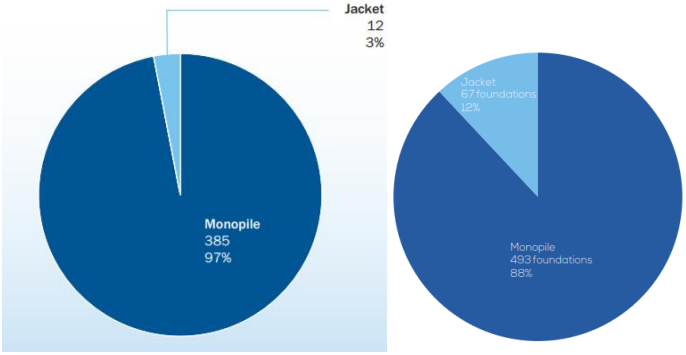

Figure 1. Foundation types installed in 2015 (left) and 2016 (right) annual market

The general trend in the offshore wind turbine industry nowadays is increase of the maximum capacity, as shown in the Fig. 2. Recently, turbines with output of 10 MW have been installed, and in the future, sizes are expected to grow up to 20MW, if proven economically and technically feasible [6, 7].

The size increase brings up the problem of larger generators, higher hub heights and larger structures and foundations, which leads to higher dynamic complexity of offshore wind turbines. As OWTs are exposed to cyclic aerodynamic, hydrodynamic and mechanical loading, they are especially prone to fatigue damage. This is a main design driving criteria, so constant research and improvements are needed in the approaches for fatigue analysis. Two mainly used approaches in the industrial design are IDA and SDA with superelements.

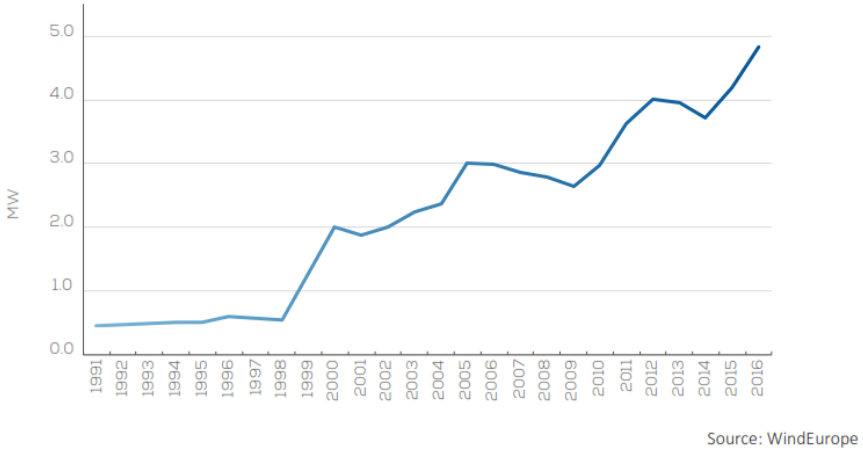

Figure 2. Average offshore wind turbine rated capacity in MW

The IDA considers the coupled structural analysis of wind and wave loads in one software only, while the SDA runs a separate aero-elastic analysis and takes only the interface loads from it for the further analysis in other offshore code. Both approaches have their own advantages, and are used depending on the case requirements and conditions. The main advantage of the SDA is that it supports the use of superelements, which allows the foundation designer to share their design for aero-elastic analysis without needing to share the detailed jacket design with the wind turbine manufacturer, as well as the fact that is can include some complex support structure elements (like shell elements) into the dynamic response of the structure.

However, the IDA has many advantages over the SDA. It includes the full coupling between wind and wave loads and the structure, while for the SDA hydro-elastic coupling is omitted, as the wave loads are given only as a simulation input. Next, by separating the simulations of wind and wave loads at SDA, the duplicated simulations must be conducted, which is not the case with IDA. Finally, the overall system optimisation is easier in fully integrated model, and that is the reason why calculation of the fatigue damage is here chosen to be conducted by means of IDA [1,4,5].

2. METHODOLOGY

The integrated FLS design is here conducted using the offshore code SESAM GeniE for structure modelling, and software Bladed for wind and wave loads computation and structural analysis. The workflow of the integrated design is visualized in the Figure 1 and described in following steps:

- Creating the jacket structure FE model in SESAM GeniE and converting it into the Bladed-readable format
- Importing the model in Bladed and adding the RNA
- Running all the analysis in Bladed
- Calculation of the SCFs for the relevant K-joint in accordance with [3]
- Including the SCFs in the stress calculations [3]
- Rainflow counting of the stress time series

- Calculating of the fatigue damage using the Efthymiou principle for 8 hot spots of the relevant brace in the K-joint.

Numerical model

The IDA workflow is shown in Fig. 3 [4]. First, the numerical model of the jacket structure is developed in the advanced offshore code SESAM GeniE. It is then converted into a Bladed format and imported into Bladed (aero-elastic solver), where it is linked to a 10 MW wind turbine based on a realistic reference design [2].

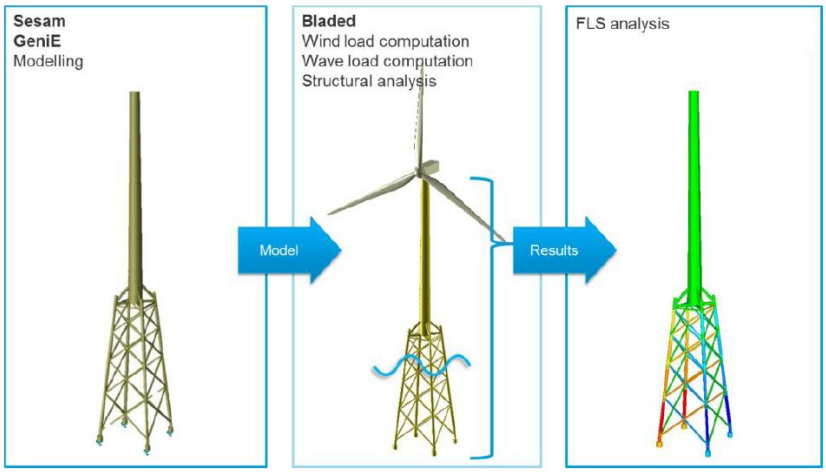

Figure 3. Workflow of the IDA using SESAM and Bladed [4]

The jacket structure is designed for an offshore site with water depth of 50m. It is supported by four piles 40 m embedded in the soil, which are here modelled by means of springs with the equivalent stiffness. The footprint disposition is 34 x 34 m. The RNA has a rotor diameter of 178.16 m with a hub height of 118.38 m (Fig. 4).

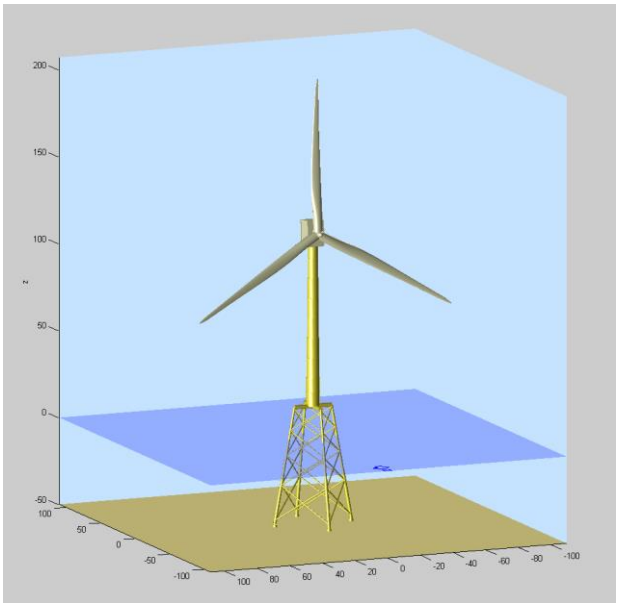

Figure 4. Numerical 3D model of the jacket structure with tower and RNA in Bladed

Loads

The jacket structure is exposed to wave loads and to wind loads mostly transferred from the tower with an RNA.

OWTs, as slender structures with a significant dynamic response, require stochastic modelling of the wave kinematics by means of irregular sea states. A sea state is defined by a wave-energy spectrum with a given significant wave height, a representative wave peak period, a mean propagation direction and a spreading function. Authors refer to [9] for a detailed explanation on modelling of irregular sea states in OWT design.

Regarding the realistic data, the mean wind speed for the target offshore site is 10 m/s. The wave energy spectra characteristics, namely significant wave height and mean zero-up crossing period, depend on the mean wind speed and in this case their values are respectively H_s=1.38 m and T_z=3.87 s. The irregular sea state is generated in Bladed and simulated 10 mins with a time step of 0.05 s. The whole process is repeated 6 times, each time changing only the randomness factor of the irregular sea state. That way, six different sea states with the same main characteristics are simulated and the fatigue damage is separately calculated for each simulation.

Wind loads are modelled by a turbulent wind field, where the basic idea is to describe spatial and temporal fluctuations with relevance for wind turbine load calculations. The turbulence has a three dimensional structure described by a spectral tensor. For a spectrum type, that describes the variance of the wind velocity fluctuations, Mann's model is chosen here, due to its good applicability for the flat, homogeneous terrains such as the sea surface. The main idea of this model is a division of the wind flow into a mean and a fluctuating part. For more detailed explanation about the Mann's model of the wind turbulence, authors refer to [10].

The Bladed software has a subprogram that defines the wind turbulence, once having all the wind turbine input parameters (dimensions of the wind field that covers the whole rotor area, simulation duration, main wind speed, height where the main wind speed is captured – hub height). The defined turbulence is an output file (.wind file) of this subprogram. Afterwards it used as an input file that defines wind loads in the final wind-wave simulation. In the similar manner as for the wave loads, six simulations have been carried out. In each simulation, different .wind file is used as a wind loads input file. Each of them six is created by the subprogram where the turbulence is defined with the same main characteristics, only the turbulence seed number is changed. The fatigue damage is here again separately calculated for each simulation.

To include the uncertainty caused by the stochastic nature of the wave and wind conditions, the final fatigue damage is taken as the mean value of the six separately calculated values.

The output of the simulations in Bladed are load time series. Comparing the loads in the members of the jacket structure, the most affected K-joint is chosen as the relevant one for this research. The most loaded K-joint is one the lowest four K-joints, as shown on the Figs. 5~6.

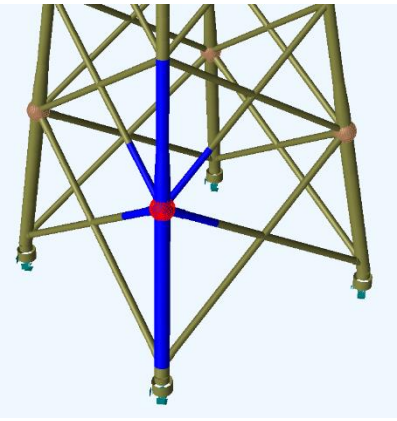

Figure 5. The most loaded K-joint of the jacket structure

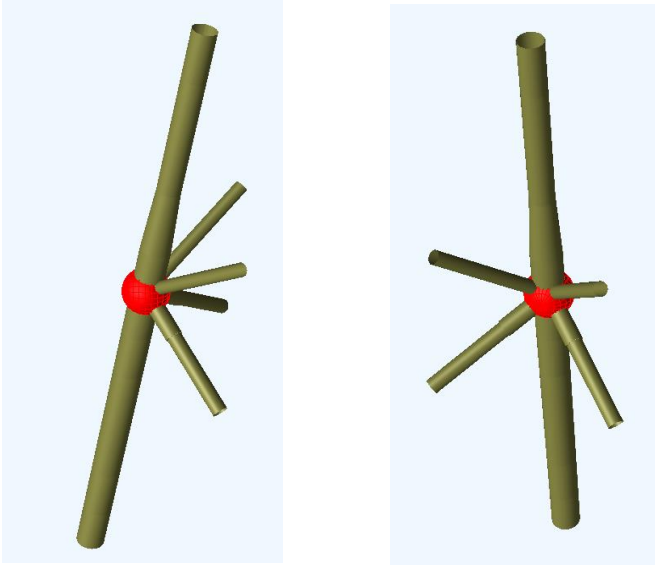

Figure 6. Detail of the reference K-joint

Since the stress time series are needed for a fatigue damage calculation, stresses are calculated by a channel combination of load series, using the Eqs 1-8 from [3]. These formulas include the stress concentration factors (SCFs) for tubular joints. Those are calculated in terms of Efthymiou principle. It considers the geometry of the joint and the type of loads applied. For the K-joints, SCFs for tubular joints are calculated as given in the Appendix B of the DNV GL-RP-C203 [3].
Once the SCFs, as well as the loads (F_x, M_y, M_z), are known, the stresses of the reference K-joint are calculated in terms of hot spot stresses. Figure 7 shows the hot spots locations on the brace circumference where the stresses are calculated, as well as the superposition of loads in the element in order to get the stresses. In each simulation, the highest of eight hot spot stresses is taken as the relevant one.

$$\sigma_1 = SCF_{AC}\sigma_x + SCF_{MIP}\sigma_{my} \tag{1}$$

$$\sigma_2 = \frac{1}{2}(SCF_{AC} + SCF_{AS})\sigma_x + \frac{1}{2}\sqrt{2}\,SCF_{MIP}\sigma_{my} - \frac{1}{2}\sqrt{2}\,SCF_{MOP}\sigma_{mz} \tag{2}$$

$$\sigma_3 = SCF_{AS}\sigma_x - SCF_{MOP}\sigma_{mz} \tag{3}$$

$$\sigma_4 = \frac{1}{2}(SCF_{AC} + SCF_{AS})\sigma_x - \frac{1}{2}\sqrt{2}\,SCF_{MIP}\sigma_{my} - \frac{1}{2}\sqrt{2}\,SCF_{MOP}\sigma_{mz} \tag{4}$$

$$\sigma_5 = SCF_{AC}\sigma_x - SCF_{MIP}\sigma_{my} \tag{5}$$

$$\sigma_6 = \frac{1}{2}(SCF_{AC} + SCF_{AS})\sigma_x - \frac{1}{2}\sqrt{2}\,SCF_{MIP}\sigma_{my} + \frac{1}{2}\sqrt{2}\,SCF_{MOP}\sigma_{mz} \tag{6}$$

$$\sigma_7 = SCF_{AS}\sigma_x + SCF_{MOP}\sigma_{mz} \tag{7}$$

$$\sigma_8 = \frac{1}{2}(SCF_{AC} + SCF_{AS})\sigma_x + \frac{1}{2}\sqrt{2}\,SCF_{MIP}\sigma_{my} + \frac{1}{2}\sqrt{2}\,SCF_{MOP}\sigma_{mz} \tag{8}$$

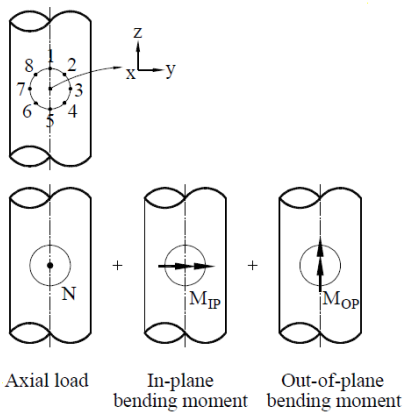

Figure 7. Hot spots and superposition of stresses in K-joint [3]

Now that the stress series for each of the six simulations are obtained, the next step for the fatigue calculation is to do a rainflow counting in order to get the number of cycles in the correspondent stress ranges.
Once the rainflow counting is done and the number of cycles are attributed to the corresponding stress ranges, fatigue damage of the K-joint is calculated by means of Markov matrices [8]. For the calculation of the fatigue damage, an S-N curve for the structures in the seawater with cathodic protection from DNV GL-RP-C203 is used (Fig. 8).

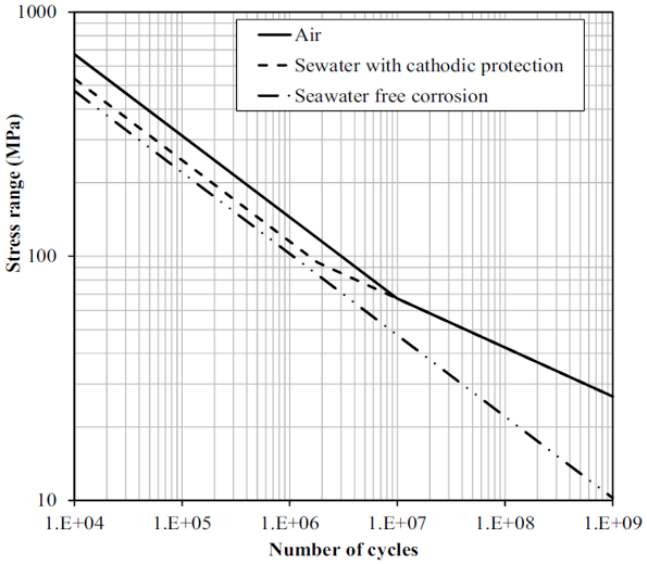

Figure 8. S-N curves for tubular joints in air and sea water with cathodic protection [3]

As mentioned, the final fatigue damage that represents the IDA is taken as a mean value of six fatigue damages obtained through six simulations where the random factor of the irregular sea state and turbulence seed number took six different values.

3. RESULTS

Six simulations were carried out, where six different wind seeds and sea state randomness factors were used. Each simulations includes applying the coupled wind and wave loads on the FE model, which is now consisting of the jacket structure, tower and an RNA, making a unique system that withstands the defined loads. Once the stress time series are obtained, the rainflow counting has been conducted using the feature of Bladed. Thus, the ranges of stresses with the corresponding numbers of cycles are obtained. The calculation of the fatigue damage from Markov matrices gave the following results, where $\boldsymbol{D_{max}}$ stands for the highest of eight hot-spot stresses pro simulation (Table 1). The final fatigue damage is a mean value of six simulations (Eq. 9).

Table 1. Fatigue damage of the relevant K-joint

Simulation	$\boldsymbol{D_{max}}$
1	1.355
2	1.232
3	0.972
4	1.051
5	1.081
6	1.616

$$\bar{D} = \frac{1}{6}\sum_{i=1}^{6} D_{max,i} = 1.218 \tag{9}$$

4. CONCLUSIONS

The examined procedure for the FLS analysis and the fatigue damage calculation proved to be less complicated and faster compared to the alternative. The IDA combined with the hydro-aero-elastic solver Bladed benefits from lower computational costs, concerning that it runs all the simulations simultaneously, without duplicated simulations in different codes. An optimised and verified compatibility of Bladed with an offshore code SESAM gives options for more detailed modelling and coupling. The next steps in the research are to carry out the same case analysis in SDA in order to closely perceive the difference in the results, methods and computational costs.

ACKNOWLEDGEMENTS

The authors acknowledge with thanks the support of the European Commission's Framework Program "Horizon 2020", through the Marie Skłodowska-Curie Innovative Training Networks (ITN) "AEOLUS4FUTURE - Efficient harvesting of the wind energy" (H2020-MSCA-ITN-2014: Grant agreement no. 643167), to the present research project.

REFERENCES

[1] W. Collier, D. McCowen,"Superelement Beta: User Guide for Bladed 4.8", DNV-GL, Doc No. 11052-UKBR-T-27-F, 2016

[2] L. Alblas, W. Collier, "Implementing an interface between Bladed and Sesam – Verification report of Sesam´s Bladed interface", DNV-GL Software, Report No. 2016-0866, 2017

[3] DNVGL-RP-C203 "Fatigue design of offshore steel structures", DNV-GL recommended practice, 2016

[4] DNV-GL "Performing FLS and ULS analysis on fixed offshore wind turbine support structures in the time domain – Integrated design approach", DNV-GL SESAM user course, 2016

[5] DNV-GL "Performing FLS and ULS analysis on fixed offshore wind turbine support structures in the time domain – Sequential and Superelement analysis approach", DNV-GL SESAM user course, 2016

[6] The European Wind Energy Association (EWEA, 2017). "Wind in power: 2016 European statistics"

[7] Wind Europe (2017). "The European offshore wind industry: Key trends and statistics 2016"

[8] Guedres Soares, C, Yeter, B, garbatov, Y (2015). "Fatigue damage assessment of fixed offshore wind turbine tripod support structures", Engineering Structures, Volume 101, pp.518-528.

[9] Glisic, A, T. Ferraz, G, Schaumann, P (2017). "Sensitivity analysis of monopiles' fatigue stresses to site conditions using Monte Carlo Simulation", The Proceedings of the 27th (2017) International Ocean and Polar Engineering Conference, ISOPE 17, San Francisco, USA.

[10] Mann, J (1998). "Stochastic wind loads on structures. Lecture notes", Risø National Laboratory.

Paper TS5.1.2

THE INTERNATIONAL CONFERENCE ON
WIND ENERGY HARVESTING 2018
21-23 March 2018
Catanzaro, Italy

HIGH STRENGTH STEEL CONNECTIONS BETWEEN POLYGONAL BUILT-UP MEMBERS: NUMERICAL INVESTIGATION AND COMPARISON WITH NORMAL STRENGTH STEEL CONNECTIONS

Slobodanka Jovašević[1*], Carlos Rebelo[2] and Marko Pavlović[3]

[1,2] ISISE, Department of Civil Engineering, University of Coimbra, Coimbra, Portugal
[3]Faculty of Civil Engineering and Geosciences, Delft University of Technology, Delft, Netherlands
Corresponding author: Slobodanka Jovašević, sjovasevic@uc.pt

ABSTRACT

The demand for high strength steel in the construction of buildings and civil engineering structures is in constant increase. However, there is a significant lack of knowledge in behaviour of high strength steel structures. Therefore, research must be focus on characterization of the strength and stiffness of members and connections. The aim of this investigation is to determine the failure modes of the elements and connections, as well as rotational stiffness and ultimate resistance of the connection. Furthermore, advantages and disadvantages of using high strength steel material for studied connections will be assessed. The focus in this paper is numerical investigation of preloaded gusset plate connections between polygonal built-up members that are composed of cold-formed pieces connected together with preloaded bolts. The connection model has been analysed through the elastic and plastic ranges up to failure. Difference in behaviour of S355 joint and S690 joint has been investigated.

NOMENCLATURE

CHS	=	Circular Hollow Section
WEC	=	Wind Energy Converter
$N_{brace.Rd}$	=	Brace design plastic resistance (kN)
M_j	=	Bending moment applied to the connection (kNm)
θj	=	Connection rotation (rad)

1. INTRODUCTION

The high demand for wind energy, due to European Union target to until 2030 at least 27% of total energy consumption is covered from renewable sources [1], [2], is leading to construction of more powerful wind energy converters. Therefore, higher towers are required. However, with the increase of the tower height, transportation, assembly, erection and maintenance of the tower becomes more difficult and more costly [2], [3]. At the moment, the most commonly used type of the tower for WEC is steel tubular tower with the height up to 100m. Proposed solution for higher tower is steel hybrid tower that uses lattice structure for lower and a tubular structure for upper portion of the tower. The use of tubular tower for upper portion takes all the advantages of optimized technology for tubular steel towers with the diameters within public road transportation limitations, while the lattice portion enables the extension of the height [4]. Another advantage is that the lattice portion can be used to facilitate installation of the upper tubular portion and the turbine, therefore avoiding the need for very high cranes.

For the lattice portion new types of bolted cross-sections are proposed (Figure). This types of cross-section are composed of cold formed pieces connected together with preloaded bolts creating polygonal (hexagonal and nonagonal) cross-section. The goal with using bolted polygonal built-up cross-section instead of CHS is to use advantage of polygonal over circular sections [5], and to improve fatigue life of the connections and members. The fatigue behaviour of preloaded high strength bolted connections

under shear or friction loads can bear higher fatigue loads than welded joints [6]. Further the use of high-strength steel was investigated as it is one of the suitable choices for construction material when durability, long lifespan, easy maintenance and aesthetic appearance are taken into consideration in design.

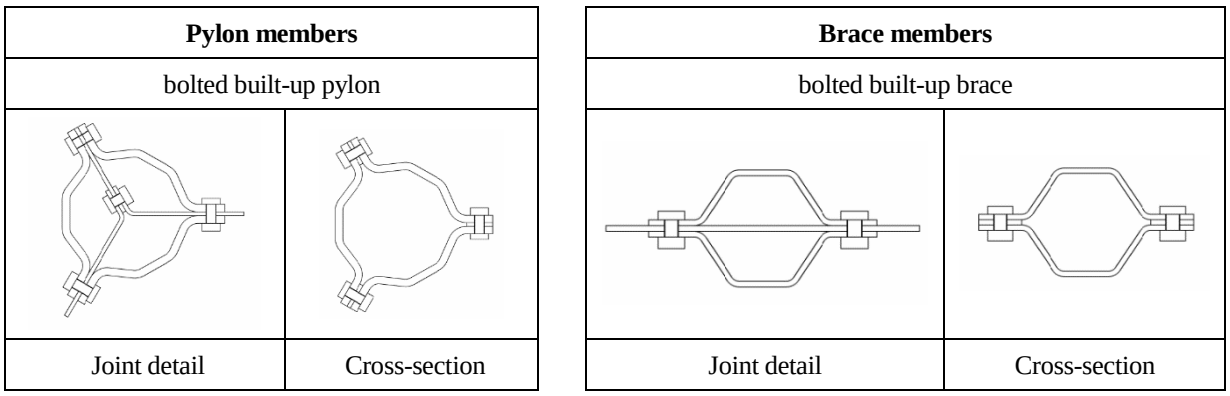

Figure 1. **Proposed cross-sections and joint details**

Since the behaviour of the joints is an important parameter in the structural global behaviour, and the current design codes lack information on this type of joints, an intensive study is carried out. This paper focuses on development of FE model and the evaluation of the resistance of joints between these types of members under bending moment. The behaviour of normal strength steel (S355) joint is compared with high-strength steel (S690) joint. The considered joint has the geometry depicted in Figure (right). The secondary member of the connection (horizontal in Figure 2 (right)) is called brace, and the main member (vertical in Figure 2 (right)) is the pylon. Connection with gusset plates and preloaded bolts is used in order to maintain simplicity of the connection bolted in-situ.

For different steel grade different thicknesses for pylon, brace and gusset plate were considered (Table).

Table 1: **Case study parameters**

Steel grade	Pylon		Brace		Bolts	Gusset Plate
	D [mm]	t [mm]	D [mm]	t [mm]		t [mm]
S355	325	12.0	200	5.0	2x4xM20 + 6xM20	6.0
		12.0		5.0		8.0
		12.0		5.0		10.0
		12.0		5.0		15.0
S690		6.0		2.6		3.0
		6.0		2.6		4.0
		6.0		2.6		5.0
		6.0		2.6		7.8

2. THE FINITE ELEMENT MODEL DESCRIPTION

The numerical model considered for this study was developed using ABAQUS [7] software. The finite element type C3D8R is adopted for steel gusset plates, high strength bolts and pylon and brace element in the region near connection. Steel pylon and brace in the region outside of the connection are modelled using finite element type SC8R. To capture accurately the stress behaviour in the region around the bolt holes, where the higher stresses are more likely to occur, an intensive mapped mesh was made within the vicinity of the bolt holes (Figure (left)). The bolt holes are modelled as 2mm larger than the bolt shank diameter, and the hexagon bolt heads were modelled as cylinders.

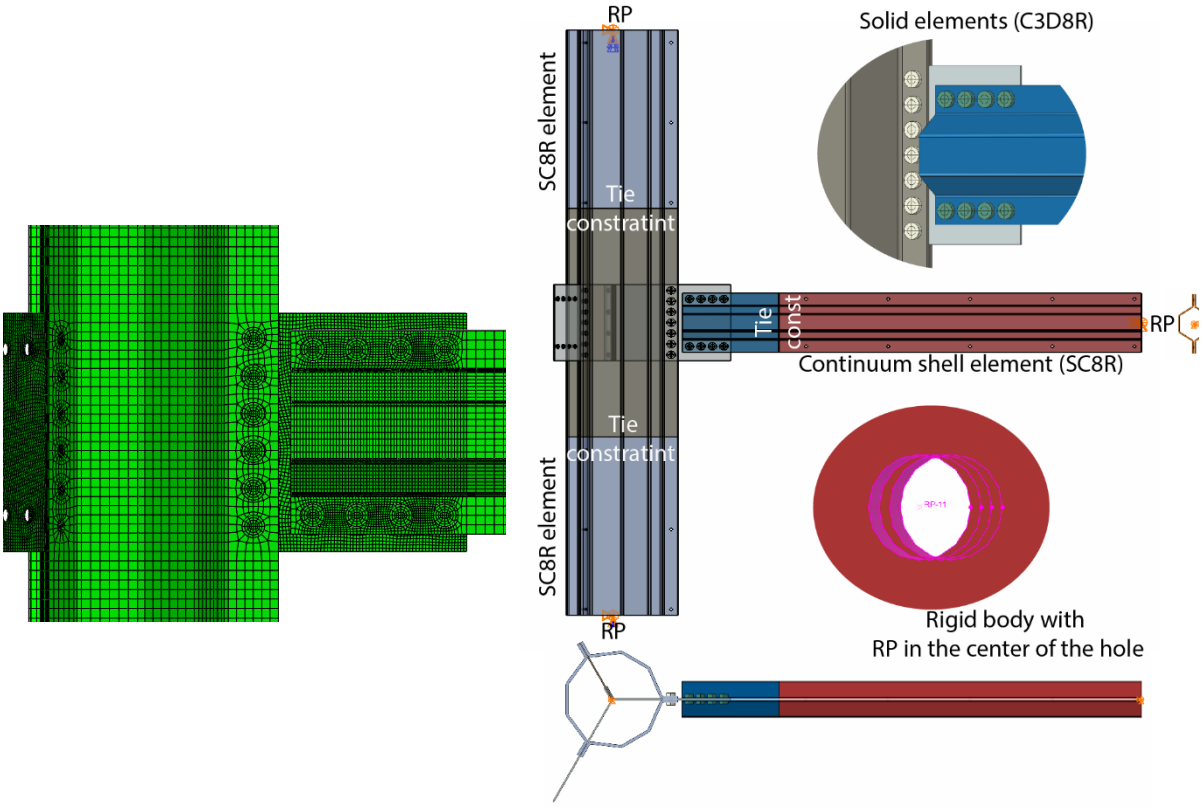

Figure 2. **Numerical model joint detail (left) and boundary conditions applied (right).**

Boundary conditions are assigned in referent points (RP) shown in Figure . The degrees of freedom of pylon bottom cross section are constrained all translations and rotation around z axis (u_1,u_2,u_3,$r_3 = 0$), while on the top cross section of the pylon vertical translation is free (u_1,u_2,$r_3 = 0$). At the brace end only translation out of the plate is constrained ($u_2 = 0$).

Three types of interactions are accounted for and implemented in FE models: (i) *Rigid-body constraints* with reference points in the centre of end cross-section (ii) *Contact interaction* using "Coulomb friction" to describe the tangential behaviour with a friction coefficient equal to 0.4, and "Hard contact" to characterize the normal behaviour (iii) *Tie constraint* that connects regions with two different element types used in the FE model.

S355 and S690 steel grades with an elastic modulus of 210GPa and 355MPa yield stress for S355 and 690MPa for S690 were adopted for pylon, brace and gusset plates. All bolts are high strength steel of grade 10.9 with Poisson's ratio of 0.3 and proof Young's modulus 210GP. The bolt shank is modelled by meshing a solid cylinder (Figure3) having a nominal circular gross area of the bolt.

The analysis type is ABAQUS/Explicit dynamic, realized in two steps: clamping and monotonic load with the final displacement equal to 200mm. The load application method is "Dynamic Explicit". The nonlinear effects of large displacements are included. Smooth amplitude functions are used for all loading steps (changes in boundary conditions) to withdraw impact behaviour and excitation of model due to inertia forces.

For the tightening force of the bolts, preload was applied as thermal contraction. In the material properties of the bolt shank expansion is defined as "ortotropic expansion" with $\alpha_{11} = \alpha_{22} = 0$ and $\alpha_{33} = \alpha$. The negative temperature is applied as "predefined field" type "temperature" in clamping step. Section variation is set as constant through region. Temperature applied is calculated using following expressions:

$$\Delta T = \alpha \frac{\Delta l}{l_{shank}} \quad (1)$$

$$\Delta l = \delta_{joint} \cdot F_{s.Rd} \quad (2)$$

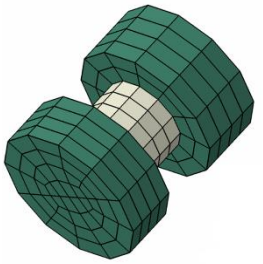

Figure 3. **Meshed bolt**

where:

α coefficient of thermal expansion

$F_{s.Rd}$ bolt preload force

δ_{joint} elastic resistance of bolted connection [8].

For ABAQUS/Explicit dynamic solver, the integration maximum stable time increment is represented by the size of the smallest finite element in a model, divided by a wave propagation speed. Therefore, computational time of a real time quasi-static analysis can be inapplicable long. Calculation speed can be increased either by a time scaling or mass scaling method [9]. These methods tend to increase inertia forces in a model, sometimes leading to a useless results. A compromise must be found between an acceptable computation time and quality of results, often by test analysis for each of the different model set-ups. Mass scaling with time increment of 0.005 was used in these analyses. FEA code automatically increases masses of finite elements such that their stable time increment matches the desired time increment [9]. Scaling is set to be variable (recomputed in every integration step) and non-uniform (different for each finite element) as it is the most efficient for the models with large spectra of elements sizes.

3. RESULTS

3.1. Moment-rotation curves

Joint behaviour may be represented by the moment-rotation curve (*M-θ*) presented in Figure5. This curve describes the relation between the bending moment ratio M_j/M_y and the corresponding rotation ratioθ_j/θ_y. Bending moment M_j is moment applied to a joint and the rotation θ_j is corresponding rotation between the connected members. Bending moment M_y is plastic resistance of brace and rotation θ_y is yield rotation of the brace calculated according to FEMA 356 [10] using following expression:

$$\theta_y = \frac{W_{pl} \cdot f_y \cdot L_b}{6 \cdot E \cdot I_b} \quad (1)$$

The bending moment acting on connection corresponds to applied load ($R3_{RP3}$ - reaction force of the brace end) multiplied by the distance between centre of the pylon and end of the brace (L_{load}).

Moment and rotation of the connection are computed using following expressions:

$$M = R3_{RP3} \cdot L_{load} \quad (2)$$

Displacement values in the reference points (P_1,P_2,B_1, B_2) of Figure 454 are used to determine rotational deformation of the joint:

$$\theta = \frac{u_{1(B1)} - u_{1(B2)}}{h_{br}} - \frac{u_{1(P1)} - u_{1(P2)}}{h_{gp}} \quad (3)$$

where:

u_1 is the horizontal displacement

h_{br} is the distance between points B_1 and B_2

h_{gp} is the distance between points P_1 and P_2

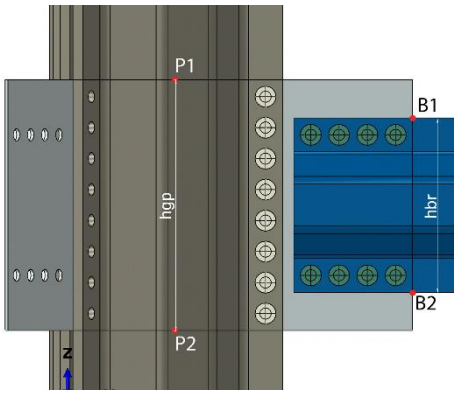

Figure 45. **Moment and rotation calculation parameters.**

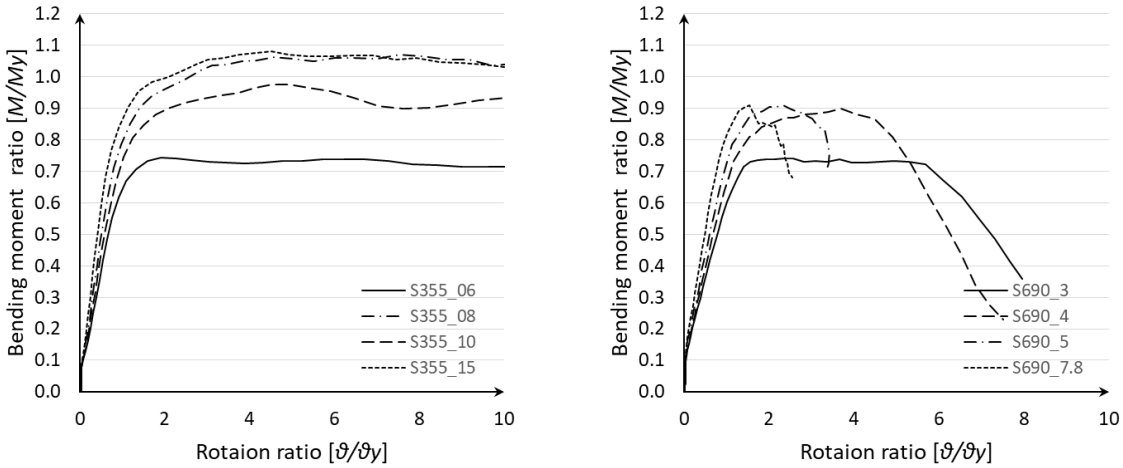

Figure 5. **Moment-rotation curves.**

3.2. PEEQ – Equivalent plastic strain

The PEEQ for the first joint configuration in the end of the second load step (monotonic load – bending) are presented in 6 (left) for S355 joint and Figure 666 (right) for S690 joint.

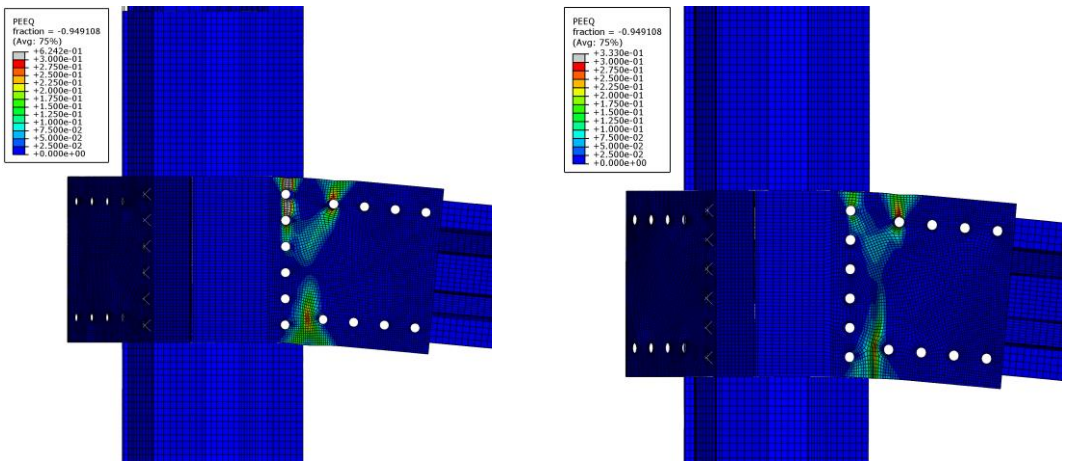

Figure 66. **PEEQ – S355 joint (left), S690 joint (right).**

For the cases with the S355 steel, with the increase in gusset plate thickness the failure mode shifts from gusset plate net section yielding Figure 666 (left) to yielding of net cross section of the brace in the last bolt row of the part in the tension. On the other hand, for S690 steel connections, yielding of the gusset plate is combined with buckling of the compression part of the gusset plate 6 (right). Also, with the increase of gusset plate thicken the failure mode shift to the local buckling of the brace member.

In both cases S355 and S690 connections, with the increase of the gusset plate thickness the bending moment ratio increases.

4. CONCLUSIONS

The results show that for the first two joint configurations for both cases (using S355 and S690 steel grade) the failure in the joint occurs in gusset plate. However, the different failure mode is observed. In the case of S355 joint the failure of the connection is yielding of the gusset plate in the net section where connected with the pylon. While for the case of S690 joint the failure is buckling of the gusset plate. For the other two joint configurations for the case of S355 connection the failure occurs in the net section of the brace member. For the S690 the failure is buckling of the brace member. Different failure mode is consequence of significantly lower thickness of gusset plate and the members in case of S690 joint.
The moment-rotation curves show increase in utilisation ratio with increase of gusset plate thickness. This increase is observed while the failure occurs in the gusset plate. When the member fails, either by yielding of net section or buckling of the member, the increase of the gusset plate thickness does not have influence on overall resistance of the connection.
In reality, this research program is going further than the development of the FE model for connection with normal strength steel and high strength steel. Experimental testing and FE model validation are in progress. In addition, a new hand-calculation method taking into account the influence of the joint tolerances for assembly is to be developed.

ACKNOWLEDGEMENTS

The authors acknowledge with thanks the support of the European Commission's Frame-work Programs "Horizon 2020" program through the Marie Skłodowska-Curie Innovative Training Networks (ITN) "AEOLUS4FUTURE – Efficient harvesting of the wind energy" (H2020-MSCA-ITN-2014: Grant agreement no. 643167) and RFCS – Research Fund for Coal and Steel program through the Grant Agreement RFSR-CT-2015-00021.

REFERENCES

[1] EWEA, "Wind energy scenarios for 2030," 2015.

[2] E. Hau, "Wind turbines: fundamentals, technologies, application, economics," *Springer Berlin, Ger.*, 2006.

[3] J. F. Manwell, J. G. McGowan, and A. L. Rogers, *Wind Energy Explained: Theory, Design and Application*. Wiley, 2002.

[4] K. Hüsemann, "Ruukki Wind towers – High truss towers for wind turbine generators," Finland, 2010.

[5] O. Garzon, "Resistance of polygonal cross-sections - Application on Steel Towers for Wind Turbines," Luleå University of Technology, 2013.

[6] J. P. Jaspart and K. Weynand, *Design of Joints in Steel and Composite Structures*. ECCS - European Convention for Constructional Steelwork, 2016.

[7] "ABAQUS/Standard, User's Manual I-III, version 6.3," 2001.

[8] M. Pavlović *et al.*, "Connections in towers for wind converters, Part II: The friction connection behaviour," *J. Constr. Steel Res.*, vol. 115, pp. 458–466, Dec. 2015.

[9] Dassault Systèmes, *Abaqus Analysis User's Manual version 6.14*. 2014.

[10] Nonlinear Static Procedure, "FEMA 356." .

Paper TS5.1.3

THE INTERNATIONAL CONFERENCE ON
WIND ENERGY HARVESTING 2018
21-23 March 2018
Catanzaro, Italy

THE HYBRID HIGHRISE WIND TURBINE TOWER: THE TRANSITION PIECE DESIGN

Mohammad Reza Shah Mohammadi[1]*, Carlos Rebelo[2], Milan Veljković[2] and Luís Simões da Silva[1]

[1] ISISE, Department of Civil Engineering, University of Coimbra, P-3004 516, Coimbra, Portugal
[2]Faculty of Civil Engineering and Geosciences, Delft University of Technology, Delft, The Netherlands
Corresponding author: Mohammad Reza Shah Mohammadi, mrsm@uc.pt

ABSTRACT

In recent years, wind farms' repowering has been started. Tower technology shows convincing potential for the increase of the electric power generation by reaching higher altitudes for stronger and less turbulent wind. Moreover, there is a potential cost reduction of wind energy by facilitating the transportation and installation procedures of the high rise supporting structures and respective foundations.

In order to achieve a competitive solution, a hybrid lattice-tubular steel tower concept has been presented. Different design scenarios were previously investigated for a185 m high study case.

This paper aims to complete the conceptual design of the hybrid tower and discuss the behaviour of the new tower's subcomponents solutions in detail.

Results present a detail design of the transition piece concepts of the proposed tower. A comparison is done between the different transition piece configuration including the shell configuration and connection. Furthermore, the ultimate limit state and post-buckling behavior of the transition piece is investigated.

NOMENCLATURE

DLC	=	Design Load Case
GMNIA	=	Geometrically and Materially Nonlinear Analysis with Imperfections
HLT	=	Hybrid Lattice-Tubular
LDST	=	Large Diameter Steel Tower
TP	=	Transition Piece

1. INTRODUCTION

By the end of 2015, more than 432 GW wind capacity is installed all around the world. Moreover, wind energy overtook the hydropower and became the third source of energy in Europe[1]. Wind farms repowering has been started and now widely is considered as a necessary policy in energy development [2]. Higher capacity wind converters are supposed to be used for repowering. To do so, two interdependent strategies are applied. Increasing the rotor blade diameter and, consequently, increasing the wind turbine tower height, which on its turn allows to take advantage of higher wind speed and more steady wind flow. However, increasing the height of wind turbine tower structure leads to new challenges in different aspects. The increase in the height of the turbine leads to large tubular tower base diameter. Therefore, the transportation and the installation become a new challenge.

The tallest installed wind turbine onshore belongs to Vestas 3 MW wind turbine with 166 m height. The innovative tower design was introduced as large diameter steel tower (LDST) for this wind turbine model with 6.2 to 6.5 m of the tower base diameter. For ease the transportation, the large segments of the tubular tower are manufactured by cutting them horizontally and longitudinally into several pieces. Figure shows both, the designed hybrid lattice tower with 6 legs and the 166 m tower using LDST[3]. The hybrid lattice-tubular tower was proposed which increase the accessible height and also facilitate the transportation and erection by using the lattice structure [4].

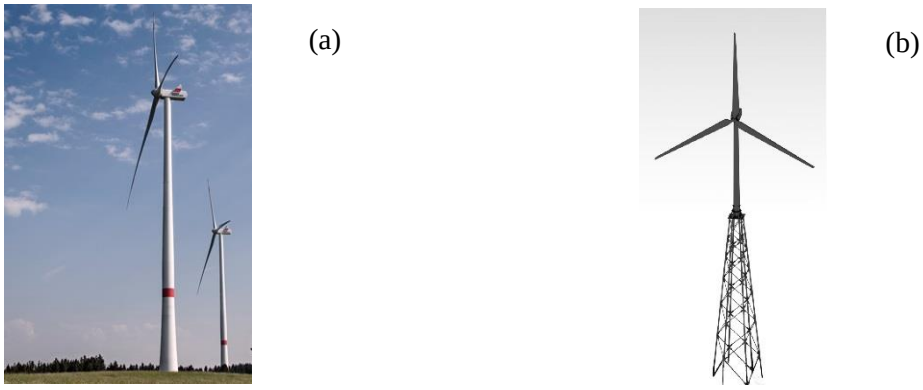

Figure 1: **The wind turbine Tower high rise concepts, (a) 166 m LDST[3], (b) 185 m HLT**

As it can be seen in Figure b, the transition piece (TP) is employed as a connection between the tubular and the lattice structure. The transition piece is one of the most crucial points as it is prone to high overturning moment of the tubular tower and fatigue from cyclic loading. The TP is supposed to withstand all operational loads and transfers the loads from the blades and the tubular tower to the ground.

2. METHODOLOGY

In order to calculate the operational loads, NREL 5MW baseline wind turbine was used and the servo-hydro-aeroelastic simulations were performed. The ultimate limit state loads were obtained based on IEC61400-1[5]. Power production during 3 m/s to 25 m/s wind speed and parked wind turbine under extreme wind condition were simulated as the selected design load cases (DLC).
Moreover, linear finite element analysis has been done for parametric study. Then, geometrically and materially analysis (GMNA) was performed to design and investigate the final TP models. Moreover, buckling analysis was performed to investigate the buckling in the TP and tubular tower shell to obtain the eigenvalues and the mode shapes of the transition piece. Furthermore, the first mode of the buckling

In this analysis, two cylindrical and conical shell configurations are considered. Moreover, two different shear and gusset plate connections are utilized to fulfil the connection of the transition piece to the lattice structure. Figure 2 shows the proposed TPs with different shell and chords.

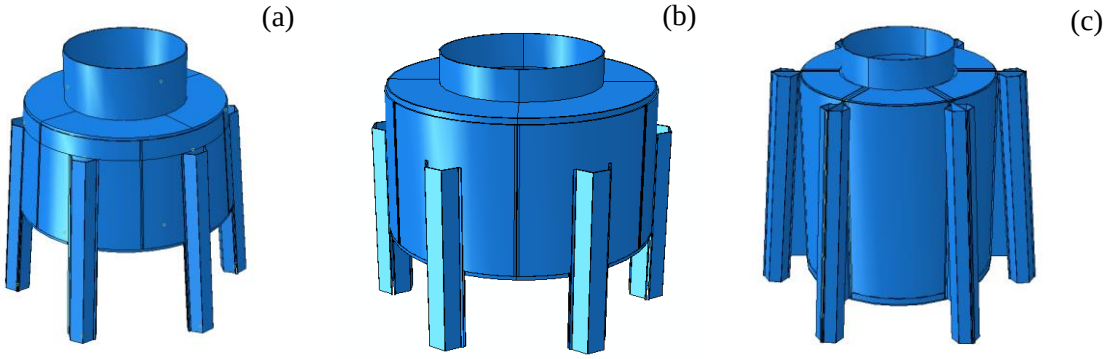

Figure 2: **Transition Piece, (a) Shear connection with conical shell, (b) Shear connection with cylinder shell, (c) Gusset connection with cylinder shell**

3. RESULTS

3.1. Mesh Study

In order to ensure adequate results from *ABAQUS* simulation a refined and good quality mesh should be used. However, the computer resources required to perform the finite element analysis increase with the level of the mesh refinement. The mesh study is done for the 8 m transition piece with shear connection and the cylindrical shell. A linear analysis was performed using a standard general procedure. Mesh study was conducted C3D8R element which is an 8-node linear brick.

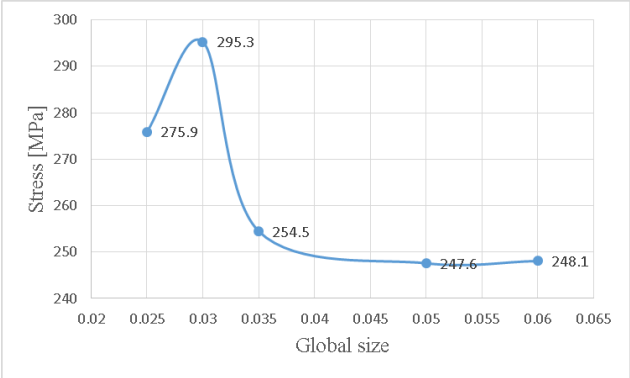

Figure 3: **Mesh analysis for the 8 m transition piece with cylindrical shell**

3.2. Parametric study

In order to dimension the TP height, shell thickness and compare the stress level in the structure, a parametric study was done. The height varies from 2 to 10 m and the thickness between 40 and 50 mm. The conical shell has slight decrease in the stress level by increasing the height of the TP but increasing the height has higher influence on the cylindrical shell stress level. Moreover, the thickness does not have huge influence on the stress level.

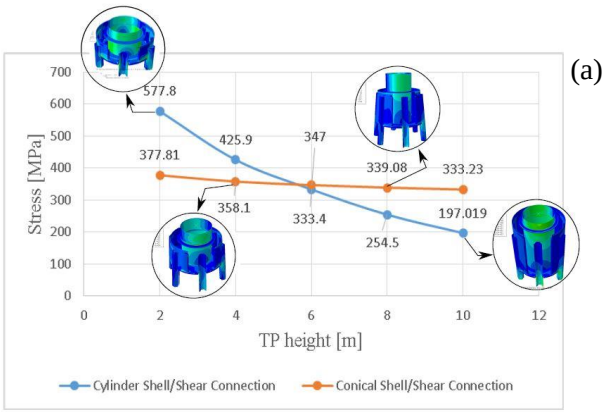

(a)

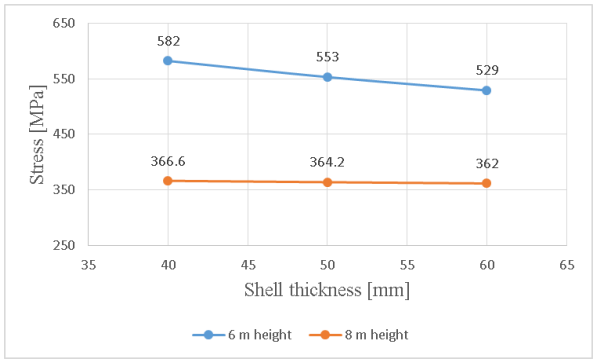

(b)

Figure 4: **Transition Piece parametric study**

3.3. Geometric Material Nonlinear Analysis

Three TPs from each group is selected as case studies for the nonlinear material and geometry analysis as below:

- 2 m cylinder shell with shear connection
- 4 m conical shell with shear connection
- 8 m cylinder shell with gusset connection

Figure 5 shows the finite element results for two TPs with shear connections and different cylindrical and conical shells with 50 mm thickness. The stress level in both of the structures are higher than normal S355 steel grade and higher steel grade like S460 is appropriate to be used. In both structures, the lower connection between tubular tower and the TPs' shell has the highest stress level. However, the 2m TP shows higher stress transfer to the chords and the lattice structure. The high stress distribution on the top plate and the upper part of the tubular tower, close to the flange connection, show the possibility of the buckling.

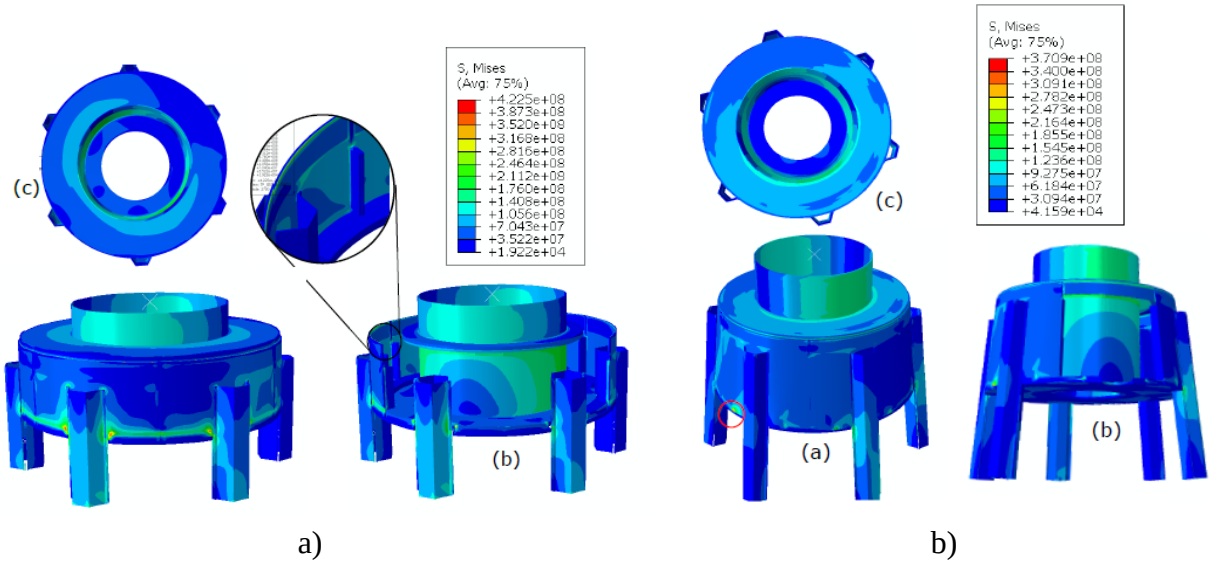

a) b)

Figure 5: **Nonlinear ULS analysis on shear connection**

The third case study is the TP with gusset connection and the 50 mm cylindrical shell as it is shown in Figure 6. The highest stress level is 391 MPa which happens at two regions. The hotspots are in the tubular segment and the flange and the other one happens at the connection between upper plate and the TP's shell. However, the upper plate and the tubular segment need to be further investigated with buckling analysis.

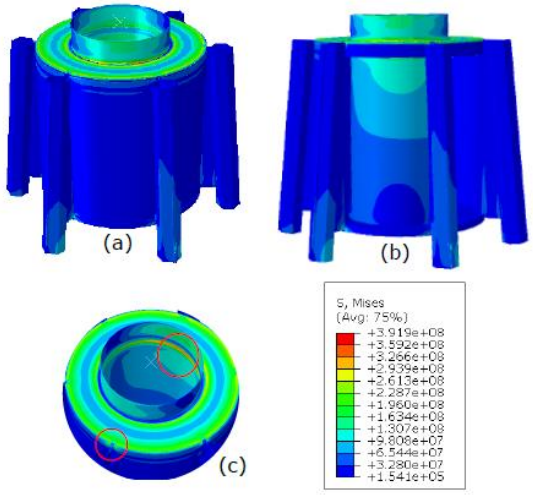

Figure 6: **Nonlinear ULS analysis on gusset plate connection**

3.4. Buckling Analysis

Due to the stress level and manufacturing feasibility, the transition piece with 8 m height and 50 mm shell thickness is considered for the further buckling and nonlinear analysis.

The buckling is the frequent failure mode of the wind turbine towers. Finding the buckling mode and eigenvalues of the model helps to avoid any buckling failure mode. ABAQUS estimates the buckling load in the format of the Equation 1.

$$P^N + \lambda Q^N \tag{1}$$

Where the λ is the eigenvalue, P consists of surface traction, body forces and prescribed displacement, and Q is small displacement gradients under additional surface traction, body force and boundary displacement.

As it can be seen in Figure 6, buckling mode shapes of the transition piece are penetrated in the lower and upper plate. Figure 6(a) shows the first buckling mode of the structure and in Figure6 (b) and (c) the further buckling modes are illustrated which have different location than in the lower plate.

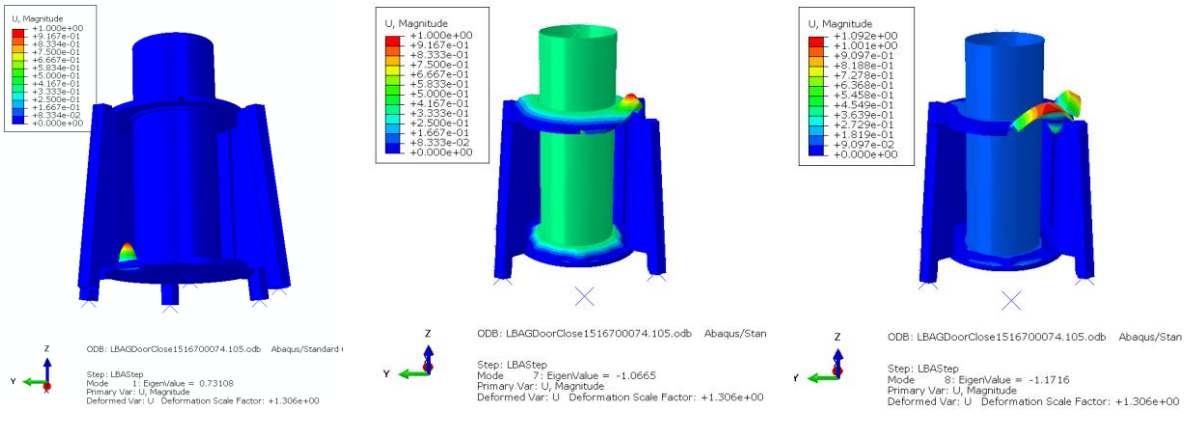

(a) (b) (c)

Figure 7: **Linear Buckling eigenvalues of the transition piece**

Moreover, the first 5 buckling eigenvalues of the transition piece are listed in Table 2.

Table 2: **the first five Eigen values of the transition piece**

Mode shape	Value
1	0.7310
2	0.7798
3	0.7908
4	0.8653
5	0.8674

3.5. Nonlinear Analysis with Imperfection

In order to calculate the nonlinear model considering the imperfection, the eigenvalues from previous section can be used as an imperfection in the analysis. The magnitude multiplier can be calculated as according to EN1993 Part 1-6[6].

Initially the I_{gx} is calculated based on the maximum radius of r and the shell thickness of t.

$$l_{gx} = 4\,.\sqrt{r}.t = 4\,.\sqrt{3750}.50 = 1732mm \tag{2}$$

Then the following formula can be used based on Eurocode recommendations. EN1993 Part 1-6 recommended value of n_i is 25 and the value of U_{n1} and U_{n2} is suggested equal to 0.016 to high fabrication quality.

$$\Delta w_{0,eq} = max\left\{\begin{matrix}\Delta w_{0,eq,1} = l_g \times U_{n1} \\ \Delta w_{0,eq,2} = n_i \times t \times U_{n2}\end{matrix}\right\} = max\left\{\frac{27.71}{20}\right\} = 27.71mm \tag{3}$$

Therefore, the magnitude multiplier of 27.71 mm for the first mode shape and the half of it for the second mode shape to consider the imperfections in the model.

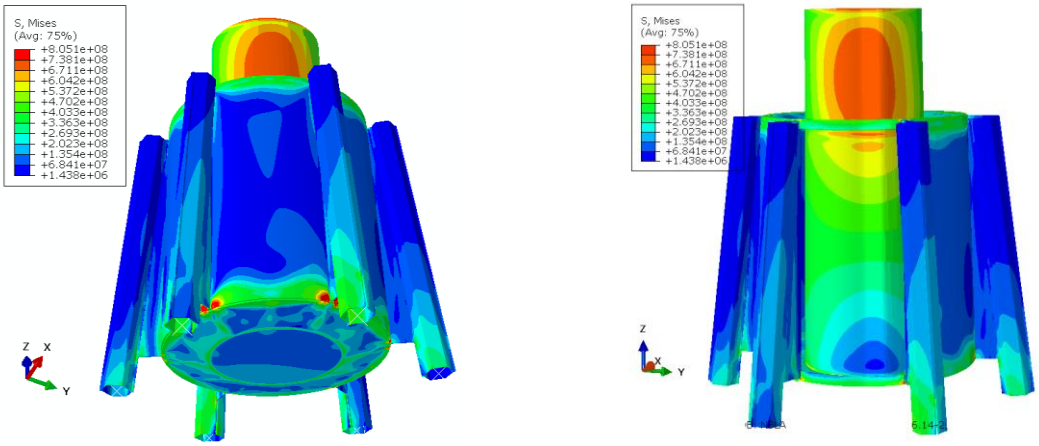

(a) (b)

Figure 8: **The nonlinear geometry and material analysis with imperfections (a) the stress concentration at lower plate, (b) at the upper and lower part of flange connection**

The GMNIA analysis captured also the same stress concentration area as the nonlinear simulation. The stress distribution are more around upper flange and the lower plate connections as the load transfers from these two connection.

4. CONCLUSIONS

The study continues the design of the hybrid lattice-tubular tower for an onshore wind turbine. The initial detail design of the transition piece concepts were proposed and investigated. The design considered both operational and lifting loads.
The parametric study shows that the cylindrical shell with shear connection can lead to shorter transition piece height. The cylindrical shell with gusset connection showed appropriate stress level with 8m height.
The initial study shows clear stress concentration in the flange connection between the tubular tower and the TP. Furthermore, the eigen analysis was performed and the mode shapes were illustrated. In order to continue with the nonlinear geometry and material, the magnitude multiplier was calculated and the mode shapes were considered as the imperfection. The GMNIA analysis showed the same stress concentration area in the model.
To conclude, the results present the transition piece design regarding the operational and installation loads. Moreover, the ultimate limit state analysis provides the sufficient height and the thickness and the hotspots are identified. Moreover, the buckling is investigated in the most crucial zones.

ACKNOWLEDGEMENTS

The authors acknowledge with thanks the support of the European Commission's Framework Programs "Horizon 2020" program through the Marie Skłodowska-Curie Innovative Training Networks (ITN) "AEOLUS4FUTURE – Efficient harvesting of the wind energy" (H2020-MSCA-ITN-2014: Grant agreement no. 643167) and RFCS – Research Fund for Coal and Steel program through the Grant Agreement RFSR-CT-2015-00021-SHOWTIME. This work was also financed by FEDER - COMPETE and by national funds within the scope of the projects POCI-01-0145-FEDER-007633 and CENTRO-01-0145-FEDER-000006.

REFERENCES

[1] GWEC, "Global Wind Report - Annual Market Update," Brussels, Belgium, 2015.

[2] E. Lantz, M. Leventhal, and I. Baring-gould, "Wind Power Project Repowering : Financial Feasibility , Decision Drivers , and Supply Chain Effects," 2013.

[3] Vestas Wind Systems A/S, "Large Diameter Steel Flanges (LDST)," 2016.

[4] S. Jovašević, M. R. Shah Mohammadi, C. Rebelo, M. Pavlović, and M. Veljković, "New Lattice-Tubular Tower for Onshore WEC – Part 1: Structural Optimization," *Procedia Eng.*, vol. 199, pp. 3236–3241, 2017.

[5] International Electrotechnical Committee, "International Electrotechnical Committee (IEC) 61400-1," 2017.

[6] CEN, "Eurocode 3 - Design of steel structures - Part 1-6: Strength and Stability of Shell Structures," 2005.

Paper TS5.1.4

THE INTERNATIONAL CONFERENCE ON
WIND ENERGY HARVESTING 2018
21-23 March 2018
Catanzaro, Italy

STRUCTURAL INVESTIGATION OF LATTICE AND TUBULAR STEEL WIND TURBINE TOWERS. A COMPARATIVE STUDY.

Nafsika Stavridou[1*], Efthymios Koltsakis[2] and Charalampos C. Baniotopoulos[1]

[1]School of Engineering, University of Birmingham, United Kingdom
[2]Department of Civil Engineering, Lulea Technical University, Sweden
Corresponding author: Nafsika Stavridou, N.stavridou@bham.ac.uk

ABSTRACT

Wind energy, being probably the most promising renewable energy source due to its great energy potential and applicability, concluded recently to a variety of impressive relevant structural applications. The most common type to support on-shore wind energy converters is the cylindrical steel tower. Research on the structural optimization of wind turbine towers is of great interest and importance due to their high manufacturing and erection costs and certain transportation limitations that prevent them from reaching greater heights. In order to increase the wind energy harvesting, the construction of taller structures and the improvement of their structural detailing is critical towards achieving greater energy production along with economy in material use and structural robustness. The present paper addresses the comparison of a classic tapered steel wind turbine tower with a hybrid lattice tower of the same height and energy production potential. Aiming to contribute to a better understanding of the structural behaviour of both types of wind turbine towers, the research work focuses on the development of reliable numerical models along with the use of analytical equations in order to predict accurately and interpret the aforementioned structural response of the two towers by conducting a comparative study between them. The present study examines the performance of each tower while attempting to minimize the total material used maintaining its endurance and robustness.

NOMENCLATURE

P	=	Total loads acting on a wind turbine
V	=	Vertical loading due to the nacelle weight (N)
H	=	Horizontal loading due to nacelle function (N)
M	=	Moment due to the rotor function (Nm)
W	=	Distributed loading on the tower shell (kN/m^2)

1. INTRODUCTION

Sustainable energy production is considered crucial in order to improve the current climate conditions and limit the use of fossil fuels that are finite and produce harmful emissions. Wind energy due to its infinite nature and due to its remarkable development during the past decades is a rather promising renewable energy source and therefore, research towards that direction is beneficial to the overall energy production. The optimized design of a wind turbine tower, being the basic structural part of a wind converter is of great importance in order to achieve more robust structures and more economic design. The most common wind turbine tower structural configurations are the cylindrical tower, the jacket one with a truss structure and the hybrid one in the sense of a combination of a truss structure for the lower part and a tube part for the upper one.

The most common wind turbine tower configuration is a steel cylindrical shell tower due to its robust structural detailing, easier mounting and limited labour done on site since the tower modules are manufactured in the factory and are only assembled on site. The tower is composed of subsequent cylindrical or conical parts that are transported and mounted on site [1]. The structural analysis of the main supporting structure of wind generators is considered of high importance since failure in such

projects has great economical, structural and safety losses. The governing loads acting on the tower are the wind pressure up the tower height, the moment and the lateral load due to the rotor operation and the vertical load that is equal to the rotor weight. The classic tubular wind turbine tower is a simple cantilever structure, which due to its geometry can carry great loads with small shell thickness. The investigation of the buckling behavior of cylindrical shells has been founded by the research work, both numerical and experimental, conducted in the past by Timoshenko and Gere [2], Bazant and Cedolin [3], Teng and Rotter [4] and a plethora of other researchers. Tubular steel wind turbine towers belong to the area of cylindrical shells under combined loading and special research work has been devoted to the behavioral analysis of those structures and the explanation of their main structural problems [5]. Lee and Bang [6] elaborated a finite element model to simulate the collapse of an actual wind turbine tower whilst Arasu *et al* [7] and Nuta *et al* [8] have performed seismic analyses of wind turbine towers. Towards taking advantage of the higher energy potential at greater heights, wind converters tend to become taller and taller. Certain transportation limitations prevent the towers to have greater cylinder diameters and longer tower subparts. The solution of lattice towers has been till now implemented on telecommunication masts mostly and its structural behaviour has been investigated by Tsitlakidou *et al.* [9] and Efthymiou *et al.* [10]. Conventional lattice towers are constructed mostly with the use of standard L shaped cross sections fabricated in the factory and mounted on site. The scale of the lattice towers which are able to support the rotor of a wind converter leads to cross sections that are well outside the range of standard industrial profiles. A lattice tower that is capable of accommodating the nacelle or a cylindrical transformation element has the form of a truncated cone with a polygon or square cross-section. The tower is a statically determinate lattice structure composed of a number of discrete structural sub-systems; the legs, the bracing trusses on the faces, horizontal braces and secondary bracings arranged inside the plane of the face bracing trusses. The aforementioned structural subsystems have a particular role in the load transfer mechanism that develops inside a lattice tower and since the tower is a statically determinate structure, the axial stresses of the legs and the bracings can be determined by closed form expressions. The present paper addresses the stability performance comparison of a tubular steel wind turbine tower and a lattice wind turbine tower of the same height and with the same loading applied at the hub height. It examines the performance of each tower while attempting to minimize the total material used maintaining its endurance and robustness.

2. METHODOLOGY

The wind turbine tower that is used for the comparative study of wind turbine tower design has a total hub height of 76.15 meters. The tubular tower consists of 3 parts that are assembled on site due to transportation limitation of longer elements. The tower is modelled with reduced integration shell elements S4R as described in the software manual [12]. The original constructed tower is divided in 3 different parts of lengths 21.8 m, 26.6 m and 27.8 m from bottom to top. The lower diameter of the tower is 4.3 m and the top one is 3 m. The thickness of the shell wall is not constant, ranging from 30mm at the bottom to 12mm at the top. In the numerical model, the concentrated loads are applied at the top of the tower to a reference point eccentrically set to the middle axis of the tower, simulating the exact position of the rotor. The gravity loads are automatically calculated through the density of the material and the wind loading is taken into account as a distributed load along the tower height. The loads acting on the wind turbine tower are given in equation (1) and are: the vertical loading due to the nacelle weight (V), the horizontal loading (H) and moment (M) due to the rotor function and the distributed wind loading (W) on the tower shell.

$$P = \{V + H + M + W\} \tag{1}$$

The lattice tower used for the comparative study shares the same height as the tubular one. As explained above the structural sub-systems that the tower consists of have distinct roles in the load transfer mechanism of the tower. Therefore, each sub-system is investigated and optimized separately. The optimal face bracing truss is the V shaped and in order to minimize the total weight of the structure while maintaining its load bearing capacity the angle of the diagonals needs to be determined. For the presented investigation, the V brace angle is set to 45 degrees and in the Mathematica script used to

calculate the optimal cross-sections secondary braces are allowed to be used. After determining the optimal diagonal angle, the only parameters needed to be characterized are the top and bottom width of the face of the tower. The two antagonistic factors that play a role in the optimal tower design at this point are:

- The parallel increase of the leg axial force along with the reduction of the face bracing weight, when closing the distance between the legs
- The parallel reduction of the leg axial force along with the total length and slenderness increase of the V braces, when increasing the distance between the legs

Since the determination of the optimal tower weight is not only dependant on the width of the tower at the top, but also by the buckling checks which is a highly non-linear procedure, a two dimensional search is demanded in order to assess the variation of the two independent parameters; B_{top} and μ. The second parameter is defined as the top tower width over the base tower width as shown in equation 2.

$$\mu = \frac{B_{top}}{B_{base,ch}} \qquad (2)$$

The script used for the optimal design of the tower uses a successive iterations scheme in order to converge to a final solution when total tower weight is minimum.

3. RESULTS

Regarding the tubular tower, material nonlinear analysis (Figure 1) is performed to examine the tower response towards this combined loading. The material data used in a non-linear analysis for steel S355 are: Poisson's coefficient 0.3, Young's modulus 210GPa and for steel class S355 the yield stress is considered 350MPa and ultimate strength 510MPa. In order to introduce plasticity data, the material properties have to be considered in terms of plastic true stress and plastic true strain. The tower shell thickness is optimized and a calculation of the total material used is also performed. The total tower mass is 127.215 tn, with the three tower subparts having 54.54 tn, 44.817 tn and 27.858 tn respectively from bottom to top.

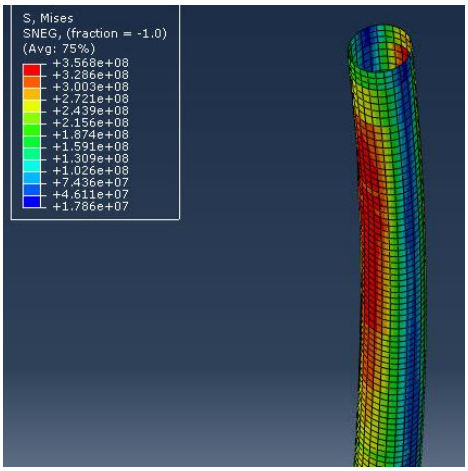

Figure 1. Tubular tower Material Non-linear Analysis.

The tubular tower subparts, in addition to having a tapered geometry, have also varying shell thickness from bottom to top. The thickness and geometry variation of the tower is presented in Table 21.

Table 3. Tubular tower diameter and thickness variation along the height

Height	Diameter	Thickness
0	4.3	0.03
4.4	4.2	0.026
8.8	4.1	0.027
13.2	4.0	0.023
22.0	3.8	0.022
28.6	3.7	0.020
39.6	3.5	0.018
45.6	3.4	0.016
54.35	3.3	0.014
63.15	3.2	0.013
71.95	3.0	0.012
74.15	3.0	0.014
76.15	3.0	0.018

As far as the lattice tower is concerned, all the tower subparts are designed and the optimum tower configuration is selected in order to minimize the total material used along with maintaining the tower load bearing capacity. The loads used for both the tubular and lattice tower are the same. The total number of cases investigated in order to optimize tower weight, are 126. The total weight for the optimal lattice tower solution is 77.47 tn. The lattice tower is lighter compared to the tubular tower for the selected hub height and critical assumptions can be made towards wind turbine tower optimal design based on the results presented in the following figures; (Figure 2), (Figure 3) and (Figure 4).

The braces used for the lattice tower are of V type, the V brace angle is set to 45 degrees and in the Mathematica script used to calculate the optimal cross-sections secondary braces are allowed to be used.

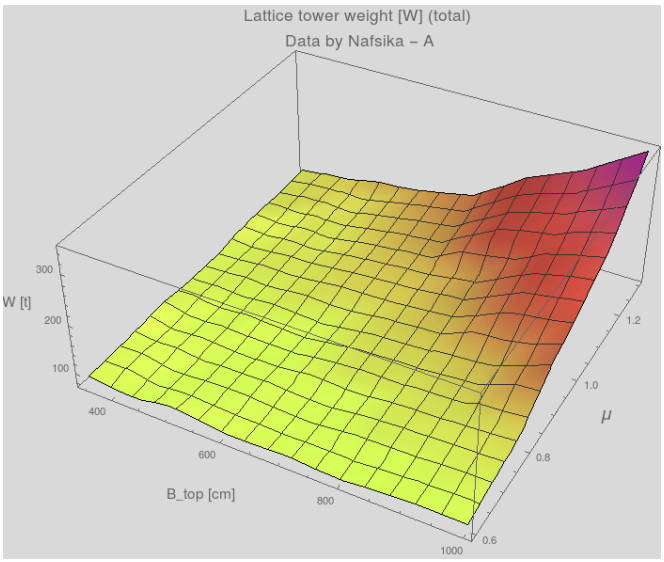

Figure 2. Total lattice tower weight in comparison to the top tower width and μ.

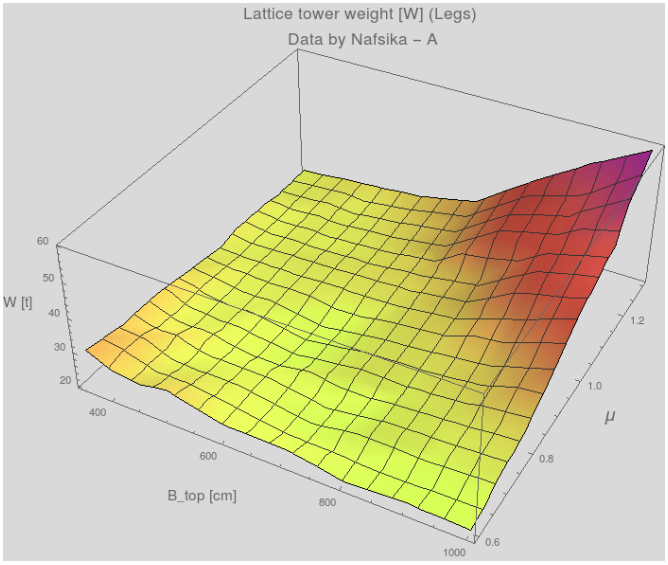

Figure 3. Tower leg weight in comparison to the top tower width and μ.

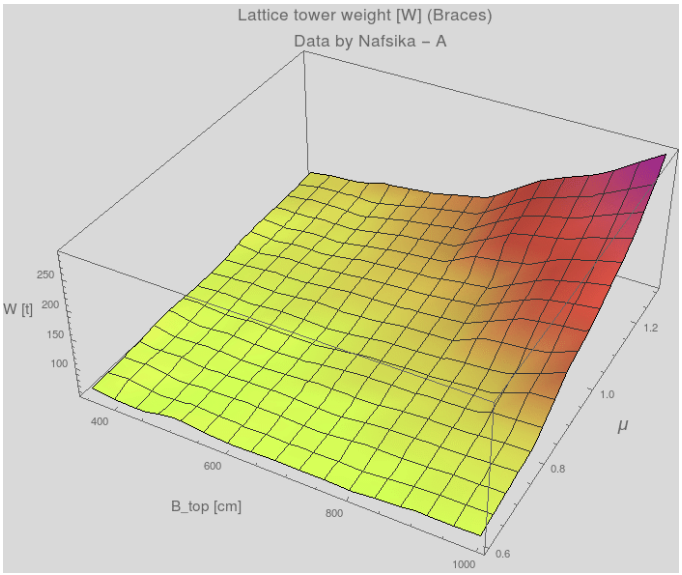

Figure 4. Braces' weight in comparison to the top tower width and μ.

The lattice tower is also divided in five levels, according to the height of the V-braces. The heights of the V-braces top elements and therefore the lattice tower subparts height is presented in Table **2**2.

Table 2. Lattice tower subpart heights

Tower subpart heights (m)					
Height	P-1	P-2	P-3	P-4	P-5
Subpart Height	34.45	55.53	68.19	75.64	76.15

As the tower is symmetric and the wind load can come from any direction, in each tower subpart the same type of elements are selected to have the same cross-sections. In our case circular hollow cross-sections are used and the optimal tower design is presented in Table **2**3.

Table 3. Lattice tower cross sections

Diameter and thickness of tower cross-sections (mm)					
Legs	P-1	P-2	P-3	P-4	P-5
Diameter	411	371	352	340	286
Thickness	8	8	7	7	5
V-Brace Diagonals	P-1	P-2	P-3	P-4	P-5
Diameter	413	385	375	363	253
Thickness	7	7	7	7	5
V-Brace Horizontals	P-1	P-2	P-3	P-4	P-5
Diameter	342	282	240	216	214
Thickness	6	5	5	4	4

The tower is almost 30 % of the initial construction cost of a wind turbine. Therefore, the reduction of the material used is of great importance in the economical aspect. As it can be observed from the comparison of the results of the two tower solutions, the total tower weight, using the lattice solution, is reduced by almost 40 %. Taking also into account the fact that in terms of transportation and in-situ construction, the lattice solution is advantageous in regards to flexibility in transportation and easiness in mounting, the lattice solution should be taken into consideration for the construction of contemporary wind turbines.

4. CONCLUSIONS

The present study investigates the potential of substituting tubular wind turbine towers with lattice ones with the project of minimizing the total structure weight while maintaining the structure load bearing capacity. With the prospect of constructing even taller structures, the minimization of the total material use is of great importance along with the transportation advantages that truss structures exhibit over the tubular ones. Cylindrical shells have been proven to be robust enough, offering higher capacity to the structure, but substantially greater amounts of material use. On the other hand, lattice structures when using the appropriate cross-sections for construction of tall structures are proved to be able to sustain great loads with minimum initial material weight. In the present comparative study, a wind turbine of 76.15 meters height has benn designed using both the tubular and the lattice solution. The design loads are identical in both types and the respective solutions are proven robust enough. In terms of total weight, the lattice tower is 40% lighter, minimizing by almost 15% the total initial construction cost. The advantages that the lattice solution offers in terms of transportation and fabrication, along with the flexibility of its configuration may lead to great and advantageous changes in the configuration concept in wind turbine tower design.

ACKNOWLEDGEMENTS

This project has received funding from the European Union's Horizon 2020 research and innovation programme under the Marie Sklodowska-Curie grant agreement No 747921.

The support of the TU1304 WINERCOST Action is also thankfully acknowledged.

REFERENCES

[1] I. Lavassas, G. Nikolaidis, P. Zervas, E. Efthimiou, I. Doudoumis and C. C. Baniotopoulos, "Analysis and design of the prototype of a steel 1-MW wind turbine tower," *Eng. Struct.*, vol. 25, no. 8, pp. 1097-1106, 2003.

[2] S. Timoshenko and J. Gere, "Theory of elastic stability," *Tata McGraw-Hill Education*, 1961.

[3] Z. Bazant and L. Cedolin, "Stability of Structures. Elastic, Inelasti, Fracture and Damage Theories," *World Scientific*, 2010.

[4] J. Teng and J. Rotter, "Buckling of Thin Metal Shells," *Taylor and Francis*, 2004.

[5] C. C. Baniotopoulos, C. Borri and T. Stathopoulos, "Environmental Wind Engineering and Design of Wind Energy Structures", *Springer Wien*, 2010.

[6] K. Lee and H. Bang, "A study on the prediction of lateral buckling load for wind turbine tower structures," *Inte. J. of Prec. Eng. and Man.*, vol. 13, no. 10, pp. 1829-1836, 2013.

[7] P. Arasu, D. Sagayaraj and J. Gowrishankar, "Seismic analysis of a wind turbine steel tower," in *"Hyper Works Technology Conference"*, 2011.

[8] E. Nuta, C. Christopoulos and J. Packer, "Methodology for seismic risk assessment for tubular steel wind turbine towers: application to Canadian seismic environment," *Can. J. of Civ. Eng.*, vol. 38, no. 3, pp. 293-304, 2011.

[9] A. Tsitlakidou, F. Lemonia, E. Koltsakis and C. C. Baniotopoulos, "Wind and ice design of ground based steel lattice masts," in *5th National Conference on Metal Structures, Xanthi, 2005*, pp. 207-214.

[10] E. Efthymiou, D. N. Kaziolas and C. C. Baniotopoulos, "On the response of steel lattice telecommunication masts under environmental actions and seismic loading," in *Nordic Steel Construction Conference NSCC 2009*, 2009.

[11] Dassault Systemes Simulia Corporation, "Abaqus Documentation," 2012.

Paper TS5.1.5

THE INTERNATIONAL CONFERENCE ON
WIND ENERGY HARVESTING 2018
21-23 March 2018
Catanzaro, Italy

INFLUENCE OF RESIDUAL STRESSES ON THE FLEXURAL BUCKLING RESISTANCE OF HIGH-STRENGTH STEEL HOLLOW SECTIONS

Gabriel Sabau[1] and Ove Lagerqvist[1]

[1]Department of Civil, Environmental and Natural Resources Engineering, Luleå University of Technology, Sweden
*Corresponding author: Gabriel Sabau, gabsab@ltu.se

ABSTRACT

Development of the wind energy industry continues to push the need for innovative solutions in terms of structural requirements. High-performance materials are thus needed to improve the efficiency of the structures and to ease the erection costs. The materials used for the towers have not improved significantly in the past years mainly because the design guidelines do not allow the efficient use of the high-strength steels. Lattice wind turbine towers could benefit from cost reductions if cold-formed high-strength steels would be used. Currently high-strength steel members have the same reductions factors for the relevant flexural buckling curve for cold-formed members regardless of the strength of steels. The paper discusses the approach towards the current European buckling curves and draws attention to potential limitations. The residual stresses present in rectangular hollow sections are discussed based on the method of fabrication. Different patterns of residual stresses are investigated by means of finite element simulations. The results indicate that the design codes slightly underestimate the flexural buckling resistance of high-strength steel members in the medium slenderness range.

NOMENCLATURE

NSS	=	Normal strength steel
HSS	=	High-strength steel (f_y >460 MPa)
RHS	=	Rectangular hollow section
EC	=	Eurocodes
f_y	=	Yield strength
t	=	Plate thickness
h_0	=	Plate width between welds
σ_{rc}	=	Longitudinal compressive residual stress
σ_{rt}	=	Longitudinal tensile residual stress
$\sigma_{rb,flat}$	=	Longitudinal bending residual stress in the flat part
$\sigma_{rb,corner}$	=	Longitudinal bending residual stress in the bent corner
χ_{EC}	=	Reduction factor for the relevant flexural buckling curve (a0,a,b,c)
χ_{FEM}	=	Reduction factor obtained through FEM simulation
N_{pl}	=	Plastic resistance of the gross cross-section
A	=	Cross-section gross area
λ_g	=	Global non-dimensional slenderness
c	=	Width of compression part (plate width)

1. INTRODUCTION

The materials used for wind turbine towers have not improved significantly in the past years mainly because the design guidelines do not cover the use of the high-strength steels. One such example is the restriction of using cold-formed or welded high-strength steel hollow sections with 0.2% proof stress resistance above 460 MPa [1]. Lattice wind turbine towers could benefit from cost reductions if cold-formed high-strength steels would be used. Furthermore, high-strength steel members have the same reductions factors for the relevant flexural buckling curve for cold-formed members regardless of the strength of steels. The hot-rolled sections have different imperfection factors corresponding to NSS and HSS.

The current European buckling curves consist of 5 different curves (a0, a, b, c, d) that represent the lower bound of the resistance of centrically compressed struts. The necessity of having more than one curve arose from the differences in geometry, boundary conditions and fabrication methods of different cross-sections. The curves were derived based on extensive experimental results conducted on compressed pin-ended columns (struts). The basis of the curves date back in the 1970 when a comprehensive study of 1067 specimens was completed with the results summarized and discussed by Sfintesco [2]. The experimental campaign covered a wide variety of cross-sections that included open sections such as 'I', 'H', 'T' and 'C' and square and cylindrical hollow sections. The experimental campaign focused on hot-rolled sections made of steel with the nominal strength of 24 kg/mm^2 (equivalent to S235 of the current European standards). A set of welded sections was also tested to form a basis of comparison. The study was conducted across different European states, such as France, Germany, Great Britain, Italy, Netherlands and Yugoslavia that comprised of a wide set of test specimens used in practice at that time. The procedure for the tests is described in the form of a report [3] and summarized later in a standardized form [4]. The preparations and initial measurements required are also presented in the aforementioned testing procedure. A series of measurements was done to evaluate the residual stresses in several different cross-sections. Yield stress and residual stress measurements were specified as complementary tests to the column testing. Procedures for measurements of the residual stresses in steel profiles were available [5] however they were not standardized.

Beer and Schulz [6] proposed a model of calculating the ultimate resistance of the compressed struts by means of accounting for the initial stresses locked in the steel bars as well as for the geometrical imperfections. The analytical formulation was then compared to the available experimental results. The fifth curve,'*a0',* was later introduced for tubular sections due to the observed reduced residual stresses and accounting for the higher strength steels used in fabrication [7].

Current European design standards for structural steel consider identical buckling curves for NSS and HSS hollow sections obtained through welding or cold forming. The recommended curves are 'b' or 'c' for welded section based on the thickness of the welds and section walls, and curve 'c' for cold-formed sections. The applied reduction assumes that in the case of HSS members the residual stresses have a proportional influence on the ultimate strength as for the NSS members since it is unreasonable to assume that the geometrical imperfections would be higher. Measurements of residual stresses performed on HSS seem to contradict this assumption [8]–[11].

The study presents a summary of the buckling experiments performed on structural high-strength steel with 0.2% proof strength higher than 460 MPa. The investigated failure mode is flexural buckling. Additionally, a FE analysis is performed with two different residual stress patterns and compared with available experimental results. The purpose is to identify if the buckling curves recommended for HSS is justified to match those of NSS.

2. METHODOLOGY

A state-of-art review was performed to identify relevant flexural buckling tests performed on HSS rectangular hollow sections. Furthermore, the results from the residual stress measurements was analyzed and discussed. The recommendation for the higher steel grades is that the curves for S460 should be used. Higher penalties are thus applied to HSS. From the premise that residual stresses have a lower impact on HSS than on normal structural steels, a comparison is made between the ultimate

strength of the HSS columns and the corresponding EC buckling curves. The experimental campaigns are generally accompanied by residual stress and imperfections measurements.

2.1. Flexural buckling

A total of 59 RHS flexural buckling experiments have been analyzed in this this paper based on the available literature, of which the most have been performed on cold-formed sections [10,12], as seen in Figure . The first experiments were performed on welded SHS [9,12] and again later in 2013 [8]. Most of the experiments have been conducted in China [8,13,14] and Hungary [12].

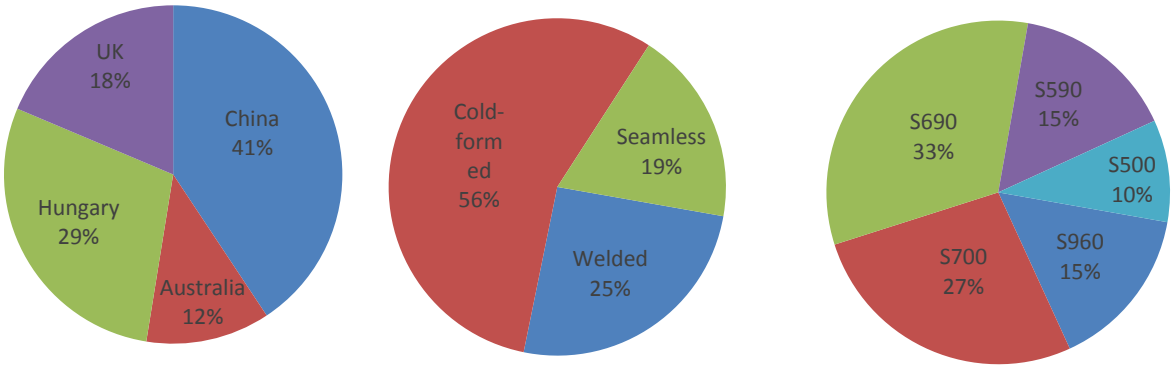

Figure 1. **Distribution of experiments on HSS RHS columns by countries and fabrication methods**

The experimental campaign conducted by Young and Lui [14] comprised specimens made of high-strength stainless steel. The two grades of steel were considered to be equivalent to S590 and S700 based on their mechanical properties as per Figure 2. Wang and Gardner[16] tested hot-rolled high-strength steel SHS and RHS. The sections were made of the steels S460NH that was subsequently normalized and S690QH that was quenched and tempered.

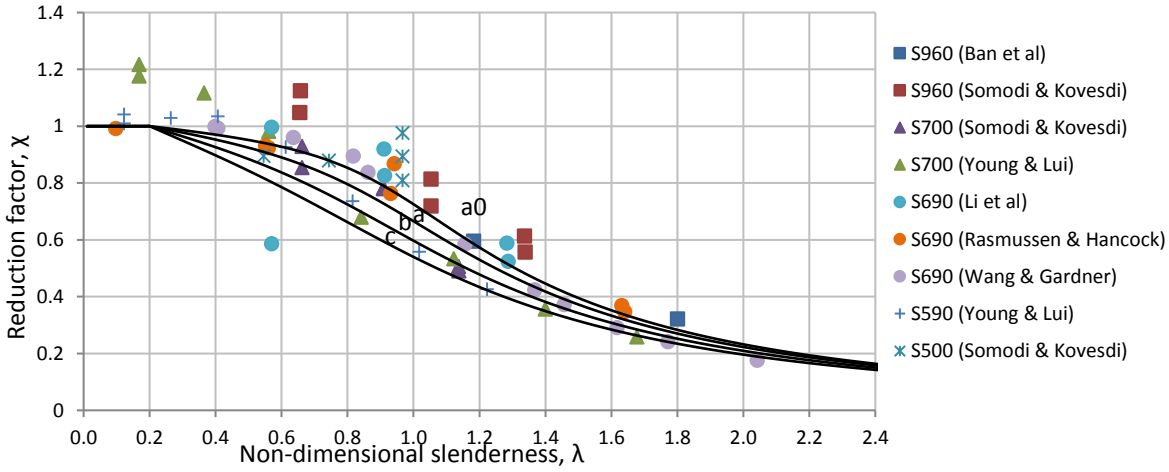

Figure 2. **Comparison of the normalized buckling strengths with the buckling design strengths according EN 1993-1-1 (SHS) – nominal values**

The experimental results from the compression tests have the buckling strength of all the columns, well above the "a0" curve in the medium slenderness range. However, in the elastic buckling range, no substantial improvement could be noticed. Somodi and Kövesdi [12] stated that in the case of S960 steel grade the buckling strength of SHS have always been above the "a" curve. Li et al [15] performed flame strengthening on one of the RHS specimens which resulted in a drastic decrease of the material performance. The outliner can be easily spotted in Figure 2. The results draw further attention to the reduced effect of the residual stresses on the higher strength steel members in the medium slenderness range.

2.2. Residual stresses

The residual stress measurements are not as extensive as the buckling tests. The main reason can be the difficulty and the time required for preparing and conducting the tests. The method most often applied was the sectioning method and the hole drilling method. The sectioning method is generally preferred since is gives a through thickness average value of the relevant residual stresses. Longitudinal stresses are considered to have the highest effect that can lead to premature yielding in the element.

Reported longitudinal residual stresses on the seamless tubes [16] have been in the range of 0.055 f_y in tension and 0.031 f_y in compression. The proposed model consisted of longitudinal tension for the corners with an amplitude of 0.025 f_y and compression in the plates with an amplitude of 0.021 f_y,. as per Figure 3c. Ban et al [8] did not report the results from the residual stress measurements, but proposed a value of 690 MPa in tension in the corners and according to Eq.(1) for the central part of the plates (Figure 3a).

$$\sigma_{rc} = -95 - 1450\left(\frac{t}{h_0}\right) - 270\left(\frac{1}{t}\right)\ [MPa] \tag{1}$$

Rasmussen and Hancock [9] reported measured values for the central part of each of the sides with the maximum compressive residual stress being -145 MPa and minimum -92 MPa, equivalent to 0.21 f_y and 0.13 f_y.

Young and Lui [14] measured the residual stress in both longitudinal and transversal directions for cold-formed high-strength stainless steel sections. The results are reported for one of the specimens (200x110x4) with the maximum value of the compressive residual stress near the weld. The measured value was approximately 200 MPa. The ratio between the maximum residual stress measured and the 0.2% proof stress becomes irrelevant since the dispersion of the results obtained from tensile test makes it difficult to classify the steel. One of the most comprehensive studies on HSS cold-formed RHS has been performed by Somodi and Kövesdi [11], covering steel grades from S460 to S960. The authors [11] emphasize the importance of the Bauschinger effect in the cold-forming of HSS, indicating that a smaller stress level can be reached at a target deformation. They proposed the analytical formulation for residual stress distribution for HSS cold-formed RHS obtained through indirect forming (cylindrical-rectangular) for the ratio of plate width to thickness of 10-40, as per Eq.(2) and Eq.(3). It is important to notice that in this case the residual stresses are not referred to as compression and tension but bending residual stresses, indicating a through-thickness stress variation. The residual stress distribution is presented in Figure 3b.

$$\sigma_{rb,flat} = \pm\left(1.28 - \frac{f_y}{1270\ MPa}\right) f_y\ [MPa] \tag{2}$$

$$\sigma_{rb,corner} = 0.55\,\sigma_{rb,flat}\ [MPa] \tag{3}$$

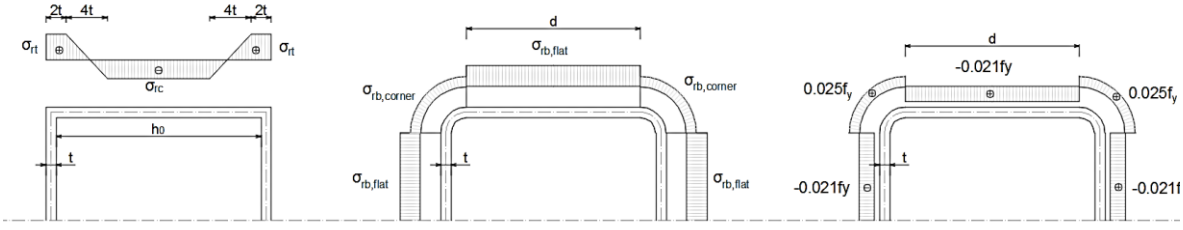

(a) (b) (c)

Figure 3. **Residual stress models for welded HSS (a), cold-formed HSS (b) and hot-rolled HSS (c)**

3. NUMERICAL STUDY

A numerical study using the FEM software Abaqus was performed to quantify the reduction in buckling resistance of SHS based on different amplitudes and distributions of residual stresses. Two distribution patterns *M1* and *M2* were chosen according to Somodi and Kövesdi [11] and Wang and Gardner[16]. The first one corresponds to cold-formed sections while the second corresponds to hot-rolled sections as seen in Figure 3(b) and (c). The global imperfections were introduced according to EN 1993-1-1 [17] and it was considered as the dominant imperfection. The local imperfection was applied as plate plate imperfections and was reduced to 70% of the recommended value based on Annex C of EN 1993-1-5 [18].

A 3D finite element model was created using 4 node rectangular shell elements with reduced integration (S4R) and 5 thickness integration points, integrated using the Simpson method. The Simpson method was preferred in order to introduce a linear distribution of the residual stresses between the two faces of the shell element as seen in Figure 4(a). The material was modelled based on the True Stress-Strain curve presented in Figure 4(b), determined from a coupon tensile test corresponding to an S700. The ultimate loads were determined using a load controlled static modified Riks analysis, commonly used in tackling stability problems. The model incorporated material non-linearity, geometrical imperfections and residual stresses (GMNIA). The residual stresses were introduced by means of predefined fields and stabilized through an initial static step. The amplitudes of the residual stresses for the two models are presented in Table 4.

Table 4. **Applied residual stresses**

	M1	M2
$\sigma_{r,flat}$	$\pm 508 MPa$	$-14.5 MPa$
$\sigma_{r,corner}$	$\pm 280 MPa$	$-17.5 MPa$

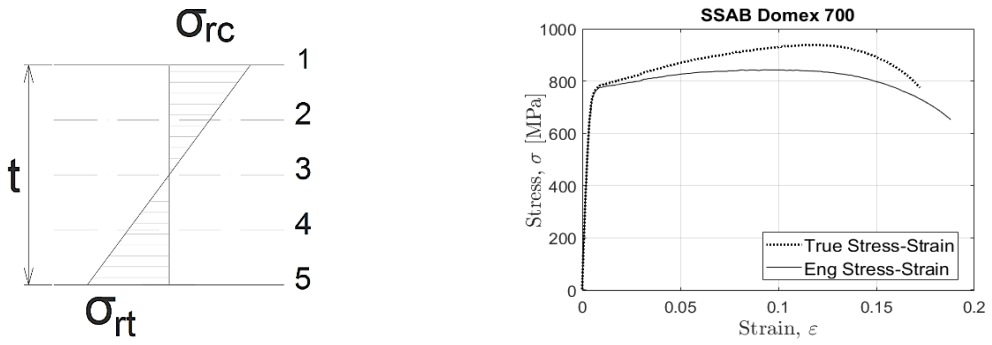

Figure 4. **Residual stress distribution over the shell thickness (a). Steel material stress-strain curve (b).**

The investigated parameters are presented in Table 5. The global and local slenderness were used as variables and the area was kept constant. The different bending radius corresponding to the different thickness causes a small variation of area of 2.1%. The bending radius was taken as $2.5t$. The slenderness range was chosen between 0.5 and 1.3. Lower slenderness would lead to plastic failure while higher values would be in the range of elastic buckling.

4. FE SIMULATION RESULTS

The resistance obtained from the FE analysis was compared to the values calculated according to EN 1993-1-1 [17] and presented in Table 5. The difference between the two models (M1 and M2) emphasize the importance of longitudinal bending residual stresses in the cold-formed sections. Although the average longitudinal stress is null for the M2 case, the stress values are higher. The resistance given by the M2 models matches the trend line of curve 'b', while still being on the safe side. This shows that the cold-formed residual stresses pattern is more detrimental for the flexural buckling scenario in the chosen

slenderness range. The hot-rolled section corresponding to model M1 showed an improvement in resistance with values above the 'a0' curve. These observations are also valid for the experimental results extracted from available literature presented in Figure 2.

Table 5. **Investigated parameters and obtained results**

Section	L_{cr} [m]	A [mm^2]	c [mm]	c/t	λ_g	N_{pl} [kN]	Class	$\chi_{EC,a0}$	$\chi_{EC,c}$	$\chi_{FEM,1}$	$\chi_{FEM,2}$
S170x12	2.030	7404	170	14.4	0.549	5109	1	0.941	0.815	0.925	0.964
	2.436				0.658			0.910	0.750	0.863	0.941
	2.843				0.768			0.869	0.682	0.791	0.902
	3.249				0.878			0.810	0.614	0.718	0.854
	3.655				0.987			0.735	0.547	0.649	0.776
	4.061				1.097			0.651	0.486	0.578	0.683
	4.467				1.207			0.568	0.431	0.513	0.589
	4.873				1.316			0.495	0.382	0.453	0.512
S200x10	2.328	7562	198	19.6	0.535	5218	2	0.946	0.823	0.931	0.960
	2.794				0.642			0.920	0.760	0.871	0.937
	3.259				0.749			0.884	0.694	0.801	0.905
	3.725				0.855			0.834	0.627	0.732	0.863
	4.190				0.962			0.768	0.562	0.661	0.795
	4.656				1.069			0.690	0.501	0.591	0.709
	5.122				1.176			0.610	0.445	0.527	0.616
	5.587				1.283			0.535	0.396	0.468	0.539
S210x9.5	2.479	7618	212	22.5	0.529	5257	3	0.947	0.824	0.923	0.954
	2.974				0.635			0.921	0.762	0.869	0.932
	3.470				0.741			0.885	0.697	0.801	0.902
	3.966				0.847			0.836	0.631	0.733	0.861
	4.462				0.952			0.771	0.566	0.663	0.796
	4.957				1.058			0.694	0.505	0.594	0.713
	5.453				1.164			0.614	0.450	0.531	0.623
	5.949				1.270			0.539	0.401	0.472	0.545

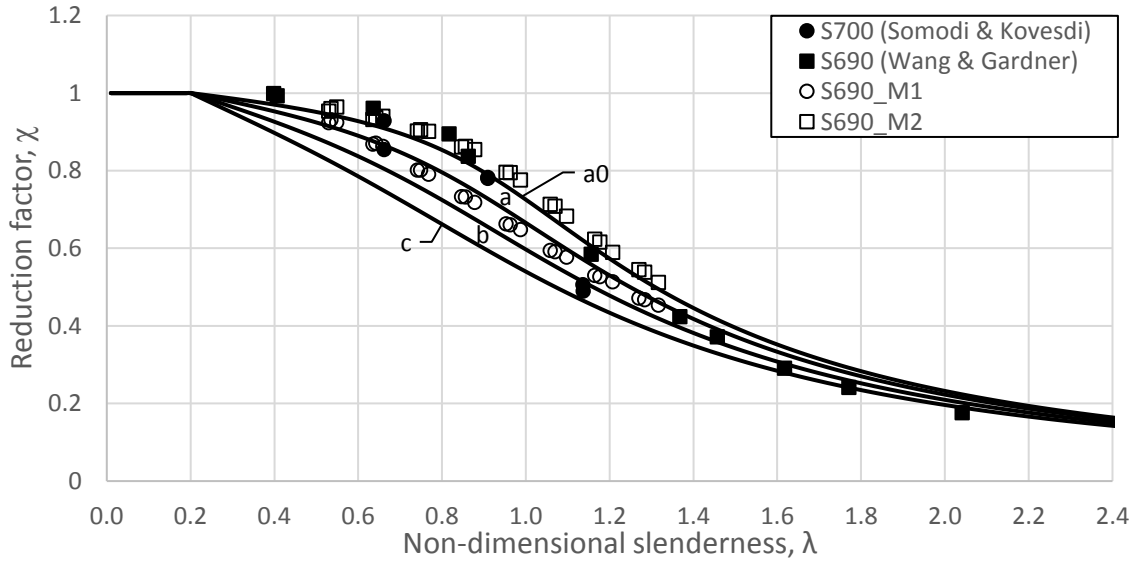

Figure 5. **Comparison of EN 1993-1-1 buckling curve and results of FEM simulations**

The results show that buckling resistance has a higher sensitivity to residual stresses in the range of 0.66 to approximately 1.2. The maximum difference 16.88% has been recorded at the slenderness 0.962. No difference has been observed between the different section classes.

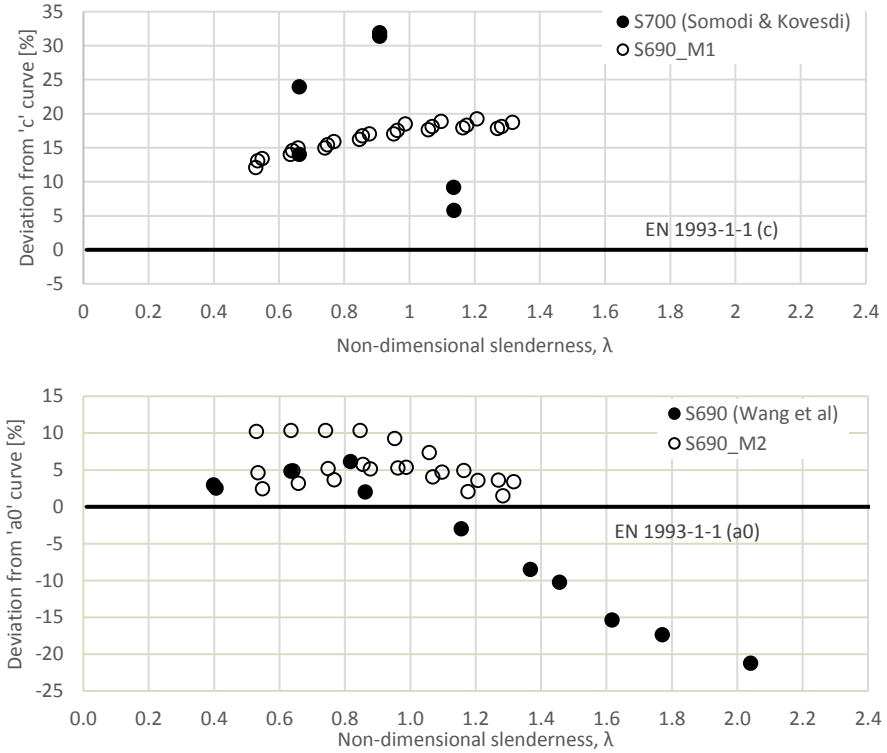

Figure 6. **Comparison of EN 1993-1-1 relevant flexural buckling curves and experimentally and numerically obtained results**

The comparison between the experimental results and the relevant buckling curves as seen in Figure 6 show that in the range of medium slenderness a more economical design can be achieved. The difference is presented in percentage, where positive values represent an increase in resistance compared to the recommended buckling curve. Good agreement is shown between the numerical and experimental values. The difference can be attributed to different amplitudes of geometrical imperfections and residual stresses.

5. CONCLUSIONS

The paper presents a state-of-art on available flexural buckling experiments performed on RHS HSS members as well as the accompanying residual stress measurements and a numerical analysis. The investigation emphasizes the importance of through thickness variation of longitudinal residual stresses. The through thickness stresses are more difficult to determine and are generally assumed as constant for thin plates. This assumption can sometimes lead to unsafe estimations.

A clear difference can be observed in the amplitude of the residual stresses between the cold-formed and seamless sections. Since many factors can influence the residual stresses resulted from welding, it is still too early to draw a general conclusion corresponding to HSS. However, the ratio between the residual stresses and the 0.2% proof strength observed in cold-formed HSS RHS have shown to have a reduced ratio compared to NSS. A holistic approach towards the buckling resistance of steel members should be considered.

A general agreement is seen between the researchers concluding that a smaller reduction should be applied to HSS, leading to less conservative flexural buckling estimations. This can be justified by the reduced amplitude of residual stresses and is mainly focused in the slenderness range susceptible to elasto-plastic buckling. The FE results have shown that members with a slenderness between 0.66 and 1.2 are highly sensitive to residual stresses. The extent of the sensitivity should be further investigated.

The experimental results gathered from the literature and the numerical simulations have shown that the Eurocodes slightly underestimate the capacity of RHS HSS members subjected to flexural buckling.

ACKNOWLEDGEMENTS

The authors acknowledge with thanks the support of the European Commission's Framework Program "Horizon 2020", through the Marie Skłodowska-Curie Innovative Training Networks (ITN) "AEOLUS4FUTURE - Efficient harvesting of the wind energy" (H2020-MSCA-ITN-2014: Grant agreement no. 643167) to the present research project.

The simulations were performed on resources provided by the Swedish National Infrastructure for Computing (SNIC) at High Performance Computing Center North (HPC2N)

REFERENCES

[1] Germanischer Lloyd Industrial Services GmbH, "Guideline for the Certification of Wind Turbines." Germanischer Lloyd, Hamburg, 2010.

[2] D. Sfintesco, "Fondement expérimental des courbes européennes de flambement," *Constr. métallique*, vol. 3, pp. 5–12, 1970.

[3] N. Tebedge and L. Tall, "Procedure for Testing Centrally -Loaded Columns," Lehigh, 1971.

[4] ECCS, "Testing Procedures," 1984.

[5] G. A. Alpsten, "Thermal Residual Stresses in Hot-Rolled Steel Members," Bethlehem, Pennsylvania, 1968.

[6] H. Beer and G. Schulz, "Theoretical basis of the European buckling curves," *Constr. métallique*, vol. 1970, no. 3, pp. 37–57, 1970.

[7] H. Beer and G. Schulz, "The European column curves," *Constr. métallique*, vol. 3, no. 23, pp. 385–398, 1975.

[8] H. Ban, G. Shi, Y. Shi, and M. A. Bradford, "Experimental investigation of the overall buckling behaviour of 960 MPa high strength steel columns," *J. Constr. Steel Res.*, vol. 88, pp. 256–266, 2013.

[9] K. J. R. Rasmussen and G. J. Hancock, "Tests of High Strength Steel Columns," *J. Constr. Steel Res.*, vol. 34, no. 1, pp. 27–52, 1995.

[10] B. Young and W. M. Lui, "Tests of cold-formed high strength stainless steel compression members," *Thin-Walled Struct.*, vol. 44, no. 2, pp. 224–234, 2006.

[11] B. Somodi and B. Kövesdi, "Residual stress measurements on cold-formed HSS hollow section columns," *J. Constr. Steel Res.*, vol. 128, pp. 706–720, Jan. 2017.

[12] B. Somodi and B. Kövesdi, "Flexural buckling resistance of cold-formed HSS hollow section members," *J. Constr. Steel Res.*, vol. 128, pp. 179–192, 2017.

[13] K. J. R. Rasmussen and G. J. Hancock, "Plate slenderness limits for high strength steel sections," *J. Constr. Steel Res.*, vol. 23, no. 1–3, pp. 73–96, 1992.

[14] B. Young and W. Lui, "Behavior of Cold-Formed High Strength Stainless Steel Sections," vol. 131, no. November, pp. 1738–1745, 2005.

[15] T. Li, G. Li, S. Chan, and Y. Wang, "Behavior of Q690 high-strength steel columns : Part 1 : Experimental investigation," *JCSR*, vol. 123, pp. 18–30, 2016.

[16] J. Wang and L. Gardner, "Flexural Buckling of Hot-Finished High-Strength Steel SHS and RHS Columns," pp. 1–12, 2017.

[17] CEN, *EN 1993: Design of steel structures - Part 1-1: General rules and rules for buildings*. European Committee for Standardization, CEN, Brussels, 2005.

[18] CEN, *EN 1993: Design of steel structures – Part 1-5: Plated structural elements*. European Committee for Standardization, CEN, Brussels, 2007.

TECHNICAL SESSION 6.1

Work Packages 4 and 6 - Wind Turbines
Loading and Monitoring

Paper TS6.1.1

THE INTERNATIONAL CONFERENCE ON
WIND ENERGY HARVESTING 2018
21-23 March 2018
Catanzaro, Italy

EARLY FAILURE DETECTION OF BOND WIRE LIFT-OFF IN A SEMICONDUCTIVE COMPONENT OF AN OPERATIONAL THREE-PHASE CONVERTER

R. Moeini[1], P. Weston[2], H. Hemida[1] and C.Baniotopoulos[1]

[1] Department of Civil Engineering, University of Birmingham, UK
[2]Department of Electronic, Electrical and Systems Engineering, University of Birmingham, UK
Corresponding author: R.Moeini@bham.ac.uk

ABSTRACT

Improved early failure detection for the IGBTs of power electronic converters can play a significant role in reducing the annual failure rate of wind turbines. The generator-side converter is the most fragile part of the converter as it encounters severe thermal stresses due to wind speed variations. IGBT modules are the most vulnerable parts of power electronic converters due to their inherent multilayer structure and the different thermal expansion coefficient of each layer. Temperature profile can be a failure detector for IGBT modules. However, direct measurement of temperature is not possible without changing the IGBT module implementation. Estimation of temperature through measurement of thermal sensitive parameters is one possible approach to detect early failure mechanisms. The collector-emitter on-state voltage of an IGBT has the potential to be a direct failure detector for bond wire lift off. One reason for choosing this parameter as a failure detector is the practicality of measuring it using the existing IGBT terminals. However, the variation trends of this parameter during the operation of an operational three-phase converter have hitherto not been well investigated.

1. INTRODUCTION

The principal failures of a wind turbine (WT) arise in the power converters (17.5 %), control system (12.9 %) and generator (5.5 %) [1, 2]. The generator-side power converter is significantly less reliable than the grid-side power converter. Failure detection of IGBTs in the generator-side converter significantly lessens the effects of failure mechanisms in this part of electrical system. Various methods have been proposed to monitor the health status of an IGBT module. As all failure mechanisms affect the temperature profile of IGBTs, monitoring temperature variations can be considered as a failure detector [3]. However, the junction temperature of an IGBT module is not directly accessible as it is a press packed module. Thus, direct measurement of temperature is not recommended. Another limitation is that temperature is not a fast response phenomenon. Estimation of temperature through thermal modelling or the measurement of TSEPs (thermo-sensitive electrical parameters) as failure detectors can be an alternative approach [4, 5]. Understanding failure mechanisms and their root causes is very important in a successful failure detector. Thermal stresses are one of the main causes of failure mechanisms in IGBTs. Bond wire lift-off (BWLO) is one of the most common failure mechanisms. In this paper, the on-state collector-emitter voltage is investigated as a failure detector for BWLO in a specially constructed three-phase converter operating with a permanent-magnet motor as a load.

2. CONVENTIONAL AC-DC GENERATOR/MOTOR CONVERTER

In this paper, a bidirectional DC to three-phase AC power electronics converter is used to run a three-phase permanent magnet motor. The converter could equally be used in reverse with the motor operating as a generator. The converter was constructed with IGBT modules which allow access to the internal bond wires, so bond wire lift off can be simulated by cutting the bond wires. Figure 1 shows the power board (the IGBT modules are on the other side) and the controller board. A dsPIC33EP508 microcontroller was used to generate the three-phase PWM signals needed to drive the IGBT gates so as to run a 3-phase AC permanent magnet (PM) machine (48 V, 450 W). Figure 2 shows IGBTs used in the three-phase IGBTs.

Figure 1. Front and rear of the power board

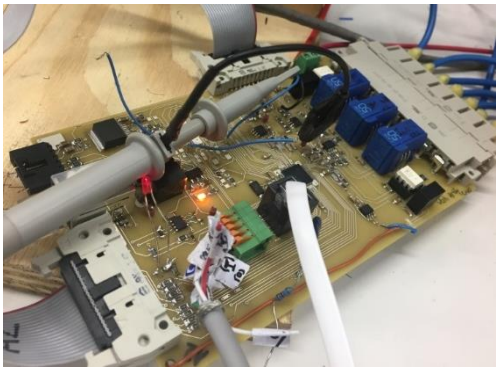

Figure 2. The controller board

The controller board includes a microcontroller and three LEM current sensors, one to measure each phase current. The switching frequency of the PWM is 20 kHz. Figure 3 shows a quadrature encoder with index pulse (500 pulses in each of two channels per revolution converted to 2000 counts per revolution inside the microcontroller) which is coupled to the machine shaft.

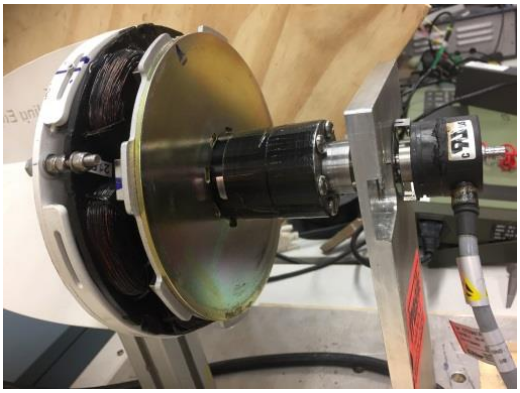

Figure 3. Permanent magnet machine coupled to a rotary position encoder

A fast vector current controller and an outer speed control loop are used to control the PM machine, as shown in Figure 4.

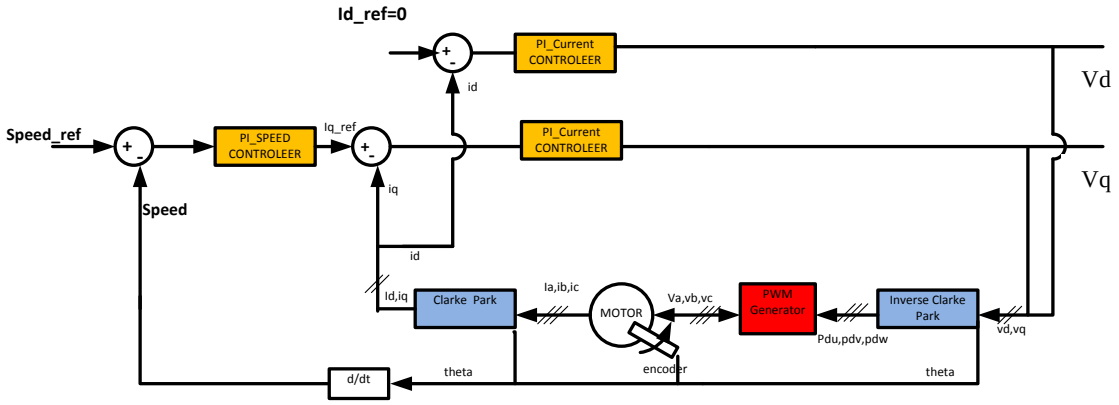

Figure 4. Control block diagram for generator/motor-side converter

A Clarke-Park transform turns three-phase current into quadrature i_d and i_q components and these are used as feedback for the current controllers to control the torque of the machine. The angle theta is fed into the Clarke-Park and inverse Clarke-Park transforms using sin(θ) and cos(θ) look-up tables. I_{d_ref} is set to zero and i_{q_ref} is set by the output of the speed controller. Speed_ref is the desired speed. Speed is measured by discrete-time differentiation of theta as given by a position encoder. V_d and V_q are set equal to PI controller outputs. Three PWM levels (pdu, pdv, pdw) are given by the inverse Clarke-Park transform. Three-phase voltage is generated from the DC-link voltage using three half-bridge IGBTs. The voltage is applied to the PM machine, which draws current.

Figure 5 shows the encoder pulse count changing as the shaft rotates at a constant rate.

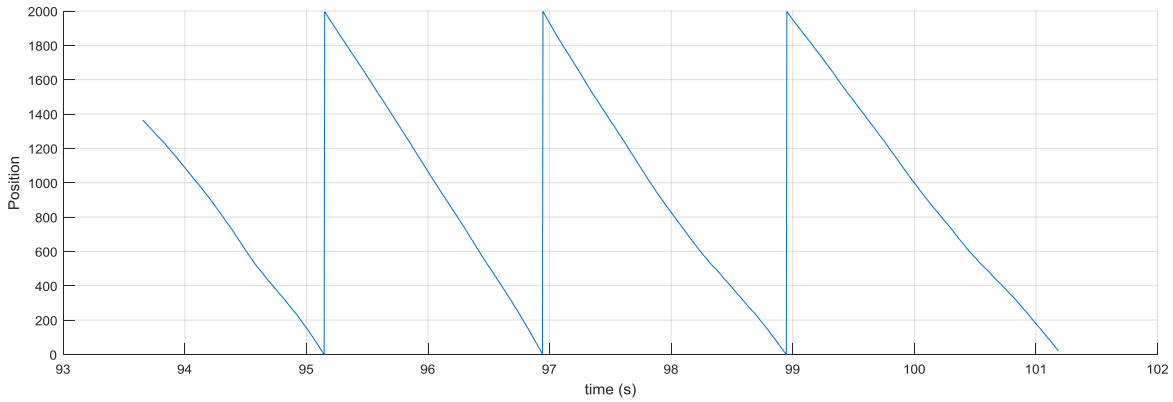

Figure 5. Pulse count vs time for constant speed of rotation

Validation of the speed controller is shown in Figure 6. Speed_ref is set as 1 at the beginning, speed_ref is set to 10 for 10 seconds and speed_ref is set to 25 for 20 seconds. Speed_ref is the number of pulses in 4 ms.

$$speed\,(rpm) = 60 \times \left(\frac{speed\_ref}{2000 \times 4 \times 10^{-3}}\right) \tag{13}$$

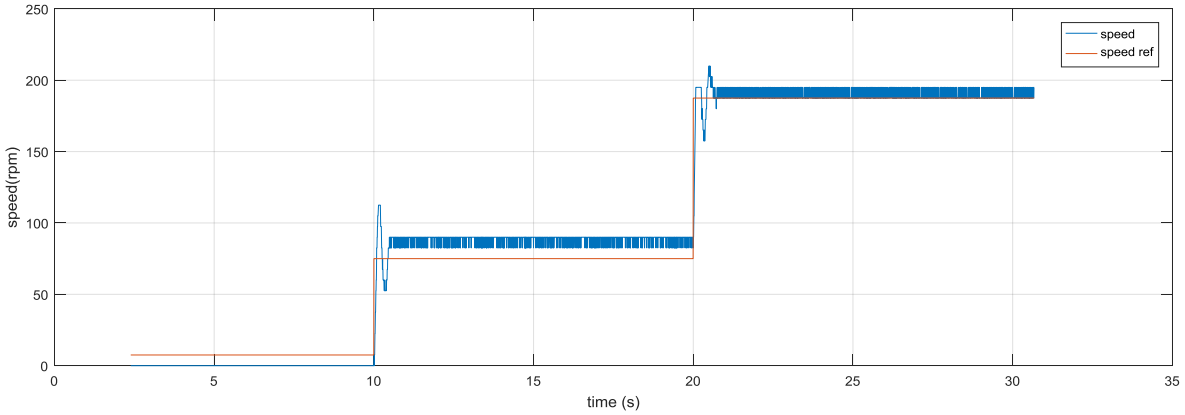

Figure 6. Validation of speed controller

The discrete-nature of the signals inside of the microcontroller code leads to a small constant error even with a PI controller. This error is of no consequence for the experimental results described in the next section.

3. ON-STATE COLLECTOR-EMITTER VOLTAGE AS A FAILURE DETECTION METHOD

The lab-built converter has been used to study the variation of V_{CE_on} with different load currents and dc bus voltages. Measuring TSEPs with the three-phase PM machine as a load has proved to be much more complicated than with a single-phase, fixed resistance and air-cored inductor load. This is because the load appears as a variable and non-linear inductance. Also, the measurements of one phase are interfered with by the switching of the other two phases.

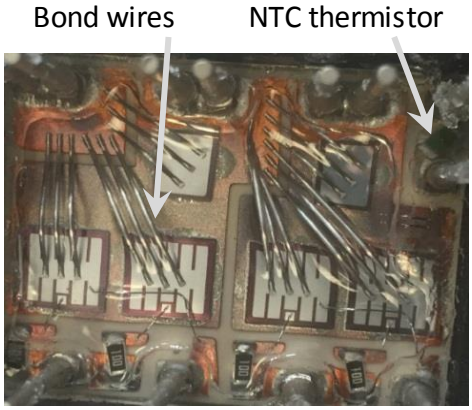

Figure 7. IGBT module

Figure 7 shows the inside of a half bridge IGBT module used for this study. Note that this module has two silicon chips in parallel in both the high and low sides. In high power IGBT modules, several parallel bond wires are used to carry the collector-emitter current. Having parallel bond wires distributes the current and helps to manage thermal distribution. In the presence of BWLO, a certain collector-emitter current is carried by fewer bond wires – increasing the resistance and the associated voltage drop. Therefore, the steady-state voltage drop between the collector and (power side) emitter terminal can, in principle, be used as a BWLO failure detection method. The modulation index varies at the AC frequency of the machine, and the positive half cycles of approximately sinusoidal current flow in each IGBT in a particular pattern. Therefore, measurements of the voltage-emitter on-state voltage are timed to coincide with the peak collector current, after switching transients have died away but before the next switching instant.

Variation in V_{CE_on} under different currents and DC-link voltages has been investigated during operation of the converter operating as a permanent magnet motor speed controller. It is also important to mention that in order to measure the small on-state collector-emitter voltage (V_{CE_on}) in the high side of half bridge IGBT chip, a high-voltage-capable and accurate differential amplifier is needed. A typical high-voltage differential probe capable of measuring hundreds of volts was not able to measure V_{CE_on} sufficiently accurately. Instead, a differential amplifier with a limited differential input range (±15 V) but a common mode voltage of up to 600 V was used. When V_{CE} is above 15 V, the output of the differential amplifier is saturated, but it quickly recovers when V_{CE_on} falls below 15 V. Temperature is measured with a NTC (negative temperature coefficient) temperature sensor inside the module. Temperature can be additionally varied through a heated heatsink attached to the IGBT under test.
Three conditions were examined: In the first, V_{CE_on} was measured with healthy IGBTs; in the second, one of the bond wires was cut as shown in Figure 8. In the third set of tests, another bond wire on the same device was cut, making two cut wires in total.

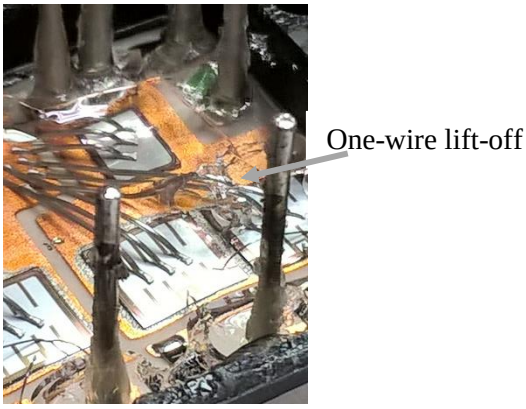

Figure 8. One wire lift-off of IGBT

Figure 9 does not show a consistent change of $V_{CE,on}$ as the dc-link voltage increases from 40 to 100 V (at 25º C). It should be noted that as the DC link voltage increases, the range of PWM period required to obtain the same rotor speed reduces. This changing PWM period at the point of measurement, which is roughly when the current is at its maximum, may affect the results somewhat as the details pf the signal traces change with switching in other phases causing interference and possible measurement errors.

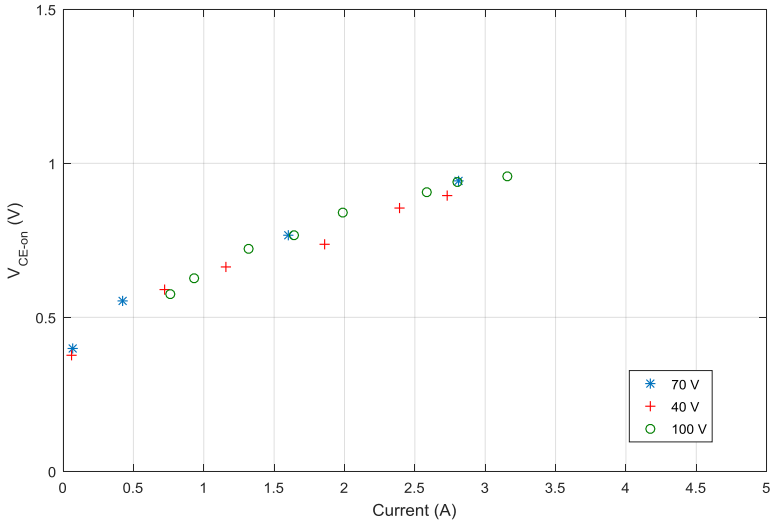

Figure 9. V_{CE_on} against current for various DC-link voltages

Figure 10, shows the measured V_{CE_on} against current for various heatsink temperatures with one bond wire cut. The temperature of the heatsink does not affect the results significantly in the presence of one wire lift off, at least from 20°C to 80°C. It might be perceived that V_{CE_on} is very slightly decreasing with increasing temperature, but the accuracy and number of measurement points is not enough to be confident in this interpretation.

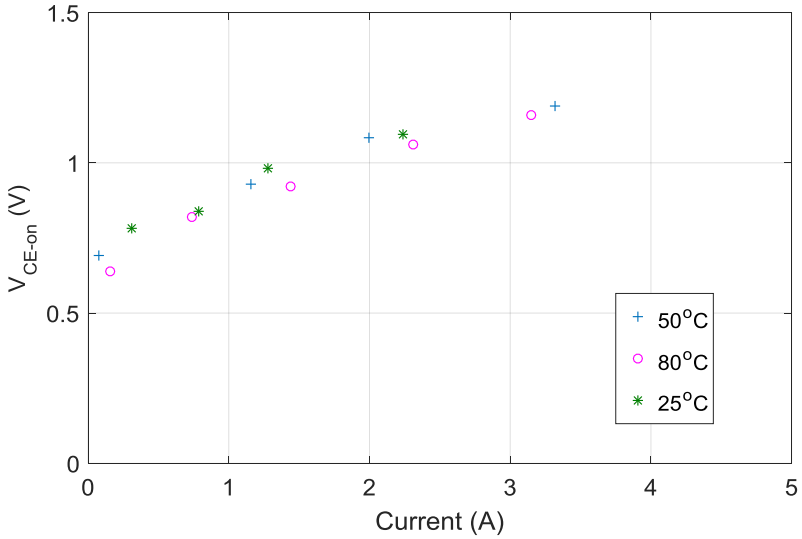

Figure 10. V_{CE_on} against current for different temperatures

Figure 11 shows the variation in $V_{CE\text{-}on}$ against collector current with zero (healthy), one and two bond wires cut. An increase of 100 mV can be observed with one of the three bond wires cut. Later, with two wires cut, an increase of 200 mV can be observed. The gradients of the points for each case suggest that the resistance is increasing as the bond wires are cut.

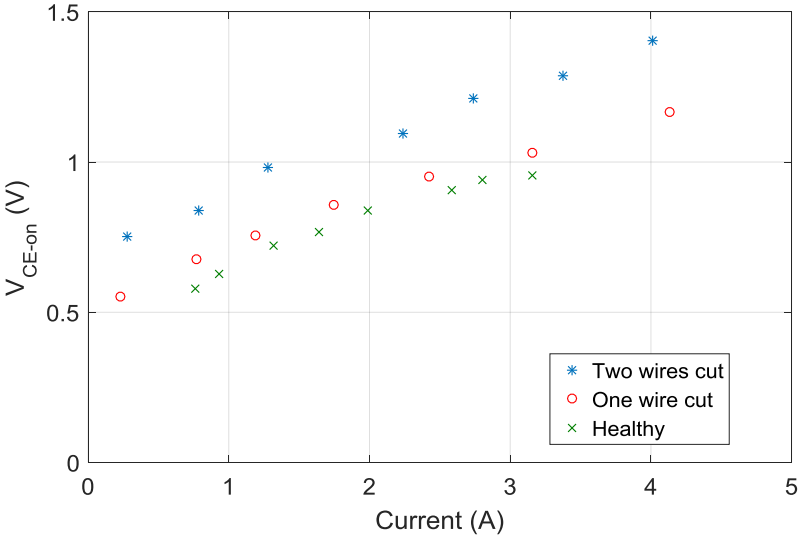

Figure 11. $V_{CE\text{-}on}$ variation in healthy and two faulty IGBT conditions, 100V DC link voltage and 25°C

Single measurements have been collected for a large number of combinations of DC link voltage, temperature, current, and number of bond wires cut in the IGBT, leading to some uncertainty in the repeatability of the measurements. By looking at the statistical distribution of many measurements taken

over time it should be possible to get a better picture of the changes that occur in $V_{CE\text{-}on}$ with DC-link voltage, temperature and current. However, it is already clear that the effect of cutting one or two bond wires changes the relationship between $V_{CE\text{-}on}$ and collector current more significantly than temperature variations or changes in the DC link voltage (which is generally known).

6. CONCLUSIONS

Early detection of failure mechanisms of IGBT modules can increase availability of power electronic converters by reducing unplanned down time. Bond wire lift-off is the most common failure found in IGBTs. The collector emitter on-state voltage is one means of detecting this failure mechanism. The on-state high-side collector-emitter voltage is measured through a high common-mode voltage-capable accurate amplifier. This failure indicator is not affected by the changing inductance presented by a PM machine as the current is briefly stationary. Variation of dc-link voltage does not appear to affect the value of collector emitter on-state voltage. The results show that bond wire lift-off increases the on-state collector emitter voltage. In addition, the method can detect bond wire lift off without being significantly affected by temperature.

ACKNOWLEDGEMENTS

This research is conducted as a part of "AEOLUS4FUTURE - Efficient harvesting of the wind energy" (H2020-MSCA-ITN-2014: Grant agreement no. 643167), founded by the European Commission's Framework Program " Horizon 2020 " (the Marie Skłodowska - Curie Innovative Training Networks (ITN)). The last two authors acknowledge the support of COST TU1304 Action in their relevant research activity.

REFERENCES

[1] F. Pedro García Márquez, A. Mark Tobia, J. María Pinar Pérez and M. Papaelias, "Condition monitoring of wind turbines: Techniques and methods," *Renewable Energy* , vol. 46, pp. 169-178, Oct 2012.

[2] M. Z. Sujod, I. Erlick and S. Engelhardt, "Improving the reactive power capability of the DFIG-based wind turbine during operation around the synchronous speed," *IEEE Trans. Energy Convers,* vol. 38, (3), p. 736–745, 2013.

[3] A. S. Bahman, K. Ma, P. Ghimire, F. Iannuzzo and F. Blaabjerg, "A 3-D-Lumped Thermal Network Model for Long-Term Load Profiles Analysis in High-Power IGBT Modules," *IEEE power electron,* vol. 4, (3), pp. 1050 - 1063, Sep 2016.

[4] S. Daliento, A. Chouder, P. Guerriero and A. Pavan, "Monitoring, Diagnosis, and Power Forecasting for Photovoltaic Fields: A Review," *Int Photoenergy,* vol. 2017, Jan 2017.

[5] R. Moeini, p. Tricoli, H. Hemida and C. Baniotopoulos, "Increasing the reliability of wind turbines using condition monitoring of semiconductor devices: A review," *RPG Conf,* London, 2016.

[6] M. Riccio, G. . D. Falco, P. Mirone, . L. Maresca, . M. Tedesco, G. Breglio and A. Irace, "Accurate SPICE Modeling of Reverse-Conducting IGBTs Including Self-Heating Effects," *IEEE Trans Power Electron,* vol. 32, (4), pp. 3088 - 3098, Apr 2017.

Paper TS6.1.2

THE INTERNATIONAL CONFERENCE ON
WIND ENERGY HARVESTING 2018
21-23 March 2018
Catanzaro, Italy

EXPERIMENT-BASED MODEL VERIFICATION FOR THE WIND LOAD IDENTIFICATION AT AN EXISTING WIND TURBINE

Mirjana Ratkovac*, Rüdiger Höffer

Wind Engineering and Flow Mechanics, Ruhr-Universität Bochum, Germany
Corresponding author: Mirjana Ratkovac, mirjana.ratkovac@rub.de

ABSTRACT

The identification of the overall wind loading including the rotor-induced thrust force at a wind turbine is a very challenging task. The paper shows results from a structural health monitoring system mounted at an operating wind turbine. First estimates about the internal forces of the turbine tower show that the measurable information seems to be insufficient to resolve the thrust forces including the head moment at the tower. Instead, a mechanical model is introduced to describe the coupling of the thrust force and the head moment using the distribution of the internal forces at the tower. First results on the identified rotor thrust force are presented and discussed for the future use. Wind tunnel experiments on a model of the wind turbine are in preparation, which serve to decouple the acting forces (thrust, head moment, pressure-induced forces at the tower). With this information it shall be made possible to verify the wind load model, to formulate the wind impact on different components of the wind turbine (rotor including nacelle, tower, foundation) and to assess the real order of internal forces based on the in-situ measurements of structural responses.

NOMENCLATURE

A	=	Rotor swept area (m^2)
c_t	=	Rotor thrust coefficient
E	=	Young's modulus of elasticity (MPa)
F_t	=	Rotor thrust force (kN)
L, ΔL	=	Base length of displacement transducer; relative displacement (mm)
M_{F_t}	=	Head bending moment from rotor thrust force
M_y, M_z	=	Bending moments in y and z direction (kNm)
M_1, M_2	=	Resulting bending moments at upper and lower section (kNm)
v	=	Horizontal wind velocity (m/s)
$q(z)$	=	Distributed wind load (kN/m)
ΔM_y, ΔM_z	=	Fluctuating bending moments in y and z direction (kNm)
σ	=	Stress (kN/cm^2)
ε	=	Strain (-)
ρ	=	Air density (kg/m^3)

1. INTRODUCTION

Direct measurement of the wind load acting on wind energy converters is often not possible due to high costs, sensor limitations or unapproachable structural components. Alternatively, wind load can be reconstructed based on the information on structural response using structural health monitoring data. In order to develop advanced structural fatigue and lifetime assessments of the complete or at least for a relevant group of loaded (structural) components of WEC, wind effects and e.g. operational impacts need to be separated. Additionally, design uncertainties due to unprecise wind load must be reduced. Using this approach for wind turbine load identification means facing many difficulties, such as solving

the ill-posed problem for the case of distributed stochastic load, dealing with the analysis for the operating structure and difficulties for the verification of the results [1,2].

It is assumed that the main cause for the measured structural response of an operating wind turbine is the wind acting on the rotor swept area, producing the thrust force on the top of the tower and an additional head bending moment due to eccentricity. In addition, the contribution of the distributed wind load over the tower height should be considered. Based on these assumptions, a mechanical model is being developed. In this paper, the full-scale data from SHM system mounted on a wind turbine structure in Dortmund, Germany is analysed. The model uses data from displacement transducers set on the wind turbine tower at two sections for the estimation of the rotor thrust force.

2. STRUCTURAL HEALTH MONITORING SYSTEM

A decentralized real-time structural health monitoring (SHM) system for remote monitoring is mounted on a 500kW wind turbine structure in Dortmund, Germany [3,4]. Wind turbine tower is a steel tubular structure with the height of 63m. The hub height is 65m with the rotor diameter of 40m. Sensors are used to measure the structural response (displacements and acceleration), together with the operational and environmental effects. The system allows automated data acquisition, storage and accessibility of the data directly from the database or through the web application. The six displacement transducers (W1-W6), which are set at the two tower sections, at 21.5m and 42.5m height, are used for the inverse wind load analysis (Figure 1). A temperature sensor (T1-T6, respectively) accompanies each displacement transducer, for the compensation of temperature effects.

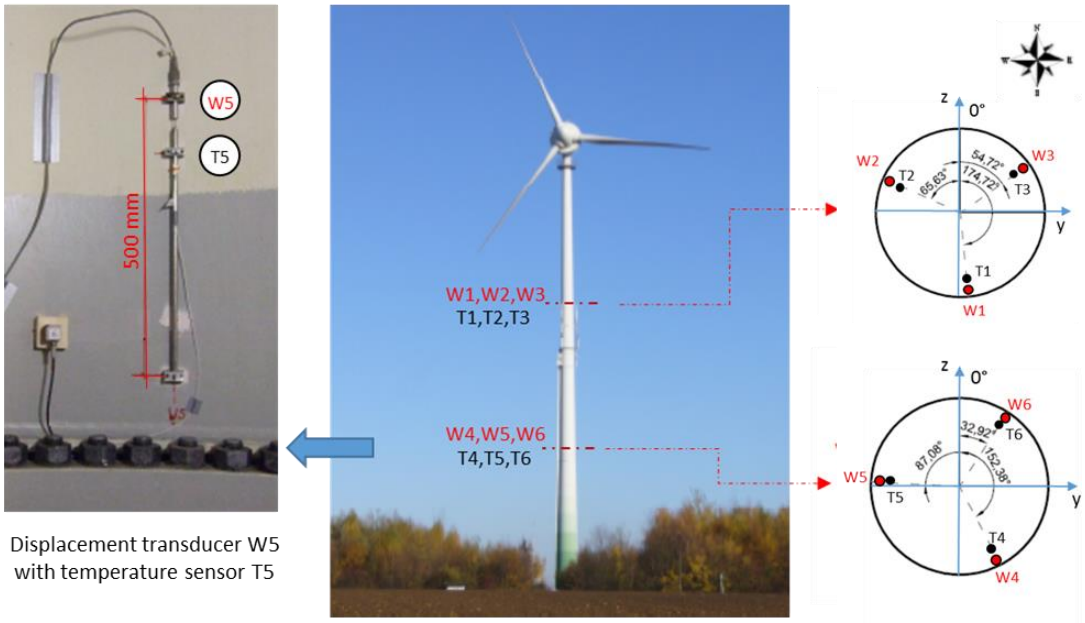

Figure 1. Overview of displacement transducers and temperature sensors at the wind turbine tower

2.1. Displacement transducers and temperature compensation

The displacement transducer, as shown in the Figure 1 (left) consist of the two legs that are fixed to the tower surface, with the base length of L= 500 mm. Between these fixed points is the holder for the sensor rod, which can move freely in vertical direction. Sensor measures change in the length (shortening or the extension) between the sensor legs, which shows the relative displacement of the tower surface, ΔL. Since the sensor rod is made from Invar, it has low temperature sensitivity and temperature effects are significant only in the low stress ranges and neglected in this study, as it is dealing with the operating phase with higher stress level. For lower stress levels, around cut-in wind velocity, temperature effects could be more influential and need to considered in the analysis.

Strain time history (ε) can easily be obtained using the displacement time history (ΔL), as shown in the Eq. (1). Assuming the linear elastic behaviour, stress time histories can be calculated based on the

Hook's law, using the Young's modulus of elasticity (E), Eq. (2). Measured time histories of the displacement for 1h data on 08.06.2010 and accordingly calculated stress time histories are shown in the Figure 2.

$$\varepsilon = \frac{\Delta L}{L} \tag{1}$$

$$\sigma = \varepsilon \cdot E \tag{2}$$

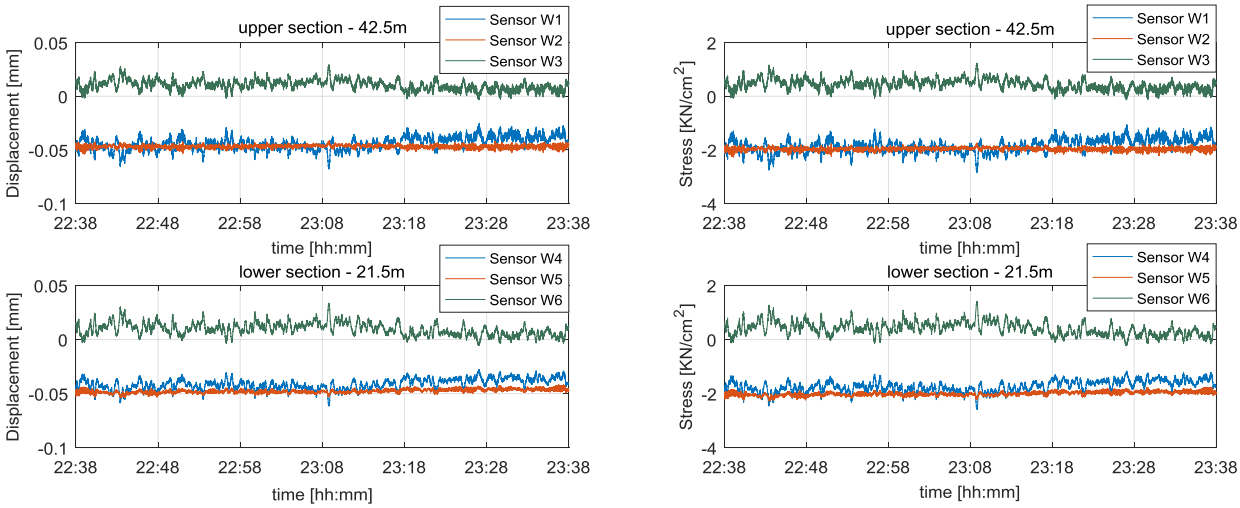

Figure 2. Time histories of displacement (left) and stress (right), 08.06.2010, 22:38-23:38h

2.2 Fluctuating bending moments calculation

Displacement transducers are installed at two levels at WEC tower and serve for the evaluation of the internal stresses. Each section contains three displacements transducers that are set symmetrically at angular distance of 120° (Figure 1). For the calculation of the bending moment at one cross section, information from two displacement transducers is sufficient, following the Eq. (3.1) and (3.2). In this study, displacement transducers W1 and W2 are used for the evaluation of the bending moment at the upper section, and for the lower section displacement transducers W4 and W5. The results are crosschecked for every combination of displacement transducers at both levels and satisfactory agreement is obtained.

$$M_{y,ij} = \left(\frac{1}{y_i}\cdot(\sigma_N - \sigma_i) + \frac{1}{y_j}\cdot(\sigma_j - \sigma_N)\right)\cdot I_y \cdot \left(\frac{z_j}{y_j} - \frac{z_i}{y_i}\right)^{-1} \tag{3.1}$$

$$M_{z,ij} = \left(\frac{1}{z_i}\cdot(\sigma_i - \sigma_N) + \frac{1}{z_j}\cdot(\sigma_N - \sigma_j)\right)\cdot I_z \cdot \left(\frac{y_j}{z_j} - \frac{y_i}{z_i}\right)^{-1} \tag{3.2}$$

Since the sensors were mounted on the structure during its lifetime, a certain stress level was already present at the structure and it is not possible to use the absolute values. Additional calibration of the sensors is required. For this reason, only fluctuating components of bending moments, i.e. RMS values are used for the first analysis. A 1h time interval of full-scale data is analysed, during which the turbine was operating with approximately constant 26 U/min. Figure 3 shows the time histories of the fluctuating bending moments, ΔM_y and ΔM_z, for measured data on 08.06.2010, from 22:38-23:38h. The remaining analysis shown in this paper refers to the aforementioned time interval with approximately constant operational conditions.

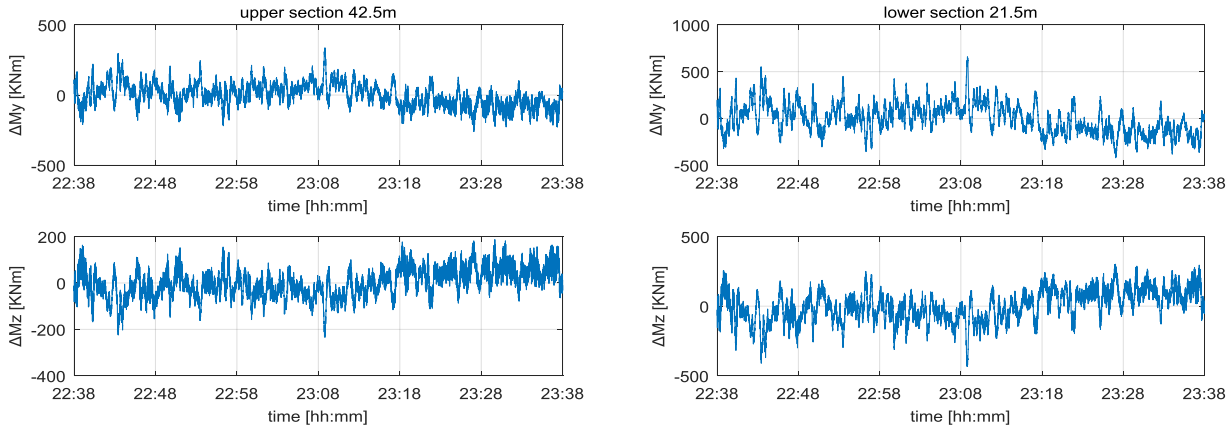

Figure 3. Fluctuating bending moments, 08.06.2010, 22:38-23:38h, upper section (left) and lower section (right)

3. DIFFICULTIES IN THE IDENTIFICATION OF THE ROTOR THRUST FORCES

The wind acting on the rotor swept area is considered to be the main cause of the measured displacements at the tower. This wind produces the thrust force on the top of the tower and an additional head bending moment due to eccentricity between the rotor thrust force and the tower. Based on these assumptions a mechanical wind load model is being developed (Figure 4), where F_t – rotor thrust force, M_{F_t} – head moment from thrust force, and q(z) – distributed wind pressure, are the main loading components.

For the first iteration, the influence of the distributed wind load at the tower is neglected and a linear distribution of the bending moments over the height due to the thrust force is considered. Fluctuating response components are manly caused by the fluctuations of the wind for quasi-stationary operational conditions with constant yaw angle and constant RPM.

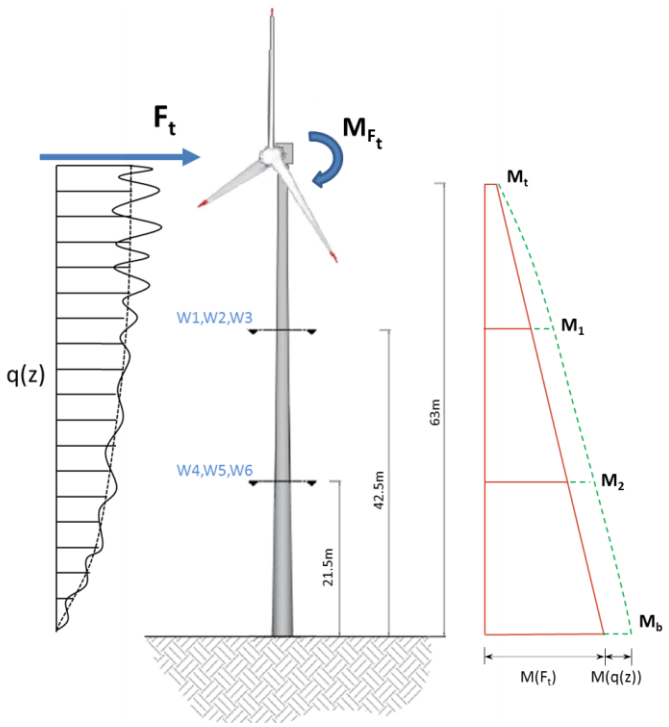

Figure 4. Schematic view of the wind load model

Assuming a linear connection between the resultant bending moments at 42.5m and 21.5m height (M_1 and M_2, respectively), first estimates on the rotor thrust force have been made. The resultant bending

moments are estimated using the geometric mean from component bending moments, M_y and M_z. In order to justify the assumption on linear distribution of the bending moments over the height, the scatter diagram of the fluctuating bending moment at the upper section and the fluctuating bending moment at the lower section is plotted for each measurement point during 1h and shown in Figure 5.

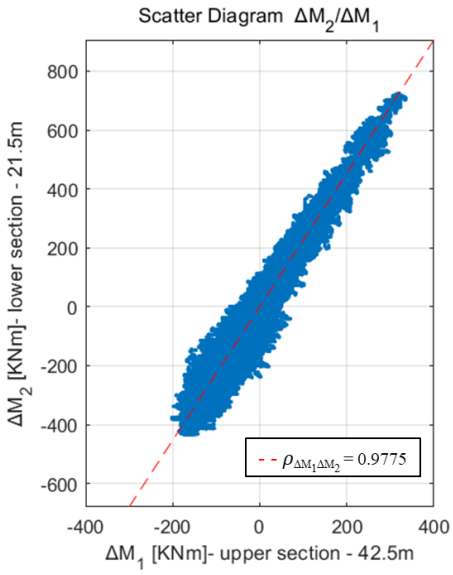

Figure 5. Scatter diagram – fluctuating bending moments ΔM_2 and ΔM_1, 08.06.2010, 22:38-23:38h

Additionally, the calculated correlation coefficient between time histories of the bending moments M_1 and M_2 is equal to 0.9775 and indicates a strong linear dependence between the two signals. As it can be seen, it is safe to assume that the thrust force is main cause of the measured response and linear connection between the bending moments can be assumed.

3.1. Estimation of the rotor thrust force

The rotor thrust force is estimated from the difference in the fluctuating bending moments at the two levels. This difference divided by the distance between the two levels gives the fluctuating thrust force that is the main cause for the measured fluctuations. In order to verify the identified thrust force, the fluctuating thrust force was calculated separately from the measured wind velocity using the theory of Betz. In Figure 6, operational data is presented, showing the measured wind velocity of nearly 7 m/s at 67m height. Pitch control for the analyzed wind turbine starts at the 12 m/s, meaning that the pitch angle does not play a role here. Wind direction is estimated using ultrasonic anemometer near the wind turbine tower at the height of 13m. As it can be seen, the yaw angle and the wind direction show good correspondence. The wind is coming from the south direction, with low fluctuations of the wind direction and the yaw angle.
According to the Betz theory, the rotor thrust force can be calculated using the Eq. (4).

$$F_t = \frac{1}{2} c_t \rho A v^2 \tag{4}$$

where, c_t is the rotor thrust coefficient, ρ is the air density, A is the rotor swept area and v is the horizontal wind velocity. The rotor thrust coefficient is considered constant for the measured wind velocity and is adopted according to [2]. Figure 7 shows the comparison between identified rotor thrust force and the force estimated using the theory of Betz.

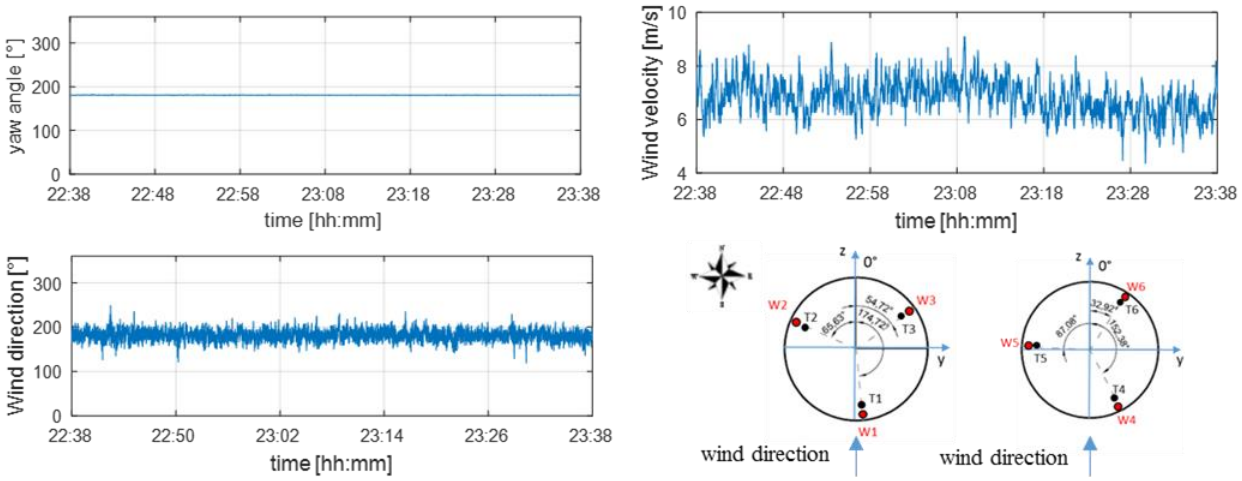

Figure 6. Operational data – wind direction and velocity; yaw angle and sensor positions in regard to the wind direction, 08.06.2010, 22:38-23:38h

The comparison of time histories of the identified rotor thrust force and the force estimated using the theory of Betz show good agreement for the whole 1h of measured data, where the standard deviation is 4.854 for the identified force and 4.646 for the Betz force.

However, the comparison of the frequency content of the both signals is required. Normalized rotor thrust force spectrums are shown in Figure 8, where larger differences can be seen. These deviations in the frequency domain are expected since the identified rotor thrust force contains also the resonant components. The first and second peak in the identified force spectrum correspond with the first and second fore-after bending modes of the wind turbine tower, 0.375Hz and 2.172Hz, respectively. Similar results for the dynamic characteristics were found in previous dynamic investigations for the same structure [5,6]. The second peak, i.e. the area with multiple peaks is found around the frequency of 1.3Hz, which corresponds to the frequency of blade passage for the rotor operation of nearly 26 U/min. The background spectrum component due to the wind load is same for the both signals for the first minutes, but later the energy content of the identified wind load is lower approaching the eigenfrequencies of the structure. The resonant component can be excluded from the signal by filtering out the resonant frequencies and extrapolating the remaining wind load spectrum. This would lead to lower variance of the identified load, i.e. to the lower thrust force fluctuations by nearly 10%. However, strategy that is more accurate should be considered for the future work. Pahn et al. [1] studied quasi-static and dynamic components of the identified thrust force for the theoretical wind turbine model, considering only the first two bending modes, using the inverse frequency response matrix. Similar approach could be considered for the real full-scale wind turbine data.

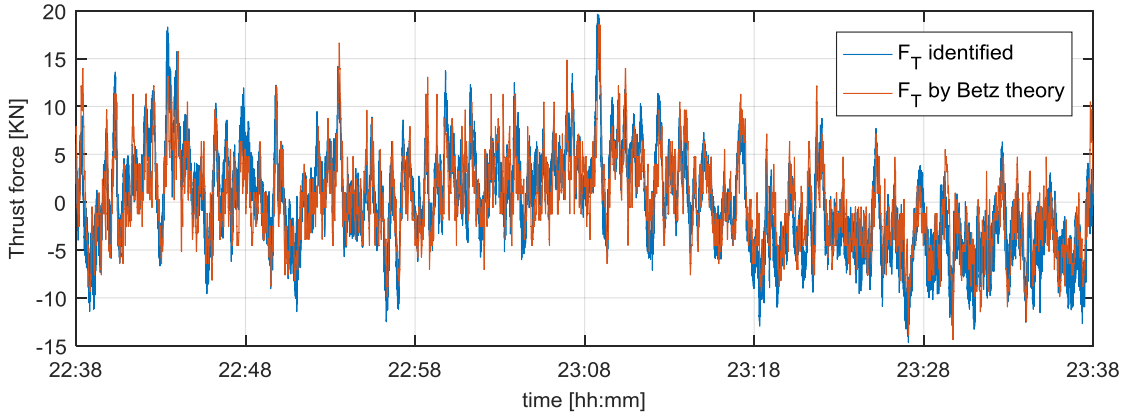

Figure 7. Fluctuating thrust force, 08.06.2010, 22:38-23:38h

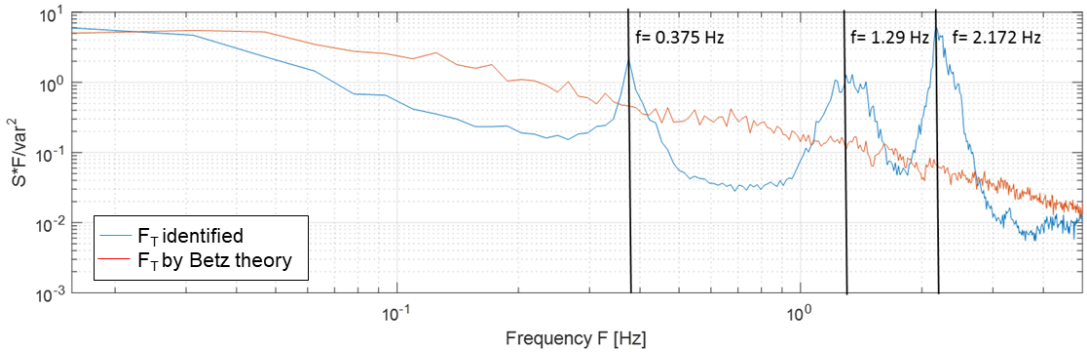

Figure 7. Normalized rotor thrust force spectrum, 08.06.2010, 22:38-23:38h

4. FUTURE WORK

The results show high potential of the proposed model for the analysis and the identification of the wind thrust force acting at an operating wind turbine. For the first iteration, number of assumptions has been made for the simplification of the model. For the future investigations, the following steps and improvements are planned:

- Background component due to the wind and resonant component of the identified thrust force need to be separated. Additionally, the influence of the operating conditions, i.e. rotor operation, gyroscopic effects and pitch control should be estimated.
- In order to determine the absolute value of the rotor thrust force, the calibration of the sensors is required. This can be achieved by analyzing the stresses during the parked time and during the low wind velocities, below the 2.5 m/s, which is the cut-in velocity.
- Dynamic coordinate system needs to be applied in order to avoid the effect of nacelle weight for nonstationary case.
- The changing wind velocity over the height of the rotor and position of the resultant force with the corresponding eccentricity should be considered.
- The separation and consideration of the distributed wind load at the tower should be considered in the next steps ((q(z)), Figure 1). This will be done by developing a wind pressure model at the tower.
- Verification of the proposed model is planned at the wind tunnel test laboratory.

4.1. Experimental verification using the wind tunnel test

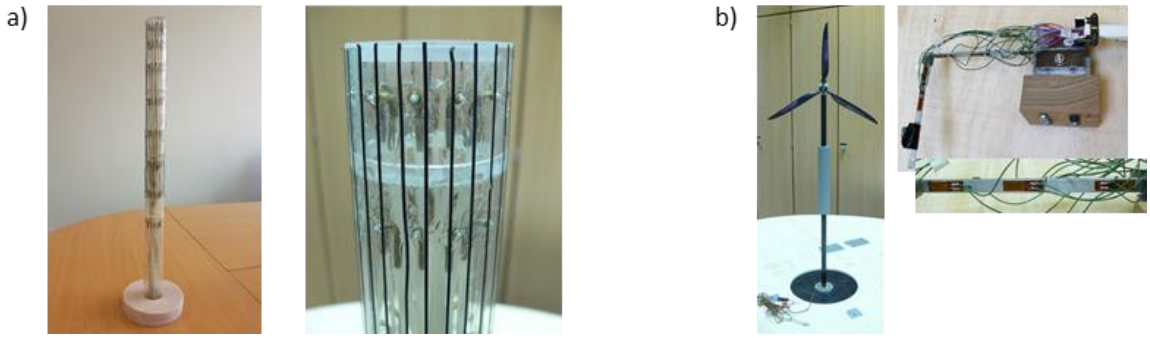

Figure 8. Wind tunnel models for measurement of pressure a) and head bending moment b)

Atmospheric boundary layer wind tunnel experiments are planned at a wind tunnel model of a wind turbine. Purpose of the experiments is the decoupling of active loads (thrust, head moment, pressure-induced forces at the tower) and the verification of the identified wind load. The model will include the measurement of the thrust force, the head moment and the measurement of wind pressures over the whole height of the model in order to develop a correlation model for pressure-induced forces at the

tower. Model for measurement of wind-induced pressures at the tower with the equipment for measuring the head bending moments is shown in Figure 8. Since the verification of the identified wind load is difficult in full-scale, especially for the distributed wind-induced pressures at the wind turbine tower, wind tunnel tests are justified alternative approach for the verification with possibility to avoid ill-posed difficulties encountered in the full-scale.

5. CONCLUSIONS

The mechanical model for the inverse wind load identification at WEC has been presented. The results show the potential of the proposed model for the dynamic analysis and the rotor thrust force identification at an operating wind turbine. Assumption on the linearity between the bending moments at two sections has been justified, due to the fact that the fluctuating rotor thrust force is the main cause of the measured response, in case of nearly constant operational conditions. Time-history of the identified rotor thrust force fluctuations shows good agreement with the theoretical rotor thrust force, calculated using the theory of Betz. However, the calculated power spectral density shows different energy content of the theoretical and the identified thrust force signal. The reason for these differences are the resonant and operational components in the identified load. The found results give insight in the complexity of the load identification problem on one side, but also the guidelines for the future improvements of the proposed mechanical model on the other side. The proposed model is also capable of capturing the dynamic characteristics of the operating structure, for nearly constant operating conditions. The achieved results and future improvements are discussed in the paper, showing the potential of the proposed mechanical model for the wind load identification at an operating wind energy converter, by using SHM data.

ACKNOWLEDGEMENTS

The authors acknowledge with thanks the support of the European Commission's Framework Program "Horizon 2020", through the Marie Skłodowska-Curie Innovative Training Networks (ITN) "AEOLUS4FUTURE - Efficient harvesting of the wind energy" (H2020-MSCA-ITN-2014: Grant agreement no. 643167) and the support of the DEW21 belonging to City of Dortmund/Germany granted to the present research project.

REFERENCES

[1] T. Pahn, R. Rolfes, J. Jonkman and A. Robertson, “Inverse Load Calculation of Wind Turbine Support Structures – ANumerical Verification Using the Comprehensive Simulation Code FAST” *Proceedings of the 53rd Structures, Structural Dynamics, and Materials Conference,* April 23 – 26 2012, Honolulu, Hawaii.

[2] M. Klinkov and C.P. Fritzen, “Wind Load Observer for a 5MW Wind Energy Plant”, *Proceedings of the IMAC-XXVIII*, February 1–4, 2010, Jacksonville, Florida, USA.

[3] D. Hartmann and R. Höffer, “Lifespan assessment of wind energy converters through system identification”, Research project funded by the German Research Foundation (DFG) through the research grant HA 1463/20-1. Ruhr-University Bochum, Bochum, Germany, 2010.

[4] S. Lachmann, “Kontinuierliches Monitoring zur Schädigungsverfolgung an Tragstrukturen von Windenergieanlagen” Ruhr-Universität Bochum, Dissertation, 2014.

[5] X. Liu, “System Identification of a Wind Energy Converter using Wavelet-based Damage Detection and Robust Model Updating Strategy”, Ruhr-Universität Bochum, Dissertation, 2013.

[6] S. Bogoevska, M. Spiridonakos, E. Chatzi, E. Dumova-Jovanoska and R. Höffer, “A novel bi-component structural health monitoring strategy for deriving global models of operational wind turbines”, *8th European Workshop On Structural Health Monitoring (EWSHM 2016), Bilbao, Spain, 5-8 July 2016*, 2016, Online: www.ndt.net/app.EWSHM2016

EXPERIMENTAL STUDY OF THE EFFECT OF FREESTREAM TURBULENCE ON THE NEAR WAKE OF A SMALL VAWT

Andreu Carbó Molina[1, 2]*, Tommaso Massai[1], Gianni Bartoli[1], and Tim De Troyer[2]

[1]Department of Civil and Environmental Engineering, University of Florence, Italy
[2] Thermo and Fluid Dynamics (FLOW), Vrije Universiteit Brussel, Belgium
*Corresponding author: Andreu Carbó Molina, andreu.carbo.molina@dicea.unifi.it

ABSTRACT

Small Vertical-Axis Wind Turbines (VAWTs) have become an important research topic within the wind energy community, as it is said that they adapt better to the complex and highly turbulent urban environment. A wind tunnel set-up has been developed in order to reproduce urban flows in a controlled environment, being able to study the effect of free stream turbulence intensity and integral length scale on a H-Darrieus VAWT in operation. The first campaign showed a significant increase of performance for high turbulence levels. Next, the near wake characteristics were measured in the same turbulent conditions, in order to understand this effect and improve the knowledge in this technology. High turbulence caused a reduction of the velocity drop behind the rotor, which is positive for wake recovery, while wake turbulence did not seem to be much affected by the free stream conditions, as the VAWT is a turbulence generator itself. Further measurements are advised to increase the knowledge on the subject, which has high potential in combination with CFD simulations. This could provide a useful insight for the optimization and combination of several VAWTs, -*e.g.* if they were placed on the rooftop of high-rise buildings.

NOMENCLATURE

A_r	=	Rotor area (m^2)
b	=	Grid bar width (m)
c	=	Turbine blade chord (m)
C_P	=	Power coefficient (-)
I_u	=	Intensity of turbulence in wind direction (-)
L_{ux}	=	Integral length scale of turbulence in wind direction (m)
M	=	Grid mesh size (m)
U	=	Wind speed (m/s)
R	=	Rotor radius (m)
P	=	Turbine mechanical power (W)
Re	=	Reynolds number (-)
x	=	Longitudinal distance from the rotor axis (m)
y	=	Transversal distance from the rotor axis (m)
λ	=	Tip-to-speed ratio (-)
ω	=	rotational speed (rad/s)
CFD	=	Computer Fluid Dynamics
HAWTs	=	Horizontal-Axis Wind Turbines
rms	=	Root mean square
VAWTs	=	Vertical-Axis Wind Turbines
$_{sf}$	=	Optimal smooth flow conditions

1. INTRODUCTION

Small wind turbines are a fast-growing research field among the smart city technologies. Placing those wind turbines on the roof of skyscrapers allows capturing the stronger winds at high elevation. Moreover, being able to harvest urban winds efficiently could reduce drastically the transportation costs by on-site consumption, and become a key factor for the autonomy of the future communities [1].

However, most of the urban wind installations have turned out to be a disappointment: still or underperforming turbines that give bad press for the technology. An important problem that urban wind turbines face is that the wind climate in cities is very complex. The wind typically has low intensity, high variability, high levels of turbulence, inclined and even reversed flows [2 - 4].

Lately, consumers and manufacturers have been investing more and more in Vertical-Axis Wind Turbines (VAWTs) for wind generation inside urban environments [5]. Their vertical rotation gives them some advantages over conventional Horizontal-Axis ones (HAWTs): they are quieter, more visually appealing and omnidirectional, which allows them to better deal with the fast-changing urban winds [6]. Roughly speaking, VAWTs can be divided in two categories: Savonius (drag based) and Darrieus (lift based). Because of their higher efficiency [7], this study will focus on the Darrieus type.

The variability of the wind inside urban environments is the main issue on the operation of those kind of turbines [8]. Most up-to-date studies of VAWT under turbulent flows have been done in real cases, comparing the performance of the installed turbines with the on-site wind turbulence measured by a meteorological station. The effect of turbulence is uncertain: some studies record an increase of performance [9, 10], others a drop [11, 12] and sometimes it depends on the wind speed [13]. Actually, as the wind speed cannot be controlled, it is very complicated to obtain, from real-life data, precise ratings or power curves of the turbines, or measure the wake characteristics without suffering external influences.

The study of urban VAWTs inside the wind tunnel is also a complicated issue, as most of the experimental facilities are designed for aeronautic purposes and have a very low background turbulence intensity (I_u < 1%). In contrast, turbulence intensity inside the cities is often higher than 10% [14], and also the typical integral length scales of this turbulence should be considered (L_{ux} in the order of 1m affecting the turbine) [15]. Several campaigns have studied in detail VAWT ratings inside the wind tunnel [16, 17] but only a few of them addressed the topic of turbulence [18, 19].

An experimental set-up and methodology was developed in the last year at the Vrije Universiteit Brussel [20], to evaluate the effect of turbulence on VAWTs performance in wind tunnel. Artificial turbulence is generated by using passive grids to increase the levels of practically homogeneous turbulence intensity, reaching I_u values up to 10%. Values of integral length scale L_{ux} reached using that set-up were lower than the ones found in urban environment but large enough to avoid local effects in the blades ($L_{ux} > c$). A considerable boost in the performance of a H-Darrieus VAWT due to turbulence was found [21].

The present study is based on measurements conducted with the same set-up at CRIACIV wind tunnel (Prato, Italy). The purpose was to better understand the effect of turbulence on a VAWT, with special interest in the near wake of the turbine. A previous study [22] on a 5-bladed rotor detected large asymmetries and differences in the wake from smooth to turbulent flow. The objective of this work is to measure the wind speed deficit in the wake and compare it with the turbine performance in smooth flow and high turbulence conditions. By contrasting the effect of free stream turbulence intensity and integral length scales, knowledge in the topic is to be expanded, in order to understand how to take advantage of turbulent flows in the future of urban wind harvesting.

2. METHODOLOGY

2.1. The facility

CRIACIV is an Inter-University Research Centre focused on the field of Building Aerodynamics and Wind Engineering, grouping eight Italian Universities. The Wind Engineering Laboratory is in Prato, close to Florence, and it is equipped with an open-circuit boundary layer wind tunnel (Figure). The facility presents a total length of about 22 m, with a nozzle at the inlet with a contraction ratio of 4.2 after the honeycomb and a T-diffuser at the outlet. The rectangular test section is 2.42 m wide and 1.60 m high. Air is aspired through a motor with a nominal power of 156 kW and the flow speed can be varied continuously up to ~ 30 m/s adjusting, by means of an inverter, the rotation speed of the fan and the pitch angle of its ten blades. In the absence of turbulence generating devices, the free-stream turbulence intensity is around 0.7 %.

Figure 1. Top view of the CRIACIV wind tunnel..

2.2. Experimental set-up

- Turbulence grids:
  Squared-mesh wooden grids are placed upstream of the VAWT to generate various levels of turbulence intensity I_u and integral length scale L_{ux}. These kinds of grids are usually employed for bluff body studies, and they are chosen for their simplicity and because they provides quasi-isotropic turbulence. Two grids are designed following the empirical relations found in literature [23, 24, 25] which describe the decay of turbulence downstream of the grid (Equations 1 and 2). Table 1 describes the characteristics of these grids.

$$I_u = 2.58\left(\frac{x}{b}\right)^{-8/9} \qquad (1)$$

$$L_{ux} = 0.2b\left(\frac{x}{b}\right)^{1/2} \qquad (2)$$

Table 1. Comparison of the turbulence grids used for the present tests.

Grid	Mesh size, M	Bar size, b	I_u range	L_{ux} range
1	10 cm	2.5 cm	2 – 5 %	5 – 7 cm
2	33 cm	7 m	5 – 12 %	9 – 18 cm

- Flow measurements:
  The mean flow speed was monitored with a Pitot tube connected to a sensor Setra AccuSense model ASL. The free stream wind speed was set placing the pitot tube in the test section, before the turbine was switched on.

The spectral properties of the induced turbulence were determined through measurements with a Dantec single-component hot-wire probe 55P11 connected to a Dantec CTA 56C01 module and a 56C17 bridge. The spatial homogeneity of the flow at the position of the model was verified prior to start the tests. The longitudinal integral length scale L_{ux} was calculated according to Taylor's frozen-eddy hypothesis and the results were confirmed by fitting a von Kármán spectrum to the measured spectrum, while the turbulence intensity was calculated as usual by using the *rms* and the mean longitudinal flow speed (Eq. 3).

$$I_u = \frac{U_{rms}}{U} \qquad (3)$$

Near wake measurements on the VAWT model tested in the CRIACIV wind tunnel test-section were performed by horizontally mounting a traversing system at a distance $x = 1.5R$ downstream the rotor, at its half height. Such test rig is composed by a stiff aluminium arm mounted on an endless-screw activated with a stepper motor controlled through an Arduino based algorithm. Three probes are mounted on the rigid fork connected to the moving aluminium arm, one central Pitot tube, to measure the mean punctual flow speed, and two hot-wire probes for measuring the fluctuating component of longitudinal wind speed. In this way an adequately refined wake profile has been obtained for each configuration tested.

- The turbine:
  It is a straight-bladed H-Darrieus model manufactured at the Vrije Universiteit Brussel, with a solidity of 0.2 and a blade chord of $c = 5$ cm. The mechanical power is measured using a torque meter, and ω is controlled using variable resistors. The axis of the turbine is coupled to a brushed DC motor/generator, allowing the start-up of the turbine.

The three components of the set-up above mentioned are shown in Figure 2.

Figure 2. Experimental set-up: a close-up view of the traverse system, with the VAWT and the turbulence grid 2 behind it.

- Test conditions:
  The experiments were done in four different turbulence conditions, to contrast the effect of I_u and L_{ux} (Table 2). The incoming wind speed was set at $U = 9$ m/s during all tests, as it was the best operational point for the VAWT prototype, resulting in a chord Reynolds of around 10^5.

Table 2. Comparison of the turbulence grids used for this experiment.

Condition	Grid	grid distance x	mean I_u	mean L_{ux}
Smooth flow	none	-	0.7 %	-
Low I_u	2	7.6 m	5.4 %	18 cm
High I_u	2	3.75 m	9.2 %	15 cm
Low I_u, low L_{ux}	1	2.1 m	4.6 %	4 cm

The turbine performance was monitored by measuring its Power Coefficient C_P (Eq. 4) and tip-to-speed ratio λ (Eq. 5). The near wake was characterized by the longitudinal wind speed U deficit and the turbulence intensity I_u. Blockage may have an influence in the measurements and wake shape [26], but as this is a preliminary study and all the measurements were taken with the same blockage conditions, no corrections were applied in that sense.

$$C_P = \frac{P}{\frac{1}{2}\rho A_t U^3} \qquad (4)$$

$$\lambda = \frac{\omega R}{U} \qquad (5)$$

3. RESULTS

3.1. Effect of turbulence on the turbine power curves

Figure 3 presents the power curves obtained with the VAWT model in the turbulence conditions presented in Table 2. The values are non-dimensionalised with the optimum C_P and λ obtained under smooth flow conditions due to confidentiality reasons. However, it is clear that the increased I_u causes a considerable boost in the turbine performance. The effect of L_{ux}, on the other hand, is not that evident, as the two curves at $I_u \sim 5\%$ show similar C_P values even when the L_{ux} levels are very different. It is interesting to mention that the error bars are larger in the high turbulence case, because when the turbine is so close to the grid the wind speed profile is not as uniform, and therefore the uncertainty in wind speed is higher [20, 21].

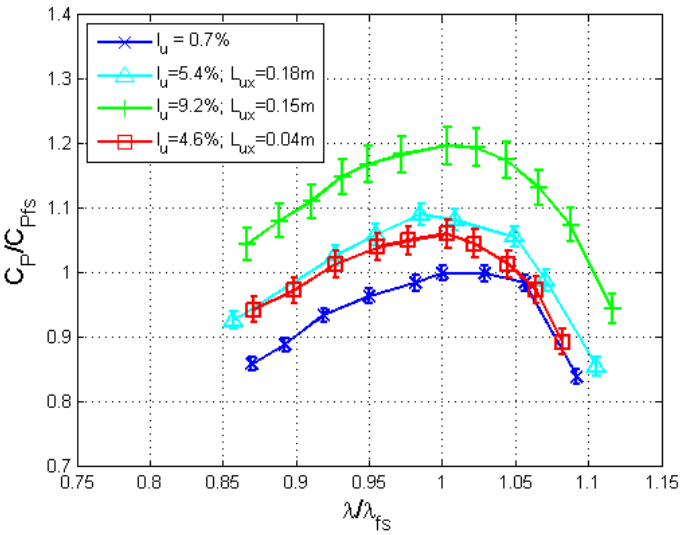

Figure 3. Non-dimensionalized power curves obtained with the VAWT under the different turbulence conditions.

3.2. Effect of turbulence on the near wake of the VAWT

- Wind speed deficit:
  Figure 4 presents the horizontal profile of the longitudinal wind speed downstream of the VAWT, taken at the optimal λ. In general, it can be noticed that the wake is shifted towards the side where the blades moves upstream, fact consistent with literature [27, 28]. The effect of turbulence is not evident in the wake shape, but only in a lower drop in wind speed deficit. In the lowest point (behind the shaft), while the wind speed in the smooth flow drops to the 20% of the free stream, in the high turbulence case the wind speed only drops to 30% of the free stream velocity. As in previous chapters, there is no evident effect of the free stream L_{ux}.

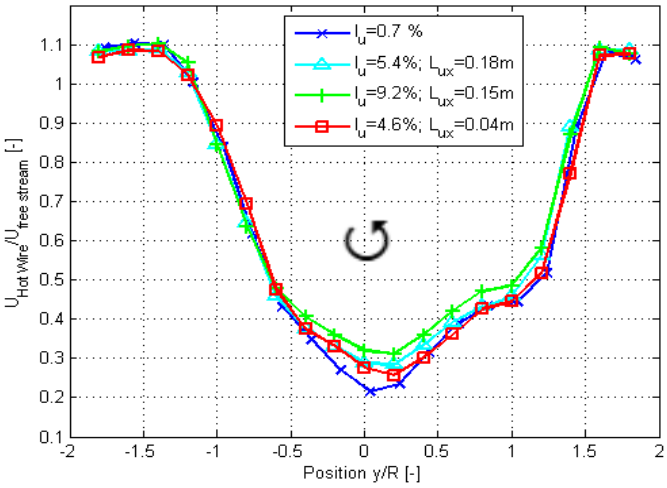

Figure 4. Wind speed deficit measured in the wake at 1.5R from the VAWT axis, under the different turbulence conditions at the optimum λ. The arrow shows the rotation sense of the rotor.

- Turbulence conditions in the wake:
  Three peaks of turbulence can be identified in Figure 5. The two in the sides are related with the interference wake/free stream, and are proportional with the free stream I_u. The central peak refers to the wake of the shaft, hence it is independent from the turbulence level, reaching in all cases a maximum I_u =25%. Free stream L_{ux} does not have evident effect in this case either.

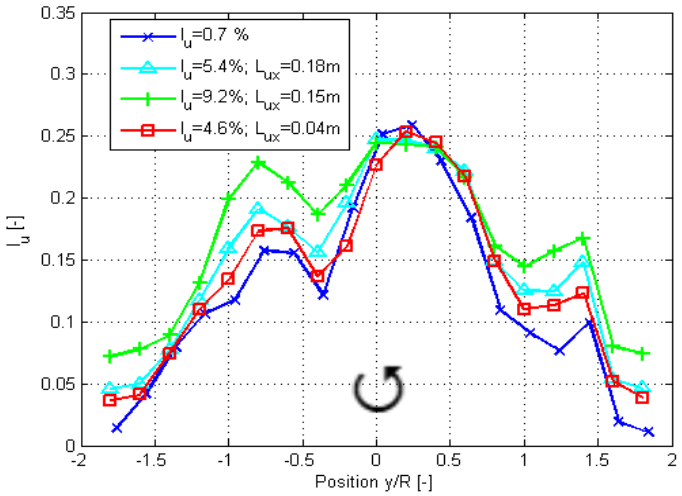

Figure 5. Turbulence intensity at 1.5R from the VAWT axis, under the different turbulence conditions at the optimum λ. The arrow shows the rotation sense of the rotor.

3.3. Interpretation of results

The effect of free stream turbulence on VAWT operation is clearly positive in the performance rating. This fact can be caused by the fact that turbulent flows are more energetic and delay the stall of the blades [29].

In contrast to previous studies [22], in the present measurements the comparison of the near-wake of the VAWT between smooth and turbulent flows showed only small variations. This can be due to differences in the turbine (5-bladed against 2-bladed) and in the operating conditions (λ, Re).

The minor drop in wind speed for turbulent flows (70% against 80% velocity deficit) seems counter-intuitive with the fact that the turbine is extracting more energy from the wind [22], but is consistent with field studies in this matter suggesting faster wake recovery in turbulent flows [30]. This is also an indicator that the aerofoil performs better in turbulent flows, causing less drag.

The turbulence intensity in the wake shows that VAWTs act like turbulence generators, increasing significantly the values of I_u downstream. The maximum levels of turbulence, reaching I_u = 25%, can be found behind the shaft, regardless of the free stream characteristics.

4. CONCLUSIONS

VAWTs are an on-growing technology still in the research phase. The increasing number of installations in high-turbulence locations (as urban environments) urges to develop a set-up to test them inside wind tunnels, in order to optimize them for complex flows.

The use of turbulent grids allows to model nearly-urban wind conditions, being able to isolate the effect of every flow parameter (U, I_u, L_{ux}). First measurements show that turbulence intensity I_u has large influence in the turbine performance, increasing its power by 20% from smooth flow to I_u =9.4 %. Integral length scales of this turbulence did not show to have relevant influence in the turbine power curves.

The study of the near wake in turbulent conditions searched to give an explanation to this performance rise, and increase the understanding of the technology. The measurements were done at the maximum power operation point 1.5R downstream the turbine, and showed that in high turbulence flows the wind speed drop is 10% lower than in smooth flow. The shape of the wake in that position does not show large differences from smooth to turbulent flows, in fact, the maximum I_u found downstream the turbine is 25% in all the cases studied.

In conclusion, also in the wake characteristics VAWT tend to perform better in turbulent flows, even though much further studies are needed in order to understand the reasons for this fact. Testing at other Re and λ should increase the knowledge in how the flow interacts with the blades, while measuring at other downstream and vertical positions will give more information about wake recovery and 3D effects. The comparison of these results with CFD-generated flow fields would be also of great utility for this research.

ACKNOWLEDGEMENTS

The present research takes part in the European Innovative Training Network (ITN) AEOLUS4FUTURE “Efficient Harvesting of the Wind Energy”. The project is funded by the Horizon 2020 research and innovation program under the Marie Skłodowska-Curie grant agreement No. 643167.

REFERENCES

[1] J. F. Barlow, D. R. Drew. Wind flow in the urban environment. From WINERCOST Work-shop 'Trends and challenges for wind energy harvesting'. Coimbra, Portugal, 2015.

[2] S. Bianchi, A. Bianchini, G. Ferrara, L. Ferrari. Small wind turbines in the built environment: influence of flow inclination on the potential energy yield. Journal of Turbomachinery, vol. 136, 2014. [DOI: 10.1115/1.4025169]

[3] C. Beller. Urban Wind Energy - State of the Art 2009. Danmarks Tekniske Universitet, Risø Nationallaboratoriet for Bæredygtig Energi. (Denmark. Forskningscenter Risoe. Risoe-R; No. 1668(EN)), 2009.

[4] D. Rabkin, M. Tomusiak. Museum of Science wind turbine lab report, Boston, 2012.

[5] T. F. Ishugah, Y. Li, R. Z. Wang, J. K. Kiplagat. Advances in wind energy resource exploitation in urban environment: a review. Renewable and Sustainable Energy Reviews 37, 2014. [http://dx.doi.org/10.1016/j.rser.2014.05.053]

[6] I. Paraschivoiu. Wind Turbine Design: With Emphasis on Darrieus Concept. Presses inter Polytechnique, 2002.

[7] M. M. Aslam Bhutta, N. Hayat, A. U. Farooq, Z. Ali, S. R. Jamil, Z. Hussain. Vertical axis wind turbine – A review of various configurations and design techniques. Renewable and Sustainable Energy Reviews 16, 2012. [doi:10.1016/j.rser.2011.12.004]

[8] W. D. Lubitz. Impact of ambient turbulence on performance of a small wind turbine. Renewable Energy 61, 2014.

[9] E. Möllerström, F. Ottermo, A. Goude, S. Eriksson, J. Hylander, H. Bernhoff. Turbulence influence on wind energy extraction for a medium size vertical axis wind turbine. Wind Energ. 19, 2016. [DOI: 10.1002/we.1962]

[10] T. Bertényi, C. Wickins, S. McIntosh. Enhanced energy capture through gust-tracking in the urban wind environment. 48th AIAA Aerospace Sciences Meeting Including the New Horizons Forum and Aerospace Exposition. Orlando, Florida, 2010.

[11] L. C. Pagnini, M. Burlando, M. P. Repetto. Experimental power curve of small-size wind turbines in turbulent urban environment. Applied Energy 154, 2015.

[http://dx.doi.org/10.1016/j.apenergy.2015.04.117]

[12] S. J. Kooiman, S. W. Tullis. Response of a vertical axis wind turbine to time varying wind conditions found within the urban environment. Wind Engineering Volume 34, No. 4, 2010.

[13] K.-Y. Lee, S.-H. Tsao, C.-W. Tzeng, H.-J. Lin. Influence of the vertical wind and wind direction on the power output of a small vertical-axis wind turbine installed on the rooftop of a building. Applied Energy 209, 2018. [http://dx.doi.org/10.1016/j.apenergy.2017.08.185]

[14] I. Janajreh, L. Su , F. Alan. Wind energy assessment: Masdar City case study. Renewable Energy 52, 2013. [http://dx.doi.org/10.1016/j.renene.2012.09.025]

[15] A. R. Dallman. Flow and turbulence in urban areas (PhD thesis). University of Notre Dame, Indiana, USA. 2013.

[16] R. E. Sheldahl. Comparison of field and wind tunnel Darrieus wind turbine data. Sandia National Laboratories energy report, 1981.

[17] V. Dossena, G. Persico, B. Paradiso, L. Battisti, S. Dell'Anna, A. Brighenti, E. Benini. An experimental study of the aerodynamics and performance of a Vertical Axis Wind Turbine in a confined and unconfined environment. Journal of Energy Resources Technology, vol. 137, 2015.

[18] J. J. Miau, S. W. Huang, Y. D. Tsai, S. Y. Liang, C. H. Hsieh, S. J. Chen, C. C. Hu, J. C. Cheng, T. S. Leu. Wind tunnel study on aerodynamic performance of small Vertical-Axis wind turbines. Cheng Kung University, Taiwan, 2012.

[19] M. Ahmadi-Baloutaki, R. Carriveau, D. S.-K. Ting. Performance of a vertical axis wind turbine in grid generated turbulence. Sustainable Energy Technologies and Assessments 11, 2015. [http://dx.doi.org/10.1016/j.seta.2014.12.007]

[20] A. Carbó Molina, G. Bartoli, T. De Troyer. Wind tunnel testing of small Vertical-Axis Wind Turbines in turbulent flows. X International Conference on Structural Dynamics, EURODYN. Rome, Italy, 2017. [DOI: 10.1016/j.proeng.2017.09.518]

[21] A. Carbó Molina, G. Bartoli, T. De Troyer. Generation of uniform turbulence profiles in the wind tunnel for urban VAWT testing. Wind Energy Exploitation in Urban Environment. TUrbWind 2017 Colloquium (to be published).

[22] H.Y. Peng, H. F. Lam. Turbulence effects on the wake characteristics and aerodynamic performance of a straight-bladed vertical axis wind turbine by wind tunnel tests and large eddy simulations. Energy 109, 2016. [http://dx.doi.org/10.1016/j.energy.2016.04.100]

[23] A. Laneville. Effects of turbulence on wind induced vibrations of bluff cylinders (Ph.D. thesis). University of British Columbia, Vancouver, Canada. 1973.

[24] P. E. Roach. The generation of nearly isotropic turbulence by means of grids. International Journal of Heat and Fluid Flow 8 (2), 1982.

[25] P. W. Bearman, T. Morel. Effect of free stream turbulence on the flow around bluff bodies. Progress in Aerospace Sciences 20(2), 1983.

[26] Q. Li, T. Maeda, Y. Kamada, J. Murata, M. Yamamoto, T. Ogasawara, K. Shimizu, T. Kogaki. Study on power performance for straight-bladed vertical axis wind turbine by field and wind tunnel test. Renewable Energy 90, 2016. [http://dx.doi.org/10.1016/j.renene.2016.01.002]

[27] G. Brochier, P. Fraunie, and C. Beguier, I. Paraschivoiu. Water Channel Experiments of Dynamic Stall on Darrieus Wind Turbine Blades. Journal of Propulsion and Power, Vol. 2, No. 5, 1986. [https://doi.org/10.2514/3.22927]

[28] G. Tescione, D. Ragni, C. He, C.J. Simão Ferreira, G.J.W. van Bussel. Near wake flow analysis of a vertical axis wind turbine by stereoscopic particle image velocimetry. Renewable Energy 70, 2014. [http://dx.doi.org/10.1016/j.renene.2014.02.042]

[29] X. Amandolèse, E. Széchényi. Experimental Study of the Effect of Turbulence on a Section Model Blade Oscillating in Stall. Wind Energ. 7, 2004. [DOI: 10.1002/we.137]

[30] J.O. Dabiri. Potential order-of-magnitude enhancement of wind farm power density via counterrotating vertical-axis wind turbine arrays, J. Renew. Sust. Energy 3, 043104, 2011. [doi:10.1063/1.3608170]

Paper TS6.1.4

THE INTERNATIONAL CONFERENCE ON
WIND ENERGY HARVESTING 2018
21-23 March 2018
Catanzaro, Italy

COMPARISON OF HYDRODYNAMIC LOADING MODELS FOR SLENDER OWT MONOPILES IN STEEP REGULAR WAVES

Agota Mockutė[1]*, Enzo Marino[1], Claudio Lugni[2] and Claudio Borri[1]

[1]Department of Civil and Environmental Engineering, University of Florence, Italy
[2]CNR-INSEAN – Maritime Research Institute - National Research Council, Italy
Corresponding author: Agota Mockutė, amockute@dicea.unifi.it

ABSTRACT

Monopile offshore wind turbines are susceptible to hazardous dynamic responses due to high nonlinearities in waves, accounting for which in the design process could contribute to driving the cost of technology down. Dangerous nonlinear phenomena seen on monopile-supported offshore structures in rough seas are not yet fully understood and are not captured by the methods commonly implemented in the industry. Therefore a comparison study is conducted on slender monopiles in very steep regular waves using fully nonlinear wave kinematics as input for three hydrodynamic loading models: Morison equation, slender-body theory and finite-depth FNV theory, comparing them to past experimental results. A fixed cylinder is analysed in various wave conditions and some discrepancies are found between all the analytical models and the experimental results available in the literature.

1. INTRODUCTION

To generate more energy per turbine, the size of offshore wind turbines keeps growing, now aiming for 8-12 MW rated capacity and reaching over 200 m in height. Combined with the wave conditions at the shallow to intermediate waters where monopile-supported offshore wind turbines are normally installed, these gigantic structures become increasingly susceptible to the effects of strong wave nonlinearities, including ringing [1-2] – hazardous transient resonant vibrations which are observed as non-Gaussian amplification of the dynamic response of slender structures, normally associated with third or higher order loading components. Ringing phenomenon is still not fully understood, but was repeatedly shown to be omitted by linear or weakly nonlinear wave theories [3-7]. From the first experiments aimed at understanding ringing, secondary load cycle has been observed on fixed cylinders in steep waves, and was immediately associated with ringing [1-2]. Just as ringing, secondary load cycle is a very nonlinear phenomena, observed as a second peak in the loading, around one quarter of the period after the main. At first this phenomena has been associated with Froude number (e.g. [2]) or wave steepness (e.g. [1]), but mostly neglecting diffraction, and only recently it has been shown to be caused by flow separation and disassociated from ringing [15-16]. As the support structure is one of the most expensive parts of offshore wind technology, better understanding and more accurate modelling of wave loads could lead to more cost-efficient designs. Therefore a comparison study of hydrodynamic loading models is being conducted, using fully nonlinear wave kinematics as input to three hydrodynamic loading models: the simplest and most commonly implemented Morison equation, slender-body theory which suggests corrections to Morison inertia term, and Faltinsen-Newman-Vinje (FNV) perturbation theory, which considers wave diffraction and directly takes third order loading components into account. This paper reviews the findings on a fixed monopile, which allows to observe the behaviour of the compared hydrodynamic loading models without the influence of cylinder motion, and where secondary load cycle is experimentally observed.

2. METHODOLOGY

The fully nonlinear wave kinematics are modelled by a potential-flow based quadratic boundary element method (BEM) model initiated by Rienecker-Fenton theory [8] for strongly nonlinear regular waves. The domain is bounded by impregnable bottom, vertical boundaries with periodic Neumann conditions and free surface with fully nonlinear dynamic and kinematic boundary conditions, stepped in time by 4th order Runge-Kutta algorithm.

The first hydrodynamic loading model in the comparison is Morison equation [9], consisting of linear inertia term '*M*' and quadratic drag term '*d*', integrated to the instantaneous undisturbed free water surface, as described by Equation 1 and illustrated on the left hand side of Figure 1.

$$F_{Mor} = \underbrace{\int_{-h}^{\eta} C_m \rho \pi R^2 \frac{\partial v_x}{\partial t} dz}_{M} + \underbrace{\int_{-h}^{\eta} C_d \rho R |v_x| v_x dz}_{d} \quad (1)$$

Where C_d, C_m – drag and inertia coefficients; η – instantaneous free surface elevation; R – cylinder radius; ρ – water density; g – gravitational constant; h – water depth; v_x – horizontal water particle velocity.

Second model is the slender-body theory by Rainey [9–10]. Following the formulation by Chaplin et al. [1], the slender-body terms which improve the Morison inertia term '*M*' are: axial divergence force '*A*' (Eq. 2), integrated along the length of the cylinder to the instantaneous undisturbed free water surface; and two point loads of surface intersection '*I*' (Eq. 3) and surface distortion '*D*' (Eq. 4), applied at the instantaneous free water surface, as illustrated on the left hand side of Figure 1.

Table 1. **Components of the slender-body theory, following [1].**

Axial divergence force	Surface intersection force	Surface distortion force
Integrated along the length to instantaneous water surface	Point load at instantaneous water surface	Point load at instantaneous water surface
$A = \int_{-h}^{\eta} \rho \pi R^2 \frac{\partial v_z}{\partial z} v_x dz$ (2)	$I = -\left(\rho \pi R^2 / 2\right) v_x^2 \, \partial \eta / \partial x$ (3)	$D = \left(\frac{7 \rho \pi R^2}{2g}\right) v_x^2 \frac{\partial v_x}{\partial t}$ (4)

Where v_z – horizontal water particle velocity.

The third loading model in the comparison is the FNV perturbation theory, directly taking into account the third-order loading components associated with ringing. The recent generalisation to finite depth by Kristiansen and Faltinsen [12] is implemented in this study. As illustrated on the right hand side of Figure 1, it consists of a horizontal inertial force integrated to the instantaneous free surface *F'* (Eq. 5) and an additional point load F^{ψ} (Eq. 6), satisfying the approximate nonlinear free-surface conditions, applied at the still water level in accordance with the original theory [13].

Table 2. **Components of the FNV theory, generalised for finite depth, following [12].**

F'	F^{ψ}
Integrated along the length to instantaneous water surface	Point load at still water level
$F' = \int_{-h}^{\eta} \left(\rho \pi R^2 \left(\frac{\partial v_x}{\partial t} + v_x \frac{\partial v_x}{\partial x} + v_z \frac{\partial v_x}{\partial z} \right) + a_{11} \left(\frac{\partial v_x}{\partial t} + v_z \frac{\partial v_x}{\partial z} \right) \right) dz$ (5)	$F^{\psi} = \left(\frac{4 \rho \pi R^2}{g} \right) v_x^2 \frac{\partial v_x}{\partial t}$ (6)

Where a_{11} is the 2D added mass coefficient.

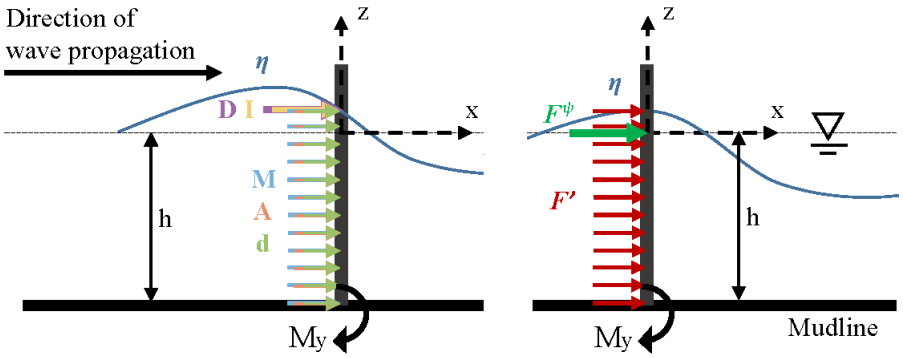

Figure 1. **Global coordinates and components of the three hydrodynamic loading models.**

3. DISCUSSION

The comparison study on a fixed rigid cylinder allows to assess the behaviour of different hydrodynamic loading models in numerically recreating wave forcing only, without the influence of body motion. A number of past experiments in a variety of wave conditions were recreated, and are each discussed in the following subsections.

3.1. Comparison with Chaplin et al. (1997)

Chaplin et al. (1997) [1] studied the response of a fixed and moving cylinder in very steep waves. Even though they started the experiments with regular waves, but due to the cylinder response lasting longer than the wave period, incoming waves disturbed the observation, therefore focused waves were used instead. In their study Chaplin et al. [1] compared the experimental results with numerical, modelled with 16th-order stream function for unsteady, and equivalent regular, wave kinematics and used Rainey corrections for hydrodynamic loading model. Comments were made on the behaviour of Morison equation too, even though no results were provided. Figure 2 shows the comparison between the experimental measurements by Chaplin et al. (1997) [1] on focused wave of steepness kA = 0.299, and the three compared hydrodynamic loading models based on fully nonlinear regular wave kinematics.

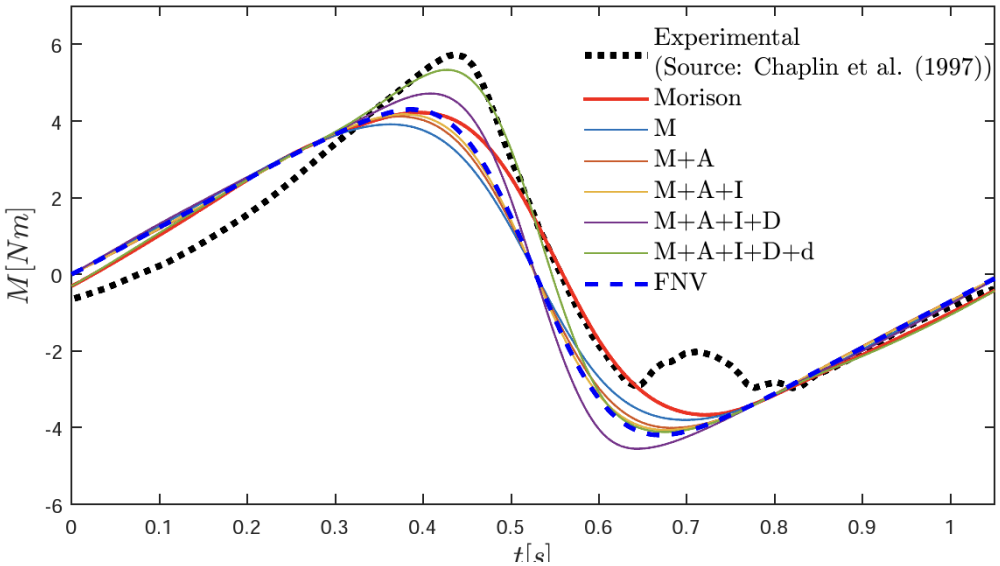

Figure 2. **Base bending moment. Steepness kA = 0.299, period τ = 1.05 s, on a fixed cylinder with diameter of 100 mm in depth of 0.525 m, measured experimentally by Chaplin et al. (1997) [1] in focused**

waves and modelled by Morison equation [9], its slender-body corrections [10-11] and FNV perturbation theory [12] with regular wave kinematics.

First of all it must be noted that the focused wave kinematics are significantly more severe than those of the corresponding regular wave, which was used in the numerical models in Figure 2, therefore the peak of loading is not expected to be recreated numerically. Validation was made by comparing the *M*, *M+A*, and *M+A+I* curves with the same ones computed by Chaplin et al. (1997) [1] with regular wave kinematics, which showed a good agreement. The *D* and *d* contributions were disregarded by [1], because when modelled with unsteady wave kinematics, which are more fitting for comparison with the focused experimental wave kinematics, they showed large discrepancies.

The secondary load cycle can be observed experimentally at time between approximately 0.6 and 0.85 seconds, but none of the models were able to capture it. The Morison equation and slender-body theory up to the combination of 'M+A+I' are both correct to second order, therefore cannot capture third order loading. The surface distortion force 'D', even though it corrects the Morison inertia term to third order, is considered inappropriate in this case because it is derived assuming small wave steepness [1] and can be seen to cause the largest deviation from the experimental values in the comparison. The FNV theory does directly take third order loads into account, therefore would have the potential to capture the nonlinearities in the force, unless they arise due to higher order forcing or mechanisms overlooked by the theory. Indeed, Kristiansen and Faltinsen [12] noted that largest discrepancies between experiments and the finite-depth FNV coincided with the observed events of flow separation, which the theory assumes negligible [12]. This observation goes along with the explanation of the secondary load cycle by wave diffraction [15-16]. With the current methods only 3D CFD solvers have successfully captured secondary load cycle numerically [12,15], but they are too complicated to be implemented in industry, therefore further work in this field is required. Nonetheless, it must be noted that it was recently suggested to disassociate secondary load cycle from ringing phenomenon [15-16], therefore not capturing the nonlinearities in the wave forcing might not necessarily lead to the omission of the amplifications in the dynamic response of the structure.

3.2. Comparison with Stansberg (1997)

Stansberg (1997) [14] conducted experiments in regular steep waves in various wave settings. For brevity only one case is presented and discussed here: Figure 3 shows one period of the normalized force from regular waves of steepness kA = 0.282, period τ = 1.52 s and amplitude of 0.162 m, measured by Stansberg [14] on cylinder of radius R = 100 mm in water depth of 10 m.

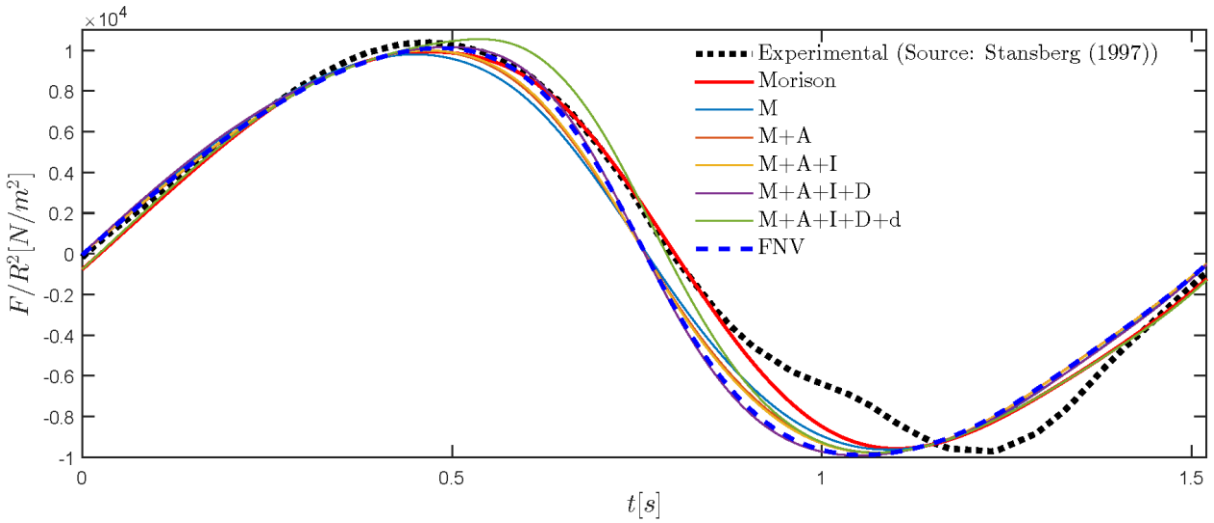

Figure 3. **Normalised horizontal force from regular waves of steepness *kA* = 0.282, period *τ* = 1.52 s and amplitude of 0.162 m, on a fixed cylinder with radius *R* = 100 mm, measured experimentally by Stansberg (1997) [14] and modelled by Morison equation [9], slender-body corrections [10-11] and FNV perturbation theory [12].**

First of all, the main trend and the peak loading was captured relatively well by all models, since the *M+A+I+D+d* curve is only added for comparison as in [1]. The Morison inertia term can be seen to underpredict the loading slightly, but when corrected by slender-body terms or the nonlinear terms of the FNV theory it can be seen to match the peak well. The full Morison equation can be seen to provide a good fit to the experimental curve as well, leading to believe that drag has a reasonable influence in these wave-cylinder conditions. Another aspect for drag consideration in this case is that a shift due to the drag component can be seen after the peak loading, at *t* between 0.6 and 0.8, where the curves including drag component, namely full Morison equation and *M+A+I+D+d*, match the experimental data better than inertia-only models.

The largest dispute between the experimental and numerical results still was observed at time *t* approximately between 0.8 and 1.4 s, where higher-order nonlinearities were observed but none of the models were able to capture them. The reasoning is expected to be the same as discussed in Subsection 3.1, just another curiosity can be observed that in this case the surface distortion component *D* is not causing such a drastic deviance as in Figure 2.

3.3. Comparison with Kristiansen and Faltinsen (2017)

Besides generalising the FNV theory for finite-depth, which is used in this study, Kristiansen and Faltinsen (2017) [12] also conducted experiments on a fixed cylinder in regular waves. These results were used to validate the FNV model implemented in this study by comparing it with the numerical results given in [12], and to assess the behaviour of the three hydrodynamic loading models in intermediate wave steepness (*kA* ranging between 0.05 and 0.16). The wave parameters were: water depth of 0.563 m, cylinder diameter of 0.144 m, wavenumber *kR* = 0.105, and various wave steepness settings, of which the smallest and the largest are shown in Figure 4, where H_1/λ = 1/60 (which approximates to around *kA* ≈ 0.05) and Figure 5, where H_1/λ = 1/60 (*kA* ≈ 0.16).

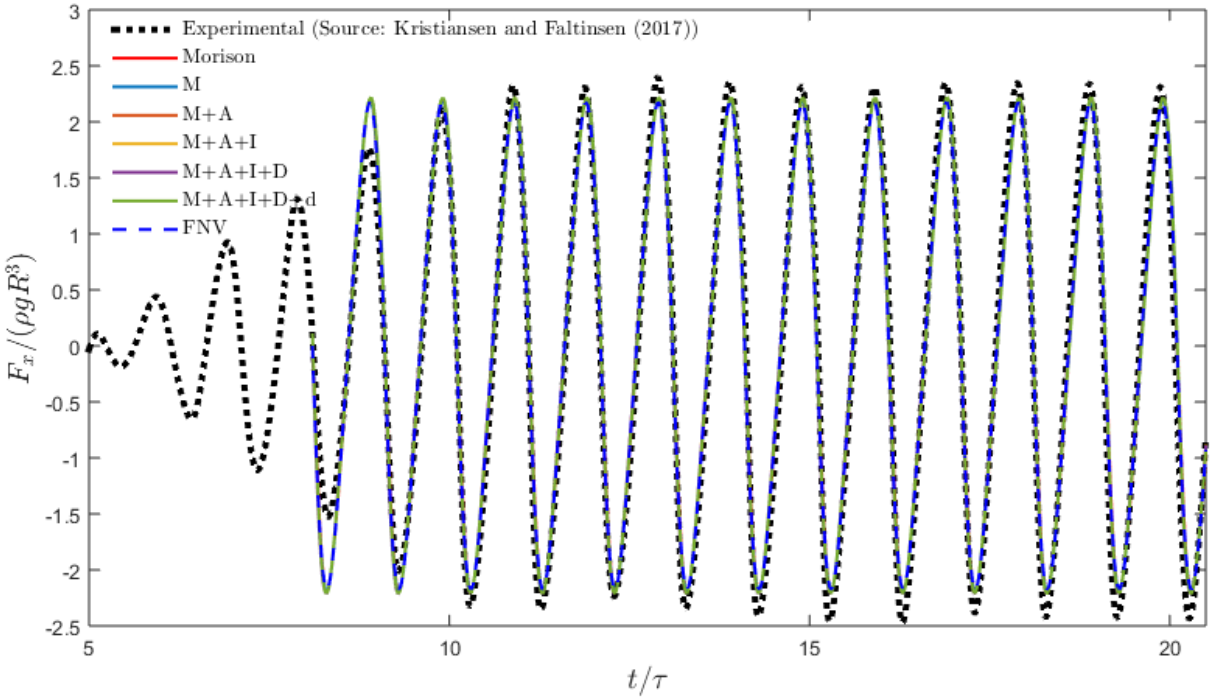

Figure 4. **Time series of horizontal force on a fixed cylinder in regular waves of steepness H_1/λ = 1/60. Comparison between experiments by Kristiansen and Faltinsen (2017) [12] and Morison equation [9], slender-body [10-11] and FNV [12] theories.**

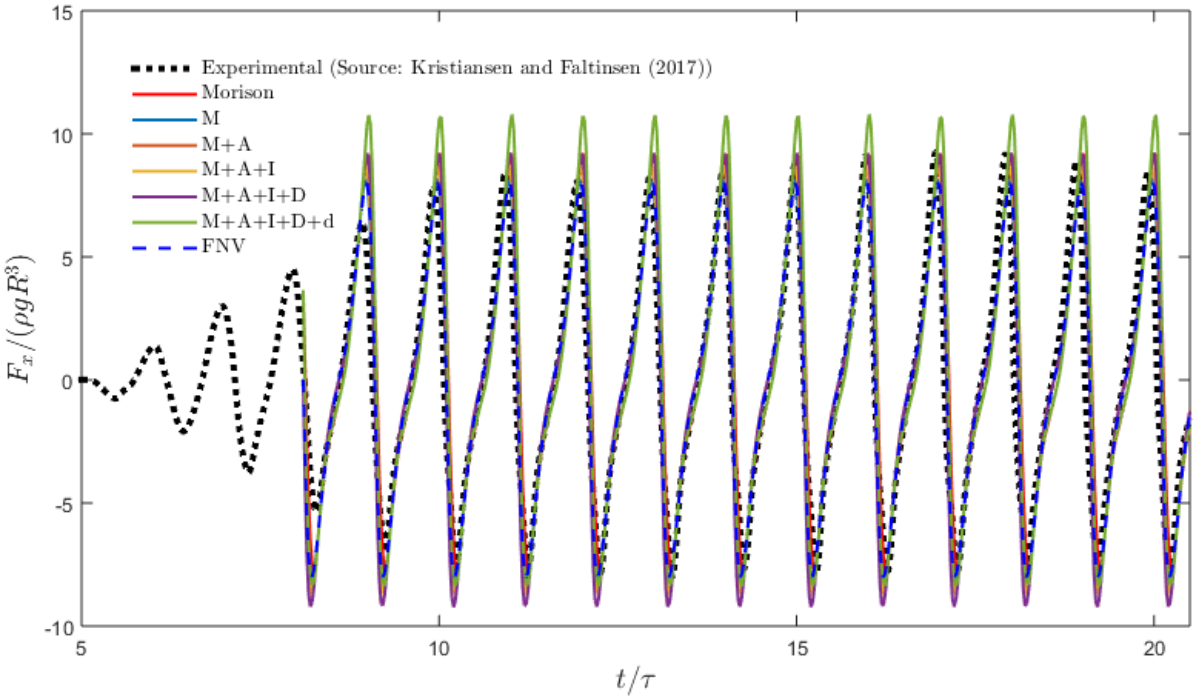

Figure 5. **Time series of horizontal force on a fixed cylinder in regular waves of steepness $H_1/\lambda = 1/20$. Comparison between experiments by Kristiansen and Faltinsen (2017) [12] and Morison equation [9], slender-body [10-11] and FNV [12] theories.**

In the smaller steepnesses all models behaved very similarly, no distinct differences could be seen, and all tended towards underprediction when compared to the experimental data. As the steepness increased the differences between models became more pronounced with Morison inertia *M* and FNV providing the most conservative results, while the slender-body theory and full Morison equation showed higher peaks. In the higher steepnesses it is hard to assess the models because the experimental peaks are not very steady, therefore for the smallest peaks the Morison inertia *M* and FNV theory show best match, while in the highest peaks - Rainey corrections or full Morison equation.

Moreover, in the comparison with Kristiansen and Faltinsen [12] no shift due to drag component is observed as it was in Figures 2 and 3, and it can be seen by the deviation of the *M+A+I+D+d* curve at the peaks in Figure 5, that additional consideration of drag for the slender-body theory (after the other corrections to the Morison inertia term) is not favourable, even though the full Morison equation (where drag term is applied together with inertia term *M* only) is behaving very similarly to the slender-body theory.

Presumably due to intermediate steepness the FNV theory stayed very similar to Morison inertia term (*M*) throughout the increase of the wave steepness, as the nonlinear terms were relatively small. Nonetheless it is interesting to observa that the nonlinear terms in the FNV theory were correcting it to lower values, compared to inertial only, instead of towards increase as was previously seen in Figures 2 and 3.

3.4. Comparison with Grue and Huseby (2002)

Grue and Huseby (2002) studied secondary load cycle and have conducted experiments in regular and irregular waves. Figure 6 shows the comparison between Grue and Huseby (2002) [2] experiments and the loading simulated with three hydrodynamic loading models in very steep (kA = 0.32) waves with period of 0.86 s, on a cylinder of 3 cm radius in water depth of 0.6 m. It should be noted that in the original paper steepness was defined as $k\eta_{max}$ = 0.34, which matched the highest peak and shallowest trough and was corrected to kA=0.32 to match the mean instead for a more meaningful comparison.

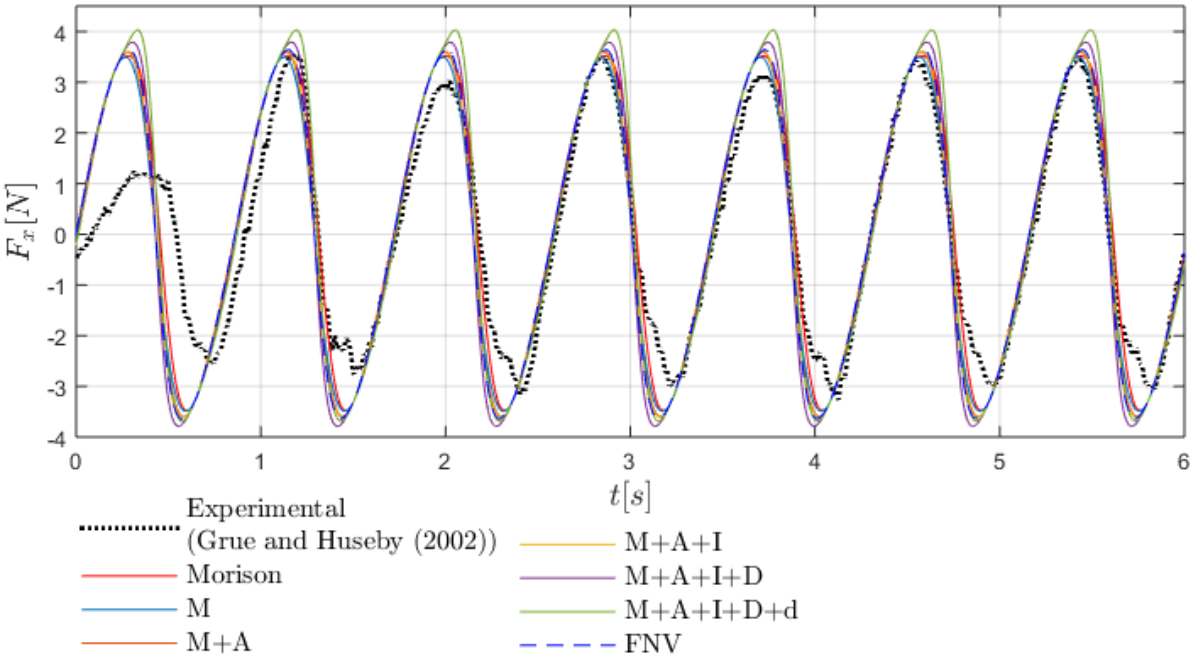

Figure 6. Time series of horizontal force on a fixed cylinder in regular waves of steepness kA = 0.32, with period of 0.86 s. Comparison between experiments by Grue and Huseby (2002) [2] and Morison equation [9], slender-body [10-11] and FNV [12] theories.

Even though the experimental peaks are rather unsteady, the general observed trend in these two cases for all models is towards overestimation, in contrary to the comparison with Kristiansen and Faltinsen (2017) seen in Subsection 3.3. Thus the model observed closest to the experimental data is the Morison inertia term (*M*), matching some of the highest experimental peaks. Interestingly, the nonlinear terms in the FNV theory deviate it from the Morison inertia term (*M*) towards the higher side in this case, increasing the prediction of peaks significantly. Slender-body theory corrects the Morison inertia term to the higher side as well, showing similar results as FNV when only *A* and *I* corrections are applied, and even larger deviation with the *D* term. This leaves full Morison equation as the closest model to inertia only, implying that drag contribution is not outstanding in these wave-cylinder conditions. Finally, the strong nonlinearities in the troughs are not captured by any of the models, as already seen in Chaplin et al. (1997) and Stansberg (1997). Potential explanation for the discrepancies could be such high wave steepness, where the small amplitude assumption and perturbation theories lose validity.

4. CONCLUSIONS AND FURTHER STUDIES

A hydrodynamic loading model comparison study is conducted for slender cylinders in very steep waves. Three hydrodynamic loading models are compared: Morison equation, slender-body theory, and finite-depth FNV perturbation theory; all using fully nonlinear wave kinematics as input. Experiments dedicated to studying ringing phenomenon were recreated and compared to, where fixed rigid cylinders were analysed in regular waves. None of the three compared loading models were able to capture the nonlinearities observed experimentally, implying the significance of three-dimensional effects or effects of higher order than third. No definite conclusions can be drawn on a recommended model for the severe wave conditions, however the findings indicate a clear need for continuing this study. Further stages are foreseen to also consider cylinder motion, irregular waves and modelling of an operating offshore wind turbine for full dynamic response. This research project is expected to contribute to better understanding of the nonlinear phenomena such as ‘ringing’ and secondary load cycle, and to lead to more accurate loading computations for more efficient future designs of offshore wind turbines.

ACKNOWLEDGEMENTS

This work was funded by the European Commission's Framework Program "Horizon 2020", through the Marie Skłodowska-Curie Innovative Training Network (ITN) "AEOLUS4FUTURE - Efficient harvesting of the wind energy" (H2020-MSCA-ITN-2014: Grant agreement no. 643167). Furthermore, the COST TU1304 action WINERCOST is gratefully acknowledged.

REFERENCES

[1] J. R. Chaplin, R. C. T. Rainey, and R. W. Yemm, "Ringing of a vertical cylinder in waves," *J. Fluid Mech.*, vol. 350, pp. 119–147, 1997.

[2] J. Grue and M. Huseby, "Higher harmonic wave forces and ringing of vertical cylinders," *Appl. Ocean Res.*, vol. 24, no. 4, pp. 203–214, 2002.

[3] E. Marino, C. Lugni, and C. Borri, "The role of the nonlinear wave kinematics on the global responses of an OWT in parked and operating conditions," *J. Wind Eng. Ind. Aerodyn.*, vol. 123, pp. 363–376, 2013.

[4] E. Marino, H. Nguyen, C. Lugni, L. Manuel, and C. Borri, "Irregular Nonlinear Wave Simulation and Associated Loads on Offshore Wind Turbines," *J. Offshore Mech. Arct. Eng.*, vol. 137, no. 2, p. 21901, 2015.

[5] S. Schløer, H. Bredmose, and H. B. Bingham, "The influence of fully nonlinear wave forces on aero-hydro-elastic calculations of monopile wind turbines," *Mar. Struct.*, vol. 50, pp. 162–188, 2016.

[6] A. N. Robertson, F. Wendt, J. M. Jonkman, W. Popko, H. Bredmose, F. Schlütter, J. Qvist, R. Bergua, A. Yde, T. Anders, J. Bernardus, D. Vaal, P. Bozonnet, L. Bouy, C. Barrera, R. Guanche, E. E. Bachynski, Y. Tu, I. Bayati, F. Borisade, H. Shin, T. Van Der Zee, and M. Guerinel, "OC5 Project Phase Ib : Validation of Hydrodynamic Loading on a Fixed , Flexible Cylinder for Offshore Wind Applications," *Energy Procedia*, vol. 94, no. January, pp. 82–101, 2016.

[7] E. Marino, A. Giusti, and L. Manuel, "Offshore wind turbine fatigue loads: The influence of alternative wave modeling for different turbulent and mean winds," *Renew. Energy*, vol. 102, pp. 157–169, 2017.

[8] M. M. Rienecker and J. D. Fenton, "A Fourier approximation method for steady water waves," *J. Fluid Mech.*, vol. 104, pp. 119–137, 1981.

[9] J. R. Morison, M. P. O'Brien, J. W. Johnson, and S. A. Schaaf, "The Force Exerted by Surface Waves on Piles," *Pet. Trans. AIME*, vol. 189, pp. 149–154, 1950.

[10] R. C. T. Rainey, "A new equation for calculating wave loads on offshore structures," *J. Fluid Mech.*, vol. 204, pp. 295–324, 1989.

[11] R. C. T. Rainey, "Slender-body expressions for the wave load on offshore structures," *Proc. Math. Phys. Sci.*, vol. 450, no. 1939, pp. 391–416, 1995.

[12] T. Kristiansen and O. M. Faltinsen, "Higher harmonic wave loads on a vertical cylinder in finite water depth," *J. Fluid Mech.*, p. 773-805, 2017.

[13] O. M. Faltinsen, J. N. Newman, and T. Vinje, "Nonlinear wave loads on a slender vertical cylinder," *J. Fluid Mech.*, vol. 289, pp. 179–198, 1995.

[14] C. T. Stansberg, "Comparing ringing loads from experiments with cylinder of different diameters - an experimental study," *BOSS '97 Behaviour of offshore structures*, vol. 2. pp. 95–109, 1997.

[15] B. T. Paulsen, H. Bredmose, H. B. Bingham, and N. G. Jacobsen, "Forcing of a bottom-mounted circular cylinder by steep regular water waves at finite depth," *J. Fluid Mech.*, vol. 755, pp. 1–34, 2014.

[16] L. Suja-Thauvin, J. R. Krokstad, E. E. Bachynski, and E.-J. de Ridder, "Experimental results of a multimode monopile offshore wind turbine support structure subjected to steep and breaking irregular waves," *Ocean Eng.*, vol. 146, pp. 339–351, 2017

AUTHORS' LIST

WINERCOST'18 & Aeolus future

"Wind Energy Harvesting...
(...focusing on exploitation of the Mediterranean Area)"

Catanzaro, Italy
21-23 March 2018

INARSVILUPPO
Centro Studi Italiano
per lo Sviluppo delle Professioni

cost
EUROPEAN COOPERATION
IN SCIENCE AND TECHNOLOGY

UNIVERSITÀ DEGLI STUDI FIRENZE

UNIVERSITY OF BIRMINGHAM

Comune di CATANZARO

COMUNE DI CIRO'
CITTA' DEL VINO E DEL CALENDARIO

ORDINEARCHITETTICATANZARO
ordine architetti pianificatori paesaggisti conservatori provincia di Catanzaro

CRIACIV

iLStudio.
Engineering & Consulting Studio

Sponsored by

GRUPPO MAZZEI 1962 50 2012